The University Of Sheffield.

Nikolaos Galanakis

Development and application of topological methods to characterise radiation damage effects in borosilicate and iron phosphate glasses

A thesis submitted in partial fulfilment of the requirements for the degree of Doctor of Philosophy

The University of Sheffield
Faculty of Engineering
Department of Materials Science and Engineering

June 1, 2019

Acknowledgments

I would especially like to express my gratitude to my research advisor, Dr. Karl P. Travis for his superb guidance and support which proved extremely helpful over the course of my PhD study and related research. His guidance was crucial on how to conduct professional research and assisted my development form a graduate student to a researcher.

Special thanks to my collaborators, Dr. Kenny Jolley and Professor Roger Smith at Loughbourough University for sharing their ideas and structures that were necessary to complete this work.

My sincere thanks also goes to Professor John Harding, Professor Karl Whittle, Dr. Colin Freeman and Dr. Amy Gandy for the insightful comments and suggestions that led me to widen the perspectives of my research.

Furthermore I would like to thank EPSRC and the University of Sheffield for providing funding to complete my research work.

I also feel the need to thank many other people, who guided and assisted me through the course of my studies and mostly Associate Professor Panagiota-Eleftheria Christopoulou for the unconditional and continuous support, from my days as an undergraduate student until today.

Last but not least, I feel the need to say *"Thank you!"* to my wife, Panagiota Papaspiliou. You are the reason for achieving it.

Abstract

The immobilization of high level nuclear waste is a very important aspect of the nuclear industry. In general, it is necessary to stabilise high level nuclear waste into a form that will retain its integrity for extended periods of time. The resulting wasteforms must be able to retain their durability and integrity for the timescale for which the incorporated radioactive elements emit radiation. This time scale extends to thousands of years and it is not possible to establish the long-term reliability of the new wasteforms only by experimental methods. Computational simulations of the wasteforms have the ability to provide detailed information regarding the structural changes in the wasteform due to the creation of an radiation damage at short timescales that can be used along with experimental approaches to predict the long term behaviour of the wasteforms. Traditional methods used to analyse radiation damage effects in computer models of glass wasteforms are based on the Wigner-Seitz method which ignores the properties of specific bonds and the number of broken bonds associated with the displacement of a particle from its initial position. Thus, it is necessary to develop novel computational methods to characterise the radiation damage effects with increased accuracy.

Work presented in this thesis, outlines the development of new topological based approaches to the characterisation of radiation damage effects in computer models of recoil damaged borosilicate and iron phosphate glasses. This method utilises a modified set of the well known Steinhardt order parameters and introduces a new set of distance-dependent order parameters, referred to as Hermite order parameters. The methods were developed using zircon crystal as a test structure, to establish the accuracy of the new approach, and then applied to the irradiated borosilicate and iron phosphate glass models to determine the behaviour of the glasses under irradiation. Additional structural analysis of the simulated structures was performed using primitive ring statistics.

The results of the analysis show that one of the topological methods proposed in this work succeeds in providing new insights regarding the effects of radiation damage in terms of bond defects. The simulated structures show significant tolerance to irradiation. For the borosilicate glass models, the Steinhardt and Hermite order parameters based methods suggest that the silica network is almost completely recovered, in contrast with the predictions of the Wigner-Seitz method, according to which a significant number of silicon particles are permanently damaged. Additionally it is found that the majority of the damage is due to broken B-O bonds. For the iron phosphate glasses the topological analysis suggest that only a small percentage of P-O bonds are affected by the creation of the damage cascade. Using the Steinhardt order parameters method it is also revealed that a radiation damage event affects the geometry of the SiO_4 and PO_4 tetrahedra in the borosilicae and iron phosphate glass models respectively, by creating variations in the values of O-Si-O, O-P-O angles and Si-O, P-O bond lengths. Primitive ring statistics analysis in the borosilicate glass models reveal that the creation of a radiation damage cascade favours the formation of higher order primitive rings. However, the distribution of the ring sizes in the

recovered structures is very close to the one of the undamaged glass models, suggesting a strong recovery of the network of the glasses. An attempt to perform a primitive ring statistics analysis in the iron phosphate glasses failed to provide any results, as no primitive rings were detected in line with existing models for the structure of phosphate glasses.

Contents

List of Figures

List of Tables

List of Abbreviations

ABWR	Advanced Boiling Water Reactor
AGR	Advanced Gas-Cooled Reactor
BEIS	UK Department of Business, Energy and Industrial Strategy
BO	Bridging Oxygen
BWR	Boiling Water Reactor
CGN	China General Nuclear
EPR	Evolutionary Power Reactor
FBR	Fast Neutron Reactor
GDF	Geological Disposal Facility
HLW	High Level Wastes
ILW	Intermediate Low Level Wastes
LEU	Low-Enriched Uranium
LLWR	Low Level Waste Repository
LLW	Low Level Wastes
LWGR	Light Water Graphite Reactor
MOX	Mixed Oxide
NBO	Non-Bridging Oxygen
NDA	National Decommissioning Authority
NWF	Network Former
NWM	Network Modifiers
PHWR	Pressurised Heavy Water Reactor
PWR	Pressurised Water Reactor
RWM	Radioactive Waste Management
SWU	Separate Work UNIT

SW Separate Work

THORP Thermal Oxide Reprocessing Plant

VLLW Very Low Level Wastes

Introduction

The immobilization of high level nuclear waste is a very important aspect of the nuclear industry. In general, it is necessary to stabilise high level nuclear waste into a form that will retain its integrity for extended periods of time. Currently, the preferred method for achieving that is vitrification. During the vitrification process, the nuclear waste is calcined, to evaporate the water and de-nitrate the radioactive fission products, and then fed into a furnace with fragmented glass. This melt is poured into stainless steel containers and when it is cooled, it vitrifies into a glass in which the radioactive elements are bonded within the glass matrix. These wasteforms are highly resistant to water and so they show good durability to corrosion. However, high level nuclear waste remains radioactive for thousands of years and so it is not possible to establish the long-term reliability of the new wasteforms only by experimental methods. For a successful study of radiation damage effects it is necessary to extract detailed information regarding the structural changes in the waste form, both at the surface and in the bulk. Consequently it is important to have a better understanding regarding the dynamics of the radiation damage process, to be able to predict the behaviour of the wasteform at large time scales.

Existing research on both borosilicate and iron phosphate glass wasteforms is mainly experimental, focusing on the structure of the glasses. The effects of radiation damage are examined from the perspective of the changes to the physical and chemical properties of the glasses due to alpha decay. To retrieve dynamic information for the material the better option is to use computational molecular dynamics simulations. For the borosilicate glasses, several molecular dynamics simulation studies exist that study the radiation damage effects. For the iron phosphate glasses on the other hand, computational simulations of radiation damage are extremely limited. The DREAM II project is a part of an EPSRC-India link, led by Professor Roger Smith of the University of Loughborough. The UK team is formed by scientific teams from the Universities of Loughborough, Sheffield, Birmingham, Cambridge and Imperial College London while the India team involves scientists from Bhabha Atomic Research Centre and the Indhira Gandhi Centre of Atomistic Research. This consortium aims to develop computer models of the radiation induced structural changes due to alpha particles and recoil nuclei damage on the structure, and speciation of redox active elements in the immobilisation materials over long time scales. The main wasteforms to be investigated are the well known borosilicate glasses and iron phosphate glasses. Both computer models and experiments will contribute to make successful predictions regarding the best materials for long time structural integrity. The successful outcome of the DREAM II project will have a serious economic impact as the expected optimization of the actinide loading might lead to a new industrial manufacturing process.

The traditional methods used to describe radiation damage effects in glass wasteforms are based in the Wigner-Seitz method which counts the number of atoms displaced by a certain distance from their initial position. However, this is not a safe method to extract accurate information regarding

the extent of damage, as it ignores the properties of specific bonds and the number of broken bonds associated with the displacement of a particle from its initial position. Thus, the development of novel computational methods to characterise the radiation damage effects with increased accuracy appears to be necessary. To make a successful characterization of the radiation damage in glasses it is necessary to develop novel computational methods utilising topological measures.

The aim of this project is to develop a new topological approach towards the characterisation of $\alpha-$recoil cascades in glass wasteforms used for the immobilisation of High Level Waste. It is expected that the new method will contribute significantly in the understanding of the dynamic behaviour of borosilicate and iron phosphate glass wasteforms under self-irradiation and provide a strong basis for future molecular dynamics simulations, targeting the improvement of the proposed methods in order to correlate topological measurements with physical and probably chemical properties of the structures.

Structure of the thesis

The first chapter of this thesis is an introduction to nuclear power. It provides information regarding the nuclear fuel cycle and the types of nuclear reactors, starting from the physics of a nuclear reactor and nuclear fission, to the production of High Level Waste. This chapter also discus the generation of nuclear power and the High Level Waste management in the UK. Chapter 2 provides a literature review on the borosilicate and iron phosphate glass wasteforms used for the encapsulation of High Level Waste. It details the glassy state and the glass structure of oxide glasses, emphasizing the borosilicate and iron phosphate glasses, and also includes a description of the radiation damage process in glass wasteforms and how it affects various properties and the structure of the glasses.

Chapter 3 details Molecular Dynamics, starting from theoretical concepts of classical and statistical mechanics. Special attention is given to the integration methods and the force fields used to describe the interaction between atoms in atomistic simulations. At the end of the chapter there is also a survey of existing work on molecular dynamics simulations on glass wasteforms. Chapter 4 presents existing methods for the characterisation of defects - the Wigner-Seitz method and the primitive ring statistics. It also describes in depth the Steinhardt order parameters and introduces the Hermite order parameters, including a detailed discussion on how these parameters are affected by the coordination number and the distribution of particles within a system and what information they provide for simple cubic systems.

Before applying the topological defect characterization techniques to the model glasses, it is important to test them in a simple crystalline material such as zircon. Chapter 6 demonstrates the relevant work starting from the creation of a radiation damaged zircon crystal model using molecular dynamics. It then considers the characterization of the defects using the simple Wigner-Seitz defect counting method, Steinhardt order parameters and Hermite Order parameters. By comparing the results obtained with these three methods, the chapter discusses the superiority of the topological methods over the traditional defect counting and how Steinhardt and Hermite order parameters and Hermite Order parameters can be used to make an accurate estimation of bond defects in both crystalline and amorphous materials.

Chapters 6 and 7 discuss the main part of this research project: a topological analysis of the

radiation damage effects in borosilicate and iron phosphate glasses. In detail, chapter 6 starts by presenting the methodology followed for the creation of irradiated models of two simplified borosilicate glasses, SBN12 and SBN14. Afterwards, the results obtained using defect counting, Steinhardt order parameters, Hermite Order parameters and primitive ring statistics methods are presented. Emphasis is given to the fact that each method can provide complementary information to others. Defect counting is useful to determine the displacement of the atoms due to the radiation damage event, Steinhardt order parameters and Hermite Order parameters can provide insights regarding the angular and radial distribution of atoms around reference particles and finally primitive ring statistics analysis is important to extract information regarding the connectivity of the network. In a similar manner, chapter 7 presents the methodology followed for the creation of three different iron phosphate glass models, provided from our collaborators at Loughborough University, Dr. Kenny Jolley and Professor Roger Smith and a comprehensive topological analysis of the three structures.

Chapter 1

Nuclear power generation

1.1 Introduction

Nuclear power is the process in which nuclear reactions are exploited to produce energy, which generates heat used for the production of electricity in nuclear power plants. In general, the nuclear reactions take place within a nuclear reactor. The heat generated by the reactions, is used to produce steam that drives a steam turbine connected to an electricity generator.

Nuclear power contributes significantly towards the generation of electricity. As of August 2018, there are 445 nuclear reactors in operation worldwide, with a combined capacity of 339.3 GW. There are also 55 reactors under construction that will increase the global capacity by 55.9 GW (Fig. 1.1). In 2017 nuclear power supplied 2487.98 TWh of electricity for commercial use, equivalent to the 10% of the global electricity production [1].

Despite the fact the amounts of greenhouse gases emitted by nuclear power plants are comparable or even lower than those from renewable sources, there is a continuous debate regarding if nuclear power generation is an environmental friendly process or not. The main criticism is due to the radioactive waste containing nuclear fission products that is discharged and deposited to the environment. These products include radioactive isotopes of several elements, such as ^{131}I, ^{90}Sr, ^{137}Cs and ^{99}Tc, with half-life varying between days and million years, that can pose a serious threat to the health of living organisms. One of the main areas of interest in the nuclear power industry, is the management of the radioactive waste and the development of wasteforms, to prevent them from becoming hazardous for the biosphere.

1.2 Nuclear reactor physics

In general, nuclear reactions are exothermic and have the ability to produce huge amounts of energy in the form of heat. Currently, nuclear energy is mainly generated from the nuclear fission of actinides. Actinides are a group of 15 slightly to highly radioactive metallic elements with atomic number $89 \leq Z \leq 103$. Most actinides, due to their moderate and high radioactivity, can produce a large variety of product nuclei, following one of the four existing α decay chains, depending on the mass number A.

- **Thorium decay series**, containing elements with $A = 4n$, $n \in \mathbb{Z}^+$.

$$^{228}\text{Th} \longrightarrow \cdots \longrightarrow {}^{208}\text{Pb} + 42.6 \text{ Mev} \tag{1.1}$$

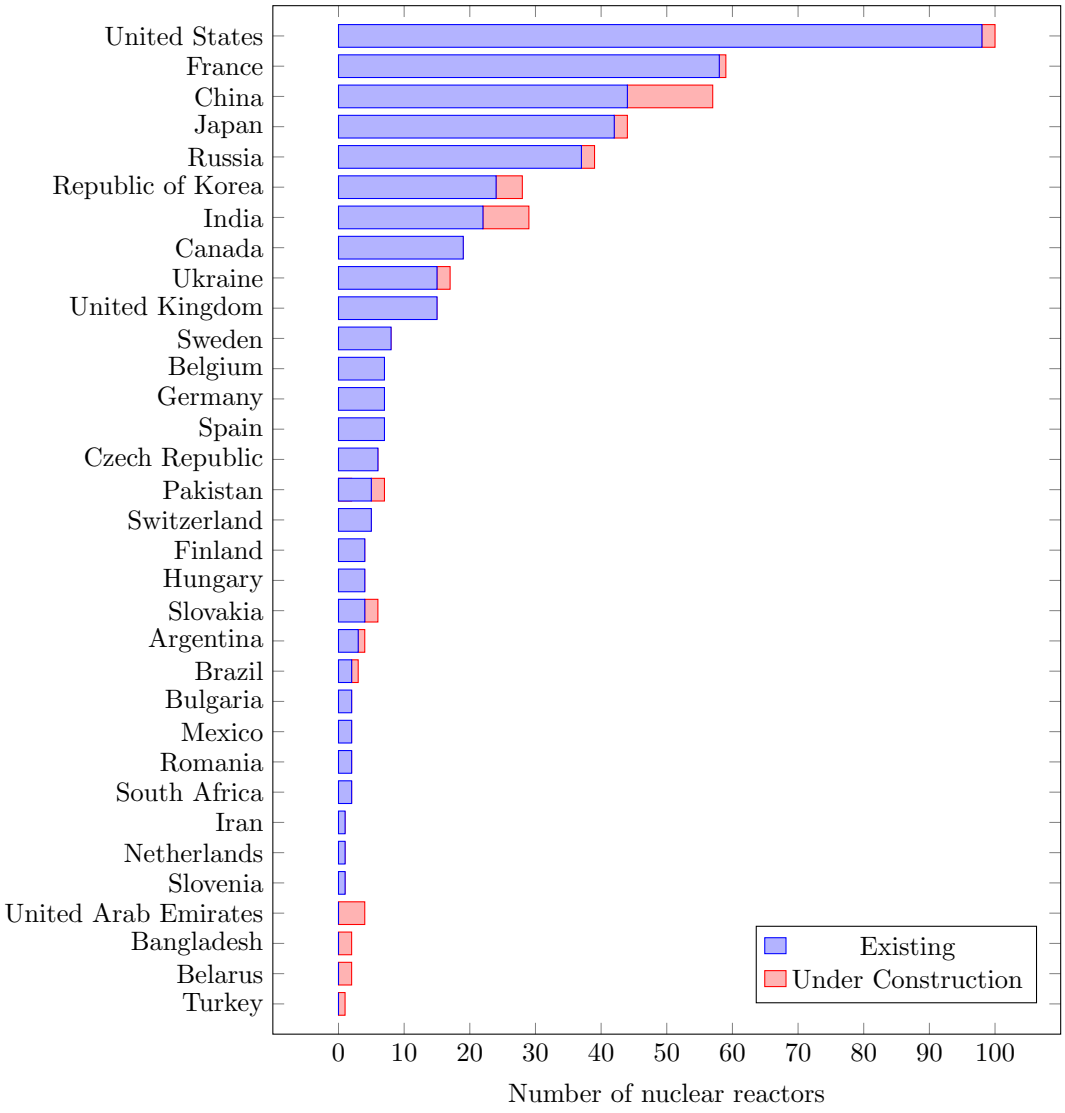

Figure 1.1: The number of existing nuclear reactors as of August 2018 and reactors under construction per country [1].

- **Neptunium decay series**, containing elements with $A = 4n + 1$.

$$^{237}\text{Np} \longrightarrow \cdots \longrightarrow {}^{205}\text{Tl} + 66.8 \text{ Mev} \tag{1.2}$$

- **Uranium decay series**, containing elements with $A = 4n + 2$.

$$^{238}\text{U} \longrightarrow \cdots \longrightarrow {}^{206}\text{Pb} + 51.7 \text{ Mev} \tag{1.3}$$

- **Actinium decay series**, containing elements with $A = 4n + 3$.

$$^{235}\text{U} \longrightarrow \cdots \longrightarrow {}^{207}\text{Pb} + 46.4 \text{ Mev} \tag{1.4}$$

Natural decay processes have the ability to produce significant amounts of energy. However in nuclear reactors the energy is produced following the more efficient nuclear fission reactions.

1.2.1 Nuclear fission

Nuclear fission is a nuclear reaction in which a mother nucleus is bombarded by a neutron and splits in two lighter daughter nuclei. The products of a nuclear fission reaction may also include neutrons and energetic photons in the form of gamma rays. The nuclear fission process is shown in Fig. 1.2. Nuclei that release neutrons during the fission reaction, such as ^{235}U, ^{233}U and ^{239}Pu, have the ability to create a nuclear fission chain reaction, since the released neutrons can trigger consecutive fission reactions that in turn release huge amounts of energy. In general, the energy released by a nuclear fission reaction is significantly higher than the energy released during a natural decay chain. In nuclear reactors, the energy is generated by the fission of ^{235}U. Following the reaction

$$^{235}_{92}\mathrm{U} + ^{1}_{0}\mathrm{n} \longrightarrow ^{141}_{56}\mathrm{Ba} + ^{92}_{36}\mathrm{Kr} + 3\,^{1}_{0}\mathrm{n} + 202.5\ \mathrm{MeV}, \tag{1.5}$$

just 1 kg of ^{235}U - corresponding to about 1400 kg of natural uranium - has the ability to produce 83.15 TJ of energy. By comparison, 1 kg of coal produces just 30.79 MJ. The above, is the most energetic fission reaction of ^{235}U, but it is not the only one. From a statistical perspective, the fission of ^{235}U can be described by

$$^{235}_{92}\mathrm{U} + ^{1}_{0}\mathrm{n} \longrightarrow \text{Fission fragments} + 2.4\,^{1}_{0}\mathrm{n} + 192\ \mathrm{MeV}, \tag{1.6}$$

which shows the average values of the neutron products and the energy produced. In any case, the above equations demonstrate the extremely high efficiency of the nuclear fission process.

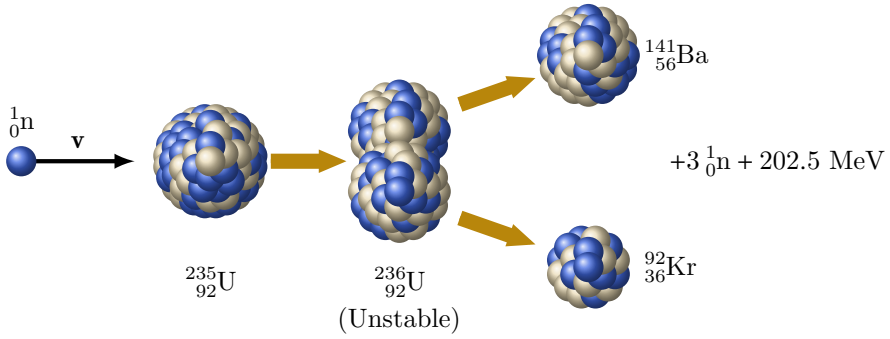

Figure 1.2: Illustration of the fission reaction described by Eq. 1.5. The mother $^{235}_{92}$U nucleus is bombarded by a neutron and converted to the excited and unstable $^{236}_{92}$U. The latter then splits into two lighter nuclei and releases 3 neutrons and a significant amount of energy in the form of gamma photons.

1.2.2 Nuclear fission products

Each nuclear fission reaction of a specific radioactive nucleus, may give a different set of daughter nuclei. However, the products of a nuclear fission reaction follow a statistical pattern that allows

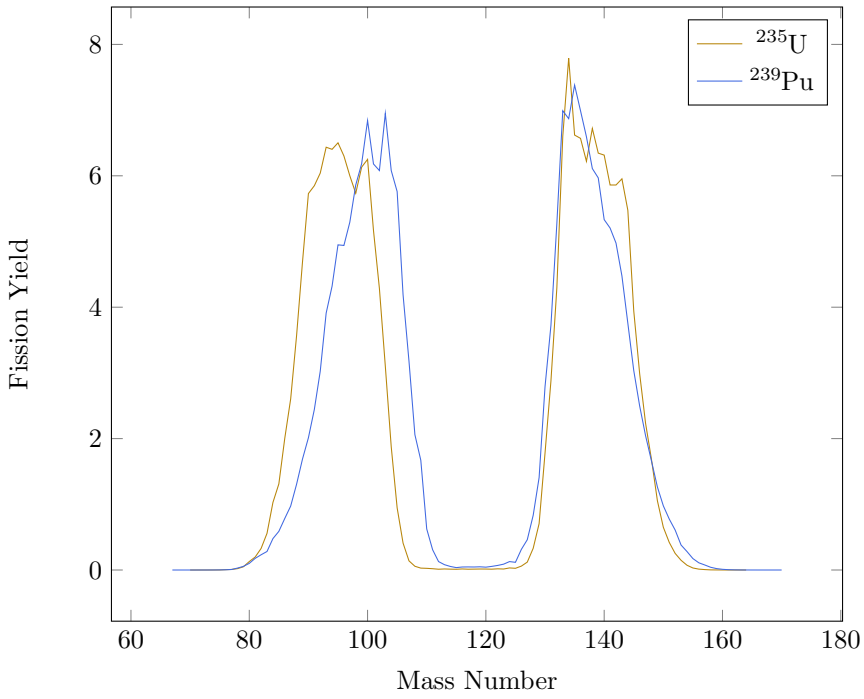

Figure 1.3: The nuclear fission product yields for the chain reactions of the thermal neutron fission of ^{235}U and ^{239}Pu, as a function of the mass of the daughter nuclei [2].

us to calculate the probability of a specific set of products. The fraction of each daughter nucleus per parent nucleus is called yield. Since each parent nuclei produces two different daughter nuclei, the sum of all product yields is equal to 200%. In general, the products of a nuclear fission reaction depend both on the parent nucleus and the energy of the incident neutron. As a rule of thumb, the mass difference of the two daughter nuclei decreases with the energy state of the nucleus and/or incident neutron. In Fig. 1.3, the fission yields for the chain reactions of the thermal neutron fission of ^{235}U and ^{239}Pu are shown, where it is clear that the valley between the two peaks for ^{235}U is wider than that for ^{239}Pu, as a result of the lower energy state of ^{235}U.

1.2.3 Criticality and control rods

The fission reaction shown in Fig. 1.2, releases three neutrons, which means that each ^{235}U nucleus that is bombarded by a neutron can in turn initialize 3 fission reactions. This chain reaction can propagate exponentially and produce uncontrolled amounts of energy. Due to the nature of nuclear fission chain reactions, the population of neutrons at a given time is a function of the rate of neutron production R_p, the rate of neutron absorption R_a and the rate of neutron leakage R_l. When $R_p = R_a + R_l$, the rate of neutron production is equal to the sum of the rates of neutron absorption and the rate of neutron leakage, the reactor's operation is referred to as critical. On the other hand, when $R_p > R_a + R_l$, the production of neutrons is higher than the losses and the operation of the reactor is referred to as supercritical and the energy production increases with time. Finally, when $R_p < R_a + R_l$, the neutron losses are higher than the production rate, and the reactor operates at a subcritical level and the production of energy declines with time. The

number of neutrons N as a function of time is given by the differential equation

$$\frac{dN}{dt} = \frac{\alpha}{\tau}N, \tag{1.7}$$

where τ is the average life-time of a neutron and α is a constant given by

$$\alpha = P_i P_f \bar{N} - P_a - P_e, \tag{1.8}$$

where P_i is the probability for a neutron to collide with a radioactive nucleus in the fuel, P_f the probability that a neutron collision with a nucleus in the fuel will trigger a fission reaction, P_a the probability that the neutron will be absorbed in the fuel before colliding with a radioactive nucleus, P_e the probability that the neutron will escape the core and $\bar{N}$ the average number of neutrons produced by a fission reaction in the fuel. For the operation of the reactor to remain at a critical level, the rate dN/dt and consequently α must be equal to zero. If $a < 0$ the number of neutrons is decreasing and the operation is subcritical, while if $a > 0$ the number of neutrons is increasing and the operation is supercritical [32].

In nuclear reactors, the number of fission neutrons must be controlled in order to produce energy at a desired and safe rate. Since the probability P_f of triggering a fission reaction depends on the fuel, to control the rate of neutron production, nuclear reactors are engineered in such a way to control the number of fission neutrons by adjusting P_a. This can be achieved by using control rods, that can absorb neutrons released by a nuclear fission reaction and prevent them from triggering further reactions. Control rods are usually made from materials such as boron, cadmium or hafnium, that exhibit high absorption cross section for thermal neutrons.

Another way to express criticality of a nuclear fission chain reaction is by using the multiplication factor k, which is equal to the ratio of number of neutrons in one generation to the number of neutrons in the preceding generation, and is given by the six-factor formula

$$k = \eta f p \epsilon P_{\mathrm{FNL}} P_{\mathrm{TNL}}, \tag{1.9}$$

where η is the thermal fission factor showing the number of fission neutrons produced per neutron absorption in the fuel material, f is the thermal utilisation factor which gives the probability of absorbing a neutron within the fuel material, p is the resonance escape probability, showing the fraction of fission neutrons that are slowed down to thermal energies without being absorbed, ϵ is the fast fusion factor, equal to the fraction of the number of fast neutron to the number of thermal neutrons produced by the fission reactions and finally P_{FNL} and P_{TNL} are the probabilities that a fast neutron and a thermal neutron will not leak out of the nuclear reactor. For $k = 1$, the operation of the reactor is critical, for $k > 1$ supercritical and for $k < 1$ subcritical [32].

1.2.4 Neutron moderators

The neutron moderators are used in thermal reactors to reduce the energy of fast neutrons generated during the fission reaction from several MeV to about 0.02 eV and convert them to thermal neutrons that have increased probability to trigger the additional fission reactions. The most effective moderators are materials with light atoms that have the ability to slow down the incident

neutrons by colliding with them without absorbing them. The most usual moderators include water (H_2O), heavy water (D_2O) and C in the form of graphite [33].

The nature and the amount of a moderator affects the controllability of a nuclear fission chain reaction. Since neutron moderators have the ability not only to slow down neutrons, but also to absorb them, the amount of the neutron moderator must be high enough to increase the probability P_f of triggering a nuclear fission reaction in the fuel, but also low enough to prevent a large number of neutrons from escaping and keep P_e term at an acceptable level. The effectiveness of a moderator is affected by temperature changes and is actually reduced with increase of the temperature. When the nuclear reactor core is overheated, the moderator temperature also increases and becomes less effective since the energy of the neutrons passing through the moderator is higher than the optimal thermal level and the reactor operates at a subcritical level, making the reactor inherently safe: the reactivity of the reactor is controlled without affecting the structure of the core and as a consequence the probability of a meltdown is decreased [33].

1.3 Nuclear fuel cycle

The Nuclear Fuel Cycle (Fig. 1.4) is the sum of activities related to the production of electricity from fission reactions. The nuclear fuel cycle can be subdivided into three major stages: the front end involving the preparation of the nuclear fuel, the service period in which the nuclear fuel is used for the production of electricity, and the back end in which the spent nuclear fuel is either disposed of or reprocessed to start a new nuclear fuel cycle. Nuclear fuel cycles in which spent fuel is not reprocessed are known as open cycles while those in which the fuel is reprocessed are called closed cycles.

1.3.1 Front end

Uranium mining and milling

The first step of the front end of the nuclear fuel cycle is to extract uranium ore, using both excavation and in-situ techniques. Traditional excavation methods recover uranium either through an open pit - when the uranium deposit is relatively close to the surface in depths less than $\sim$ 120 m, or directly from the underground. In-situ techniques use oxygenated groundwater that is circulated through a porous deposit of natural uranium, to dissolve the uranium oxide (UO_2) and make it emerge to the surface. In 2017, the majority of uranium was extracted in three countries: Kazakhstan (39%), Canada (22%) and Australia (10%), with the remaining 10 countries extracting about 29% of world production, as shown in Fig. 1.5.

This then undergoes a milling process in which the ore is ground and uranium is separated from the waste rock to produce a type of uranium concentrate powder, known as yellowcake, containing about 80% uranium oxide (U_3O_8), which is significantly higher than the $\simeq$ 0.1% of uranium in the extracted ore [34, 35].

Uranium enrichment

Natural uranium primarily consists of ^{238}U (99.28 w%) while the amount of fissile ^{235}U accounts only for 0.71 w% - the rest 0.01 w% is mainly ^{234}U. For most types of reactors, this amount of

^{235}U is not adequate to sustain a nuclear fission chain reaction and consequently the concentration of the fissile ^{235}U must be increased to between 3.5% and 5%, depending on the reactor. This can be achieved with a process known as isotope separation. However, isotope separation requires uranium in a gaseous form. In conversion facilities, the uranium oxide mixture is initially refined into uranium dioxide UO_2. The conversion of the uranium oxide mixture to UO_2 can by achieved

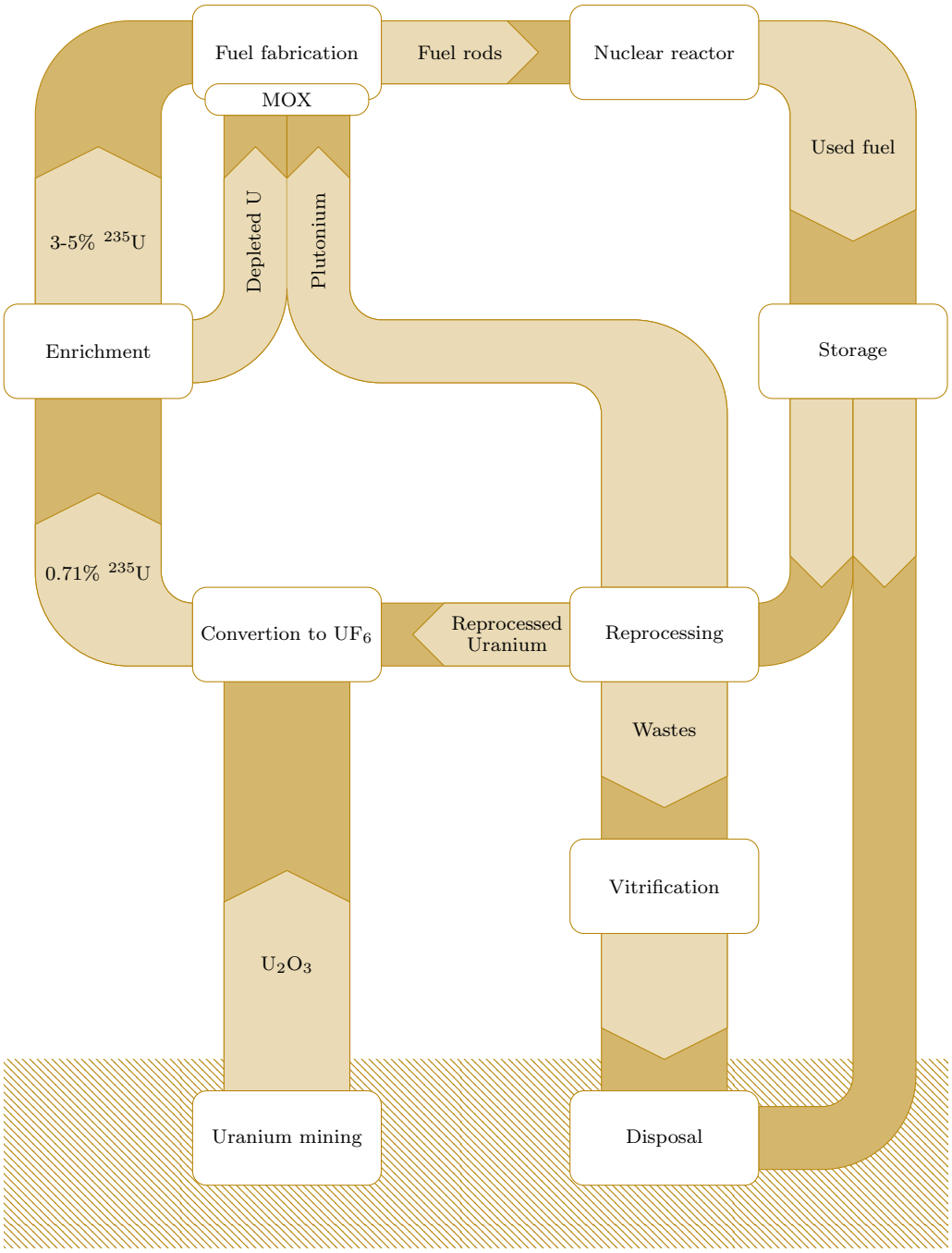

Figure 1.4: Schematic diagram of the nuclear fuel cycle [35].

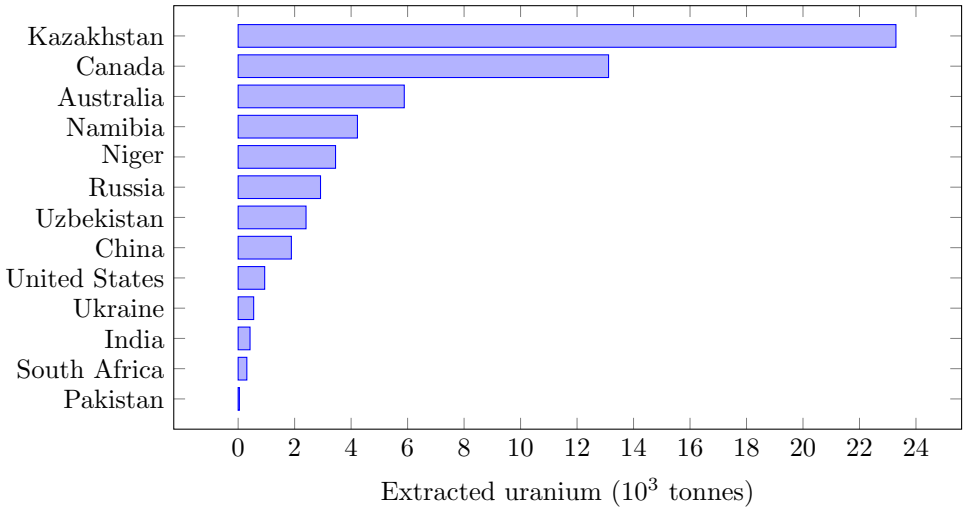

Figure 1.5: The production of uranium in tonnes in 2017 [3].

using two different methods, the dry, that produces U_3O_8 or the wet which gives UO_3, following the reactions

$$U_3O_8 + 2\,H_2 \longrightarrow 3\,UO_2 + 2\,H_2O - 109\ \text{kJ/mole}, \tag{1.10}$$

or

$$UO_3 + H_2 \longrightarrow UO_2 + H_2O - 109\ \text{kJ/mole}, \tag{1.11}$$

that can be used directly in graphite-moderated and heavy-water reactors. Most of the UO_2 is converted into uranium hexafluoride UF_6 using the two step process

$$UO_2 + 4\,HF \longrightarrow UF_4 + 2\,H_2O - 176\ \text{kJ/mole}, \tag{1.12}$$

and

$$UF_4 + F_2 \longrightarrow UF_6, \tag{1.13}$$

which is in a gaseous form at the relatively low temperature of 57 °C. The UF_6 is then cooled into a liquid form that is drained into 14-tonne cylinders and solidifies into a solid form [34, 35, 36].

During the enrichment process, gaseous UF_6 is separated into two streams. The important stream contains the low-enriched uranium and the secondary, containing up to 96% of the byproduct of the process is gradually depleted in ^{235}U that can be used in a series of other applications. The enrichment of the uranium can be accomplished following three different processes: gaseous diffusion, gas centrifuge and laser separation. The final product in the main stream is enriched UF_6 that is reconverted into UO_2 ready to be used in a fuel fabrication facility [34, 35].

In the UK, the gas centrifuge method is used. To separate the ^{235}U and ^{238}U isotopes, the UF_6 gas is fed into several cylindrical vacuum tubes. Each of these tubes contains a rotor 20 cm in diameter and between 3 and 5 m tall, that spins rapidly, between 50×10^3 and 70×10^3 rpm. This process moves the heavier ^{238}U nuclei towards the outer parts of the tubes, while the lighter ^{235}U nuclei accumulate near the centre. A temperature gradient between the top and bottom of

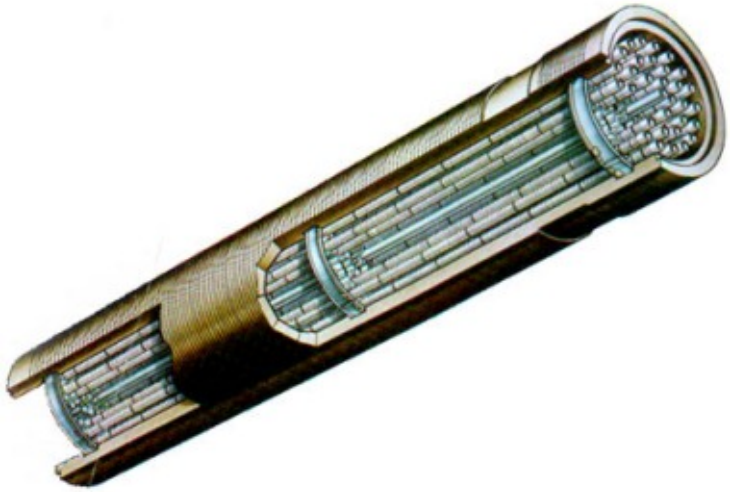

Figure 1.6: Cutaway of a fuel assembly used in the Advanced Gas-Cooled Reactors [4].

the tubes creates a convention current that moves the ^{235}U nuclei to the top of the tubes, where it is collected, while the ^{238}U nuclei are moved to the bottom. The enriched gas can be used directly as feed for the next stages of the nuclear cycle, while the depleted UF_6 goes back to the previous stage [37].

Fuel fabrication

The enriched UF_6 resulted from the previous stage, is converted to UO_2 powder which is sintered in the form of ceramic pellets at a temperature above 1400 °C. These pellets are then ground to become uniform in size and stacked into cylindrical tubes of metal alloy specially designed to have a high resistance to corrosion to create the fuel rods [35]. The size of the rods is defined by the specifications of the specific nuclear reactor core but it is usually 10-15 *mm* long and 8-15 *mm* in diameter [38]. The fuel rods are finally grouped in assemblies that form the nuclear fuel core of the nuclear reactor.

In the Advanced Gas-Cooled Reactors used in the UK (Section 1.4.1), the fuel assembly is a circular array consisting of 36 fuel rods, as shown in Fig. 1.6. Each of these rods contains 20 fuel pellets of uranium, enriched to about 3.5%. The fuel rods clad are made of stainless steel that offers higher operating temperatures. Each reactor contains 8 assemblies, stacked end on end through the top of the nuclear reactor [4].

1.3.2 Service period

A nuclear reactor requires several hundred fuel rods to operate - for an electricity output of 1000 MW the core needs to be loaded with 75 tonnes of low-enriched uranium. Once the fuel is loaded a controlled fission process is initiated. The fission of ^{235}U nuclei produces large amounts of heat, used to boil water and produce steam at high pressure. This steam, is directed to a turbine that sets in motion a generator that produces electricity [35]. During the ^{235}U chain reaction, a fraction of ^{238}U of the core absorbs neutrons emitted from the decay of ^{235}U and decays to plutonium.

About 50% of this plutonium is also fissioned, contributing about 30% or more of the reactor's electricity output [34, 35].

The full fuel load has a service period of 3 to 6 years (5 years for the Advanced Gas-Cooled Reactors used in the UK [4]), depending on the size and the production power of the reactor. To ensure the continuous functionality of the reactor, over a period of about one year to 18 months, known as a cycle, the 25-30% of the fuel is removed from the core and replaced with new fuel [35, 38].

1.3.3 Back end

Spent fuel

The amount of fissile ^{235}U in the fuel rods declines over time and after 18-36 months, the nuclear fuel contains about 1% of ^{235}U. At the same time, the nuclear fission reactions produce 1% plutonium with 0.6% of the fissile isotope ^{239}Pu, 3% fission products and minor actinides and the rest 95% is in the form of ^{238}U. The main fission products are presented in Table 1.1. When the fuel is removed from the reactor, the fission products will emit significant amounts of radiation and heat. In order to reduce the levels of radiation and heat, immediately after removal from the reactor, the fuel is submerged in water ponds located next to the nuclear reactor. The water within the ponds absorbs both the radiation and heat which causes the temperature of the water to increase. To maintain the temperature of the water at an acceptable level, it is circulated to external heat exchangers. This way, the spent fuel rods can remain in the ponds for months or even years [35]. In the final stage, spent fuel is either reprocessed to recycle the portion that is usable or it can be prepared for long-term storage and final disposal without any reprocessing.

Table 1.1: The characteristics of the different fission products of nuclear fuel cycle [39].

	Isotope	**Half-life (y)**	**Yield (%)**	**Q (keV)**	**Radiation type**
Medium-lived	^{155}Eu	4.76	0.0803	252	β, γ
	^{85}Kr	10.76	0.2180	687	β, γ
	^{113m}Cd	14.1	0.0008	316	β
	^{90}Sr	28.9	4.505	2826	β
	^{137}Cs	30.23	6.337	1176	β, γ
	^{121m}Sn	43.9	0.00005	390	β, γ
	^{151}Sm	96.6	0.5314	77	β
	Isotope	**Half-life (My)**	**Yield (%)**	**Q (keV)**	**Radiation type**
Long-lived	^{99}Tc	0.211	6.1385	294	β
	^{126}Sn	0.230	0.1084	4050	β, γ
	^{79}Se	0.327	0.0447	151	β
	^{93}Zr	1.53	5.4575	91	β, γ
	^{135}Cs	2.3	6.9110	269	β
	^{107}Pd	6.5	1.2499	33	β
	^{129}I	15.7	0.8410	194	β, γ

Reprocessing of spent fuel

The main scope of the reprocessing of spent fuel is to separate the uranium and plutonium from the fission products and the cladding of the fuel rods. For this the fuel rods are chopped and dissolved in acid to separate the materials comprising the fuel rod. This way, the uranium and plutonium can be recycled to create new fuel while the remaining 3% of the spent fuel is the radioactive waste [40]. The treatment of the radioactive waste is presented in detail in Section 1.6.

Uranium and plutonium recycling

The uranium produced during the reprocessing of the spent fuel, contains about than 1% of fissile ^{235}U, which is about 40% higher than the percentage of ^{235}U in the natural uranium. Consequently, it can be used directly as a feed to the front end of the nuclear fuel cycle in order to be converted and enriched as discussed in the previous sections [35].

The concentration of the various plutonium isotopes however, depends strongly on the burn-up level of the original fuel in the core. In general, when the burn-up level is higher, most plutonium isotopes in the spent fuel are non-fissile and the concentration of the fissile ^{239}Pu is lower [40]. Usually, the spent fuel contains about 1% plutonium of which 0.5% and 0.15% are the fissile isotopes ^{239}Pu and ^{241}Pu respectively [41]. The majority of the separated plutonium can be used directly to produce Mixed Oxide (MOX), that acts as a substitute for the uranium oxide fuel [34, 35, 38, 41]. The standard process is to mix the recycled plutonium with depleted uranium produced during the enrichment phase. The generated MOX fuel contains both UO_2 and PuO_2 [41]. MOX fuel generated by mixing depleted uranium and recycled plutonium with concentration about 7-11%, is equivalent to enriched uranium with concentration of about 4.5% ^{235}U. In terms of power generation, MOX fuel generated from natural uranium and recycled plutonium is about 12% more efficient than natural uranium, while MOX fuel containing recycled plutonium and uranium is about 22% more efficient [41].

1.4 Nuclear reactor types

Currently, there is a variety of existing nuclear reactor types. The majority of existing nuclear reactors are improvements of the two types developed in the 1950s: the thermal reactors and the fast neutron reactors. The main component of a nuclear reactor is the nuclear reactor core which is actually the fuel of the reactor, surrounded by a neutron moderator (in the case of thermal reactors) and fitted with control rods.

Additional components of a nuclear reactor are the coolant, which is a fluid flowing in a circuit through the core to transfer the heat, the pressure vessel/tubes that contain the nuclear reactor core, the moderator and the coolant, the steam generator, used in the Pressurised Water Reactors and the Pressurised Heavy Water Reactors to generate the steam necessary to drive the turbine and finally the containment, a structure surrounding the reactor and associated with the steam generators, used to protect the surrounding environment from the effects of radiation in case of a malfunction of the nuclear reactor, and also to protect the reactor from outside intrusion [14]. Depending of the nature of the moderator and the coolant, nuclear reactors can be categorised as shown in Table 1.2.

Table 1.2: Existing nuclear reactor types as of August 2018 [14]

Reactor type	Main countries	Number	Fuel	Coolant	Moderator
Pressurised Water Reactor (PWR)	US, France, Japan Russia, China	299	Enriched UO_2	Water	Water
Boiling water Reactor (BWR)	US, Japan, Sweden	74	Enriched UO_2	Water	Water
Pressurised Heavy Water Reactor (PHWR)	Canada, India	49	Natural UO_2	Heavy Water	Heavy Water
Gas-Cooled Reactor (AGR & Magnox)	UK	14	Natural U Enriched UO_2	CO_2	Graphite
Light Water Graphite Reactor (LWGR)	Russia	15	Enriched UO_2	Water	Graphite
Fast Neutron Reactor (FBR)	Russia	3	PuO_2 & UO_2	Liquid Sodium	-

1.4.1 Thermal reactors

The majority of nuclear reactors use moderators in order to lower the kinetic energy of neutrons participating in a nuclear fission reaction and convert them to thermal neutrons with kinetic energy of about 0.025 eV, and consequently increase the probability for a successful fission reaction. These reactors are known as thermal reactors and they are able to use minerals with very low fissile isotope concentration. Additional categorisation of the thermal nuclear reactors is based on the nature of the moderator and the coolant.

Reactors using natural water as moderator, are known as light water reactors and are further categorized into Pressurised Water Reactors (Fig. 1.7a) and Boiling Water Reactors (Fig. 1.7b). The difference between the two types is that in a PWR the reactor heats pressurised water at a temperature above 300 °C, that then exchanges heat with a secondary lower pressure system of water, which generates the steam to drive the turbine, while in a BWR the steam is produced directly by the main water system, in which the water is heated at around 285 °C to produce the necessary steam. LWRs require fuel enriched in fissile isotopes. For those using uranium, which is the majority, it is required to enrich the element in order to contain 3-5% of the radioactive isotope ^{235}U. This is because the water moderator, apart from slowing down the neutrons, can also absorb a large number of them, and consequently the probability of creating and sustaining a nuclear fission chain reaction is reduced. The enrichment of the fuel is actually a countermeasure for the absorption of neutrons from the water moderator. As an alternative to the low-enriched uranium (LEU), LWR can also operate by using MOX fuels, consisting of plutonium mixed with depleted or natural uranium. These reactors are very useful as they utilise the excess of plutonium used for nuclear weapons.

An alternative to the LWR is the Pressurised Heavy Water Reactor (Fig. 1.7c), which operates in a similar way but has two main differences. It can use natural uranium oxide as fuel and consequently it is not necessary to perform the enrichment step, thus reducing the fuel preparation time and cost. On the other hand it requires heavy water to operate, the production cost of which is equivalent to the cost of uranium enrichment. In addition, the construction costs of a PHWR

are higher in comparison with the LWRs. The purpose of using heavy water is that in contrast with water, it absorbs neutrons at a much lower rate and consequently the probability of triggering a nuclear fission reaction in ^{235}U is high enough to sustain a nuclear fission chain reaction in the natural uranium fuel.

The Light Water Graphite Reactor that was developed in the former Soviet Union, is a cheaper alternative to the PHWR. The heat is generated in the main water system as in the BWRs but the moderator is made of carbon in the form of graphite. Carbon has a lower neutron absorption rate in comparison with water and consequently LWGR can operate by using low enriched UO_2 containing about 2% of fissile ^{235}U as a fuel.

Finally, the Gas-Cooled Reactors developed in the UK, use graphite as moderator and CO_2 as a coolant. The major advantage of this reactor type, is that it can use natural uranium as a fuel, avoiding the enrichment process. The Magnox reactors, was the first generation of nuclear reactors developed in the UK. They were designed with a dual purpose, to produce electricity and also ^{239}Pu to be used for nuclear weapons. Their name derives from the magnesium-aluminium used to clad the fuel rods within the core. This allow has the advantage of having a low neutron absorption cross-section. However it exhibits two major disadvantages. At high temperatures, magnox reactivity increases and the operational temperature of the reactor had to remain relatively low, at around 380 °C, thus limiting the efficiency of the reactor. Additionally the magnox alloy reacts with the water and this prevents the long term storage of the spent fuel in a water pool. These factors limited the economic performance of the design and led to the development of a new design, the Advanced Gas-Cooled Reactors (AGR) (Fig. 1.7d), which would make the power generation more profitable. The AGRs were designed to have a thermal efficiency of 41%, higher than the 34% offered by the LWRs. To achieve that, the AGRs had to run at considerably higher temperatures (650 °C) and for this, the magnox alloy cladding of the core was replaced with stainless steel. This however required the core to use enriched UO_2 as fuel. Although the enrichment process increased the operational costs of the AGRs, the overall economic performance was better than that of the Magnox reactors.

1.4.2 Fast neutron reactors

In contrast with thermal reactors, fast neutron reactors use fast neutrons with kinetic energy of about 1 MeV to initiate the fission of the nuclear fuel and instead of moderators, these reactors use coolants. Fast neutrons have very low probability to collide with a nuclei and initiate a fission reaction. Consequently, fast neutron reactors require highly enriched fuel, including more than 20% of fissile material. Additionally they are more difficult to build and expensive to operate in comparison with thermal reactors. However, all actinides in the nuclear fuel are involved in fission reactions [42] with fast neutrons and so they produce less transuranic radioactive waste.

1.5 Nuclear power in the UK

The United Kingdom was the first country in the world establishing a civilian nuclear programme. The first nuclear power station opened in 1956 at Calder Hall, Windscale. Between 1956 and 1971, 26 Magnox nuclear reactors were connected in the UK electricity grid, followed by 14 AGRs,

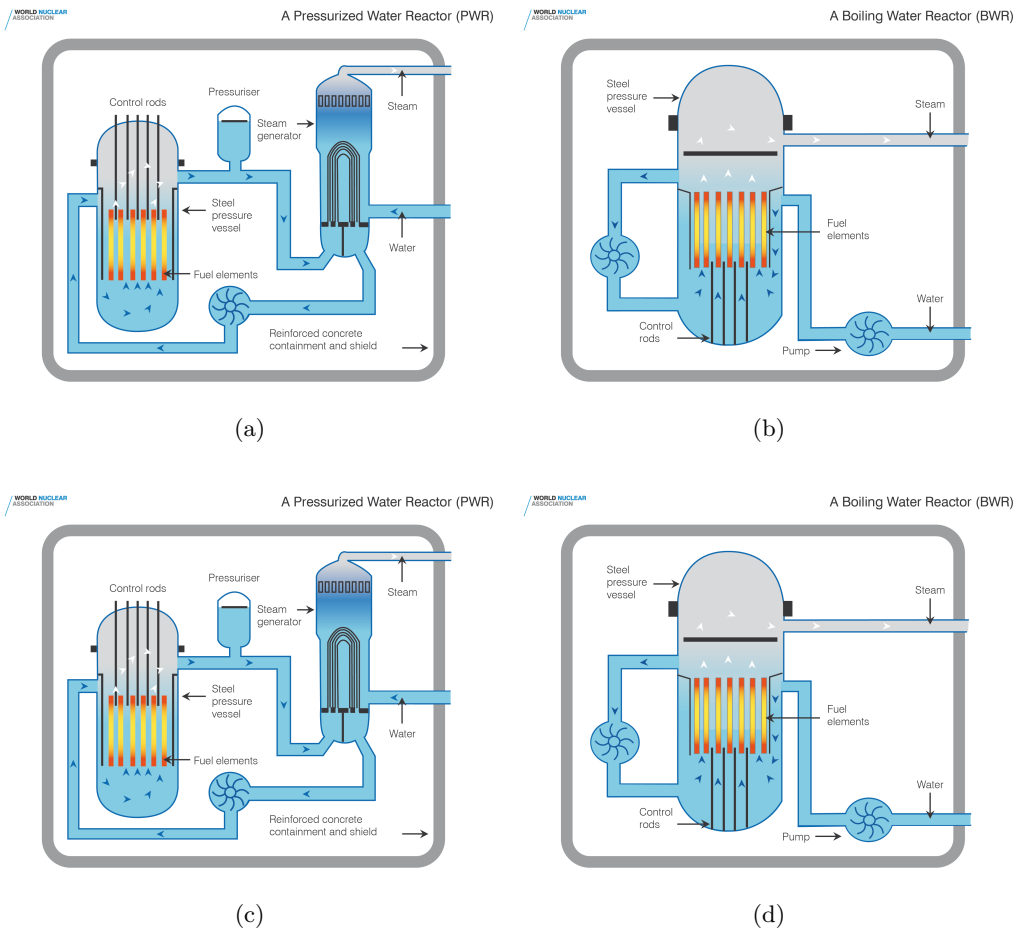

Figure 1.7: Diagrams of the main nuclear reactor types: (a) a Pressurised Water Reactor [5], (b) a Boiling Water Reactor [6], (c) a Pressurised Heavy water reactor [7] and (d) an Advanced Gas-Cooled Reactor [8].

between 1976 and 1988 and a single PWR in 1995. All Magnox reactors were gradually decommishioned between 1986 and 2015. The operation of the nuclear reactors contributes significantly in the electricity generation in the UK. In 1997, electricity produced by nuclear reactors accounted for the 26% of the total electricity production in the UK. However, due to the shutdown of the Magnox reactors this percentage declined and in 2018 it was around 21% [9].

As of August 2018, in the UK there are 14 graphite-moderated advanced gas-cooled reactors operating at Dungeness (2), Hinkley Point B (2), Hunterston B (2), Hartlepool (2), Heysham (2), Torness (2) and one PWR at Sizewell, producing in total 8.883 GW of electricity. Existing nuclear power plants, operated by EDF energy are planned to gradually shut-down by 2035. However, on March 2017, EDF energy started building two new, third generation PWRs, at Hinkley Point. China General Nuclear (CGN) company is also involved in this project and they also expressed their interest to build their own nuclear power plants at Bradwell in Essex and at Sizewell in Suffolk. Additionally there are plans from Horizon Nuclear Power for 4-6 new PWR and from NuGeneration for 3 new PWR at Sellafield [9]. In Table 1.3 a summary of the planned and proposed reactors in the UK are presented.

Table 1.3: Planned and proposed nuclear reactors in the UK [9].

Proponent	Site	Type	Capacity (MWe)	Comission
EDF Energy	Hinkley Point C1	EPR	1670	2026
	Hinkley Point C2	EPR	1670	2027
	Sizewell C1	EPR	1670	N/A
	Sizewell C2	EPR	1670	N/A
Horizon	Wylfa Newydd 1	ABWR	1380	2015
	Wylfa Newydd 2	ABWR	1380	2015
	Oldbury B1	ABWR	1380	Late 2020s
	Oldbury B2	ABWR	1380	Late 2020s
NuGeneration	Moorside 1	AP1000/APR1400	1135/1520	2025
	Moorside 2	AP1000/APR1400	1135/1520	2026
	Moorside 2	AP1000	1135	2027
China General Nuclear	Bradwell B1	Hualong One	1150	Proposed
	Bradwell B2	Hualong One	1150	Proposed

Notes: The EPR (Evolutionary Power Reactor) is a third generation Pressurised Water Reactor, developed in France by Areva and Germany by Siemens. The ABWR (Advanced Boiling Water Reactor) is a third generation Boiling Water Reactor developed in Japan by Toshiba. The AP1000 is an advanced Pressurised Water Reactor developed by Westinghouse Electricity Company. The APR1400 is an advanced Pressurised Water Reactor developed by the Korea Electric Power Corporation. The Hualong One is a Pressurised Water Reactor developed in China by China General Nuclear Power Group and the China National Nuclear Corporation.

1.5.1 The front end of the nuclear cycle in the UK

Since in the UK there are no sources of natural uranium, all the uranium that was used in the front end of the nuclear fuel cycle was imported. The conversion of UO_2 into UF_6 used to take place at a facility at Springfields, near Preston, operated by Westinghouse Electric Company, a group company of Toshiba Corporation, with a UF_6 production capacity of 6000 tonnes U per year. However, this facility was shut down at the end of August 2014 [9].

The enrichment process is assigned to Urenco, operating three centrifugal enrichment plants at Capenhurst with a capacity of 1.1×10^6 tonnes SWU[1] per year. Another Urenco enrichment facility is currently being built at Capenhurst, with a capacity of 7000 tonnes U per year and is expected to start commission by the end of 2018 [9].

A fuel fabrication facility for the AGRs and the future PWRs is located at Springfields, where a Magnox fuel fabrication facility was located, but was shut down in May 2008 [9].

1.5.2 The back end of the nuclear cycle in the UK

The reprocessing of spent nuclear fuel takes place at Sellafield by Sellafield Ltd. The reprocessing plant started operations in 1964 and has a capacity of 1500 tones/year. It is used to reprocess the spent fuel from the first generation Magnox reactors and it is planned to cease operations by 2020, when all the Magnox fuel will be reprocessed. A second reprocessing facility at Sellafield, known as Thermal Oxide Reprocessing Plant (THORP) is responsible for the reprocessing of oxide fuel from the Advanced Gas-Cooled Reactors overseas. This plant was commissioned in 1994 and is planned

[1]SWU stands for Separate Work Units (SWU). 1 SWU equals to 1 kg of Separate Work (SW) which is the effort necessary to separate the ^{235}U and ^{238}U isotopes [43].

to close by the end of 2018. The original capacity of THORP was for 1200 tonnes/year, but due to a leak incident in 2005, the capacity was reduced to 900 tonnes/year. A MOX reprocessing facility, the Sellafield MOX Plant operated between 2001 and 2011, with an original capacity of 120 tonnes/year which was decreased to 40 tonnes/year in 2005. This plant was not efficient in terms of production since the plant managed to produce only 8 tonnes of fuel. In 2010, the Nuclear Decommission Authority (NDA) reached an agreement with 10 Japanese utilities for the refurbishment of the facility, in order to export reprocessed MOX fuel to Japan. However, in August 2011, following the Fukushima accident, NDA reassessed the project and decided to close the facility [9].

1.6 Radioactive waste management in the UK

Despite the fact that the amount of radioactive wastes produced during the nuclear fuel cycle is very small when compared with the amount of the produced energy, the nuclear wastes may contain highly radioactive fission products that are extremely hazardous for the environment. As it makes sense, the wastes must be treated properly is order to minimize or even eliminate the impact in the surrounding biosphere. Radioactive wastes are produced in every step of the nuclear fuel cycle and also in other sectors involving radioactive materials, such as research, medicine, manufacturing, agriculture and mineral exploration. There are different types of wastes, each containing a variety of radioactive materials.

1.6.1 Types of radioactive waste

The classification of nuclear waste varies between countries. In the UK, radioactive wastes are classified depending on the types and the intensity of the emitted radiation and heat into four categories: Very Low Level Wastes (VLLW), Low Level Wastes (LLW), Intermediate Level Wastes (ILW) and High Level Wastes (HLW). The main characteristics of each type of radioactive waste are presented in Table 1.4.

Table 1.4: The characteristics of the different radioactive waste types [44, 10].

Waste	**Alpha**	**Beta**	**Heating**
Very Low Level Wastes (VLLW)	–	<4 MBq/t	No
Low Level Wastes (LLW)	<4 GBq/t	<12 GBq/t	No
Intermediate Level Wastes (ILW)	>4 GBq/t	>12 GBq/t	No
High Level Wastes (HLW)	>4 GBq/t	>12 GBq/t	Yes

The majority of the radioactive wastes in the UK, are products of the nuclear power development programme. Only a fraction of the total waste is produced during the nuclear fuel cycle [9]. In the UK, 57.02% of the total radioactive waste is characterised as VLLW, 33.54% is LLW, 9.41% is ILW and only 0.03% is HLW. In Fig. 1.8 an area chart of the relative percentages of each type is shown. It is predicted that by 2125, the total volume of the radioactive wastes in the UK will be 4.77×10^6 m^3 (Table 1.5). However, HLW are responsible for the majority of the radioactivity,

producing about 95% of the radiation, with the remaining 5% mainly produced by the ILW. The LLW and VLLW are only responsible for 0.00001% of the radioactivity [10].

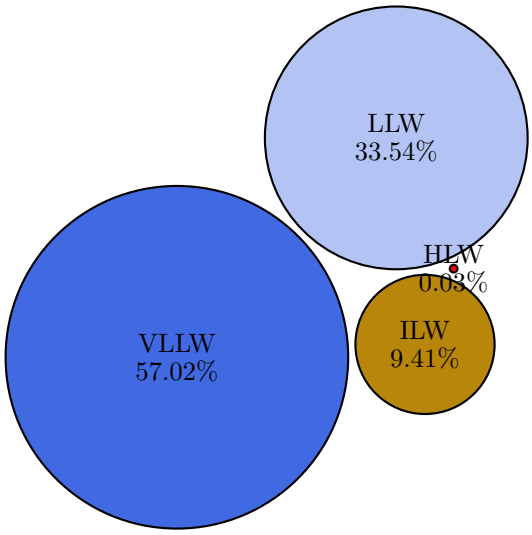

Figure 1.8: Area chart of the radioactive waste in UK by percentage [9].

Table 1.5: The forecast for the volume of the radioactive waste in the UK by 2125 [10].

Waste type	VLLW	LLW	ILW	HLW	**Total**
Volume (m^3)	2720000	1600000	449000	1500	4770500

Very Low Level Wastes

The Very Low Level Wastes, are actually a sub-category of the Low Level Wastes described in the following section and they include materials left over and byproducts of the uranium ore process as well as materials produced during demolishing or rehabilitation of nuclear industrial sites. They emit very low amounts of β radioactivity, less that 4 MBq per tonne, but they also contain heavy metals such as As and Pb that are chemical hazardous.

Low Level Wastes

Low Level Wastes contain radioactive elements emitting less than 4 GBq/tonne of α radiation and less than 12 GBq/tonne β radiation [44]. They include materials such as clothing, filters, papers and tools and they are mainly generated from industry and hospitals and also from the nuclear fuel cycle. Although they are more radioactive than uranium tailings, they are also characterized by a relatively low emission of radiation [44].

Intermediate Level Wastes

Includes contaminated materials from nuclear reactor decommissioning, nuclear fuel cladding, chemical sludge and resins. They contain higher amounts of radioactive nuclei in comparison

to uranium tailings and LLW, and require shielding to protect the environment. ILW emit more than 4 GBq/tonne of α radiation and more than 12 GBq/tonne of β radiation. However, the radioactive elements do not heat up the waste so no cooling is necessary [44]. They are usually disposed of by solidification in concrete canisters. Depending on the half-life of the encapsulated radioactive elements, ILW are either buried in shallow repositories or deposited in a geological repository facility [44].

High Level Wastes

High Level Wastes are mainly the product of spent fuel reprocessing and can be found in either raffinate form created during the nuclear reprocessing or in the form of vitrified HLW [45]. Additional HLW may be generated during the operation and decommissioning of nuclear reactors. Although they account for a small amount of the total volume of radioactive waste, HLW are responsible for 95% of the emitting radiation, since they contain all the fission products created during the nuclear fuel cycle as well as actinides. They are highly radioactive since they emit the same levels of α and β radiation as the ILW but they also have the ability to heat up, since the radioactivity produces energy greater than 2 kW/m^3. For this reason, the treatment of HLW require cooling and shielding operations [44].

1.6.2 Treatment and conditioning of radioactive waste

After a radioactive material is characterised as radioactive waste, it must be converted into a form that will be convenient for the subsequent transportation, storage and final disposal. For this the wastes must be treated properly to minimise the volume and then conditioned into an appropriate solid form that can be immobilised and prevent contamination of the biosphere. There are several processes that can be used for the treatment and conditioning of the radioactive wastes, depending on the type of the waste, the radioactivity of the material and the nuclear waste management policies of each country [46]. The most energetic LLW may require shielding to handle or transport but in general all LLW can be disposed of by burying them on land in shallow repositories [44]. Liquid LLW and ILW are solidified in cement, a process known as cementation, while HLW are calcined and then vitrified in a glass matrix, a process known as vitrification [44].

Vitrification

The immobilisation of HLW is based on vitrification (Fig. 1.9), a process in which the waste is transformed into a glass wasteform [11] that does not react or degrade for long periods of time [45]. Vitrified glasses show great resistance to corrosion, making them a favourite option for the immobilisation of HLW [47]. In the West, the main glass wasteforms are normally borosilicate glasses while in countries of the former Soviet Union, phosphate glasses are more common [48].

In the UK, the vitrification takes place at the Sellafield Waste Vitrification Plant. At the first stage of the vitrification process, the HLW liquor is transferred from the storage facility to the waste vitrification plant where it is then mixed with sugar, to enhance the de-nitration process and reduce as far as possible ruthenium volatilization. Afterwards the mix passes through a electrically-controlled rotary calciner, to dehydrate the waste and also partially de-nitrate the radioactive elements, producing a dry powder to increase the stability of the glass wasteform [49, 50]. The

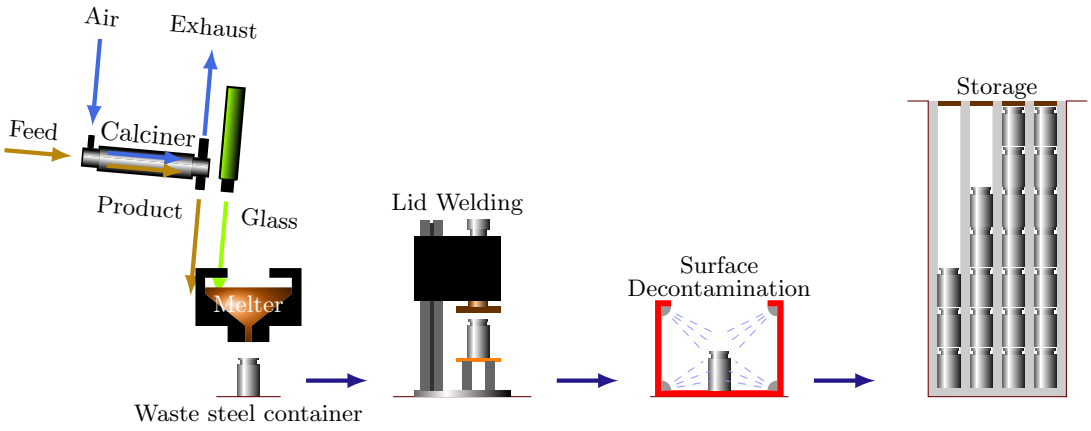

Figure 1.9: Illustration of a typical vitrification process.

calcined mix is then discharged by gravity along with a measured quantity of fragmented glass in an induction-heated melter and heated to a temperature of about 1050 °C. The calcine mix reacts with the melted glass, resulting in a homogeneous melt which is then poured periodically into steel containers. The product containers are allowed to cool for a period of at least 24 hours, which is sufficient for the product to solidify into a glass in which the radioactive waste elements are incorporated into the glass matrix. The cylinder canisters are then welded and decontaminated before being stored in the Vitrified Product Store, located at Sellafield.

1.6.3 Storage and disposal of radioactive waste

Radioactive waste may be stored at any stage of the management process, after being treated and conditioned appropriately. The main purpose of the storage is to maintain the radioactive waste accessible and at the same time isolate it from the environment and prevent any pollution [44]. HLW are stored for at least 50 years before disposal, to allow the radioactivity level to decrease. Spent nuclear fuel is usually stored under water for at least 5 years, until the amount of generated heat is reduced to an acceptable level, and then moved to a dry storage facility [51].

To manage the radioactive waste in a more sustainable way, a waste hierarchy has been established (Fig. 1.10). The main concept is to prevent or minimise as much as possible the production of radioactive waste. When it is possible, radioactive wastes are decontaminated and then re-used or recycled. In some cases, radioactive waste may be incinerated and the disposal to a radioactive waste repository is the least preferred option [10].

In the UK, an active LLW National Waste Programme is responsible for the sustainable management of the LLW across the country. The main scope of this programme is to ensure that the capacity of the Low Level Waste Repository (LLWR), located in Cumbria will remain sufficient for the future needs. A metal recycling facility, also located at Cumbria, is responsible for minimising the amount LLW sent for disposal. As of 2016, about 10^6 m^3 of LLW have been delivered to the LLWR. Initially, the wastes delivered to the LLWR were disposed of in shallow landfills and covered with soil and stone. However, the large amount of LLW made it necessary to minimize the volume of the disposed material. Today, the LLW are compacted to decrease their volume. Afterwards

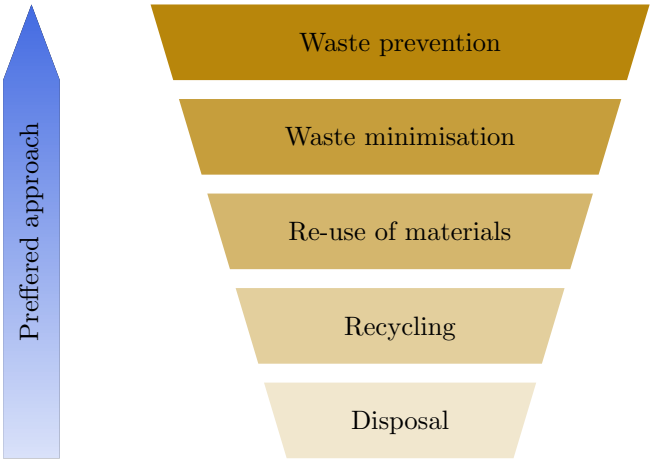

Figure 1.10: The waste hierarchy implemented in the UK for the radioactive waste management [10].

they are placed in large metal containers that are then filled with cement grout. As of 2016, there have been produced more than 10000 containers. In 2014, a new LLW disposal facility was opened at Dounreay that will receive LLW produced from the decommissioning of the Dounreay Nuclear Power Development Establishment and also waste packages produced from LLW retrieved from the LLWR landfills [10].

In contrast with the LLW, no plan has been implemented so far for the disposal of the ILW. As a result, most ILW are stored in on-site drums, silos, vaults and tanks. The majority of ILW are stored without any treatment process while the rest are immobilised in cement. The NDA plans to dispose of ILW alongside vitrified HLW in a Geological Disposal Facility (GDF) [9].

The vitrified HLW are temporarily stored in the Vitrified Product Store at Shellafield, with a capacity of 7960 steel canisters [50], which is currently almost 75% occupied. While the glass remains within the Vitrified Product Store it is heated due to the incorporated radioactive elements. To ensure that the temperature of the glass remains well below the glass transition temperature, the storage facility is passively cooled by convection. Sellafield's Vitrified Product Store is planned to continue operation until the planned completion of reprocessing of the existing HLW liquor. It is estimated that Sellafield's vitrification facility will produce about 8620 steel canisters of which about 1850 will be returned to overseas customers while the remaining packages will be disposed of in the UK in an appropriate Geological Disposal Facility [50].

Deep Geological Disposal

In the UK and for the long-term management of the radioactive nuclear waste, the government is working along with local communities, regulators and technical specialists to design the best possible route for the disposal of ILW and HLW. Currently, the preferred option is Deep Geological Disposal. In order to develop and implement a plan for geological disposal in the UK, NDA established a public organisation known as Radioactive Waste Management (RWM). In addition, the safety policies required for HLW and ILW management are developed by the UK Department of Business, Energy and Industrial Strategy (BEIS) and the Scottish government.

The concept of geological disposal involves the isolation of ILW and HLW in sealed vaults,

placed in tunnels at depths between 200 m and 1000 m below the surface, the containment of the radiation emitted by the radioactive waste to prevent it reaching the surface at levels harmful for the biosphere. For this, the tunnels must be created within solid rock formations and the packaged radioactive wasteforms that are placed in the tunnels, are additionally surrounded by cement (for the ILW) or clay (for the HLW). This multi-barrier approach minimises as much as possible the probability of contaminating the surrounding environment with the hazardous radioactivity of the wastes [52]. The GDF is expected to cost 12 million GBP and is expected to become operational around 2040 with a prospected decommissioning at 2100.

According to the initial plans, the site selection process was expected to start at 2025. After an invitation from the UK government three communities in Cumbria volunteered to site the facility. Once the location would be selected, three research studies were expected to take place: a 4-year geological study, a 10-year surface study and a 15-year underground study, construction and commissioning. However, this plan was cancelled in 2013 after the Cumbria County Council decided to halt the project. Following that, the UK government issued a white paper in July 2014, describing the new plans for the establishment of the GDF. According to this, during the first two years of the process, the RWM alongside with the government would provide the communities that are interested in hosting the GDF with detailed information regarding the development of a GDF. It was planned for the site of the GDF to be selected in 2017, but this was postponed due to local elections that complicated the process [9, 53]. According to RWM, the site selection and investigation process will take about 15-20 years [9].

Chapter 2

Glass wasteforms

2.1 Introduction

The relatively high concentration of medium-lived and long-lived radioactive elements makes it necessary to treat and solidify HLW before they are disposed of in an appropriate repository. Vitrified nuclear waste products incorporate radioactive elements within the glass matrix. These nuclei can undergo a spontaneous decay, releasing α, β and γ radiation. While only β and γ particles can heat the wasteform, highly energetic recoil nuclei, resulting from α decay, can have a serious impact on the physical and chemical properties of the wasteform in a way that can cause it to lose its mechanical coherence, and it can lead to unwanted phenomena such as corrosion, degradation and leaching. Additionally, the incorporated radioactive elements, such as ^{99}Tc, retain their radioactivity for $10^5 - 10^6$ years. In order to prevent the radiation from escaping the wasteform and contaminating the surrounding environment, it is important to develop new wasteforms with increased resistance to corrosion and leaching induced by the self irradiation that will be reliable over the time for which the containing elements remain significantly radioactive, a period that can expand even to millions of years. Thus the research on wasteforms that can maintain their chemical durability and physical properties for all the time that the incorporated radioisotopes remain radioactive, is of crucial importance [54].

Early efforts to develop wasteforms for the immobilisation of HLW started in the 1950s. These attempts were focused on the incorporation of nuclear radioactive waste into various glasses with different compositions. The first wasteforms developed were nepheline syenite glasses [55]. Nepheline syenite glasses have a relatively high melting point of about 1350 °C, which is much higher than the respective borosilicate glasses, ranging between 1100 °C and 1150 °C. Additionally, the high processing temperature of nepheline syenite glass leads to leaching of radioactive elements by volatilization and incorporation of radioactive waste without phase separation, reducing the durability of the wasteform. These facts directed the research in United States, United Kingdom, Canada, France, Italy, Japan and Soviet Union to the development of new glass wasteforms with lower melting point to make the manufacturing and processing easier. The lower processing temperatures also help to manufacture glasses at an industrial scale. This research led to the development of the well-known borosilicate glasses, used as vitrified wasteforms since 1978 [54], and to phosphate glasses [56].

The search for alternative wasteforms was continued and between 1977 and 1982 a large variety of new wasteforms were developed [56]. In the US, this research ended with the establishment of borosilicate glasses as wasteform [57]. The alternative to borosilicate glasses is SYNROC, a ceramic titanate wasteform, developed initially in the US and afterwards at the Australian National University and Australian Nuclear Science and Technology Organization, with the collaboration

of the Japanese Atomic Energy Research Institute and AERE Harwell in the UK [54].

Through the years, a series of alternative wasteforms has been developed such as tailored ceramics such as zirconolite, perovskite, hollandite and pyrochlore [58], TiO_2 ceramics [59], glass ceramics such as the aluminosilicate glasses[60], monazite [61].

As the highly energetic recoil nuclei are moving within the glass wasteform, they transfer their kinetic energy to the glass atoms that are displaced from their initial position. In computer simulations of crystalline materials it is easy to identify the defects by comparing the damaged structure with the ideal crystalline assembly [62]. In amorphous materials, such as glass wasteforms things are more complicated and defects are associated with under-coordinated or over-coordinated atoms [63] or empty regions [64]. Consequently, the research in radiation damage effects in crystalline materials is quite extensive, especially for zircon, zirconolite and pyrochlore. In glass wasteforms, existing research is not as wide as for crystalline materials and is limited mainly to silicate glasses - for iron phosphate glasses, the study of radiation damage effects is still at an early stage.

2.2 The glassy state

A glass is in general an amorphous solid resulting from a melt by rapid cooling to a rigid body without crystallization. The atomic structure of glasses is characterised by the absence of order at long-range level. However, amorphous materials such as glasses appear to have a short to medium-range order due to the chemical bonding and the interactions between the atoms comprising the glass. For example, silicate glasses, such as borosilicate glasses, are characterised by tetrahedral structures formed by the one silicon and 4 oxygen atoms. Early X-ray diffraction studies of vitreous SiO_2 and GeO_2 showed that the structure of these glasses is typical of that of an amorphous solid [65].

2.2.1 The glass transition temperature

In general, when a melt is cooled at a relatively low rate from a high temperature to the melting point T_m, it solidifies in a crystalline form. The transition between the two forms is not smooth. Instead at the transition temperature T_m, the volume decreases significantly, as shown in Fig. 2.1. The slope of dV/dT, which represent the thermal expansivity of the material, is different for $T < T_m$ and $T > T_m$ and is actually higher at temperatures above the melting point [66].

In order to create a glass, a melt must be rapidly supercooled to a temperature below the melting point, in a way that prevents the recrystallisation of the structure. In this case the specific volume of the quenched material does not exhibit a discontinuity and decreases smoothly until the glass transition temperature, at which the volume change rate with the temperature decreases. The liquid to glass transition curve, is identical to the liquid to crystal transition up to T_m. Below T_m however the rate remains the same until the melt reaches the glass transition temperature T_g, at which the rate of dV/dT gradually decreases, until the material reaches the glassy state in which dV/dT is constant. The value of the transition temperature depends on the rate of cooling $Q = -dT/dt$, and in general T_g increases with the cooling rate. For the curves of Fig. 2.1, T_{g2} corresponds to a higher cooling rate [11, 66, 67]. The curve between the super cooled region and the line corresponding to the glassy state is known as the glass transition region. The departure

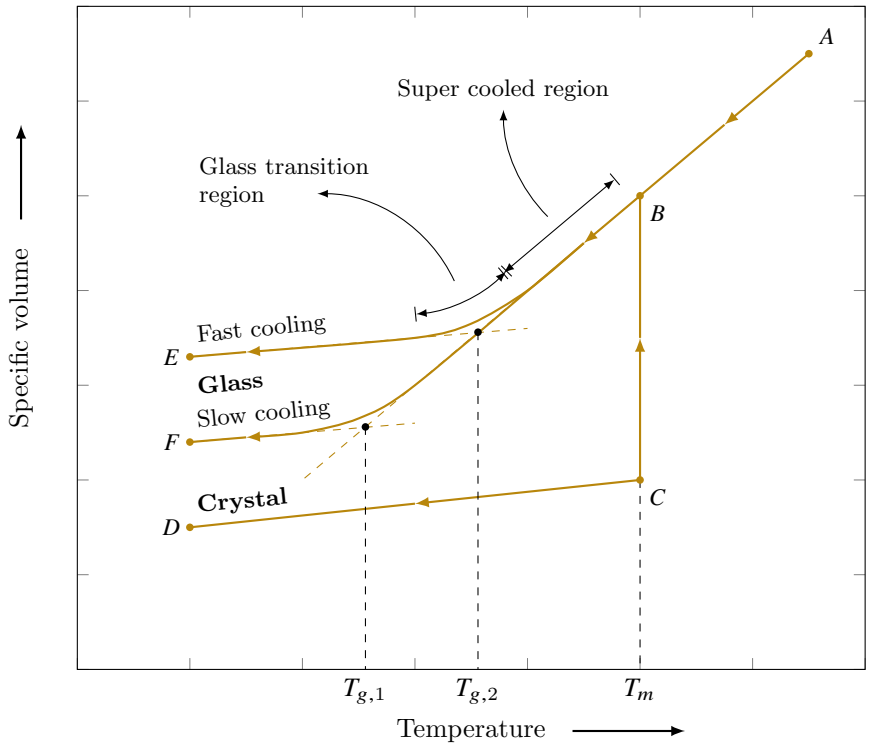

Figure 2.1: Diagram of the specific volume against the temperature for the liquid to crystal and liquid to glass transitions [11].

from the super cooled region depends on the cooling rate. A slow cooling rate allow the glass to have a lower volume and hence a higher density [11].

To avoid the crystallisation and obtain a glass, the cooling rate must be rapid and is determined by the crystallisation velocity v_c, given by

$$v_c = \frac{L}{3\pi a^2 \eta} \frac{T_m - T}{T_\infty}, \tag{2.1}$$

where L is the fusion heat, a is a parameter of the order of the lattice spacing and describes the distance an atom needs to move during crystallisation and η is the melt viscosity of the material. During a rapid quench, viscosity increases exponentially and consequently the crystallisation velocity also decreases rapidly, preventing atoms from relaxing at a position in a crystal lattice and allowing glass formation [66].

In the case of glass forming materials such as SiO_2 and B_2O_3, used in borosilicate glasses, and P_2O_5 used in phosphate glasses, the maximum crystallisation velocities are very low and consequently the quench rate can also be relatively low. For SiO_2 the rate is just 22 Å/s while for P_2O_5 it is 15 Å/s [68, 69]. Furthermore, for B_2O_3 glasses, crystallisation only occurs when the melt is pressurised when quenched [66].

From a thermodynamical perspective, the entropy and enthalpy during the liquid to glass and liquid to crystalline transitions show the same behaviour as the specific volume. However, other thermodynamic properties, such as the heat capacity behave quite different. In Fig. 2.2 the plot of C_p for the liquid to crystal and liquid to glass transition is shown. It is clear that the heat capacity

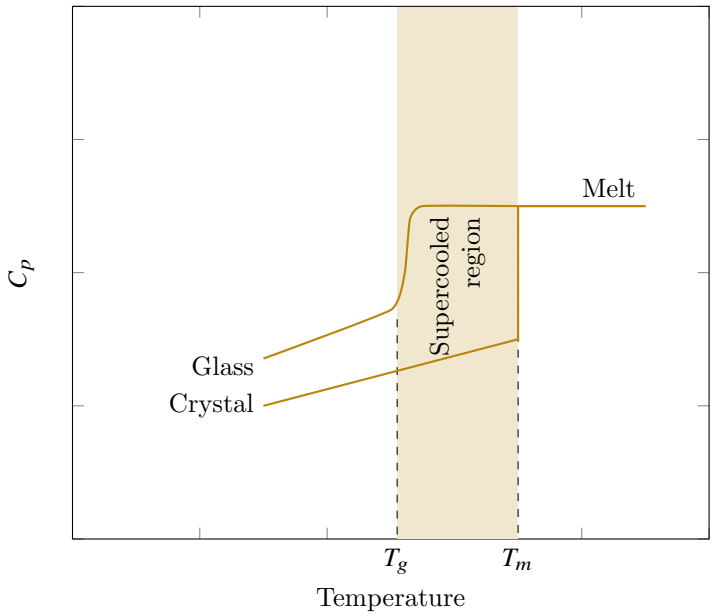

Figure 2.2: Diagram of the specific heat against the temperature for the liquid to crystal and liquid to glass transitions [11].

exhibits a sudden drop at T_g which can be explained by the change at the enthalpy values near the glass transition temperature [66]. Using the Gibbs free energy function G, that changes with temperature T and pressure P according to the equation

$$dG = -SdT + VdP, \tag{2.2}$$

where S is the entropy and V the volume, the main thermodynamical properties can be expressed as functions of the pressure and temperature. For the volume and entropy we have

$$V = \left(\frac{\partial G}{\partial P}\right)_T, \tag{2.3}$$

$$S = -\left(\frac{\partial G}{\partial T}\right)_P, \tag{2.4}$$

while for the heat capacity C_p, the thermal expansivity α and compressibility β

$$C_p = \left(\frac{\partial^2 G}{\partial T^2}\right)_P = -\left(\frac{\partial S}{\partial T}\right)_P, \tag{2.5}$$

$$\alpha = \frac{1}{V}\left(\frac{\partial^2 G}{\partial P \partial T}\right) = -\frac{1}{V}\left(\frac{\partial S}{\partial P}\right) = \frac{1}{V}\left(\frac{\partial V}{\partial T}\right), \tag{2.6}$$

$$\beta = -\frac{1}{V}\left(\frac{\partial^2 G}{\partial P^2}\right)_T = \frac{1}{V}\left(\frac{\partial V}{\partial P}\right)_T \tag{2.7}$$

The above equations, along with Fig. 2.2 show that the heat capacity, the thermal expansion and the compressibility undergo characteristic sudden and major changes at the glass transition temperature [66].

2.3 Glass structure

Early efforts to study glass formation by Zachariasen [70] led him to develop 4 rules for the glass structure. For a glass forming oxide in the form A_mO_n the rules imply that

1. An oxygen atom can be connected to up to two alkali metal atoms,
2. Each A atom must be surrounded by a small number of oxygen atoms,
3. Polyhedra formed by an A atom and the surrounding oxygen atoms can share only corners and not edges,
4. The minimum number of shared corners of each polyhedron is three.

These rules are based on the fact that the crystalline and the glass form of a material that can undergo a glass transition contain the same types of oxygen polyhedra. The difference between the crystalline and the glass form is due to the large variations in the A-O-A bond angles of the glassy state, leading to the loss of the long-range periodicity and the formation of a network of corner-sharing oxygen polyhedra with random orientations [66]. While glass formers such as B_2O_3 and SiO_2 obey all the rules suggested by Zachariasen, oxygen polyhedra of highly ionic compounds, such as MgO, Al_2O_3 and TiO_2, are connected by sharing edges or faces and consequently they are not efficient glass formers [66].

However, glasses can also be formed using alkali oxides which act as network modifiers. Network modifiers can alter the network of a glass by breaking A-O-A chains and forming A-O^- terminations. For example, as seen in Fig. 2.3, consider a SiO_2 glass, in which the structural units are $[SiO_{4/2}]$ tetrahedra sharing all the oxygens residing on the corners. Consequently, each oxygen forms a Si-O-Si unit with two silicon atoms. The addition of an ionic oxide, such as Na_2O triggers the reaction

$$2[SiO_{4/2}] + Na_2O \longrightarrow 2[SiO_{3/2}O]^- + 2Na^+ \tag{2.8}$$

As a result, the Si-O-Si chain is broken, forming SiO^- terminations, and the structure is modified or depolymerised. Oxygen atoms in the Si-O-Si chains are known as bridging oxygens (BO) while those in the SiO^- link are known as non-bridging oxygens (NBO). Additionally Na_2O, the ionic oxide that is responsible for the transformation of BOs to NBOs, is the network modifier and SiO_2, the unit that formed the glass, is called the network former.

In this case, the number of shared corners between the oxygen polyhedra is reduced, which seems contradictory to the Zachariasen rules. Through the years, the Zachariasen rules were also modified to be in line with the observation for alkali oxide glasses [66] as:

1. The majority of cations acting as network formers are surrounded by tetrahedral oxygen configurations,
2. Polyhedra formed by an A atom and the surrounding oxygen atoms can share only corners and not edges,
3. A number of oxygen atoms can be linked to only two cations and cannot form additional bonds with other cations.

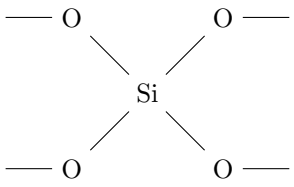

Initial [$SiO_{4/2}$] tetrahedra.

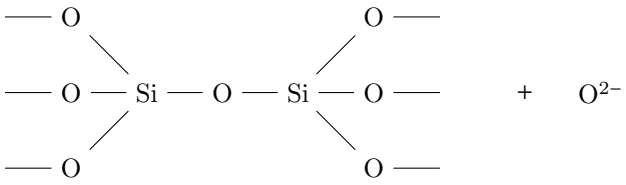

Reaction between two [$SiO_{4/2}$] sharing an oxygen atom and a O^{2-} cation.

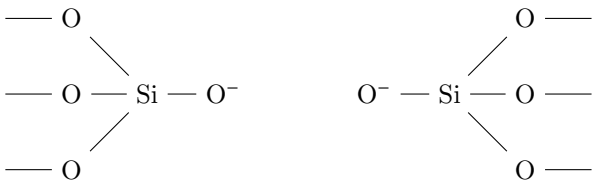

Depolymerization of the structure

Figure 2.3: The modification of a simple silicate glass network due to the addition of an alkali oxide.

2.3.1 The continuous random network model

For the description of the glass structure, the most widely accepted model is the continuous random network model, introduced by Zachariasen in 1932. The continuous random network model assumes that the network formed in a glass is extensive and consequently continuous as well as random due to the absence of periodicity. The oxygen polyhedra structural units in the glass are considered to be the same as in the respective crystalline material, defining a short-range order with a size defined by the distance of the first neighbours. In some cases, second or higher order neighbours are also observed to have fixed geometries, creating a medium-range order within the glass. However, the large variety in bond lengths and bond angles at large distances results in the complete absence of long-range order.

The continuous random network model ignores the nature of the bonds between atoms in a glass. Zachariasen's rules do not take into account whether a bond is ionic or covalent. Early efforts to explore the nature of bonds within a glass network conducted in the early 1950s, showed that glass formation requires both ionic and covalent bonds, as the existence of only one type of bond will result in crystalline order [71]. Additionally, bond strength can also affect the glass formation. In detail, high bond strength values result in increased glass forming ability [72]. But this is only valid if the melting temperatures are high enough to favour bond breaking [73].

For a detailed description of a glass network, it is required not only to know the primary structural polyhedra, but also the way they are connected to each other to form the network, consisting of closed paths, known as rings. In a simple silica glass, the smallest possible ring consists of 2 silicon and two oxygen atoms forming 4 Si-O bonds. However, such a ring requires heavy distortions in the Si-O-Si angle, which in normal [$SiO_{4/2}$] tetrahedra is normally equal to 109.28^o and thus it is very difficult to form. Thus, rings with 6 or more Si-O bonds are more favourable but very large rings, with more than 12 bonds are not easy to form as such formation reduces the cohesive energy of the structure [66, 74]. Additionally, the absence of Si-Si and O-O bonds forbids the formation of odd rings.

Despite the success of the continuous random network model, there are some significant exceptions. In oxides, oxygen atoms are 2-coordinated and the polyhedra formed by the structural unit are connected via their corners. However, in $GeSe_2$ and B_2S_3 glasses, that are similar to SiO_2 and B_2O_3 respectively, their polyhedra are mainly connected via an edge. As a result, the sizes of the rings are generally of lower order and the long range order of the network is decreased. Consequently, the Zachariasen's rules cannot be applied to non-oxide glasses. Despite that, the continuous random network model can predict the distribution in the bond angles that leads to a large distribution in the ring sizes and in turn an alteration in the local connectivities, known as topological disorder [66].

2.3.2 Single bond strength criterion

In order for the supercooled liquid to form a glass, there must be a mechanism that prevents the rearrangements of the bonds towards a crystalline state. Additionally this mechanism must be able to explain the fact that some materials are better glass formers as discussed previously. Sun [75] proposed that this mechanism is related to the strength of the bond and that the ability of a material to form a glass increases with the bond strength. By calculating the strength of the A – O bonds in the A_mO_n oxides, Sun was able to show that if the single bond strength is higher than 80 kcal/mol, the oxide acts as a glass network former (NWF). Oxides with single bond strength between 60 and 80 kcal/mol are classified as intermediates and those with single bond strength lower than 60 kcal/mol are considered to be glass network modifiers (NWM). Based on Sun's results it was found that among other materials, 3- and 4- coordinated boron, 4-coordinated silicon, 4-coordinated aluminium, 6-coordinated zirconium and 4-coordinated phosphorus are classified as network formers, 3-coordinated aluminium, 6-coordinated titanium and 8-coordinated zirconium are intermediates and 6-coordinated magnesium and 6-coordinated sodium are network modifiers.

2.4 Oxide glasses

Oxide glasses are the oldest existing glasses and those with the most widespread industrial exploitation. The most common oxide glasses are made from combinations of SiO_2, B_2O_3, Al_2O_3, Na_2O, K_2O, MgO, CaO and PbO at various compositions [66]. For the purposes of this work, the interested is limited to the borosilicate and phosphate glasses, the structure of which is discussed in more detail in the following sections.

2.4.1 Silica glasses

Silica glasses are considered the simplest of all existing glasses. A typical silica glass is formed by supercooling a silica melt at a moderate rate to a glass transition temperature around T_g = 1200 °C. They are typical examples of a tetrahedral glass structure in which each silicon atom is connected to 4 oxygen atoms and each oxygen atom is connected to 2 silicon atoms [66]. Each of the slightly distorted [$SiO_{4/2}$] tetrahedra are connected together via a bridging oxygen. All the oxygens in the glass structure act as bridging oxygens. The distortions on the [$SiO_{4/2}$] tetrahedra geometry are due to variations in the values of the Si−O−Si bond angles and the O−Si−O−Si torsional angles [11]. The Si-O-Si bond angles vary between 120 and 180 degrees, with a peak at around 144° [11, 66].

The short range order of the silica glasses extends to about 5.0 Å and includes the two nearest neighbour distances between the bonded Si−O pairs and the non bonded O−O pairs comprising the tetrahedron up to 2.65 Å and the Si−O−Si bond angles and the O−Si−O−Si torsional angles at distances between 2.65 Å and 5.0 Å (Fig. 2.4). The radial distribution function demonstrates five dominant peaks: the first at 1.62 Å corresponding to the first coordination shell of the Si-O pairs ($Si_1-O_{1/2/3/4}$), the second at 2.65 Å formed by the O−O pairs formed by oxygen atoms of the same tetrahedron ($O_1-O_{2/3/4}$, $O_2-O_{3/4}$, O_3-O_4), the third at 3.12 Å due to the Si−Si pairs of the Si−O−Si bond angles (Si_1-Si_2), the fourth at 4.15 Å formed by the second coordination shell of the Si−O pairs from the Si−O−Si−O dihedral angles ($Si_1-O_{5/6/7}$) and the fifth at around 5.0 Å formed by the second coordination shell of the Si−Si and O−O pairs (Si_1-Si_3, $O_{1/2/3}-O_{5/6/7}$) [11].

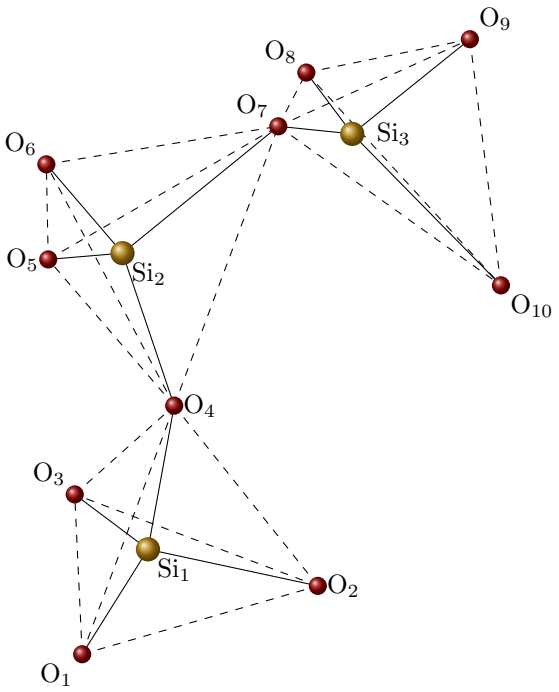

Figure 2.4: A typical short range silica glass structure formed by three [$SiO_{4/2}$] tetrahedra connected via bridging oxygens O_4 and O_7.

2.4.2 Borate glasses

Borate glasses have been used extensively and especially in combination with SiO_2. Due to the high glass forming abilities of the boron atoms, B_2O_3 melts have the ability to avoid crystallisation and form glass structures even when they are cooled at the slowest possible rates. The main building block of borate glasses are the $[BO_{3/2}]$ units, formed by 3 covalent bonds between a boron atom and three oxygen atoms. However, these units are electron deficient (the p_1 orbital has 6 electrons) and have the ability to accept two more electrons. Consequently, borate glasses also consist of tetrahedral $[BO_{4/2}]^-$ units [66]. The average B−O bond length in the $[BO_{3/2}]$ units is 1.38 Å, which is shorter than the theoretical length of 1.53 Å.

This suggests that more than 80% of the boron atoms of a borate glass, form $[BO_{3/2}]$ that are connected in triplets to form boroxol rings [76, 77]. The boroxol rings in turn are connected together through simple $[BO_{3/2}]$ units [78]. The addition of alkali oxides in the structure, destroys the boroxol network, by transforming one $[BO_{3/2}]$ unit in the boroxol ring into a $[BO_{4/2}]$ tetrahedron. In a binary borate glass, this transformation is described by the reactions

$$2[BO_{3/2}]^0 + O^{2-} \longrightarrow 2[BO_{4/2}]^- \qquad \text{and} \qquad 2B_3 + O^{2-} \longrightarrow 2B_4. \tag{2.9}$$

The transformation of B_3 to B_4 is favoured when the concentration of the B_3 is less than 50%. However, when it exceeds 50%, the concentration of B_4 is rapidly decreasing. This phenomenon is known as the borate anomaly and it affects significantly the properties of the borate glasses [11, 66]. The tetrahedral $[BO_{4/2}]$ units are not associated with any non-bridging oxygens and in general they are not connected directly [79]. For alkali fractional concentrations of less than 1/3, the connectivity of the $[BO_{4/2}]$ units creates an open borate glass structure. In contrast, when the alkali fractional concentration exceeds 1/3, the tetrahedral $[BO_{4/2}]$ units are transformed to $[BO_{1/2}O_2]^{2-}$ units via

$$2[BO_{4/2}]^- + O^{2-} \longrightarrow 2[BO_{1/2}O_2]^{2-} \qquad \text{and} \qquad 2B_4 + O^{2-} \longrightarrow 2{B_3}^{2-}. \tag{2.10}$$

This way, the glass network partially collapses and the utilisation of the volume increases [66].

2.4.3 Alkali and sodium borosilicate glasses

Alkali borosilicate glasses consists of an alkali oxide, SiO_2 and B_2O_3 in various compositions. The general formula of an alkali borosilicate glass is RA$_2$O-KSiO$_2$-B$_2$O$_3$. As it is clear, two glass network formers exist: boron and silicon. The addition of the alkali oxide can be associated either with the silicon atom and create SiO^-A^+ units containing a NBO, or with the boron atoms and convert BO_3 units to BO_4 tetrahedra. In the second case, no NBOs are formed during the process [11]. The exact glass forming mechanism depends on the concentration of alkali oxide. The association of the alkali oxide with the boron atoms is favoured for $R < 0.5$ and for higher R values the alkali oxide is associated also with silicon atoms at a fraction depending on the K value, therefore creating NBOs [80].

Sodium borosilicate glasses, consisting of SiO_2, B_2O_3 and Na_2O are studied extensively. The effects of sodium addition to a binary SiO_2-B_2O_3 glass was first studied during 1979-1983 by Nuclear Magnetic Resonance (NMR) [81, 82, 83] and it was shown that the structure depends on

the fractions $R = [Na_2O]/[B_2O_3]$ and $K = [SiO_2]/[B_2O_3]$. Later studies revealed that sodium acts as a network former and leads to the complete transformation of $[BO_{3/2}]$ to $[BO_{4/2}]$ tetrahedra, leaving the silica network undisturbed with no NBOs [84]. This process occurs while $R < 0.5$. For $0.5 < R < R_{max}$, where $R_{max} = 0.5 + K/16$ the silica network is also altered resulting in the formation of reedmergnerite ($\frac{1}{2}Na_2OB_2O_38\,SiO_2$) units consisting of four silica tetrahedra bonded with one four-coordinated boron [83, 85]. For even higher R values up to $R_1 = 0.5 + K/4$, the additional Na_2O molecules are shared between reedmergnerite and the diborate units, resulting in the formation of NBOs on the silica units forming the reedmergerite groups [81, 82, 83, 84]. This process is also characterised by the transformation of diborate units to pyroborate consisting of 1 three-coordinated boron atom with 2 NBOs at a rate given by $(2 - K/4)/(2 + K)$ and the transformation of reedmergnerite into silica tetrahedra and pyroborate units with also 2 NBOs per silicon atom at a rate $(K + K/4)/(2 + K)$, until all the three-coordinated boron atoms are associated with at least one NBO. This happens for $R = R_2 = 1.5+3K/4$ [81, 82, 83, 84]. These transformations continue to occur until all borate units are transformed into pyroborate and all silica units have no NBOs.

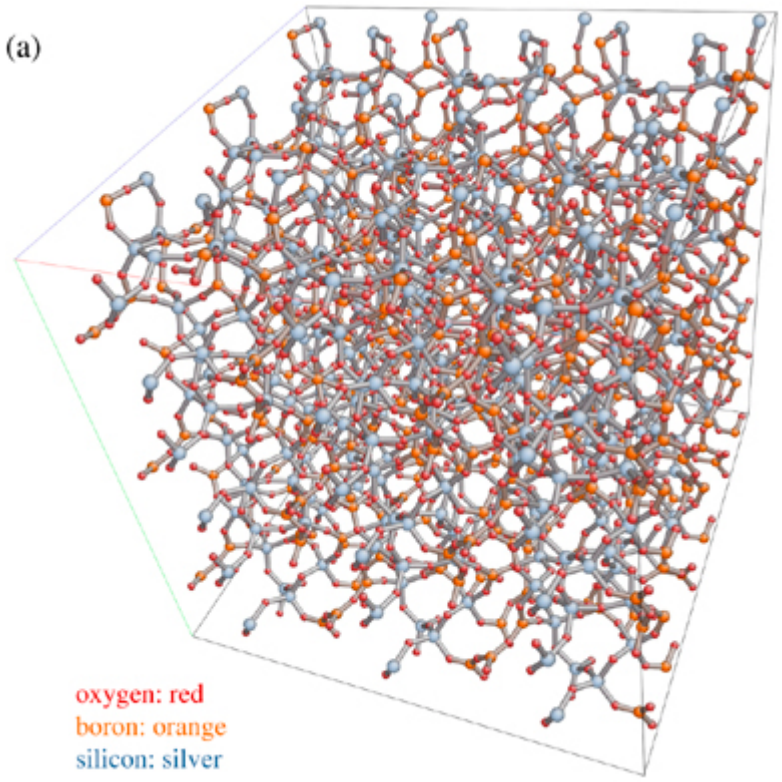

Figure 2.5: Structure of a typical borosilicate glass. [86]

2.4.4 Phosphate and iron phosphate glasses

Although phosphorus is a network former, only P_2O_5 has the ability to form a glass. Crystalline P_2O_5 can be found in three different forms: hexagonal, orthorhombic and tetragonal, which can form a glass [11]. The simplest possible phosphate glasses can be made using a P_2O_5 melt. However,

the manufacturing of such a glass is very difficult due to the complex preparative procedures [87]. The basic building units of a phosphate glass are the trigonal [$PO_{3/2}$] and the tetrahedral [$PO_{4/2}$]. In the tetrahedral unit, the phosphorus atom is connected with 3 oxygen atoms via a single bond of length equal to 1.581 Å, while the bond with the fourth oxygen is double with length equal to 1.432 Å. In a single component P_2O_5 phosphate glass, the three single bonded oxygens are actually bridging oxygens, while the double bonded is a terminal oxygen (TO) that cannot be connected with any other atom. The addition of an alkali oxide, results in the reduction of the non-bridging oxygens in the PO_4 [66]. This is one of the main differences between the phosphate and the silica glasses, in which all four oxygens of the SiO_4 units are BOs. As a result, the phosphate glasses are less rigid when compared to silica glasses [11]. Using the notation Q_i, where i is the number of NBOs, all the structural units in pure P_2O_5 glasses are described as Q_3. The addition of one alkali oxide in the glass results in the gradual transformation of Q_3 units to $Q_2 \rightarrow Q_1 \rightarrow Q_0$ as the abundance of the alkali oxide increases [66, 88]. The different structures formed as the alkali oxide concentration increases consist of ultraphosphates Q_3 tetrahedra, Q_2 metaphosphate chains, Q_1 pyrophosphates and Q_0 orthophosphate ions. Consequently, the structure of an alkali oxide phosphate glass consists of chains instead of rings [11].

Basic iron phosphate glasses are binary oxides consisting only of Fe_2O_3 and P_2O_5. The atomic structure of iron-phosphate glasses and how it affects physical and chemical properties is well studied. The basic structural unit is the PO_4 tetrahedron and depending on the composition of the glass, these tetrahedra can be isolated. In the case where the O/P ratio is equal to 4, like the $FePO_4$ glasses, the structure is known as orthophosphate [89]. For binary glasses consisting only of Fe_2O_3 and P_2O_5, the glass formation is achieved for a content of 15 to 45 mol% in Fe_2O_3. Lower iron oxide content may also form glass but with very low chemical durability, while higher concentrations crystallise rapidly [90, 91]. For vitrification applications, it is common to use 30 to 40 mol% Fe_2O_3 [89]. The maximum waste load of iron phosphate glasses depends on the composition of both the glass frit and the HLW. Recent studies also show that an iron phosphate glass with composition of 42% P_2O_5, 25% Na_2O, 5% Al_2O_3, 10% CaF_2 and 18% Fe_3O_4 shows great potential for the immobilisation of HLW containing ^{99}Tc [92].

Mössbauer spectroscopy studies of sodium iron phosphate glasses showed clearly that iron ions can be found both as Fe^{2+} and Fe^{3+} redox states [93]. Melting conditions can affect the concentration of Fe^{2+}. Increase of Fe^{2+} will result in the increase of both the viscosity and the tendency to crystallise. To create an iron-phosphate glass with the desired properties it is important to maintain the fraction Fe^{2+}/Fe^{3+} at an appropriate level. This fraction is found to depend on the melting temperature, the glass composition, the melting time and the atmospheric composition [90, 93]. Although the Fe^{2+}/Fe^{3+} fraction tends to decrease during the cooling stage of the vitrification, for normal melting conditions, the variations are quite small and it is generally accepted that both the melt and the glass consist of the same Fe^{2+}/Fe^{3+} fraction. However, at low temperatures and when the resulting glass wasteform is heated in the air, it seems that the fraction increases with a rate depending on the air temperature. This oxidation can be explained by assuming that the increase of the temperature results into the transformation of FeO to Fe_2O_3 [89].

The structure of iron phosphate glasses are far more complicated due to the existence of redox states. The local structure of iron atoms depends on the Fe^{2+}/Fe^{3+} fraction. In general, iron atoms can have a coordination number varying from 4 to 6. In any case the basic structural units are

the $FePO_4$ tetrahedra. The first attempts to create a model which describes with accuracy the structure of iron phosphate glasses belong to Wedgwood and Wright [94]. According to this model, the basic structural units of iron phosphate glasses are $[FeO_4]^-$ and $[PO_4]^-$ tetrahedra sharing all four corners and also PO_4 tetrahedra with 3 NBOs and one BO. Additionally, all Fe^{2+} cations are 8-coordinated and act as network modifiers. A second model was developed by Marasinghe et. al. more than two decades later [95]. This model is based on the crystalline $Fe_3(P_2O_7)_2$ structure, in which two Fe^{3+} ions are found in octahedral coordination and one Fe^{2+} ion is in trigonal prismatic coordination. DFT simulations of a simple iron phosphate glass consisting of 60% P_2O_5 and 40% Fe_2O_3 performed by Stoch et. al. [88], assisted efforts to develop a third model, according to which the basic structural units are both $[FeO_4]^-$ and $[PO_4]^-$ tetrahedra. The glass network structure depends on the Fe^{2+}/Fe^{3+} ratio.

2.5 Radiation damage process in glass wasteforms

The radioactive decay of the actinides and other fission products incorporated within glass wasteforms, results in self-heating and self-irradiation of the wasteform that can gradually affect the structure, performance and stability of the wasteform [96, 97]. Fissile radioactive products contained within nuclear spent fuel have the potential to undergo a spontaneous radioactive decay to form lighter and more stable elements. During the decay process, the initial nuclei loses energy by emitting α, β or/and γ radiation.

2.5.1 Alpha decay effects

In alpha decay, a radioactive nucleus undergoes a spontaneous decay in which the initial nucleus is transformed to a nucleus with atomic number Z reduced by two and a mass number A reduced by four, with the simultaneous emission of an alpha particle, identical to a ${}^4_2$He nucleus. Alpha decay is described by the equation

$$ {}^A_Z X \xrightarrow{\alpha} {}^{A-4}_{Z-2} Y + \alpha \qquad \text{or} \qquad {}^A_Z X \xrightarrow{\alpha} {}^{A-4}_{Z-2} Y + {}^4_2 He \tag{2.11} $$

For a single decay event, the kinetic energy of α particles is given by the Geiger-Nuttall law [98]

$$ E_\alpha = \left(\frac{\alpha_1 Z}{\alpha_2 - \ln \lambda} \right)^2 - E_\mathrm{r}, \tag{2.12} $$

where E_r is the kinetic energy of the recoil nucleus, Z the atomic number of the mother nuclei and α_1, α_2 are constants. This law limits the kinetic energy of α particles in the range between 4.5 MeV and 5.5 MeV, corresponding to a speed of about 0.045 c to 0.055 c or 13.5×10^6 m/s to 16.5×10^6 m/s. The recoil nuclei, depending on the mass, has a much lower kinetic energy between 70 keV to 100 keV [54].

In nuclear wasteforms, radiation damage results mainly from the α decay of actinides. Although the kinetic energy of α particles can be from 45 to almost 80 times greater that the one of the recoil nuclei, it is the latter that is responsible for the majority of the damage. When the fast moving α particles collide with atoms of the glass matrix because of their extremely high velocity,

they deposit their energy inelastically to the atoms with the energy transferred to the electrons of the atoms. Consequently, α particles contribute only about 4% in the displacement energy of an alpha decay event and their energy is deposited over a relatively large distance varying from 10 μm to 20 μm, while the maximum damage occurs near the end of the α's particle trajectory [99]. Furthermore, each α particle collides with a small number of atoms in the glass matrix and the resulting damage is limited to small clusters of atoms spread over a large area of the structure and surrounded by undamaged regions, making possible the recovery of the damaged regions. As a result, the generic effect of α particles in the wasteform is the heating of the structure although it has been observed that borosilicate glasses may decompose when absorbing ionizing energy and consequently forming molecular oxygen [100]. Noble gases, such as helium, are insoluble in most materials. Consequently, accumulation of α particles in different regions within the glass matrix can lead to helium bubble formation, resulting in induced mechanical strains reducing the mechanical integrity of the wasteform [54, 101]. Aggregation of helium bubbles within the wasteform is a continuous process - as long as radioactive materials within the glass undergo α decay, the concentration of helium nuclei will increase. However, the estimated helium bubble concentration after 100,000 years is about 30 times lower than that required to start affecting the mechanical integrity of the wasteform [101].

In contrast, the massive recoil nuclei are responsible for 96% of the displacement energy [99]. Although recoil nuclei from an alpha decay event can travel only about 10 *nm* within the wasteform, they have low velocity and transfer their energy elastically, displacing a large number of atoms from the glass matrix in a small volume and creating a radiation damage cascade. The fact that damaged atoms of the glass matrix are surrounded by displaced atoms makes the recovery of the structure less possible. The accumulation of damaged regions from multiple decay events within the glass wasteform results in permanent damage to the glass matrix [54].

2.5.2 Beta and gamma decay effects

During a beta decay process, the radioactive nuclei transforms a neutron to a proton by emitting an electron (β^- particle) and an anti-neutrino (β^- decay), or a proton to neutron with simultaneous emission of one positron (β^+ particle) and one neutrino (β^+ decay), according to equations

$$ {}^{A}_{Z}X \xrightarrow{\beta^-} {}^{A}_{Z+1}Y + \beta^- + \bar{\nu}_e \qquad \text{and} \qquad {}^{A}_{Z}X \xrightarrow{\beta^+} {}^{A}_{Z-1}Y + \beta^+ + \nu_e. \tag{2.13} $$

or

$$ {}^{A}_{Z}X \xrightarrow{\beta^-} {}^{A}_{Z+1}Y + e^- + \bar{\nu}_e \qquad \text{and} \qquad {}^{A}_{Z}X \xrightarrow{\beta^+} {}^{A}_{Z-1}Y + e^+ + \nu_e. \tag{2.14} $$

Because of the large difference in masses between the emitted β particle and the recoil nuclei, almost all the kinetic energy is transferred to the β particle and it is generally accepted that the kinetic energy of the recoil nuclei is negligible.

The contribution of the small β particles to the displacement energy of the structure is also very small. Since electrons and positrons have a very small mass, 5 orders of magnitude lower than a typical nucleus, they can only participate in single displacement events and most of their energy is dissipated in the structure of the wasteform by ionisation effects. These effects result in

the heating of the wasteform for a period of about 500-600 years from their manufacture [54, 97]. The main heating sources, are the short-lived fission products ^{90}Sr and ^{137}Cs.

In gamma decay, a nucleus excited to a higher energy level relaxes to the ground state by emitting a photon (γ particle) with energy equal to the energy difference between the two states, via

$$ {}^{A}_{Z}X^{*} \xrightarrow{\gamma} {}^{A}_{Z}X + \gamma. \tag{2.15} $$

The energy of the emitting photon depends on the energy levels of the mother nuclei but in general is of the order of 100 keV. Photons resulting from γ decay processes within the wasteform, can have significant effect only when the wasteform is subjected to a radiolysis process.

2.6 Borosilicate glass wasteforms

The first country to use borosilicate glasses as wasteforms for the immobilisation of HLW was France in 1981, followed by United states in 1982 and progressively by other countries [102, 103]. The establishment of borosilicate glasses as the main wasteform in the USA was based on early stage experimental studies of the radiation damage effects conducted in the early 1980s at the Savannah River Laboratory. These studies focused on the effects of radiation on physical and chemical properties and mainly on the leaching rates, volume change and damage accumulation. In general, the results of these studies enhanced the reliability of borosilicate glass wasteforms as they showed that α and γ particles have no effect on the leaching of the glass [104, 105]. Radiolysis of the borosilicate glass leachant using ^{244}Cm α radiation, ^{90}Sr β radiation and ^{60}Co γ radiation also has a small effect on the leaching rates of the wasteforms [106]. However, leach rates may increase under the oxidative conditions resulting from the formation of HNO_3.

The main advantages of borosilicate glass waste forms are [107]:

1. The ability to incorporate the large variety of actinides and fission products comprising HLW,
2. They have a relatively low melting point, about 1150 ^{o}C or lower, depending on the composition,
3. They have a high waste load, up to 40 wt%, again depending on the composition,
4. They maintain their tolerance for a large variety of glass compositions,
5. They are proved to be resistant to radiation induced degradation,
6. They have low leaching rates in aqueous environments,
7. They can be manufactured at an industrial scale.

2.6.1 Composition effects on physical and chemical properties of the wasteform

Through the years, several borosilicate glass compositions have been proposed for vitrification applications. In order to achieve the maximum chemical durability, a borosilicate glass wasteform should have the maximum possible concentration of SiO_2. However, large silica concentrations

increase the melting point to more than 1700 °C. At such high temperatures, fission products such as Cs, Tc and Se become volatile and cannot be incorporated into the vitrified glass matrix. Thus, it is necessary to use additional glass forming components to decrease the melting temperature. In Table 2.1, typical compositions of glass frits used for the vitrification of HLW are presented [56]. The only glass consisting of the three basic components of borosilicate glasses, SiO_2, B_2O_3 and Na_2O, is developed at Atelier de Vitrification Marcoule and is known as AVM frit.

Each of the components of a borosilicate glass can modify specific physical and chemical properties and the composition is based on the desired properties. Alkaline species, such as sodium and lithium affect the electrical conductivity and viscosity of the melt. Lithium in general is a network modifier and consequently it helps to decrease the specific electrical resistance and the melting point of the glass [108]. To achieve the desired melting temperature, it is required to use both Li_2O and Na_2O with a weight percentage of about 0.5. However, alkaline materials may result in very low viscosities, making it difficult to pour the melt into the steel containers. To set the viscosity at a convenient value, it is necessary to use oxide additives and mainly Al_2O_3, CaO, MgO, ZnO and TiO_2.

Aluminium oxide is used to increase the chemical durability of the glass, as aluminium forms tetrahedra with four oxygen atoms. High concentrations of aluminium however, may increase the viscosity to levels at which the glass produced will be inhomogeneous [109]. Calcium, Magnesium and Zinc have the ability to increase the chemical durability of the glass by stabilizing the glass structure. They also increase the viscosity of the glass at low temperatures, from 400 °C to 600 °C and decrease it at temperatures in the range from 1000 °C to 1300 °C [110]. The effect of magnesium depends strongly on the composition of the glass. Substitution of CaO by MgO in specific amounts may significantly reduce the viscosity [111]. ZnO at a concentration of 20 wt% or more, on the other hand, may devitrify the glass to form willemite (Zn_2SiO_4). Finally, TiO_2 can

Table 2.1: Typical compositions of borosilicate glass frits use for the vitrification of HLW [56]

	Composition in weight percent									
	SRL165	SON168	SM513	PNL76-68	UP209	GP98/12	P0522	SM539	AVM	SRL131
SiO_2	68.0	54.9	58.6	59.4	68.5	58.5	61.0	45.5	56.1	58.7
B_2O_3	10.0	16.9	14.7	14.3	15.0	11.0	19.9	33.0	25.3	14.9
Li_2O	7.0	2.4	4.7	–	5.4	–	4.3	4.5	–	5.8
Na_2O	13.0	11.9	6.5	11.3	11.2	17.5	1.4	10.5	18.6	18.0
K_2O	–	–	–	–	–	–	2.8	–	–	–
TiO_2	–	–	5.1	4.5	–	3.6	–	–	–	1.04
CaO	–	4.9	5.1	2.9	–	4.5	2.8	6.5	–	–
MgO	1.0	–	2.3	–	–	3.3	–	–	–	2.1
Al_2O_3	–	5.9	3.0	–	–	1.6	5.0	–	–	–
ZnO	–	3.0	–	7.6	–	–	2.8	–	–	–
ZrO_2	1.0	–	–	–	–	–	–	–	–	0.45
La_2O_3	–	–	–	–	–	–	–	–	–	0.45

also decrease the viscosity of the glass because it forms TiO_4 tetrahedra. However, large titanium concentrations can produce crystalline phases within the glass [112]

The composition has been proved to have a significant effect on the leaching and thermal stability of the glasses, but it has no or only a minor effect on other physical properties. The optimum borosilicate glass compositions are 51-53% SiO_2, 24-28% Na_2O and B_2O_3 and 21-25% Al_2O_3, Fe_2O_3 and waste products [57].

One of the problems associated with the use of borosilicate glass is that many HLW wastes contain phosphates P_2O_5, with mass concentrations that reaches 15 wt%. The high concentration of P_2O_5 may lead to phase separation in borosilicate glasses, resulting in loss of chemical durability [113]. To prevent phase separation, one possibility is to minimise as much as possible the concentration of P_2O_5 in the wasteform. Depending on the composition of the borosilicate glass, the maximum acceptable concentration of P_2O_5 varies from 0.5 wt% to 7 wt% [114, 115]. For most common borosilicate glass compositions, this limit is even smaller, from 2 wt% to 3 wt%, which is far less than the common 15 wt%.

2.6.2 Damage accumulation and energy storage

Continuous α decay events within the wasteform result in the accumulation of radiation dose. In Table 2.2 the cumulative decay events in typical borosilicate glass wasteforms used by the US nuclear industry and tested in the Savannah River Laboratory are demonstrated. The energy stored in the wasteform, as a function of cumulative dose, shows a sigmoid behaviour, with an exponential growth for low cumulative doses and a saturation for higher doses. From 10^{16} to 10^{17} α decays/g the stored energy remains almost constant and equal to the maximum values mentioned previously [96, 116].

Table 2.2: Cumulative decay events in typical borosilicate glass wasteforms used by the US nuclear industry and tested in the Savannah River Laboratory [117]

Time (years)	**Alpha decays (per gram)**	**Beta decays (per gram)**	**Alpha decay dose (rad)**	**Beta decay dose (rad)**
1	2×10^{14}	5×10^{16}	2×10^{7}	6×10^{8}
10	2×10^{15}	5×10^{17}	2×10^{8}	6×10^{9}
10^2	2×10^{16}	2×10^{18}	2×10^{9}	3×10^{10}
10^3	1×10^{17}	5×10^{18}	9×10^{9}	6×10^{10}
10^4	3×10^{17}	5×10^{18}	3×10^{10}	8×10^{10}
10^5	5×10^{17}	5×10^{18}	4×10^{10}	1×10^{11}
10^6	1×10^{18}	5×10^{18}	8×10^{10}	1×10^{11}

The amount of stored energy was also calculated using molecular dynamics simulations. Results show that the stored energy in a radiation damaged simplified borosilicate glass model is about 70 J/g [15], which is very close to the experimental findings by Weber et. al. [96, 116]. Later studies of the CJ1 borosilicate glass conducted by Dewan et. al. [20], estimated that after 200×4 keV cascades, the stored energy is almost 100 times higher and approaches 8 kJ/g. However, these authors note that in a real glass wasteform such a high radiation dose would be achieved after 10^4-10^5 years and so it is not possible to make a direct comparison of the simulation results with real world glasses.

2.6.3 Coordination changes due to alpha decay

Molecular dynamics simulation studies in simplified borosilicate glasses consisting of 63.8% SiO_2, 17.0% B_2O_3, 13.4% Na_2O_3, 4.0% Al_2O_3 and 1.8% ZrO_2, with incident energy of about 800 eV or less, showed that oxygen and sodium are the most frequently displaced atoms. A displaced atom was defined by the authors as one that was moved away from its initial position by more than 10 Å. This is because oxygen and sodium cohesive energies are lower than those of the network formers of the glass network and also because Na-O bonds are longer than the other bonds of the structure ($\simeq$ 2.5 Å), and consequently these species have the largest free volume surrounding them in which they can move [15].

The formation of a damage cascade affects the coordination number of particles and the geometric characteristic and local angles of bonds. Simulations of a simplified glass model revealed that there is a net reduction of the coordination of oxygen atoms. This transformation of oxygens results in the transformation of three-coordinated boron atoms to four-coordinated. Additionally the mean O-B-O angle for the four-coordinated boron atoms is reduced in the damaged structures regardless of the kinetic energy of the impact particle, varying between 109.27° and 109.29°. For the three-coordinated boron atoms that were transformed to four-coordinated during the cascade formation, the variations in the angle were more significant and varied between 109.14° and 109.37°. In any case, these angles are smaller than the equilibrium angle θ_0 [15]. In a multiple cascade simulation of the French borosilicate glasses SON68 consisting of 63.8% SiO_2, 17.0% B_2O_3, 13.4% Na_2O, 1.83.5% ZrO_2, 4.0% Al_2O_3 and $\simeq$0.1% UO_2, by calculating the mean Voronoi volumes of the three and four-coordinated boron atoms, it was demonstrated how the change in the coordination numbers is proportional to the number of decay events [17]. Molecular dynamics simulations on a simplified borosilicate CJ1 glass consisting of only three oxides at composition 67.7% SiO_2, 18.0% B_2O_3 and 14.2% Na_2O also revealed that the change of the boron coordination number results in a change in the B-O-B and Na-O-Na angles but also in the Si-O-Si. In glasses with high sodium concentrations, the Na-O bond length becomes shorter and this affects the structure of network formers, forcing them away from the central oxygen atom and consequently reducing the values of B-O-B, Na-O-Na and Si-O-Si angles [18]. The changes in the local structure of the glass within the damage cascade, have been found to be similar to the effect observed when increasing the temperature of the glass near to the melting point, suggesting that radiation damage effects are of a similar nature to thermal effects [118]

2.6.4 Volume changes due to alpha decay - Swelling

Alpha decay of radioactive isotopes within the glass wasteform results into a change in the volume of the glass. The relative volume change is given by

$$\frac{\Delta V}{V_0} = A\left[1 - e^{-BD}\right], \tag{2.16}$$

where V_0 is the initial volume, A the saturation volume change, B the amount of damaged glass per unit dose and D the total radiation dose. Normally, the saturation volume changes for $D = 10^{18}$ α decays per gram of glass, are limited within ±1.2% [54, 119, 120, 96]. The volume saturation depends on the composition and the network of the glass, but in general the volume saturation

dose is higher than 2×10^{18} α decays/g [121].

By comparing with the energy storage saturation doses, it is obvious that volume change saturation occurs at much higher doses and this suggests that the storage energy, associated with the defects formed from α particles released from the decay events, has a different origin from the network rearrangements that are responsible for the volume changes, associated with the recoil nuclei. This argument is also supported by the fact that the amount of energy stored in the glass is independent of whether the glass undergoes contraction, swelling or negligible changes in the volume [121].

Volume changes in irradiated borosilicate glass were also investigated in several molecular dynamics simulation studies. For a structure comprising 56.1% SiO_2, 17.1% B_2O_3, 12.3% Na_2O, 3.5% ZrO_2, 6.1% Al_2O_3 and 4.9% CaO and for damage cascades created by heavy atoms with kinetic energies of 300, 500 and 700 eV, the volume changes were found to be respectively +0.21%, +0.33% and +0.19% [122]. In the simulation of the French borosilicate glasses SON68, it was shown that the increase of the kinetic energy of the projectile results in a decrease of the swelling. To explain this behaviour, authors suggested that the higher kinetic energy of the impact particle results in a higher thermal wave that enhances the restoration of the structure. Consequently, the swelling of the glasses is mainly due to the low energy recoil particles. This is supported by the observation that structures irradiated with high kinetic energy projectiles (>700 eV) have almost identical ring distributions as undamaged structures. In contrast, impact particles with lower kinetic energy have the ability to change the ring distribution, by increasing the number of higher order rings and decreasing lower order rings [122]. The total swelling observed in multiple decay events accompanied by multiple damage cascades is correlated with the structural changes at the atomic level. This is because of the changes in the coordination numbers of the atoms, resulting in the increase of the mean ring size and consequently increasing the size of the network [17]. In general, the swelling of the structure is mainly observed around Na and Ca atoms, acting as network modifiers [122]. However, multiple cascade molecular dynamics simulations of the simplified borosilicate CJ1 glass, showed that computer simulations may overestimate the change in the volume by a factor of 2.5 [123]. In the work done by Dewan et. al. [20] the volume expansion saturates at about 9%, much higher than observed in real glasses, but this can also be explained by the fact that the radiation dose in the simulations was much higher that those observed in current real glasses.

2.6.5 Polymerisation of the glass due to alpha decay

The effect of polymerisation in the cascade morphology also has been studied using molecular dynamics. It is argued that the impact particle behaves in a different way in polymerised regions, where it displaces many atoms and its momentum is not reduced significantly, resulting in the formation of heavily damaged regions, while in depolymerised zones containing sodium, the impact particle only displaces a few atoms with a faster loss of kinetic energy [16]. In a later molecular dynamics study of polymerisation the results suggested that the development of the cascade can be separated into two different stages, a initial one, during the first 0.1 ps, in which the cascade is created and the glass is depolymerized, followed by the second stage during which the structure relaxes and the glass is repolymerised [19].

2.7 Iron phosphate glass wasteforms

The problems related to the high P_2O_5 concentration in borosilicate glasses, led to the search for alternative glass wasteforms. A proposed alternative is the iron phosphate glasses that take advantage of the high P_2O_5 and Fe_2O_3 concentration in the HLW to produce wasteforms that can retain their physical and chemical properties at high phosphate and metal oxides loading. In later years, the interest in iron phosphate glasses focused on their low melting temperatures and their large thermal expansion coefficients [124].

Phosphate glass wasteforms were developed in the same period as borosilicate glass wasteforms [54]. However, for almost three decades, until the mid 1990s, it was thought that they had lower chemical durability and research was abandoned [102]. It was then proven that binary and tertiary iron phosphate glasses result in having the same or higher chemical durability in comparison with borosilicate glasses in water at 90 °C [125, 93]. Additionally, iron-phosphate glasses have a lower melting point, ranging between 950 °C and 1150 °C which makes their manufacturing process relatively straightforward [125, 93, 126].

2.7.1 Composition effects on physical and chemical properties

Iron phosphate glasses are in general more fluid than borosilicate glasses with significantly lower viscosity. The addition of CaF_2 decreases further the viscosity and makes the glass formation much easier. 3 to 7% CaF_2 also has the ability to reduce the melting point by almost 100 °C and additionally increase the durability of the glass [113]. Fluorides such as ZnF_2, AlF_3 and MgF_2 and additions like Si_3N_4 or CaO have the same effects such as CaF_2, but in lower degree.

Sodium-iron phosphate glasses demonstrate a dissolution rate that is heavily dependent on the Fe_2O_3 concentration of the wasteform. In general, durability increases with the iron content [126, 127]. At 20 mol% Fe_2O_3, the dissolution rate is of order of 10^{-6} g/cm^2 while for 30 mol% Fe_2O_3 it decreases by three orders of magnitude, to about 10^{-9} g/cm^2 [93]. In sodium iron phosphate glasses, the P-O-P bonds forming the PO_4 tetrahedra give place to P-O-Fe^{2+} and P-O-Fe^{3+} bonds that demonstrate increased chemical resistance and are responsible for the enhanced chemical durability and lower thermal expansion coefficient of glasses with high Fe_2O_3 concentration [113, 126]. Dissolution rates also depend on the oxygen and phosphorus content of the glass and become a minimum for O/P ratio equal to 3.5, corresponding to a structure of two PO_4 tetrahedra, with one common oxygen, joined to form a pyrophosphate group P_2O_7 bonded by iron ions [113].

Displacement energy threshold depends on the nature and the coordination of the ions of iron phosphate glasses. However, the total stored energy seems to be independent of the amount of Fe^{2+} and P ions. Additionally, the peak displacement energy threshold of the Fe^{3+} and O atoms is higher that that for Fe^{2+}, suggesting that iron phosphate glasses used for the immobilisation of HLW should contain as few Fe^{2+} ions as possible.

2.7.2 Alpha decay effects on iron phosphate glasses

Until 2002, there was no research on the radiation damage effects in iron phosphate glasses containing actinides [128]. Since then, research has been mainly focused on the encapsulation of LLW by the US nuclear industry. In recent years, the Indian nuclear industry expressed interest in

using iron phosphate glasses for the immobilisation of spent nuclear fuel containing ^{99}Tc [129] and consequently, involved parties started investigating the effects of α decay on iron phosphate wasteforms.

To date, there is very limited research on the radiation effects in iron phosphate glasses. From the existing literature it is found that the irradiation of iron phosphate glasses with 2 MeV Bi ions results in the depolymerisation of the glass and the breaking of P-O-P and Fe-O-P bonds. In contrast, 750 keV Bi ions irradiation results in the polymerisation related with the heating of the structure during irradiation [130]. Finally, molecular dynamics simulations show that the extent of damage during the cascade formation seems to be inversely proportional to the Fe^{2+} content. However, the final damage, after the relaxation of the structure is independent of the amount of Fe^{2+}. In terms of the P atoms with a coordination number less than 4 which is observed in the undamaged structures, it can be argued that radiation damage has limited effects in iron phosphate glasses [13].

Chapter 3

Molecular dynamics

3.1 Introduction

Molecular dynamics is a computational method for studying the behaviour of matter at the atomic scale, using Classical Mechanics. The technique is based on Newton's equations of motion

$$\mathbf{F} = m\frac{d^2\mathbf{r}}{dt^2}, \tag{3.1}$$

that are solved for a given force field $\mathbf{F}$ to yield the positions $\mathbf{r}$ and velocities $\dot{\mathbf{r}}$ of a set of N atoms after a finite set of timesteps. The positions and velocities of atoms at each timestep of the simulation define the trajectory of the atom in phase space. Boltzmann's formulation of Statistical Mechanics links the trajectories of atoms to equilibrium thermodynamic properties. Linear response theory enables time-dependent properties, such as transport properties, to be extracted. A basic Molecular Dynamics algorithm represents an isolated thermodynamic system in which volume and energy are conserved.

3.2 Classical mechanics in molecular dynamics

In Molecular Dynamics simulations, the first step is to define the potentials $\phi(\mathbf{r})$ between the atoms. For a conservative force field, we can then calculate the forces between the atoms of the system using the relation

$$\mathbf{F} = -\nabla\phi(\mathbf{r}), \tag{3.2}$$

and from this the acceleration. With the acceleration known, we can calculate the velocity $\mathbf{v}$ and the position $\mathbf{r}$ of a particle by simply integrating equations

$$\mathbf{a} = \frac{d\mathbf{v}}{dt} = \frac{\dot{\mathbf{p}}}{m} \qquad \text{and} \qquad \mathbf{v} = \frac{d\mathbf{r}}{dt} = \dot{\mathbf{r}} = \frac{\mathbf{p}}{m}. \tag{3.3}$$

For a system of N particles, the integration of these first order ordinary differential equations will introduce $6N$ constants that can be calculated using the initial conditions for the positions and velocities. While initial positions depend on the structure under investigation and are set according to that structure, initial velocities can be assigned using a Maxwell-Boltzmann distribution. For example, the x component of the initial velocity of particle i we will have

$$\mathcal{P}(v_{x,i}) = \left(\frac{m_i}{2\pi k_B T}\right)^{1/2} e^{\frac{m_i v_{x,i}^2}{2k_B T}}, \qquad i = 1, 2, 3, \ldots N. \tag{3.4}$$

Using similar relations the $\hat{y}$ and $\hat{z}$ components of the initial velocities can be also assigned. Additionally, in molecular dynamics it is usual to choose a reference frame moving with the centre of mass of the system. Since Newton's equations of motion conserve total momentum, without loss of generality this can be set to zero. So the initial momenta can be assigned to satisfy the equation

$$\mathbf{p}(t=0) = \sum_{i=1}^{N} \mathbf{p}_i(t=0) = 0. \tag{3.5}$$

The Hamiltonian of the motion of a particle will be

$$\mathcal{H}_i = \frac{\mathbf{p}_i^2}{2m_i} + \phi_i(\mathbf{r}). \tag{3.6}$$

We can easily show that

$$\frac{d\mathcal{H}}{dt} = 0 \qquad \text{and} \qquad \frac{d\mathbf{p}}{dt} = 0, \tag{3.7}$$

Thus, for a system governed by Newton's equation of motion (3.1) the total energy and total momentum are conserved. Additionally, since there is no net torque in the system the total angular momentum is also a conserved variable. However, in molecular dynamics simulations, we are concerned only for the conservation of energy and linear momentum, since periodic boundary conditions used for the simulation (section 3.7) destroy the conservation of angular momentum.

The knowledge of linear momentum at any timestep of the simulation is crucial, as it can be used to calculate, among others, two very important variables: the total kinetic energy of the system

$$K_{\text{tot}}(t) = \frac{1}{2} \sum_{i=1}^{N} \frac{\mathbf{p}_i^2(t)}{m_i}, \tag{3.8}$$

and the pressure, from the Clausius virial theorem

$$P = \frac{1}{3V} \left(\sum_{i=1}^{N} \frac{\mathbf{p}_i^2}{m_i} + \sum_{i=1}^{N} \mathbf{r}_i \cdot \mathbf{F}_i \right). \tag{3.9}$$

which for pairwise additive forces becomes

$$P = \frac{1}{3V} \left(\sum_{i=1}^{N} \frac{\mathbf{p}_i^2}{m_i} + \sum_{i=1}^{N-1} \sum_{j>i}^{N} \mathbf{r}_{ij} \cdot \mathbf{F}_{ij} \right). \tag{3.10}$$

Kinetic energy and pressure play very important role in molecular dynamics simulations because, as will be discussed in section (3.4), they are used to control the conditions of a simulation.

3.3 Statistical mechanics

In molecular dynamics, all the information regarding the properties of a system is provided at the microscopic level by calculating atomic positions, velocities and accelerations at each timestep of the simulation. The knowledge of the position and velocities of the particles at every timestep

is crucial in order to calculate the thermodynamic properties of the structure. For example, the kinetic energy can be calculated from the equipartition theorem and in the case where the structure has no net momentum, we can calculate the instantaneous temperature via

$$T(t) = \frac{2}{3fk_B} K_{\text{tot}}(t), \tag{3.11}$$

where f is the number of degrees of freedom in the system, given by

$$f = 3N - 3, \tag{3.12}$$

where N is the number of particles of the system. In basic molecular dynamics simulations the total momentum is conserved and this imposes 3 constraints, reducing the total number of degrees of freedom by 3.

However, it is of equal importance to get information at the macroscopic level for observables such as the energy, the pressure, the heat capacities and the elastic properties. In order to convert microscopic variables to macroscopic observables, it is required to use statistical mechanics.

> *Statistical mechanics is a branch of physics that combines probability theory with classical physics and quantum mechanics, to determine the thermodynamic behaviour of large systems consisting of a large number of particles.*

3.3.1 Statistical ensembles in molecular dynamics

Statistical mechanics is based on the concept of a microstate, which is a microscopic configuration of the system with a specific probability. Each microstate is defined by the positions and the momenta of the particles of the system that form the phase space. Since both position and momentum are three dimensional vectors, for a system of N particles, the phase space will have $6N$ dimensions and the state of the system will be described by a point in the phase space. As the particles of a system fluctuate around their equilibrium position, the microstates of the system change and the state of the system will move in phase space. Although the microstates of the system may change with time, some of the macroscopic variables will remain constant and will define a macrostate. The set of the points in the phase space that correspond to a specific macrostate define a statistical ensemble.

In typical molecular dynamics simulations, the total linear momentum $\mathbf{p}$ and the total energy E are constants of motion and consequently, molecular dynamics produce trajectories very close to the microcanonical NVE ensemble. However, a molecular dynamics simulation in the microcanonical ensemble cannot provide information regarding the fluctuations of energy. In general the choice of a specific ensemble determines the thermodynamic properties of which the fluctuations can be measured. Thus, apart from the microcanonical ensemble, we are able to perform molecular dynamics simulations in different ensembles, such as the canonical NVT ensemble or the isobaric-isothermal NPT ensemble.

3.3.2 The microcanonical NVE ensemble

The microcanonical ensemble represents a set of microstates of a system for which if the number of particles N and the volume V remains constant, the total energy will also be constant. In order to be in statistical equilibrium, the system must be isolated and the exchange of energy between the particles and the environment is not possible. In case the system consists of more than one atomic species, the number of particles of each species N_1, N_2, N_3, ... is also constant. In the microcanonical ensemble, each microstate $r = r(q_i, p_i; i = 1, 2, \ldots, N)$ is characterized by the same probability

$$\mathcal{P}_r = \frac{1}{\Omega} \tag{3.13}$$

where Ω is the number of microstates of the system. An immediate consequence of this is that all the microstates of the system are characterized by the same energy and so all the particles belonging in the ensemble must have the same total energy. Although the microcanonical ensemble provides a very convenient framework to study the evolution of a system, it may not give realistic results since no real world system is actually isolated from the environment.

3.3.3 The canonical NVT ensemble

The canonical ensemble represents all the possible microstates of a system that are in thermal equilibrium with a surrounding heat bath of fixed temperature. To preserve thermal equilibrium, the system must be closed and so it is not allowed to exchange particles with the environment, keeping the total number of particles N constant. However, the system can exchange heat either with the environment or with other systems that are described by any ensemble at the same temperature and it can describe real systems with increased accuracy in comparison with the microcanonical ensemble.

The Boltzmann factor and the partition function

In the canonical ensemble, the particles do not have the same energy. One of the tasks of statistical mechanics is to find the distribution of the total energy of the system in the particles. For this, it is necessary to introduce the Boltzmann factor and the partition function.

The Boltzmann factor is actually a dimensionless weighting factor, that describes the relative probability to find a particle of a system - which is at thermodynamic equilibrium with a heat bath at temperature T, in a specific energy state. For a system at temperature T, in a state of energy E_i, the Boltzmann factor is given by

$$b_i = e^{-\beta E_i}, \tag{3.14}$$

where

$$\beta = \frac{1}{k_B T}. \tag{3.15}$$

In contrast with the microcanonical ensemble, the microstates of the system in the canonical ensemble are not characterized by the same energy. For each particle of specified energy, there is a specific number of microstates with the same energy that it can occupy, a number that defines the multiplicity Ω_R of the microstate. The least energy principle requires the system to have the least possible energy. Thus, it is reasonable to assume that the multiplicity of the microstates

will decrease as the energy of the microstate increases and the particles will have an increased probability of occupying a state of lower energy. This probability is proportional to the multiplicity of the microstate and is given by

$$P_i \propto \Omega_R(E_i), \tag{3.16}$$

resulting in

$$\mathcal{P}_i = \frac{1}{Z_{\mathrm{NVT}}} e^{-\beta E_i}, \tag{3.17}$$

where

$$Z_{\mathrm{NVT}} = \sum_i e^{-\beta E_i}, \tag{3.18}$$

is the partition function, which contains all the information regarding the statistical properties of a system at thermodynamic equilibrium. The importance of the partition function lies in the fact that the knowledge of the exact form of partition function allow us to know how the particles of a system are distributed in the different energy states and additionally to calculate all the basic thermodynamic variables.

3.3.4 Isothermal-Isobaric NPT ensemble

For simulations of homogeneous fluids, it is common to use the isothermal-isobaric NPT ensemble, in which the number of particles N, the pressure P and the temperature T of the system remain constant, allowing the volume and the total energy to change. The probability density is given by

$$\mathcal{P} = \frac{1}{Z_{\mathrm{NPT}}} e^{-\beta(E+PV)} \tag{3.19}$$

where the partition function can be written as a combination of the partition functions of the canonical ensembles as

$$Z_{\mathrm{NPT}} = \sum_V e^{-\beta PV} Z_{\mathrm{NVT}} \tag{3.20}$$

3.3.5 The ergodic hypothesis

As discussed in the previous paragraphs, the great power of statistical mechanics is based on the calculation of average variables, achieved by averaging all the points of the phase space. Phase space defines a continuous 6N-dimensional volume and the average variables cannot be calculated using the above summation. For a given thermodynamic observable $A(\mathbf{p}^N, \mathbf{r}^N)$ which is a function of the positions $\mathbf{r}$ and momenta $\mathbf{p}$, the canonical ensemble average is given by

$$\langle A \rangle_e = \iint \mathcal{P}(\mathbf{p}^N, \mathbf{r}^N) A(\mathbf{p}^N, \mathbf{r}^N) d\mathbf{p}^N d\mathbf{r}^N. \tag{3.21}$$

In this equation, $\mathcal{P}(\mathbf{p}^N, \mathbf{r}^N)$ is the probability density written as a function of $\mathbf{r}$ and $\mathbf{p}$, given by

$$\mathcal{P}(\mathbf{p}^N, \mathbf{r}^N) = \frac{1}{Z} e^{-\beta \mathcal{H}(\mathbf{p}^N, \mathbf{r}^N)}, \tag{3.22}$$

where $\mathcal{H}(\mathbf{p}^N, \mathbf{r}^N)$ is the Hamiltonian and

$$Z = \iint e^{-\beta \mathcal{H}(\mathbf{p}^N, \mathbf{r}^N)} d\mathbf{p}^N d\mathbf{r}^N \tag{3.23}$$

is the partition function in the classical limit. However, in molecular dynamics simulations it is impossible to access all the points of the phase space and instead, time averaged variables are calculated using equation

$$\langle A \rangle_t = \lim_{\tau \to \infty} \left[\frac{1}{\tau} \int_0^\tau A(\mathbf{p}^N(t), \mathbf{r}^N(t)) \right] dt \simeq \frac{1}{n_{\text{ts}}} \sum_{t=1}^{n_{\text{ts}}} A(\mathbf{p}^N, \mathbf{r}^N), \tag{3.24}$$

where τ is the total simulation time, n_{ts} the number of timesteps and $A(\mathbf{p}^N, \mathbf{r}^N)$ the instantaneous value of observable A. In order for the two approaches to be equivalent, it is necessary to assume that over long periods of time, the time spent by a particle in some region of the phase space of microstates with the same energy is proportional to the volume of this region. This is known as the ergodic hypothesis and plays a very crucial role in molecular dynamics simulations. Because of this hypothesis the statistical ensemble averages are equal to time averages of the system and can be calculated using

$$\langle A \rangle_e = \langle A \rangle_t. \tag{3.25}$$

3.4 Molecular dynamics at constant temperature

Basic molecular dynamics simulations produce trajectories in the microcanonical NVE ensemble and require the total energy of the system to be constant. However, as mentioned in section 3.3.2, the microcanonical ensemble only simulates isolated systems. That is unrealistic. Additionally, the use of the NVE ensemble does not give access to all the properties of a system. In order to make simulations related more closely to laboratory experiments and be able to access more features of the simulated system, it is necessary to use the canonical NVT ensemble that requires the temperature of the system to be constant. This would be a very easy task if we could solve the equations of motions analytically. Molecular dynamics simulations however, involve the numerical integration methods described in section 3.6 that allow the temperature to fluctuate. To control the temperature in a molecular dynamics simulation, at least four different methods can be used:

1. Velocity scaling.
2. Gaussian constraints
3. Addition of stochastic forces.
4. Use of extended Lagrangian formalism.

3.4.1 Deterministic thermostats

Velocity scaling: Isokinetics and Berendsen thermostat

The simplest way to control the temperature is to use the equipartition theorem, according to which the temperature of the system is a linear combination of the linear momenta of the particles

consisting the system given by

$$T = \frac{1}{3fk_B} \sum_{i=1}^{N} \frac{\mathbf{p}_i^2}{m_i}, \tag{3.26}$$

and rescale the velocities at every timestep of the simulation by multiplying them with a scale factor so that

$$\gamma = \left[\frac{T_{\text{req}}}{T(t)} \right]^{1/2}, \tag{3.27}$$

where T_{req} is the required temperature and $T(t)$ the kinetic temperature at time t. This thermostat conserves the kinetic energy and is called the ad-hoc thermostat.

A preferable temperature control method involves the Berendsen thermostat [131]. Unlike ad-hoc rescaling, the momenta scale factor is

$$\gamma = \left[1 + \frac{\Delta t}{\tau} \left(\frac{K_{\text{req}}}{K_{\text{tot}}} - 1 \right) \right]^{1/2}, \tag{3.28}$$

where Δt is the timestep of the simulation, τ is the coupling constant of the thermostat that indicates how strong is the coupling of the system with a hypothetical heat bath at constant temperature T_{req} and is proportional to the time needed by the thermostat to set the temperature to the required value, K_{tot} is the total kinetic energy of the system and finally

$$K_{\text{req}} = \frac{f}{2} k_B T_{\text{req}}, \tag{3.29}$$

is the total kinetic energy corresponding to the desired temperature. As it can be easily shown, when $\tau = \Delta t$ Berendsen and ad-hoc rescaling are identical. Both the ad-hoc and Berendsen thermostats can be easily implemented in a molecular dynamics scheme. However, if we choose to rescale temperature at every timestep of the simulation, the temperature will remain constant during the simulation and energy fluctuations will not be captured correctly. Consequently these thermostats, when applied to every timestep of the simulation, fail to produce trajectories in the canonical ensemble.

Gaussian constraints: Evans thermostat

In this scheme, the kinetic energy of the system is assumed to be a constant of motion [132]. The scheme uses a modified set of equations of motion, based on Gauss's principle of least constraint

$$\dot{\mathbf{r}}_i = \frac{\mathbf{p}_i}{m_i}, \tag{3.30}$$

$$\dot{\mathbf{p}}_i = \mathbf{F}_i - \gamma \mathbf{p}_i, \tag{3.31}$$

where γ is a kinetic temperature constraint that can be easily calculated from the equipartition theorem

$$\sum_{i=1}^{N} \frac{\mathbf{p}_i^2}{2m_i} = \frac{f}{2} k_B T. \tag{3.32}$$

Since the kinetic energy and the temperature are constants of motion, by taking the time derivatives we have

$$\sum_{i=1}^{N} \frac{\dot{\mathbf{p}}_i \cdot \mathbf{p}_i}{m_i} = 0, \tag{3.33}$$

and if we substitute $\dot{\mathbf{p}}_i$ from (3.31)

$$\sum_{i=1}^{N} \frac{(\mathbf{F}_i - \gamma \mathbf{p}_i) \cdot \mathbf{p}_i}{m_i} = 0. \tag{3.34}$$

Solving this equation for gamma, we can easily find that

$$\gamma = \frac{1}{2K_{\text{tot}}} \sum_{i=1}^{N} \frac{1}{m_i} (\mathbf{p}_i \cdot \mathbf{F}_i). \tag{3.35}$$

The Evans thermostat conserves the kinetic energy and generates trajectories in the NVE_{kin} ensemble. For this reason it is known as the isokinetic thermostat.

The Nosé-Hoover thermostat

In 1984, Nosé proposed an alternative deterministic thermostat, based on a more general formulation of mechanics based on the Hamilton, Lagrange and Gauss formalisms, involving an extended phase space, by reformulating Newton's equations of motion [133]. In detail, Nosé added two additional degrees of freedom to the Hamiltonian of the system, which he re-wrote as

$$\mathcal{H} = \frac{1}{2} \sum_{i=1}^{N} \frac{\mathbf{p}_i^2}{m_i} + \sum_{i=1}^{N-1} \sum_{j>i}^{N} \phi_i(\mathbf{r}_{ij}) + \frac{\mathbf{p}_s^2}{2Q} + (3N+1) k_B T_{\text{req}} \ln s, \tag{3.36}$$

where $\mathbf{s}$ and $\mathbf{p}_s$ are the generalized position and momentum of an imaginary heat bath coupled to the system and Q an effective mass, related to position $\mathbf{s}$, as

$$\mathbf{p}_s = Q\dot{\mathbf{s}}. \tag{3.37}$$

The third and fourth terms on the right hand side represent the kinetic and potential energy of the imaginary heat bath. The momentum of each particle is scaled to satisfy the equation

$$\mathbf{p}_i = m_i \mathbf{v}_i s. \tag{3.38}$$

It can be proven that the Nosé thermostat produces trajectories in the canonical ensemble and since the evolution of the system is deterministic instead of stochastic, it can be used to approximate the true dynamics of the system. In order to deploy this thermostat in a simulation, the constant Q needs to be specified, as it determines the energy exchange rate between the system and the imaginary heat bath.

However, the above formulation of the thermostat is not convenient, as the momenta scaling by the factor s requires the time t to be an additional variable of the simulation. To eliminate this problem, Hoover [134] developed a different formulation of the Nosé thermostat by writing the

Hamiltonian as

$$\mathcal{H} = \frac{1}{2}\sum_{i=1}^{N}\frac{\mathbf{p}_i^2}{m_i} + \sum_{i=1}^{N-1}\sum_{j>i}^{N}\phi_i(\mathbf{r}_{ij}) + \frac{\gamma^2(t)Q}{2} + 3Nk_BT_{\text{req}}\ln s, \tag{3.39}$$

in which γ is a friction coefficient that replaces p_s and actually represents the scaled velocity of the particles. To calculate the evolution of the position of the particles, Hoover used the equations

$$\dot{\mathbf{r}}_i = \mathbf{v}_i, \tag{3.40}$$

$$\dot{\mathbf{p}}_i = \mathbf{F}_i - \gamma\mathbf{v}_i, \tag{3.41}$$

$$\dot{\gamma} = \frac{1}{Q}\left[\frac{1}{2}\sum_{i=1}^{N}\frac{\mathbf{p}_i^2}{m_i} - 3Nk_BT_{\text{req}}\right], \tag{3.42}$$

The third equation can be written in a more convenient form that demonstrates the strength of the coupling as

$$\dot{\gamma} = -\frac{1}{\tau_T^2}\left[\frac{T_{\text{req}}}{T} - 1\right], \tag{3.43}$$

where

$$\tau_T^2 = \frac{Q}{Nk_BT_{\text{req}}}, \tag{3.44}$$

is the effective relaxation time of the thermostat. To apply the Nosé-Hoover thermostat, it is necessary to use an integration scheme designed for 1st order equations of motion ,consistent with the above equation, such as the fourth order Runge-Kutta method.

3.4.2 Stochastic NVT thermostats

Andersen thermostat

As discussed in section 3.2, initial velocities of the particles in a molecular dynamics simulations can be assigned using a Maxwell-Boltzmann distribution. The basic idea behind the Andersen thermostat [135], is to add a stochastic element to the temperature, by assuming random collisions of the particles with an imaginary heat bath. In this scheme, every particle of the system is assumed to collide with imaginary particles of the heat bath with a frequency ν. After the assumed collision, all the components of particle's velocity are reassigned using a Maxwell-Boltzmann distribution. The probability of the collisions is described by a Poisson process given by

$$P_c(t) = 1 - e^{-\delta t/\tau_T}, \tag{3.45}$$

where τ_T is the relaxation time of Andersen thermostat. In the hardest collision scenario, the collided particles undergo a complete reset of their momentum using a Maxwell-Boltzmann distribution. It can be proven that infinitely long trajectories, generated using the Andersen thermostat and averaged over a large number of collisions, belong to the canonical ensemble.

Langevin thermostat

An alternative to the Andersen thermostat is the Langevin thermostat [136, 137], which adds a stochastic friction force to reassign the velocities of the particles. The Langevin thermostat controls

temperature by using the modified Newton's equations of motion

$$\begin{aligned}\dot{\mathbf{r}}_i(t) &= \mathbf{v}_i(t),\\ \dot{\mathbf{p}}_i(t) &= \mathbf{F}_i(t) - \gamma(t)\mathbf{p}_i(t) + \mathbf{r}_i(t),\end{aligned} \tag{3.46}$$

where $\gamma(t)$ is the friction coefficient and $\mathbf{r}_i$ a random force on atom i due to stochastic collisions of the particles with the imaginary heat bath, with a dispersion σ_i related to the friction coefficient $\gamma(t)$ via

$$\sigma_i = \frac{2m_i\gamma(t)k_BT}{\delta t}. \tag{3.47}$$

In order to produce trajectories in the canonical ensemble, the random force $\mathbf{r}_i$ must oppose the viscous force. Additionally, $\mathbf{r}_i(t)$ is uncorrelated in time and its mean value is given by

$$\langle \mathbf{r}_i(t), \mathbf{r}_j(t')\rangle = 6k_B m_i\gamma(t)T(t)\delta_{ij}\delta(t-t') \tag{3.48}$$

Just like the Andersen thermostat, the Langevin thermostat also destroys momentum transport so it is not recommended in simulations where transport properties are to be calculated.

The great advantage of the Langevin thermostat is that it thermostats the system on a local scale. Particles with high kinetic energies are slowed down by the friction term while those with low kinetic energies are given additional energy by the random force term.

3.5 Molecular dynamics at constant pressure

In some applications of molecular dynamics it is important to conserve the pressure of the system. To achieve that it is necessary to use barostats to control the pressure during the simulation. In general, pressure is controlled by adjusting the size of the unit cell and rescaling the positions of atoms at each timestep.

3.5.1 Berendsen barostat

The most widely used barostat for the pressure control is the Berendsen barostat [131], based on the instantaneous pressure, given by (3.9). The Berendsen barostat applies a scale factor η, given by

$$\eta = \left[1 - \frac{\Delta t}{\tau_P}[P - P_{\text{req}}]\right]^{1/3}, \tag{3.49}$$

where τ_P is the relaxation time of the barostat, to rescale the lengths of the system according to

$$\mathbf{r}_i(t) \longrightarrow \eta\mathbf{r}_i \qquad \text{and} \qquad L \longrightarrow \eta^3 L. \tag{3.50}$$

3.5.2 Nosé-Hoover barostat

As for the control of temperature, we can use a deterministic approach to control pressure based on the Nosé-Hoover thermostat, proposed by Melchionna et. al. [138]. The Nosé-Hoover equations

of motion are modified as

$$\dot{\mathbf{r}} = \mathbf{v} + \eta[\mathbf{r} - \mathbf{r}_{\mathrm{cm}}], \tag{3.51}$$

$$\dot{\mathbf{p}} = \mathbf{F} - [\gamma + \eta]\mathbf{p}, \tag{3.52}$$

$$\dot{\gamma} = \frac{1}{\tau_T^2}\left[\frac{T}{T_{\mathrm{req}}} - 1\right], \tag{3.53}$$

$$\dot{\eta} = \frac{1}{Nk_B T_{\mathrm{req}}\tau_P^2}[P - P_{\mathrm{req}}], \tag{3.54}$$

$$\dot{V} = 3\eta V, \tag{3.55}$$

where $\mathbf{r}_{\mathrm{cm}}$ is the position of the centre of mass of the system at time t. With the Nosé-Hoover barostat, the conserved quantity is

$$\mathcal{H}_{NPT} = \mathcal{H}_{NVE} + P_{\mathrm{req}}V(t) + \frac{3Nk_B T_{\mathrm{req}}}{2}\eta^2(t)\tau_P^2, \tag{3.56}$$

and represents within a constant the Gibbs free energy of the system (and can be used to check the dynamics of the system).

3.6 Integrating the equations of motion

As mentioned in the previous sections, molecular dynamics simulations require the solution of Newton's equations of motion. For a three dimensional system of N particles, we need to solve $3N$ second order differential equations in the form of (3.1), where the force depends on the $3N$ positional coordinates. For $N > 2$, this task cannot be performed analytically and it is necessary to seek a numerical solution.

All numerical methods are based on the initial value problem

$$\frac{dy}{dt} = f(t, y), \qquad y(t_0) = y_0. \tag{3.57}$$

In molecular dynamics simulations we cannot calculate the position and velocity of a particle as a continuous function of time and consequently it is impossible to calculate the analytical form of the differentials $\dot{\mathbf{r}}$ and $\dot{\mathbf{v}}$. However, since we are only interested in finding the position and velocities of the particles at each timestep of the simulation, we can use the same initial value problem in the form

$$\frac{\Delta y}{\Delta t} = f(t, y), \qquad y(t_0) = y_0. \tag{3.58}$$

where Δt is the timestep of the simulation, and give approximate solutions at discrete times $t_0, t_1, t_2, \ldots$ for which $\Delta t = t_{n+1} - t_n = h$. In general the distance h between two consecutive points is known as the step and in the case of molecular dynamics simulations it is equivalent to the timestep of the simulation. The size of this step determines the accuracy of the solution and in general, the smaller the step, the greater the accuracy of the solutions.

The basic idea behind this algorithm is that if we know the initial position $\mathbf{r}(t = 0)$, the initial velocity $\mathbf{v}(t = 0)$ and the initial acceleration $\mathbf{a}(t = 0)$ of the particles, we can use them to find the

position, velocity and acceleration at Δt. Then, using $\mathbf{r}(\Delta t)$, $\mathbf{v}(\Delta t)$ and $\mathbf{a}(\Delta t)$ as reference values, we can calculate the position, velocity and acceleration at $2\Delta t$. Repeating this process for a desired number of n timesteps Δt, it is possible to calculate the position, velocity and acceleration at any discrete moment $n\,\Delta t$.

The integration of the equations of motion may be performed using simple numerical integration techniques, such as Euler's method or more complex algorithms, developed for molecular dynamics simulations, such as Verlet's algorithm, Verlet's velocity algorithm and the leapfrog algorithm or the even more complicated but also more accurate Runge-Kutta method.

3.6.1 Euler's method

In this method we consider the Taylor's expansion of position and velocity vectors around time t for a timestep $\Delta t = h$, given by

$$\mathbf{r}(t+h) = \mathbf{r}(t) + \mathbf{v}(t)h + O(h^2), \tag{3.59}$$

$$\mathbf{v}(t+h) = \mathbf{v}(t) + \dot{\mathbf{v}}(t)h + O(h^2). \tag{3.60}$$

By keeping only the first two terms of the expansion we can write these equations in the form of linear recurrence equations as

$$\mathbf{r}_{n+1} = \mathbf{r}_n + \mathbf{v}(t)h, \tag{3.61}$$

$$\mathbf{v}_{n+1} = \mathbf{v}_n + \dot{\mathbf{v}}(t)h. \tag{3.62}$$

Considering that $\dot{\mathbf{v}}(t) = \mathbf{v}(t)$ and $\dot{\mathbf{v}}(t) = \mathbf{F}(t)/m$ we have

$$\mathbf{r}_{n+1} = \mathbf{r}_n + \mathbf{v}_n h, \tag{3.63}$$

$$\mathbf{v}_{n+1} = \mathbf{v}_n + \frac{\mathbf{F}_n}{m}h. \tag{3.64}$$

With the initial positions, velocities and forces known, these equations give directly the position and velocity at time $t + \Delta t$. Then, using $\mathbf{v}(t + \Delta t)$, $\mathbf{v}(t + \Delta t)$ and $\mathbf{F}(t + \Delta t)$ as reference values, we can calculate the position and velocity at time $t + 2\Delta t$ and so on.

Although this method is quite simple and straightforward, for small step values, it is associated with large errors of order of h^2 in the calculation of the trajectories, because all the higher order terms of the position and velocity expansions are discarded. To minimize error it is necessary to use more terms from the Taylor's expansion.

3.6.2 Explicit Runge-Kutta method

Euler's method take into account the first two terms of Taylor's expansion, up to the first derivative. To increase the accuracy we can use explicit Runge-Kutta methods[1] of order s that include in the calculation the first s derivatives.

[1] Explicit Runge-Kutta methods are used for the integration of ordinary differential equations. For partial differential equations it is necessary to use implicit Runge-Kutta methods.

Second order Runge-Kutta method takes into account the first two derivatives of the Taylor's expansion of the position and velocity, and the solution of an initial value problem is given by

$$y_{n+1} = y_n + \frac{1}{2}(k_1 + k_2), \tag{3.65}$$

where

$$k_1 = hf(t_n, y_n) \qquad \text{and} \qquad k_2 = hf(t_n + h, y_n + k_1). \tag{3.66}$$

The error in the second order Runge-Kutta method is of order h^3 which is smaller than the one resulting from Euler's method but it can still be significant. To further reduce the error we can use the fourth order Range-Kutta method, according to which

$$y_{n+1} = y_n + \frac{1}{6}\left(k_{n,1} + 2k_{n,2} + 2k_{n,3} + k_{n,4}\right), \tag{3.67}$$

where

$$k_{n,1} = hf(t_n, y_n), \tag{3.68}$$
$$k_{n,2} = hf(t_n + h/2, y_n + k_{n,1}/2), \tag{3.69}$$
$$k_{n,3} = hf(t_n + h/2, y_n + k_{n,2}/2), \tag{3.70}$$
$$k_{n,4} = hf(t_n + h, y_n + k_{n,3}). \tag{3.71}$$

The fourth order Runge-Kutta method uses the first four derivatives of the Taylor's expansion and consequently the resulting errors are of order h^5.

For Newton's second law, we can determine velocities and positions according to the equations

$$\dot{\mathbf{v}}(t) = \frac{\mathbf{F}(t)}{m}, \qquad \text{and} \qquad \dot{\mathbf{r}}(t) = \mathbf{v}(t). \tag{3.72}$$

We can apply Runge-Kutta methods to these equations, for each component of the position and velocity, to determine with increased accuracy the trajectories of the particles. However, this method is more demanding in terms of calculation time in comparison with Euler's method.

3.6.3 Numerical solution of the simple harmonic oscillator

To investigate the effect of the truncation of Taylor's series, we can apply the previous integration methods in a one dimensional system, such as the simple harmonic oscillator. This system describes the movement of a mass m, experiencing a restoring harmonic force

$$F = -kx, \tag{3.73}$$

where k is a positive constant, related to the mass and the angular frequency ω via

$$k = m\omega^2. \tag{3.74}$$

The corresponding potential is given by

$$V(x) = \frac{1}{2}m\omega^2 x^2. \tag{3.75}$$

The analytical solution for the simple harmonic oscillator is

$$x(t) = x_0 \cos(\omega t) + \frac{v_0}{\omega}\sin(\omega t), \tag{3.76}$$

$$v(t) = v_0 \cos(\omega t) - \omega x_0 \sin(\omega t), \tag{3.77}$$

where x_0 and v_0 are the initial position and velocity respectively. The total energy of the system is given by

$$E_{\text{tot}} = \frac{1}{2}mv^2(t) + \frac{1}{2}kx^2(t) = \frac{1}{2}mv_0^2 + \frac{1}{2}kx_0^2 = \text{constant}. \tag{3.78}$$

Using Euler's method with a timestep Δt, we will have

$$x(t+\Delta t) = x(t) + v(t)\Delta t \qquad \text{and} \qquad v(t+\Delta t) = v(t) - \frac{k}{m}x(t)\Delta t. \tag{3.79}$$

For the Runge-Kutta methods, we need to solve the set of coupled differential equations

$$\frac{dx(t)}{dt} = v(t) \qquad \text{and} \qquad \frac{dv(t)}{dt} = -\frac{k}{m}x(t). \tag{3.80}$$

For the second order Runge-Kutta method, the position and velocity at time $t + \Delta t$ will be given by (3.65) and since the right hand side of equations (3.80) are only functions of time, k_1 and k_2 will be

$$k_{1,x} = v(t)\Delta t, \qquad k_{1,v} = -\frac{k}{m}x(t)\Delta t, \tag{3.81}$$

$$k_{2,x} = v(t+\Delta t)\Delta t, \qquad k_{2,v} = -\frac{k}{m}x(t+\Delta t)\Delta t. \tag{3.82}$$

For the calculation of $x(t + \Delta t)$ and $v(t + \Delta t)$, we use the first three terms of the respective Taylor series.

In a similar approach, the position and velocity in the fourth order Runge-Kutta method is given by (3.67) where

$$k_{1,x} = v(t)\Delta t, \qquad k_{1,v} = -\frac{k}{m}x(t)\Delta t \tag{3.83}$$

$$k_{2,x} = v(t+\Delta t/2)\Delta t, \qquad k_{2,v} = -\frac{k}{m}x(t+\Delta t/2)\Delta t \tag{3.84}$$

$$k_{3,x} = v(t+\Delta t/2)\Delta t, \qquad k_{3,v} = -\frac{k}{m}x(t+\Delta t/2)\Delta t \tag{3.85}$$

$$k_{4,x} = v(t+\Delta t)\Delta t, \qquad k_{4,v} = -\frac{k}{m}x(t+\Delta t)\Delta t, \tag{3.86}$$

and for the calculation of position and velocity at $t + \Delta t/2$ and $t + \Delta t$ we use the first five terms of the Taylor series.

The truncation of Taylor's expansion of the position and velocity plays a crucial role in the stability of the solution. This is demonstrated in Fig. (3.1), in which the amplitude of the vibration

is plotted as a function of time, for a simple harmonic oscillator with mass $m = 1\,kg$, $k = 100\,N/m$, $x_0 = 0$ and $v_0 = 10\,m/s$. For such a system, the maximum amplitude of the vibration must be equal to $A = 1\ m$. The simulation was performed for just 200 timesteps of 0.02 s each. In the first, we can see that Euler's method provides an unstable solution as the amplitude of the vibration diverges rapidly. Second order and fourth order Runge-Kutta methods provide relatively stable solutions that are not easy to distinguish for such a short simulation. To explore the differences between the two methods, we simulated the system for 1000 timesteps of 0.02 s each (Fig. 3.2). For this longer run, it is clear that the second order Runge-Kutta integrator also diverges while the fourth order integrator manages to keep the amplitude in the range $|A| \leq 1\,m$ as expected from the analytical solution of the system. At this point it is worth mentioning that the stability of the solution is also affected by the timestep Δt. By choosing a smaller timestep we can make the second order Runge-Kutta method give more accurate results. However, for long simulations the solutions will always diverge far more rapidly in comparison with fourth order Runge-Kutta method. A similar behaviour is observed for the velocity as a function of time, resulting in the divergence of the total mechanical energy of the system. Consequently, it is preferable to use the fourth order Runge-Kutta method although its implementation is more complicated in comparison with Euler's and second order Runge-Kutta methods.

3.6.4 Verlet's algorithm

This algorithm was introduced in 1791 by Delambre and rediscovered many times since, including most recently by Verlet in the 1960s [139]. Verlet's algorithm is more complex than Euler's in-

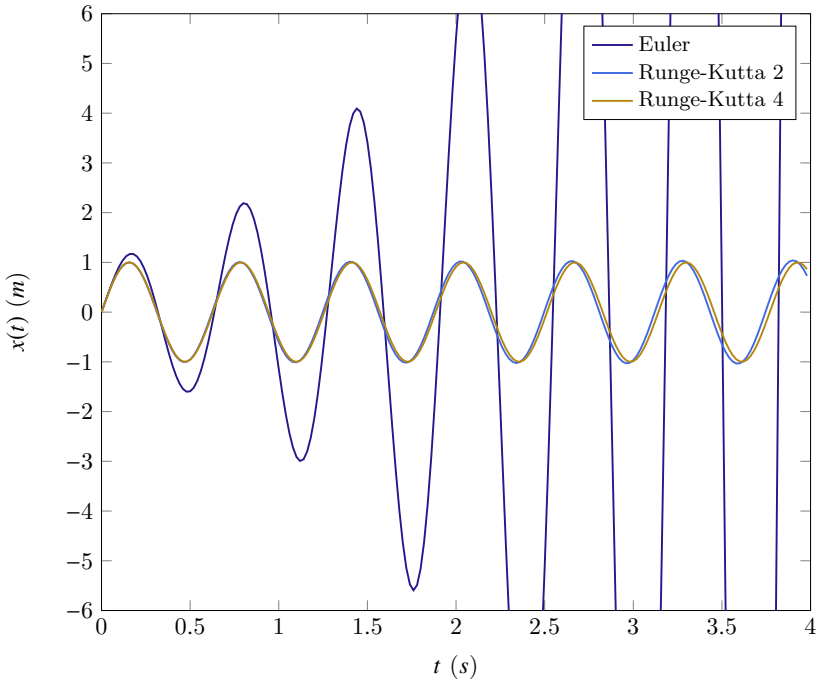

Figure 3.1: The amplitude of the vibration as a function of time, for a simple harmonic oscillator, as calculated using Euler's, second and fourth order Runge-Kutta integration methods.

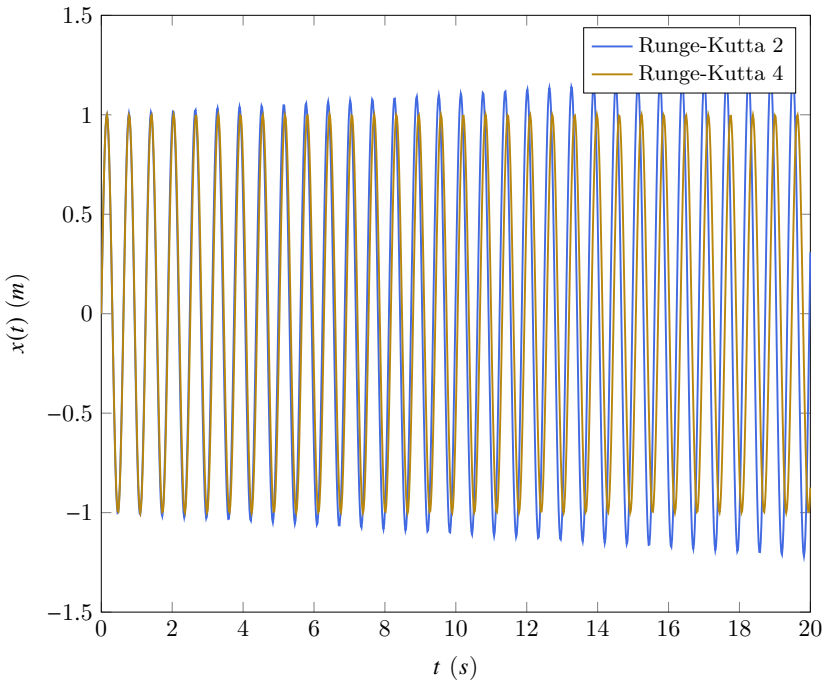

Figure 3.2: The amplitude of the vibration of a simple harmonic oscillator as calculated using the two different Runge-Kutta methods for a longer simulation.

tegration method and with no significant additional computational cost, it offers greater stability and time-reversibility in phase space, properties that are quite important in physical systems.

Verlet's algorithm is based on the Taylor's expansion of the position vector around time t for two different steps $\pm h$

$$\mathbf{r}(t+h) = \mathbf{r}(t) + \dot{\mathbf{r}}(t)h + \frac{1}{2}\ddot{\mathbf{r}}(t)h^2 + O(h^3), \tag{3.87}$$

$$\mathbf{r}(t-h) = \mathbf{r}(t) - \dot{\mathbf{r}}(t)h + \frac{1}{2}\ddot{\mathbf{r}}(t)h^2 + O(h^3). \tag{3.88}$$

Summing these two equations and rearranging gives

$$\mathbf{r}(t+h) = 2\mathbf{r}(t) - \mathbf{r}(t-h) + \ddot{\mathbf{r}}(t)h^2 + O(h^4). \tag{3.89}$$

In this algorithm, the velocity is not calculated by the integration of the equations of motion. Instead, the Störmer-Verlet method is used, according to which the velocity can be calculated by subtracting (3.87) and (3.88), in which case

$$\mathbf{v}(t) = \dot{\mathbf{r}}(t) = \frac{1}{2h}\left[\mathbf{r}(t+h) - \mathbf{r}(t-h)\right] \tag{3.90}$$

From the above equations it is obvious that the calculation of the position vector and velocity at time $t + \Delta t$ requires the knowledge of the position vectors $\mathbf{r}(t)$ and forces $\mathbf{F}(t)$ on each particle at the current timestep, but it also requires the knowledge of the position vector at time $t - \Delta t$ and this is a problem in molecular dynamics simulations since the algorithm is not self starting.

3.6.5 Verlet's velocity algorithm

To solve the problem with the calculation of positions at time $t - \Delta t$ in the Verlet algorithm and most importantly to be able to calculate velocities directly from the integration of equations of motion, a modification of the method known as Verlet's velocity algorithm was introduced that apart from the Taylor's expansion of the position vector at time $t + \Delta t$, involves the expansions of velocity [140]. Thus, we start using equations

$$\mathbf{r}(t+h) = \mathbf{r}(t) + \dot{\mathbf{r}}(t)h + \frac{1}{2}\ddot{\mathbf{r}}(t)h^2 + O(h^3), \tag{3.91}$$

$$\mathbf{v}(t+h) = \mathbf{v}(t) + \frac{d\mathbf{v}(t)}{dt}h + \frac{1}{2}\frac{d^2\mathbf{v}(t)}{dt^2}h^2 + O(h^3), \tag{3.92}$$

or, in a better form

$$\mathbf{r}(t+h) = \mathbf{r}(t) + \mathbf{v}(t)h + \frac{1}{2}\frac{\mathbf{F}(t)}{m}h^2 + O(h^3), \tag{3.93}$$

$$\mathbf{v}(t+h) = \mathbf{v}(t) + \frac{\mathbf{F}}{m}h + \frac{1}{2m}\frac{d\mathbf{F}(t)}{dt}h^2 + O(h^3). \tag{3.94}$$

Although the calculation of the position can be performed directly using (3.93), the calculation of the velocity requires the first derivative of the force. To eliminate this term, we additionally use the Taylor's expansion of the force

$$\mathbf{F}(t+h) = \mathbf{F}(t) + \frac{d\mathbf{F}(t)}{dt}h + O(h^2), \tag{3.95}$$

from which

$$\frac{d\mathbf{F}(t)}{dt}h^2 \simeq h\left[\mathbf{F}(t+h) - \mathbf{F}(t)\right]. \tag{3.96}$$

Substituting this to (3.94) we get

$$\mathbf{v}(t+h) = \mathbf{v}(t) + \frac{1}{2}\frac{\mathbf{F}}{m}h + \frac{1}{2}\frac{\mathbf{F}(t+h)}{m}h + O(h^3). \tag{3.97}$$

Discarding higher order terms, equations (3.93) and (3.97) can be written in recurrence form as

$$\mathbf{r}_{n+1} = \mathbf{r}_n + \mathbf{v}_n h + \frac{1}{2m}\mathbf{F}_n h^2, \tag{3.98}$$

$$\mathbf{v}_{n+1} = \mathbf{v}_n + \frac{1}{2}\frac{\mathbf{F}_n}{m}h + \frac{1}{2}\frac{\mathbf{F}_{n+1}}{m}h. \tag{3.99}$$

The obvious advantages of Verlet's velocity algorithm over the basic Verlet's algorithm is that it calculates the velocities directly from the force fields and also does not require the calculation of the position vector at the previous timestep, making it a more favorable option. Additionally, it follows the logic of the simple Euler's method but offers greater accuracy due to the fact that it includes in the calculations the second derivatives of the Taylor's expansion for both the position and the velocity. However, the implementation of this algorithm require two steps in the calculation, and this because, for the calculation of the velocities at time $t+h$ we must first update the forces acting

on the particles. The first step to achieve that is to write (3.93) and (3.97) in the form

$$\mathbf{r}(t+h) = \mathbf{r}(t) + h\left[\mathbf{v}(t) + \frac{h}{2}\frac{\mathbf{F}(t)}{m}\right], \tag{3.100}$$

$$\mathbf{v}(t+h) = \left[\mathbf{v}(t) + \frac{1}{2}\frac{\mathbf{F}(t)}{m}h\right] + \frac{h}{2}\frac{\mathbf{F}(t+h)}{m}. \tag{3.101}$$

The terms in the brackets are the expression of the velocity in Euler's method for half a timestep $h/2$. Thus, the four steps of the implementation are:

1. Calculate velocities at half timestep $h/2$ using Euler's method,

$$\mathbf{v}(t+h/2) = \mathbf{v}(t) + \frac{h}{2}\frac{\mathbf{F}(t)}{m}. \tag{3.102}$$

2. Use the Störmer-Verlet method for $t \longrightarrow t + h/2$ and $t - h \longrightarrow t$ to update the positions at time $t + h$,

$$\mathbf{r}(t+h) = \mathbf{r}(t) + h\mathbf{v}(t+h/2). \tag{3.103}$$

3. Use $\mathbf{r}(t+h)$ to update forces at $t + h$ directly from the interaction potential.

4. Update velocities at $t + h$

$$\mathbf{v}(t+h) = \mathbf{v}(t+h/2) + \frac{h}{2}\frac{\mathbf{F}(t+h)}{m}. \tag{3.104}$$

3.7 Periodic boundary conditions

Integration of the equations of motion requires the calculation of all the interactions between the particles of the system. In general, for a small system consisting of a few hundred or thousand particles, this is not a problem, since the system is finite and we will have a finite number of interactions - for a system of N particles the total potential energy is proportional to N^2. Additionally, the surface of such a system is well-defined and the cohesive forces between the particles are sufficient to hold the system stable [137].

However, if we want to study bulk systems things are more complicated since we practically want to study an infinite system. Additionally, particles near the surface of the simulation box will experience different forces from the particles in the bulk, leading to unnatural behaviour of the simulated system. To overcome these inconveniences, we can implement periodic boundary conditions [141], introduced by Born & von Karman in 1912. The basic idea is to create periodic images of the original simulation box and so the motion of the particle within the original simulation box is replicated in every one of the periodic images. This way, a particle can travel through the surface of the original simulation box and simultaneously, an image particle enters the simulation box through the opposite face. This way, both the total number of particles in the system as well as the number density of particles in the original box are conserved. The great advantage of the method, however, is that during the simulation we need to calculate the positions and velocities only for the particles within the original simulation cell - although a pseudo-infinite system is investigated, we can extract all the necessary information from a small and finite portion of the

infinite structure.

However, the number of interactions increases rapidly with N. If there are N particles in the original simulation box, the number of interactions will be equal to $\frac{1}{2}N(N-1)$. For the 3D case and for $N \gg 1$, the replication of the cell a times in each direction, will increase the number of interactions by a factor equal to $a^3(a^3N-1)/(N-1) \simeq a^6$. For example, if $a = 3$ this factor is equal to 729 meaning that the simulation time will be 729 times longer. To avoid increasing the number of interactions, the minimum-image convention method is used, according to which, every particle only interacts with the closest of the images or equivalently only with the particles within a volume identical to the volume of the original box, in which the reference particle is found in the centre of the volume.

A simple example of periodic boundary conditions in a two dimensional system is illustrated in Fig. 3.3. Every time a particle leaves the original simulation box (central square) through the top side, another particle enters the cell from the symmetric point at the bottom side of the cell. The procedure is exactly the same for all the periodic images of the simulation cell. To avoid enormously increasing the number of interactions between particles, the minimum-image convention method suggests to take into account only the interactions of a reference particle (particle A) with the particles within the shaded area, which has the same shape as the original box and where the reference particle lies in the centre of the area.

Special attention needs to be paid to the way the interactions between particles are handled. Periodic boundary conditions can be applied only in cases where the size of the original box is sufficient to prevent a molecule from interacting with its own image. Additionally the shape of the

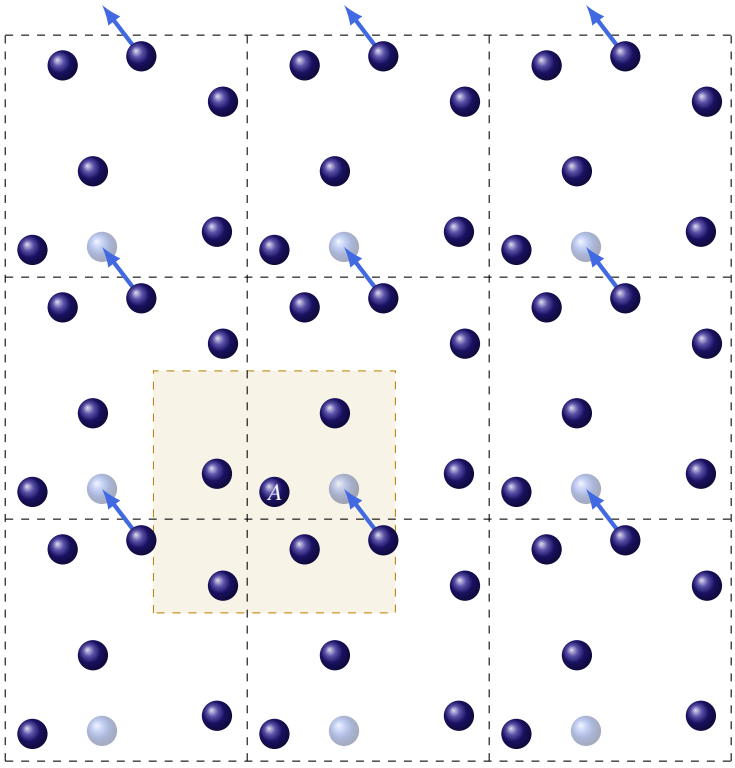

Figure 3.3: Illustration of periodic boundary conditions in a simple two dimensional system.

original simulation cell must have a geometry that will allow the periodic images to exactly fill the 3D space, without leaving any voids or overlapping. It also places a restriction on the maximum correlation length and correlation time [137].

3.8 Interaction potentials

In a real system, the total internal energy is a quantity depending on the positions and momenta of all the nuclei and electrons comprising the structure. However, it is extremely difficult to calculate the exact form of electronic interactions and thus it is necessary to use approximate interacting potentials. In general, for a system consisting of N particles, the total potential energy function can be expressed as

$$\Phi_{\text{tot}}(\mathbf{r}_i, \mathbf{r}_j, \ldots, \mathbf{r}_N) = \sum_{i=1}^{N} \phi_1(\mathbf{r}_i) + \sum_{i=1}^{N-1} \sum_{j>i}^{N} \phi_2(\mathbf{r}_i, \mathbf{r}_j) + \sum_{i=1}^{N-2} \sum_{j>i}^{N-1} \sum_{k>j}^{N} \phi_3(\mathbf{r}_i, \mathbf{r}_j, \mathbf{r}_k) + \cdots, \tag{3.105}$$

where $\phi_1(\mathbf{r}_i)$ on the right hand side describes the single particle energy which is zero unless an external field is applied to the system, $\phi_2(\mathbf{r}_i)$ the two body pair interactions, $\phi_3(\mathbf{r}_i)$ the three body interactions etc. In molecular dynamics simulations of crystalline or amorphous materials, we only take into account pair interactions.

3.8.1 Electrostatic interactions

To describe electrostatic interactions we use Coulomb's law of electrostatics, according to which, the force between two particles of charge q_1 and q_2 at a distance r_{12} is given by

$$\mathbf{F}_{12} = \frac{1}{4\pi\epsilon_0} \frac{q_1 q_2}{r_{12}^2} \hat{r}_{12}, \tag{3.106}$$

where $\hat{r}_{12}$ is the unit vector pointing from charge q_1 to q_2 or to the opposite, depending on the charge on which the force is calculated. The respective electrostatic energy is given by

$$\phi_e = \frac{1}{4\pi\epsilon_0} \frac{q_1 q_2}{r_{12}}. \tag{3.107}$$

These relations are valid for particles interacting in a vacuum. For dielectric materials, the electric permittivity ϵ_0 of the vacuum must be replaced with the electric permittivity $\epsilon = k_e \epsilon_0$ of the dielectric material, where k_e is the dielectric constant of the material.

Inside a typical atomic system, the only kind of electrostatic interactions taking place are the ionic interactions, describing the attractive and repulsive forces between ions with full formal charges.

3.8.2 Van-der-Waals interactions

Van-der-Waals interactions are a subset of electrostatic forces describing the interaction between any kind of dipoles or multipoles. They are separated into three different categories:

1. Permanent dipole-permanent dipole interactions, also known as Keesom forces, that align the molecules parallel to each other in order to minimize the potential energy of a structure.

2. Permanent dipole-induced dipole interactions, alternatively known as Debye forces resulting from the polarisation of a molecule with no permanent dipole due to the electric field of an approaching molecule with a permanent dipole.

3. Induced dipole-induced dipole interactions, or London dispersion forces, generated by the temporary repulsion of the electronic clouds between two molecules with no permanent dipoles and resulting in the creation of one partially positive and one partially negative dipole.

In general, interactions between dipoles are proportional to r^{-6} and also depend on the orientation of dipoles. It can be proven that the total Van-der-Waals energy is given by the sum of the above three terms as

$$\phi_{\mathrm{vw}} = -\frac{c_{\mathrm{vw}}}{r^6}, \tag{3.108}$$

where c_{vw} is a positive constant. From this equation it is clear that Van-der-Waals interactions are inversely proportional to the sixth power of the distance between dipoles.

3.8.3 Short range potentials and the Lennard-Jones potential

Electrostatic interactions, as described in the previous section are very accurate for large distances. However, close to atoms they are invalid because atoms and particles do not behave like point charges as assumed by Coulomb's law. The main reason is that when two atoms approach, the electronic orbitals of the two atoms overlap, resulting into a relatively strong repulsive Pauli force, the detailed calculation of which is very complicated as it requires quantum mechanical perturbation theory. The perturbation terms of the Coulombic potential consist of the interactions between the electrons of the two orbitals, the spin-spin interactions and the spin-orbital angular momentum interactions. From a computational perspective this is an extremely demanding and expensive task. To overcome these complications, John Lennard-Jones proposed an approximate interaction potential, that takes into account both the Van-der-Waals interactions and Pauli repulsion term [142]. In the most common form, the Lennard-Jones potential is expressed as

$$\phi_{\mathrm{LJ}} = 4\epsilon \left[\left(\frac{\sigma}{r}\right)^{12} - \left(\frac{\sigma}{r}\right)^{6} \right], \tag{3.109}$$

or

$$\phi_{\mathrm{LJ}} = \epsilon \left[\left(\frac{r_m}{r}\right)^{12} - 2\left(\frac{r_m}{r}\right)^{6} \right], \tag{3.110}$$

where ϵ is the depth of the potential well, σ is the distance at which the potential is equal to zero and r_m is the distance for which the respective force is zero and the Lennard-Jones potential has its minimum value.

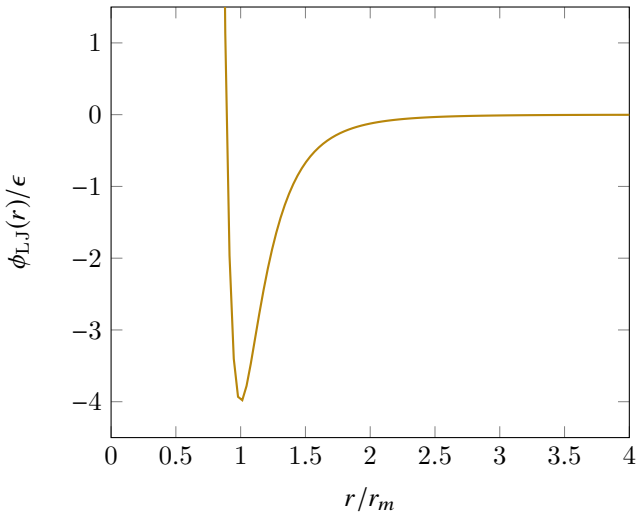

Figure 3.4: Plot of $\phi_{\mathrm{LJ}}(r)/\epsilon$ versus r/r_m of the Lennard-Jones pair potential.

Although the attractive Van-der-Waals term is well justified, the repulsive r^{-12} term has no clear physical basis. However, it approximates with very good accuracy the Pauli repulsion and its calculation is very easy and inexpensive since it is proportional to the square of r^6.

The calculation of the exact interaction energy between atoms in molecular dynamics simulations is an extremely demanding task and there are several limitations associated with the Lennard-Jones potential. First, the Lennard-Jones potential is empirical. It has only two parameters that can be fitted to up to two physical quantities using experimental data, and consequently it is not applicable to systems where more than two physical properties need to be fitted into the potential. Additionally, the Lennard-Jones bonds are spherically symmetrical and so it cannot be used in systems where directional bonding is important. Furthermore, the coordination number of an atom does not affect the strength of the bond and the bond energy is a linear function of the coordination number, in contrast with experimental data showing that the bond energy per atom increases quadratically with the coordination number [143]. Finally, the potential diverges when two atoms approach. This may lead to instabilities in molecular dynamics simulations involving highly energetic particles. Thus, in molecular dynamics simulations of atomic systems, it is common to use alternative potentials, such as the Buckingham potential, the Ziegler-Biersack-Littmark short range potential and the Stillinger-Weber potential.

3.8.4 Buckingham potential

A more flexible potential, that can be fitted to three physical parameters, is the Buckingham potential [144] given by

$$\phi_{\mathrm{Buck}}(r) = Ae^{-r/\rho} - \frac{C}{r^6}, \tag{3.111}$$

where the first term describes the Pauli repulsion energy and the second the Van-der-Waals interaction energy. In the Buckingham potential the Pauli repulsion term has a more natural exponential form in comparison with the $(r_m/r)^{12}$ Lennard-Jones term [145]. However, as shown in Fig. 3.5, Buckingham potential has a divergent region at short distances with $\lim_{r\to 0}[\phi_{\mathrm{Buck}}(r)] = -\infty$. This

may create problems in simulations of systems with either very short interatomic distances that due to the nature of the potential will converge to zero, or with energetic particles that may overcome the potential barrier and simultaneously lose energy due to collisions with other atoms and consequently be trapped in the infinite potential well. Additionally, for $r \longrightarrow 0$, Buckingham potential is attractive despite the fact that the force between two nuclei is repulsive.

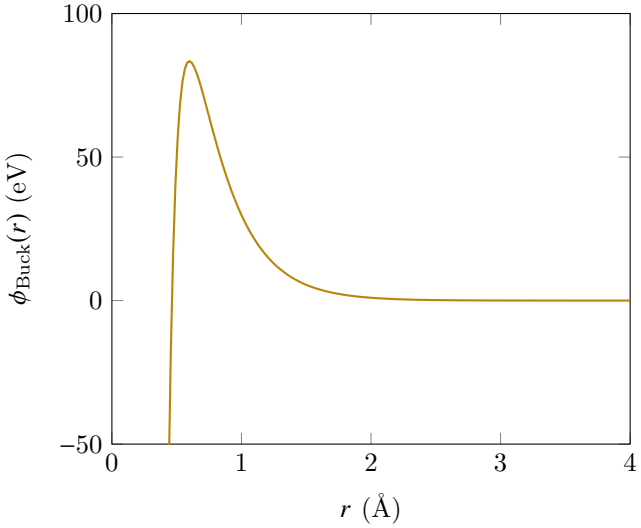

Figure 3.5: A typical form of the Buckingham potential with $A = 1000$ eV, $\rho = 0.30$ Å and $C = 1.00$ Å^6.

3.8.5 Ziegler-Biersack-Littmark short range potential

To eliminate the effects of the divergence region of the Buckingham potential, in simulations with short interatomic distances or in cases where energetic particles are involved, the Buckingham potential is combined with the short range Ziegler-Biersack-Littmark (ZBL) potential (Fig. 3.6), that describes the nuclear repulsion resulting from high-energy collisions between atoms [146]. The ZBL potential between two atoms with atomic number Z_i and Z_j is given by

$$\phi_{\mathrm{ZBL}} = \frac{1}{4\pi\epsilon_0}\frac{Z_i Z_j e^2}{r_{ij}}\sum_{k=1}^{4} c_k e^{-b_k \frac{r_{ij}}{a}}. \tag{3.112}$$

where

$$a = \frac{0.46850}{Z_i^{0.23} + Z_j^{0.23}}\ \text{Å} \tag{3.113}$$

and

$$\begin{aligned} b_1 &= 0.18175, \quad b_2 = 0.50986, \quad b_3 = 0.28022, \quad b_4 = 0.02817, \\ c_1 &= 3.19980, \quad c_2 = 0.94229, \quad c_3 = 0.40290, \quad c_4 = 0.02817. \end{aligned} \tag{3.114}$$

A ZBL potential has no natural joining point with a Buckingham potential. In order to work together, the two potentials must be truncated at distances r_{ZBL} and $r_{\mathrm{Buck}} > r_{\mathrm{ZBL}}$. They may be joined with a 3$^{\mathrm{rd}}$ or higher order spline or even with a Fermi switching function, in such a way that the total potential energy function is continuous and smooth.

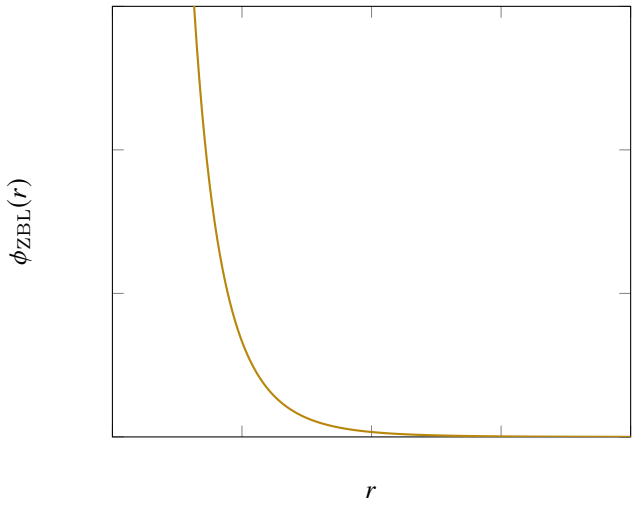

Figure 3.6: A typical form of the short range ZBL potential.

Cubic spline interpolations

To fit the two truncated potentials, the most common method is to use a cubic spline in the form

$$Q(x) = \sum_{k=0}^{3} c_k x^k. \tag{3.115}$$

The first step is to choose a set of $n+1$ points (x_i, y_i), $i = 0, 1, 2 \ldots n$ and rewrite $Q(x)$ in the parametric form

$$Q_i = (1-t)f_{i-1} + tf_i + t(1-t)[a_i(1-t) - b_i t], \tag{3.116}$$

where

$$t = t(x) = \frac{x - x_{i-1}}{x_i - x_{i-1}}. \tag{3.117}$$

In (3.116), Q_i are 3^{rd} order polynomials interpolating f in the interval $x_{i-1} < x < x_i$ for $i = 1, 2, 3 \ldots n$ such that

$$\left(\frac{dQ_i}{dx}\right)_{x_i} = \left(\frac{dQ_{i+1}}{dx}\right)_{x_i} \qquad \textit{and} \qquad \left(\frac{d^2Q_i}{dx^2}\right)_{x_i} = \left(\frac{d^2Q_{i+1}}{dx^2}\right). \tag{3.118}$$

Since there are n steps between points x_0 and x_n, we must calculate n polynomials $Q(x)$ to fill the gap between the two truncated curves. Equations (3.118) secure the continuity of the first and second derivatives of polynomials $Q(x)$, while the continuity of the polynomials is ensured using the relations

$$Q_i(x_i) = Q_{i+1}(x_i) = Q(x_i), \qquad i = 1, 2, 3, \ldots, n-1. \tag{3.119}$$

To simplify the above equations we can set

$$Q(x_i) = y_i, \qquad \text{and} \qquad \left(\frac{dQ_i(x)}{dx}\right)_{x_i} = k_i. \tag{3.120}$$

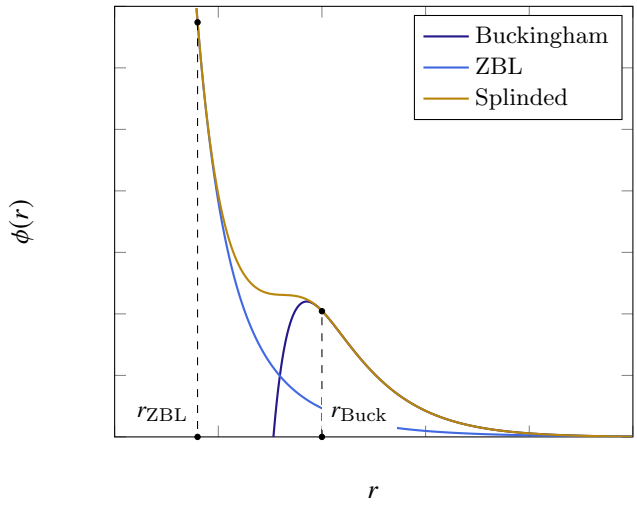

Figure 3.7: A typical splined interaction potential, along with the Buckingham and ZBL potentials. The Buckingham potential was truncated at r_{Buck} and the ZBL at r_{ZBL}. These distances are chosen so that the splined potential won't form a potential well for $r_{\text{ZBL}} < r < r_{\text{Buck}}$. Additionally the value of r_{Buck} was selected to be significantly smaller than the distance between oxygen atoms in the initial crystal.

Using this notation, parameters a_i and b_i in equation (3.116) can be calculated via

$$a_i = k_{i-1}(x_i - x_{i-1}) - (y_i - y_{i-1}), \tag{3.121}$$

and

$$b_i = -k_i(x_i - x_{i-1}) + (y_i - y_{i-1}), \tag{3.122}$$

respectively. Since there are n polynomials to be calculated, parameters a_i and b_i define a system of $2n$ equations. However, by using the continuity of the second derivatives of $Q_i(x)$, this system can be simplified into a $n \times n$ system in respect to k_i.

Three body Stillinger-Weber potential

The Lennard-Jones, Buckingham and ZBL potentials are used to describe the pair interactions between the particles of a system. But in certain cases, it is necessary to include in the simulations three body terms used to describe three particle interactions. Through the years, several three body potentials have been proposed [147, 148, 149, 150]. The most commonly used three body potential for the simulation of glasses however, is the Stillinger-Weber three body potential [148], given by

$$\phi_{\text{SW}}(r_{ij}, r_{ik}, \theta_{jik}) = \lambda e^{\left(\frac{\gamma}{r_{ij}-r_c} + \frac{\gamma}{r_{ik}-r_c}\right)}(\cos\theta_{jik} - \cos\theta_0)^2, \tag{3.123}$$

where r_{ij} and r_{ik} are the distances of the outer atoms j and k from the middle atom i of an atomic triplet $(j-i-k)$, θ_{jik} is the angle of the bonds formed by atoms j and k with atom i, r_c is the cutoff distance that defines the maximum distance for which the three body potential is applied and finally λ and θ_0 are adjustable parameters, with the latter describing the ideal bond angle.

3.8.6 Long range electrostatic potentials

All pair potentials described in the previous sections have infinite range. For large bulk systems, this will lead to a huge increase of the computational time. An alternative method is to use truncated and shifted potentials. For the Lennard-Jones potential it is common to truncate the potential at a distance $r_c = 2.5\sigma$, and shift the potential upwards so that $U_{\mathrm{LJ}}(2.5\sigma) = 0$. The final expression of the potential is

$$\phi_{\mathrm{LJ}}^{\mathrm{tr.}}(r) = \begin{cases} 4\epsilon\left[\left(\frac{\sigma}{r}\right)^{12} - \left(\frac{\sigma}{r}\right)^{6}\right] - \phi_{\mathrm{LJ}}(r_c), & \text{for} \quad r < r_c, \\ \\ 0, & \text{for} \quad r > r_c \end{cases} \tag{3.124}$$

We can follow the same approach with all pair potentials and with the electrostatic forces, for which the truncated potential can be written as

$$\phi_{\mathrm{e}}^{\mathrm{tr.}}(r) = \begin{cases} \frac{1}{4\pi\epsilon_0}\frac{q_i q_j}{r} - \phi_{\mathrm{e}}(r_c), & \text{for} \quad r < r_c, \\ \\ 0, & \text{for} \quad r > r_c \end{cases} \tag{3.125}$$

For every potential however we need to pay special attention on how to choose the truncation distance. The Lennard-Jones potential converges very fast to zero due to its dependency on r^{-6} and r^{-12}. But electrostatic forces are proportional to $1/r$ and so they converge much slower. Thus, the cutoff distance for the electrostatic forces must be much greater than the cutoff for the Lennard-Jones potential. It is common to truncate electrostatic forces to a distance equal to the half of the minimum dimension of the simulation box, to avoid a particle interacting with its own image when we use periodic boundary conditions.

Direct sum and Ewald sum of electrostatic forces

Even if the electrostatic potential is truncated, we will still have a huge number of interactions to calculate, making simulations quite expensive. One way to reduce the computation time, is to take advantage the periodic boundary conditions and perform a direct sum of the electrostatic potentials for all the images of the original simulation box. In case of a cubic cell of size L, all the electrostatic interactions can be calculated using equation

$$\Phi_{\mathrm{e}}(r) = \frac{1}{8\pi\epsilon_0}\sum_{i=1}^{N}\sum_{j\neq i}^{N}\frac{q_i q_j}{r_{ij}} + \frac{1}{8\pi\epsilon_0}\sum_{\mathbf{n}\neq\mathbf{0}}\sum_{i=1}^{N}\sum_{j=1}^{N}\frac{q_i q_j}{|\mathbf{r}_{ij} + \mathbf{n}L|}, \tag{3.126}$$

where $\mathbf{n}$ is a three-dimensional vector used to identify the positions of the image particles. The first term on the right hand side of the above equation describes the interactions of particle i with all the other particles in the original simulation box, where it cannot interact with itself, and the second the interaction of the particle with all the other particles of the image cells, include the images of the particle itself. Even with this method, the potential energy conditionally converges very slowly and even more importantly, if we model infinite bulk structures, the sum over vectors $\mathbf{n}$ must also be infinite making the computation impossible.

The faster way to compute electrostatic forces is to use the Ewald summation [151], in which the potential energy is split into two terms: one for the short range interactions, treated with a simple cutoff and one for the long range interactions which is periodic and can be approximated with satisfactory accuracy by a finite Fourier series. To perform the splitting, the first step is to neutralize every point charge of the system by using a surrounding charge distribution of equal magnitude and opposite sign, treated in real space. To remove the effects of this artificial charge distribution Ewald summation method also uses a slowly varying periodic charge density, treated in reciprocal space.

For the surrounding charge distribution, a screening function is used, most commonly in the form of a Gaussian distribution

$$\rho_s(r) = -q_i \left(\frac{\alpha}{\pi}\right)^{3/2} e^{-\alpha r^2}. \tag{3.127}$$

To compensate for the contribution of this charge density in the Coulombic energy, we use a charge distribution

$$\rho_c(r) = \sum_{\mathbf{n}} \sum_{j=1}^{N} q_j \left(\frac{\alpha}{\pi}\right)^{3/2} e^{-\alpha |\mathbf{r}-(\mathbf{r}_j+\mathbf{n}L)|}, \tag{3.128}$$

for which the Fourier transform is given by

$$\tilde{\rho}_c(r) = \sum_{j=1}^{N} q_j e^{-i\mathbf{k}\cdot\mathbf{r}_j} e^{-k^2/4\alpha}. \tag{3.129}$$

Using the Fourier's transform of Poisson's equation

$$k^2 \tilde{\phi}(k) = \frac{1}{\epsilon_0} \tilde{\rho}(k), \tag{3.130}$$

we can find that the Fourier's transformation of the respective potential energy is

$$\tilde{\phi}_j(k) = \frac{1}{k^2 \epsilon_0} \sum_{j=1}^{N} q_j e^{-i\mathbf{k}\cdot\mathbf{r}_j} e^{-k^2/4\alpha}, \tag{3.131}$$

and by using inverse Fourier's transformation, we find that the compensating potential function is

$$\phi_j(r) = \frac{1}{V} \sum_{\mathbf{k}\neq 0} \tilde{\phi}(k) e^{i\mathbf{k}\cdot\mathbf{r}} = \frac{1}{\epsilon_0 V} \sum_{\mathbf{k}\neq 0} \sum_{j=1}^{N} \frac{q_j}{k^2} e^{i\mathbf{k}\cdot(\mathbf{r}-\mathbf{r}_j)} e^{-k^2/4\alpha}. \tag{3.132}$$

The contributing of the compensating term in the potential energy is

$$\Phi_c(r) = \frac{1}{2} \sum_{i=1}^{N} q_i \phi_j(r) = \frac{1}{2\epsilon_0 V} \sum_{\mathbf{k}\neq 0} \sum_{i=1}^{N} \sum_{j=1}^{N} \frac{q_i q_j}{k^2} e^{i\mathbf{k}\cdot(\mathbf{r}-\mathbf{r}_j)} e^{-k^2/4\alpha}. \tag{3.133}$$

This term includes an interaction of particle i at $\mathbf{r}_i$ with the compensating charge distribution at the same point, described by a potential due to the Gaussian charge distribution, given by

$$\phi_{i,G}(r) = \frac{1}{4\pi\epsilon_0} \frac{q_i}{r} \operatorname{erf}(\sqrt{\alpha} r), \qquad \text{where} \qquad \operatorname{erf}(x) = \frac{2}{\sqrt{\pi}} \int_0^x e^{-r^2} dr. \tag{3.134}$$

at the centre of the distribution, for $r = 0$. This interaction corresponds to a potential energy

$$\Phi_{\text{self}}(r) = \left(\frac{\alpha}{\pi}\right)^{1/2} \sum_{i=1}^{N} q_i^2, \tag{3.135}$$

that needs to be subtracted from the total Coulombic energy.

We also need to calculate the real space contribution for the short range interactions, given by

$$\phi_{j,\text{sh}} = \frac{1}{4\pi\epsilon_0}\frac{q_j}{r} - \phi_{j,G}(r) = \frac{1}{4\pi\epsilon_0}\frac{q_j}{r}(\text{erfc}\,\sqrt{\alpha}r), \tag{3.136}$$

resulting into a potential energy term given by

$$\Phi_{\text{sh}}(r) = \frac{1}{8\pi\epsilon_0}\sum_{i=1}^{N}\sum_{j\neq i}^{N}\frac{q_i q_j}{r_{ij}}\,\text{erfc}(\sqrt{\alpha}r_{ij}) \tag{3.137}$$

Finally, the Coulombic energy calculated with Ewald summation method is

$$\Phi_{\text{e}}(r) = \Phi_c(r) - \Phi_{\text{self}}(r) + \Phi_{\text{sh}}(r). \tag{3.138}$$

For a successful implementation of the Ewald summation method one needs to specify the cutoffs for the real and the reciprocal space and also Gaussian parameter α. This step is quite important as a poor estimation of these parameters may lead to large errors in the results of the simulation.

3.9 Molecular dynamics simulations on glass wasteforms

To model the structure of borosilicate and iron phosphate glasses as well as the the effects of radiation damage, several molecular dynamics simulations have been conducted, using a large variety of interatomic potentials. In the following paragraphs, a concise and detailed description of these studies is provided to point out the necessity of a topological approach towards the characterisation of radiation damage effects in glass wasteforms.

To study simplified borosilicate glass wasteforms, Delaye & Ghaleb [15, 16, 17] used a Buckingham pair potential in the form

$$U_{\text{Buck}}(r) = Ae^{-\frac{r}{\rho}}, \tag{3.139}$$

along with the three body Stillinger-Weber potential

$$U_{\text{SW}}(r_{ij}, r_{ik}, \theta_{jik}) = \lambda e^{\left(\frac{\gamma}{r_{ij}-r_c}+\frac{\gamma}{r_{ik}-r_c}\right)}(\cos\theta_{jik} - \cos\theta_0)^2 \tag{3.140}$$

where A, ρ, λ and γ are adjustable parameters. For the short range pair interactions, the authors also used a Ziegler-Biersack-Littmark (ZBL) potential (details in section 4.9). To combine the Buckingham with the ZBL potential, the two potentials were truncated and joined with a fifth order spline.

Results of their work showed that in a simplified nuclear glass consisting of 63.8% SiO_2, 17.0% B_2O_3, 13.4% Na_2O_3, 4.0% Al_2O_3 and 1.8% ZrO_2 the number of atoms displaced from their initial positions due to irradiation increases with the kinetic energy of the incident particle, ranging form

300 to 800 eV. The authors considered a particle to be displaced if the distance between its final and initial position is larger than 1 Å. The majority of the displaced particles are sodium and oxygen atoms, with the displaced sodium atoms found near the limits of the damage cascade, while the displacement distance of the particles is independent of the atomic species. Additionally, it was observed that boron atoms are transformed from 4-coordinated to 3-coordinated and BOs are transformed to NBOs, minimizing the connectivity of the network [15]. Delaye & Ghaleb also investigated the origins of volume change in irradiated borosilicate glasses, by performing molecular dynamics simulations in a glass with the same composition [17]. Multiple damage cascades were created using impact particles with kinetic energy equal to 700 eV. Results revealed that the swelling of the glass is rapid in the first stages of the simulation and reached a saturation volume after the creation of 10 consecutive cascades. The swelling was accompanied with a depolymerisation of the structure, since the coordination number of the boron atoms was decreased and consequently the mean size of the rings was increased. The swelling was mainly due to the increase of the local volume of boron and silicon particles, as a result of the decrease in the coordination of boron atoms.

Simulations of a different glass, consisting of 60% SiO_2, 20% B_2O_3, 13% Na_2O, 5% Al_2O_3 and 2%ZrO_2, using incident particles with kinetic energies between 500 eV and 6 keV to model the irradiation process, revealed that network formers behave differently from network modifiers during the creation of damage cascades. In detail, the number of particles displaced by more than 1 Å in the polymerised regions of the structure is significantly larger from the one in the depolymerised zones [16].

The behaviour of a borosilicate glass with composition 60.2% SiO_2, 15.8% B_2O_3, 12.7% Na_2O_3, 3.9% Al_2O_3, 1.8% ZrO_2 and 5.6% CaO under α irradiation was investigated by Abbas et al. [19].

Table 3.1: Parameters of the potentials used by Delaye & Ghaleb [15, 16, 17], Delaye et al. [18], Abbas et al. [19] and Dewan et al. [20] to study the radiation damage effects in a simplified borosilicate glass.

Buckingham potential parameter A in keV ρ = 0.29 Å except for the O-O interactions for which $\rho_{\text{O-O}}$ = 0.35 Å.						
	Si	O	B	Na	Zr	Al
Si	836.42	1571.11	361.41	862.02	2557.35	961.27
O		362.670	760.90	1396.34	4805.09	1734.03
B			121.09	374.52	1031.80	366.37
Na				842.05	2637.87	976.25
Zr					7822.47	2940.61
Al						1100.46

Stillinger-Weber potential parameters. λ is expressed in eV, γ and r_c in Å and θ_0 in degrees.			
	O-Si-O	Si-O-Si	O-B-O
λ	149.808	6.242	11984.64
γ	2.6	2.0	2.27
θ_0	109.47	160.0	109.47
r_c	3.0	2.6	2.1

These authors used the same potentials as Delaye & Ghaleb [15, 16, 17] and the impact particle was given a kinetic energy of 700 eV. Results showed that the number of particles displaced by more than 1 Å increases during the first 0.1 ps, where the damage cascade is created and the structure is depolymerised, and then it decreases significantly as the structure relaxes and repolymerises.

Delaye et al. [18] performed simulations of an irradiated CJ1 glass with molecular composition 67.7% SiO_2, 18.1% B_2O_3 and 14.2% Na_2O_3, using again the same potentials as Delaye & Ghaleb [15, 16, 17]. The kinetic energy of the impact particle was selected to be equal to 600 eV and it was found that the creation of the damage cascade resulted in the disorder within the glass. In contrast with previous results, these authors found that the mean ring size of the irradiated structure decreased in comparison with the one of the initial undamaged glass. The same glass structure was also simulated by Dewan et al. [20] who performed a topological analysis of the structure. The system was subjected to 300 cascades of 4 keV each. The results revealed that the number of 4-coordination boron atoms decreases with the number of cascades, leading to the domination of 3-coordinated boron atoms while the average ring size increases, indicated a depolymerisation of the structure.

Gu et al. [152], examined the chemistry of sodium borosilicate glasses with various compositions given by $(B_2O_3)_x(Na_2Si_2O_5)_{1-x}$ for $x = 0.3, 0.5, 0.7$, using a Born-Mayer-Huggins potential in the form

$$U_{\mathrm{BMH}}(r_{ij}) = \left(1 + \frac{Z_i}{n_i} + \frac{Z_j}{n_j}\right) b_{ij} e^{\frac{\sigma_i + \sigma_j - r_{ij}}{\rho_{ij}}} + \frac{1}{4\pi\epsilon_0} \frac{Z_i Z_j e^2}{r_{ij}}, \tag{3.141}$$

where n_i, n_j are the number of valence electrons of atoms i and j respectively, σ_i, σ_j the atomic sizes and b_{ij}, ρ_{ij} constants. For the three body interactions, these authors used the same three body Stillinger-Weber potential used by Delaye & Ghaleb [15, 16]. They concluded that the tetrahedral coordination of silicon atoms remains invariant with the increase of B_2O_3 concentration, while the boron tetrahedra are decreased in favour of 3-coordinated boron atoms.

Abbas et al. [21] performed molecular dynamics simulations to study the structure and surface dynamic behaviour of a borosilicate glass consisting of 53.3% SiO_2, 14.05% B_2O_3, 11.3% Na_2O_3, 3.4% Al_2O_3, 1.6% ZrO_2 and 5.0% CaO, using a Buckingham pair potential in the form of (3.139) supplemented with a three body Stillinger-Weber potential, with parameters given in Table 3.2. The results suggested that the glass behaves in a different manner on the surface, as the structural properties deviate from those in the bulk glass. The reason behind this behaviour is the accumulation of alkali oxides near the surface of the glass resulting in the lower coordination of atoms at the outer layers of the structure. This depolymerisation near the surface results in the formation of slightly larger rings in comparison with those in the bulk.

Kieu et al. [22] developed composition dependent empirical potentials for the study of sodium borosilicate glasses by assuming fractional charges for the different atoms, unlike previous studies in which the charges of the atoms were integers. They used only a pair Buckingham potential with parameters given in Table 3.3. Kieu assumed that the charges of atoms in the sodium borosilicate glasses are given by

$$q'_{\mathrm{B}} = -q'_{\mathrm{O}} \left(C_6 K^2 + \sum_{i=0}^{5} C_i R_i\right) \tag{3.142}$$

Table 3.2: Parameters of the potentials used by Abbas et al. [21] to study the structure and surface behaviour of borosilicate glasses.

Buckingham potential parameter A in keV ρ = 0.29 Å except for the O-O interactions for which $\rho_{\text{O-O}}$ = 0.35 Å.							
	Si	O	B	Na	Zr	Al	Ca
Si	876.02	1645.89	353.45	903.59	2679.25	956.46	4000.81
O		369.31	769.92	1462.63	5034.05	1725.23	6873.07
B			126.76	392.61	1080.99	394.48	1691.08
Na				882.37	2763.58	971.38	3990.64
Zr					8185.01	2925.38	12236.19
Al						1039.67	4326.64
Ca							17898.94

Stillinger-Weber potential parameters. λ is expressed in eV, γ and r_c in Å and θ_0 in degrees.				
	O-Si-O	Si-O-Si	O-B-O	O-Al-O
λ	124.840	6.242	9363.000	149.808
γ	2.6	2.0	2.27	2.6
θ_0	109.47	160.0	109.47	109.47
r_c	3.0	2.6	2.1	3.0

and

$$q_i' = q_i - \frac{N_{\text{B}}}{N_{\text{Si}} + N_{\text{O}} + N_{\text{Na}}}(q_{\text{B}}' - q_{\text{B}}), \qquad \text{where} \qquad i = \text{Si, O, Na}, \tag{3.143}$$

where

$$\begin{aligned} C_0 &= 1.49643, & C_1 &= -0.2950, & C_2 &= -0.2565, \\ C_3 &= 0.08721, & C_4 &= -0.01323, & C_5 &= 0.00073, \end{aligned} \tag{3.144}$$

and

$$C_6 = 0.00315 \qquad \text{for } R > 0.55 \qquad \text{or} \qquad C_6 = 0 \qquad \text{for } R \leq 0.55. \tag{3.145}$$

Using this approach Kieu managed to control bond angles to the desired values without using the three body Stillinger-Weber potential.

Table 3.3: Buckingham potential parameters used by Kieu et al. [22]

Bond	A (eV)	ρ (Å)	C (eV·Å^6)
Si-O	45296.72	0.161	46.1395
Na-O	120360.22	0.17	0
O-O	9027.03	0.265	85.0321
Si-Si	834.40	0.29	0
Si-B	337.70	0.29	0
B-B	121.10	0.35	0

Potentials used by Delaye & Ghaleb [15] and Kieu et al. [22] were evaluated by Jolley et al. [24]. These authors found that the potentials proposed by Kieu et al. provide the highest accuracy regarding the calculation of bond lengths and bond angles and additionally these models have the lowest melting point.

For the investigation of the structure of iron phosphate glasses, Al-Hasni & Mountjoy [23] used a Buckingham pair potential, with parameters given in Table 3.4. Authors simulated 10 different glass compositions with P_2O_5, Fe^{2+} and Fe^{3+} compositions varying in the ranges 50-70%, 0-50% and 0-50% respectively. They also used a three body potential in the form

$$V_{iji}(\theta) = \frac{1}{2} k_{iji} \left(\theta - \theta_{iji}\right)^2, \tag{3.146}$$

where j is the central atom, to describe the bond angle stretch of O-P-O and P-O-P triplets, with k_{OPO} = 3.5 eV, k_{POP} = 3.0 eV, θ_{OPO} = 109.47^o and θ_{POP} = 135.5^o. Results revealed a well-defined phosphate network and different bond lengths for the Fe^{2+}–O and Fe^{3+}–O bonds, equal to 2.12 Å and 1.89 Å respectively. The mean coordination of iron ions was calculated equal to $\simeq$ 4.5. Finally, they suggested that an iron phosphate glass consisting of 60% P_2O_5 and 40%Fe_2O_3 has increased durability because of the relatively low number of P-O-P bonds and the increased number of Fe-O-P bonds.

Table 3.4: Parameters of the Buckingham potential used by Al-Hasni & Mountjoy et al. [23], Jolley et al. [24] and Jolley & Smith [13] to model iron phosphate glasses.

Bond	A (eV)	ρ (Å)	C (eV·Å^6)
Fe^{2+}-O	11777	0.2071	21.642
Fe^{3+}-O	19952	0.1825	4.6583
O-O	1844	0.3436	192.58
P-O	27772	0.1819	86.860

Kitheri et al. [31] and Jolley & Smith [13] used the same potentials to investigate the displacement energy thresholds and radiation damage tolerance respectively. In contrast with Al-Hasni & Mountjoy, Jolley et al. [24] and Jolley & Smith [13] used a three body Stillinger-Weber potential with λ_{OPO} = 5.351617 eV, λ_{POP} = 8.299695 eV, θ_{OPO} = 109.47^o, θ_{POP} = 135.5^o, γ = 0.5 Å and r_c = 2.5 Å.

The work done by Kitheri et al. [31] revealed that the displacement energy of Fe^{2+} in an iron phosphate glass consisting of 60% P_2O_5 and 40% Fe_2O_3 is lower than the one for Fe^{3+}. Additionally, the cohesive energy of the glasses reduces as the Fe^{2+} content increases and consequently, iron phosphate glass wasteforms are suggested to have as low Fe^{2+} content as possible.

Jolley & Smith [13] simulated five different compositions of iron phosphate glasses: 3 resulting from crystalline phases $Fe^{2+}Fe_2^{3+}(P_2O_7)_2$, $Fe_4^{3+}(P_2O_7)_3$, $Fe^{3+}(PO_3)_3$ and two from the 40% Fe_2O_3 and 60% P_2O_5 iron phosphate glass with two different Fe^{2+} concentrations, 4% and 17%. For the creation of the damage cascade authors used 4 keV impact particles. Results show that the majority of particles displaced by more than 1.2 Å are oxygen atoms and also that the number of displaced particles increases significantly during the first 0.5 ps of the simulation and is slightly reduced (about 10%) during the final relaxation stage. The number of displaced particles during the creation of the cascades was found to be proportional to the Fe^{2+} content. However, the

absence of Fe^{2+} ions in the $Fe_4^{3+}(P_2O_7)_3$ glass resulted in a higher number of displaced atoms in comparison with the other simulated structures. In the relaxed structures in contrast, it was found that the Fe^{2+} concentration has no effect on the final number of displaced particles.

In the existing literature it is apparent that radiation damage studies focus on the number of displaced particles. A particle is identified as displaced if the distance between the position of the particle in the damaged structure and the position in the initial undamaged structure exceeds a certain value depending on the structure. However, this approach ignores the specific bond lengths and characteristics and may lead to inaccurate estimation of damage effects. Additionally, rings play a crucial role in the understanding of glass structure. Especially for irradiated glass wasteforms, ring statistics can improve our understanding on the effect of radiation damage and contribute significantly in the efforts to develop the best possible wasteforms. However, until now, the exploitation of ring statistics in the research of glass wasteforms is very limited.

Chapter 4

Defect characterization techniques

4.1 Introduction

Radiation damage characterization requires the identification and analysis of the defects that play a crucial role in materials properties and behaviour. In general, point defects can be categorized as vacancies and interstitials. It is relatively easy to spot them in a crystal, like zircon, where a simple comparison between the damaged structure and the initial reference crystal is sufficient for their identification. DLPOLY 4[132] offers an in-build algorithm based on the Wigner-Seitz method, to estimate the number of defects. The Wigner-Seitz method compares the configuration of a system at a time t, which contains the point defects, with a reference configuration that defines the defect-free structure of the system and is usually a perfect crystal lattice. But as Hobbs [153] points out, this method cannot be used for an accurate estimation of defects during radiation damage simulation, since the crystal may suffer heavy distortions during the procedure. In addition, in amorphous materials such as glasses there is no reference lattice structure to refer to and a topological approach becomes necessary. In this work three topological methods are proposed, involving Steinhardt order parameters, Hermite order parameters and ring statistics.

4.2 Defect counting: The Wigner-Seitz method

The Wigner-Seitz method is the most wide-spread method for defect characterization in crystalline materials. It is based on the concept of a Wigner-Seitz cell (Fig. 4.1), a type of primitive Voronoi cell. To construct a Wigner-Seitz cell, the process is quite straightforward. From a chosen atomic site, the planes that are perpendicular to the midpoint of the position vector of all the neighbours are drawn. From the cells that are formed, the one with the least volume defines the Wigner-Seitz cell of the specific atomic site.

In a crystalline structure, each atomic site defines a unique Wigner-Seitz cell. The number of atoms in each Wigner-Seitz cell defines the occupancy o_i of the cell. In typical undamaged structures, each Wigner-Seitz cell is occupied by one and only one atom, so for the undamaged structure we will have

$$o_i(t = 0) = 1. \tag{4.1}$$

To find defects in the damaged structure, the positions of the atoms are compared with their positions in the initial structure in order to determine the occupancy of the atomic sites in the damaged configuration (Fig. 4.2). An empty atomic site i for which

$$o_i(t > 0) = 0, \tag{4.2}$$

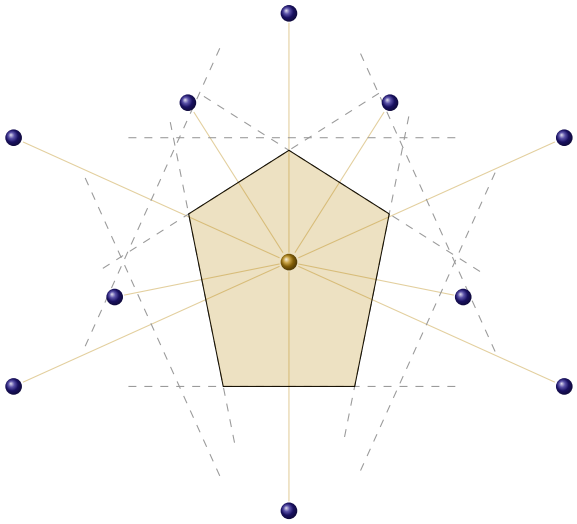

Figure 4.1: Construction of a Wigner-Seitz cell in a simple 2D case: A reference atomic site (gold color) is connected with all the neighbours. From the midpoint of the position vector of each neighbour, a perpendicular line is draw (grey dashed lines). The Wigner-Seitz cell (light gold area) is defined by the black lines that form the cell with the least possible area.

defines a vacancy defect, while a site for which

$$o_i(t > 0) > 1, \tag{4.3}$$

has excess atoms and the number of excess atoms $o_i(t > 0) - 1$ defines the number of interstitial defects of the site. Obviously, the total number of vacancies of the system is equal to the number

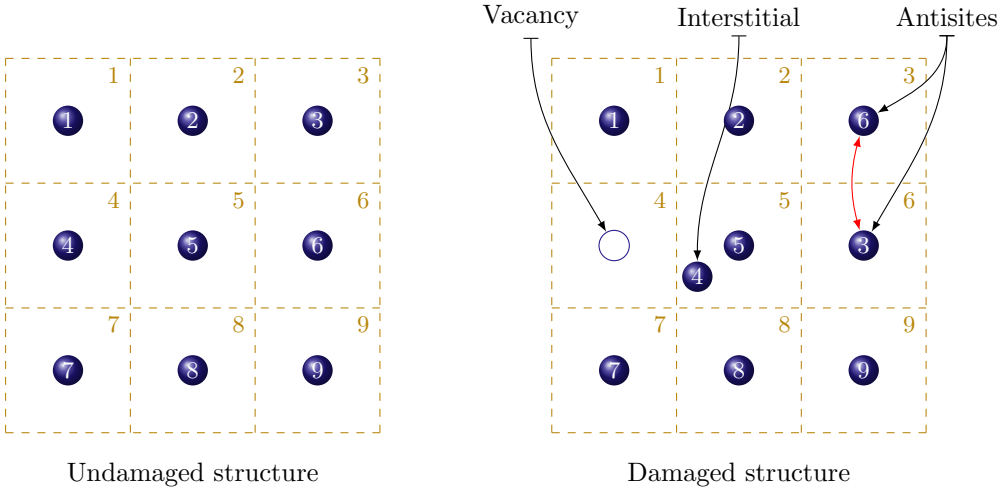

Figure 4.2: Typical defects in a simple crystalline structure. The empty atomic site previously occupied from atom 4 forms a vacancy. Atomic site 5 in the damaged structure is occupied by two atoms forming an interstitial. Atoms 3 and 6 that exchanged their atomic sites are characterized as antisite defects.

of atomic sites with occupancy equal to zero, so

$$n_v(t) = \sum_i \delta_{o_i(t>0),0}, \tag{4.4}$$

and the total number of interstitials is equal to the total number of excess atoms of the system, so

$$n_i(t) = \sum_i [o_i(t) - 1](1 - \delta_{o_i(t>0),0}). \tag{4.5}$$

In the above relations, $\delta_{i,j}$ is the Kronecker delta, defined by

$$\delta_{i,j} = \begin{cases} 0, & \text{for} \quad i \neq j \\ \\ 1, & \text{for} \quad i = j \end{cases}, \tag{4.6}$$

In the case that the total number of atoms of the system is conserved, the number of vacancies is equal to the number of interstitials.

When a vacancy is created in a damaged structure, the empty atomic cell may be re-occupied by a different atom. Thus the occupancy of this site is equal to 1, meaning it cannot be characterized as vacancy or as interstitial. However, since the atom that originally occupied this site is displaced from its initial position, this defines an antisite defect.

4.2.1 The necessity of a topological approach

Although this method is quite simple, it is not accurate to estimate radiation damage effects, mainly because it is based on the displacement of the particle from the initial position. In a real damaged structure there is no information regarding the distance a particle is moved from its initial position. In crystalline materials this distance can be estimated by comparing the position of the particle in the damaged structure with the position of a reference frame but again this is just an estimation, while in amorphous materials there is no reference structure to compare with. Additionally and especially in amorphous materials, the displacement distance of a particle from its initial position is not a foolproof way to classify if the structure is damaged or not. The displacement of the particles from their initial positions will result in broken bonds between the atoms, known as bond defects. These bond defects are responsible for any change in the properties of a material under irradiation. As demonstrated in Fig. 4.3, a point defect is not necessarily accompanied by bond defects and via versa. In the first case, particle 9 is displaced away from its initial position it occupied in the undamaged structure (Fig. 4.2), resulting into two broken bonds previously formed by pairs 6-9 and 8-9. However, particle 9 is still within the boundaries of its Wigner-Seitz cell and consequently the Wigner-Seitz method will not identify this particle as a defect. In the second case, a group af atoms may move as a whole away from the positions occupied in the undamaged structure, without breaking any bonds between the atoms forming the group. All the atoms of the group in the damaged structure are found outside their respective Wigner-Seitz cells and the Wigner-Seitz method will classify them as defects, ignoring the fact that the relative geometry of the group is unaffected by the radiation damage event. It is important to retrieve information about *both* point defects *and* bond defects and for this we need to apply a

topological approach.

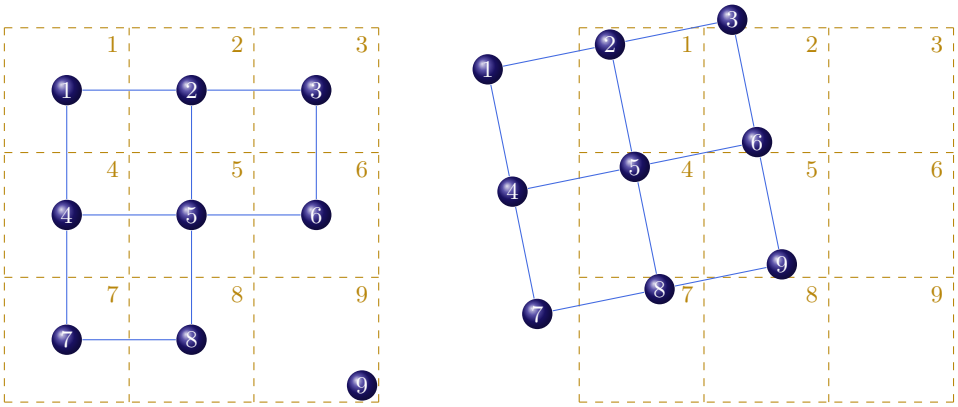

Damaged structure 1 Damaged structure 2

Figure 4.3: Problems associated with Wigner-Seitz defect counting method. **Left:** Radiation damage may displace a particle away from its initial position, breaking the bonds with the neighbouring atoms. However, if this particle stays within its Wigner-Seitz cell, the Wigner-Seitz method will not identify it as a defect. **Right:** In this case, radiation damage may displace a small cluster away from its reference position, without breaking any bonds. The Wigner-Seitz method will identify a large number of point defects even though there is no broken bond in the structure.

4.3 Steinhardt order parameters

In 1983, P. Steinhardt and his group formulated a set of bond-orientational parameters based on spherical harmonics, in order to study the structure of liquids and glasses [154]. For a reference particle i of the system, these parameters are given by

$$\langle Q_{\ell,m} \rangle^{(i)} = \frac{1}{N_b} \sum_{j=1}^{N_b} Y_\ell^m(\theta_j, \phi_j), \tag{4.7}$$

where N_b is the number of neighbours of particle i, θ_j, ϕ_j are the spherical polar and azimuth angles of the neighbouring particle j in the reference system of particle i and ℓ, m are integers that obey the conditions

$$\ell \geq 0 \qquad \text{and} \qquad -\ell \leq m \leq \ell. \tag{4.8}$$

Spherical harmonics on the other hand are given by

$$Y_\ell^m(\theta, \phi) = (-1)^m \sqrt{\frac{2\ell+1}{4\pi} \frac{(\ell-m)!}{(\ell+m)!}} e^{im\phi} P_\ell^m(\cos\theta), \qquad -\ell \leq m \leq \ell, \tag{4.9}$$

where $P_\ell^m(\cos\theta)$ are the associated Legendre polynomials, given by

$$P_\ell^m(\xi) = \frac{1}{2^\ell \ell!} (1-\xi^2)^{m/2} \frac{d^{\ell+m}}{d\xi^{\ell+m}} (\xi^2 - 1)^\ell, \qquad 0 \leq m \leq \ell. \tag{4.10}$$

for positive m values, while for the negative values of m we have

$$P_\ell^m(\xi) = (-1)^m \frac{(\ell+m)!}{(\ell-m)!} P_\ell^{|m|}(\xi), \qquad -\ell \le m < 0. \tag{4.11}$$

It can also be shown that associated Legendre polynomials can be expressed as a series of ξ in the form

$$P_\ell^m(\xi) = \frac{1}{2^\ell}(1-\xi^2)^{m/2} \sum_{k=0}^{\ell-m} d_k(\ell,m)\xi^k, \tag{4.12}$$

where

$$d_k(\ell,m) = (-1)^{\frac{1}{2}(\ell-m-k)} \frac{(\ell+m+k)!}{k!\left(\frac{\ell-m-k}{2}\right)!\left[\ell-\left(\frac{\ell-m-k}{2}\right)\right]!} \tag{4.13}$$

for

$$\begin{aligned} &\ell - m = \text{odd} \quad \text{and} \quad k = 1, 3, 5, \ldots, \ell - m \\ &\qquad\qquad \text{or} \qquad\qquad , \\ &\ell - m = \text{even} \quad \text{and} \quad k = 0, 2, 4 \ldots, \ell - m \end{aligned} \tag{4.14}$$

and $d_k = 0$ for all the other cases. The calculation of spherical harmonics at the poles where the angle ϕ is not defined requires special attention. Using the cartesian form of the spherical harmonics we can find that for $\theta = 0$ and $\theta = \pi$, all the spherical harmonics with $m \neq 0$ should be zero. This leads us to define the angle ϕ_p for $\theta = 0$ according to the relation

$$\phi_p = \begin{cases} 0 & \text{for} \quad m \le 0 \\ \dfrac{\pi}{2m} & \text{for} \quad m > 0 \end{cases} \tag{4.15}$$

Because spherical harmonics, for a given value of ℓ, are members of the $SO(3)$ rotational group that represents all the rotations in the $3D$ Euclidian space under the operation of composition, they are coordinate system dependent. This dependence is transferred directly to the first kind of Steinhardt order parameter given by equation (4.7). To avoid this inconvenience, a second kind of Steinhardt order parameter was introduced, given by

$$Q_\ell^{(i)} = \left[\frac{4\pi}{2\ell+1} \sum_{m=-\ell}^{\ell} \left|\langle Q_{\ell,m}\rangle^{(i)}\right|^2\right]^{1/2}, \tag{4.16}$$

which are independent of the coordinate system - they depend only on the relative position of the reference particle i with its neighbours. In general, Steinhardt Order Parameters can give useful information regarding the degree of symmetry in a system and more particularly about the angular distribution of atoms around a reference particle. Details regarding the information that can be retrieved for the symmetry of both crystalline and amorphous materials will be discussed in the following paragraphs.

4.3.1 Tesseral spherical harmonics

Spherical harmonics are in general complex functions, due to the exponential term $e^{im\phi}$. Thus, the sum in equation (4.7) has both real and imaginary parts. For example, if a reference particle has N_b neighbours, the first kind of Steinhardt order parameters will be given by

$$\begin{aligned}\langle Q_{\ell,|m|}\rangle^{(i)} =& \frac{1}{N_b}\sum_{j=1}^{N_b} Y_\ell^m(\theta_j,\phi_j) = \\ =& \frac{1}{N_b} c_{\ell,m}\left[\sum_{j=1}^{N_b}\cos(m\phi_j)P_\ell^m(\cos\theta_j) + i\sum_{j=1}^{N_b}\sin(m\phi_j)P_\ell^m(\cos\theta_j)\right].\end{aligned} \tag{4.17}$$

where

$$c_{\ell,m} = (-1)^m\sqrt{\frac{2\ell+1}{4\pi}\frac{(\ell-m)!}{(\ell+m)!}}. \tag{4.18}$$

Second kind Steinhardt order parameters require the calculation of the squared norm of the first kind Steinhardt order parameters, which in this case is

$$\begin{aligned}\left|\langle Q_{\ell,m}\rangle^{(i)}\right|^2 = \frac{1}{16}c_{\ell,m}^2\Bigg[&\left(\sum_{j=1}^{4}\cos(m\phi_j)P_\ell^m(\cos\theta_j)\right)^2 + \\ &+\left(\sum_{j=1}^{4}\sin(m\phi_j)P_\ell^m(\cos\theta_j)\right)^2\Bigg],\end{aligned} \tag{4.19}$$

and results in

$$\begin{aligned}\left|\langle Q_{\ell,m}\rangle^{(i)}\right|^2 = \frac{1}{N_b^2}c_{\ell,m}^2\Bigg[&\sum_{j=1}^{N_b}\left[P_\ell^m(\cos\theta_j)\right]^2 + \\ &+\sum_{j=1}^{N_b-1}\sum_{k>i}^{N_b}\cos\left[m(\phi_j-\phi_k)\right]P_\ell^m(\cos\theta_j)P_\ell^m(\cos\theta_k)\Bigg].\end{aligned} \tag{4.20}$$

From a computational perspective, this practice is not very efficient as it requires $N_b(N_b+1)$ calculations for each particle of the system. To make the calculation more efficient and reduce the computation time, the real form of the spherical harmonics is used. Real spherical harmonics, also known as tesseral spherical harmonics, are given by

$$Y_{\ell,m}(\theta,\phi) = \begin{cases}\sqrt{2}c_{\ell,|m|}P_\ell^{|m|}(\cos\theta)\sin(|m|\phi), & \text{for} \quad m<0\\ c_{\ell,0}P_\ell^0(\cos\theta), & \text{for} \quad m=0\\ \sqrt{2}c_{\ell,m}P_\ell^m(\cos\theta)\cos(m\phi), & \text{for} \quad m>0\end{cases}. \tag{4.21}$$

Using tesseral spherical harmonics, the calculation of $\left|\langle Q_{\ell,m}\rangle^{(i)}\right|^2$ becomes proportional to the number N_b of neighbours of the reference particle, reducing significantly the computation time.

4.3.2 Symmetry of tesseral spherical harmonics

Tesseral spherical harmonics obey symmetry relations that are transferred into Steinhardt order parameters, which in turn give useful information regarding the structure of a system. As can be seen from Fig. 4.4, for a cubic lattice, for every particle at position (r, θ, ϕ) there are three particles at positions $(r, \theta, \pi + \phi)$, $(r, \pi - \theta, \phi)$ and $(r, \pi - \theta, \pi + \phi)$. In general it can be shown that tesseral spherical harmonics obey the symmetry relations

$$\begin{aligned} Y_{\ell,m}(\pi - \theta, \phi) &= (-1)^{\ell-m} Y_{\ell,m}(\theta, \phi), \\ Y_{\ell,m}(\theta, \pi \pm \phi) &= (-1)^{m} Y_{\ell,m}(\theta, \phi), \\ Y_{\ell,m}(\pi - \theta, \pi \pm \phi) &= (-1)^{\ell} Y_{\ell,m}(\theta, \phi). \end{aligned} \tag{4.22}$$

From the final equation it is obvious that the sum of the spherical harmonics for two particles in opposite directions from the reference particle will be zero for ℓ = odd.

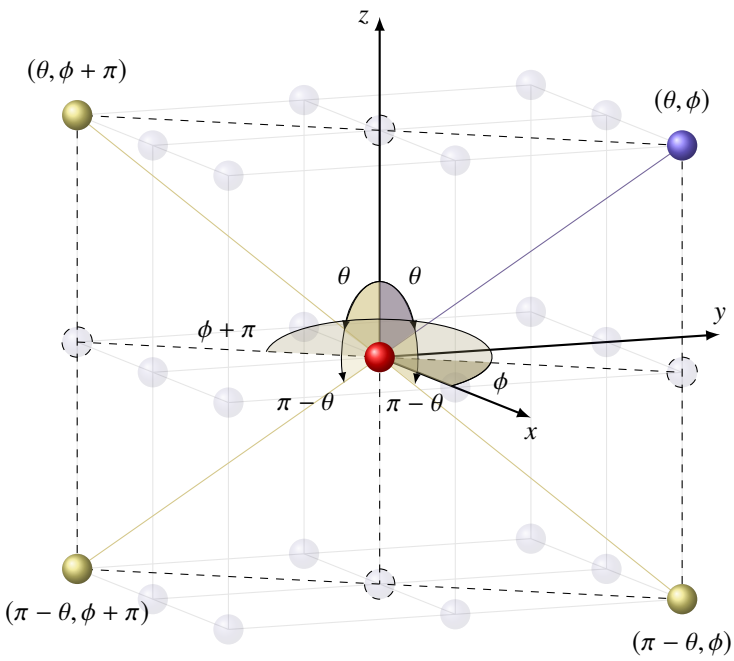

Figure 4.4: The symmetry in a simple cubic lattice. For the coordinate system of the central red atom and for every particle at position (r, θ, ϕ) (blue atom) there are three particles at positions $(r, \theta, \pi + \phi)$, $(r, \pi - \theta, \phi)$ and $(r, \pi - \theta, \pi + \phi)$. The dashed lines show the projections of the positions on the Oxy plane and on the z axis. Same symmetries apply for every cubic based lattice system, such as the bcc and the fcc.

4.3.3 Calculation of Steinhardt order parameters

In radiation damage simulations, it is important not only to estimate the total damage in the system, but also to know the extent of the damage for the different species comprising the structure. Thus, Steinhardt order parameters are calculated separately for each species. Additionally, since we are interested in bond defects, separate calculations are carried out for each of the neighbouring species of the reference particle. For the calculation, the algorithm displayed in Fig. 4.5 is followed.

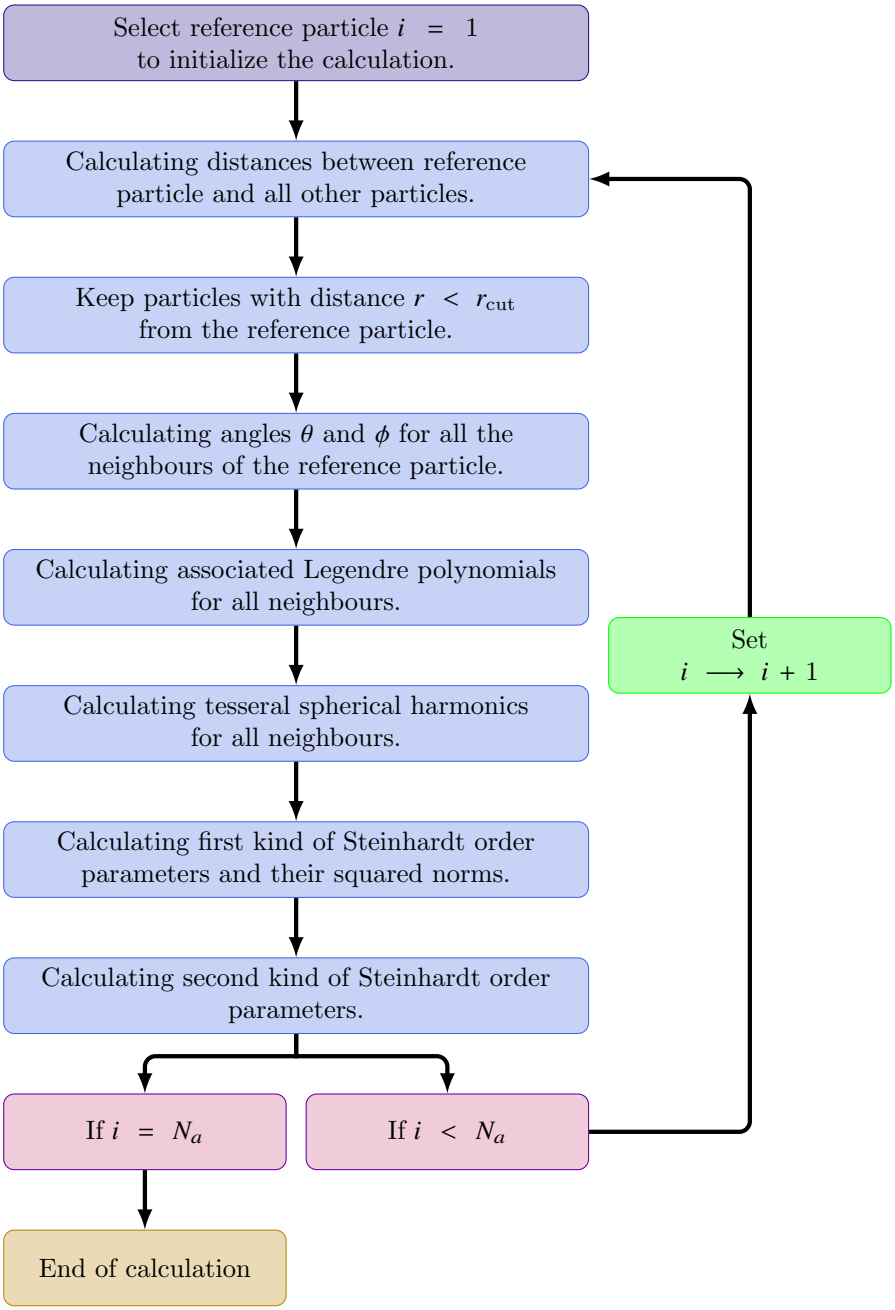

Figure 4.5: Algorithm for the calculation of Steinhardt order parameters. N_a is the total number of atoms of the same species.

The calculation is initialized by selecting the first reference particle of the system. The next step is to find all the neighbours of the particle that lie within a sphere of radius r_{cut}, usually equal to the distance of the first minimum of the partial radial distribution function for the species under investigation. To identify those neighbours, the distances r_{ij} between the reference particle and all the other particles of the systems must be calculated. The calculation time of common codes is proportional to the square of the number N_a of the atoms. But since the calculation of Steinhardt order parameters for the reference particle is limited to the neighbours inside the sphere

of radius r_{cut}, the calculation time can be significantly reduced using a modified cell algorithm. This is based on the fact that since $r_{ij} \leq r_{\text{cut}}$, the components x_{ij}, y_{ij} and z_{ij} must also satisfy the relations $x_{ij} \leq r_{\text{cut}}$, $y_{ij} \leq r_{\text{cut}}$ and $z_{ij} \leq r_{\text{cut}}$. Based on that, the initial structure is expanded by a distance r_{cut}, and then the cell is split into smaller cells with dimensions larger and as close as possible to r_{cut}. To identify all the bonds, we just need to calculate the distances between the particles of each of the smaller cells, with the particles in its 26 neighbouring cells. This way, the calculation time is proportional to $27N_a^2(d/a)^3$ instead of N_a^2, where a is the dimension of the original cell and d the dimension of the smaller cells. Fraction a/d is an integer and for $a/d > 3$, the calculation time is significantly reduced. For example, for a system of 10^6 particles, a/d can take a value $a/d > 50$ and the running time with the modified cell algorithm can be more than 10^4 times lower in comparison with conventional methods.

Once all the neighbours with $r \leq r_{\text{cut}}$ are identified, spherical angles θ_{ij} and ϕ_{ij} can be calculated. Angle θ_{ij} appears in the associated Legendre polynomials, not explicitly, but in the form of $\cos\theta_{ij}$ and $\sin\theta_{ij}$. Thus, there is no need to calculate angle θ_{ij} itself. Instead, $\cos\theta_{ij}$ and $\sin\theta_{ij}$ are calculated using

$$\cos\theta_{ij} = \frac{z_{ij}}{r_{ij}} \qquad \text{and} \qquad \sin\theta_{ij} = \sqrt{1-\cos^2\theta_{ij}}. \tag{4.23}$$

However, the calculation of ϕ_{ij} involves a lot of details that needs to be considered. In general, angle ϕ_{ij} is given by

$$\phi_{ij} = \arccos\left(\frac{x_{ij}}{\sqrt{x_{ij}^2 + y_{ij}^2}}\right) \tag{4.24}$$

The problems arise when x_{ij} or y_{ij} or both are equal to zero. In the poles of the reference particle, where $x_{ij} = y_{ij} = 0$ and so $\theta_{ij} = 0$ or $\theta_{ij} = \pi$, angle ϕ_{ij} is defined by

$$\phi_{ij} = \begin{cases} 0, & \text{for} \quad m \leq 0 \\ \\ \frac{\pi}{2m}, & \text{for} \quad m > 0 \end{cases}. \tag{4.25}$$

If the component y_{ij} of the distance between two particles is zero and $x_{ij} \neq 0$, then

$$\phi_{ij} = \arccos\left(\frac{x_{ij}}{|x_{ij}|}\right), \tag{4.26}$$

and ϕ_{ij} can take two possible values, 0 if $x_{ij} > 0$ and π if $x_{ij} < 0$. Finally, special consideration needs to be taken for particles with $\pi < \phi_{ij} \leq 2\pi$ since the inverse cosine function provides values in the range $0 \leq \phi_{ij} \leq \pi$. To solve this issue, for particles with $y_{ij} < 0$ the transformation $\phi_{ij} \longrightarrow 2\pi - \phi_{ij}$ is necessary.

The calculation of associated Legendre polynomials can be performed using equation (4.9) for $m \geq 0$. It is not required to calculate $P_\ell^m(\cos\theta_{ij})$ for $m < 0$, since tesseral spherical harmonics are expressed using associated Legendre polynomials for $m \geq 0$. However, this way, associated Legendre polynomials need to be written in their analytical form and this requires a rigid code that will have a prefixed limit for the maximum value of ℓ and the respective maximum order of

the Steinhardt order parameters. To make the code more flexible and have the freedom to choose the maximum number ℓ for the calculations, associated Legendre polynomials can be calculated using the recursion relations

$$P_\ell^m(\cos\theta_{ij}) = \frac{1}{\ell - m}\left[(2\ell-1)\cos\theta_{ij}P_{\ell-1}^m(\cos\theta_{ij}) - (\ell+m-1)P_{\ell-2}^m(\cos\theta_{ij})\right], \tag{4.27}$$

for $\ell \geq 2$ and

$$P_\ell^m(\cos\theta_{ij}) = -2(m-1)\cot\theta_{ij}P_\ell^{m-1}(\cos\theta_{ij}) - (\ell+m-1)(\ell-m+2)P_\ell^{m-2}(\cos\theta_{ij}), \tag{4.28}$$

for $\ell, m \geq 2$. This calculation requires initial values for $P_0^0(\cos\theta_{ij})$, $P_1^0(\cos\theta_{ij})$, $P_1^1(\cos\theta_{ij})$ and $P_2^1(\cos\theta_{ij})$ given by

$$\begin{aligned} P_0^0(\cos\theta_{ij}) &= 1, & P_1^0(\cos\theta_{ij}) &= \cos\theta_{ij}, \\ P_1^1(\cos\theta_{ij}) &= -\sin(\theta_{ij}), & P_2^1(\cos\theta_{ij}) &= -3\sin\theta_{ij}\cos\theta_{ij}. \end{aligned} \tag{4.29}$$

The first two are used to calculate all polynomials with $m = 0$, using (4.27),

$$P_\ell^0(\cos\theta_{ij}) = \frac{1}{\ell}\left[(2\ell-1)\cos\theta_{ij}P_{\ell-1}^0(\cos\theta_{ij}) - (\ell-1)P_{\ell-2}^0(\cos\theta_{ij})\right], \tag{4.30}$$

while $P_1^1(\cos\theta_{ij})$ and $P_2^1(\cos\theta_{ij})$ are used in (4.27) for the calculation of all polynomials with $m = 1$,

$$P_\ell^1(\cos\theta_{ij}) = \frac{1}{\ell - 1}\left[(2\ell-1)\cos\theta_{ij}P_{\ell-1}^1(\cos\theta_{ij}) - \ell P_{\ell-2}^1(\cos\theta_{ij})\right]. \tag{4.31}$$

The knowledge of all polynomials with $m = 0, 1$ allows the calculation of all the other polynomials using (4.28), up to the desired value of integer ℓ.

To find the tesseral spherical harmonics it is required to calculate first the $c_{\ell,m}$ coefficients from equation (4.18). One approach is to use directly this equation. However, the calculation of the factorial can be extremely expensive, especially for large values of ℓ. It is far more efficient to use the following recursion relations

$$c_{\ell,0} = \sqrt{\frac{2\ell+1}{4\pi}} \tag{4.32}$$

to find all the coefficients for $m = 0$ and then use

$$c_{\ell,m} = \frac{(-1)^m}{\sqrt{(\ell+m)(\ell-m+1)}}c_{\ell,m-1}, \tag{4.33}$$

to calculate all the required coefficients. These coefficients, since they do not depend on the position of the particles, can be calculated just one time, before the initialization of the algorithm, to save computational time. With $c_{\ell,m}$ and $P_\ell^m(\cos\theta_{ij})$ already known, tesseral spherical harmonics can be calculated for the different values of m directly from equation (4.21).

First kind Steinhardt order parameters are calculated by summing the tesseral spherical harmonics for all the neighbours and then dividing by the number N_b of the neighbours. $\langle Q_{\ell,m}\rangle^{(i)}$ are then squared and summed for all possible m values and substituted in (4.16) in order to find the second kind Steinhardt order parameters for the reference particle. This process is repeated N_a times, until the parameters are calculated for all the atoms of the system.

4.3.4 The effect of the coordination number

Steinhardt order parameters not only depend on the angular distribution of the particles around a reference particle, but also on the number of neighbours. In a radiation damage event, where the recoil nuclei displace atoms from their initial positions, the coordination number of the atoms changes constantly during the cascade formation. We can explore the dependence of Steinhardt order parameters on the number of nearest neighbours in order to predict the effect of radiation damage.

As shown in detail in Appendix A.1.1, for a reference particle with only one neighbour we will have

$$Q_\ell^{(i)}(N_b = 1) = \left[\frac{4\pi}{2\ell+1} \sum_{m=-\ell}^{\ell} |Y_\ell^m(\theta,\phi)|^2 \right]^{1/2} = 1. \tag{4.34}$$

From this relation we can also show that the sum of the squares of the spherical harmonics for all possible m values satisfy the relation

$$\sum_{m=-\ell}^{\ell} |Y_\ell^m(\theta,\phi)|^2 = \frac{2\ell+1}{4\pi}. \tag{4.35}$$

When the reference particle has two or more neighbours, it can be proven (Appendix A.1.2) that the second kind of the Steinhardt order parameters is given by

$$Q_\ell^{(i)} = \frac{1}{N_b} \left[N_b + \frac{8\pi}{2\ell+1} \sum_{m=-\ell}^{\ell} \sum_{j=1}^{N_b-1} \sum_{k>j}^{N_b} Y_\ell^m(\theta_j,\phi_j) Y_\ell^m(\theta_k,\phi_k) \right]^{1/2}. \tag{4.36}$$

From this relation it is obvious that each particle contributes in two ways to the values of Steinhardt order parameters. Each of the neighbours has a single-particle contribution to the values of Steinhardt order parameters resulting in the N_b terms inside the brackets of the above relation and we also have the two-particle contributions described by the sum over all the neighbour pairs. It can be shown that the pair terms are also independent of the values of angles θ and ϕ and can be expressed using only the angular differences $\theta_j - \theta_k$ and $\phi_j - \phi_k$. For example, for $\ell = 1$ each of the pair terms can be written as

$$\begin{aligned} \sum_{m=-1}^{1} Y_1^m(\theta_j,\phi_j) Y_1^m(\theta_k,\phi_k) =& \frac{3}{8\pi} \cos(\theta_j - \theta_k)[1 + \cos(\phi_j - \phi_k) + \\ &+ \frac{3}{8\pi} \cos(\theta_j + \theta_k)[1 - \cos(\phi_j - \phi_k). \end{aligned} \tag{4.37}$$

The result of this behaviour is that Steinhardt order parameters do not depend on the position vectors of the neighbours surrounding the reference particle, but only on the number of neighbours and the relative position of them. To obtain detailed results of the effect of coordination number we calculate Steinhardt order parameters for a reference particle and for different numbers of neighbours that are placed in random positions around the reference particle. In this way, simulations were carried out for up to 8 neighbours and repeated 1000 times in order to have a good statistical sample.

We can plot Q_ℓ values against any other variable, but there is no real point in doing that. When

we need to study a real material, the most common structural parameter that can be measured, apart from the coordination number, is the average bond length, which is equal to the average distance of the nearest neighbours. Also there is no point in trying to find a relation between the values of the Steinhardt order parameters and the displacement of the particles from their initial positions for the reasons described in section 4.2.1. The displacement of the particles from their initial positions will result in broken bonds between the atoms and consequently the average neighbour distance and the coordination number of the particles will change. Thus, it is much more sensible to try to identify possible relations between Steinhardt order parameter values and either the average neighbour distance or the coordination number.

Figs. 4.6 and 4.7 show plots of Q_4 and Q_6 against the average neighbour distance. The first observation is that for 1 neighbour the parameters are equal to 1 - as expected - and for 2 neighbours the values of Steinhardt order parameters are greater than 0.5. For the 2 neighbours, we can see also an upper limit in the values, with only a few particles receiving a higher value. These data points correspond to a pair of almost diametrically opposite particles, for which, as we can easily prove from equation 4.37, Steinhardt order parameters have values close or equal to 1. As the number of neighbours increases, the distribution of the data points becomes more uniform since the range of values of both Q_ℓ and r_{av} is becoming narrower. Additionally, Steinhardt order parameters values become lower. This observation is quite important when we study radiation damage effects. Figs. 4.6 and 4.7 show that Steinhardt order parameters are sensitive to the change of the coordination number. Thus, we will be able to use Steinhardt order parameters in order to identify any broken bonds in a structure. The only disadvantage of this method seems to be the fact that for coordination numbers greater that 2, the values of Steinhardt order parameters overlap. However, it must be pointed out that these plots correspond to randomly placed atoms around the reference particle. In real systems - even in amorphous materials - there is a kind of symmetry that will be reflected in the Steinhardt order parameters values. For example, the silica network in both crystalline and amorphous materials usually forms tetrahedral structures with the neighbouring oxygen atoms. In these structures, the relative positions of the oxygen atoms around the silicon reference particle are almost fixed. Thus the range of Q_ℓ values will be narrowed significantly. When a radiation damage event occurs, the coordination number of silicon atoms will be reduced to 3 or perhaps to 2 or 1, with the oxygen atoms having a more random distribution around the silicon atom, resulting into a wide range of Q_ℓ values, that will make the identification of bond defects possible.

Things become clearer when Q_6 values are plotted against Q_4, as shown in Fig. 4.8. For 1 neighbour, all Q_ℓ values are equal to 1, and so all (Q_4, Q_6) pairs are reflected at $(1,1)$. For 2 neighbours, the $Q_6(Q_4)$ plot forms an α shaped curve that is very easy to distinguish. As the number of neighbours increases, the area occupied by the data points becomes smaller and becomes elliptic in shape. Once again there is overlapping in the Steinhardt order parameter values. However, in real systems - crystalline or amorphous - the local geometry of the structures is quite consistent and we expect to have a much more compact distribution of data points which can be used to explore effectively the radiation damage effects.

Although in this section only the effect of the coordination number on the values of Q_4 and Q_6 are presented, we can do a similar analysis for any $(Q_\ell, Q_{\ell'})$ pair and identify similar behaviour in terms of their relation with the coordination number. However, as it is demonstrated in the

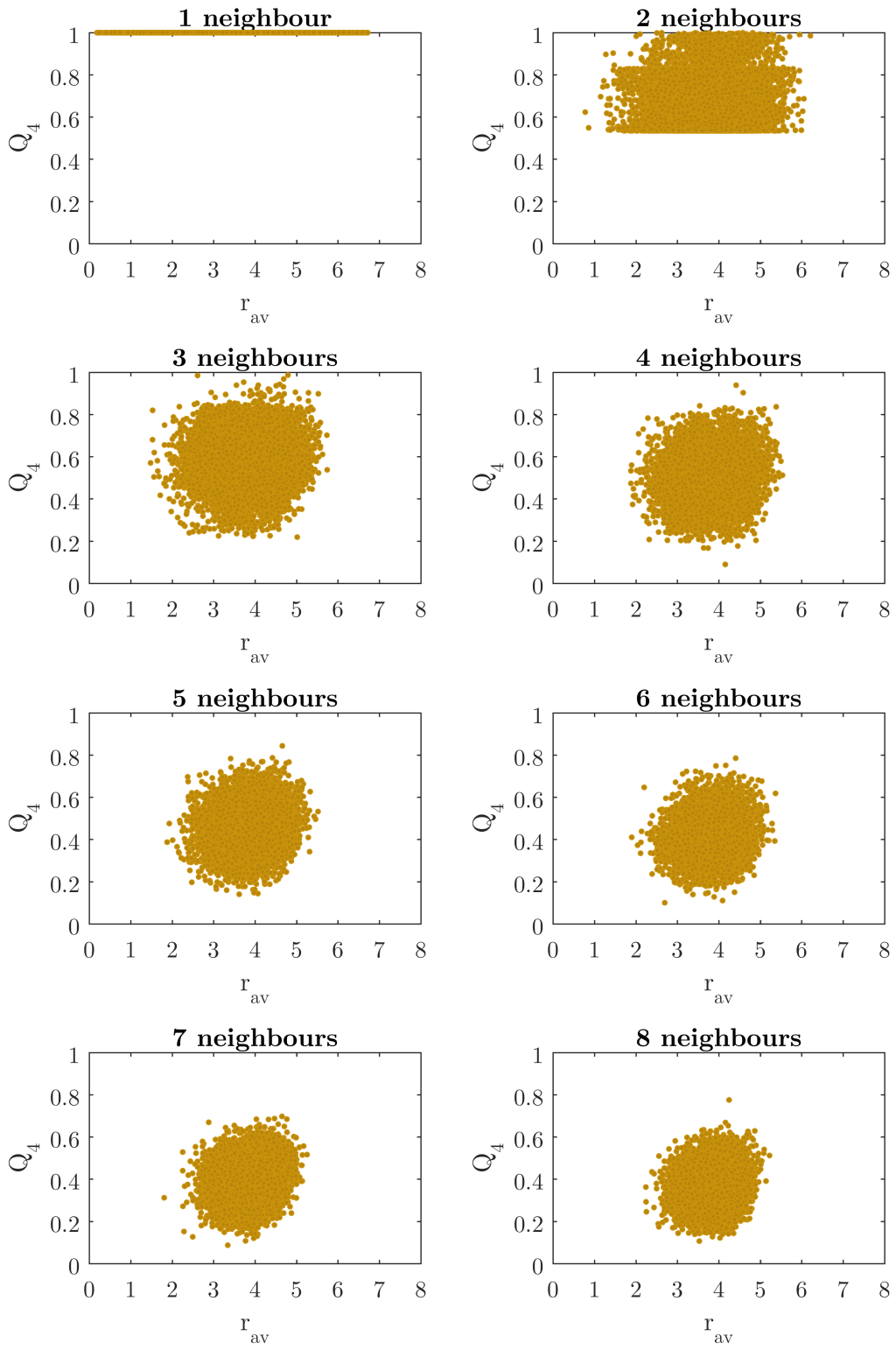

Figure 4.6: Plots of Q_4 values against the average neighbour distance for a reference particle with 1-8 neighbours located at random positions.

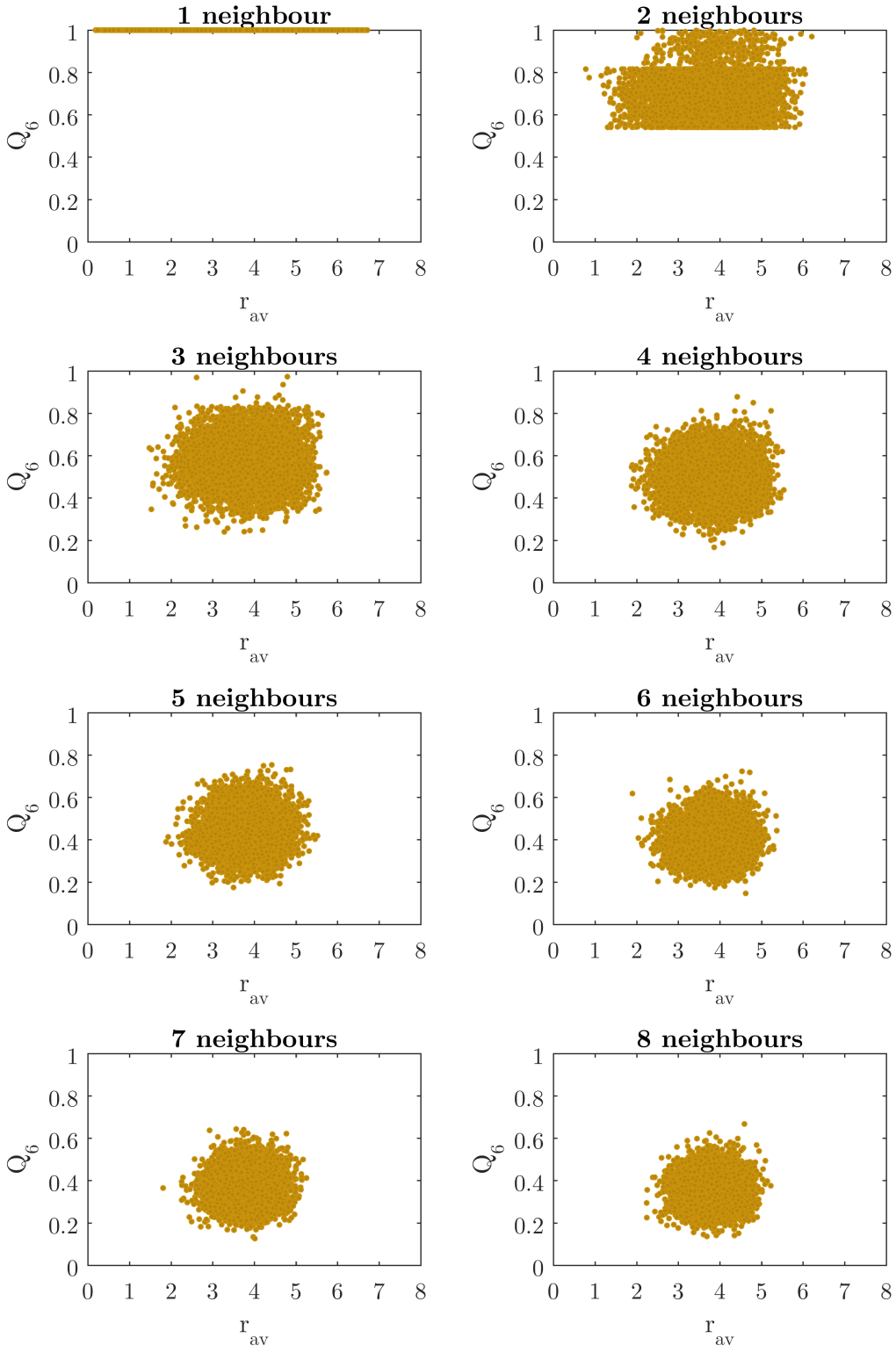

Figure 4.7: Plots of Q_6 values against the average neighbour distance for a reference particle with 1-8 neighbours located at random positions.

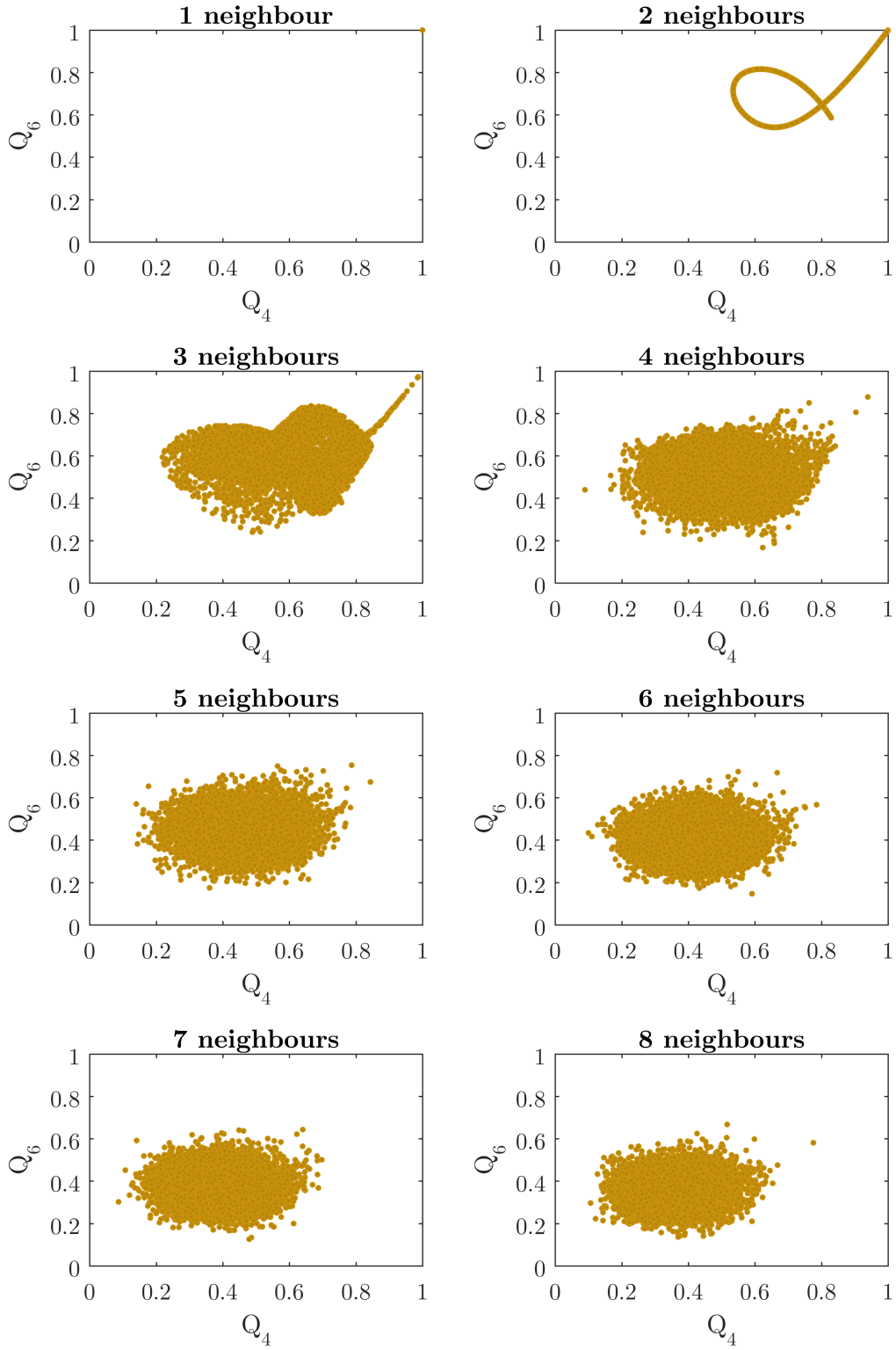

Figure 4.8: Plots of Q_6 against Q_4 values for a reference particle with 1-8 neighbours located at random positions.

following section, for cubic crystals, all the odd Steinhardt order parameters as well as Q_2 are equal to zero. So Q_4 and Q_6 are the first non-zero Steinhardt order parameters.

4.4 Steinhardt order parameters of simple cubic crystals

The values of Steinhardt order parameters, depend on the structure of the system. More specifically, the local environment of each particle and the positions on the neighbouring particles define the parameter values. To explore the way that local structure affects Steinhardt order parameter values, simple cubic structures were investigated for the three first neighbouring cells.

4.4.1 Primitive cubic cell

The primitive cubic cell structure consists of one atomic site in each corner of a cube (Fig. 4.9). The first neighbour shell consists of 6 atoms, the second has 12 atoms and the third 8. In order to determine the values of Steinhardt order parameters for the primitive cubic cell, it is required to calculate tesseral spherical harmonics for the different neighbouring atoms. For the first three neighbouring cells, angle θ can take the values 0, $\pi/4$, $\cos^{-1}(1/\sqrt{3})$, $\pi/2$, $\cos^{-1}(1/\sqrt{3})$, $3\pi/4$ and π. But using the symmetry of tesseral spherical harmonics, only terms with $0 \leq \theta \leq \pi/2$ require calculation. These calculations contain tedious mathematical details presented in Appendix A.2. For the first neighbouring shell, the second kind of the Steinhardt order parameters is given by

$$Q_\ell^{(i)} = \frac{1}{3}\left[\left[1 + \frac{1}{2^{\ell-1}} d_0(\ell,0)\right]^2 + \frac{1}{2^{2\ell-1}} \sum_{m=0}^{\ell} \frac{(\ell-m)!}{(\ell+m)!} d_0^2(\ell,m) e_{m,4k+4}\right]^{\frac{1}{2}} e_{\ell,2k}, \tag{4.38}$$

For the atoms that lie exclusively in the second neighbour shell

$$\begin{aligned} Q_\ell^{(i)} = &\frac{1}{3\cdot 2^\ell}\left[\left[2\left[\sum_{k=0}^{\ell} 2^{-\frac{k}{2}} d_k(\ell,0)\right] + d_0(\ell,0)\right]^2 + \right. \\ &\left. + \frac{1}{2}\left[\sum_{m=0}^{\ell} \frac{(\ell-m)!}{(\ell+m)!} d_0^2(\ell,m) e_{m,4k+4}\right]\right]^{\frac{1}{2}} e_{\ell,2k}, \end{aligned} \tag{4.39}$$

Finally, for the third neighbouring shell,

$$\begin{aligned} Q_\ell^{(i)} = &\frac{1}{2^\ell}\left[\left[\sum_{k=0}^{\ell} 3^{-\frac{k}{2}} d_k(\ell,0)\right]^2 + \right. \\ &\left. + \frac{1}{2}\sum_{m=0}^{\ell}\left(\frac{2}{3}\right)^m \frac{(\ell-m)!}{(\ell+m)!}\left[\sum_{k=0}^{\ell-m} 3^{-\frac{k}{2}} d_k(\ell,m)\right]^2 e_{m,4k+4}\right]^{\frac{1}{2}} e_{\ell,2k}. \end{aligned} \tag{4.40}$$

In the above relations, the terms $e_{\ell,2k}$ and $e_{m,4k+4}$ are a sum over various Kronecker's delta terms, given by

$$e_{i,jk+l} = \sum_{k=0}^{\infty} \delta_{i,jk+l}. \tag{4.41}$$

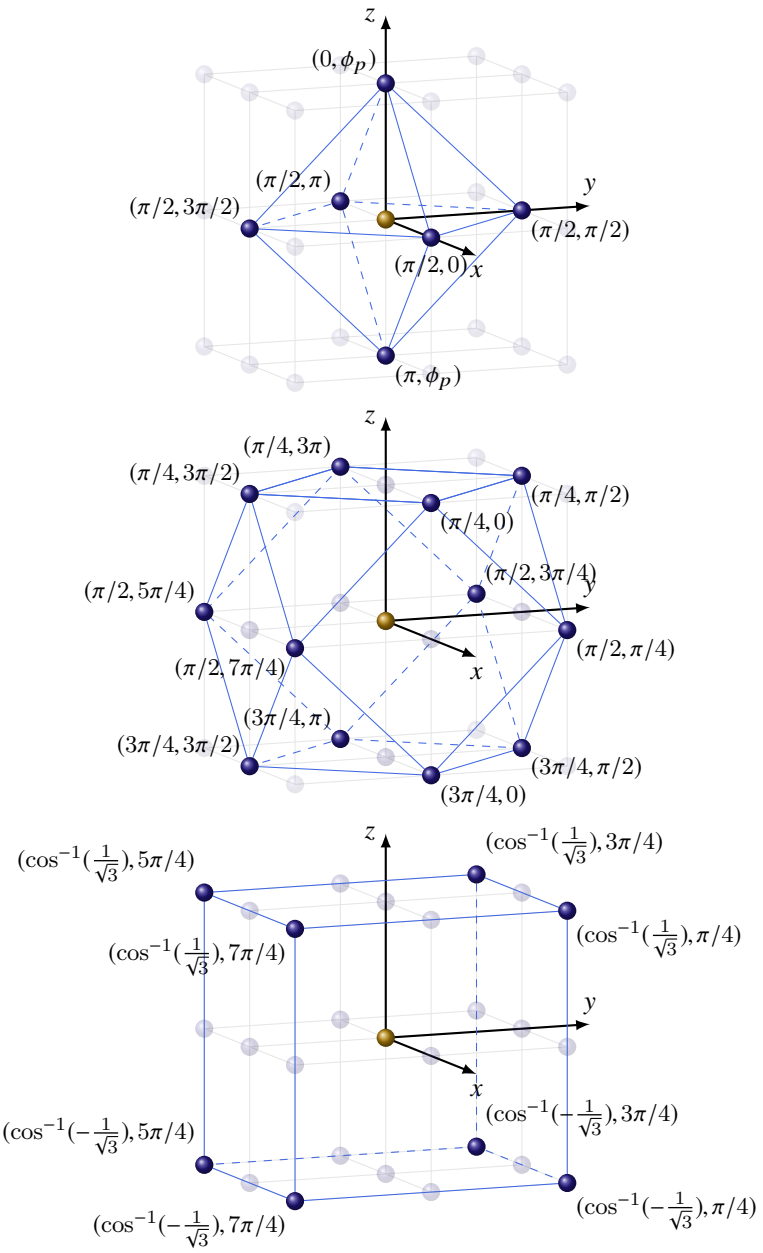

Figure 4.9: The first three coordinate shells of a primitive cubic cell system. **Top**: Atoms in the first neighbour shell of a primitive cubic lattice form an octahedron. There are six atoms at certain distance a from the reference particle, equal to the dimension of the cell, that can be grouped in three pairs, $[(\pi/2,0)-(\pi/2,\pi)]$, $[(\pi/2,\pi/2)-(\pi/2,3\pi/2)]$ and $[(0,\phi_p)-(\pi,\phi_p)]$, symmetric to the origin. **Middle:** The 12 atoms of the second neighbour shell form a tetradecahedron. All atoms are found at distance $a\sqrt{2}$ from the reference particle. The symmetry of the tesseral spherical harmonics makes possible the calculation of all spherical harmonics by using just the for atoms at $(\pi/4,0)$, $(\pi/4,\pi/2)$, $(\pi/2,\pi/2)$ and $(\pi/2,3\pi/4)]$. **Bottom:** The third neighbour shell consists of 8 atoms at the corners of the cubic cell and at distance $a\sqrt{3}$ from the reference particle. All tesseral spherical harmonics can be calculated by using the two particles at $(\cos^{-1}(1/\sqrt{3}),\pi/4)$ and $(\cos^{-1}(1/\sqrt{3}),3\pi/4)$.

Table 4.1: The non-zero values of second kind Steinhardt order parameters for the first three neighbour cells of the primitive cubic cell and for $0 \leq \ell \leq 10$

	ℓ	0	4	6	8	10
1st	Neighbour cell	1	$\frac{\sqrt{21}}{6}$	$\frac{\sqrt{2}}{4}$	$\frac{\sqrt{33}}{8}$	$\frac{\sqrt{390}}{48}$
2nd	Neighbour cell	1	$\frac{\sqrt{21}}{24}$	$\frac{13\sqrt{2}}{32}$	$\frac{9\sqrt{33}}{128}$	$\frac{\sqrt{390}}{1536}$
3rd	Neighbour cell	1	$\frac{\sqrt{21}}{9}$	$\frac{4\sqrt{2}}{9}$	$\frac{\sqrt{33}}{27}$	$\frac{8\sqrt{390}}{243}$

This expression is used to distinguish the non-zero terms contributing to the values of the Steinhardt order parameters. The presence of the terms $e_{\ell,2k}$ and $e_{m,4k+4}$ in Eqs. (4.38), (4.39) and (4.40), reveals that all the parameters with ℓ = odd are zero and for ℓ = even only terms with $m = 4k$ contribute to the values of the Steinhardt order parameters. The non-zero second kind Steinhardt order parameters values for the first three neighbour cells of the primitive cubic cell are given in Table 4.1.

Combination of different neighbouring cells

If we need to calculate the Steinhardt order parameters for all the atoms within the second neighbour shell, there is no need to perform an analytical calculation as in the case of separate cells. It can be proven that the first kind Steinhardt order parameters for all the atoms within the $n-$th neighbouring cell are given by

$$\langle Q_{\ell,m}\rangle^{(i)} = \frac{1}{N_n}\sum_{j=1}^{n} N_j \langle Q_{\ell,m}\rangle_j^{(i)}, \tag{4.42}$$

where N_j are the atoms of the $j-$th neighbouring cell and $\langle Q_{\ell,m}\rangle_j^{(i)}$ the respective first kind Steinhardt order parameters. Thus, the squared norm will be

$$|\langle Q_{\ell,m}\rangle^{(i)}|^2 = \frac{1}{N_n^2}\left[\sum_{j=1}^{n} N_j^2 |\langle Q_{\ell,m}\rangle_j^{(i)}|^2 + 2\sum_{j=1}^{n}\sum_{k>j}^{n} N_j N_k \langle Q_{\ell,m}\rangle_j^{(i)} \langle Q_{\ell,m}\rangle_k^{(i)}\right] \tag{4.43}$$

Using this relation we can also prove that second kind Steinhardt order parameters are given by

$$Q_\ell^{(i)} = \frac{1}{N_n}\left[\sum_{j=1}^{n} N_j^2 Q_{\ell,j}^{(i)} + 2\sum_{j=1}^{n}\sum_{k>j}^{n} N_j N_k \sum_{m=-\ell}^{\ell} \langle Q_{\ell,m}\rangle_j^{(i)} \langle Q_{\ell,m}\rangle_k^{(i)}\right]^{\frac{1}{2}} \tag{4.44}$$

For example, in the case of the first two cells, first order Steinhardt order parameters are given by

$$\langle Q_{\ell,m}\rangle^{(i)} = \frac{1}{3}\langle Q_{\ell,m}\rangle_1^{(i)} + \frac{2}{3}\langle Q_{\ell,m}\rangle_2^{(i)}, \tag{4.45}$$

and the second kind Steinhardt order parameters

$$Q_\ell^{(i)} = \frac{1}{3}\left[Q_{\ell,1}^{(i)} + 4Q_{\ell,2}^{(i)} + 4\sum_{m=-\ell}^{\ell} \langle Q_{\ell,m}\rangle_1^{(i)} \langle Q_{\ell,m}\rangle_2^{(i)}\right]^{\frac{1}{2}} \tag{4.46}$$

This methodology is also extremely helpful in case we need to calculate Steinhardt order parameters for particles with neighbours of different species. We can perform calculations of the parameters for each of the neighbouring species separately and then use equation (4.44) to calculate the parameters for all the neighbours, instead of recalculating them from scratch, which will be a more expensive procedure.

4.4.2 BCC lattice

In a bcc lattice, the first three neighbour shells are identical to the third, the first and the second neighbour shells of a primitive cubic cell, as demonstrated in Fig. 4.10. Thus, second kind Steinhardt order parameters will be given by (4.40), (4.38) and (4.39) respectively.

Thus, by estimating the Steinhardt order parameters of the first and only neighbouring cell it will be quite easy to distinguish the two crystal systems. However, if the parameters are calculated for all the atoms in the first three neighbouring cells, they will be identical for the two structures and any identification of the crystalline structure will be impossible.

4.4.3 FCC lattice

For the fcc lattice, the first neighbour cell is identical to the second neighbouring cell of the primitive cubic cell and the second to the first cell. Additionally, the third cell is quite different from and much more complicated than the neighbour cells of the primitive cubic cell (Fig. 4.10). It forms a tetradecahedron consisting of 24 atoms at a distance $a\sqrt{10}/2$ from the reference particle. This tetradecahedron is formed by 6 squares and 8 hexagons, while the tetradecahedron of the first neighbour cell (which is identical to the second neighbour cell of the primitive cubic cell structure) consists of 6 squares and 8 equilateral triangles.

Again, to distinguish the different cubic crystal systems using Steinhardt order parameters, we need to calculate them only for the first neighbour cell, since it is different in the three basic cubic crystal systems.

4.5 Hermite order parameters

Steinhardt order parameters depend only on the angular distribution of the particles around a reference atom. If we can develop a similar method to characterize damage that will be independent of the angles θ_{ij} and ϕ_{ij} between particles that will give identical results, then the two can provide a self validating set of methods to characterize radiation damage. In this direction, we can develop an additional methodology that will depend only on the distance r_{ij} between the particles using a set of polynomial functions. The first step is to decide which kind of polynomials we must use in order to get the required results.

In all systems, particles are vibrating around their initial position. So the force in their vicinity must have a dominant harmonic term of the form

$$\mathbf{F} = -kr\,\hat{r}, \tag{4.47}$$

which describes the well known Hooke's law. In classical mechanics, this equation of motion can

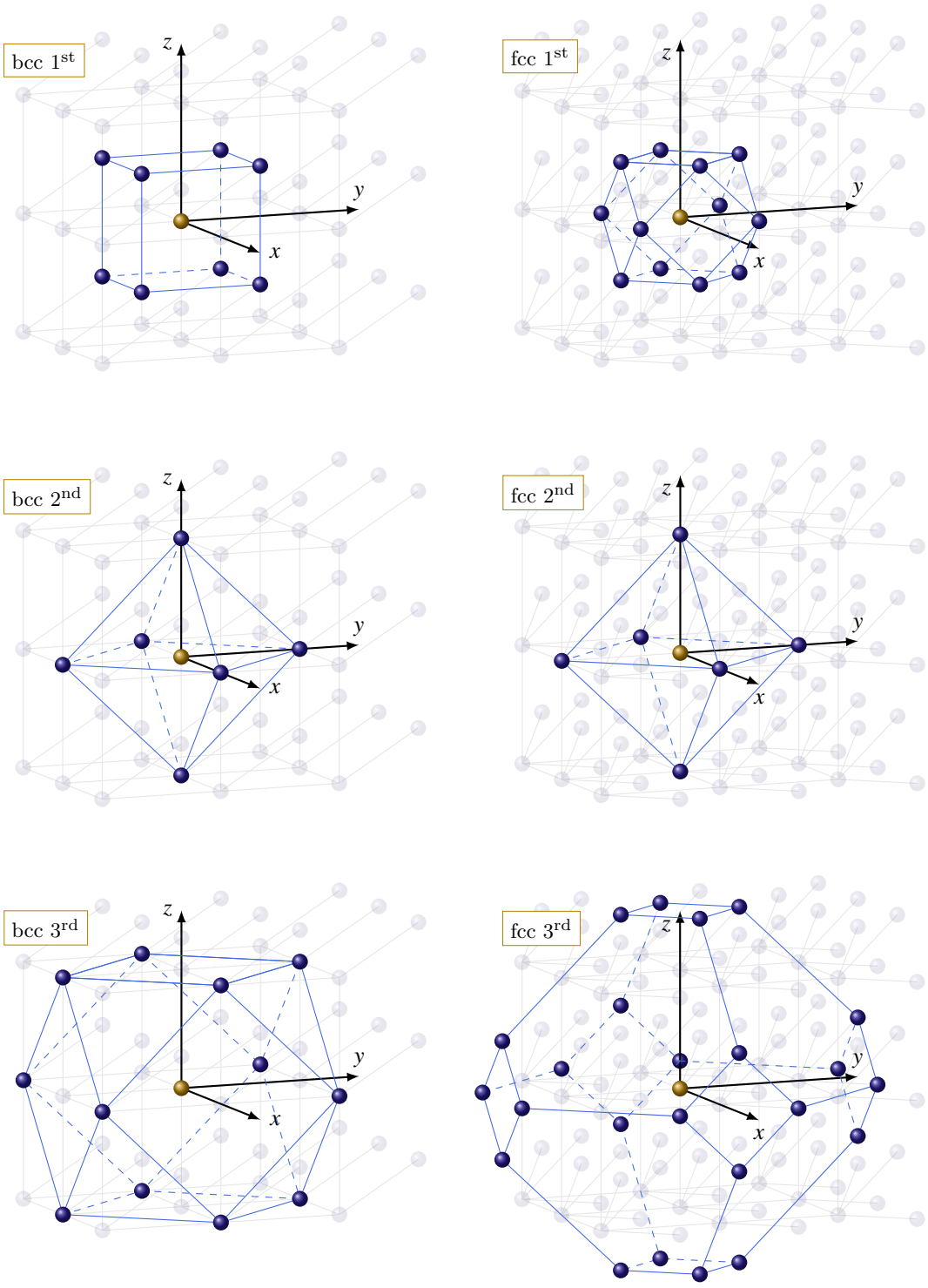

Figure 4.10: The first three neighbour cells of a bcc lattice (left) and a fcc lattice (right). For the bcc it is quite easy to see that the first three cells are identical to the third, the first and the second cell of a primitive cubic cell. For the fcc lattice, the first cell is identical to the second and the second to the first shell of the primitive cubic cell. However, the third cell is much more complicated and very different from the neighbour cells of a primitive cubic cell.

be solved analytically giving the position of the particle as a function of time in the form

$$r = A\cos(\omega t) + B\sin(\omega t), \tag{4.48}$$

where

$$\omega = \sqrt{\frac{k}{m}}, \tag{4.49}$$

is the frequency of the vibrational movement and m the mass of the particle. If we know the initial conditions (the initial position and velocity) it is easy to find the position of the particle as a function of time. However this approach cannot give us the required information as it involves only the displacement of a particle from its initial position. For crystalline systems, this information might be enough to characterize radiation damage. But in amorphous materials, where the displacement of a particle from its initial position cannot determine with accuracy if it is damaged or not, we need something more sophisticated.

If we use a quantum mechanics approach things become more interesting. The solution of Schrödinger's equation for a harmonic potential results is the well known Hermite polynomials, given by

$$H_n(\xi) = (-1)^{\xi} e^{\xi^2} \frac{d^n}{d\xi^n} e^{-\xi^2}. \tag{4.50}$$

These polynomials are probably the best functions to describe vibrational motions around a reference point. These polynomial are orthogonal and satisfy the relation

$$\int_{-\infty}^{\infty} H_n(\xi) H_m(\xi) e^{-\xi^2} d\xi = \sqrt{\pi}\, 2^n n!\, \delta_{m,n}. \tag{4.51}$$

For large n or ξ values, the Hermite polynomials take on very large values. To limit their values to a more reasonable and workable range, we use the orthonormal polynomials

$$\tilde{H}_n(\xi) = \frac{(-1)^n}{\pi^{1/4}\sqrt{2^n n!}} e^{\xi^2/2} \frac{d^n}{d\xi^n} e^{-\xi^2}, \tag{4.52}$$

so that

$$\int_{-\infty}^{\infty} \tilde{H}_n(\xi) \tilde{H}_m(\xi) d\xi = \delta_{m,n}. \tag{4.53}$$

The disadvantage of this form is that because of the exponential term and the high order terms, these polynomials are extremely sensitive to any change in the distance. But as in the case of Steinhardt order parameters, we do not attempt to find a relation between the Hermite order parameters and the displacement of the particles. We are only interested in finding a relation between the parameters and the coordination number. To reduce the effect of the distance, instead of using the distance between the neighbouring particles we can use the relative distance

$$\tilde{r}_j = \frac{r_j}{r_{\mathrm{av}}}, \tag{4.54}$$

where r_{av} is the average neighbour distance. In a similar approach to Steinhardt order parameters,

we can calculate the Hermite polynomials for all the nearest neighbours and average them taking

$$\langle \tilde{H}_n(\tilde{r}) \rangle^{(i)} = \frac{1}{N_b} \sum_{j=1}^{N_b} \tilde{H}_n(\tilde{r}_j) \tag{4.55}$$

Using the above expression for the average Hermite polynomials we define the Hermite order parameters for a reference particle as

$$R_n^{(i)} = \frac{1}{N_b} \left[\sum_{j=1}^{N_b} \left| \tilde{H}_n(\tilde{r}_{ij}) \right|^2 \right]^{1/2} . \tag{4.56}$$

For a damaged system, where both the coordination number and the distances between the particles change, it is expected that these parameters will take values that depend on both the number of neighbours and the neighbour distances, providing important information regarding radiation damage.

4.5.1 Calculation of Hermite order parameters

The algorithm to calculate the Hermite order parameters is similar to the one for Steinhardt order parameters and is presented in Fig. 4.11. The first step is to select a reference particle to initialize the calculation. For this particle, all the neighbours that are inside a sphere of radius r_{cut} are selected, following the same procedure as in the calculation of Steinhardt order parameters.

The calculation of the even Hermite polynomials can be performed using equation (4.52) for $\xi = r_{ij}$. Once the Hermite polynomials are determined, we can also calculate their squared values and average them over all the nearest neighbours. The Hermite order parameters can then be calculated by just taking the square root of the averaged squared Hermite polynomials, as described in equation (4.56).

4.5.2 The effect of coordination number

As in the case of Steinhardt order parameters we can examine the effect of coordination number on the values of Hermite order parameters. In the case where the reference particle has only one neighbour, the relative distance $\tilde{r}$ will be equal to 1. As we can show, orthonormal Hermite polynomials for $\xi = 1$ are given by

$$\tilde{H}_n(1) = \frac{1}{\pi^{1/4}\sqrt{2^n\, n!}} \sum_{k=0,2,4,\ldots}^{n} (-1)^{k/2} \frac{2^{n-k}\, n!}{(n-k)!(2k)!} \tag{4.57}$$

and so Hermite order parameters will be given by

$$R_n^{(i)}(N_b = 1) = \frac{1}{\pi^{1/4}\sqrt{2^n\, n!}} \left| \sum_{k=0,2,4,\ldots}^{n} (-1)^{k/2} \frac{2^{n-k}\, n!}{(n-k)!(2k)!} \right|, \tag{4.58}$$

and their values are actually equal to the absolute value of the orthonormal Hermite polynomials at $\xi = 1$. We can divide each of the Hermite order parameters with $R_n^{(i)}(N_b = 1)$ in order to make all the Hermite order parameters for $N_b = 1$ to be equal to 1, just like the respective Steinhardt order

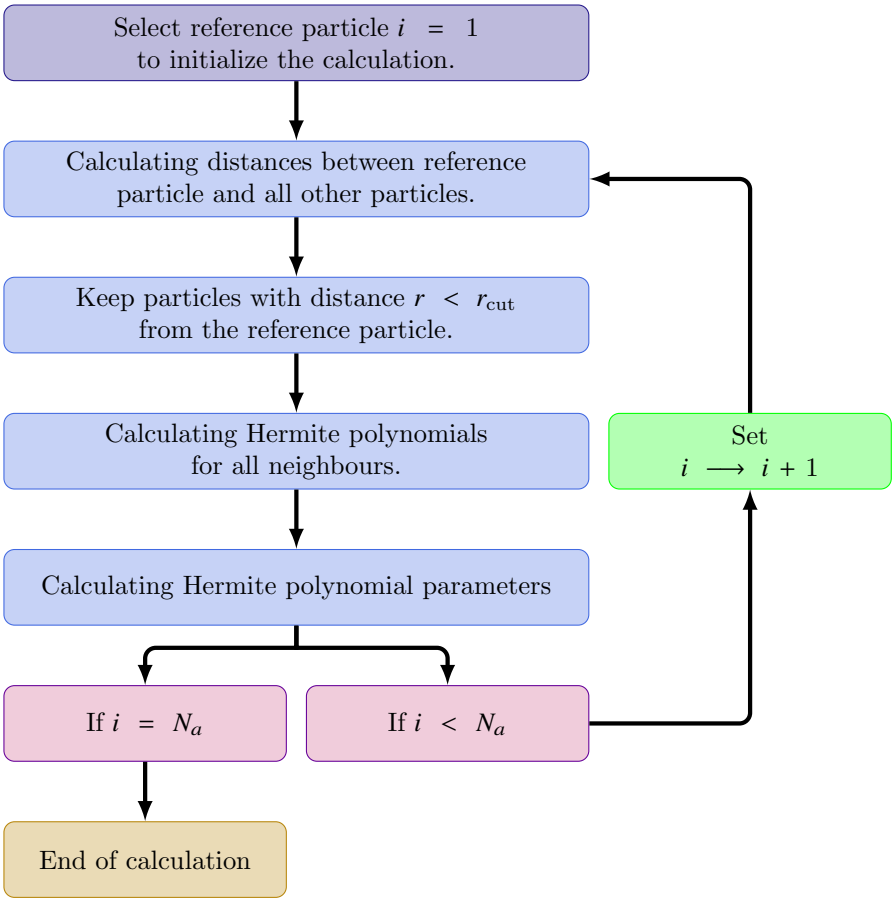

Figure 4.11: Algorithm for the calculation of the Hermite order parameters. N_a is the total number of atoms of the same species.

parameters. This will allow the immediate identification of particles with coordination number equal to 1, but it will not affect the way that the Hermite order parameters behave.

To explore the relation of the higher order Hermite order parameters with the average neighbour distance and the coordination number, simulations similar to those used for Steinhardt order parameters were carried out. In Fig. 4.12 the plots of R_4 against the average neighbour values are shown. From these plots it is obvious that for a coordination number $N_b \geq 3$ the Hermite order parameters present very small variations in their values. This behaviour is observed for all the parameters with $n \geq 2$. However, these plots can lead to the incorrect conclusion that the values of the Hermite order parameters are almost constant. To avoid such misconceptions, it is better to adjust the values of R_n axis properly, according to the range of the parameter values, as demonstrated in figure 4.13, where R_6 is plotted against r_{av}. From this plot we can observe that in general, R_n values form triangular-shaped regions, in which the Hermite order parameters converge as the average neighbour distance increases. For up to 4 neighbours, the triangles have a well defined base at the bottom of the plots, while for higher coordination numbers the base appears at the top of the plots. The disadvantage of $R_n(r_{\text{av}})$ plots is that there is large overlapping in the values of the Hermite order parameters for different coordination numbers - exactly as observed for Steinhardt order parameters.

For the Hermite order parameters however, it is quite easy to overcome this obstacle. In Fig. 4.14 the plots of R_6 against R_4 are shown, for the various coordinate numbers. Although it is quite easy to distinguish the areas occupied for up to four neighbours, particles with higher coordination numbers seems to occupy the same areas in the plots. As in the case of $R_n(r_{\rm av})$ plots, these cannot give any information, unless the scales of both axes are adjusted, as in Fig. 4.15, which demonstrates $R_4 - R_6$ pairs for coordination numbers $4 \leq N_b \leq 8$. In this plot it is obvious that particles with different coordination numbers occupy different position in the diagram, which makes very easy to distinguish them. There is a small overlapping for particles with 4 and 5 neighbours, however this is for only a few particles in a total of 8000 data points, which means that the error in the estimation will be extremely small. For the Hermite order parameters there is no need in modify their values by using a weight function dependent on the coordination number.

As is obvious, we can create similar plots for any pair of the Hermite order parameters and get similar information. The choice of R_4 and R_6 is just made for symmetry reasons, in order to have the same order as in the Steinhardt order parameters.

Similarly to the Steinhardt order parameters, the Hermite order parameters are also sensitive to both the coordination number of the particles as well as to the average neighbour distance. It is therefore expected that the use of the Hermite order parameters will provide important information regarding the radiation damage in a structure. In fact, it is expected that both Steinhardt and Hermite order parameters will provide consistent information regarding bond defects. This is extremely important, as the two sets of parameters depend on different variables. Steinhardt order parameters depend only on the spherical angles θ and ϕ between the reference particle and it's nearest neighbours, while the Hermite order parameters depend only on the separation distance. Thus, if the results of the two methods are consistent with each other, the Steinhardt and Hermite order parameters can be used as a self-validating set of methods in order to retrieve information regarding the topology of a structure.

4.6 Hermite order parameters of simple cubic crystals

In contrast with Steinhardt order parameters, the calculation of the Hermite order parameters of simple cubic crystals is quite straightforward. In these systems, all the nearest neighbours are found at the same distance from the reference particle, and so $\tilde{r}_{ij} = r_{ij}/r_{\rm av} = 1$. This means that all the orthonormal Hermite polynomials will be given by equation (4.57) and the Hermite order parameters are

$$R_n^{(i)} = \frac{1}{N_b} \frac{1}{\pi^{1/4}\sqrt{2^n\, n!}} \left[\sum_{j=1}^{N_b} \left| \sum_{k=0,2,4,\ldots}^{n} (-1)^{k/2} \frac{2^{n-k}\, n!}{(n-k)!(2k)!} \right|^2 \right]^{1/2} . \tag{4.59}$$

The second sum, over the k values, does not depend on the coordination number and so the above relation results in

$$R_n^{(i)} = \frac{1}{\sqrt{N_b}} \frac{1}{\pi^{1/4}\sqrt{2^n\, n!}} \left| \sum_{k=0,2,4,\ldots}^{n} (-1)^{k/2} \frac{2^{n-k}\, n!}{(n-k)!(2k)!} \right| , \tag{4.60}$$

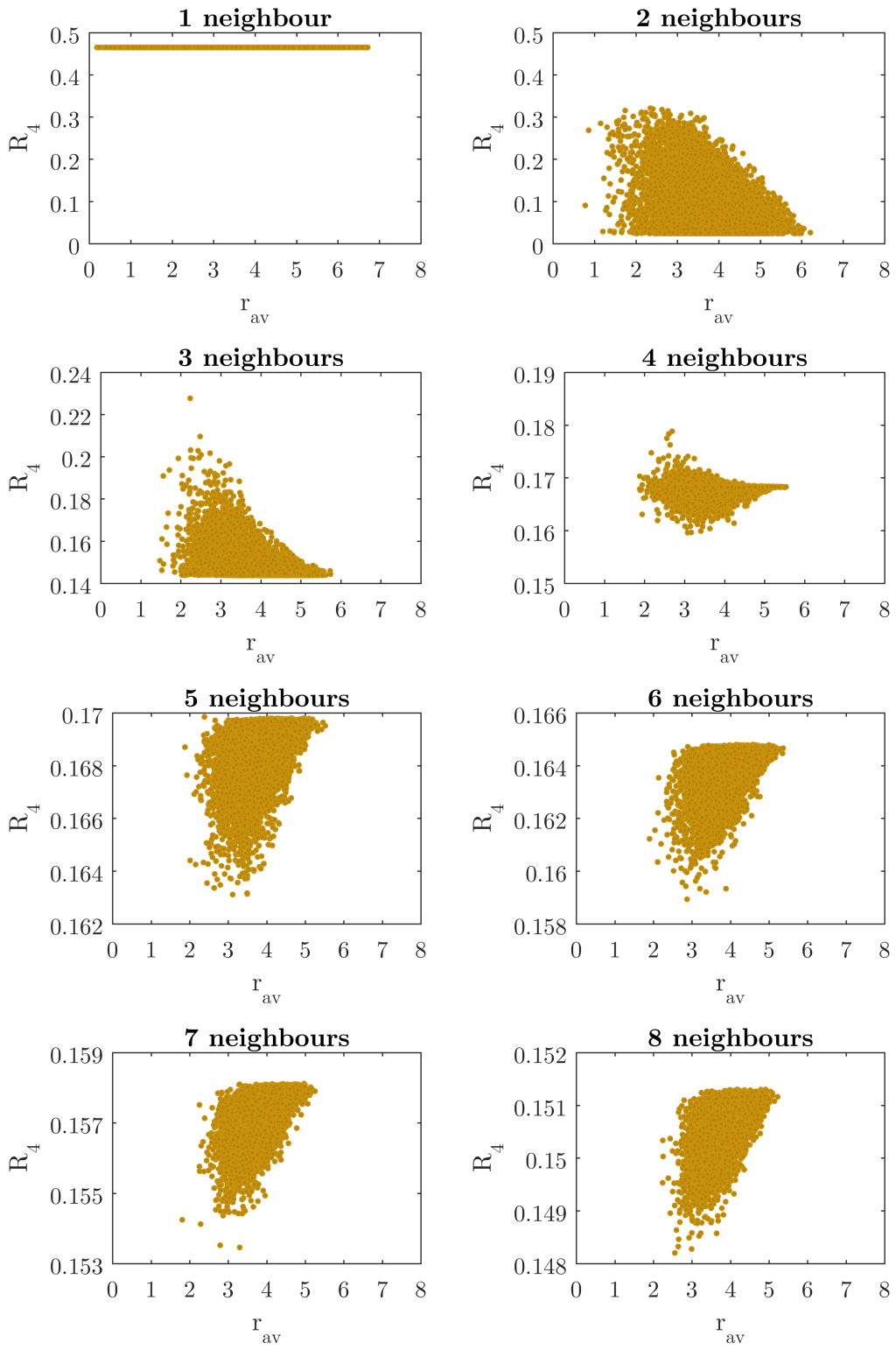

Figure 4.12: Plots of R_4 values against the average neighbour distance for a reference particle with 1-8 neighbours located at random positions.

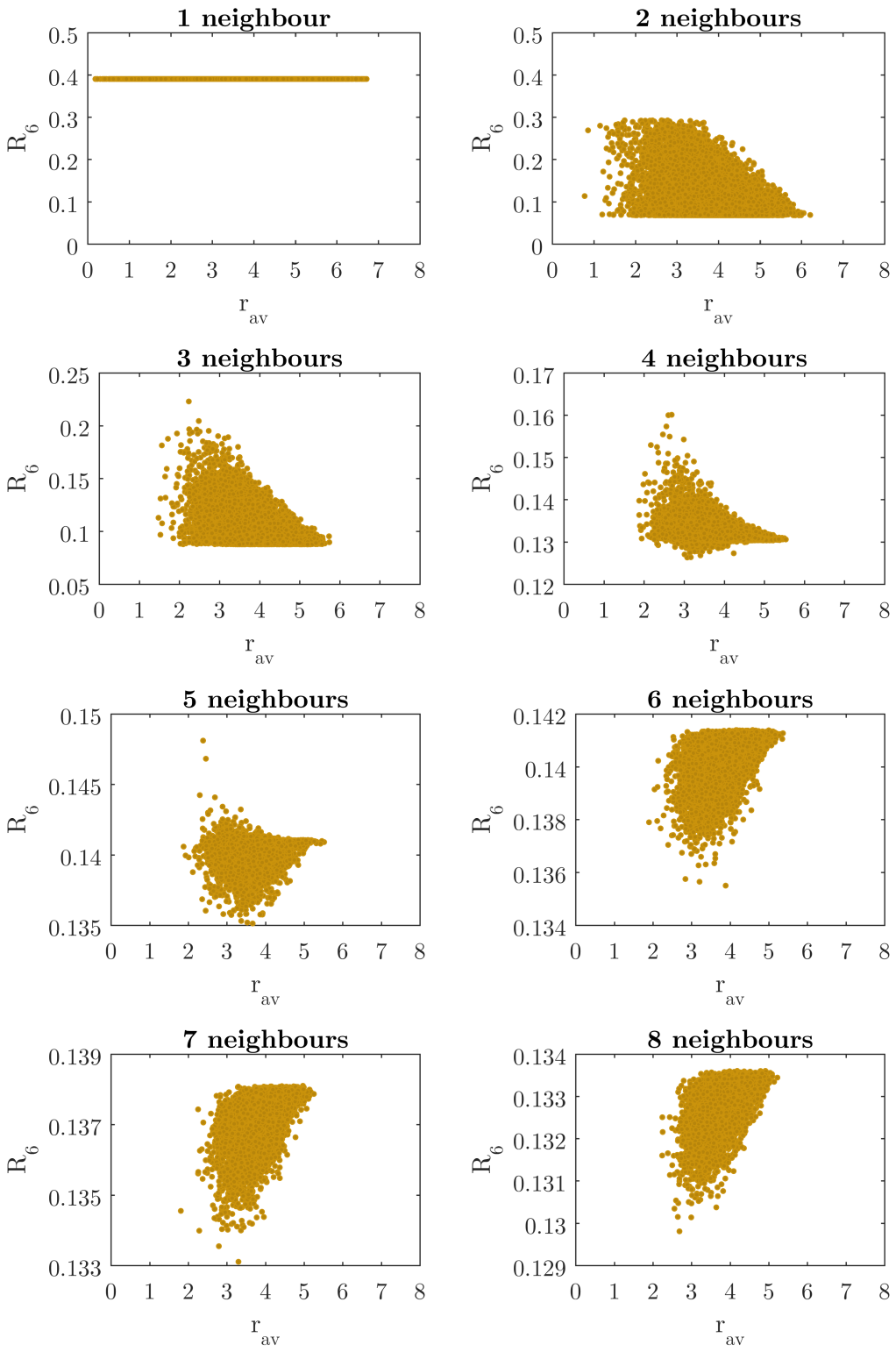

Figure 4.13: Plots of R_6 values against the average neighbour distance for a reference particle with 1-8 neighbours located at random positions.

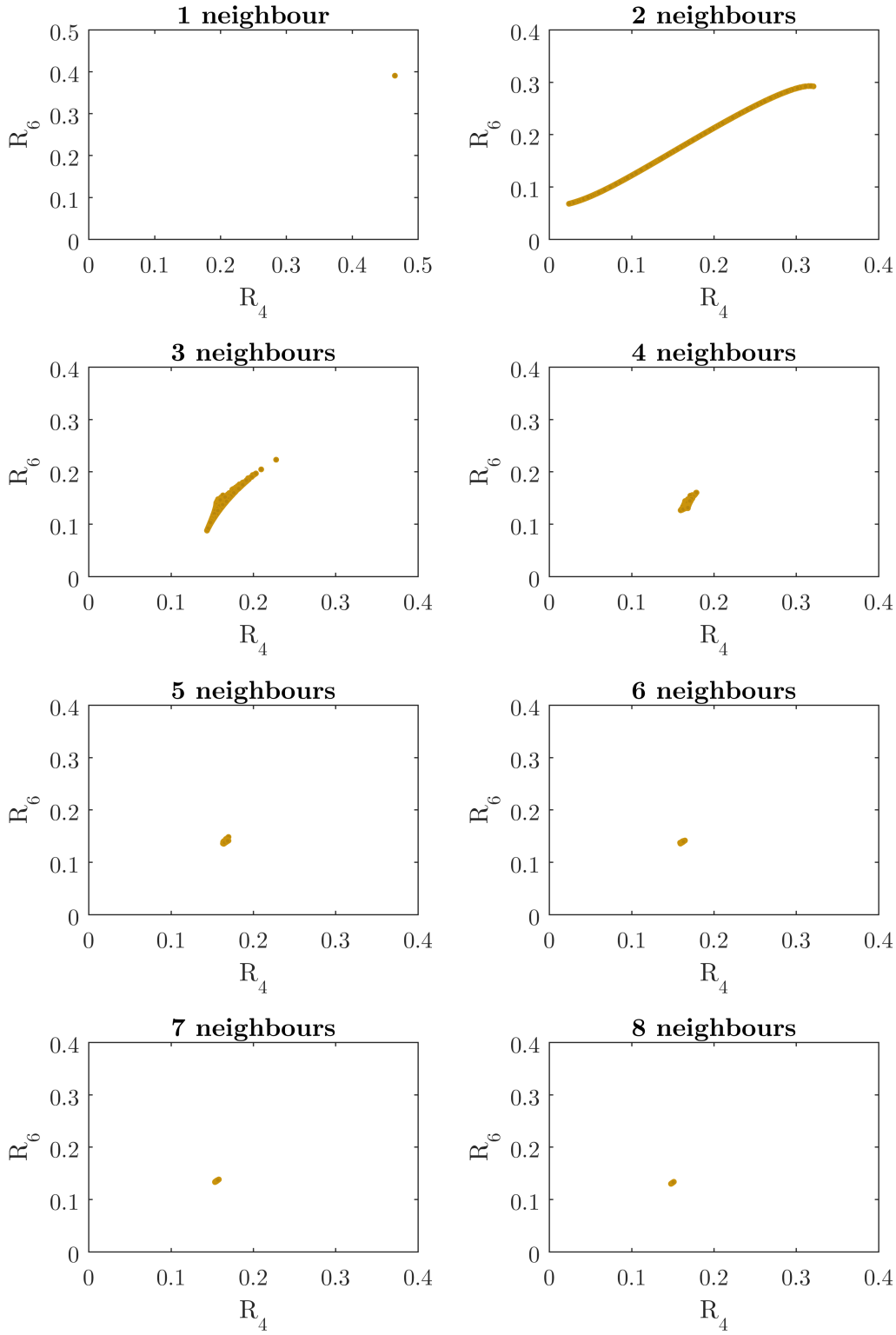

Figure 4.14: Plots of R_6 against R_4 values for a reference particle with 1-8 neighbours located at random positions.

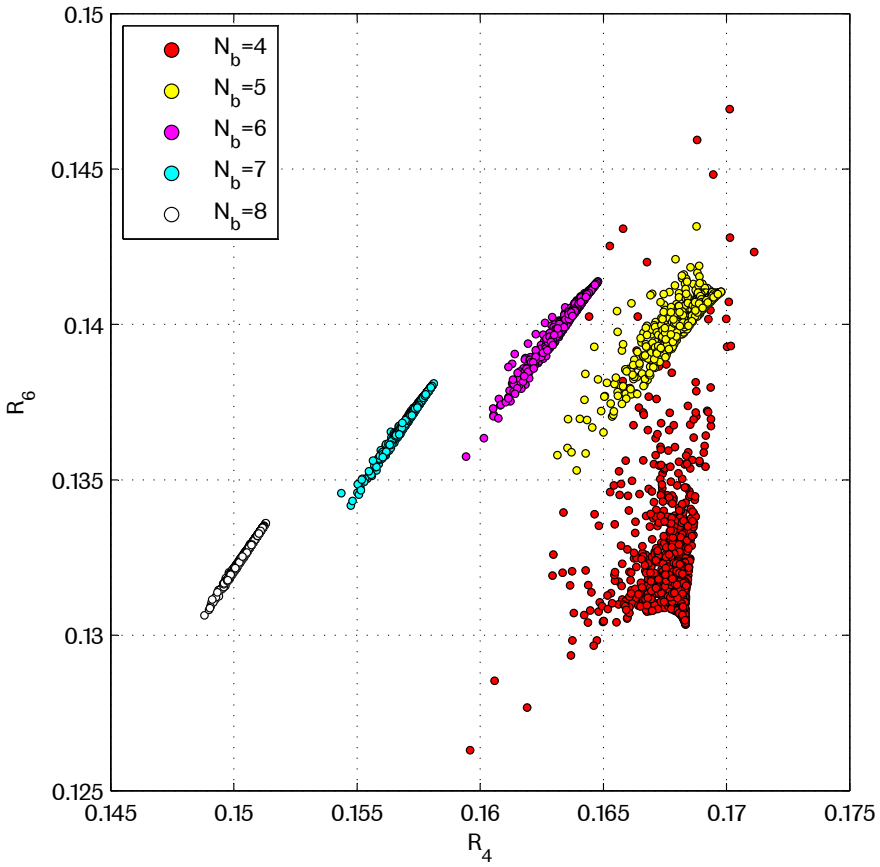

Figure 4.15: Plots of R_6 against R_4 values for 4 to 8 neighbours with adjusted axis scales.

and all the parameters are inversely proportional to the square root of the coordination number. For example, for the different n values up to 8 we get

$$\begin{aligned} R_0^{(i)} &= \frac{1}{\sqrt{N_b}}, & R_1^{(i)} &= \frac{1}{\sqrt{N_b}}\sqrt{2}, & R_2^{(i)} &= \frac{1}{\sqrt{N_b}}\frac{1}{\sqrt{2}}, \\ R_3^{(i)} &= \frac{1}{\sqrt{N_b}}\frac{1}{\sqrt{3}}, & R_4^{(i)} &= \frac{1}{\sqrt{N_b}}\frac{5}{4\sqrt{6}}, & R_5^{(i)} &= \frac{1}{\sqrt{N_b}}\frac{1}{2\sqrt{5}}, \\ R_6^{(i)} &= \frac{1}{\sqrt{N_b}}\frac{23}{12\sqrt{5}}, & R_7^{(i)} &= \frac{1}{\sqrt{N_b}}\frac{29}{6\sqrt{70}}, & R_8^{(i)} &= \frac{1}{\sqrt{N_b}}\frac{103}{24\sqrt{70}}. \end{aligned} \tag{4.61}$$

For the first neighbouring cells of the simple cubic lattice, for which $N_b = 6$ we have the values demonstrated in table 4.2. With these values known, the parameters for any other neighbouring shell can be directly calculated using the relation

$$R_n^{(i)} = \sqrt{\frac{6}{N_b}} R_{n,\mathrm{pcc}}^{(i)}. \tag{4.62}$$

In Table 4.2 the Hermite order parameters for the second and third neighbour shells of a primitive cubic structure are also shown. It is obvious that the parameters depend on the structure, although they do not have the symmetry of Steinhardt order parameters. Consequently, the Hermite order

parameters can also be used to retrieve information regarding the structure of a material. However, as in the case of Steinhardt order parameters, it is impossible to distinguish the 1st neighbour shell of the primitive cubic cell (pcc) from the 2nd cell of the bcc and fcc structures, the 2nd pcc from the 3rd bcc and the 3rd pcc from the first bcc. Thus, to distinguish the different structures, we need to calculate the Hermite order parameters for all the atoms within the first two neighbour shells.

Table 4.2: The first 9 Hermite order parameters for the first three neighbour shells of a primitive cubic system.

n	0	1	2	3	4	5	6	7	8
1st	$\frac{1}{\sqrt{6}}$	$\frac{1}{\sqrt{3}}$	$\frac{1}{2\sqrt{3}}$	$\frac{1}{3\sqrt{2}}$	$\frac{5}{24}$	$\frac{1}{2\sqrt{30}}$	$\frac{23}{12\sqrt{30}}$	$\frac{29}{12\sqrt{105}}$	$\frac{103}{48\sqrt{105}}$
2nd	$\frac{1}{2\sqrt{3}}$	$\frac{1}{\sqrt{6}}$	$\frac{1}{2\sqrt{6}}$	$\frac{1}{6}$	$\frac{5}{24\sqrt{2}}$	$\frac{1}{4\sqrt{15}}$	$\frac{23}{24\sqrt{15}}$	$\frac{29}{12\sqrt{210}}$	$\frac{103}{48\sqrt{210}}$
3rd	$\frac{1}{2\sqrt{2}}$	$\frac{1}{2}$	$\frac{1}{4}$	$\frac{1}{2\sqrt{6}}$	$\frac{5}{16\sqrt{3}}$	$\frac{1}{4\sqrt{10}}$	$\frac{23}{24\sqrt{10}}$	$\frac{29}{24\sqrt{35}}$	$\frac{103}{96\sqrt{35}}$

Combination of different neighbouring shells

With Steinhardt order parameters, if we know the parameters for each of the first m neighbour shells, the parameters for all the atoms within these shells are given by equation 4.44. For the Hermite order parameters the calculation needs to be performed from scratch, since the average neighbour distance changes as more and more neighbouring cells are added in the calculation. For example, for the first two shells of the primitive cubic cell, we have 6 atoms at distance α and 8 at distance $\alpha\sqrt{2}$. Thus, the average neighbour distance will be

$$r_{\text{av}} = \frac{1}{14}\left(6 + 8\sqrt{2}\right)\alpha. \tag{4.63}$$

Thus, the Hermite polynomials will be given by

$$\tilde{R}_n^{(i)} = \frac{1}{N_b}\left[\sum_{j=1}^{6} |\tilde{H}_n((6+8\sqrt{2})/14)|^2 + \sum_{j=7}^{14} |\tilde{H}_n((3\sqrt{2}+8)/14)|^2\right]. \tag{4.64}$$

In any case, there is no analytical form that can be extracted that will give the Hermite order parameters of m neighbouring shells as a function of the parameters for each of the cells.

4.7 Ring statistics

The Steinhardt and Hermite order parameters, provide information regarding the short-range structure of a material, based on the position of particles within the first coordination cell of a reference particle. By increasing the radius of the sphere used to identify neighbours, the range can be increased, but it will be difficult to retrieve information regarding bond defects. Thus, for long-range information it is preferable to use ring statistics, a topological approach that provides a mathematical description of the connectivity between the atoms of a structure [153, 155, 156, 157, 158].

4.7.1 Rings definitions

Ring statistics are based in the concept of a *topological network*, consisting of *nodes*, that are points in a network connected with *links*. In a real system, nodes represent atoms and links represent bonds between them. However, in contrast with actual structures, both nodes and links in a topological network are non-directed and have equivalent weights. Thus, all nodes are independent of the atomic species while links do not depend on the bond types and properties [159]. Sequentially connected nodes that do not overlap form *paths*, and if the path is closed it forms a *ring*. Each ring is characterized by a size or an order that is equal to the number of nodes comprising the ring.

Fig. 4.16 illustrates a sample topological network consisting of 11 nodes and 12 links. Several paths can be identified in this network. For example, just for node 1, 30 paths can be identified. However, Node sequences such as $(1-2-3-4-5-6-7-2-8)$ are not paths, since one node (2) appears more than once. However, this sequence forms the ring $r_1 : (2-3-4-5-6-7-2)$. In this network, apart from the one previously mentioned, another two rings can be identified: $r_2 : (2-8-9-10-11-4-3-2)$ and $r_3 : (2-8-9-10-11-4-5-6-7-2)$. The size of these rings is respectively 6, 7 and 9.

Primitive rings

In the network demonstrated in Fig. 4.16, we can see that nodes 2 and 4 can be connected through three different paths: $p_1 : (2-3-4)$, $p_2 : (2-8-9-10-11-4)$ and $p_3 : (2-7-6-5-4)$. The length of these paths is $l_1 = 2$, $l_2 = 5$ and $l_3 = 4$ respectively. The path with the shortest length that connects two nodes is known as *shortest path*. For the rings r_1 and r_2, this shortest path forms an edge of the rings. For these rings, all the shortest paths between any pair of nodes belongs to the perimeter of the rings. In contrast, for ring r_3 the shortest path between nodes 2 and 4 does not belong to the perimeter. Thus, for this ring, path p_1 defines a *shortcut*. Any ring for which there is no shortcut between any two nodes that form the ring is called a *primitive ring*. Thus, rings r_1 and r_2 are primitive rings, while ring r_3 is not. One important property of primitive rings, is that they cannot be decomposed into two rings of lower order. In contrast, any non-primitive ring can be decomposed into two rings of which at least one is of lower order. In Fig. 4.16, the non-primitive 9-order ring r_3 can be decomposed into a 6-order ring r_1 and a 7-order ring r_2.

An equivalent definition of primitive rings, that clarifies the previous argument, is given by Marians & Hobbs [160], who define a primitive ring as one with at least one shortest path between any pair of nodes. For this definition we can give a mathematical description. Consider three paths of lengths l_1, l_2 and l_3 between 2 nodes, forming three rings, r_{12}, r_{13} and r_{23}. If all paths have the same length, so that $l_1 = l_2 = l_3$ then all three rings are primitive, since all paths between the two nodes are shortest paths. If $l_1 = l_2 < l_3$, then for ring r_{12} both paths are shortest while rings r_{13} and r_{23} contain one shortest path (l_1 and l_2 respectively). All three rings are primitive. Finally, when $l_1 < l_2 = l_3$ or $l_1 < l_2 < l_3$, rings r_{12} and r_{13} include the shortest path, while ring r_{23} does not include the shortest path and consequently is not primitive.

An important concept in the primitive rings, is the *prime-mid-node* [159]. For an even ring of any given source node, there is one node, the prime-mid-node, for which both paths that connect the source node with the prime-mid-node are shortest paths. For odd rings, a prime-mid-node is defined

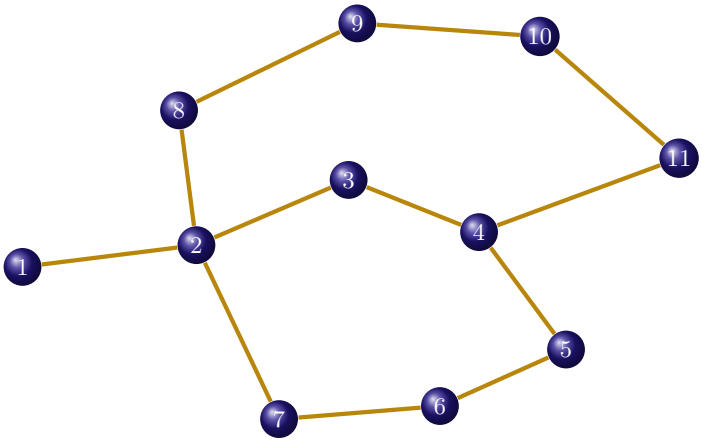

Figure 4.16: A sample topological network with 11 nodes and 12 links. In this network, 3 rings are identified: 2 primitive $r_1 : (2-3-4-5-6-7-2)$ and $r_2 : (2-8-9-10-11-4-3-2)$ and one non-primitive $r_3 : (2-8-9-10-11-4-5-6-7-2)$ that can be decomposed into r_1 and r_2.

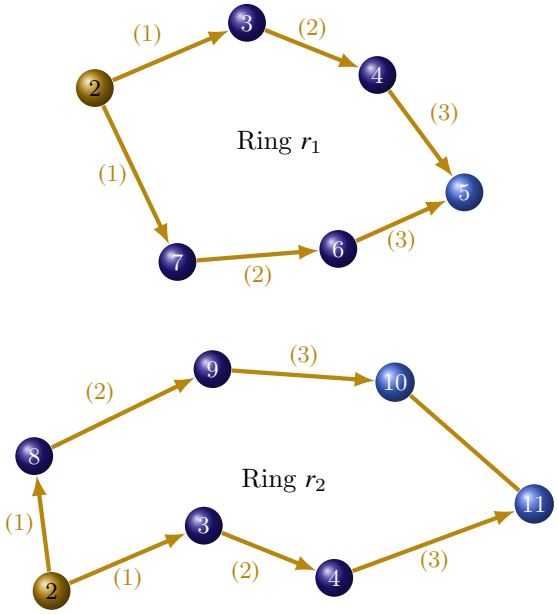

Figure 4.17: The concept of prime-mid-node for the even ring $r_1 : (2-3-4-5-6-7-2)$ and the odd $r_2 : (2-8-9-10-11-4-3-2)$. Taking node 2 as a source node, in the even ring r_1 has only one prime-mid-node, node 5, while in the odd ring r_2, nodes 10 and 11 form a pair of prime-mid-nodes.

as a node for which the length of the two paths connecting the node with the source node differ by one. To understand this concept, consider node (2) in Fig. 4.17. Ring $r_1 : (2-3-4-5-6-7-2)$ has six nodes and so it is an even ring. For node 2, there are two paths $2-3-4-5$ and $2-7-6-5$ connecting it with node 5. Thus, node 5 is the prime-mid-node of source node 2 and via versa. For the ring $r_2 : (2-8-9-10-11-4-3-2)$ we can see that there are two paths, $2-3-4-11$ and $2-8-9-10-11$, with respective lengths 3 and 4, connecting node 2 with node 11. Since the length of these paths differs by 1, node 11 is a prime-mid-node of source 2. However, node 10 is also connected with node 2 with two paths, $2-8-9-10$ and $2-3-4-11-10$, with lengths 3

and 4 respectively, so this is also a prime-mid-node. This stands for every odd ring. In general, for every source node of an even ring there is one prime-mid-node, while for a source node of an odd ring there are two prime-mid-nodes, linked with each other and forming a pair of prime-mid-nodes [159].

4.7.2 Identifying primitive rings

To analyse a structure using primitive rings, the first step is to identify the shortest paths from a *source node* - a node for which the ring structure will be determined, to any other source of the network. For this process, several methods have been proposed, including algorithms proposed by Goetzke & Klein [161] and by Hobbs et. al. [158]. For a system consisting of N nodes, these methods require the calculation of a $N \times N$ matrix that stores the shortest path distances for any pair on nodes in the system [158, 161]. For large systems where $N \sim 10^6$, the shortest distant matrix should contain $\sim 10^{12}$ elements, which makes the calculation quite expensive. Yuan and Cormack [159], proposed a new efficient algorithm to identify primitive rings. This algorithm involves 6 main calculation steps, described in detail in Appendix B. According to the authors, this method is significantly faster than traditional ring searching algorithms. For example, in case of a silica-based glass network and for a maximum ring size of 24, the new algorithm is about 1000 times faster.

Chapter 5

Developing topological methods towards radiation damage characterisation

5.1 Introduction

The development of new methods to analyse structural properties of materials needs validation. However, methods that involve the analysis of radiation damage effects in amorphous materials are very difficult to validate, since there are no data in the literature with which to compare the results. Thus, it is necessary to develop the new methodologies on a well studied crystalline structure, for which the existing literature studies will contribute to the validation of the methods. A zircon crystal was selected as a test structure, as it is one of the most well-studied crystalline structures under radiation damage events. This structure was used to identify how the radiation damage affects Steinhardt order parameters and Hermite order parameters and what information can be retrieved from these topological measurements regarding the bond defects and the extent of the damage in the material.

This structure is ideal for radiation damage studies, since all the atoms of the same species of the undamaged structure have the same coordination number. As several atoms will be displaced from their initial positions during the radiation damage event, the coordination numbers will change significantly and we anticipate being able to identify these changes - and consequently the bond defects - by plotting Q_4 against Q_6 and R_4 against R_6, as shown in the previous chapter.

At this point it is important to emphasise that although the results from the topological measurements will be compared with results from the traditional Wigner-Seitz method, they are not expected to converge. The Wigner-Seitz method only identifies atoms that are displaced from their initial position. Each of these atoms may be involved with more than one broken bond and so the number of broken bonds will be much higher than the number of displaced atoms, especially in the case of atoms with higher coordination. However, the number of broken bonds is not directly related to the displacement of one particle.

5.2 Zircon crystal structure

Zircon is the common name of zirconium silicate, a mineral crystal with chemical formula $ZrSiO_4$, which crystallizes in the I41/amd space group. Its structure is well studied in the past, mainly by Robinson et.al. [25], Hazen and Finger [26] and Finch et.al. [27]. The structure data determined by these studies are presented in Table 5.1. As Robinson et.al. [25] concluded, the main structural

unit of zircon is a Si-Zr chain, parallel to the *c* axis, consisting of ZrO_8 dodecahedra and SiO_4 tetrahedra that share one edge, as illustrated in Fig. 5.2 [162]. Each of the oxygen atoms forms one bond with a silicon atom and two bonds of different length with zirconium atoms, forming a triangular plane, as demonstrated in Fig. 5.1.

The SiO_4 units in zircon are distorted from the regular SiO_4 tetrahedron to a shape elongated parallel to [001], due to the repulsion between the Si^{4+} and Zr^{4+} cations of adjusted SiO_4 tetrahedra and ZrO_8 dodecahedra that share a common edge [163]. The values of the two O−Si−O angles in the SiO_4 unit are 116° and 97° [26, 27]. The O−O distance opposite the 116° angle and along the edge that is not shared between the SiO_4 tetrahedron and the adjusted ZrO_8 dodecahedron is 2.75 Å, while the O−O distance opposite to the 97° angle and along the shared edge is 2.43 Å. Similarly, the zirconium atom located at the centre of the ZrO_8 dodecahedron forms 4 short (2.131 Å) and four long (2.268 Å) bonds with the neighbouring oxygen atoms [162].

5.3 Creating a zircon crystal model

To create the crystal model, the General Utility Lattice Program (GULP) [147] was used. Although GULP was originally developed to perform fitting of potential energy functions to the physical and structural properties, it now offers a wide variety of simulation tasks using boundary conditions, including the energy minimization of a structure. Instead of using molecular dynamics, the program uses lattice dynamics in order to find still numerical solutions. GULP can automatically create the ideal initial structure just by using the space group and the chemical formula of the structure. However, to create a realistic structure, it is required to minimize Gibbs free energy and for this, the correct interaction potentials must be selected.

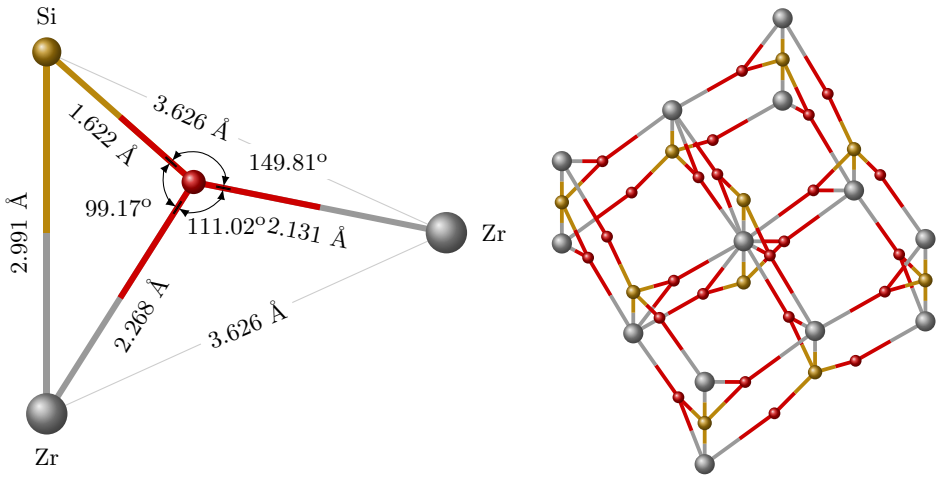

Figure 5.1: Zircon unit cell structure. **Left:** The triangular plane formed by one oxygen, one silicon and two zirconium atoms, along with the respective bond length and angles. **Right:** 3D image of zircon crystal unit cell. Although it is difficult to identify the SiO_4 tetrahedra - the cell must be expanded at least in one dimension to make them obvious - it is very easy to distinguish the ZrO_8 dodecahedron in the centre of the cell, formed by the central zirconium atoms and the 8 oxygen atoms that are bonded with it.

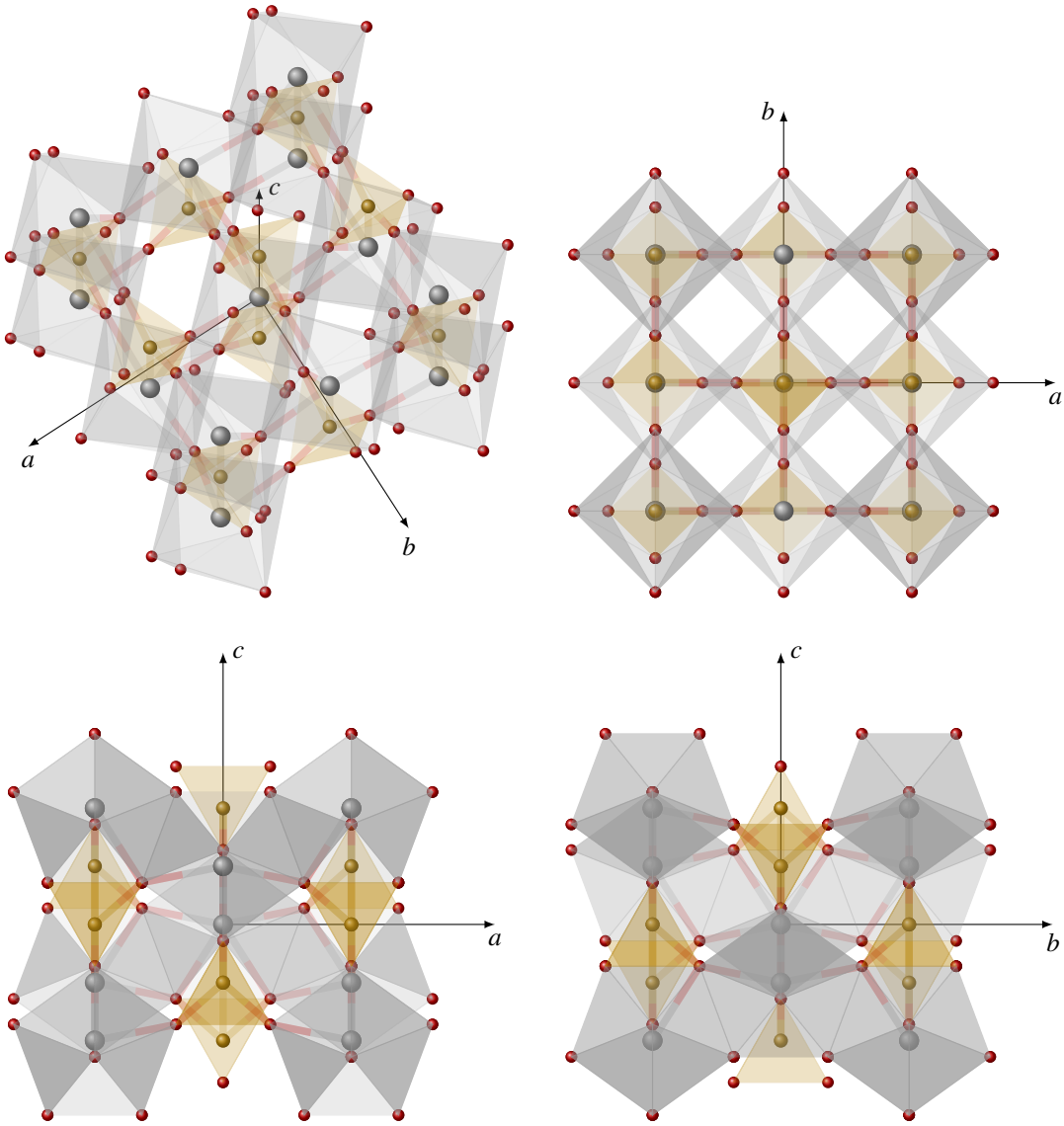

Figure 5.2: 3D representation of the SiO_4 tetrahedra and ZrO_8 dodecahedra, as seen from the same angle as the unit cell in Fig. 5.1 and 3 cuts parallel to the Oxy, Oxz and Oyz planes.

5.3.1 Potentials for radiation damaged zircon simulations

There are several potentials proposed in the literature for the zircon structure. Most common is a Buckingham type potential, used to describe Si-O, Zr-O and O-O interactions. Electrostatic interactions in all existing studies are described by the Coulombic term and calculated using an Ewald summation method. Trachenko et al. [28] (2001), used a Buckingham potential with the parameters shown in Table 5.2 to study radiation damage effects in a zircon crystal. To keep the Zr-Si-O angle constant at 99.17^o, these authors used three body potentials proposed by Sanders et al. [164]. Electrostatic interactions were calculated using the standard integer charges $q(\mathrm{Si}) = q(\mathrm{Zr}) = +4e$ and $q(\mathrm{O}) = -2e$. To avoid problems associated with the divergence region of the Buckingham potential, the short range ZBL potential was also used.

Table 5.1: Zircon crystal structure data as published in the studies of by Robinson et.al. [25], Hazen and Finger [26] and Finch et.al. [27]. In this, a, b, c are the unit cell distances, Z is the number of $ZrSiO_4$ units in the unit cell, ρ is the density and x, y, z are the relative positions of the atoms within the unit cell.

	Robinson et al.	**Hazen and Finger**	**Finch et al.**
a (Å)	6.6070	6.6042	6.6139
b (Å)	6.6070	6.6042	6.6139
c (Å)	5.9820	5.9796	5.9850
a/b	1.0000	1.0000	1.0000
b/c	1.1045	1.1045	1.1051
c/a	0.9054	0.9054	0.9049
Z	4	4	4
ρ (g/cm^3)	4.66	4.67	4.65
x(Zr)	0.0000	0.0000	0.0000
y(Zr)	0.7500	0.7500	0.7500
z(Zr)	0.1250	0.1250	0.1250
x(Si)	0.0000	0.0000	0.0000
y(Si)	0.2500	0.2500	0.2500
z(Si)	0.3750	0.3750	0.3750
x(O)	0.0000	0.0000	0.0000
y(O)	0.0661	0.0660	0.0658
z(O)	0.1953	0.1951	0.1954

Table 5.2: Buckingham potential parameters used by Trachenko et al. [28] (2001) to study the radiation damage effects in a zircon crystal.

Buckingham	A (eV)	ρ (Å)	C (eV·Å^6)
Si-O	1354.9546	0.3104097	5.33
Zr-O	8000000	0.14	0
O-O	22764	0.149	27.879

In a later study, Trachenko et al. [12] (2004) replaced the Si-O Buckingham potential with a Morse potential (Table 5.3) and used the fractional charges q(Si) = 1.356, q(Zr) = 3.428 and q(O) = −1.196 for the electrostatic interactions.

Table 5.3: Buckingham and Morse potential parameters used by Trachenko et al. [12] (2004).

Buckingham	A (eV)	ρ (Å)	C (eV·Å^6)
Zr-O	1477	0.317	0
O-O	9245	0.2617	100
Morse	$D\,(eV)$	a (Å^{-1})	r_e (Å)
Si-O	1.252	2.83	1.627

To study radiation damage effects in disordered zircon, Devanathan et al. [29] also used a Buckingham potential with $C = 0$ for all pair interactions, coupled with a ZBL short range potential.

For the electrostatic interactions, these authors used the fractional charges $q(\mathrm{Si}) = 2.00e$, $q(\mathrm{Zr}) = 3.80e$ and $q(\mathrm{O}) = -1.45e$. To join the Buckingham potential with the ZBL potential, instead of using the usual splines, this author used a Fermi switching function, given by

$$f(r) = \frac{1}{1 + e^{-b_f(r-r_f)}}, \tag{5.1}$$

where b_f and r_f are adjustable parameters such that the first derivative of the total potential energy function is continuous and monotonic for every $r \in [0, +\infty)$.

Table 5.4: Buckingham potential and Fermi switching function parameters used by Devanathan et al. [29].

Buckingham potential			Fermi switching function					
Pair	A (eV)	ρ(Å)	Pair	b_f(Å^{-1})	ρ_f(Å)	Pair	b_f(Å^{-1})	ρ_f(Å)
Si-O	1277.0	0.227225	Si-Si	6.0	1.00	Zr-Zr	6.0	1.00
Zr-O	1967.0	0.305004	Si-Zr	6.0	1.00	Zr-O	6.0	0.87
O-O	1755.0	0.306820	Si-O	6.0	0.62	O-O	6.0	0.30

Yu et al. [30] proposed an alternative potential, given by

$$U(r) = Ae^{-\frac{r}{\rho}} - \frac{C}{r^6} + 4\epsilon\left[\left(\frac{\sigma}{r}\right)^{18} - \left(\frac{\sigma}{r}\right)^{6}\right], \tag{5.2}$$

which is the sum of a Buckingham potential with a (18-6) Lennard-Jones potential, that applies to simulations of $ZrSiO_4$, ZrO_2 and SiO_2 systems. For the electrostatic interactions, the charges of atoms are: $q(\mathrm{Si}) = q(\mathrm{Zr}) = 2.4$ and $q(\mathrm{O}) = -1.2$.

Table 5.5: Buckingham and (18-6) Lennard-Jones parameters used by Yu et al. [30].

Pair	A (eV)	ρ(Å)	C (eV·Å^6)	ϵ (eV)	σ(Å)
Si-O	18003.7572	0.2052	133.5381	0.019	1.36
Zr-O	17243.3940	0.2265	128.3513	0.010	1.30
O-O	1388.7730	0.3623	175.0000	0.002	2.05

5.3.2 Optimization results: Choosing the correct potential

To validate the proposed potentials described in the previous section, three different energy minimization procedures were performed using a 2×2×2 supercell, containing 192 atoms in total. As demonstrated in Table 5.6, by comparing with experimental results it is obvious that the potentials proposed by Trachenko et al. [28] (2001) give relatively small errors for the structural properties, from 0.88% for the density to 3.26% for the c vector. However, the results for the elastic properties are associated with large relative errors, up to 198.8% for C_{13} and furthermore they give a negative C_{66} coefficient, observed in systems that store energy. From the other three potentials, those proposed by Trachenko et al. [12] (2004) give the best structural properties while those proposed by Devanathan et al. [29] give the best elastic properties.

Table 5.6: The cell parameters and properties calculated with the four different proposed potentials using a 2×2×2 supercell, containing 192 atoms. a, b, and c are the unit cell distances, V is the volume of the unit cell, ρ the density C_{ij} the non-zero elastic constants and K_s the bulk modulus.

Parameter	**Trachenko (2001)**	**Trachenko (2004)**	**Devanathan (2004)**	**Yu (2009)**	**Experimental**
a(Å)	6.4571	6.6410	6.6020	6.5583	6.607†
b(Å)	6.4571	6.6410	6.6020	6.5583	6.607†
c(Å)	6.1173	5.8998	6.0934	6.1445	5.982†
V(Å^3)	255.9977	260.2002	265.5928	264.2809	261.1†
$\rho(gr/cm^3)$	4.7012	4.6794	4.5844	4.6072	4.66‡
$C_{11}(GPa)$	1148.4924	434.3904	445.3640	455.3635	424†
$C_{33}(GPa)$	1283.3937	519.0305	479.1945	436.4143	490†
$C_{44}(GPa)$	139.4096	106.5761	84.3542	96.1216	114†
$C_{66}(GPa)$	-0.3274	31.5165	63.8702	63.5743	49†
$C_{12}(GPa)$	109.5501	47.9927	64.0769	118.6705	70†
$C_{13}(GPa)$	385.4487	146.8824	133.1748	146.3562	129†
$K_s(GPa)$	593.4749	230.1474	225.6417	241.0992	225†

† Results from Devanathan et al. [29]
‡ Results from Robinson et al. [25]

To explore the effect of the cell size, additional optimization simulations were performed for the three potentials qualified from the first round of optimization, using a 6×6×6 supercell containing 5184 atoms (Table 5.7). By comparing the results for the 2×2×2 and the 6×6×6 structures it is clear that the size of the simulation cell has negligible effects in the optimization results. For the 6×6×6 supercell, Trachenko's potentials give the best structural properties with a median error equal to 0.633% while the median error for the structural properties calculated with Devanathan's and Yu's potentials are equal to 1.072% and 1.308% respectively. For the elastic properties, the median errors for the three proposed potentials are equal to 16.0%, 12.5% and 24.5% respectively. Thus, it is clear that Devanathan's potentials provide the best estimation of the elastic properties. For radiation damage simulations it is important to preserve the structural properties and thus it is important to create models with structural properties as close as possible to the experimental values and so to create the irradiated zircon crystal model, the potentials proposed by Tracheno et al. [12] were used.

5.3.3 Creating a radiation damage cascade

The radiation damage cascade formation process was performed using the DL_POLY_4 molecular dynamics simulations package [132]. The first step was to equilibrate the 5184 atoms structure created by GULP at 300 K for 10 ps under the NVT ensemble and by using periodic boundary conditions. For the interaction between atoms, pair potentials proposed by Trachenko et al. [12] (2004) were used, as they give the most accurate structural data in comparison with experiments. To avoid problems associated with the divergence region of the O-O Buckingham potential, a short range ZBL potential was also used. To fit the two potentials, the `atsim.potentials` package was used [165], that fits a third order spline between the truncation points. The truncation distances

for the two potentials where selected so that:

1. The resulting potential is a smooth function of distance r,
2. The Buckingham potential is truncated as close as possible to the distance $r_{\max}$ for which the potential receives the maximum value,
3. The distance $r_{\text{Buck}} - r_{\text{ZBL}}$ is as small as possible.

These conditions are satisfied for $r_{\text{Buck}} = 1.0\,\text{Å}$ and $r_{\text{ZBL}} = 0.4\,\text{Å}$. The resulting potential was tabulated and incorporated within DL_POLY_4, and had the general form

$$U_{\text{O-O}}(r) = \begin{cases} U_{\text{ZBL}}(r), & \text{for} \quad r < 0.4\,\text{Å} \\ f(r), & \text{for} \quad 0.4\,\text{Å} \le r \le 1.0\,\text{Å} \\ U_{\text{Buck}}(r), & \text{for} \quad r > 1.0\,\text{Å} \end{cases}, \tag{5.3}$$

where $f(r)$ is the third order spline. For the calculation of electrostatic interactions the Ewald summation method routine provide by DL_POLY_4 was used.

A zirconium atom of the crystal was used as impact particle and assigned an excess of kinetic energy equal to 4 keV along the direction [111]. This kinetic energy is very high for a system of just 5184 atoms. However, the purpose of the simulation was not to estimate the radiation damage effects in the zircon crystal, but to create significant damage and find correlations between the extent of the damage and the topological parameters described in the previous chapter.

Radiation damage is a highly non-equilibrium process. To handle the excess of kinetic energy, a Langevin thermostat boundary layer was used, to emulate an infinite heat bath at a constant temperature of 300 K. The boundary layer relaxes locally the buffer region of the simulation cell

Table 5.7: The cell parameters and properties calculated with the three qualifying potentials using a 6×6×6 supercell, containing 5184 atoms. a, b, and c are the unit cell distances, V is the volume of the unit cell, ρ the density C_{ij} the non-zero elastic constants and K_s the bulk modulus. The relative errors of each calculation in comparison with the experiment can be seen in the brackets.

Parameter	**Trachenko (2004)**		**Devanathan (2004)**		**Yu (2009)**	
a(Å)	6.6410	(0.515)	6.6020	(0.076)	6.5583	(0.737)
b(Å)	6.6410	(0.515)	6.6020	(0.076)	6.5583	(0.737)
c(Å)	5.8998	(1.374)	6.0934	(1.863)	6.1445	(2.716)
V(Å^3)	260.2002	(0.345)	265.5929	(1.721)	264.2807	(1.218)
$\rho(gr/cm^3)$	4.6794	(0.416)	4.5844	(1.622)	4.6072	(1.133)
$C_{11}(GPa)$	434.3900	(2.450)	445.3641	(5.038)	455.3637	(7.397)
$C_{33}(GPa)$	519.0304	(5.925)	479.1946	(2.205)	436.4192	(10.935)
$C_{44}(GPa)$	106.5760	(6.512)	84.3541	(26.005)	96.1221	(15.682)
$C_{66}(GPa)$	31.5165	(35.681)	63.8702	(30.347)	63.5740	(29.743)
$C_{12}(GPa)$	47.9926	(31.439)	64.0768	(8.642)	118.6685	(69.521)
$C_{13}(GPa)$	146.8823	(13.862)	133.1748	(3.216)	146.3532	(13.452)
$K_s(GPa)$	230.1472	(2.288)	225.6415	(0.286)	241.0996	(7.155)

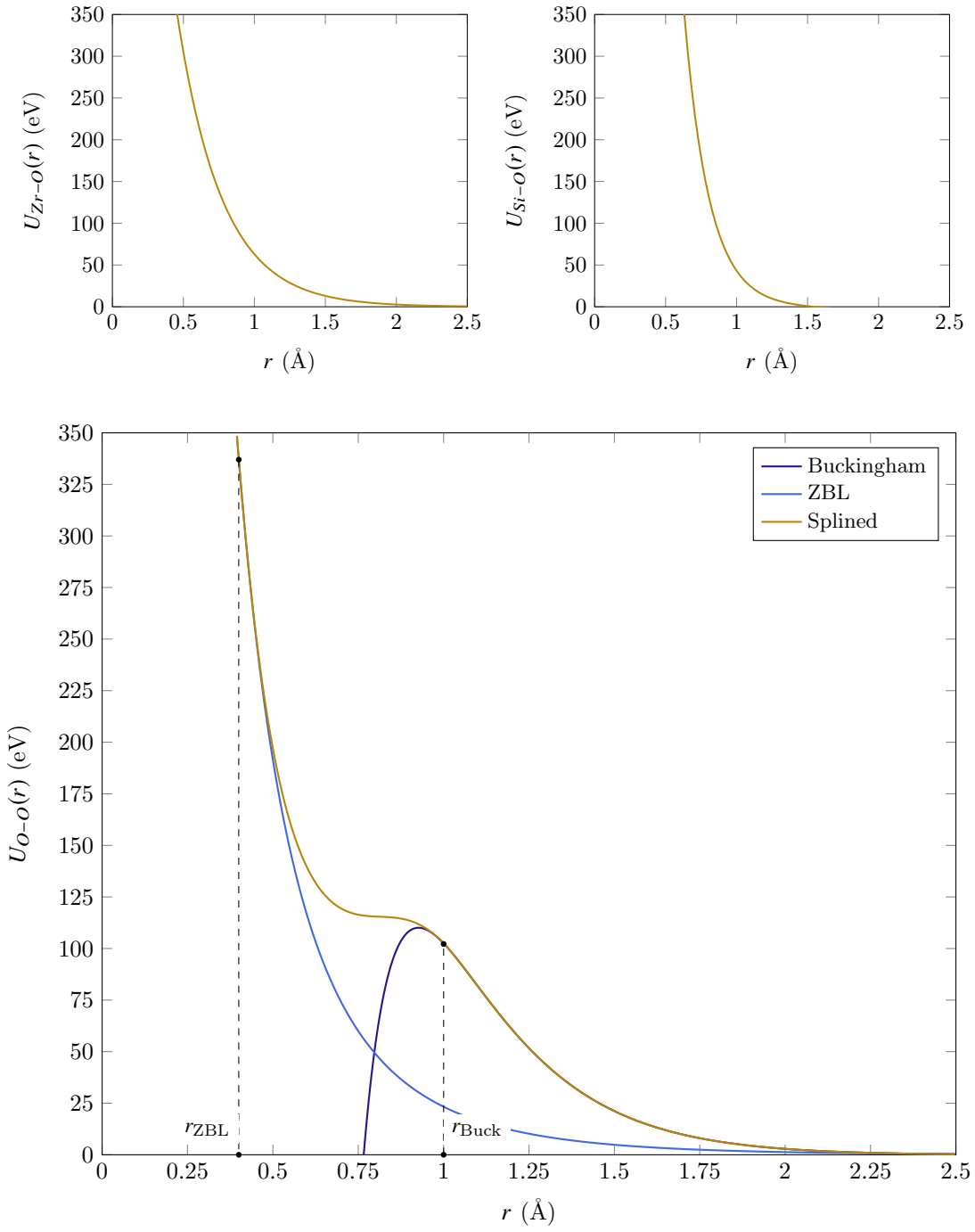

Figure 5.3: Potentials proposed by Trachenko et al. [12] (2004). **Top:** The Buckingham potential of the Zr-O interactions (left) and the Morse potential of the Si-O interactions (right) are monotonic, strictly decreasing functions and there is no need to truncate them and join them with the short range ZBL potential. **Bottom:** The O-O potential diverges to $-\infty$ as $r \longrightarrow 0$ and this can cause serious problems in the simulation in case two oxygen atoms approach to a distance closer than r_{max}, equal to the distance for which the interaction potential receives it's maximum value. For this, Buckingham potential is truncated and fitted to a short range ZBL potential.

and dissipates the excess kinetic energy, preventing energetic atoms from travelling through the boundaries of the simulation cell and re-entering through the mirror point, forming an unrealistic damage cascade. The thickness of the boundary layer was selected equal to 2 Å, the smallest possible value offered by DL_POLY_4, which was sufficient to block the energetic atoms. The highly energetic atoms travel relatively large distances at the initial stages of the simulation. To form the trajectories as accurate as possible, a variable timestep algorithm was applied for 50,000 timesteps. The initial and final timesteps set to 10^{-5} ps and 10^{-4} ps respectively, allowing the atoms to travel a distance between 0.01 Å and 0.05 Å per timestep.

5.3.4 Thermostat evaluation

The accuracy of the simulation heavily depends on the thermostat used to control the temperature. To explore this dependence and evaluate the efficiency of the different thermostats in controlling the temperature during the simulation of the radiation damage event, four different runs were performed at 300 K, using respectively NVE ensemble, NVT Nose-Hoover, NVT Berendsen and NVT Langevin thermostats. In all four simulations, a 2 Å boundary layer was used to emulate a heat bath at 300 K. In Fig. 5.4 the plot of the temperature versus time is illustrated. It is obvious

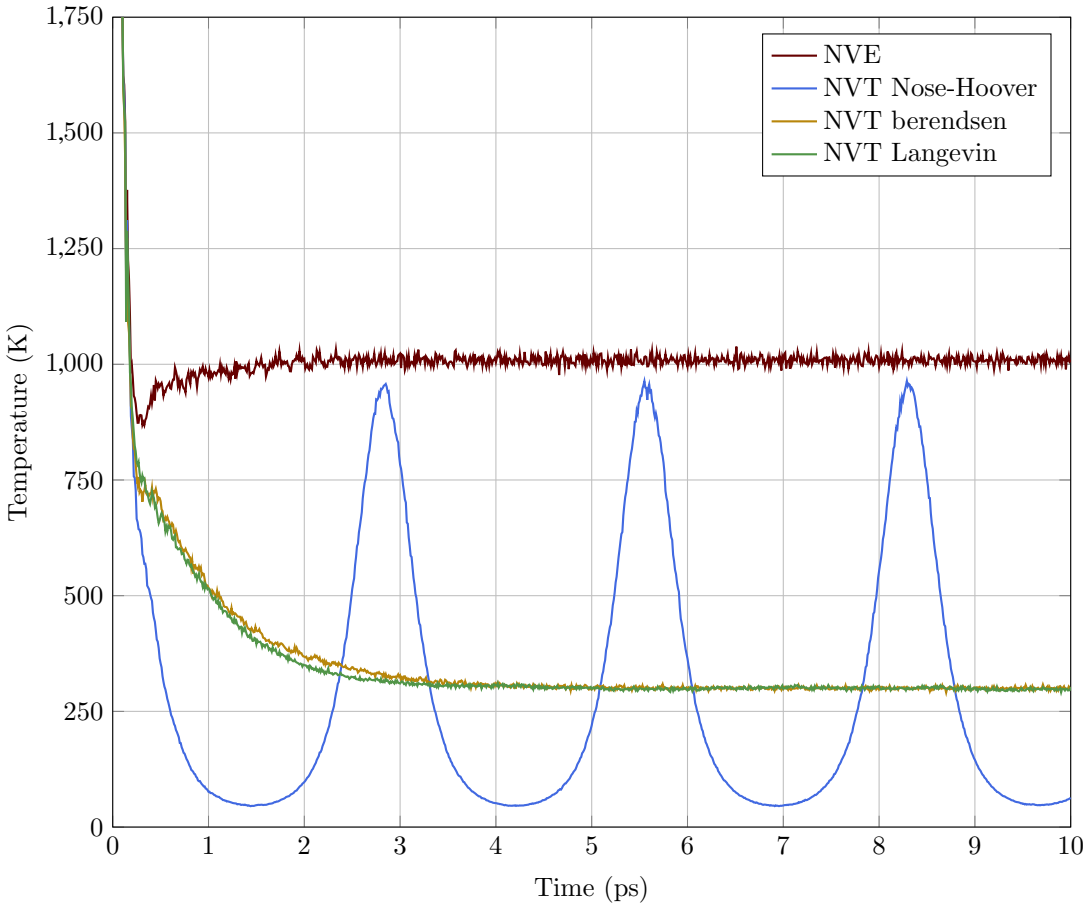

Figure 5.4: Temperature plot vs. time of a irradiated system simulated using four different constant volume thermostats, NVE, NVT Nose-Hoover, NVT Berendsen and NVT Langevin.

that the NVE ensemble fails to control sufficiently the temperature, as the system relaxes at a final temperature of around 1000 K. This is explained by the fact that the excess of energy given to the impact particle is only dissipated if a particle enters the boundary layer. The NVT Nose-Hoover thermostat on the other hand allows huge fluctuations in the temperature. This could be avoided by using a smallest timestep for the simulation. However, a timestep smaller by a factor of 10^k will increase the time of simulation K times, resulting in a very expensive simulation. In contrast, both NVT Berendsen and NVT Langevin thermostats control the temperature very efficiently. However, the best option is to use a Langevin stochastic thermostat since it is especially designed to dissipate excess energy in a system.

5.4 Algorithmic details for defect analysis

The defect analysis process was conducted using the output of the simulation, which recorded the trajectories of the atoms every 100 timesteps. A total of 501 configurations (frames) were created, with the first one corresponding to the initial undamaged structure and the remaining 500 to the damaged structure. Each of these frames was analysed with both the traditional defect counting method and two different sets of topological methods, each one utilizing both the Steinhardt and the Hermite order parameters.

5.4.1 Defect counting

The standard way to estimate damage effects is to use the Wigner-Seitz method to identify defects and vacancies in the system. The process was carried out using the DL_POLY_4 in-built defect identification routine based on the Wigner-Seitz method. For this it is necessary to define a site-interstitial distance r_{si}, which is equal to the minimum distance that a particle needs to travel from its lattice position to be regarded as a defect. In the existing literature, this distance is usually set equal to half of the minimum bond-length of the system under investigation or equal to the half of the distance corresponding to the first maximum of the total radial distribution function. For the modelled zircon crystal, the first maximum of the total radial distribution function is observed at 1.55 Å (Fig. 5.5) and the site-interstitial distance was set to 0.75 Å.

5.4.2 Global and partial order parameters

To characterize the radiation damage effects in the system, we explored various approaches to calculate Steinhardt and Hermite order parameters. These approaches are using the algorithms illustrated in Figs. 4.5 and 4.11 and the only differences are related to the definition of the neighbours that are used for the calculation of the order parameters.

The first and most common approach used in this work, is to select a reference particle and for each timestep of the simulation identify all the atoms that lie within a sphere of radius r_{cut} and calculate order parameters for these atoms. However, this approach ignores the identity of neighbours and the nature of specific bonds. For example, if a zirconium atom is selected as reference particle and the cutoff distance set equal to 3.2 Å to include silicon and oxygen atoms within the first neighbour shell, and given that Zr-Si and Zr-O bond lengths are ≃2.99 Å and ≃2.27 Å respectively, a silicon particle will leave the sphere if the distance from the reference zirconium

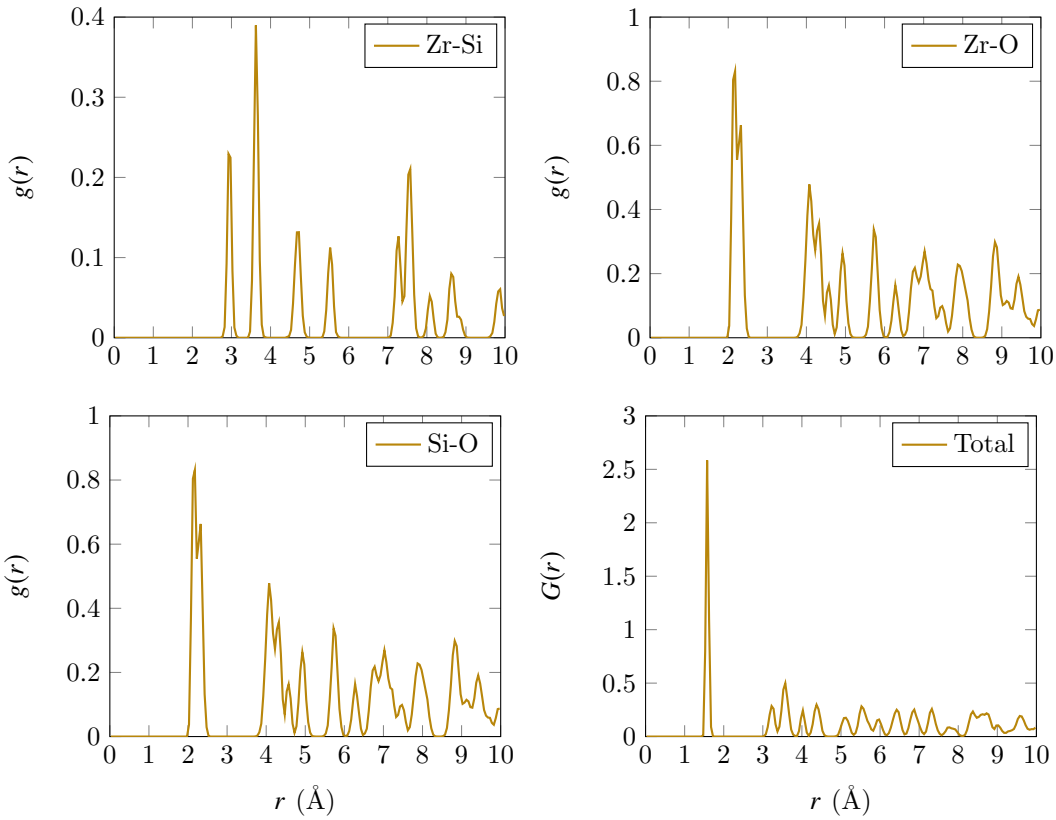

Figure 5.5: Radial distribution functions for the Zr-Si, Zr-O and Si-O pairs and the total radial distribution function of the undamaged zircon crystal.

atom is increased by just 0.3 Å while the distance of the oxygen particle must increase by more than 0.9 Å. These distances are not related to actual bond lengths and as a result, the characterization of a particle as a defect is not physical and the results will involve large errors.

To overcome the problems related with the selection of a global cutoff distance, a different approach is used that takes into account the bond lengths between atoms of different species. Instead of setting a global cutoff distance, a species dependent distance is used, defined by the first minimum of the partial radial distribution functions. The order parameters are then calculated not only for all the neighbours, but also for neighbours of each species separately. For example, for a zirconium reference atom, the cutoff distances for the silicon and oxygen neighbours are different and defined by the first minimum of the Zr-Si and Zr-O radial distribution functions and the parameters are calculated for all the neighbours - referred to from now on as global order parameters, as well as for the silicon oxygen neighbours separately - referred to as partial order parameters. The identification of bond defects can be achieved by using only Q_4 and Q_6 for the Steinhardt order parameters and R_4, R_6 for the Hermite order parameters.

Another issue that needs to be addressed is rising from the fact that the distances between a reference particle and its neighbours may alter significantly during the damage process. In Fig. 5.6, the evolution of the local environment around a reference particle and of the parameter Q_6 during the radiation damage process is illustrated. From this figure it is apparent that at the initial stages of the damage process where the damage cascade is formed, there is a significant increase

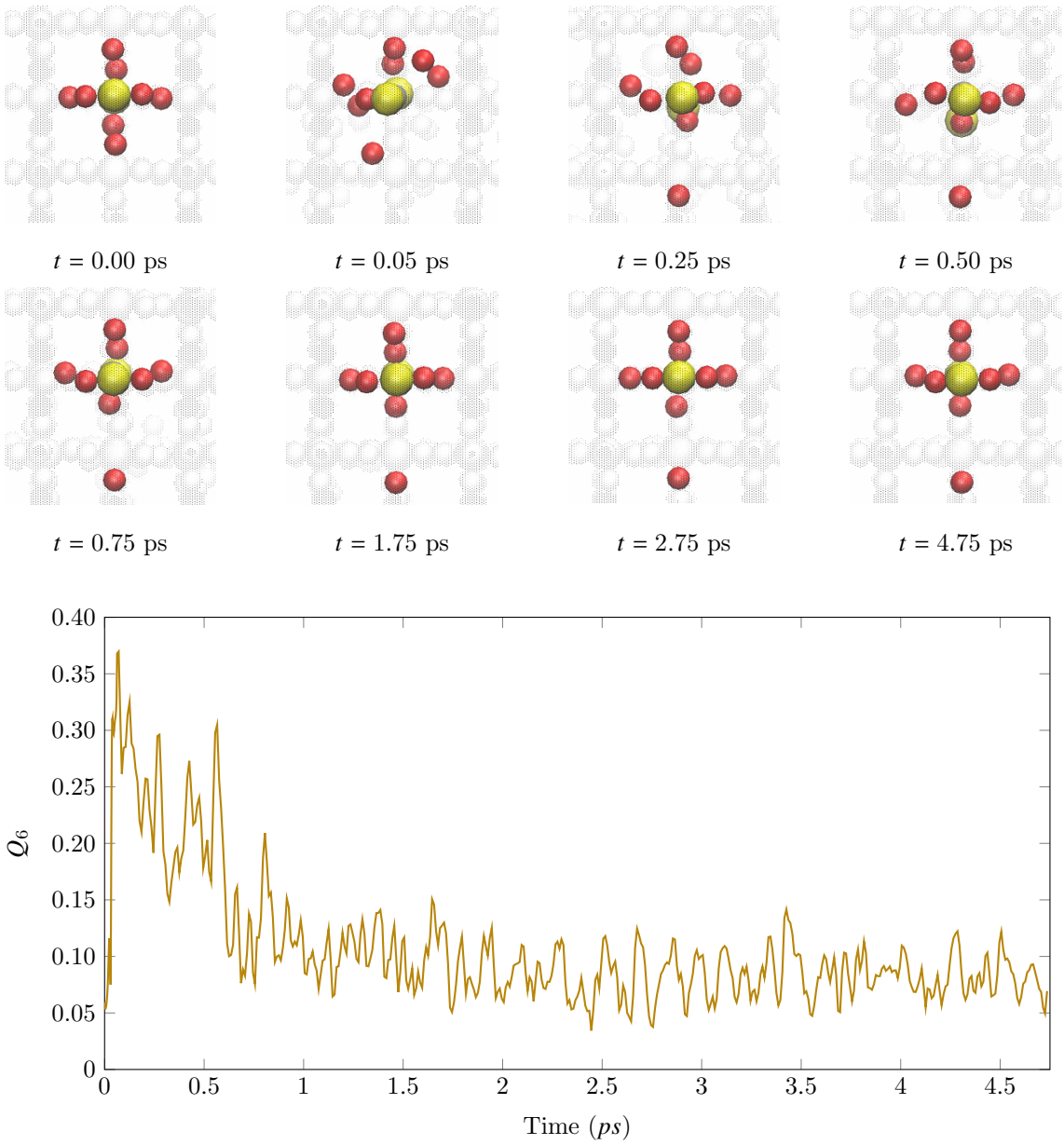

Figure 5.6: Evolution of Steinhardt order parameters during the radiation damage process of a zirconium atom.

in the value of Q_6. As the displaced atoms recover their initial positions, Q_6 also recovers close to the initial value, with small variations due to the vibrational movement of the atoms. For $t > 0.05$ ps it is obvious that the bottom particle of the configuration left its initial position and resided at a different final position. However, the relative angle of the displaced particle is almost the same as in the initial structure, and since Steinhardt order parameters are independent on the distance between the atoms, this movement is not recorded in the final Q_6 value and the particle is not identified as a defect.

To avoid such misleading results, it is necessary to apply the cutoff distance to every snapshot, to

identify the neighbours at the specific timestep. If a particle is displaced by a distance large enough to be found at a distance greater than r_{cut} from the reference particle, it will no longer contribute to the value of Steinhardt order parameters. This way, when a particle leaves the calculation sphere, the values of the Steinhardt order parameters are expected to alter significantly and reflect this event. This process requires the calculation of the distance between all the atoms of the system and this is an expensive procedure. To reduce the calculation time without losing information regarding the defect atoms, the neighbour list can be updated in larger time increments - but not too large as in this case the results might appear discontinuous. For this study, the neighbour list was updated every 5 timesteps.

5.4.3 Species specific order parameters

The previous two methods are able to provide information regarding the bond defects of the system. However it is not possible to use them to estimate the number of defect atoms. For this, a different and more complicated approach is implemented. The zircon structure is separated into three substructures, each containing only atoms of the same species. For each of these substructures, a nearest neighbour list is created for each reference particle, containing atoms within a distance shorter than the first minimum of the respective partial radial distribution function (Fig. 5.7). For each of the 501 snapshots of the simulation and for each of the substructures, the species specific Steinhardt order parameters with $0 \leq \ell \leq 10$ and the species specific Hermite order parameters with $0 \leq n \leq 16$ were calculated. At each snapshot, the average value of the parameters is calculated along with the number of atoms $n_g(t)$ with an order parameter value greater than the average of the respective snapshot, and for all the available ℓ and n values.

To avoid identifying as damaged an atom that undergoes a simple thermal vibration around its equilibrium position, a special condition is applied. At each snapshot, the distances r_{ij} between every reference particle and its neighbours are calculated, along with the differences $d_{ij}(t) = |r_{ij}(t) - r_{ij}(0)|$ of the distance between the initial undamaged structure at $t = 0$ and the distance at the time t of the snapshot under investigation. To characterize a particle as defect, it is required that at least one of the distances between the reference particle and its neighbours at the snapshot corresponding to the damaged structure will be greater than the distance r_{cut} corresponding to the first minimum of the respective partial radial distribution function. If all the distances are less than r_{cut}, the order parameters values for the specific reference particle are set to the values calculated for the same particle in the snapshot corresponding to the initial undamaged structure.

However, this method will overestimate the number of defect atoms. When $d_{ij}(t) > r_{\text{cut}}$, we will also have $d_{ji}(t) > r_{\text{cut}}$. Consequently, the values of the species specific order parameters will be affected for both the reference particle i and its neighbour j and both atoms will be identified as defects, even where only one of them is actually a defect. To avoid such an erroneous estimation, a correlation map between the numbers $n_g(t)$ and the actual number of defect atoms is created. In each of the three substructures corresponding to the initial undamaged configuration, a number of atoms equal to 10% of the total atoms of the substructure, are displaced deliberately from their equilibrium positions by a distance greater than r_{cut}. In these artificially damaged substructures, the number $n_g(t)$ is calculated and compared with the actual number of deliberately displaced atoms. The process is repeated 100 times to increase the statistical accuracy by calculating the

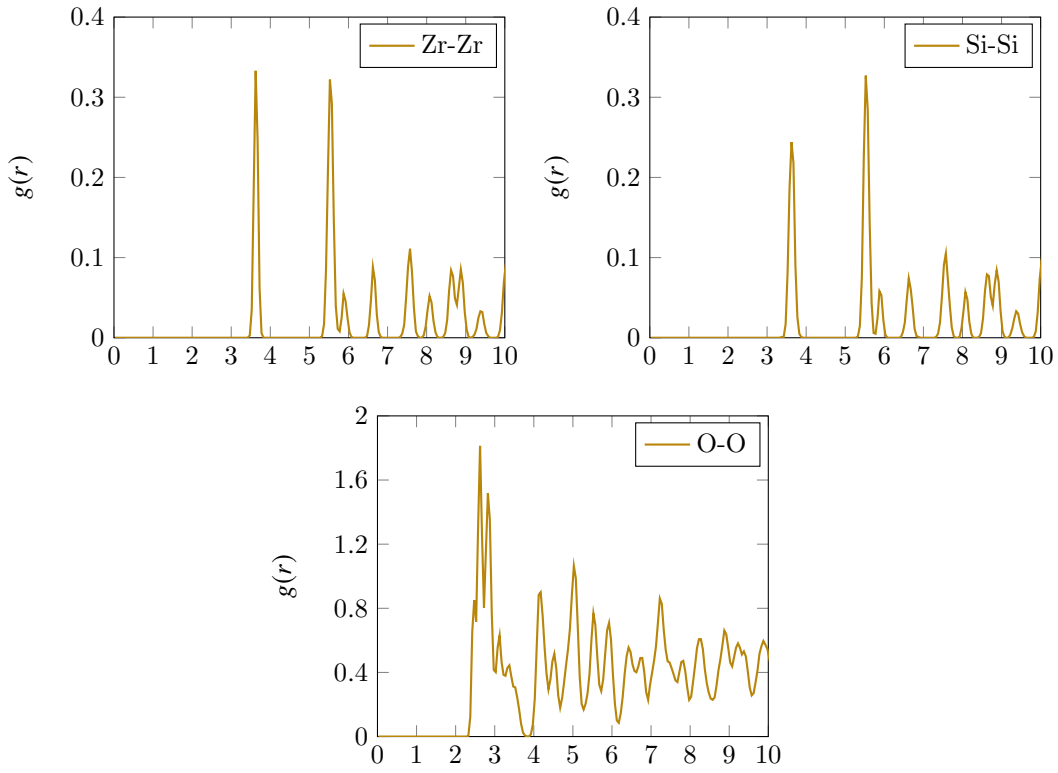

Figure 5.7: Radial distribution functions for the Zr-Zr, Si-Si and O-O pairs.

average $n_g(t)$ values.

Not all the Steinhardt and Hermite order parameters are appropriate to estimate the number of defect atoms. To get a satisfactory estimation it is necessary to select only the Steinhardt and Hermite order parameters that demonstrate a qualitative evolution similar to the evolution of number of defects. For these ℓ and n values, the respective correlation coefficients between the number of deliberately displaced atoms and the number of defects are calculated and used to estimate the number of defect atoms in the actual structure. For example, for the zirconium atoms and for $\ell = 6$, the number of defect atoms $n_d(t)$ is given by

$$n_d(t) = \frac{86}{35.13} n_g(t). \tag{5.4}$$

The number of defect atoms is calculated for all the selected ℓ and n values and then averaged to get the final estimation of the number of defects in the system.

5.4.4 Treatment of surface effects

In all the above approaches, it is crucial to deal with surface effects. Atoms close to the edges of the simulation box have fewer neighbours than atoms in the bulk. Consequently the value of Steinhardt order parameters for these atoms will be different and they need special treatment to clarify if they are defective or not. To avoid this complexity, one could use periodic boundary conditions during the calculation of the parameters. However, periodic boundary conditions may

transfer a defect particle residing near one edge of the box to its mirror position, in an undamaged area, leading to overestimation of the damage. To deal with this problem, instead of applying periodic boundary conditions, we used a periodic expansion of the initial undamaged cell and at each timestep of the simulation, only the atoms within the original simulation box are replaced with those of the current timestep. This way, surface effects are neglected and also damaged atoms are not transferred to undamaged regions of the structure. Additionally, during the simulation of the damage cascade and due to periodic boundary conditions, it is common for atoms to travel through the boundaries and settle to the mirror point of the simulation box. These atoms needs to be identified at each timestep and returned to their initial positions.

5.5 Results

In Fig. 5.8, four stages of the radiation damage simulation are illustrated. From this figure it can be safely assumed that the damage progresses very rapidly at the beginning and also that the crystal is well recovered at the end of the process.

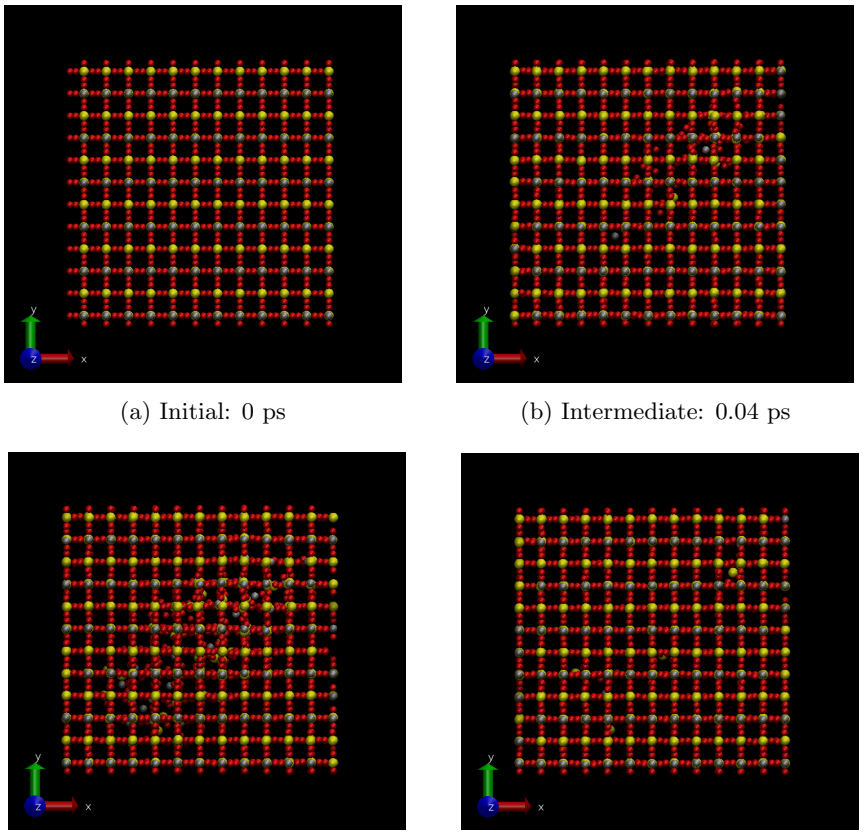

(a) Initial: 0 ps (b) Intermediate: 0.04 ps

(c) Maximum damage: 0.11 ps (d) Final equilibrium: 5.0 ps

Figure 5.8: Screenshots of the zircon crystal at four different stages of the damage cascade creation. The initial undamaged structure, the structure after 0.04 ps as the damaged atoms are increasing, the configuration at 0.11 ps where the maximum damage occurred and the structure at the final equilibrium state, after 4.75 ps. Zirconium atoms are in gray, silicon in yellow and oxygen in red.

5.5.1 Defect counting

In Fig. 5.9, the number of vacancies, as calculated at every 100 timesteps, is illustrated for each of the three species. From this plot, it is clear that the damage progresses rapidly in the first 0.15 ps, where it reaches a maximum for all the atomic species. The recovery phase is also very fast, as after just 1 ps the system reaches a new equilibrium state in which only about 20 vacancies remain. While during the creation of the damage cascade the majority of the displaced atoms are oxygen atoms, in the final equilibrium state, about half of the damaged atoms are silicon atoms.

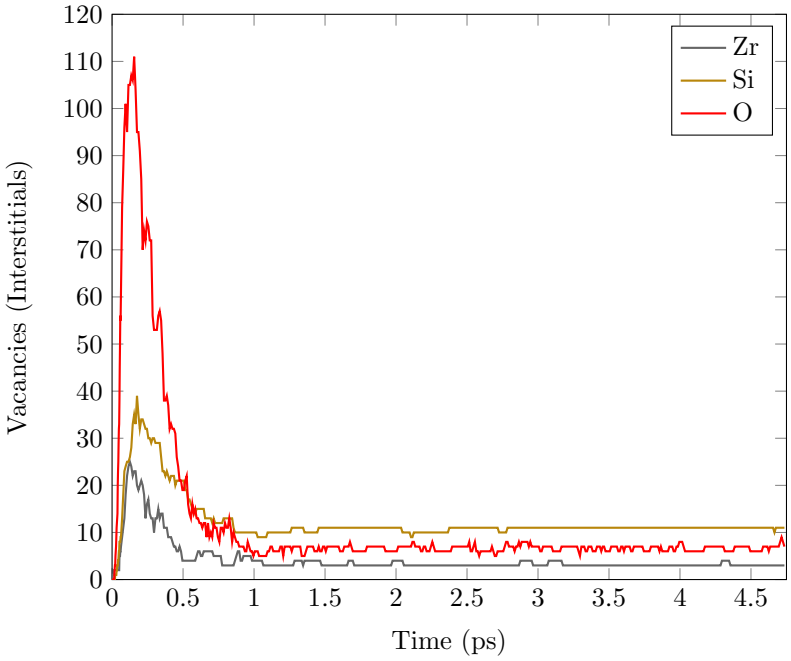

Figure 5.9: Evolution of vacancies (interstitials) in the damaged zircon structure.

At this point, it is important to note that the in-built defect counting method provided by the DL_POLY_4 routine, identifies only vacancies and interstitials and does not identify antisites. Also, this method assumes that all the bonds of the system have the same "strength" and the characterization of a particle as a defect is independent of the bond length and the forces between atoms. This approximation may lead to inaccurate results as, depending on the species forming a bond, a particle needs to travel a different distance so that the bond is broken. Additionally, the Wigner-Seitz cell is not spherical, as assumed in the DL_POLY_4 routine. Instead the shape depends on the crystal structure. However it is extremely difficult to define Wigner-Seitz cells with accuracy to better estimate the number of defects. Furthermore, as stated in the previous chapter, even if Wigner-Seitz cells were properly defined, this method will not provide any details regarding the number of broken bonds in the system.

5.5.2 Global Steinardt order parameters

In Fig. 5.10, the $Q_6(Q_4)$ scatter of global Steinhardt order parameters of the initial undamaged crystal is illustrated. In this Fig. it is obvious how the local geometry affects the distribution of

Q_4 and Q_6 values. Zirconium atoms are 10-coordinated, forming 2 bonds with neighbouring silicon atoms and 8 with oxygen, silicon atoms are 6-coordinated, forming 2 bonds with zirconium atoms and 4 with oxygen and finally oxygen atoms are 3 coordinated, forming 2 bonds with zirconium atoms and 1 with a silicon atom. Ideally, atoms of the same species should have exactly the same local geometry and occupy the same point on the $Q_6(Q_4)$ plots. However, small variations in the bond angles and the relative angles of atoms around a reference particle, result in the observed spread in the values of the parameters. Since atoms in the crystalline structure are located in places corresponding to minima of the free energy, it can be safely argued that the data points in this plot correspond to the minima of free energy. During a radiation damage event, atoms are excited to a higher free energy state and it is expected that this increase of free energy will be reflected in the $Q_6(Q_4)$ plot, represented by data points away from the initial well-defined regions.

Indeed, for t = 0.15 ps, where according to the DL_POLY_4 defect counting routine the maximum damage occurs, the distribution of the data points on the plot is very different (Fig. 5.11). A large number of data points for all the species are distributed away from the initial well-defined areas, indicating a major change in the local geometry of these atoms. By comparing this plot with Fig. 5.8, it is clear that several oxygen atoms are transformed from 3-coordinated to 2-coordinated forming the characteristic α-like space on the upper right corner of the diagram while some others are either 1-coordinated, located at point $(1, 1)$ of the diagram and others are completely free, found

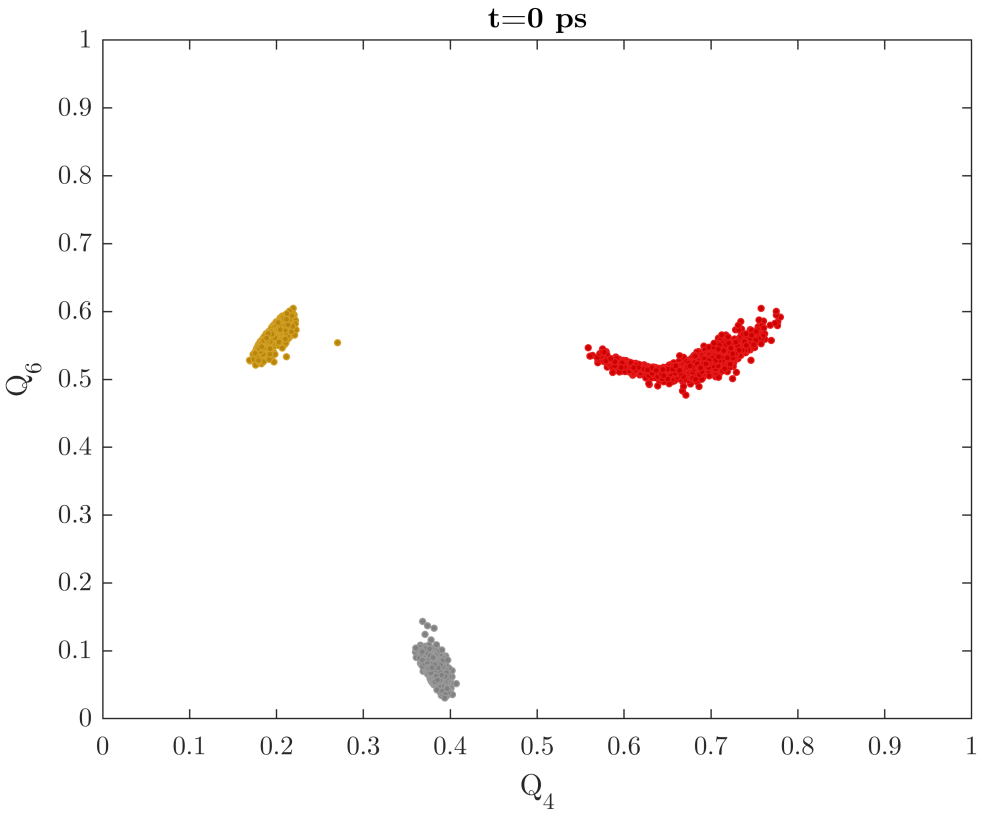

Figure 5.10: $Q_6(Q_4)$ scatter of global Steinhardt order parameters for the initial undamaged zircon crystal. Zirconium atoms are in grey colour, silicon in yellow and oxygen in red.

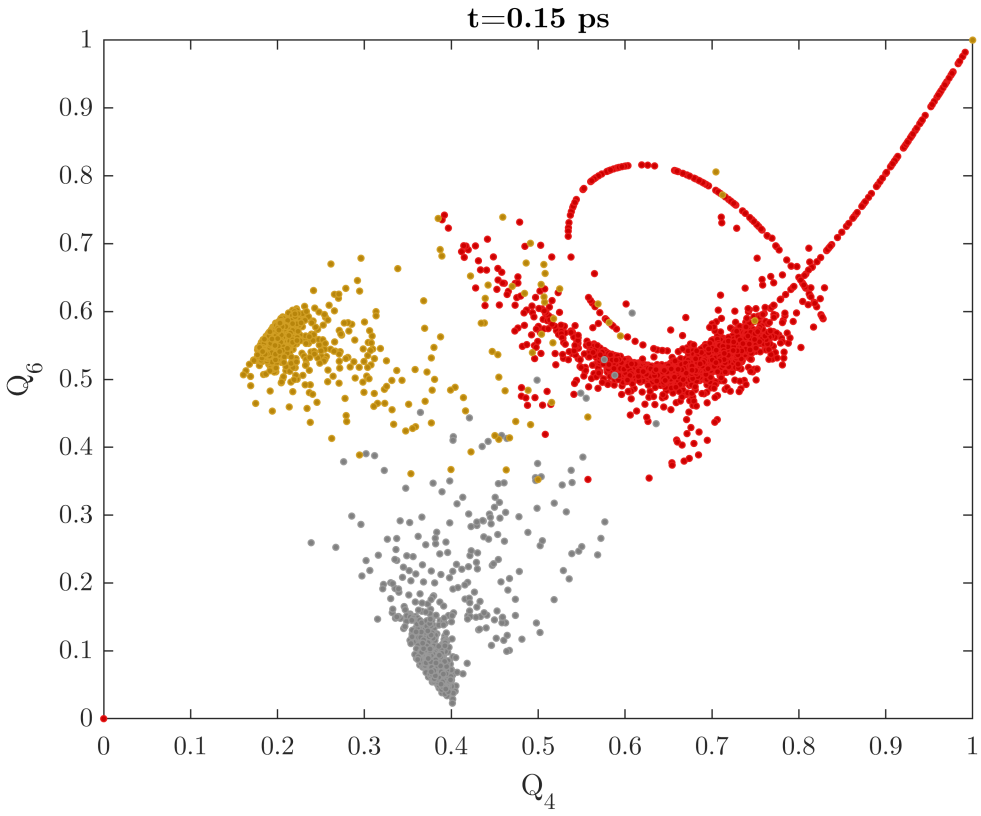

Figure 5.11: $Q_6(Q_4)$ scatter of global Steinhardt order parameters for t = 0.15 ps. Zirconium atoms are in grey colour, silicon in yellow and oxygen in red.

on the lower corner of the plot, at (0,0). Consequently, a number of O-Zr/Si bonds are broken. However, for the silicon and zirconium atoms it is not easy to distinguish the original 6-coordinated and 10-coordinated configurations from the damaged one.

In Fig. 5.12, $Q_6(Q_4)$ is illustrated for the final equilibrated structure at t = 4.75 ps. It is quite clear that the structure is almost recovered, as only a few atoms (in comparison with the 5184 atoms comprising the structure) are found away from the well defined areas formed for t = 0. Thus, the local geometry in the final configuration is almost identical to the one of the initial structure, apart from the damaged atoms. For oxygen atoms it is again easy to spot those that are converted from 3-coordinated to 2-coordinated. However it is again impossible to identify the change in the coordination number of silicon and zirconium atoms.

For this, each of the species is plotted separately, highlighting the coordination number of the atoms. In Figs. 5.13, 5.14 and 5.15, the scatter $Q_6(Q_4)$ plots for each species are illustrated at t = 0.15 ps and t = 4.75 ps. From these plots it is safe to argue that non-defect atoms, e.g. atoms with no broken bonds, remain concentrated in a compact region, with similar shape to the initial well-defined area and slightly expanded. Defect atoms tend to leave this well-defined area. For zirconium and silicon atoms, the distance from the well-defined area seems to be proportional to the change in the coordination number. However, in both the intermediate damaged configuration at t = 0.15 ps and the final recovered structure, there are atoms that although they have no

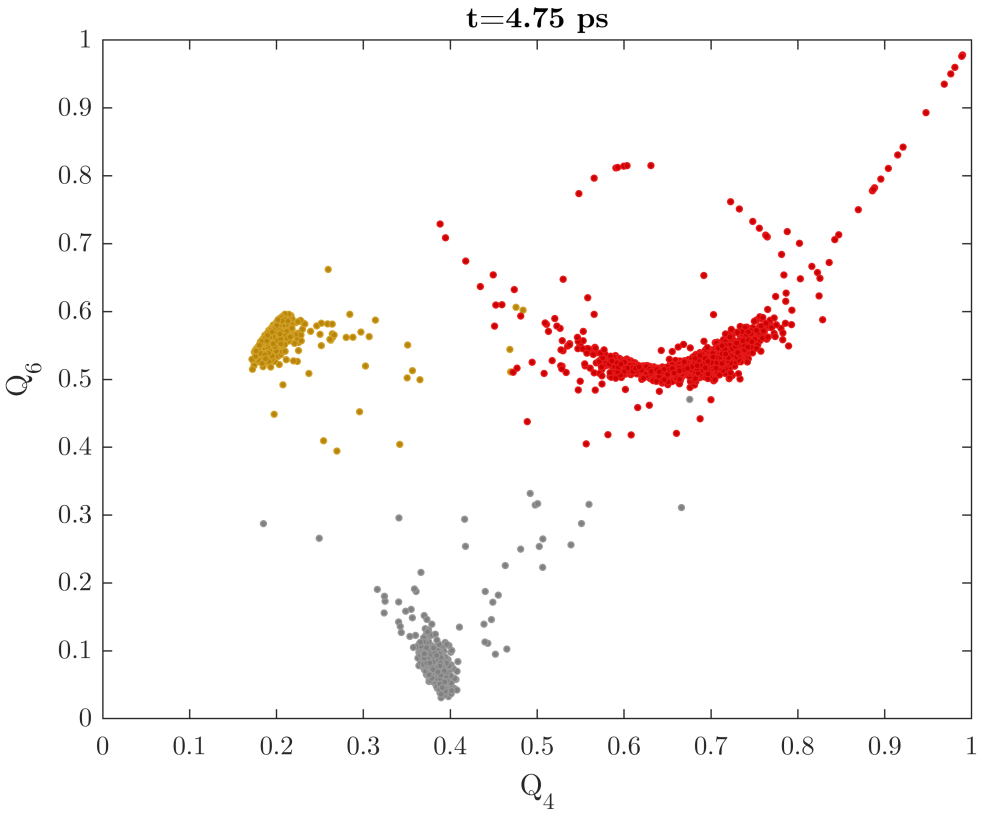

Figure 5.12: $Q_6(Q_4)$ scatter of global Steinhardt order parameters for t = 4.75 ps. Zirconium atoms are in grey colour, silicon in yellow and oxygen in red.

broken bonds, since the coordination number is unchanged, they are away from the initial well-defined area. This suggests a change in their local geometry because either the particle itself or its neighbours are displaced from their initial positions in a way that the bonds remain unaffected.

As for the final configuration and based on the coordination numbers of the atoms, 31 zirconium atoms with broken bonds are identified, 23 silicon atoms and 44 oxygen atoms. Although these scatter plots can be used to identify atoms of specific species associated with broken bonds, it is not possible to identify the species of the second atom of the damaged bond. Additionally, the total number of atoms associated with at least one broken bond is not given by the total number of atoms with altered coordination number, as a broken bond affects both atomic species that originally formed the bond.

5.5.3 Partial Steinhardt order parameters

To identify specific species associated with a broken bond, partial Steinhardt order parameters were calculated for all the possible bond pairs (Zr-Si, Zr-O and Si-O). For the Zr-O and Zr-Si pairs, the results at t = 0.00 ps, t = 0.15 ps and t = 4.75 ps are illustrated in Figs. 5.16, 5.17 and 5.18 respectively. As expected, Zr-O and Zr-Si bonds occupy different areas in the plots, that are characteristic of the geometry of the central zirconium atom with the bonded oxygen and silicon atoms. Each zirconium atom is bonded with 8 oxygen atoms, forming dodecahedra and also with

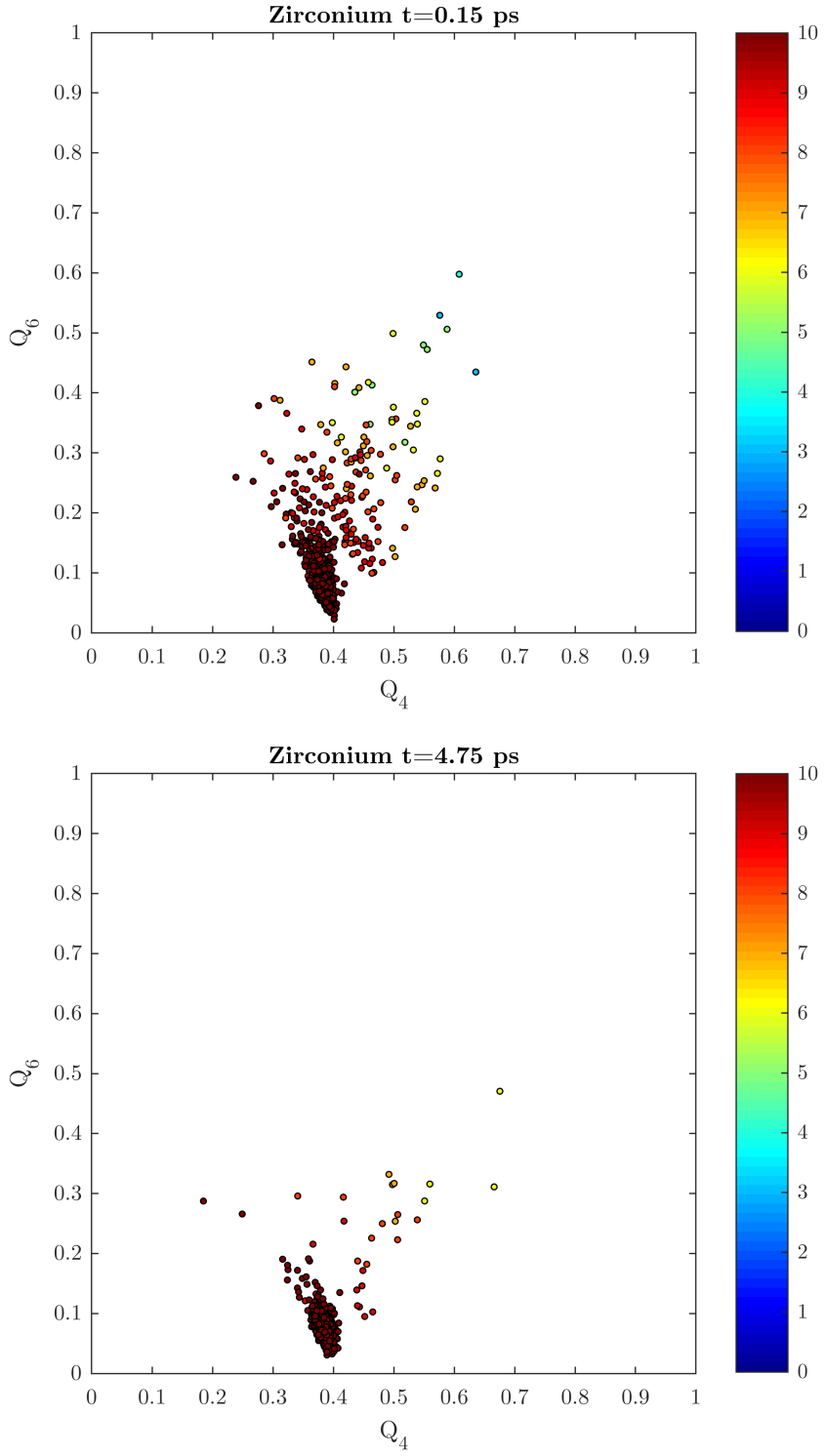

Figure 5.13: $Q_6(Q_4)$ scatter of the global Steinhardt order parameters for the zirconium atoms at t = 0.15 ps and t = 4.75 ps, highlighting the coordination number, as indicated in the colourbar next to the plots.

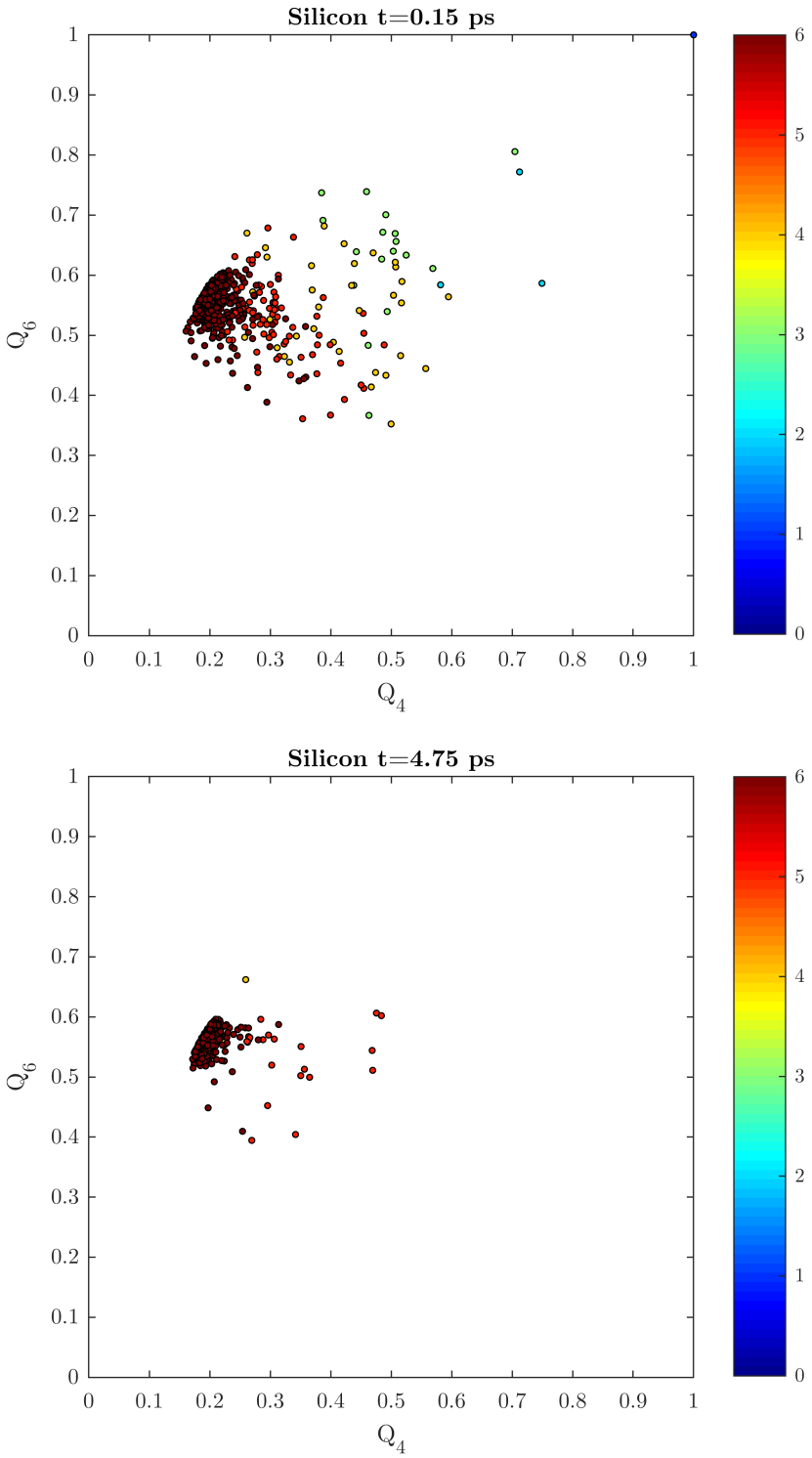

Figure 5.14: $Q_6(Q_4)$ scatter of the global Steinhardt order parameters for the silicon atoms at t = 0.15 ps and t = 4.75 ps, highlighting the coordination number, as indicated in the colourbar next to the plots.

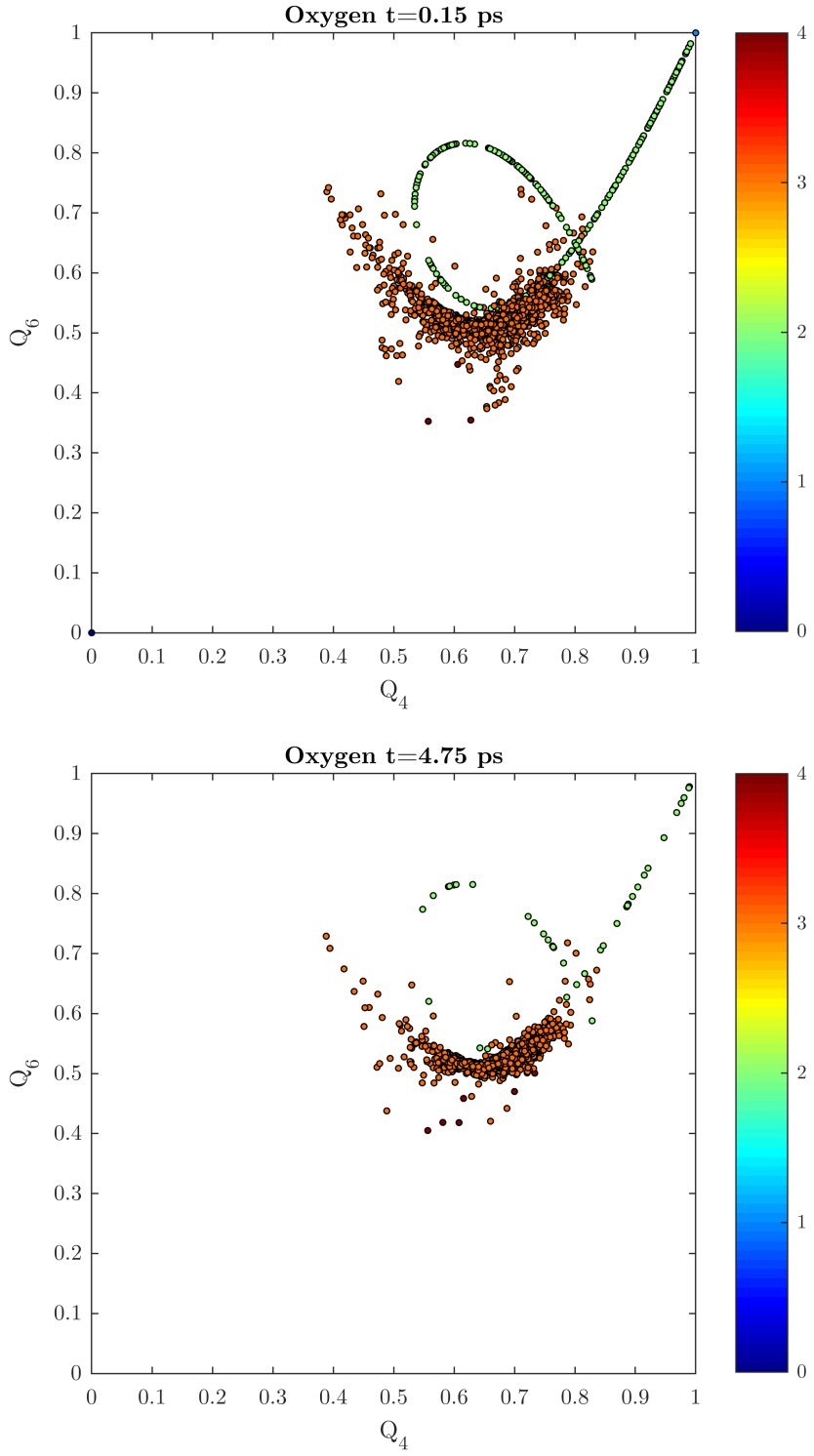

Figure 5.15: $Q_6(Q_4)$ scatter of the global Steinhardt order parameters for the silicon atoms at t = 0.15 ps and t = 4.75 ps, highlighting the coordination number, as indicated in the colourbar next to the plots.

2 silicon atoms with a bond angle ≃180 degrees. The small variations of the Si-Zr-Si bond angle from the ideal value of 180 degrees, are reflected in the fact that the Zr-Si $Q_4 - Q_6$ data points have small deviations from the ideal (1, 1) point.

As the damage progresses, at $t = 0.15$ ps, data points corresponding to the Zr-Si bonds tend to form the characteristic $\alpha-$ shape curve on the upper right part of the plot, indicating large variations in the Si-Zr-Si angles. Also, a large number of Zr-Si bonds are broken, since 108 zirconium atoms are now connected with less than 2 silicon atoms. For the Zr-O bonds, it is observed that a large number are broken and 147 zirconium atoms are related to at least one Zr-O broken bond. The dispersion of $Q_4 - Q_6$ data points for the Zr-O pairs away from the compact initial region is characteristic of the changes in the number and the relative positions of the oxygen atoms that are bonded with reference zirconium atoms. In the recovered structure on the other hand, only a few atoms are dispersed away from their initial positions. Actually, only 22 zirconium atoms are identified to have at least one Zr-Si bond broken and 27 at least one Zr-O broken bond.

For the Si-O pairs, a similar behaviour is observed, but with a significantly higher degree of recovery. At $t = 0$ ps, the plots are characteristic of the tetrahedral geometry of silicon atoms with bonded oxygen atoms. At $t = 0.15$ ps, 81 silicon atoms have at least one broken bond with an oxygen atom while for $t = 4.75$ ps only 3 silicon atoms are associated with a broken Si-O bond. Thus it is safe to assume that a radiation damage event mostly affects the Zr-Si and Zr-O bonds, while the Si-O tetrahedral formations remain almost undamaged.

The question that arises is: Can the number of damaged bonds for specific species pairs be estimated without calculating the coordination number? This is possible if we know the specific geometry of the reference particle and the bonded neighbours. For the zircon crystal structure, the geometry is well defined. Each zirconium atom is bonded with 2 silicon atoms in a straight chain and with 8 oxygen atoms forming dodecahedra, while each silicon atom is connected with 2 zirconium atoms in a straight chain and 4 oxygen atoms forming tetrahedra. In frozen structures, each of these geometries would be represented in the $Q_6(Q_4)$ scatter plots as a single point. But the vibrations[1] of the atoms from their equilibrium positions create wider areas in which the $Q_6(Q_4)$ values lie. These vibrations can be simulated in order to define the area in which data points corresponding to atoms with no broken bonds can be found. In a zircon crystal, the Zr-Si chain, the Zr-O dodecahedra and the Si-O tetrahedra can be simulated. The maximum distance a particle can travel - e.g. the amplitude of the simulated vibrations - is equal to the difference $r_a = r_{\min} - r_{\max}$ between the first minimum and the first maximum of each partial radial distribution function, so that the distance of the neighbours from the reference particle will be less than the Steinhardt order parameters cutoff distance. In Fig. 5.19, the effect of atomic vibrations in the values of the partial Steinhardt order parameters for the Zr-Si (blue), Zr-O (gray) and Si-O (yellow) pairs are illustrated. By comparing these plots with Fig. 5.16 corresponding to the initial undamaged structure, it is clear that atomic vibrations significantly expand the areas covered by $Q_4 - Q_6$ data points.

These plots can be used as a guide to identify damaged bonds without the calculation of coordination numbers. As illustrated in Fig. 5.20, in which the partial Steinhardt order parameters are compared with those of the vibrational effect for $t = 0.15$ ps where the maximum damage occurs,

[1] During a simulation, atoms are not frozen at their equilibrium positions but they vibrate with a small amplitude in the order of 0.1 Å.

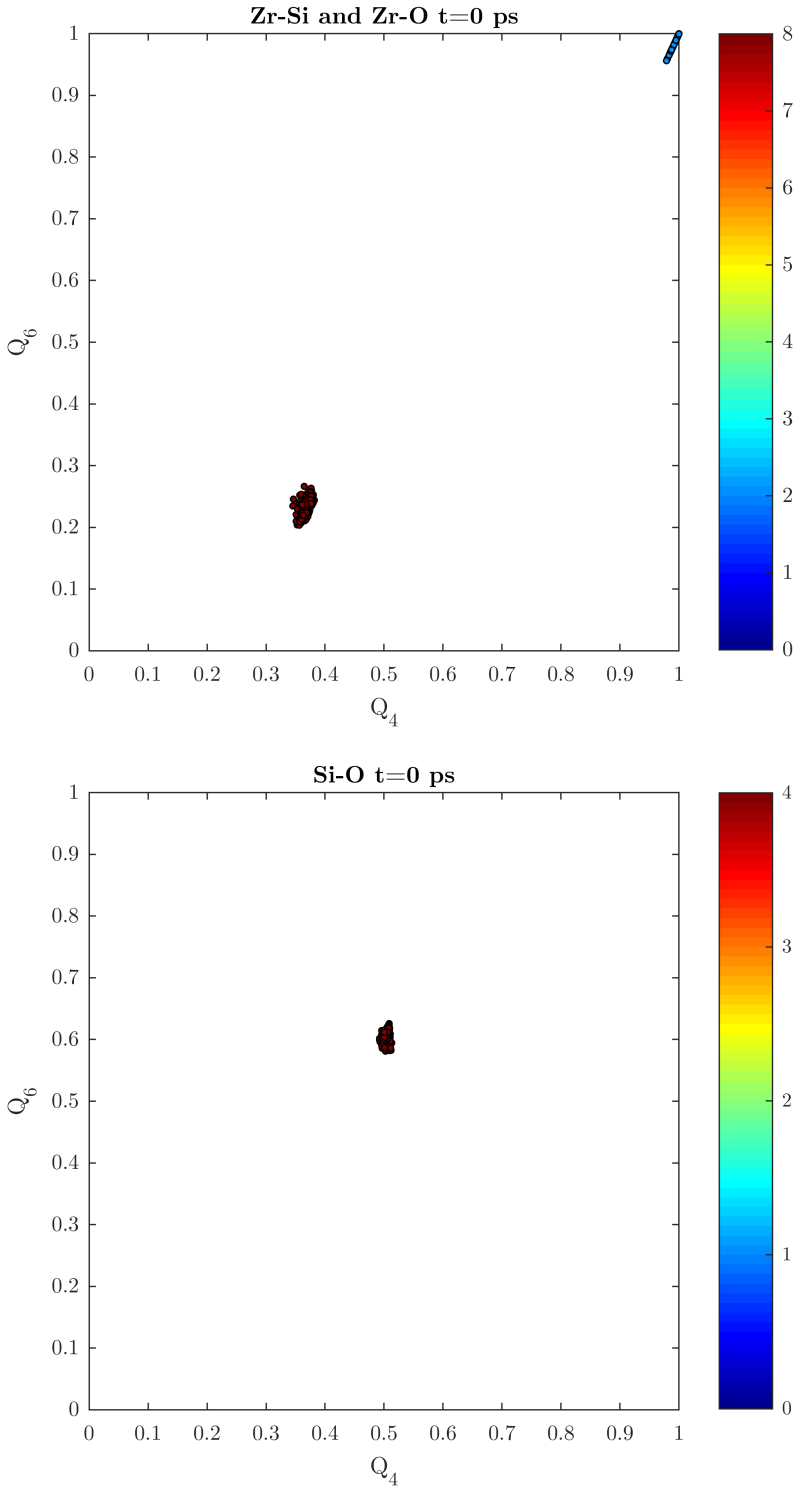

Figure 5.16: $Q_6(Q_4)$ scatter of Zr-Si and Zr-O (top) and Si-O (bottom) partial Steinhardt order parameters for t = 0.00 ps, highlighting the coordination number, as indicated in the colourbar next to the plots.

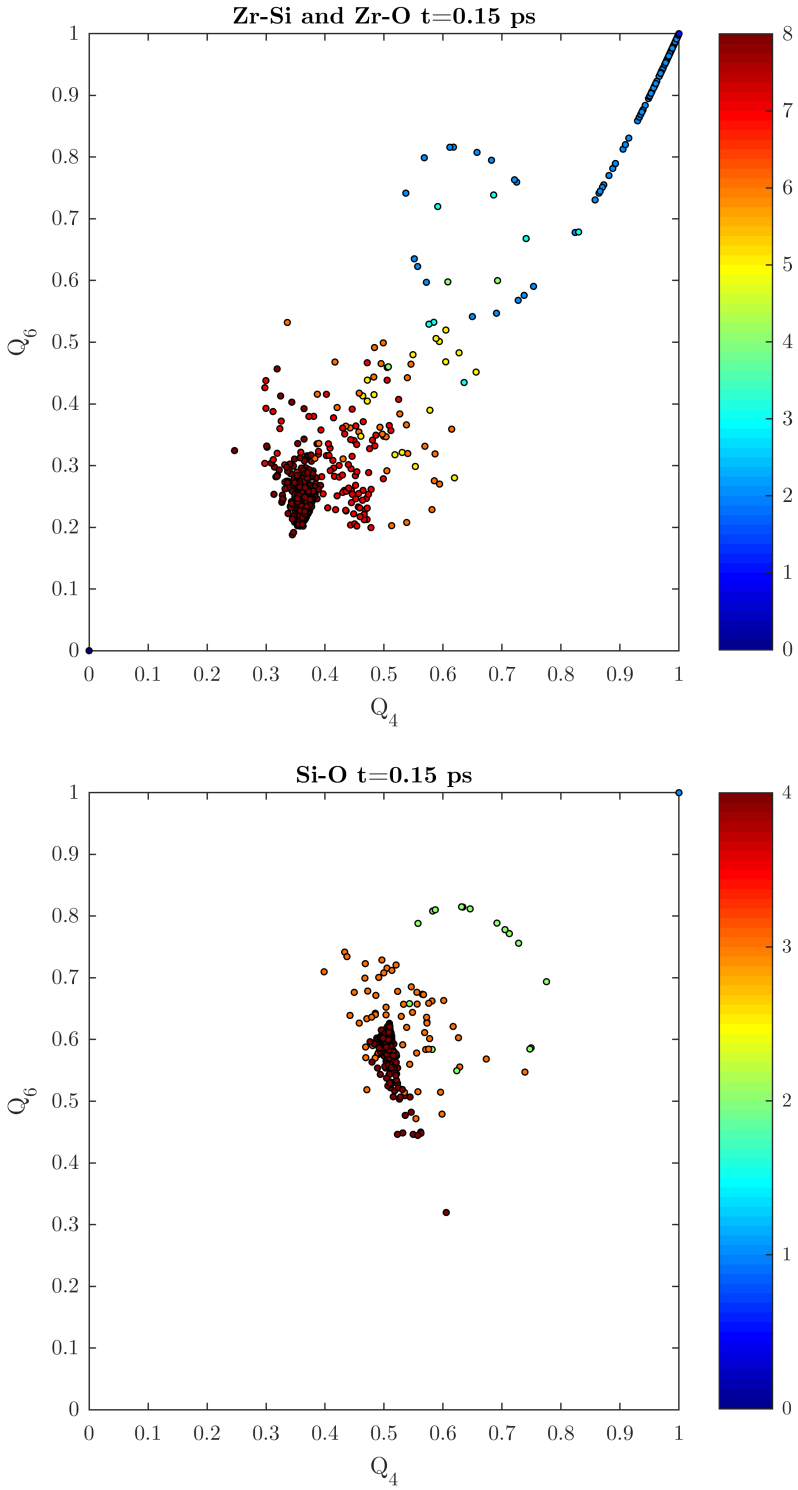

Figure 5.17: $Q_6(Q_4)$ scatter of Zr-Si and Zr-O (top) and Si-O (bottom) partial Steinhardt order parameters for t = 0.15 ps, highlighting the coordination number, as indicated in the colourbar next to the plots.

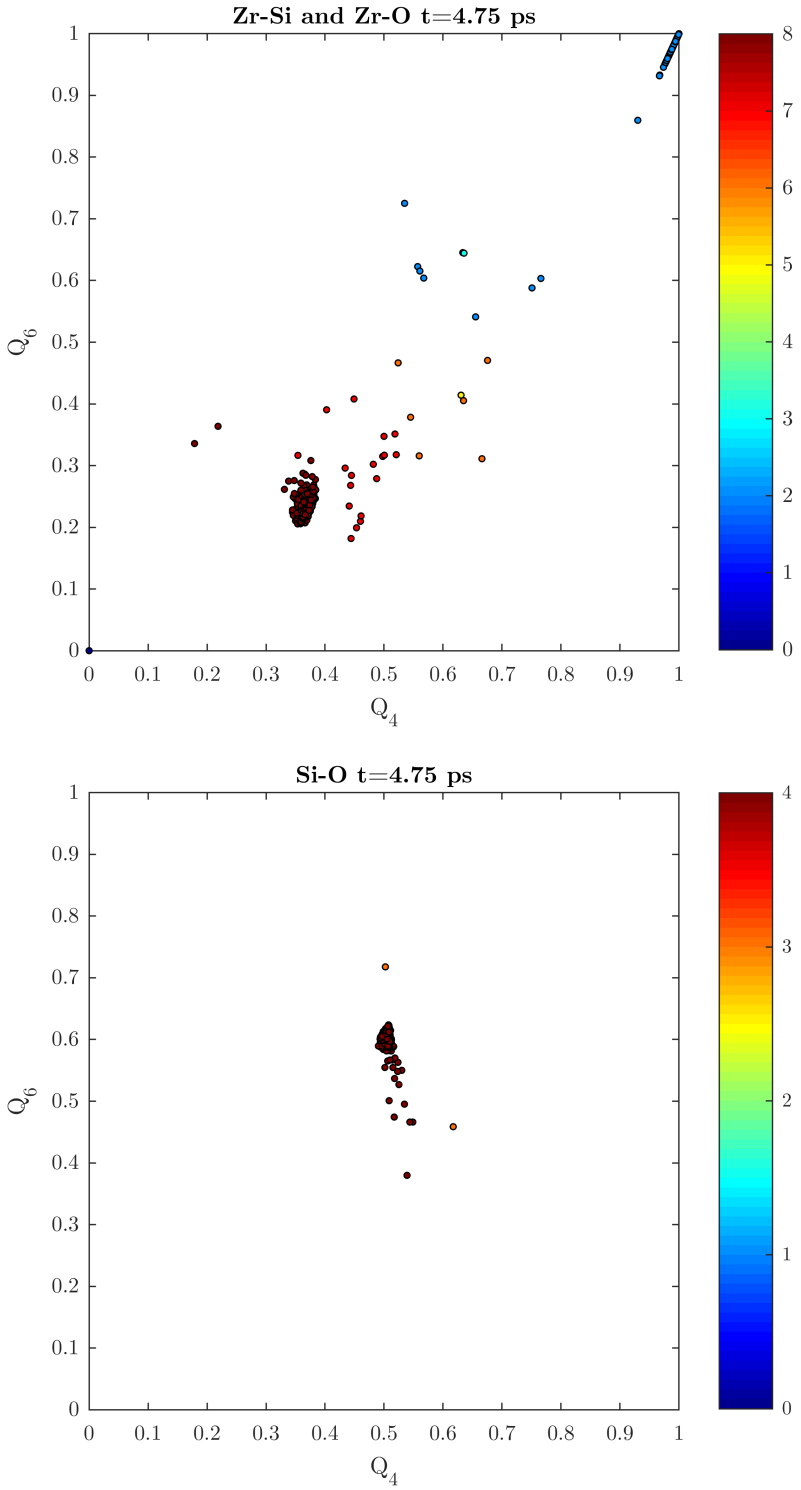

Figure 5.18: $Q_6(Q_4)$ scatter of Zr-Si and Zr-O (top) and Si-O (bottom) partial Steinhardt order parameters for t = 4.75 ps, highlighting the coordination number, as indicated in the colourbar next to the plots.

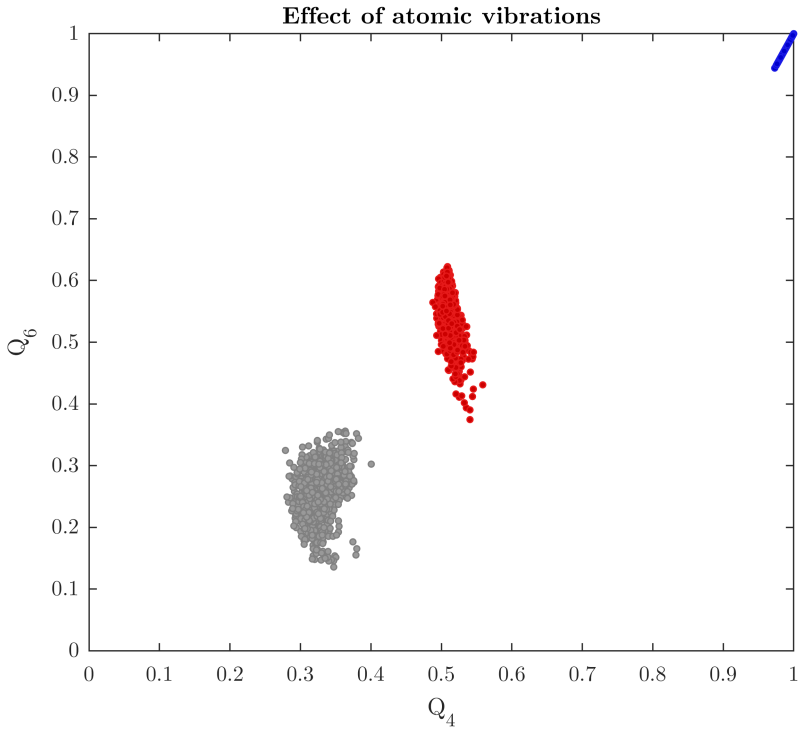

Figure 5.19: The effect of atomic vibrations in the $Q_6(Q_4)$ values of partial Steinhardt order parameters of a zircon crystal. Grey points correspond to Zr-O bonds, red to Si-O and blue to Zr-Si.

it is clear that almost all zirconium and silicon atoms associated with at least one damaged bond with an oxygen atom are found outside the area defined by the vibrations of atoms. For the Zr-Si pairs, things are not that clear, as the Si-Zr-Si angles in the damaged structure are not as limited due to the atomic vibrations. However, zirconium atoms are originally bonded with 2 silicon atoms. 2-coordinated atoms are easily identified in the $Q_6(Q_4)$ plots due to the characteristic $\alpha-$ shape curve they form. Zirconium atoms with one broken Zr-Si bond will have $Q_4 = Q_6 = 1$ while those with two broken Zr-Si bonds will have $Q_4 = Q_6 = 0$, making it possible to identify defect atoms without examining if their $Q_6(Q_4)$ values are within the area defined by the vibrational moves. As demonstrated if Fig. 5.21, at $t = 4.75$, where the crystal is almost completely recovered, it is much easier to identify the zirconium and silicon atoms associated with at least one damaged bond.

By defining the area corresponding to atomic vibrations and calculating at each timestep the number of atoms found outside this area, it is possible to get a clear and accurate estimation of bond defects. In Fig. 5.22 the evolution of Zr-Si, Zr-O and Si-O bond defects is illustrated. It is clear that the number of defects versus time follow a pattern similar to the number of damaged atoms calculated by the DL_POLY_4 in-built routine, as shown in Fig. 5.9. Additionally, these numbers are compared with the respective calculation using the coordination number as a function of time. The agreement between the two methods is impressive, reflecting the accuracy of the partial Steinhardt order parameters method and establishing the latest as a successful defect characterization technique for crystalline materials. The accuracy of the method is mainly due to the fact that in an undamaged crystalline material, all atoms of the same species have the same

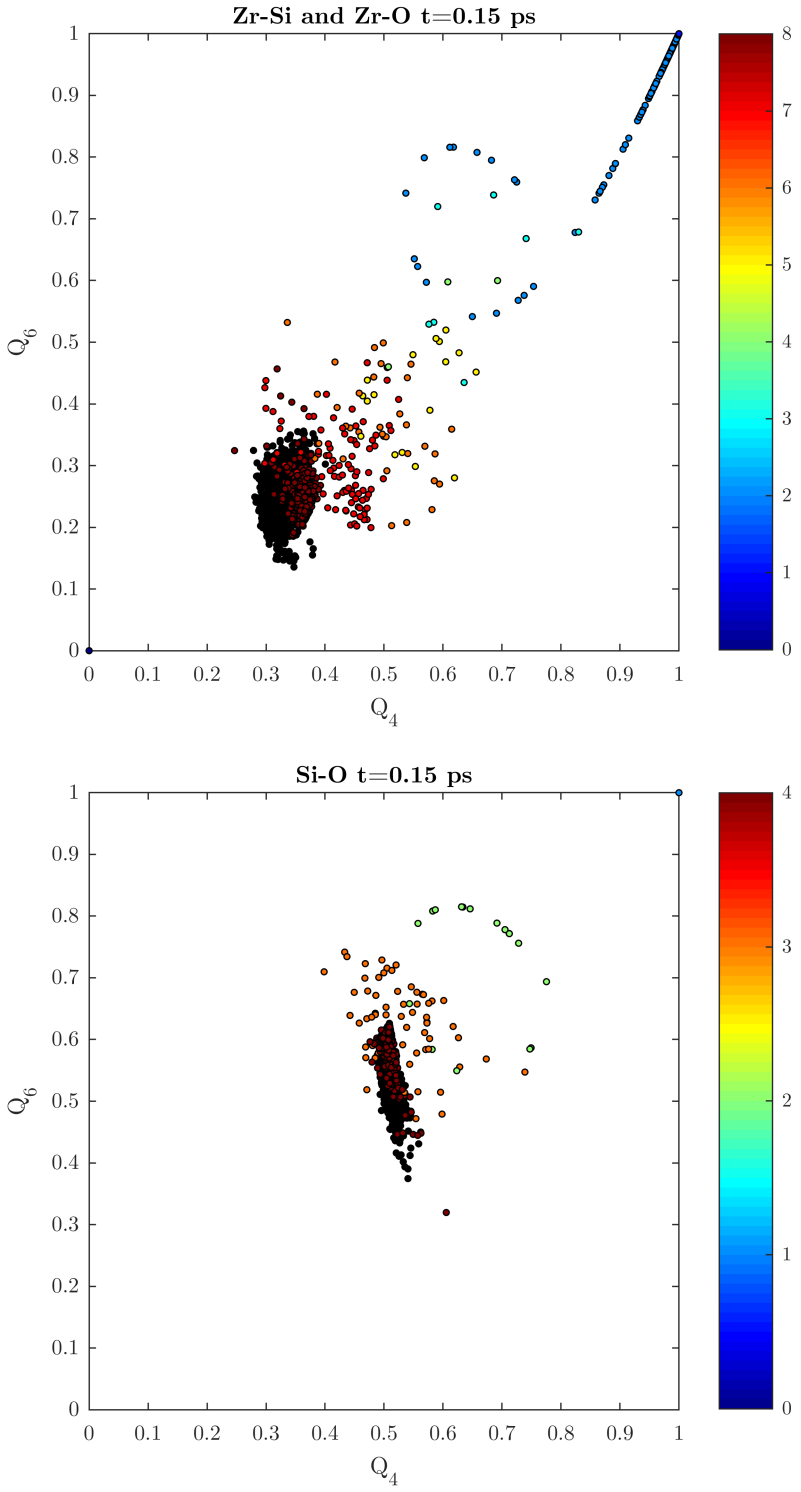

Figure 5.20: Comparison of $Q_6(Q_4)$ data points between the structure at maximum damage with those of the vibrational effect for the Zr-Si and Zr-O pairs (top) and Si-O pairs (bottom), highlighting the coordination number, as indicated in the colourbar next to the plots

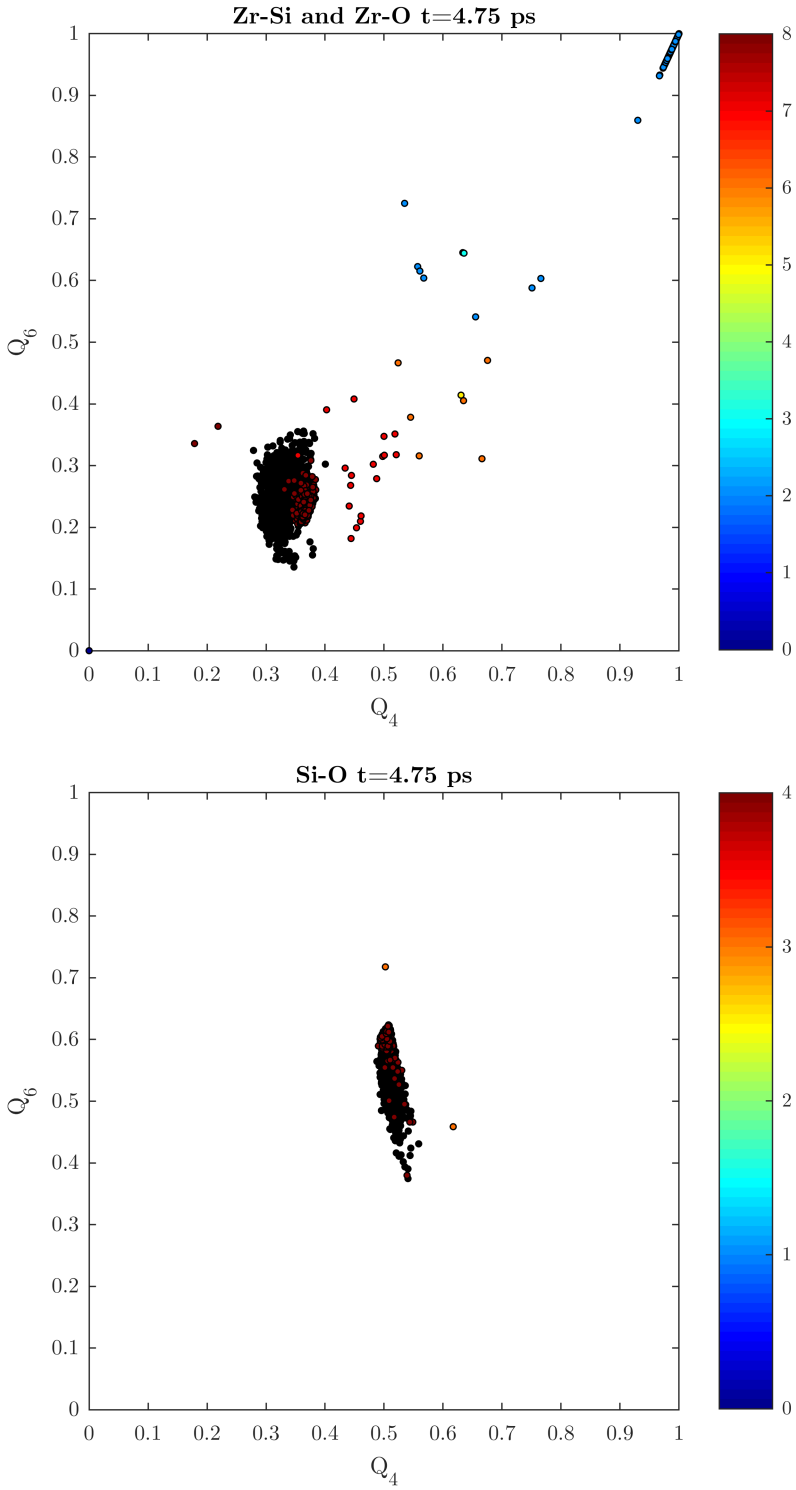

Figure 5.21: Comparison of $Q_6(Q_4)$ data points between the structure at t = 4.75 ps, with those of the vibrational effect for the Zr-Si and Zr-O pairs (top) and Si-O pairs (bottom), highlighting the coordination number, as indicated in the colourbar next to the plots

initial coordination number and a specific local geometry, making easy to define the $Q_6(Q_4)$ area due to atomic vibrations and consequently identify the atoms of the damaged structure associated with at least one bond defect. In amorphous materials, atoms of the same species in an undamaged structure may have more than one coordination number and a variety of local geometries. Thus, the task to define areas in $Q_6(Q_4)$ plots due to the vibrational movements remains challenging.

Since Steinhardt order parameters depend on the relative angular positions of the atoms around a reference particle, it is expected that, if the relative positions of the neighbours surrounding different reference atoms are similar, then the corresponding data points on the $Q_6(Q_4)$ plots will be close to each other. This is actually shown in Fig. 5.19. For the SiO_4 units, the geometry of the respective tetrahedra is similar - the only variations are due to the vibration of the atoms around their equilibrium positions. Consequently, the corresponding data points form a well defined compact area. Similar arguments can be made for the ZiO_8 dodecahedra and also for the almost linear Si-Zr-Si triplets. During the creation of the radiation damage cascade, it is clear that the data points corresponding to the SiO_4 pairs (or the 4-coordinated silicon atoms) remain inside the area defined by these vibrations. Thus, the angular geometry of the SiO_4 tetrahedra is not affected by the radiation damage event. However, the distribution of data points corresponding to defect silicon atoms is quite extended. It can be argued that the angular distribution of the bonded oxygen neighbours of both the 3- and 2-coordinated silicon atoms created during the irradiation event does not converge. Similar arguments can be made for the zirconium atoms associated with at least one bond defect, as the distribution of low coordinated atoms in the $Q_6(Q_4)$ plots is arbitrary for the Zr-O pairs. For the Zr-Si pairs, it is also clear from Fig. 5.20 that during the

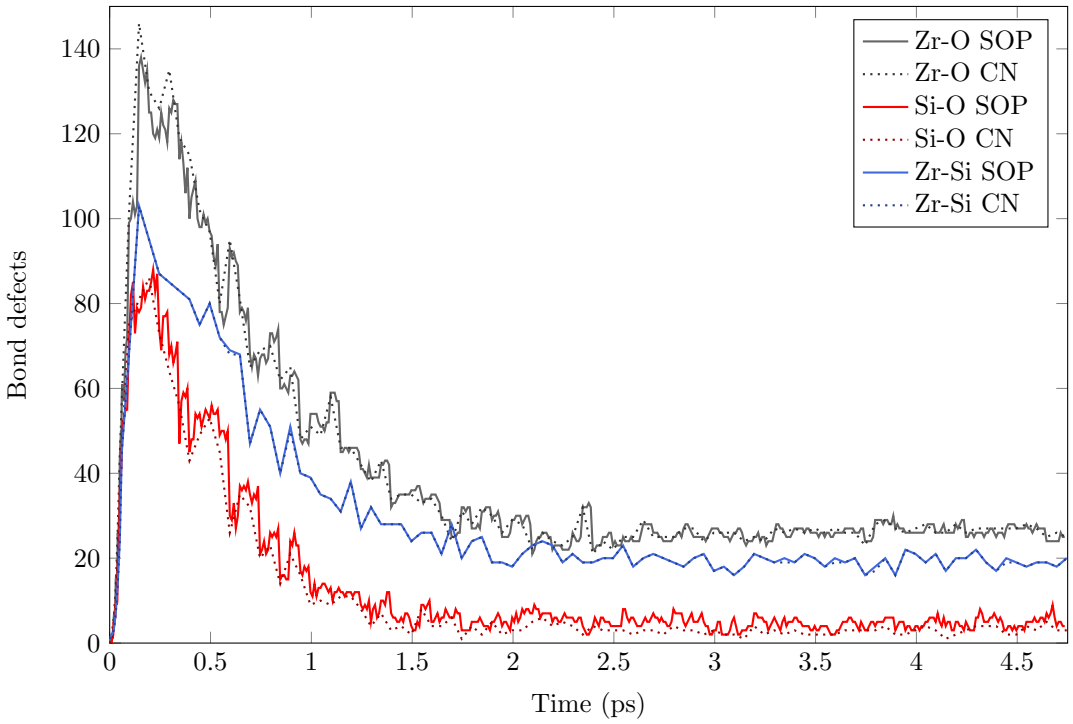

Figure 5.22: Comparison of number of bond defects for Zr-Si, Zr-O and Si-O pairs calculated using partial Steinhardt order parameters and by simple calculation of coordination numbers.

creation of the damage cascade, several data points are found away from the upper right corner, meaning that the Si-Zr-Si bond angle is affected and taking values away from the ideal angle of 180°. By the end of the simulation however (Fig. 5.21), it is clear that the angular geometry of the SiO_4 tetrahedra and ZrO_8 dodecahedra is almost completely restored and there is also a high recovery of the Si-Zr-Si bond angles.

5.5.4 Partial Hermite order parameters

For the Hermite order parameters, a similar approach is applied. Using the cutoff distances defined for the calculation of Steinhardt order parameters, partial Hermite order parameters were calculated in order not only to identify atoms with damaged bonds, but also to extract information regarding the nature of broken bonds. Using partial Hermite order parameters it is quite simple to retrieve all the necessary information, as atoms with broken bonds are clearly distinguished from non-defect atoms. Figs. 5.23 - 5.25 show the distribution of $R_6(R_4)$ data points in three different states of the damage process, the initial undamaged structure at t = 0 ps, the maximum damage phase at t = 0.15 ps and the final recovered structure at t = 4.75 ps.

For t = 0 ps and for the Zr-Si pairs, all data points (apart for one corresponding to the primary knocked zircon atom) are found in a small area around $(R_4, R_6) = (0.328, 0.275)$. For the Zr-O pairs the $R_6(R_4)$ data points of the undamaged structure are concentrated around point $(0.163, 0.136)$ and for the Si-O pairs the $R_6(R_4)$ data points of the undamaged structure are concentrated around point $(0.232, 0.195)$. As the damage progresses and several Zr-Si, Zr-O and Si-O bonds are broken, resulting in zirconium and silicon atoms with at least one bond defect, data points for the Zr-Si pairs accumulate at $(0.465, 0.391)$ corresponding to 1 silicon neighbour and at $(0, 0)$ corresponding to no Zr-Si bond. Data points corresponding to the Zr-O and Si-O pairs are dispersed in several regions according to the number of damaged Zr-O and Si-O bonds respectively. For the Zr-Si pairs it is possible to estimate the number of defect zircon atoms just by counting the number of atoms at each data point. For the Zr-O and Si-O pairs, it is also very easy to identify damaged bonds between specific pairs. Using the same approach as for partial Steinhardt order parameters, the areas in the $R_6(R_4)$ plots formed using data from the undamaged structure can be defined and the number of atoms associated with bond defects can be calculated. As in the case with partial Steinhardt order parameters, the number of bond defects calculated using partial Hermite order parameters is compared with the one calculated using the coordination number of atoms (Fig. 5.26). The agreement between the results is once again impressive.

In terms of bond defects, Hermite order parameters give the same results as the Steinhardt order parameters method. As a result, it is natural to question the usage of Hermite order parameters. However, Hermite order parameters can give additional information regarding the radial distribution of atoms around a reference atom, that the Steinhardt order parameters are unable to provide. For example, we can refer to Fig. 5.24, where R_6 is plotted against R_4 for the Zr-O bonds and for t = 0.15 ps. Apart from the obvious argument, that several zirconium atoms are associated with at least one broken Zr-O bond, zirconium atoms with the same coordination number are not located in the same position in the diagram. For example, the three 4-coordinated zirconium atoms are found in three different points on the plot. Since Hermite order parameters are a function of distance r, but also dependent on the average neighbour distance, it is safe to

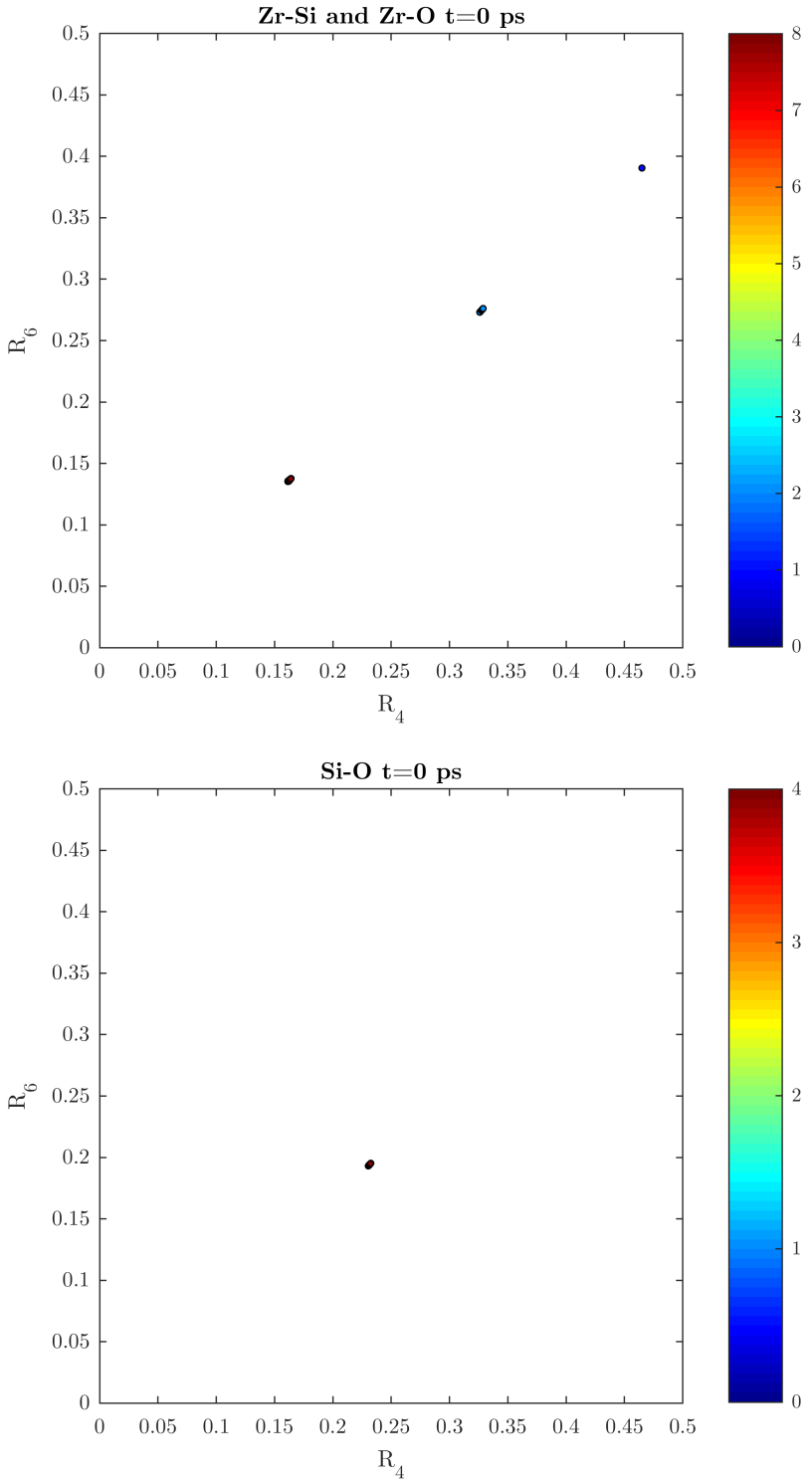

Figure 5.23: $R_6(R_4)$ scatter of Zr-Si and Zr-O (top) and Si-O (bottom) partial Hermite order parameters for t = 0.00 ps, highlighting the coordination number, as indicated in the colourbar next to the plots.

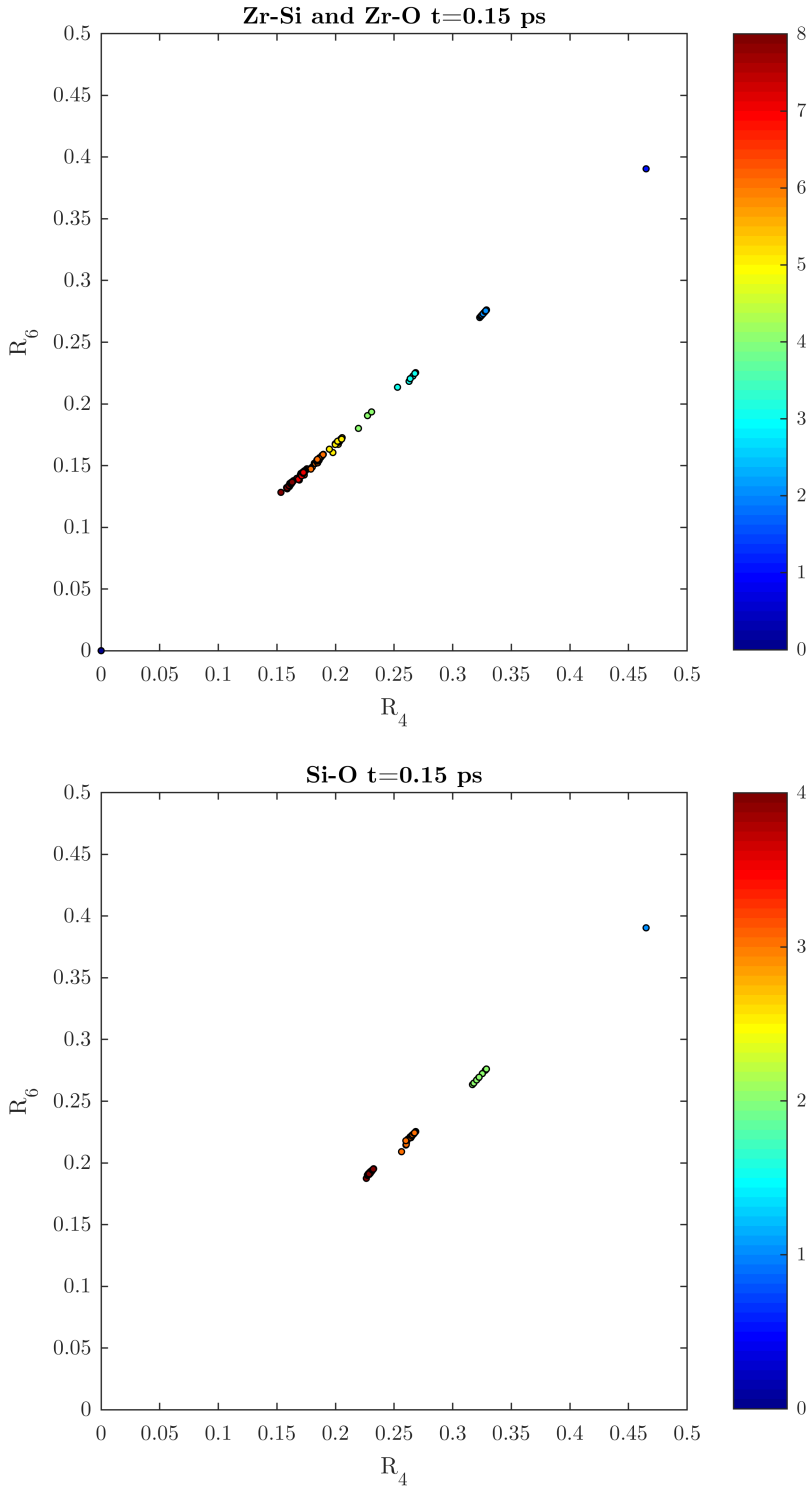

Figure 5.24: $R_6(R_4)$ scatter of Zr-Si and Zr-O (top) and Si-O (bottom) partial Hermite order parameters for t = 0.15 ps, highlighting the coordination number, as indicated in the colourbar next to the plots.

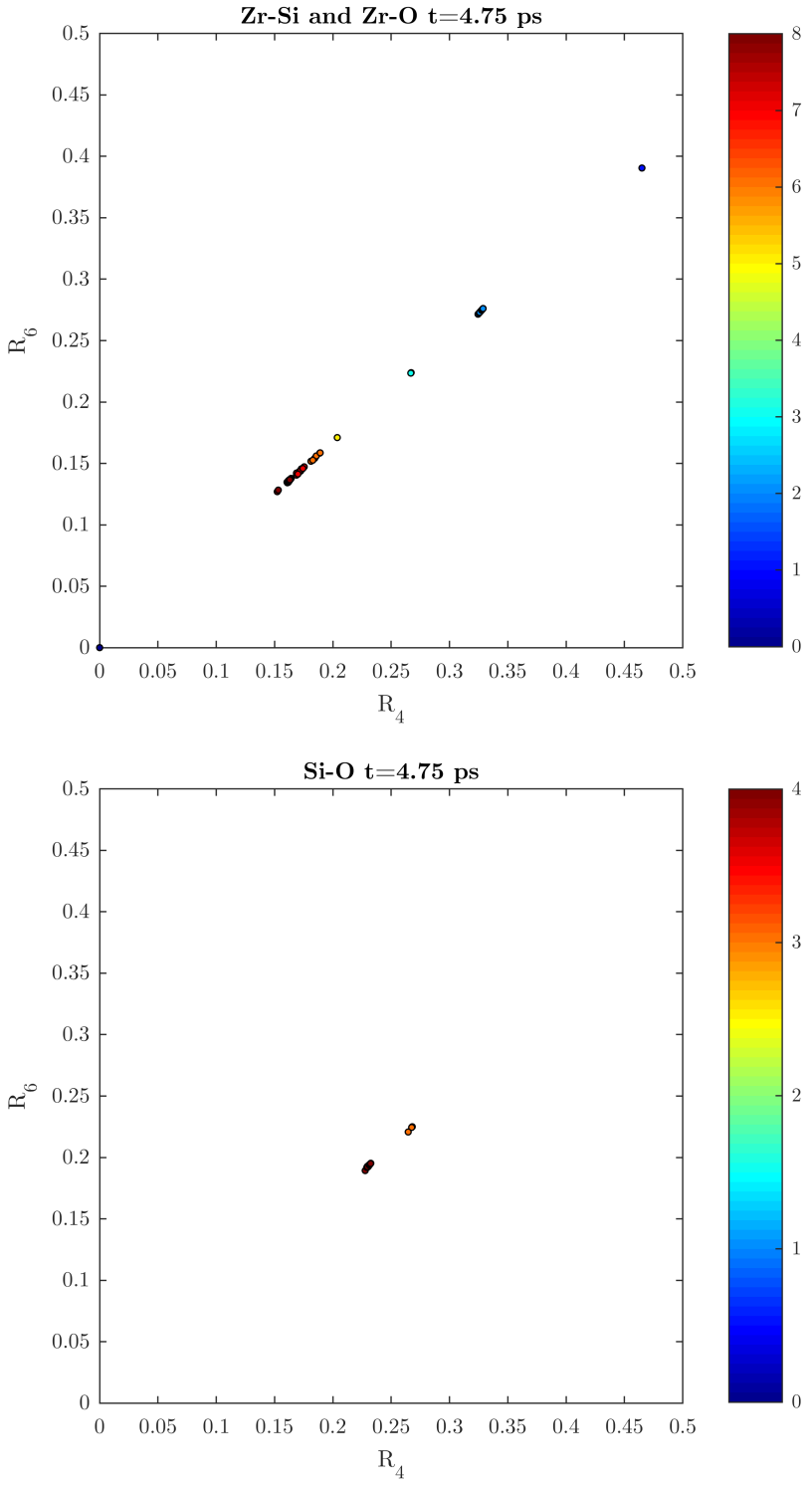

Figure 5.25: $R_6(R_4)$ scatter of Zr-Si and Zr-O (top) and Si-O (bottom) partial Hermite order parameters for t = 4.75 ps, highlighting the coordination number, as indicated in the colourbar next to the plots.

assume that although these three atoms have 4 neighbouring oxygens, the radial distribution of these neighbours is different for each zirconium atom.

For the Zr-O bonds and for $t = 0.15$ ps (Fig. 5.24), apart from the zirconium atoms associated with bond defects, the area corresponding to the 8-coordinated atoms are expanded in comparison with the respective area for the initial undamaged structure (Fig. 5.23). This is due to the change of the local geometry around reference zirconium atoms during the creation of the damage cascade, resulting in variations in the average distance of the oxygen neighbours. At the final stage of the simulation, for $t = 4.75$ ps (Fig. 5.25), the area is again more compact and close to the one of the initial structure and so it is safe to assume that the local geometry of the Zr-O bonds in terms of the average neighbour distance is restored. Si-O bonds behave in a similar manner. During the generation of the damage cascade (Fig. 5.24), silicon atoms show some variations in the radial geometry of the neighbours, regardless of the coordination number, while the geometry of the 4-coordinated silicon atoms is restored at the end of the simulation.

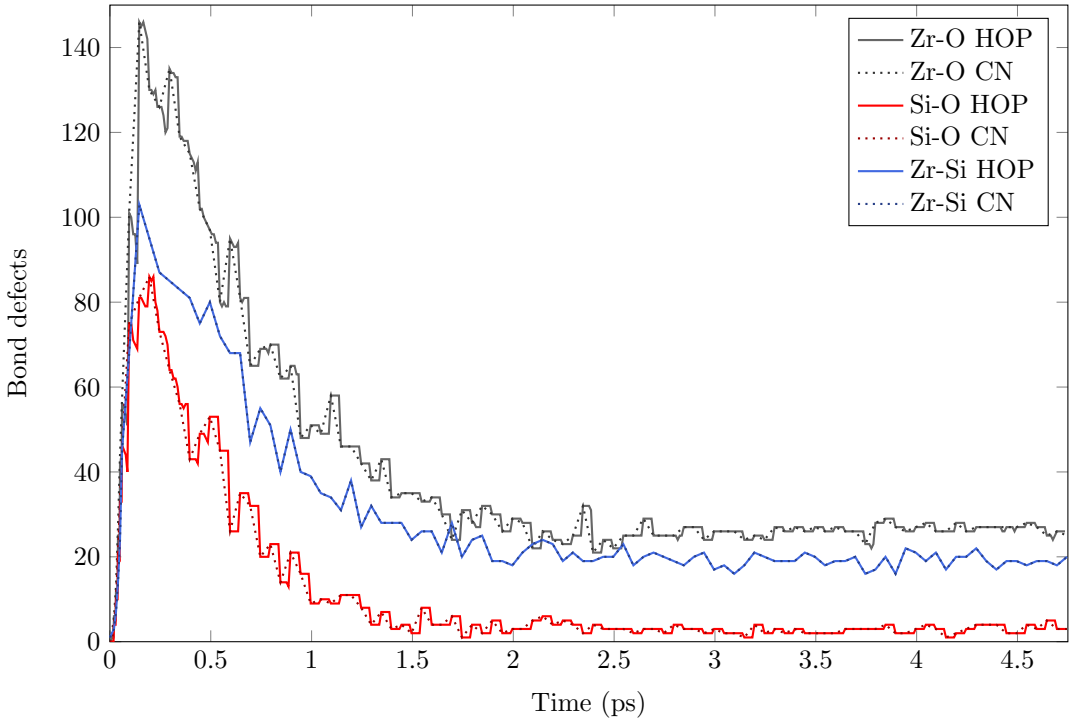

Figure 5.26: Comparison of number of bond defects for Zr-Si, Zr-O and Si-O pairs calculated using partial Hermite order parameters and by simple calculation of coordination numbers.

5.5.5 Species specific Steinhardt order parameters

The evolution of the majority of the species specific Steinhardt order parameters, follows an arbitrary pattern that is not related with the evolution of the number of defects, as shown in Fig. 5.9. However, some of the parameters demonstrate similar behaviour to the evolution of the number of defects. As shown in Fig. 5.27 of the zirconium and silicon atoms of the structure it was found that Q_1, Q_6 and Q_9 are evolving qualitative the same way as the number of defects, by reaching a maximum value near the time of the maximum damage and forming a plateau at $0.5 < t < 1$

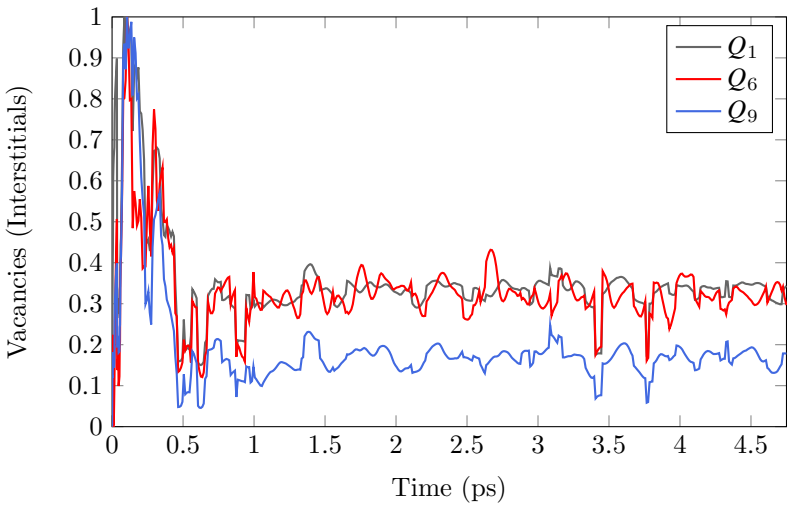

Figure 5.27: The time evolution of Q_1, Q_6 and Q_9 for the zirconium species. The plot demonstrates the values of $Q_\ell(t) - Q_\ell(0)$ normalized to give unit maxima. These three were the only SOPs that presented a damaged-like behaviour.

ps, while for the oxygen atoms it was Q_9 and Q_{10}. Since our effort is to correlate the Steinhardt order parameters with the number of defect atoms, it makes sense to use these parameters. It can be argued that the time evolution of these parameters is directly related to the evolution of the number of defect atoms of the system. Actually, the average number of defect atoms for the zirconium and silicon atoms, as calculated using the Steinhardt order parameters method, for the above ℓ values, is in good agreement with the number of defects calculated using the traditional defect counting method (Fig. 5.28). For the oxygen atoms however, there is a disagreement in the recovery region which can be explained by considering the fact that the DL_POLY in-built defect counting routine cannot identify antisites, which in this system are numerous.

A simple way to make an estimation of the total number of defects for each species is to find for each of the frames corresponding to the damaged structure the atoms that are displaced by a distance $r > r_d$. As can seen in Fig. 5.28, the total number of defect oxygen atoms is again smaller than the one estimated using the Steinhardt order parameters method, but this time, the difference is much smaller. A solution to this problem is to use higher order Steinhardt order parameters, in order to be able to average the number of defect atoms for even more ℓ values and get a better statistical distribution. However, this comes with a significant computational cost, since to compute the Steinhardt order parameters for $\ell = 16$ and $\ell = 24$, the computational times becomes 2.4 and 5.2 times higher respectively. However, since in amorphous materials there are no antisites, it is expected that the accuracy of this method will not be affected by such effects.

5.5.6 Species specific Hermite order parameters

For the species specific Hermite order parameters, a similar approach is followed. For the zirconium atoms, R_9, R_{10}, R_{11}, R_{12}, R_{14} and R_{15} demonstrated a desired damage-like time evolution while for silicon atoms R_{10}, R_{11}, R_{14} and R_{15} were used. For the oxygen atoms on the other hand, only R_2 demonstrated the desired behaviour. As seen in Fig. 5.28, the results obtained with the Hermite

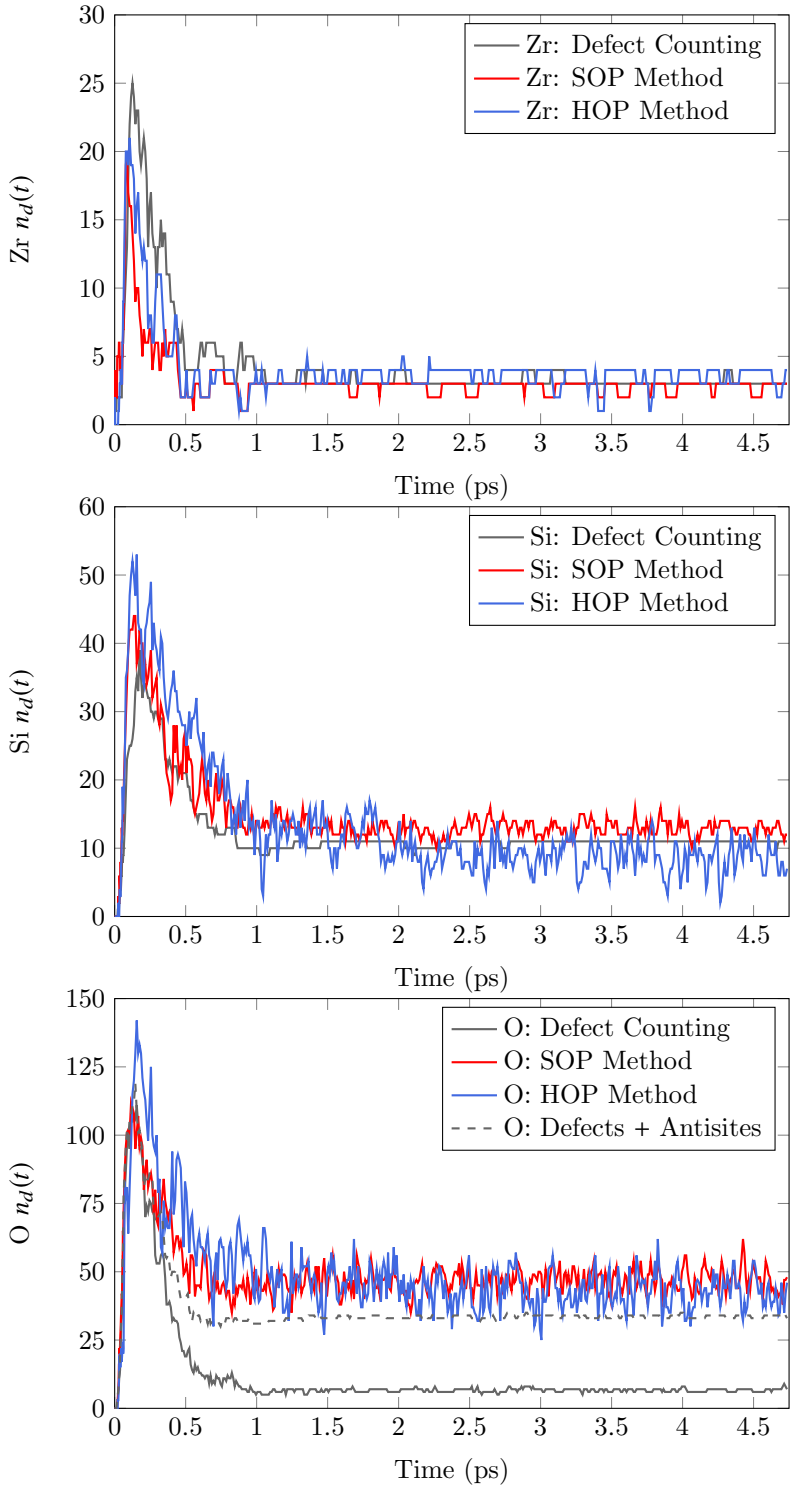

Figure 5.28: Comparison between the number of defects of the zirconium, silicon and oxygen atoms calculated using Wigner-Seitz method and the number of oxygen damaged atoms calculated using SOP and HOP methods. For the oxygen atoms, the dashed gray line corresponds to the total number of displaced oxygen atoms: damaged atoms and antisites.

order parameters method are in good agreement with the results obtained with both the Steinhardt order parameters and defect counting methods. This can be considered as a self-validation of the two proposed methods for systems with no antisites.

5.6 Conclusions

Zircon crystal is a well studied crystalline system regarding the effects of radiation damage and thus it is an ideal structure to develop and test new methods to characterise radiation damage effects that can be also applied in amorphous materials. When calculated Steinhardt order parameters using the standard approach, in which a reference particle is selected and the parameters are calculated using all the atoms within a sphere of specific radius, centred on the reference atoms, it was found that it is not possible to extract information regarding the bond defects. As a result, two novel approaches were proposed. The first approach, utilises the partial Steinhardt order parameters, calculated using as neighbours the atoms that form a physical bond with a reference particle. The goal of this method is to identify the number of atoms that are associated with at least one bond defect. The second approach, estimates the effects of radiation damage in terms of defect particles, by calculating the species specific Steinhardt order parameters, in which the neighbours of a reference atom of species A, are all the atoms of the same species within the first coordination shell of the $g_{A-A}(r)$ radial distribution function.

The results obtained using the partial Steinhardt order parameters method were compared with the number of low coordinated atoms created during the radiation damage event and the accuracy was very good. By comparing the results with the number of defected atoms estimated using the Wigner-Seitz defect count method, it was found that the latter fails to predict with accuracy the number of atoms associated with bond defects. The displacement or not of a particle from its initial lattice position is not directly related with the number of bond defects. The Wigner-Seitz method seems to underestimate the total number of defect atoms by a factor of 2.5 and in parallel overestimates the respective number of silicon atoms. This is due to the fact that the Wigner-Seitz method fails to identify antisites that in general may assist the recovery of a damage structure by reforming broken bonds.

The species specific Steinhardt order parameters method was proved accurate for the estimation of the number of defect particles resulting from a radiation damage event. For the silicon and zirconium atoms there was a very good agreement with the Wigner-Seitz method. However, for the oxygen atoms, the species specific Steinhardt order parameters method show a good agreement with the Wigner-Seitz method only at the first stages of the simulation, where the damage cascade is created. In the recovery region, our method seems to significantly overestimate the number of defect atoms. However, the species specific Steinhardt order parameters method has the ability to identify and count as defect atoms the antisites, that are not calculated using the DL_POLY 4 in built routine. When calculating the number of defect particles using the Wigner-Seitz method and taking into account the antisites, the results are much close to those obtained by our method. However, there is still a considerable difference between the two methods that needs to be addressed.

Apart from that, it was possible to use the partial Steinhardt order parameters to explore how the impact event affects the angular geometry of the SiO_4 tetrahedra, the ZrO_8 dodecahedra and the Si-Zr-Si triplets and the resulting low coordination structures associated with a bond defect. It

was found that during the creation of the damage cascade , the non-defect SiO_4 and ZrO_8 structures are only a little affected by the impact event. However, the low coordination units, demonstrate a large variety of angular geometry - the relative angular positions of remaining oxygen atoms surrounding the reference atoms do not converge. Additionally, several Si-Zr-Si triplets become non linear, as there are several zirconium atoms for which the Si-Zr-Si angle is very different from the ideal value of 180°. However, by the end of the simulation, when the crystal exhibits a large degree of recovery, most of the Si-Zr-Si triplets are restored to an almost linear conformation.

Hermite order parameters methods were developed in order to have an additional method to identify bond-defect atoms, using only the distance between bonded atoms and to extract information regarding the effect of radiation damage on the bond length between different species. In terms of the number of atoms associated with at least one bond defect, partial Hermite order parameters provide almost the same results as the partial and partial Steinhardt order parameters methods. In terms of the number of defect atoms, species specific Hermite order parameters provide results that are in good agreement with the respective results of the species specific Steihnhardt order parameters method. Since the two sets of parameters depend on different variables - Steinhardt order parameters depend on the spherical angles θ and ϕ while Hermite order parameters on the spherical distance r - it can be argued that they can be used as a self validating set of methods for the estimation of bond-defect atoms in a system. In terms of the average bond length between the different bonded species, Hermite order parameters revealed that the impact event affects the length of all the bond lengths of the system. In the $R_6(R_4)$ plots, the compact areas formed by the data points for the undamaged structure, are replaced in the damaged structures by extended areas due to the changes in the average distance of the bonded neighbours.The recovery of the system at the end of the simulation is also reflected in the average neighbour distance, as the final areas in the $R_6(R_4)$ plots are more compact compared with the respective areas at the stage of maximum damage.

Chapter 6

Radiation damage in borosilicate glasses

6.1 Introduction

Since borosilicates represent the most common glass wasteform for the encapsulation of HLW, it is important to explore their tolerance to self irradiation. In the UK, the most common borosilicate glass for nuclear waste encapsulation consists of 47.2% SiO_2, 16.9%B_2O_3, 4.8% Al_2O_3, 5.3% MgO, 8.4% Na_2O and 17.4% of other elements [166]. However, this glass composition cannot be simulated with accuracy, as the accurate potentials developed to describe the pair interactions in borosilicate glasses are limited to Si-O, B-O and Na-O interactions. Consequently, in this work, the behaviour of the simpler sodium borosilicate glasses SBN12 and SBN14 (Table 6.1) is explored.

Table 6.1: Composition of the SBN12 and SBN14 sodium borosilicate glasses in mol%.

	SiO_2	B_2O_3	Na_2O
SBN12	59.66	28.14	12.20
SBN14	67.73	18.04	14.23

These glasses were selected on the basis of their molar compositions and on the extent of current research. The ratios R = $[Na_2O]/[B_2O_3]$ and K = $[SiO_2]/[B_2O_3]$ for the UK nuclear glass are R = 0.497 and K = 2.793. From the sodium borosilicate glasses that are currently used in molecular dynamics simulations, SBN12 has a molar composition close to the UK glass with R_{12} = 0.434 and K_{12} = 2.120, while SBN14 glass has a composition with ratios R_{14} = 0.789 and K_{14} = 3.754, very close to those of the R7T7 glass used in the French nuclear industry. Although R7T7 glass has no current applications in the UK nuclear industry, SBN14 was selected in this work as it has been extensively researched and it can be used for comparison with our models.

The two irradiated glass models were analysed using the methods described in the previous chapters: defect counting, partial Steinhardt and Hermite order parameters, species specific Steinhardt and Hermite order parameters and primitive ring statistics. However, the species specific Steinhardt and Hermite order parameters methods failed to provide any trustworthy information regarding the extent of radiation damage in terms of defect atoms. Following the same procedure as in the radiation damaged crystal structure, the method failed to identify appropriate order parameters following a damage like evolution and so it was not possible to find a relation between $n_d(t)$ and $n_g(t)$ as described in section 5.4.3.

6.2 Creating SBN12 and SBN14 borosilicate glass models

The first step to create accurate borosilicate glass models is to select the correct pair potentials. Jolley et. al. [24] conducted a comprehensive comparison between existing potentials for sodium borosilicate glasses and concluded that potentials proposed by Kieu et. al. [22] predict the bond lengths and the density of the structure with increased accuracy and additionally have lowest melting points. Kieu model potentials are described in detail in section 3.9. The partial charges presented in Table 6.2 for each of the species were calculated using equation (3.143).

Table 6.2: Partial charges used in SBN12 and SBN14 borosilicate glass models.

	q_{Si}	q_{B}	q_{Na}	q_{O}
SBN12	1.869128	1.528756	0.451628	-0.965872
SBN14	1.869425	1.588015	0.451925	-0.965580

For the simulation of the glasses, the DLPOLY_4 molecular dynamics simulation package was used [132]. For the SBN12 glass a cubic fcc cell consisting of 4093 atoms in total (686 silicon, 646 boron, 230 sodium and 2481 oxygen atoms) randomly placed on the lattice points was created while for the SBN14 glass the cubic cell contained 4094 atoms (825 silicon, 440 boron, 346 sodium and 2483 oxygen atoms). The difference in the total number of atoms in the two structures was necessary in order to have the respective compositions as close as possible to those presented in Table 6.1 and also have a neutral crystal with zero total charge. Electrostatic interactions were taken into account using the Ewald summation routine provided by the DLPOLY_4 package. The size of the cell was selected appropriately to give densities about 5% lower than the experimental values, in order to relax close to the experimental value after the quench, and set to 37.999 Å for the SBN12 glass and to 37.686 Å for the SBN14. The initial structures were equilibrated for 100 ps at 5000 K under the NVT ensemble and then rapidly quenched to room temperature at a rate of 5×10^{12} K/s under constant volume. Finally, both structures were equilibrated at 300 K following a two step procedure: for 20 ps under the NPT ensemble to relax to the desired density and for 10 ps using the NVE ensemble, to remove the excess pressure. The procedure of glass creation [24] is illustrated in Fig. 6.1.

To verify the glassy nature of the quenched structures, the radial distribution functions (Figs. 6.2 and 6.3) are examined. All radial distribution functions are characteristic of an amorphous material. For both structures, the curves representing the radial distribution functions of the Si-O and B-O pairs are plotted separately, as their first peak, corresponding to the first coordination shell, is found at a distance smaller than the first minimum of the total radial distribution function. This property will be exploited later, for the calculation of the Steinhardt order parameters, Hermite order parameters and primitive rings. Also, the Si-O and B-O radial distribution functions clearly demonstrate the local order corresponding to the silica and boron network that is limited to the first coordination shell.

The accuracy of the two glass models can also be tested by calculating their density. For the SBN12 glass, the final density is calculated ρ_{SBN12} = 2.378 g/cm^3 while for the SBN14 it was ρ_{SBN14} = 2.482 g/cm^3. These values are very close to the experimental ones, which are 2.37 g/cm^3 and 2.45 g/cm^3 respectively [22]. The average coordination number of the boron atoms was

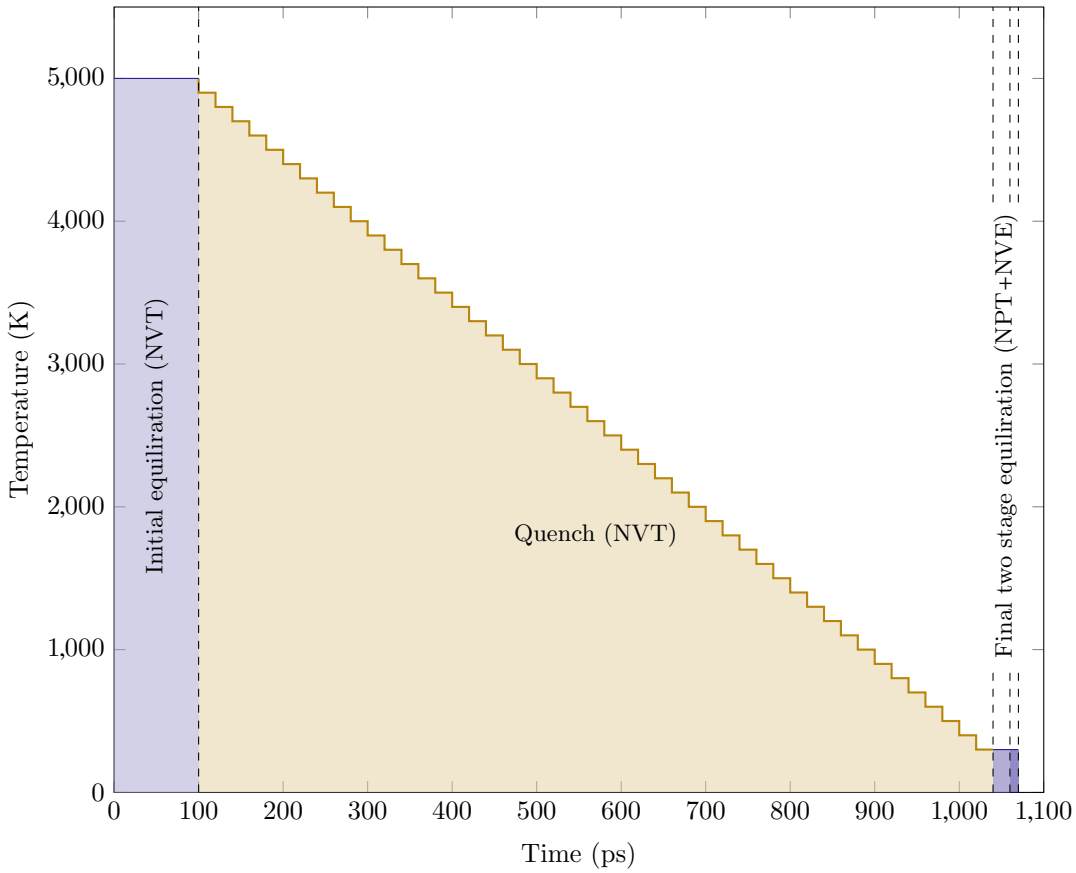

Figure 6.1: The melt-quench routine for the creation of borosilicate glass models.

calculated equal to $C_{\mathrm{B,SBN12}}$ = 3.30 and $C_{\mathrm{B,SBN14}}$ = 3.46, very close to the experimental values which are 3.43 and 3.72 respectively. The Si-O, B-O and Na-O bond lengths for the two glasses, as given in Table 6.3, are close to the experimental values.

Table 6.3: Structural data of the modeled SBN12 and SBN14 glasses. The experimental values [22] are in parentheses.

	$d_{\mathrm{Si\text{-}O}}$		$d_{\mathrm{B\text{-}O}}$		$d_{\mathrm{Na\text{-}O}}$	
SBN12	1.61	(1.60-1.62)	1.42	(1.41)	2.42	(2.30-2.62)
SBN14	1.62	(1.60-1.62)	1.42	(1.44)	2.43	(2.30-2.62)

6.2.1 Creating a radiation damage cascade

The radiation damage cascade formation process was performed using the DLPOLY_4 molecular dynamics simulations package [132]. One silicon atom of the system was selected as primary knock atom (PKA) and given an excess of kinetic energy equal to 1 keV along the direction ($x = y = z$). To avoid problems associated with the divergence region of the Si-O, B-O and O-O Buckingham potentials, a short range ZBL potential was used. This potential was truncated and fitted to the Buckingham potentials using the `atsim.potentials` package [165]. As in the case of the damage

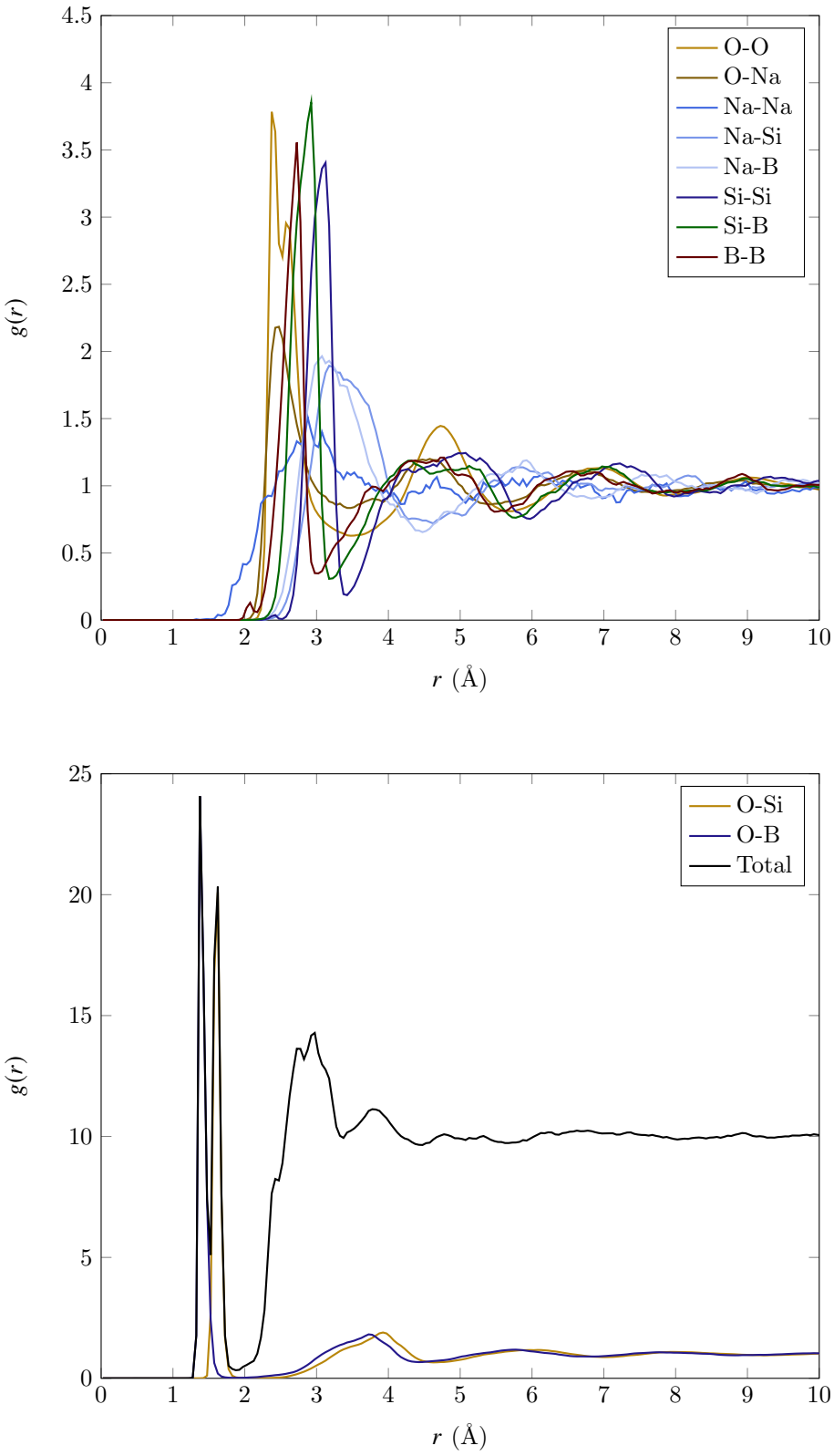

Figure 6.2: Partial and total radial distribution functions of the SBN12 borosilicate glass.

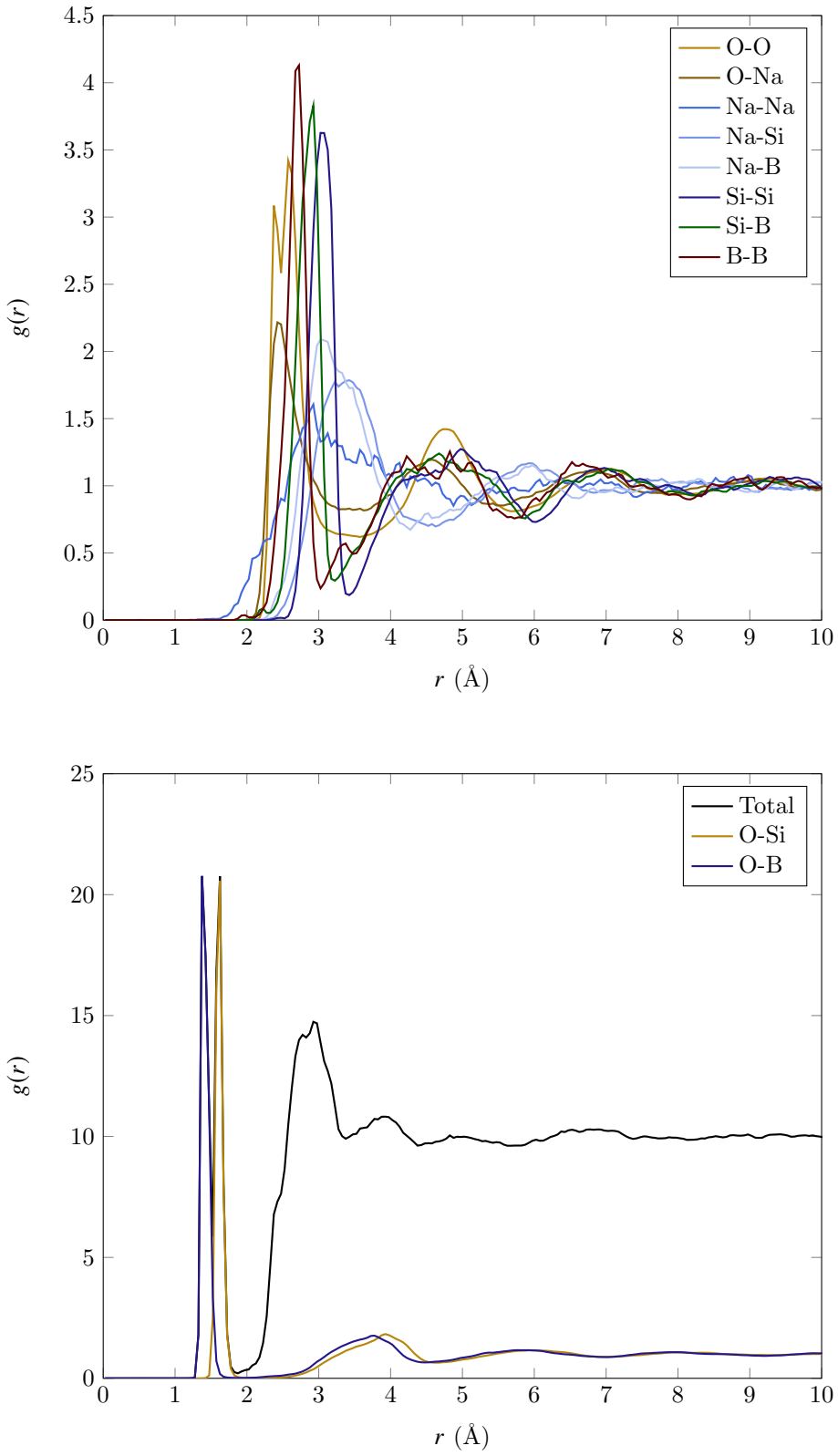

Figure 6.3: Partial and total radial distribution functions of the SBN14 borosilicate glass.

cascade creation in zircon crystal, a boundary layer was applied to dissipate the excess of kinetic energy as well as a variable timestep algorithm. The simulation was run for 50000 timesteps, corresponding to 4.75 ps, under the NVT dynamics.

6.3 Algorithmic details of defect analysis

The method followed for the defect analysis is similar to the one used in the zircon crystal. An output file was generated, containing the trajectories of the atoms at every 100 timesteps of the simulation, generating 501 snapshots in total to be analysed using the defect counting and the partial SOP/HOP methods. Additionally, for each snapshot, a primitive ring statistics analysis was performed, to get detailed information regarding the effect of the radiation in the silica network of the glasses.

For the defect counting method and since the smallest interatomic distance for both structures is 1.42 Å, equal to the average B-O bond distance, a particle is identified as damaged, if the distance between the position it occupies in the damaged frame from the position in the initial undamaged structure is greater than 0.7 Å.

Partial Steinhardt order parameters are calculated for a reference particle using all the bonded neighbours of the same species. For the calculation of the parameters it is assumed that a bond between two atoms A and B exists if the distance r_{AB} between two atoms is less than the first minimum $r_{\mathrm{min}}^{\mathrm{RDF(A,B)\ Par.}}$ of both the respective partial radial distribution function and the first minimum of the total radial distribution functions $r_{\mathrm{min}}^{\mathrm{RDF(A,B)\ Tot.}}$,

$$r_{\mathrm{AB}} \leq r_{\mathrm{min}}^{\mathrm{RDF(A,B)\ Par.}} \qquad \text{and} \qquad r_{\mathrm{AB}} \leq r_{\mathrm{min}}^{\mathrm{RDF(A,B)\ Tot.}} \tag{6.1}$$

By these criteria, the only bonds existing in the structure are the B-O and Si-O bonds.

6.4 Results

6.4.1 Defect counting

In Figs. 6.4 and 6.5, the number of displaced atoms versus time is demonstrated, for the SBN12 and SBN14 borosilicate glasses, as calculated using the DL_POLY 4 defect counting routine. From these plots it is obvious that the two glasses show similar behaviour. The majority of displaced atoms are oxygen atoms, while boron atoms demonstrate the greater resistance to radiation damage.

For the SBN12 glass, at the maximum damage, almost 10.7% of the total atoms of the system are displaced from their initial position. The fraction of displaced atoms is 9.0% for the boron atoms, 44.8% for the sodium atoms, 7.7% for the silicon atoms and 10.4% for the oxygen atoms. The respective percentages for the SBN14 glass are 9.8% for the total atoms, 6.6% for the boron atoms, 36.7% for the sodium atoms, 7.5% for the silicon atoms and 8.7% for the oxygen atoms. Thus, in terms of number of displaced atoms, it is obvious, that SBN14 glass is slightly more resistant to radiation damage in comparison with SBN12 glass. The high percentage of displaced sodium atoms for both structures can be justified by considering that sodium atoms are actually network modifiers and consequently it is much easier to displace them from their position during

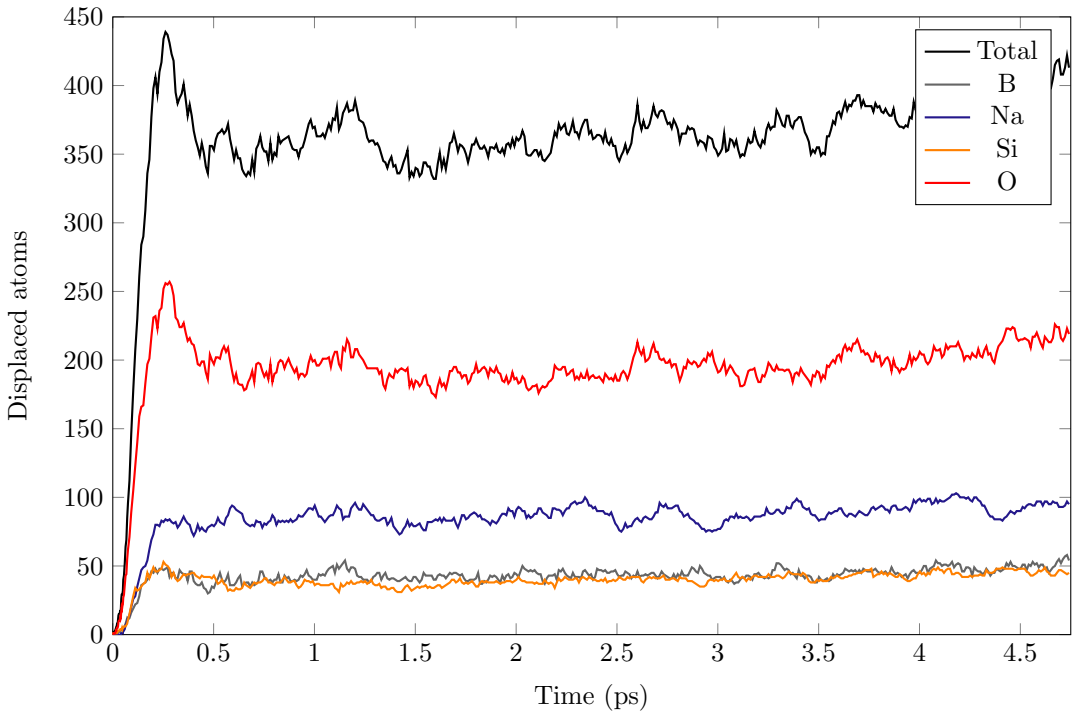

Figure 6.4: Number of displaced atoms versus time for the radiation damaged SBN12 glass calculated using defect counting method.

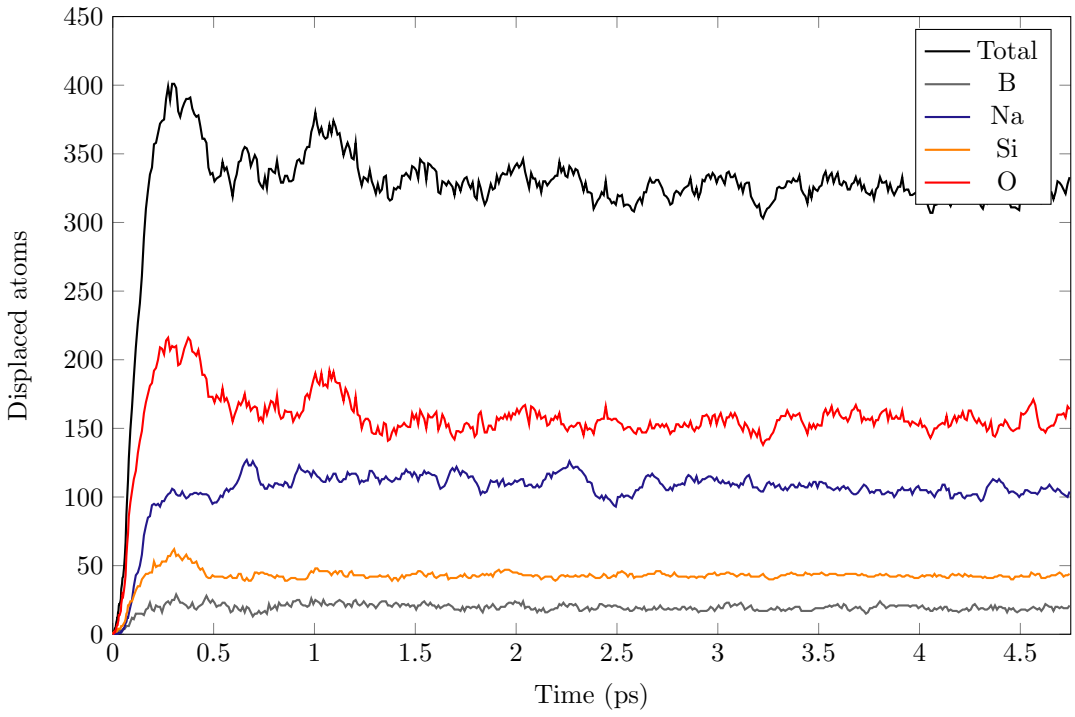

Figure 6.5: Number of displaced atoms versus time for the radiation damaged SBN14 glass calculated using defect counting method.

a decay event in comparison with bonded atoms. In terms of recovery, only a few of the displaced oxygen and silicon atoms manage to recover to their initial positions, while boron and sodium atoms are permanently displaced.

However, the number of displaced atoms is in total disagreement with the changes in the coordination number of the atoms. In Figs. 6.6 and 6.7, the changes in the coordination number of boron and silicon atoms during the simulation are clear. For both glasses, the number of 3-coordinated boron atoms and 4-coordinated boron and silicon atoms at the end the simulation, is almost the same as the numbers in the initial undamaged structure. For the SBN12 glass, there is a small increase in the number of 4-coordinated boron atoms and a small decrease in the number of 3-coordinated boron atoms, suggesting that due to the irradiation, a small number of boron atoms transform from 3- to 4-coordinated, while for the SBN14 glass we observe the reverse. Additionally, the maximum number of boron and silicon atoms undergoing a change in their coordination number is much lower than the maximum number of displaced atoms for each of the species. Thus it is clear that the defect counting method does not provide an accurate estimation of the radiation damage effects in terms of bond defects.

6.4.2 Partial Steinhardt order parameters

In Figs. 6.8-6.13 the plots of Q_4 against Q_6 for the B-O and Si-O bonds of the SBN12 glass are shown for the initial structure at t = 0.00 ps, t = 0.35 ps (a moment in which the maximum damage occurs according to the defect counting method), and for the final structure at t = 4.75 ps. In Figs. 6.14-6.19 the same plots for the SBN14 glass are displayed.

For the undamaged structures it is clear that boron atoms are concentrated in two regions, one corresponding to the 3-coordinated boron atoms and one to the 4-coordinated (figs. 6.8 and 6.14). These regions are in general well defined, meaning that there is a consistency in the geometry for both 3 and 4-coordinated boron atoms. However, a small number of the initially 3-coordinated boron atoms are found outside the well defined regions and it can be argued that the angular distribution of the oxygen neighbours around this atoms is slightly different than the average. The initially 4-coordinated boron atoms on the other hand appear to have a most consistent initial angular distribution of their oxygen neighbours. For the silicon atoms (figs. 6.11 and 6.17), it is observed that a few of them are three coordinated and distributed in a wide area of the $Q_6(Q_4)$ plots, underlying the large variations of the angular distribution of the three oxygen neighbours. In a similar manner, data points corresponding to the initially 4-coordinated silicon atoms cover a relatively wide area showing a variety in the geometry of the tetrahedra of the silica network.

For the damaged structures, it is clear that for both glasses, the changes in the values of partial Steinhardt order parameters show agreement with the behaviour of the coordination number of the boron and silicon atoms. For both glasses and for t = 0.35 ps, only a few boron (Figs. 6.15) and silicon atoms (Figs. 6.18) have a $Q_6(Q_4)$ value away from the region defined by the undamaged structure. Boron atoms are found either 3- or 4-coordinated, with the exception of some located in the low left corner of the plots and corresponding to 0-coordinated atoms. Similar to the undamaged structure however, the angular distribution of the oxygen neighbours of a small number of the 3- and 4-coordinated boron atoms appear to be different from the average. For the silicon atoms this is more obvious as several 4-coordinated atoms are clearly distributed away from

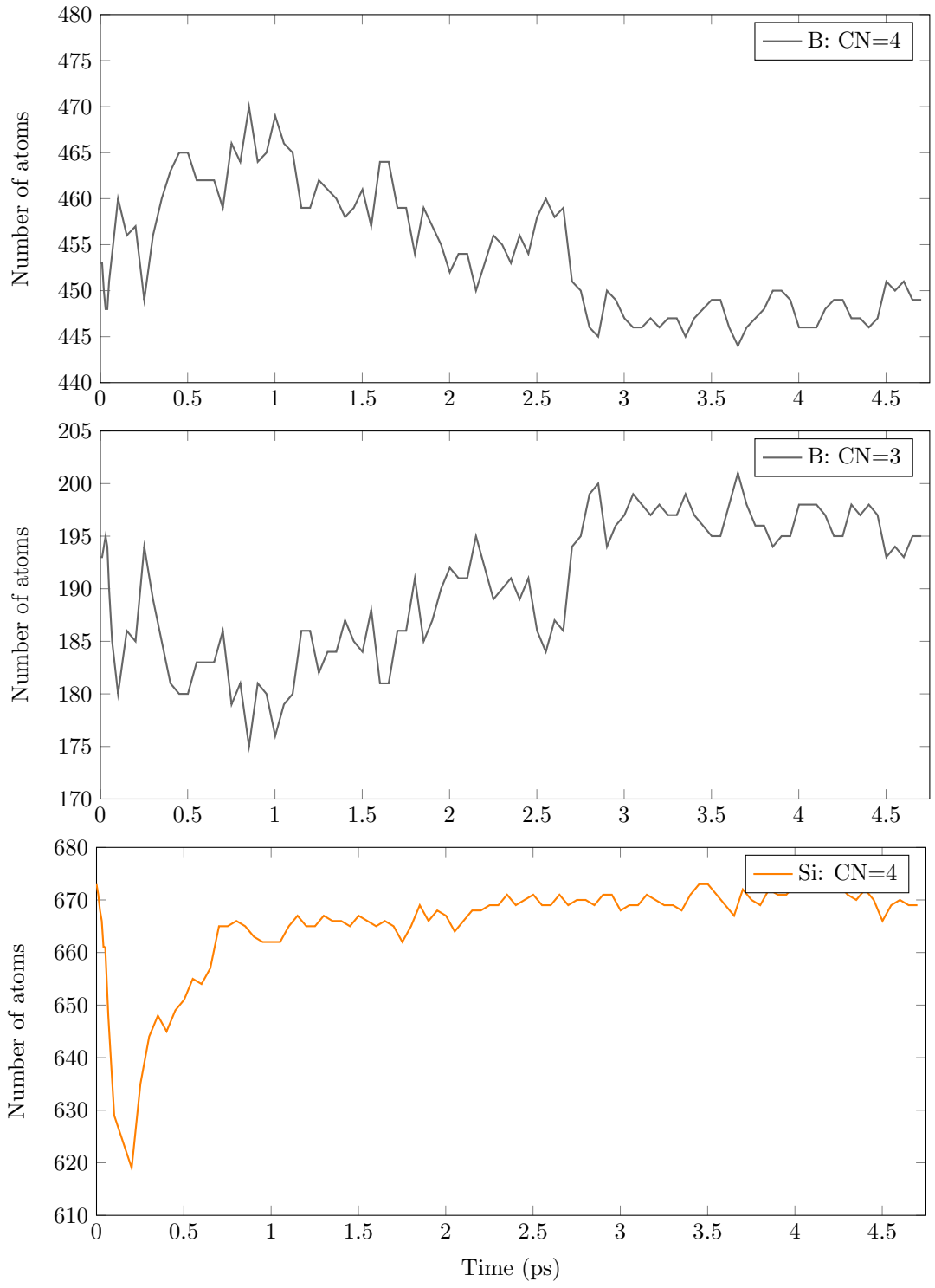

Figure 6.6: The evolution of the number of 4-coordinated boron atoms (**top**), of 3-coordinated boron atoms (**middle**) and 4-coordinated silicon atoms (**bottom**) of the SBN12 radiation damaged glass.

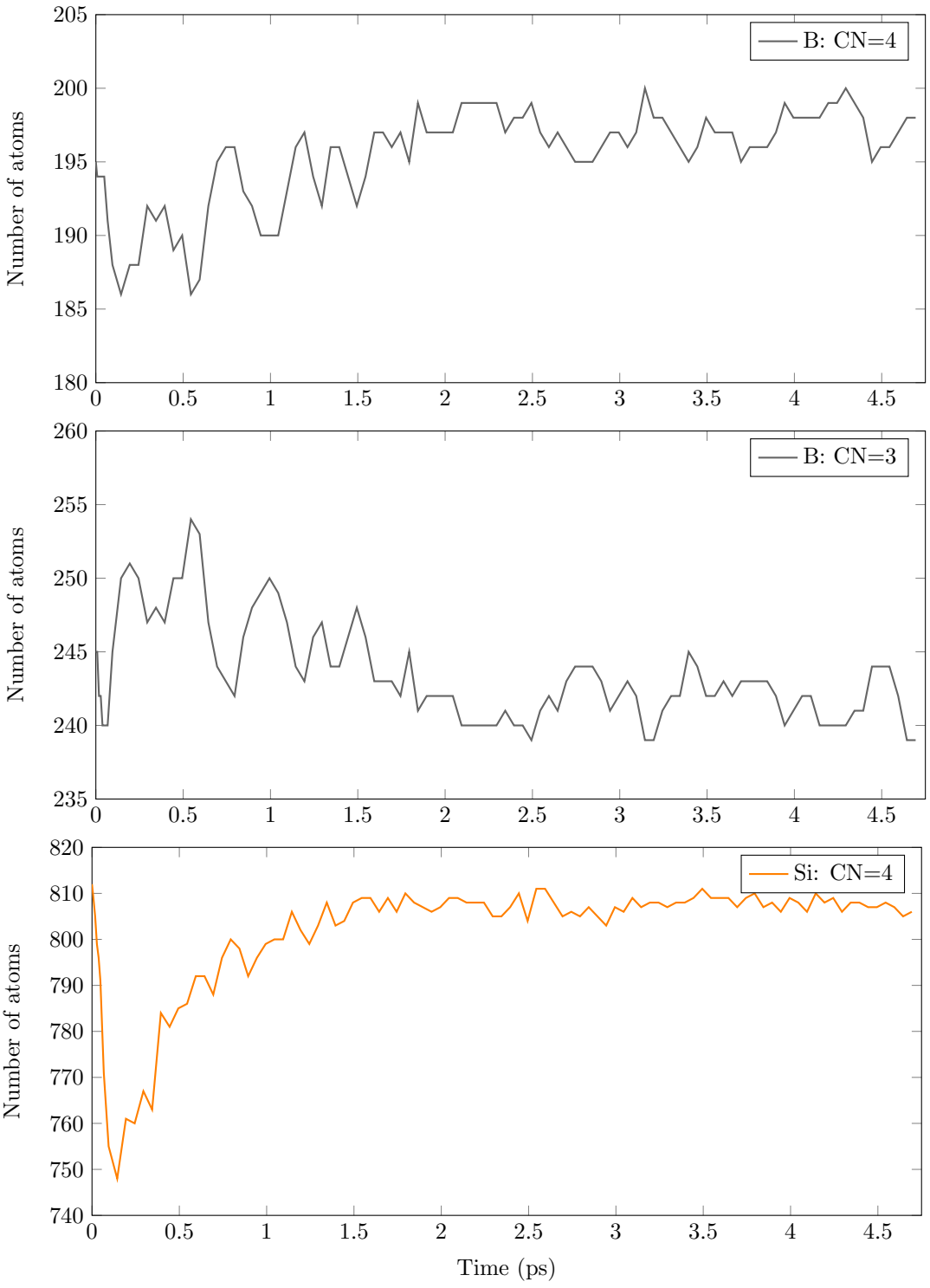

Figure 6.7: The evolution of the number of 4-coordinated boron atoms (**top**), of 3-coordinated boron atoms (**middle**) and 4-coordinated silicon atoms (**bottom**) of the SBN14 radiation damaged glass.

the region defined by the atoms with the standard geometry, while the 3-coordinated damaged silicon atoms have an arbitrary geometry. In the final structures, at t = 4.75 ps, the distribution of data points is very close to the one of the initial undamaged structure implying a high degree of structural recovery.

The transformation of 3-coordinated boron atoms to 4-coordinated and vice versa can be explored, by identifying 3- and 4- coordinated boron atoms of the initial undamaged structure and calculating partial Steinhardt order parameters at every timestep for each of these separately. In Figs. 6.20-6.23 and 6.24-6.27 the $Q_6(Q_4)$ plots of the 3- and 4-coordinated boron atoms are demonstrated for the SBN12 and SBN14 glasses. It is clear from these plots that some boron atoms that were originally 3-coordinated, leave the area defined by this atom and move in the area of the four coordinated atoms and vice versa. Additionally all boron atoms found at some point to have zero coordination number were initially 3-coordinated. During the creation of the damage cascade, at t = 0.35 ps, the 3-coordinated boron atoms transform to 4-coordinated with a relatively fixed angular distribution of oxygen neighbours - with only a few exceptions - very close to the one of the originally 4-coordinated boron atoms. Thus it is safe to assume that the initially 3-coordinated boron atoms are transforming to BO_4 tetrahedra during every stage of the simulation. On the contrary, during the creation of the damage cascade, the initially 4-coordinated boron atoms are transformed into 3-coordinated with arbitrary angular distribution of the 3 oxygen neighbours. At the end of the simulation however, the 3-coordinated boron atoms resulting from the transformation of 4-coordinated, demonstrate a consistent geometry similar to the one of the undamaged 3-coordinated boron atoms.

For both boron and silicon atoms, the number of atoms associated with at least one bond defect can be calculated, the same way it was calculated for the zircon crystal: the areas in the $Q_6(Q_4)$ plots occupied by atoms in the undamaged structure is defined and all the atoms in the damaged structure and for each timestep lying outside these areas are identified (Figs. 6.28 and 6.29). For the silicon atoms, there is a good agreement between the number of atoms associated with at least one bond defect and the number of 4-coordinated silicon atoms demonstrated in Figs. 6.6 and 6.7. For the boron atoms it seems to have a lower agreement. However, in Figs. 6.6 and 6.7 the number of 4-coordinated boron atoms is the sum of those having no bond defects and those transformed from 3-coordinated to 4-coordinated and in a similar manner, the number of 3-coordinated atoms are the actual one and those transformed from 4-coordinated to 3-coordinated. Thus, the coordination number fails to give information regarding the transformation of boron atoms between the two different coordination number, a task that can be successfully completed using partial Steinhardt order parameters.

By comparing the number of boron and silicon atoms associated with bond defects for both structures it is clear that SBN14 shows slightly increased tolerance to radiation damage. The percentage of maximum displaced silicon atoms is 7.1% for the SBN12 glass and 7.4% for the SBN14. However for the boron atoms the percentage of defect atoms is 8.8% for the SBN12 glass and 6.4% for the SBN14. In the final equilibrated structures, silicon atoms are almost completely recovered in terms of bond defects. On the contrary after the time at which the maximum damage is observed, the number of boron atoms associated with at least one broken B-O bond remains almost constant. Consequently, it can be argued that B-O bonds are unable to recover after a radiation damage event and the majority of the damage in both structures is related to broken

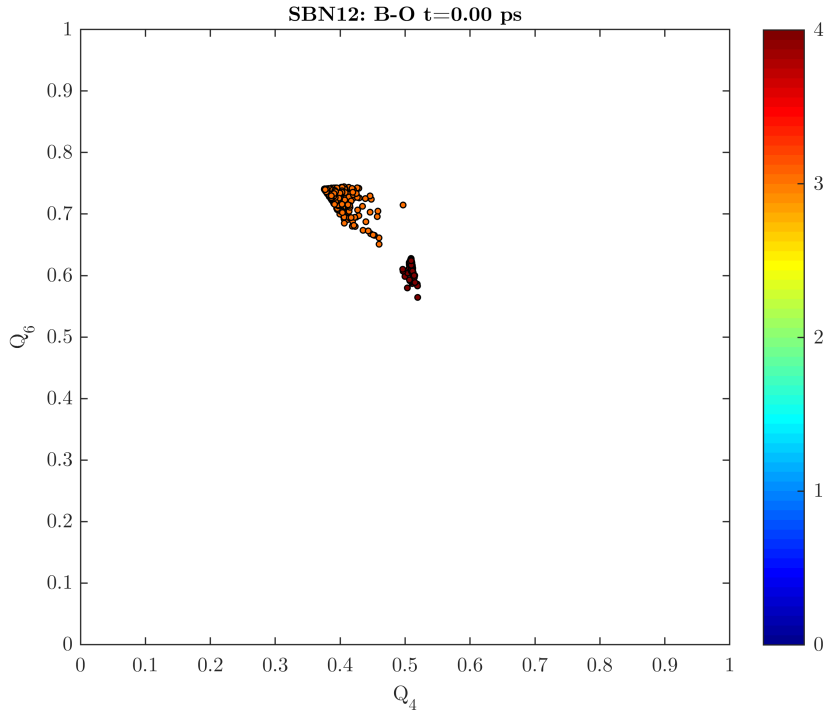

Figure 6.8: $Q_6(Q_4)$ plot of the boron atoms in the initial undamaged structure of the SBN12 glass, highlighting the coordination number, as indicated in the colourbar next to the plots.

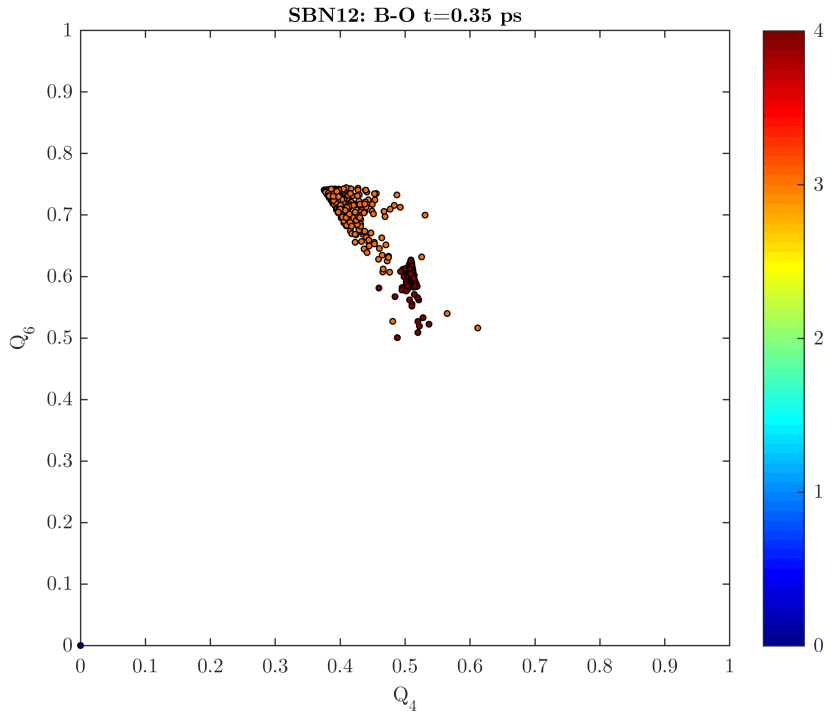

Figure 6.9: $Q_6(Q_4)$ plot of the boron atoms at t = 0.35 ps for the SBN12 glass, highlighting the coordination number, as indicated in the colourbar next to the plots.

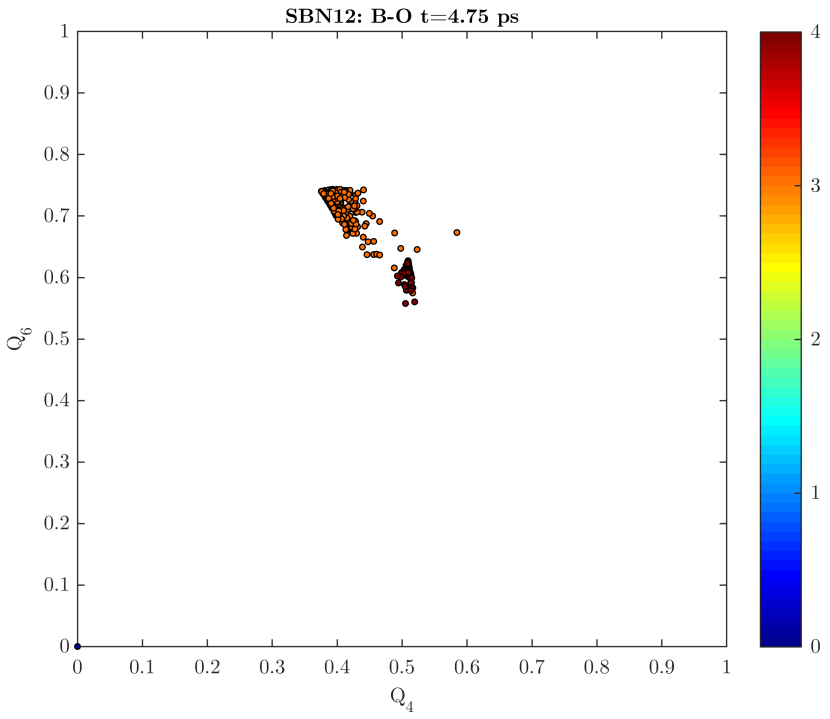

Figure 6.10: $Q_6(Q_4)$ plot of the boron atoms in the final damaged structure of the SBN12 glass, highlighting the coordination number, as indicated in the colourbar next to the plots.

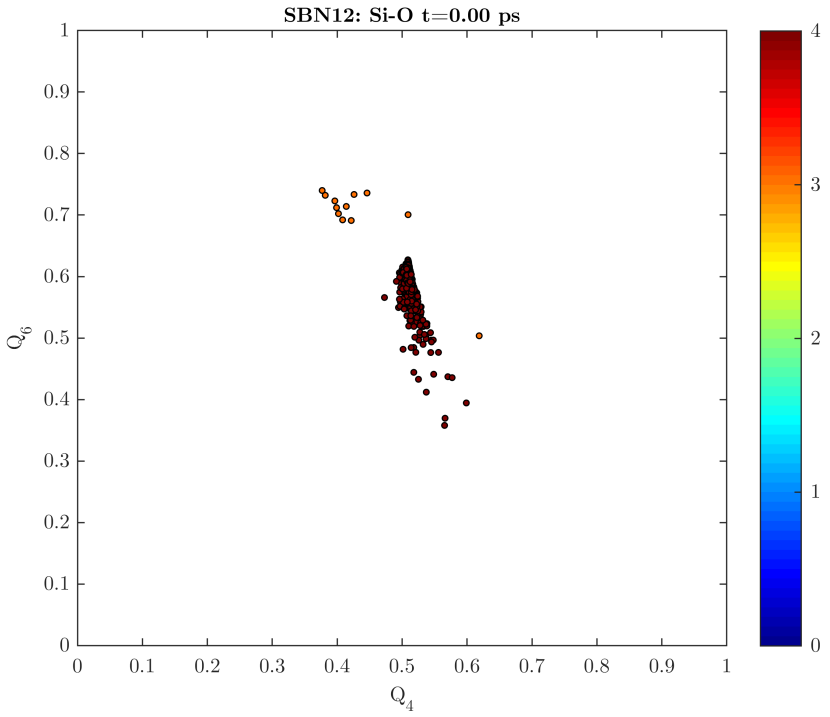

Figure 6.11: $Q_6(Q_4)$ plot of the silicon atoms in the initial undamaged structure of the SBN12 glass, highlighting the coordination number, as indicated in the colourbar next to the plots.

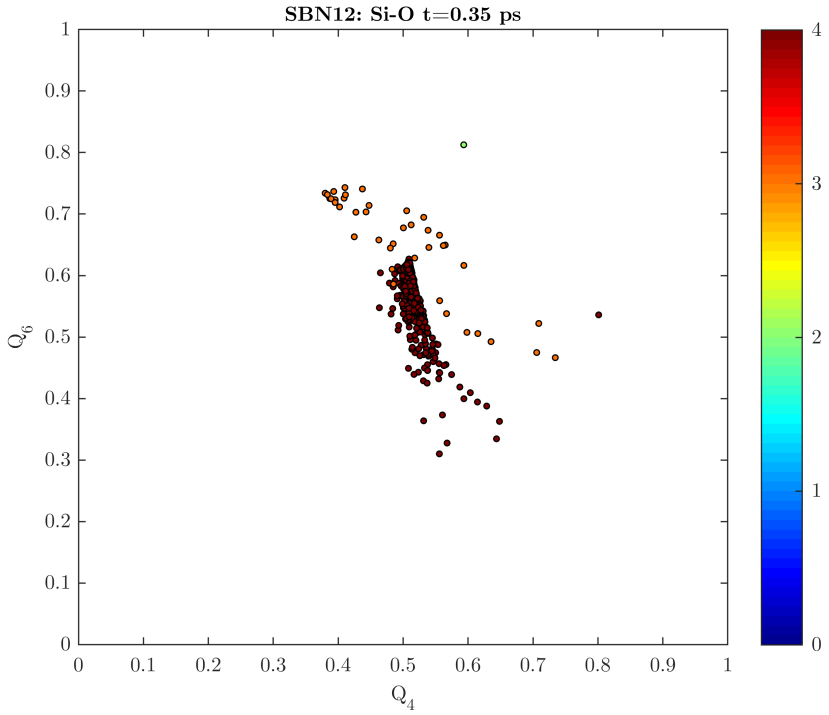

Figure 6.12: $Q_6(Q_4)$ plot of the silicon atoms at t = 0.35 ps for the SBN12 glass, highlighting the coordination number, as indicated in the colourbar next to the plots.

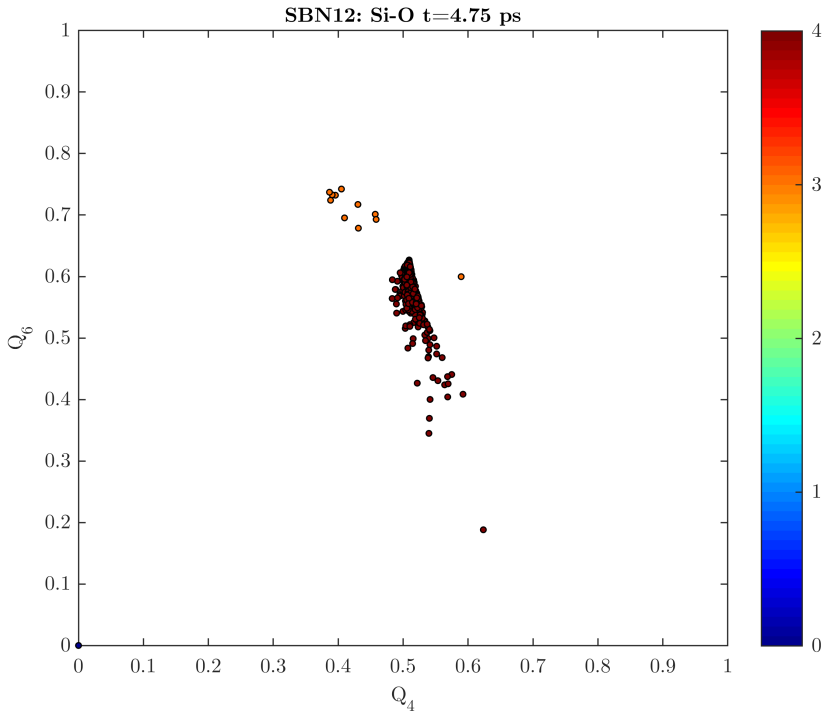

Figure 6.13: $Q_6(Q_4)$ plot of the silicon atoms in the final damaged structure of the SBN12 glass, highlighting the coordination number, as indicated in the colourbar next to the plots.

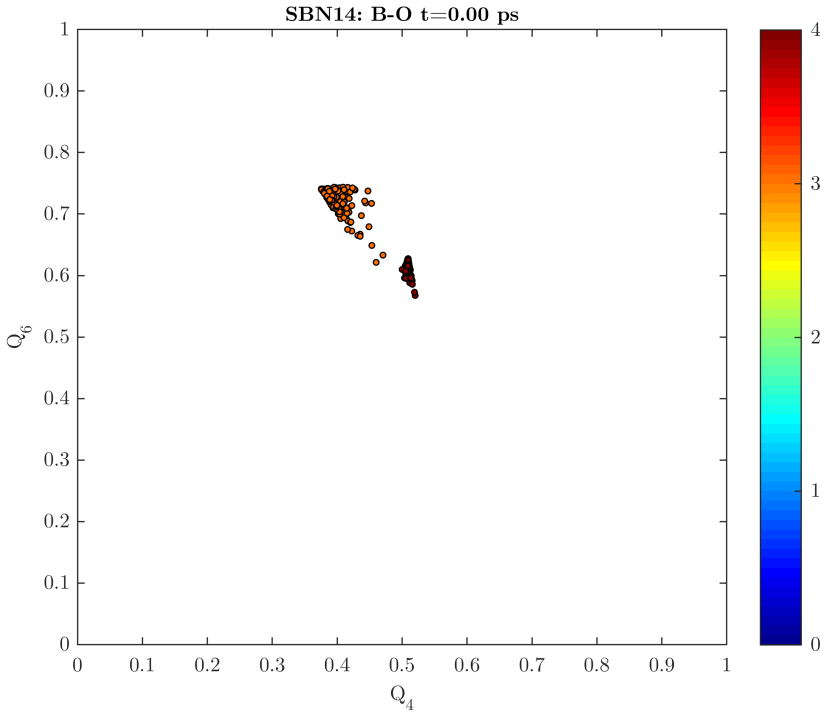

Figure 6.14: $Q_6(Q_4)$ plot of the boron atoms in the initial undamaged structure of the SBN14 glass, highlighting the coordination number, as indicated in the colourbar next to the plots.

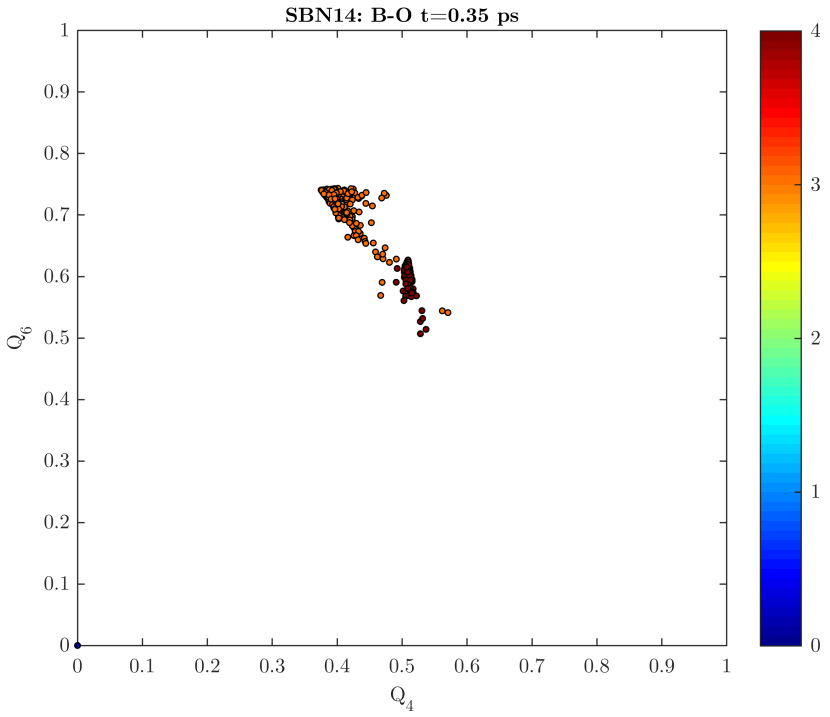

Figure 6.15: $Q_6(Q_4)$ plot of the boron atoms at t = 0.35 ps for the SBN14 glass, highlighting the coordination number, as indicated in the colourbar next to the plots.

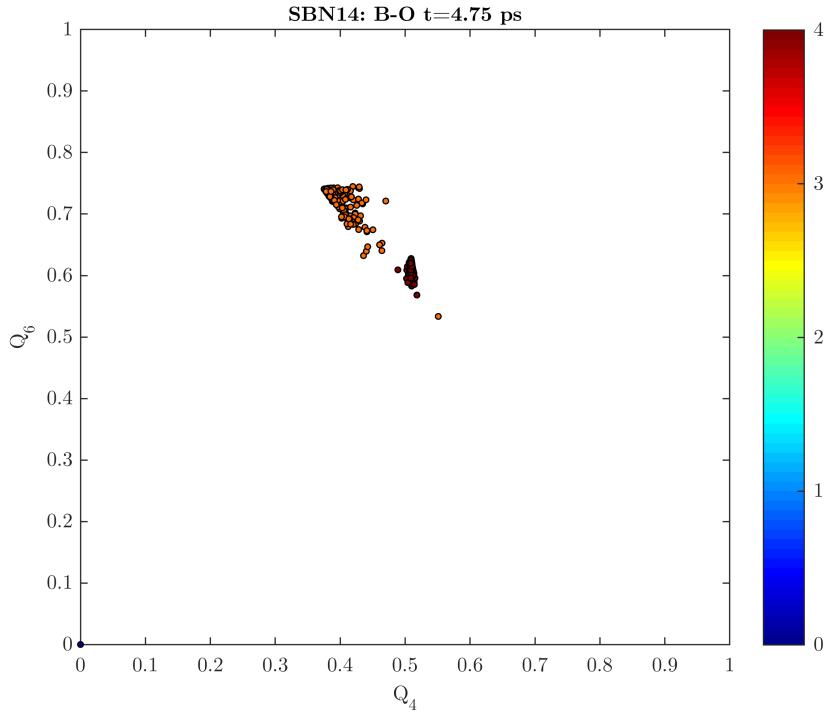

Figure 6.16: $Q_6(Q_4)$ plot of the boron atoms in the final damaged structure of the SBN14 glass, highlighting the coordination number, as indicated in the colourbar next to the plots.

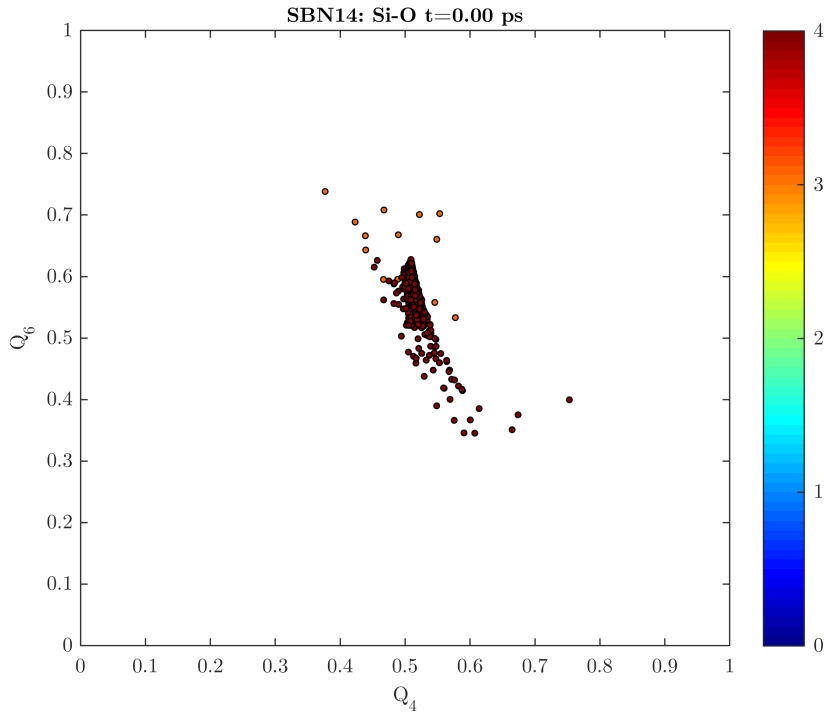

Figure 6.17: $Q_6(Q_4)$ plot of the silicon atoms in the initial undamaged structure of the SBN14 glass, highlighting the coordination number, as indicated in the colourbar next to the plots.

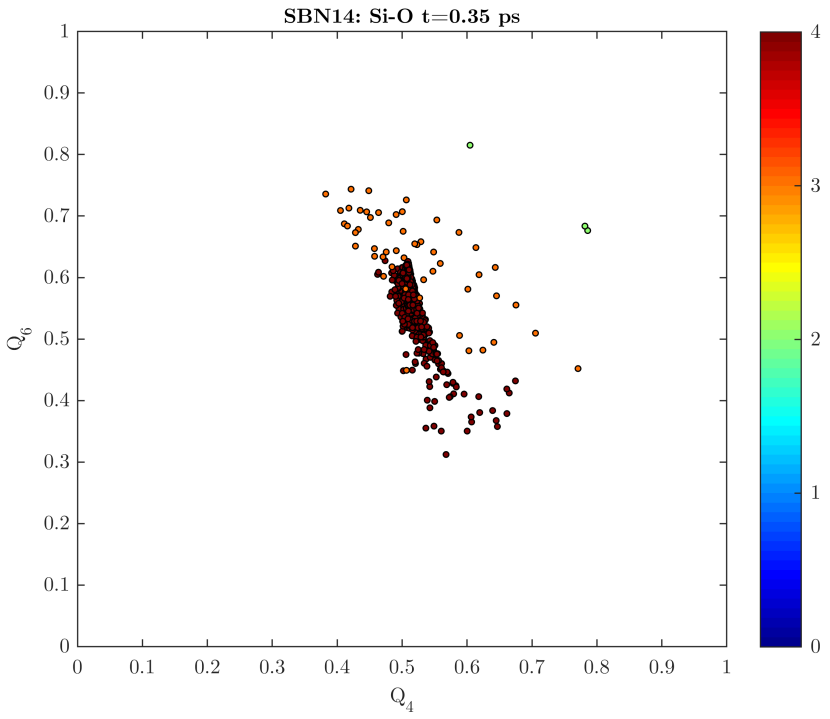

Figure 6.18: $Q_6(Q_4)$ plot of the silicon atoms at t = 0.35 ps for the SBN14 glass, highlighting the coordination number, as indicated in the colourbar next to the plots.

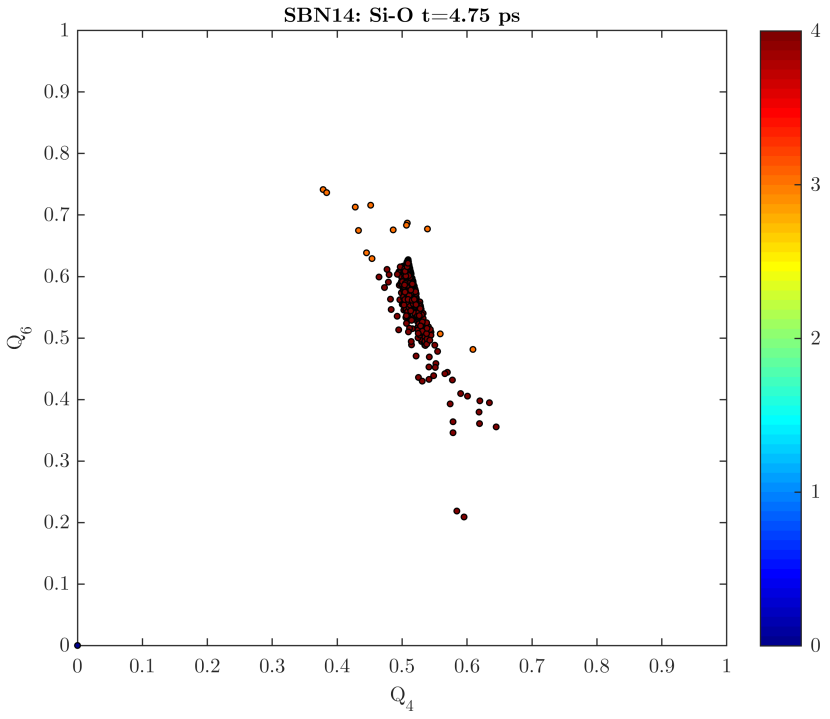

Figure 6.19: $Q_6(Q_4)$ plot of the silicon atoms in the final damaged structure of the SBN14 glass, highlighting the coordination number, as indicated in the colourbar next to the plots.

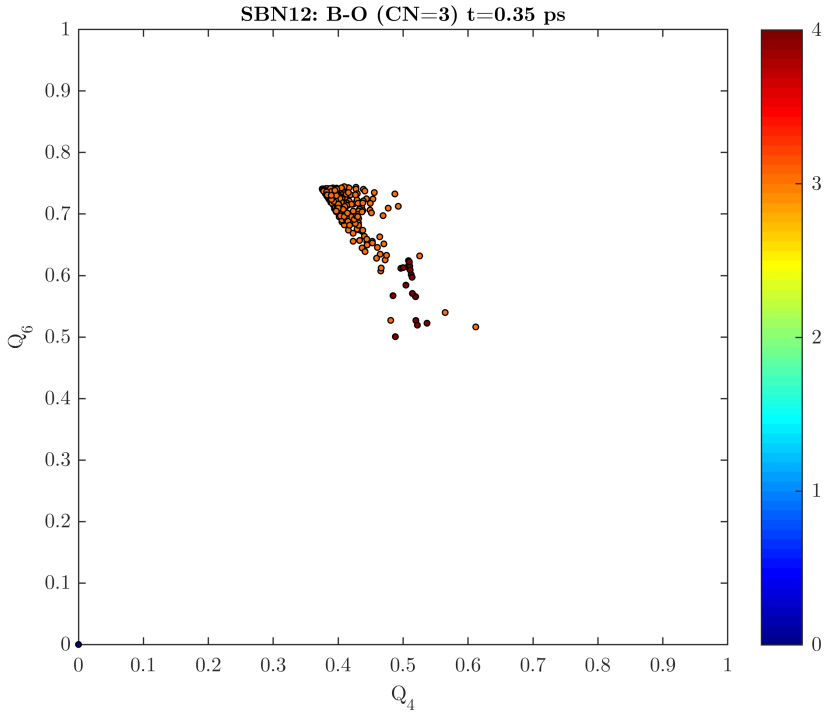

Figure 6.20: $Q_6(Q_4)$ plot of the initially 3-coordinated boron atoms at t = 0.35 ps for the SBN12 glass, highlighting the coordination number, as indicated in the colourbar next to the plots.

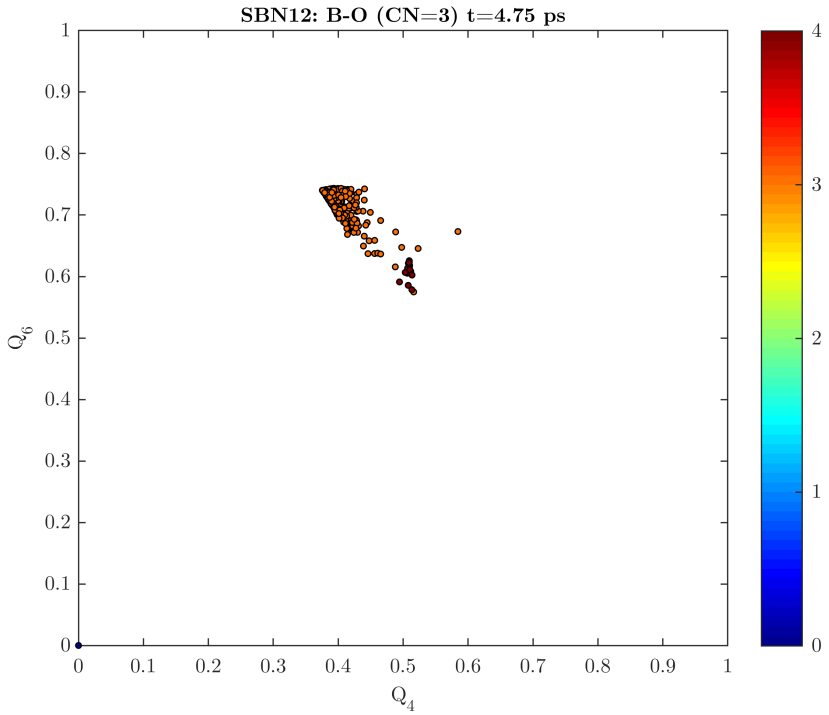

Figure 6.21: $Q_6(Q_4)$ plot of the initially 3-coordinated boron atoms in the final structure of the SBN12 glass, highlighting the coordination number, as indicated in the colourbar next to the plots.

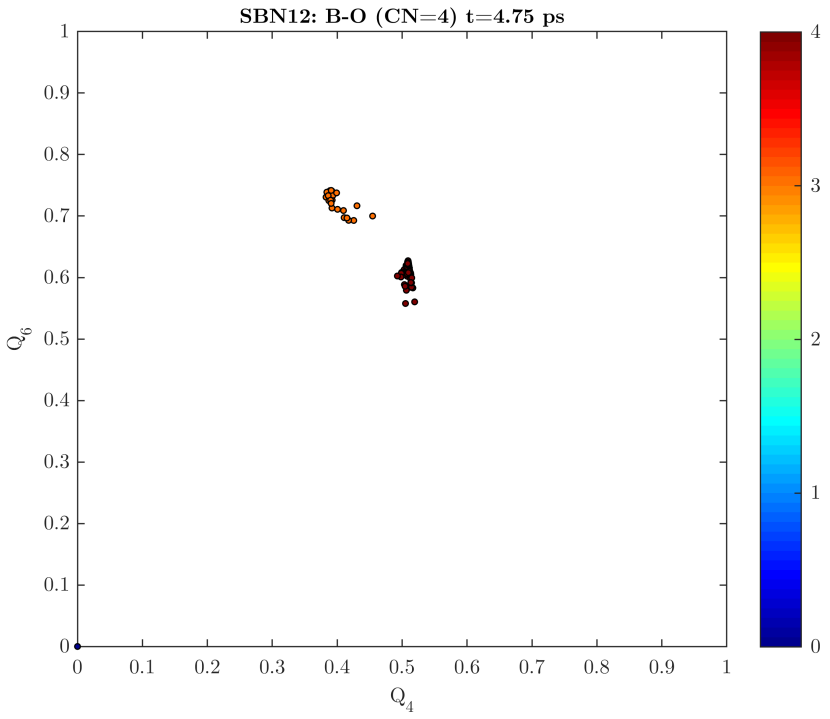

Figure 6.22: $Q_6(Q_4)$ plot of the initially 4-coordinated boron atoms at t = 0.35 ps for the SBN12 glass, highlighting the coordination number, as indicated in the colourbar next to the plots.

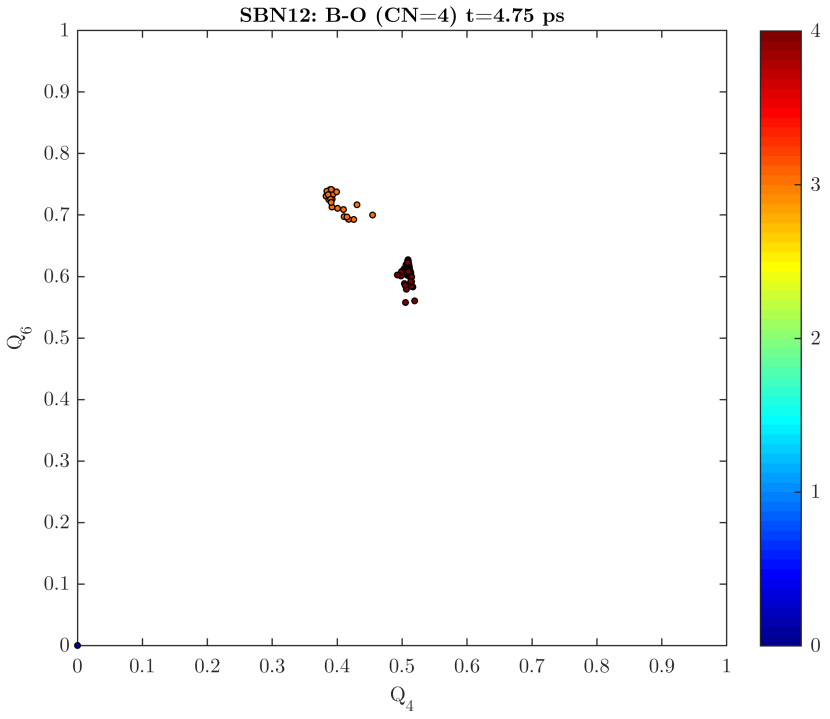

Figure 6.23: $Q_6(Q_4)$ plot of the initially 4-coordinated boron atoms in the final structure of the SBN12 glass, highlighting the coordination number, as indicated in the colourbar next to the plots.

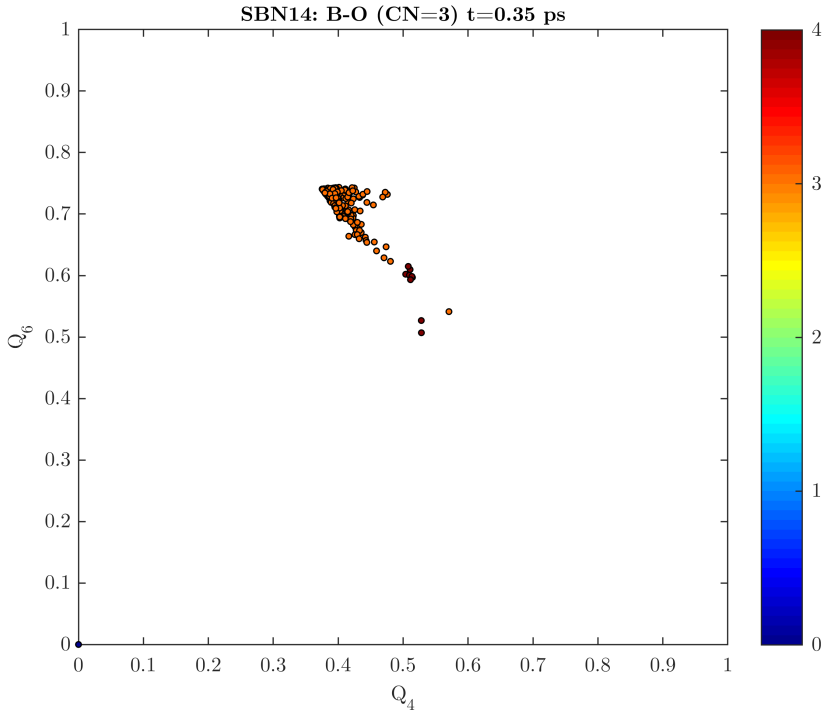

Figure 6.24: $Q_6(Q_4)$ plot of the initially 3-coordinated boron atoms at t = 0.35 ps for the SBN14 glass, highlighting the coordination number, as indicated in the colourbar next to the plots.

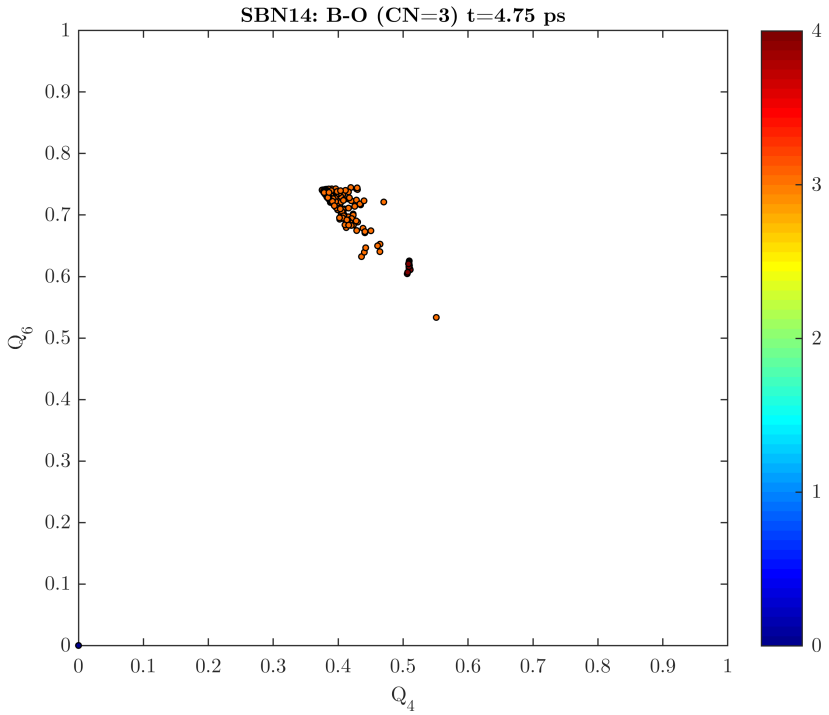

Figure 6.25: $Q_6(Q_4)$ plot of the initially 3-coordinated boron atoms in the final structure of the SBN14 glass, highlighting the coordination number, as indicated in the colourbar next to the plots.

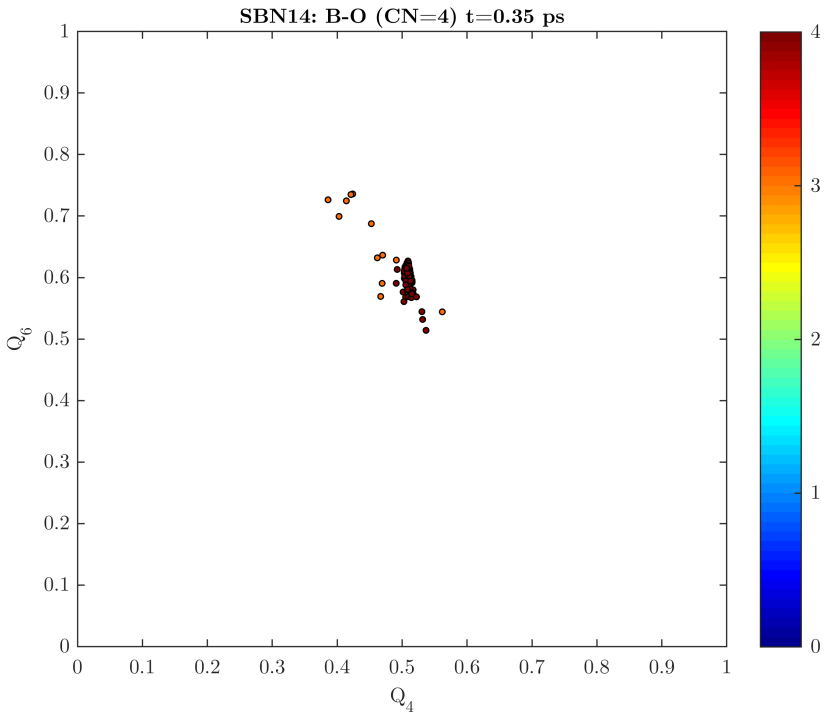

Figure 6.26: $Q_6(Q_4)$ plot of the initially 4-coordinated boron atoms at t = 0.35 ps for the SBN14 glass, highlighting the coordination number, as indicated in the colourbar next to the plots.

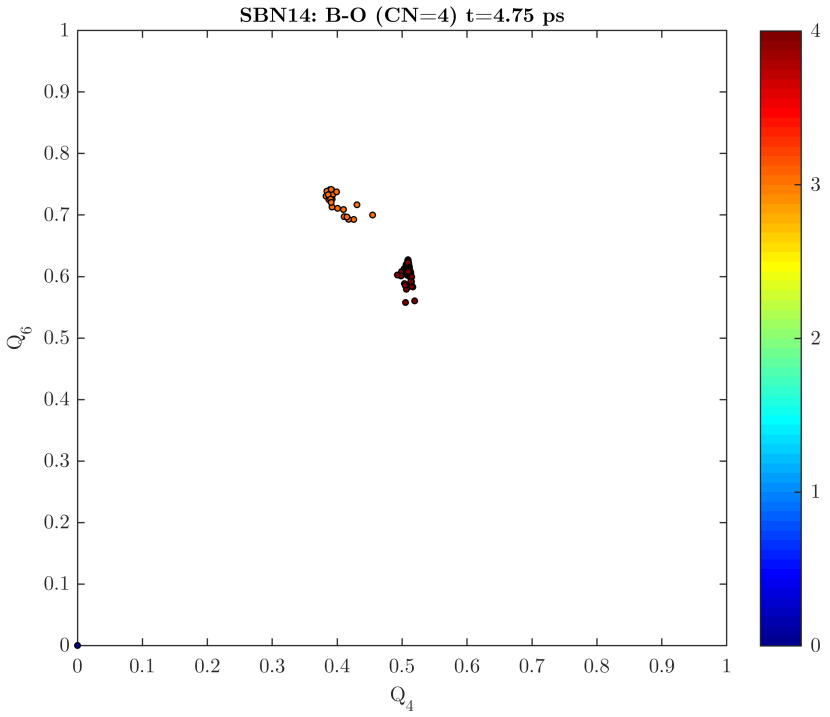

Figure 6.27: $Q_6(Q_4)$ plot of the initially 4-coordinated boron atoms in the final structure of the SBN14 glass, highlighting the coordination number, as indicated in the colourbar next to the plots.

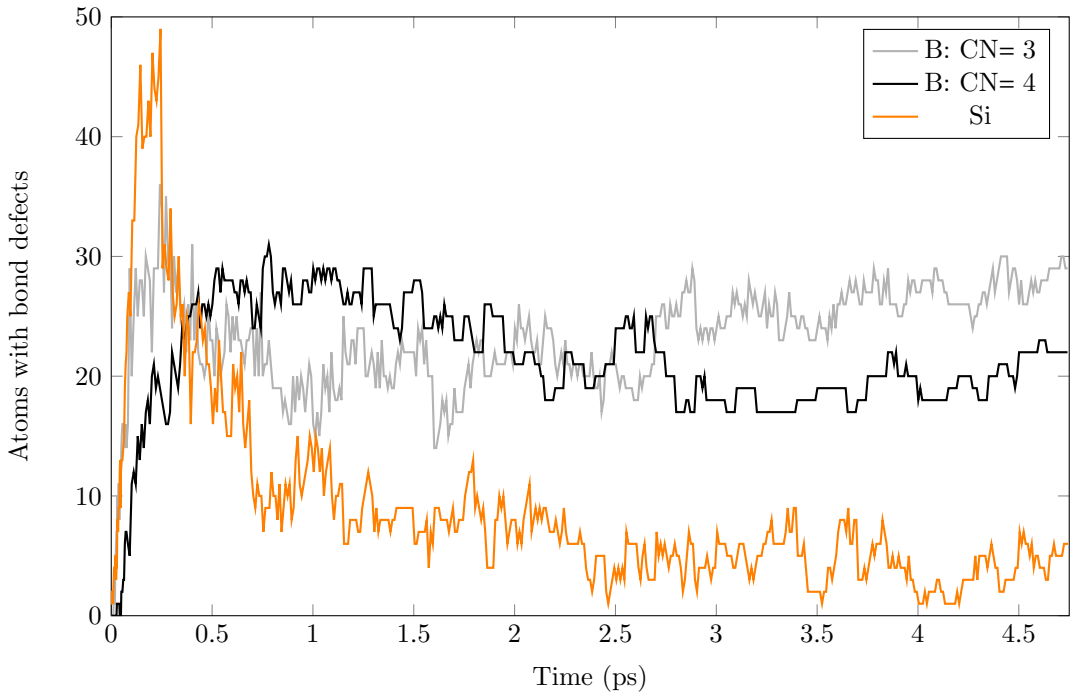

Figure 6.28: Number of atoms associated with bond defects for the radiation damaged SBN12 glass, calculated using the partial Steinhardt order parameters method.

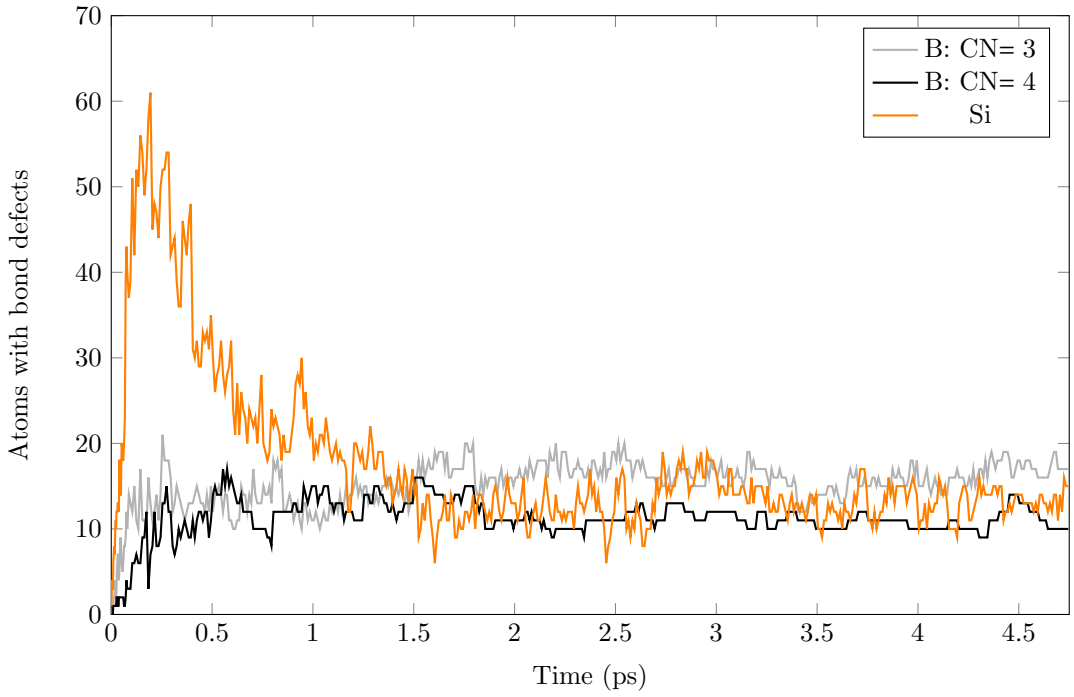

Figure 6.29: Number of atoms associated with bond defects for the radiation damaged SBN14 glass, calculated using the partial Steinhardt order parameters method.

B-O bonds.

6.4.3 Partial Hermite order parameters

As is expected, Hermite order parameters reveal similar information to partial Steinhardt order parameters regarding bond defects. In Figs. 6.30-6.35 and 6.36-6.41, Hermite order parameters of the boron and silicon atoms of the SBN12 and SBN14 glasses respectively are shown for t = 0.00 ps, t = 0.35 ps and t = 4.75 ps. From these plots it is obvious that radiation damage alters the distribution of $R_4 - R_6$ data points for both boron and silicon atoms. However, as in the case of Steinhardt order parameters cannot be used to directly identify boron atoms that transform from 3-coordinated to 4-coordinated during the creation of the radiation damage cascade and vice versa. In Figs. 6.42-6.44 the parameters of the 3- and 4-coordinated boron atoms of the SBN12 glass for t = 0.35 ps and t = 4.75 ps are shown while the respective plots for the SBN14 glass are illustrated in Figs. 6.46-6.48. These plots provide information regarding the transformation between the 3- and 4- coordinated boron atoms.

As discussed in the previous chapter, Hermite order parameters are able to provide information regarding the radial distribution of atoms around the reference particle. In the initial structure of both glasses (figs. 6.30 and 6.36) it is clear that the average oxygen neighbour distance for the 3-coordinated boron atoms is almost constant - the $R_6(R_4)$ data points form a very compact area. On the other hand, the dispersion of the $R_6(R_4)$ data points of the 4-coordinated boron atoms is due to the variations of the average B-O bond length of the BO_4 units. During the simulation, 3-coordinated boron atoms are transformed into 4-coordinated, for which the average neighbour distance varies, while the radial geometry of the BO_3 units resulted from the transformation of 4-coordinated boron atoms to 3-coordinated is more consistent. At the end of the simulation however, the radial geometry of the resulting BO_4 units converges. Finally, for the silicon atoms it can be argued that the average neighbour distance in the initial undamaged SiO_4 units shows some variations reflected in the non-compact distribution of the $R_6(R_4)$ data points. At the time of maximum damage, the variations are larger and it can be safely assumed that the average neighbour distance is affected significantly during the creation of the damage cascade. At the end of the simulation, the region formed by the $R_6(R_4)$ data points for the silicon atoms is very close to the one of the undamaged structure. There is a slightly increased dispersion of the data points which can be explained by assuming that the radial geometry of the recovered SiO_4 units is slightly different from the one of the undamaged structures.

As in the case of Steinhardt order parameters the number of atoms associated with at least one bond defect can be calculated, by identifying at each timestep the number of atoms found outside the area defined by the undamaged atoms in the $R_6(R_4)$ plots. In Figs. 6.50 and 6.51, the number of atoms associated with at least one bond defect for the SBN12 and SBN14 glasses respectively is displayed. The results are in very good agreement with those extracted using the Steinhardt order parameters method and consequently we can argue that the results of the two methods are validating each other.

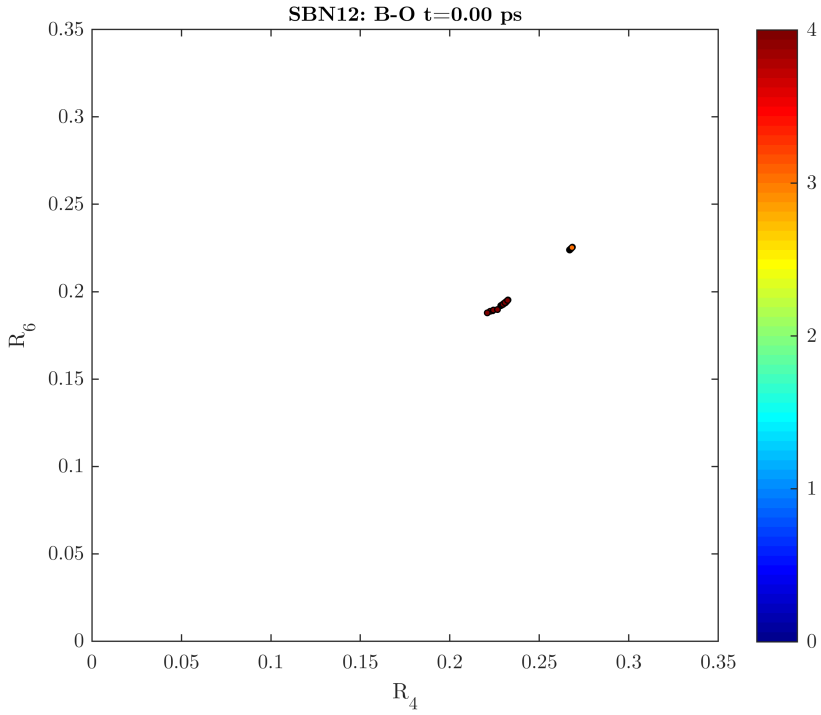

Figure 6.30: $R_6(R_4)$ plot of the boron atoms in the initial undamaged structure of the SBN12 glass, highlighting the coordination number, as indicated in the colourbar next to the plots.

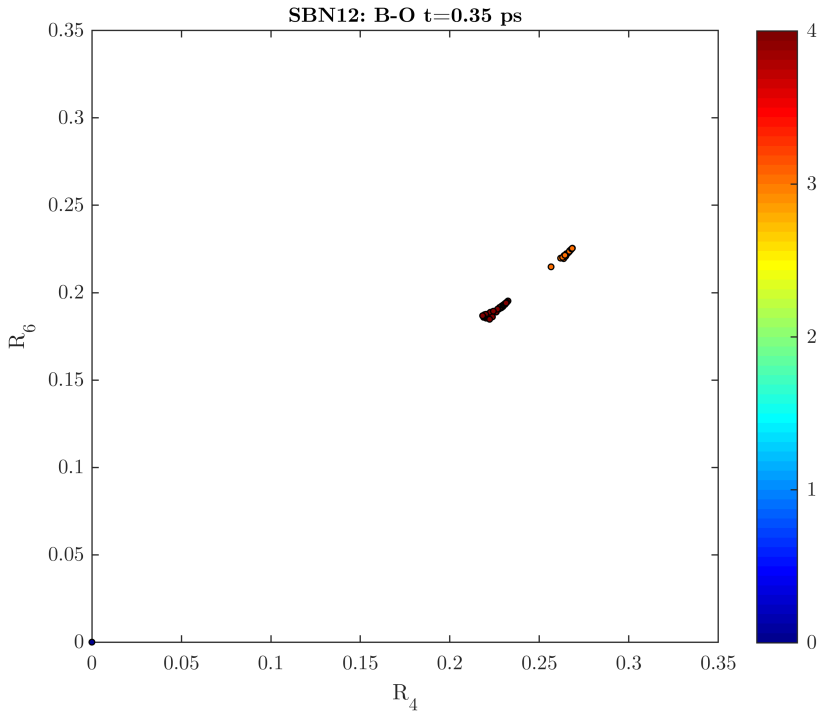

Figure 6.31: $R_6(R_4)$ plot of the boron atoms at t = 0.35 ps for the SBN12 glass, highlighting the coordination number, as indicated in the colourbar next to the plots.

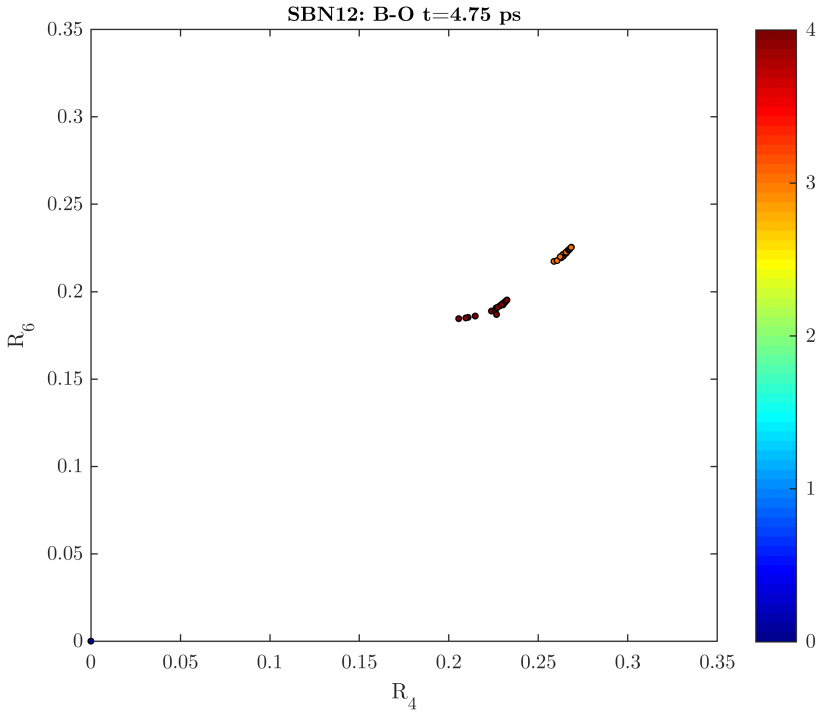

Figure 6.32: $R_6(R_4)$ plot of the boron atoms in the final damaged structure of the SBN12 glass, highlighting the coordination number, as indicated in the colourbar next to the plots.

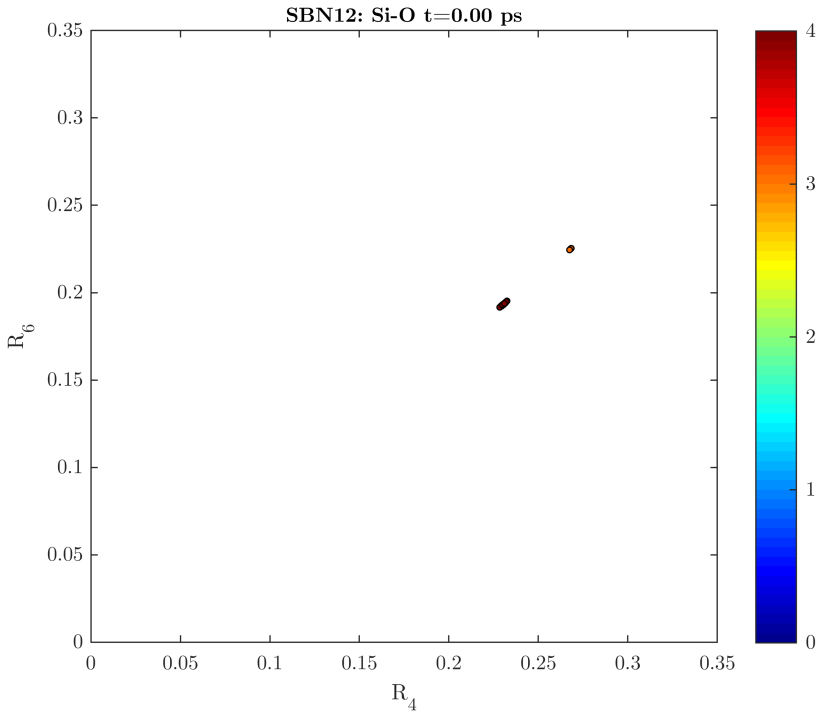

Figure 6.33: $R_6(R_4)$ plot of the silicon atoms in the initial undamaged structure of the SBN12 glass, highlighting the coordination number, as indicated in the colourbar next to the plots.

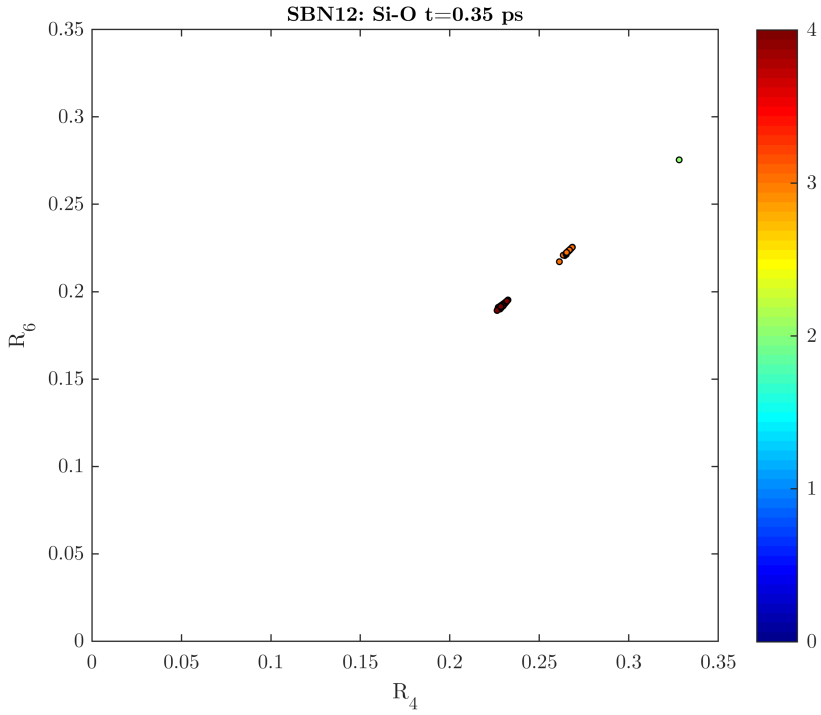

Figure 6.34: $R_6(R_4)$ plot of the silicon atoms at t = 0.35 ps for the SBN12 glass, highlighting the coordination number, as indicated in the colourbar next to the plots.

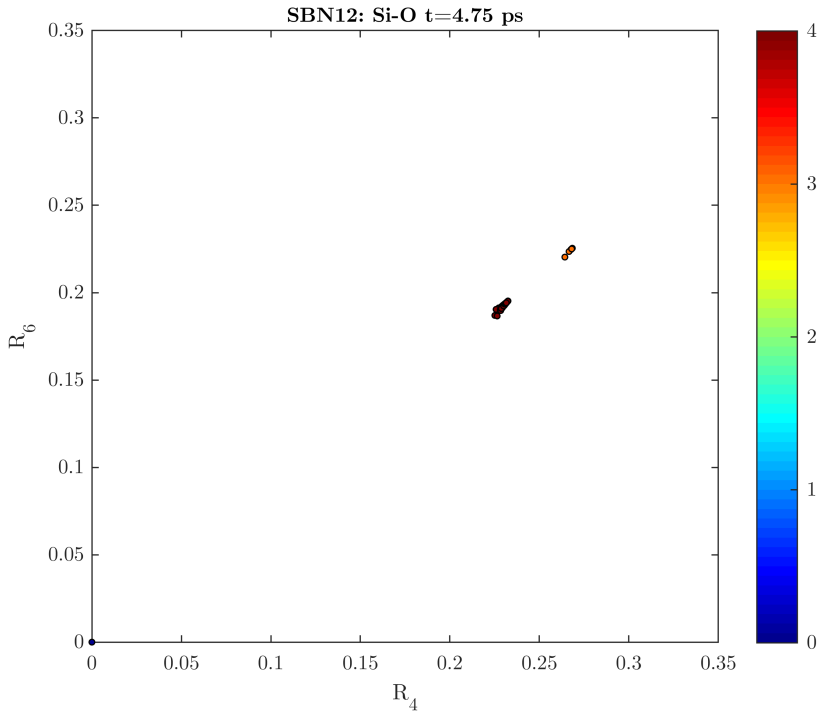

Figure 6.35: $R_6(R_4)$ plot of the silicon atoms in the final damaged structure of the SBN12 glass, highlighting the coordination number, as indicated in the colourbar next to the plots.

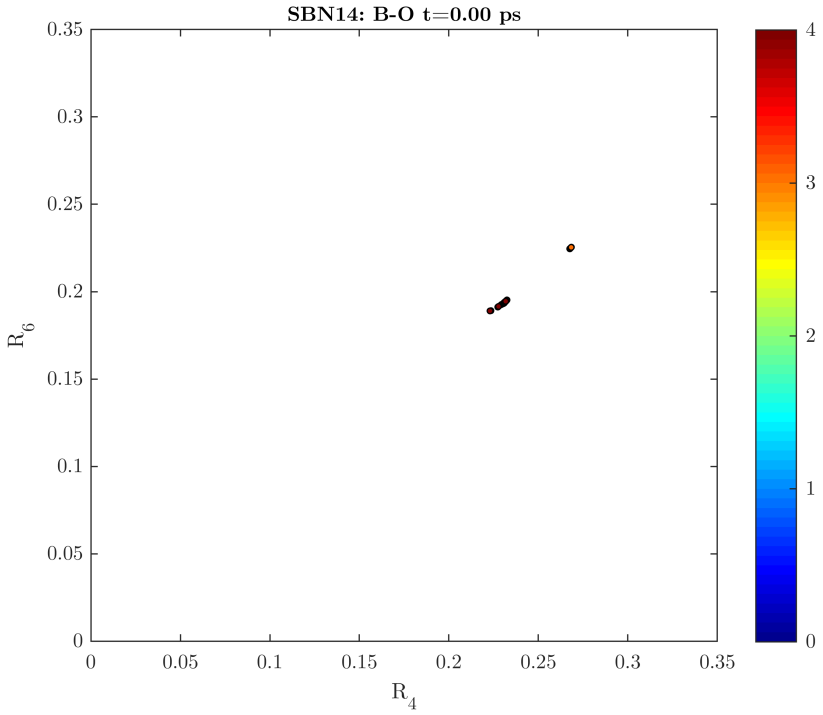

Figure 6.36: $R_6(R_4)$ plot of the boron atoms in the initial undamaged structure of the SBN14 glass, highlighting the coordination number, as indicated in the colourbar next to the plots.

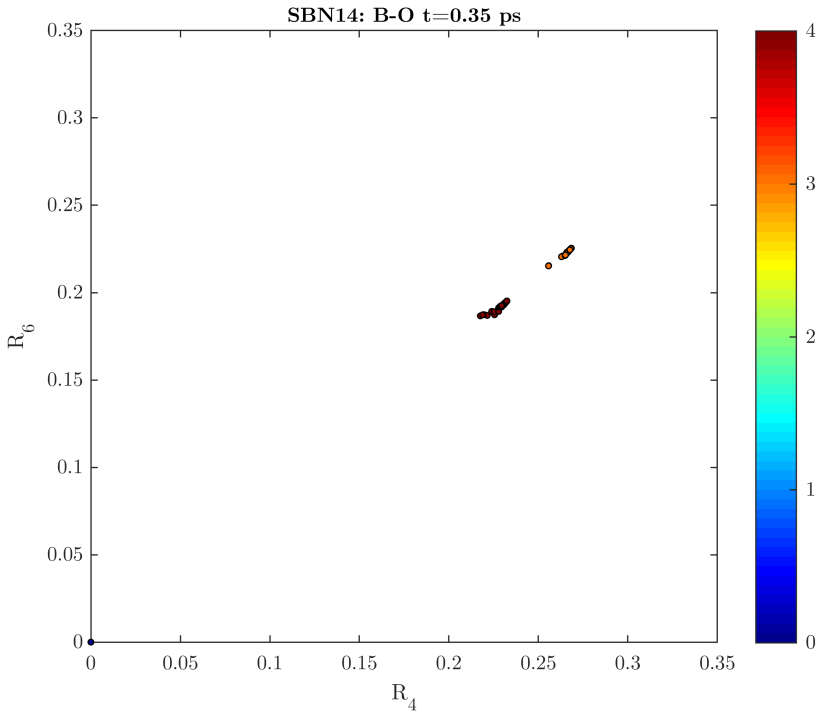

Figure 6.37: $R_6(R_4)$ plot of the boron atoms at t = 0.35 ps for the SBN14 glass, highlighting the coordination number, as indicated in the colourbar next to the plots.

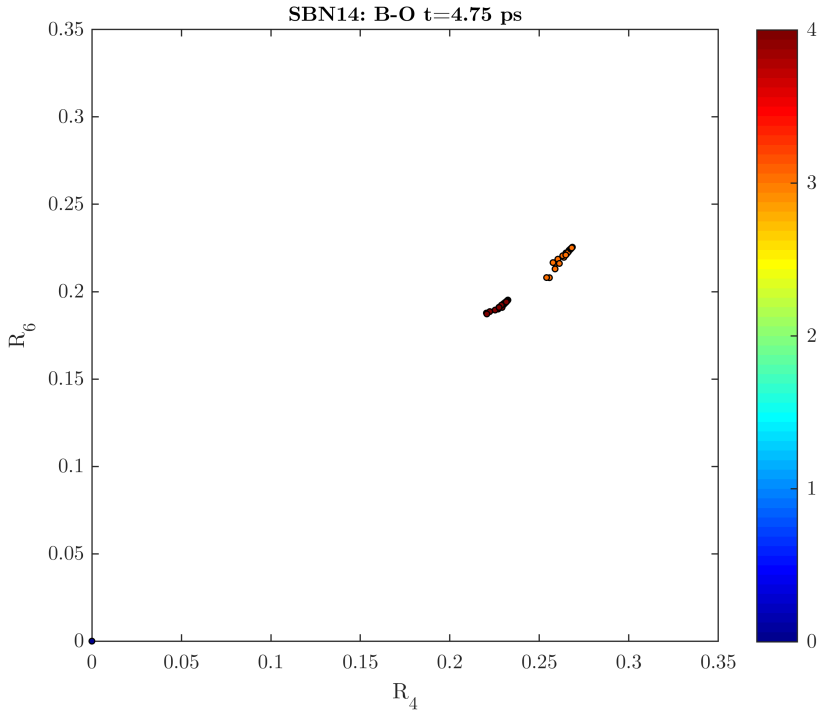

Figure 6.38: $R_6(R_4)$ plot of the boron atoms in the final damaged structure of the SBN14 glass, highlighting the coordination number, as indicated in the colourbar next to the plots.

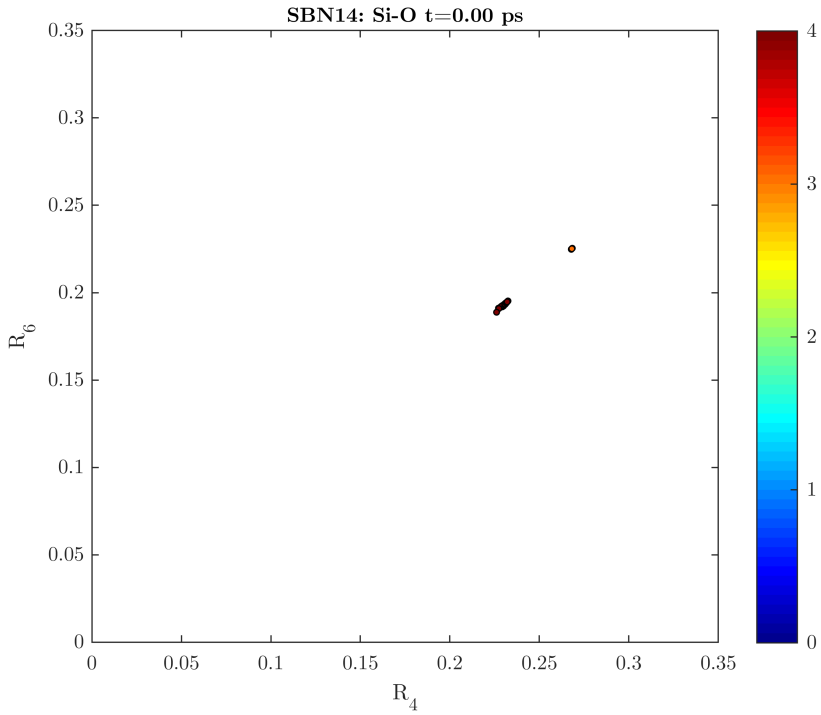

Figure 6.39: $R_6(R_4)$ plot of the silicon atoms in the initial undamaged structure of the SBN14 glass, highlighting the coordination number, as indicated in the colourbar next to the plots.

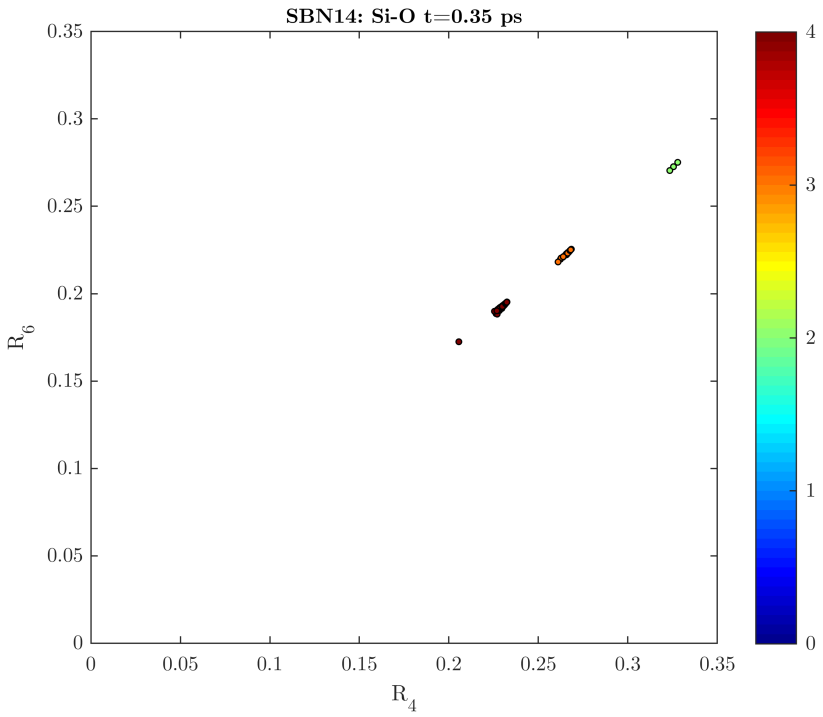

Figure 6.40: $R_6(R_4)$ plot of the silicon atoms at t = 0.35 ps for the SBN14 glass, highlighting the coordination number, as indicated in the colourbar next to the plots.

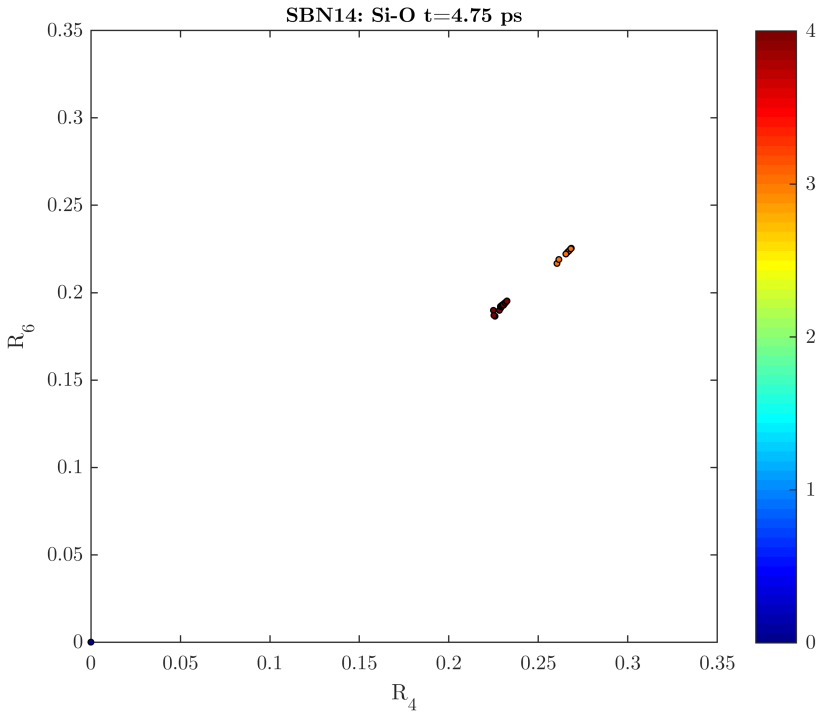

Figure 6.41: $R_6(R_4)$ plot of the silicon atoms in the final damaged structure of the SBN14 glass, highlighting the coordination number, as indicated in the colourbar next to the plots.

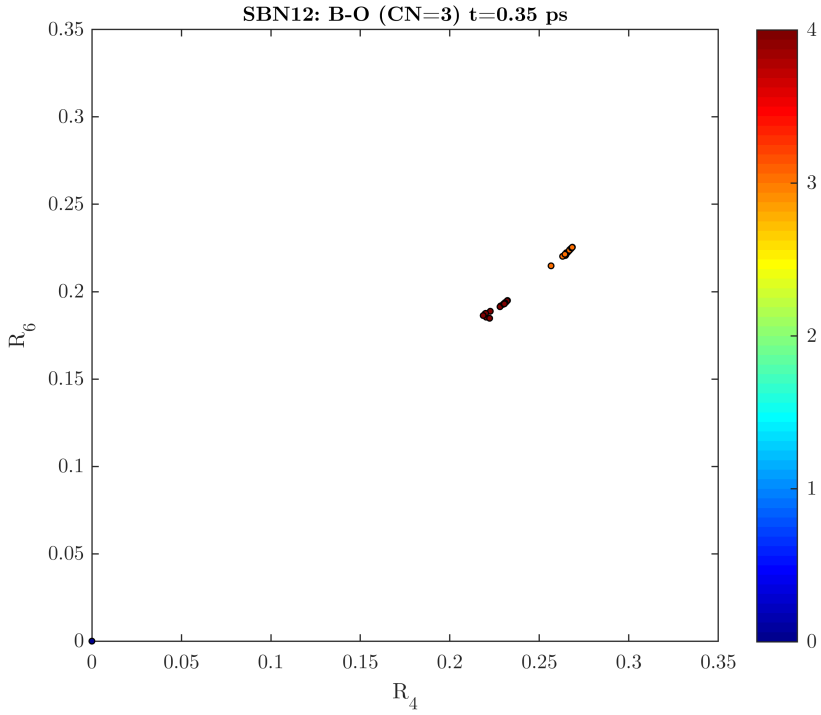

Figure 6.42: $R_6(R_4)$ plot of the initially 3-coordinated boron atoms at t = 0.35 ps for the SBN12 glass, highlighting the coordination number, as indicated in the colourbar next to the plots.

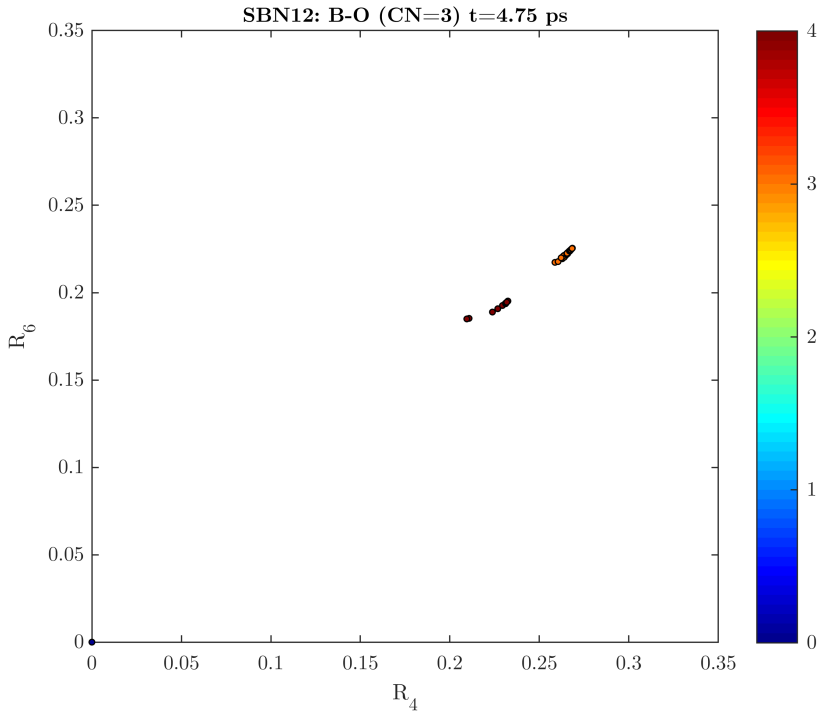

Figure 6.43: $R_6(R_4)$ plot of the initially 3-coordinated boron atoms in the final structure of the SBN12 glass, highlighting the coordination number, as indicated in the colourbar next to the plots.

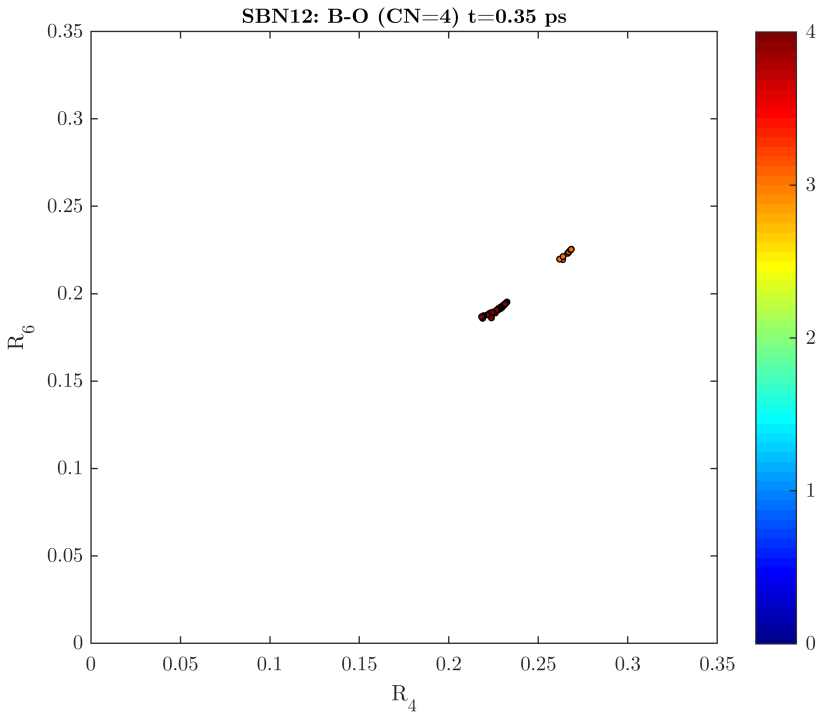

Figure 6.44: $R_6(R_4)$ plot of the initially 4-coordinated boron atoms at t = 0.35 ps for the SBN12 glass, highlighting the coordination number, as indicated in the colourbar next to the plots.

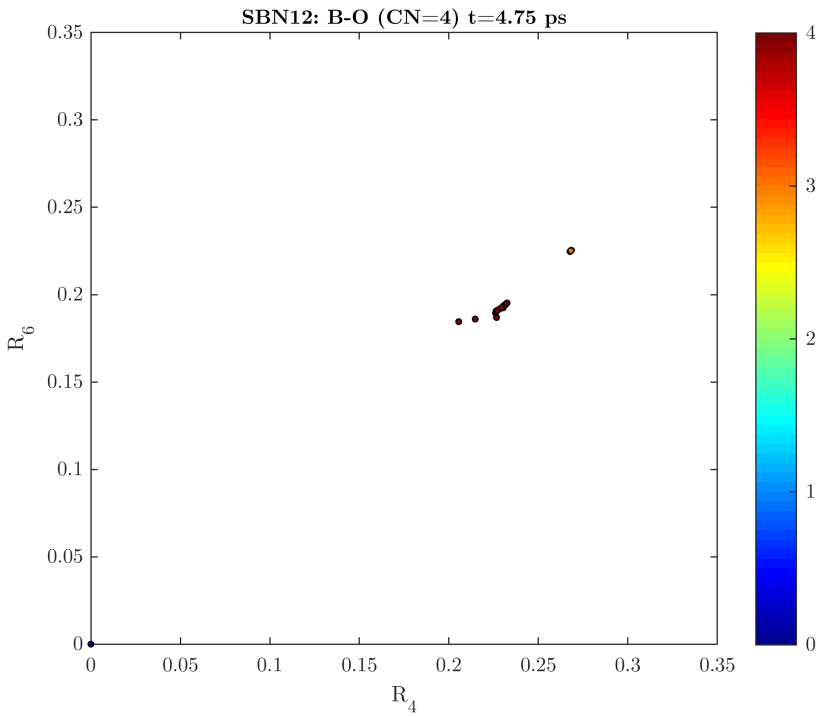

Figure 6.45: $R_6(R_4)$ plot of the initially 4-coordinated boron atoms in the final structure of the SBN12 glass, highlighting the coordination number, as indicated in the colourbar next to the plots.

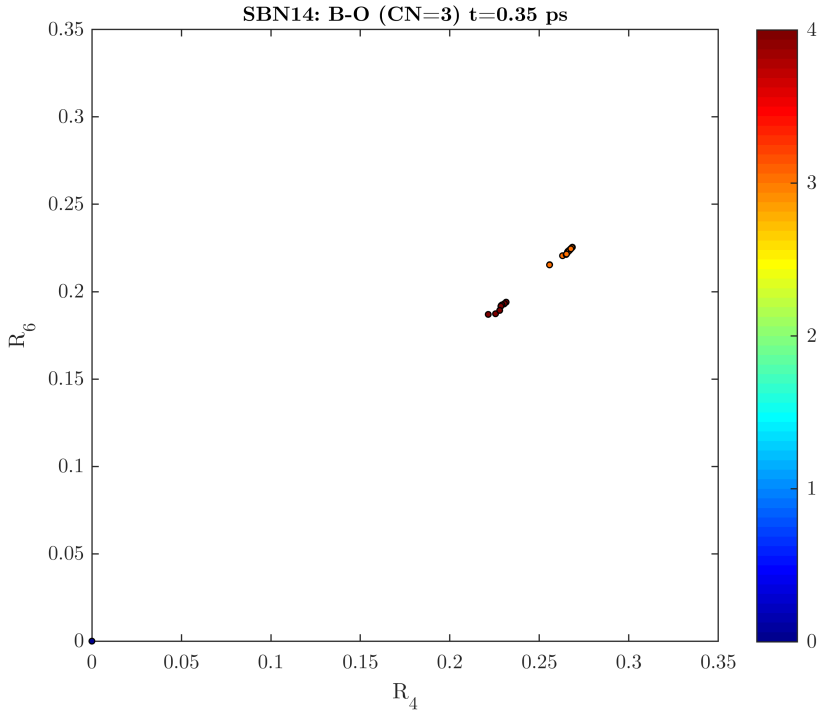

Figure 6.46: $R_6(R_4)$ plot of the initially 3-coordinated boron atoms at t = 0.35 ps for the SBN14 glass, highlighting the coordination number, as indicated in the colourbar next to the plots.

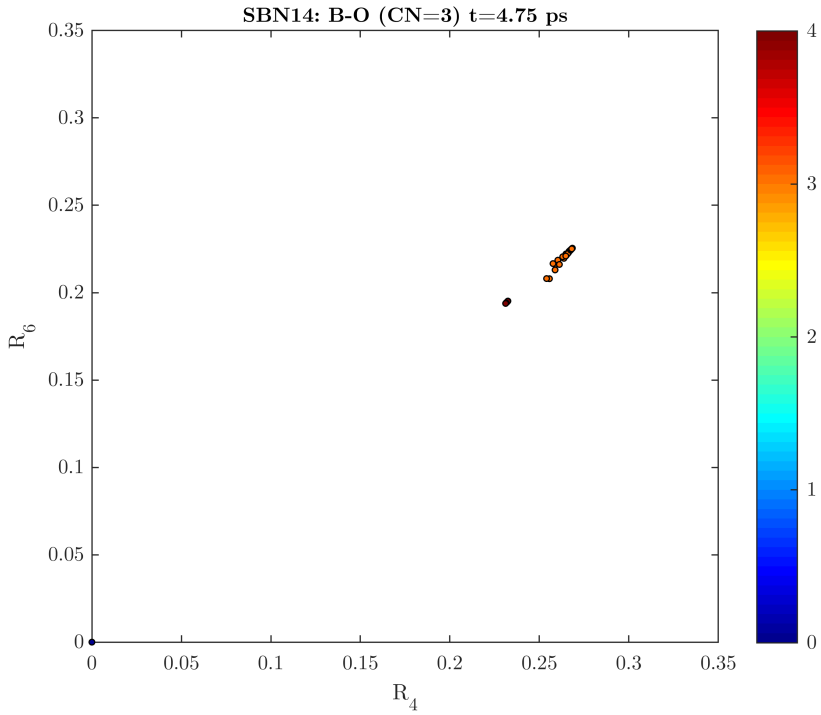

Figure 6.47: $R_6(R_4)$ plot of the initially 3-coordinated boron atoms in the final structure of the SBN14 glass, highlighting the coordination number, as indicated in the colourbar next to the plots.

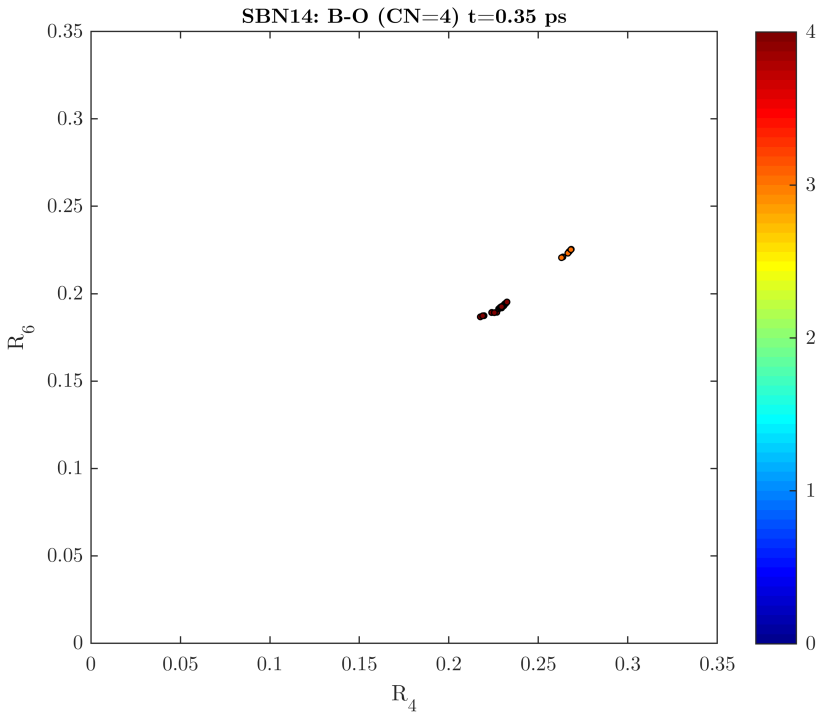

Figure 6.48: $R_6(R_4)$ plot of the initially 4-coordinated boron atoms at t = 0.35 ps for the SBN14 glass, highlighting the coordination number, as indicated in the colourbar next to the plots.

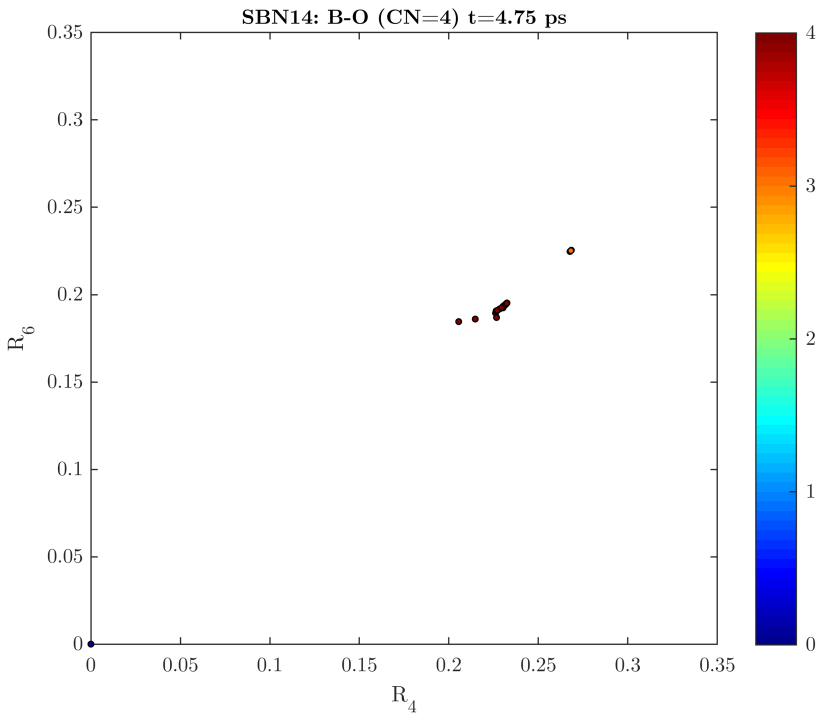

Figure 6.49: $R_6(R_4)$ plot of the initially 4-coordinated boron atoms in the final structure of the SBN14 glass, highlighting the coordination number, as indicated in the colourbar next to the plots.

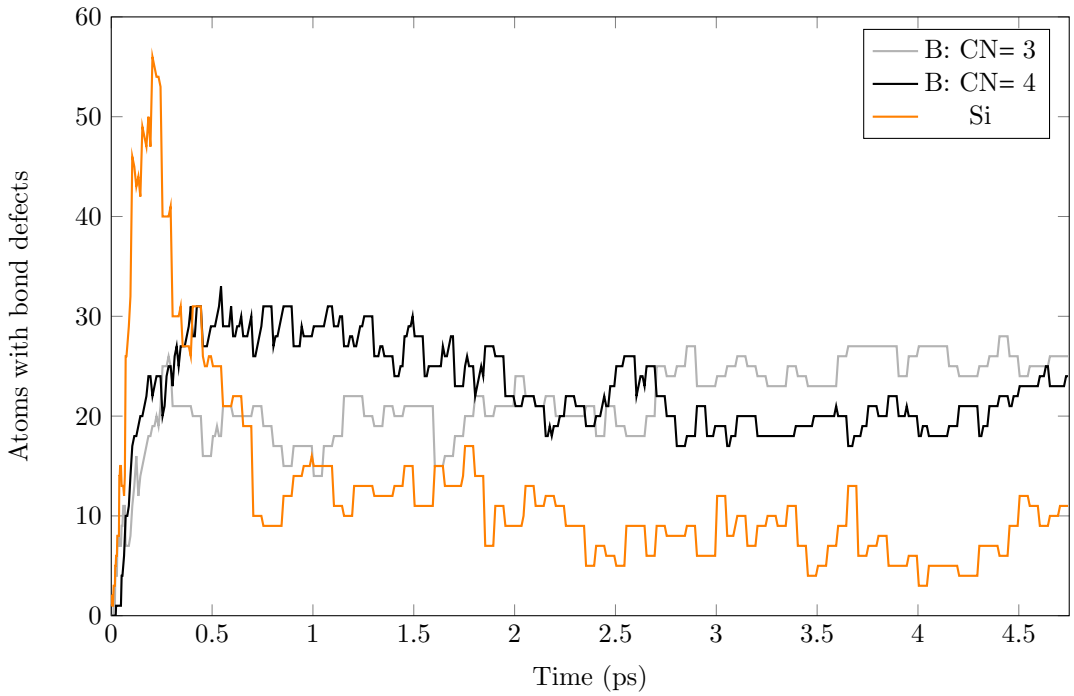

Figure 6.50: Number of atoms associated with bond defects for the radiation damaged SBN12 glass, calculated using the partial Hermite order parameters method.

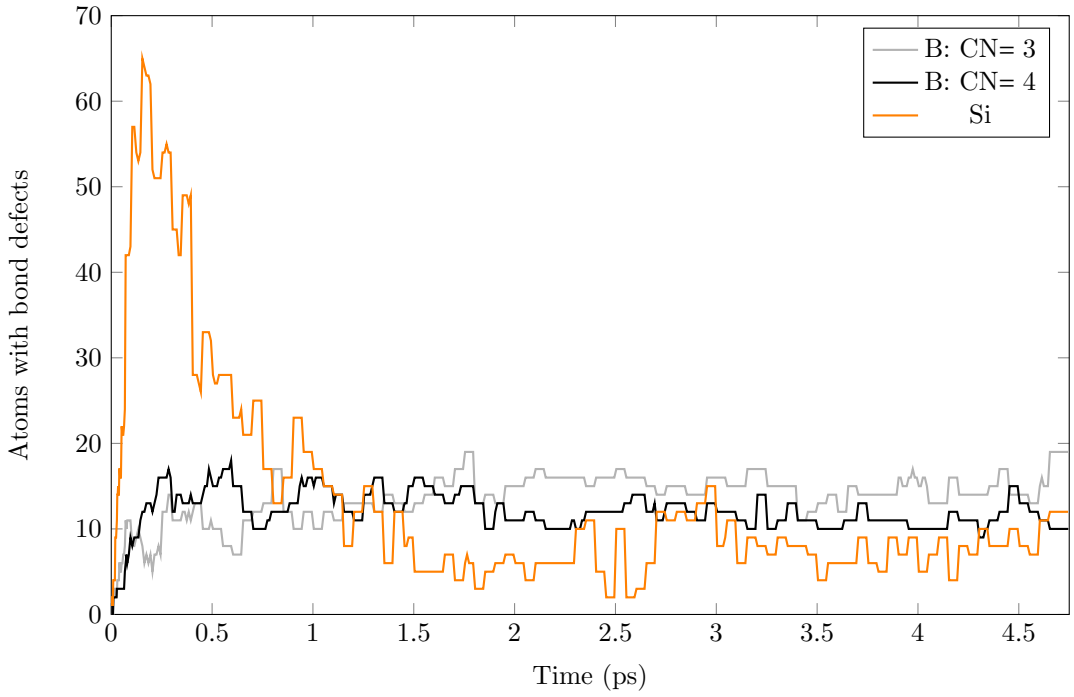

Figure 6.51: Number of atoms associated with bond defects for the radiation damaged SBN14 glass, calculated using the partial Hermite order parameters method.

6.4.4 Primitive ring statistics

Primitive rings statistics provide important information regarding the connectivity between the atoms of the glasses. All boron and silicon atoms of the systems are connected together through oxygen atoms. Consequently, all the rings of the borosilicate glass structures are even numbered. We performed a search of primitive rings up to 40 nodes. Since the maximum bond length is 1.61 Å for the SBN12 glass and 1.62 Å for the SBN14 glass, equal to the respective Si-O bond lengths, to identify all possible rings up to the required size, the initial structure was expanded by 32.4 Å and 32.2 Å in each direction respectively, distances corresponding to 20 Si-O bond lengths. In each step in which ring statistics was performed, the expanded cell was the same as for the initial undamaged structure and we replaced the original cell with the one corresponding to the current timestep. In the expanded structure, rings were identified for all nodes of the original cells. Since the identification of rings is an expensive task, we performed a ring statistics analysis every 2000 timesteps of the simulation.

In Figs. 6.52 and 6.53 the number of rings per boron atom of the SBN12 glass as a function of ring size are shown and for t = 0.00 ps, t = 0.35 ps and t = 4.75 ps. The respective plots for the SBN14 glass are shown in Figs. 6.54 and 6.55. For the SBN12 glass, it is obvious that for the initial structure the most common rings are of size 16 for both boron and silicon nodes. For each boron and silicon atom we have 1.53 and 1.97 rings of size 16 per node respectively. As the damage progresses, the number of medium sized rings consisting of 12 to 16 nodes decreases significantly. The most obvious change in the distribution of rings per node is observed for the 16-sized rings, the number of which is reduced by 14.4% for the boron nodes and 15.3% for the silicon nodes of the SBN12 glass at t = 0.35 ps. At this stage, there are more 14 and 18 sized rings that 16 sized rings in the structure. We also observe an increase in number of rings of size 20 and 26. For the latter, there is a clear peak in the plots making it easy to distinguish the damaged structures from the undamaged.

The initial structure of the SBN14 glass is dominated by rings of size 14 and 18 and also there is a strong peak at the 28 numbered rings. During the damage, the number of 14, 18 and 28 sized rings is reduced significantly and in parallel we observe an increase in the number of higher order rings consisting of 34 and 38 nodes.

Most importantly, for t = 4.75 ps it is clear that the ring distribution for both structures is very close to the one for the undamaged glasses, implying the recovery of the structure. For the SBN12 glass we observe a small decrease in the number of 14, 16 and 18 membered rings of the boron nodes and of the 16 sized rings of the silicon nodes, accompanied by an increase in the number of 20 and 22 sized rings for both species. For the SBN14 glass and for both species, the final result of the damage is to decrease the number of the dominant 18 membered rings and increase the 28 sized rings.

We can also explore the average ring size of each structure and for each species of nodes versus time (Figs. 6.56 and 6.57). Initially the average ring size for the boron and silicon nodes and for the SBN12 glass is 17.78 and 17.68 respectively, while for the SBN14 glass is 17.08 and 17.22. Thus, initially there are only minor differences in the local cluster level between boron and silicon atoms. Also, despite the fact that the composition of the two glasses is quite different, they have initially similar average ring sizes. During the creation of a damage cascade, the average ring size

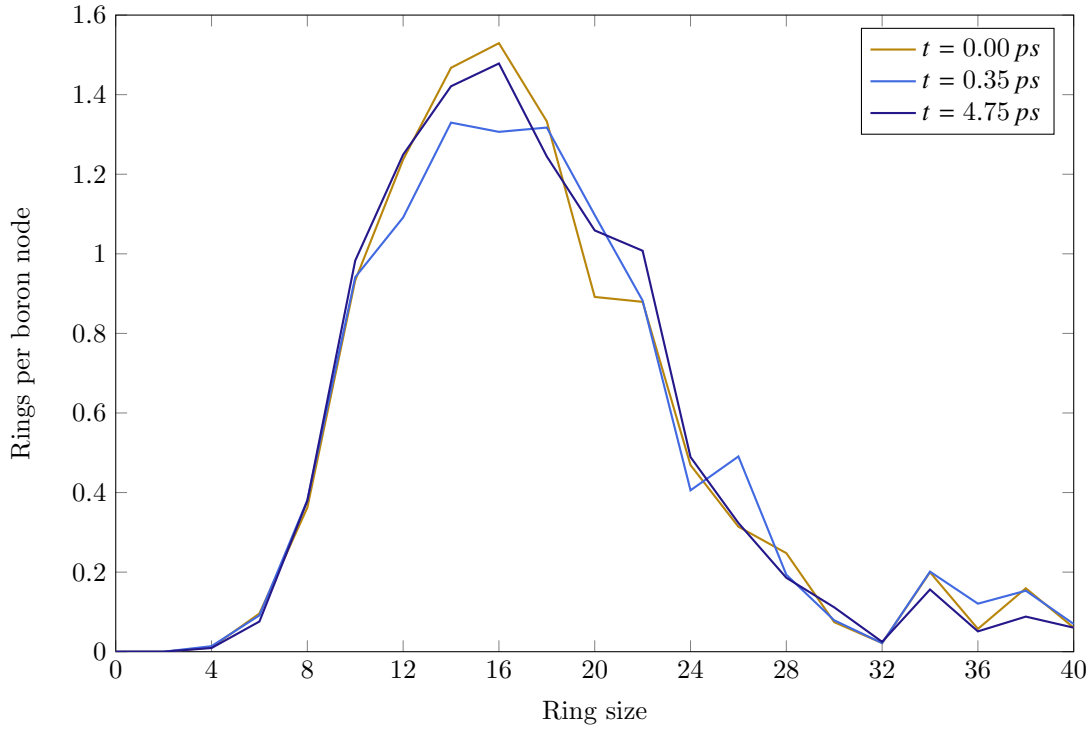

Figure 6.52: Rings per boron node for the radiation damaged SBN12 glass.

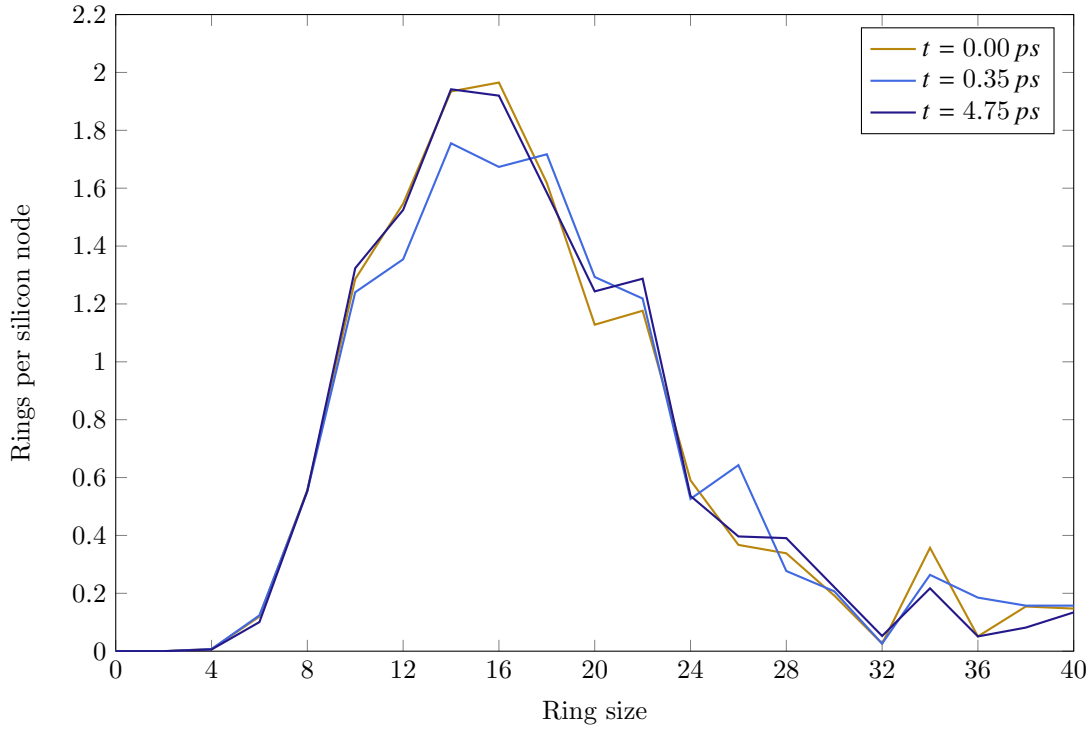

Figure 6.53: Rings per silicon node for the radiation damaged SBN12 glass.

is increasing for both structures which is expected.

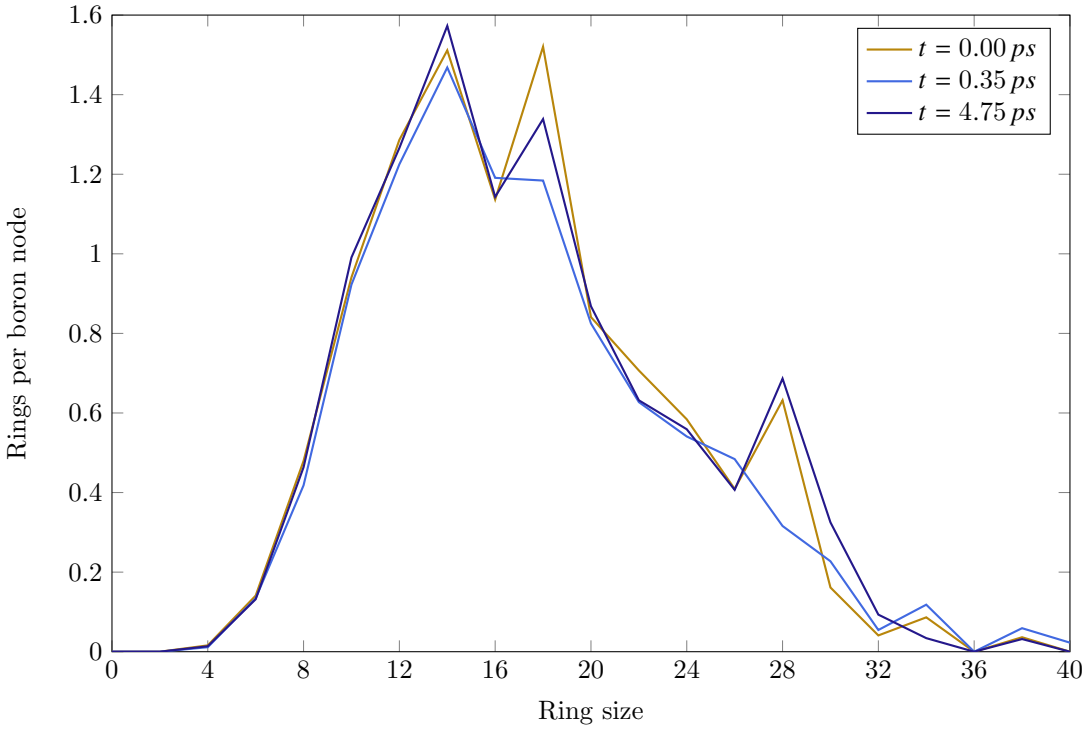

Figure 6.54: Rings per boron node for the radiation damaged SBN14 glass.

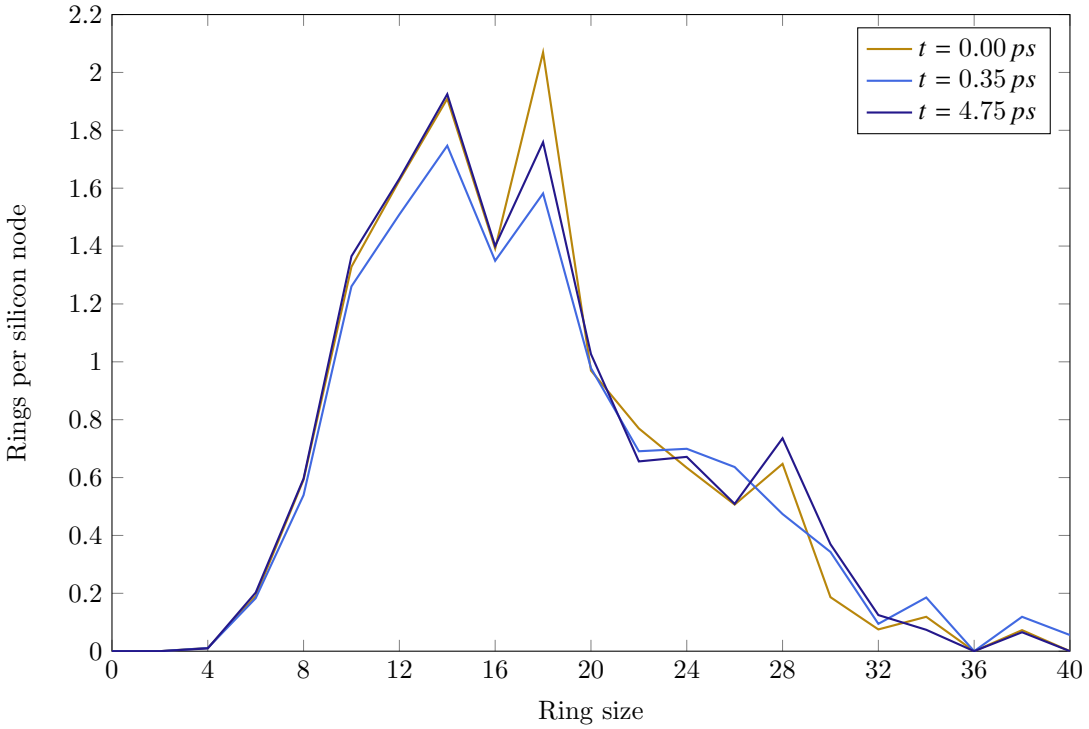

Figure 6.55: Rings per silicon node for the radiation damaged SBN14 glass.

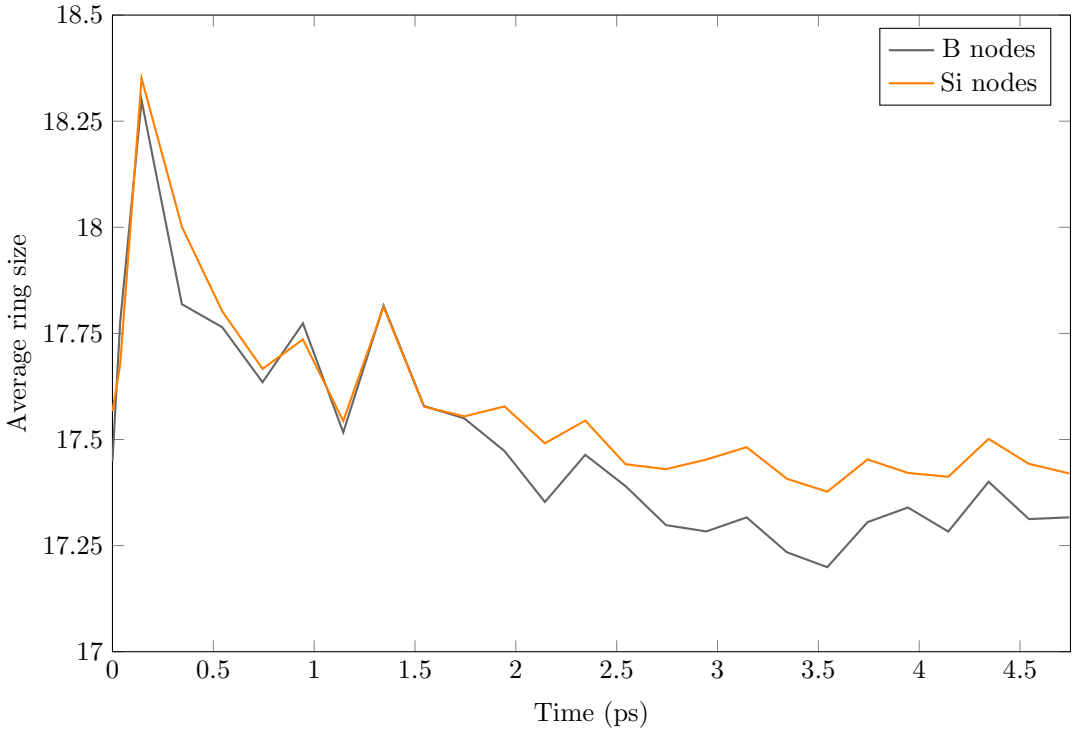

Figure 6.56: Rings per boron node for the radiation damaged SBN12 glass.

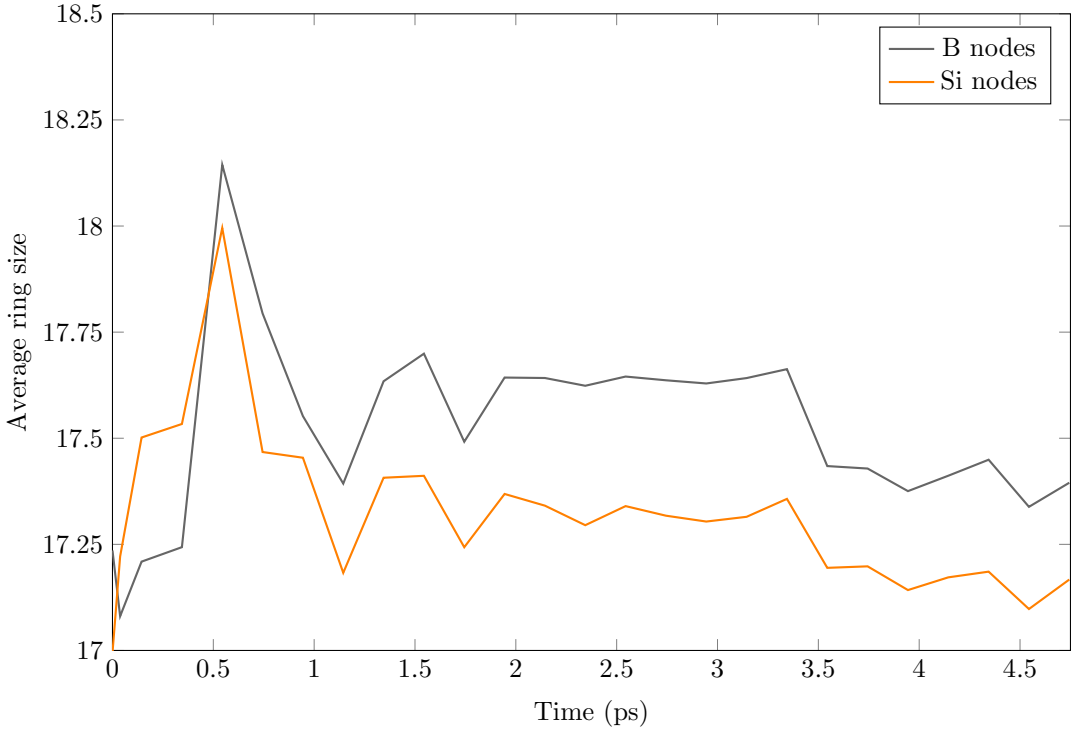

Figure 6.57: Rings per silicon node for the radiation damaged SBN14 glass.

The radiation damage event will result in the breaking of smaller size rings and favours the formation of higher order rings. However the two glasses behave quite differently. For the SBN12 glass, there is a sudden increase in the average ring size, reaching its maximum for $t \simeq 0.15$ ps, before the time where the maximum number of bond defects is observed. On the contrary, SBN14 glass demonstrates the maximum of average ring size at $t \simeq 0.55$ ps, after the maximum of the bond defects. Thus the network of the SBN14 glasses demonstrates a slower response to the bond defects induced by radiation damage. Also, for the first 1.5 ps of the simulation and for the SBN12 glass, the average ring size for the boron nodes varies almost the same way as the average ring size of the silicon nodes, but after that time, the average ring size of the boron atoms decreases to a higher degree. The average ring size for the final structure, at $t = 4.75$ ps is about 2% lower in comparison with the initial one for both boron and silicon nodes. For the SBN14 glass however, during the creation of the damage cascade, boron nodes demonstrate a significantly higher average ring size in comparison with silicon atoms. In the final structure, the average ring size for the boron atoms is increased about 2% in comparison with the initial structure while for the silicon atoms is almost at the same level.

6.5 Conclusions

Radiation damage simulations performed in SBN12 and SBN14 borosilicate glass models, show that both glasses demonstrate high tolerance to radiation damage. Using the simple Wigner-Seitz method, it is found that the percentage of permanently displaced silicon and boron atoms for the SBN12 glass is 7.3% and 7.7% respectively while for the SBN14 glass the respective numbers are 5.5% and 5.0%. In terms of the number of bond defects, all three methods used to estimate the number of atoms associated with broken bond suggest that Si-O bonds are almost completely recovered - which is in contrast with what the Wigner-Seitz method predicts - while B-O bonds are unable to recover. The majority of the damage is related to broken B-O bonds. For the SBN12 glass, it is estimated that about 8.8% of the boron atoms are associated with at least one broken B-O bond while for the SBN14 glass this percentage is about 6.4%. Using these numbers it can be argued that the Wigner-Seitz method overestimates significantly the damage of the silicon atoms and on the other hand slightly underestimates the damage effects on the boron atoms. By comparing the number of atoms associated with at least one bond defect it is safe to assume that SBN14 glass demonstrate a slightly increased tolerance to the irradiation effects.

Using Steinhardt order parameters, it is possible to extract additional information regarding the angular distribution of oxygen atoms around reference boron and silicon atoms at every stage of the simulation. For both glasses, it is clear that the geometry of the SiO_4 tetrahedral units in the undamaged structures is not fixed. The relative positions of the oxygen neighbours around the reference silicon atoms show variations. Consequently it can be assumed that the O-Si-O angles in the SiO_4 tetrahedra, as well as the distance between the oxygen atoms forming the tetrahedra can take a wide range of values. BO_4 tetrahedra on the other hand appear to have a very consistent geometry. During the creation of the damage cascade, several silicon atoms are related to at least one broken Si-O bond and the resulting 3-coordinated silicon atoms demonstrate large variations in the angular distribution of the bonded oxygen atoms. As for the boron atoms, there is a transformation of 4-coordinated atoms to 3-coordinated and vice versa. While the 3-

coordinated atoms transforming to 4-coordinated appear to create BO_4 tetrahedral units with geometry very close to the one of the undamaged structure, the 4-coordinated atoms transform to 3-coordinated with arbitrary angular geometry, different from the one of the initially 3-coordinated atoms. However, the geometry of the resulting 3-coordinated boron atoms progressively converges to the one of the undamaged BO_3 units. By the end of the simulation, it is observed that the BO_3 units resulting from the transformation of a 4-coordinated boron atom to a 3-coordinated demonstrate a geometry identical to the initial BO_3 units.

Hermite order parameters provide information regarding the radial distribution of the oxygen atoms around the reference boron and silicon atoms. For the silicon atoms, in the undamaged structure there are some variations in the radial distribution of the oxygen neighbours. During the creation of the damage cascade, the radial geometry of the oxygen neighbours initially diverges, until the maximum damage is observed and then gradually converges to the initial one. At the end of the simulation, the radial geometry of the SiO_4 tetrahedra is slightly expanded in comparison with the initial one, suggesting that the bond lengths in the recovered SiO_4 tetrahedra are slightly different from the initial. For the boron atoms, in contrast with the angular distribution of the neighbouring oxygen atoms of the BO_3 and BO_4 units, which is more consistent for the BO_4 tetrahedra, the radial distribution appears more consistent for the BO_3 units.

Primitive ring statistics analysis was used to explore the effect of radiation damage in the size of the primitive rings in the network of the glasses. For the SBN12 glass, the number of rings per node as a function of the ring size, follows a bell-shaped curve. The most common rings in the undamaged structure consists of 16 nodes. As the damage progresses, the number of 12-, 14- and 16-sized rings is reduced, while there is a significant increase in the number of rings consisting of 20 and 26 nodes, accompanied with the formation of a characteristic peak corresponding to the 26-sized rings. Additionally, several rings consisting of 34, 36 and 38 nodes are formed. In the final structure, the rings distribution is quite similar to the one of the undamaged structure. The only significant difference that can be observed is the small decrease of the 14-, 16- and 18-sized rings and the increase in the number of 10- and 22-sized rings. The number of 36-sized rings is restored to close to the initial value while the number of 34- and 38- sized rings remains higher than in the initial structure. For the SBN14 glass, the results suggest that in the undamaged structures, the network is slightly different in comparison with the SBN12 glass. The most common rings consist of 14 and 28 nodes. There is also a characteristic peak in the 28-sized rings. During the formation of the damage cascade, the number of rings of this size reduces significantly, especially, for the 18 and 28-sized. At the maximum damage phase, the peak formed by the 28-sized rings is actually diminished. At the end of the simulation, the distribution of ring sizes is very close to the one of the initial structure, suggesting a recovery of the network of the glass. It is worth pointing out that there is a small decrease in the number of the 18-sized rings and an increase in the 20-, 22- and 28-sized rings. In addition to the previous observations, the average ring size in the final structures is decreased for the SBN12 glass and increased for the SBN14. These results suggest that the network of the two structures behaves differently during the irradiation process and for the first glass results in the formation of smaller rings, while for the SBN14 it favours the formation of rings with increased size.

Chapter 7

Radiation damage in iron prosphate glasses

7.1 Introduction

Although borosilicate glasses are generally accepted as effective wasteforms for the immobilization of HLW and spent fuel, there is a need to develop the best possible glass wasteforms that will retain their chemical durability for all the time period for which the incorporated radioactive nuclei remain active. In this direction, the Indian nuclear industry shows great interest in the development and fabrication of new iron phosphate glass wasteforms, and for this they formed a link with UK's Engineering and Physical Sciences Research Council (EPSRC) that led to the DREAM II consortium. Although experimental research can provide very useful information regarding the effects of radiation damage in a material, many radioactive components incorporated within nuclear waste remain radioactive for thousands or millions of years and consequently it is not straightforward to establish the reliability of the new vitrified wasteforms only by experimental methods. For a successful study of these radiation damage effects it is important to acquire detailed information regarding the structural changes in the waste form, both at the surface and in the bulk. It is important to retrieve dynamic information for the material and thus the better option is to use a method that directly yields this, Molecular Dynamics.

The iron phosphate glass models used in this study, were created by Jolley et. al. [13], collaborators from Loughborough University. In detail, Jolley et. al. created 3 different iron phosphate glasses with different compositions, presented in Table 7.1, subjected to radiation damage. These authors also performed a defect counting analysis of the damaged structures which is presented briefly later in this chapter, in section 7.4.1.

In this work, we performed additional analysis of the irradiated structures, by utilising partial Steinhardt and Hermite order parameters methods, alongside with primitive rings statistics. As in the case of the borosilicate glass models, the species specific Steinhardt and Hermite order

Table 7.1: Composition of the three iron phosphate glass models used in this study, in mol%. N_a is the total number ot atoms of the structures.

	Structure	N_a	Fe^{2+}	Fe^{3+}	P	O
IPG1:	$Fe^{2+}Fe_2^{3+}(P_2O_7)_2$	453600	4.76	9.52	19.05	66.67
IPG2:	$Fe_4^{3+}(P_2O_7)_3$	455328	–	12.90	19.36	67.74
IPG3:	$Fe^{3+}(PO_3)_3$	454896	–	7.69	23.08	69.23

parameters failed to identify appropriate parameters to be used for the estimation of the number of defect particles and consequently, this method was not used to analyse the irradiated iron phosphate glass models. Additionally, in the last section of this chapter, a topological description of the redox states of the irradiated IPG1 glass is given, to acquire information regarding the local structure around the iron atoms comprising the glass.

7.2 Creating iron phosphate glass models

Jolley et. al. [13] generated the iron phosphate glass models used in this study using the potentials proposed by Al Hasni & Mountjoy [23]. P-O, Fe-O and O-O interactions were described using a Buckingham potential in the form

$$\phi(r) = A_{ij}e^{-\frac{r}{\rho_{ij}}} - \frac{C_{ij}}{r^6} + \frac{1}{4\pi\epsilon_0}\frac{q_i q_j}{r}, \tag{7.1}$$

with parameters A_{ij}, C_{ij} and ρ_{ij} given in Table 3.4. To control P-O-P and O-P-O bond angles a three body Stillinger-Weber potential

$$\phi(r_{ij}, r_{ik}, \theta_{ijk}) = \lambda e^{\left(\frac{\gamma}{r_{ij}-r_c}+\frac{\gamma}{r_{ik}-r_c}\right)}(\cos\theta_{ijk} - \cos\theta_0)^2 \tag{7.2}$$

was used, with parameters λ, γ, r_c and θ given in Table 7.2.

Table 7.2: Parameters of the three body Stillinger-Weber potential used by Jolley et. al. [13] for the creation of the iron phosphate glass models used in this work.

Triplet($j-i-k$)	λ (eV)	γ (Å)	r_c (Å)	θ_0 (°)
P-O-P	8.299695	0.5	2.5	135.50
O-P-O	5.351617	0.5	2.5	109.47

For the short range interactions, Jolley et. al. [13] used a short range ZBL potential, truncated and fitted to the Buckingham pair potentials with a fifth order spline in the form

$$f(r) = a_0 + a_1 r + a_2 r^2 + a_3 r^3 + a_4 r^4 + a_5 r^5, \tag{7.3}$$

where the parameters a_i were chosen such that the resulting potential energy functions as well as their first and second derivatives were continuous and given in Table 7.3.

Table 7.3: Parameters used to truncate and fit the Buckingham potential used for the creation of iron phosphate glass models with the short range ZBL potential [31]. In this table, r_{Buck} and r_{ZBL} are the truncation distances for the Buckingham and ZBL potentials respectively. r_{ZBL} and r_{Buck} are in Å and a_n in Å^{-n}.

Pair	r_{ZBL}	r_{Buck}	a_0	a_1	a_2	a_3	a_4	a_5
$Fe^{2+}-O$	0.2	0.85	11.274280	-21.233242	44.802056	-69.570862	60.519843	-21.948215
$Fe^{3+}-O$	0.5	1.25	13.468756	-36.254018	82.390627	-109.921757	74.401925	-20.216820
O–O	0.35	1.80	9.273627	-11.288100	8.398709	-2.456703	-0.030643	0.093801
P–O	0.25	1.03	11.166080	-26.912807	75.626106	-136.453869	116.256770	-36.456113

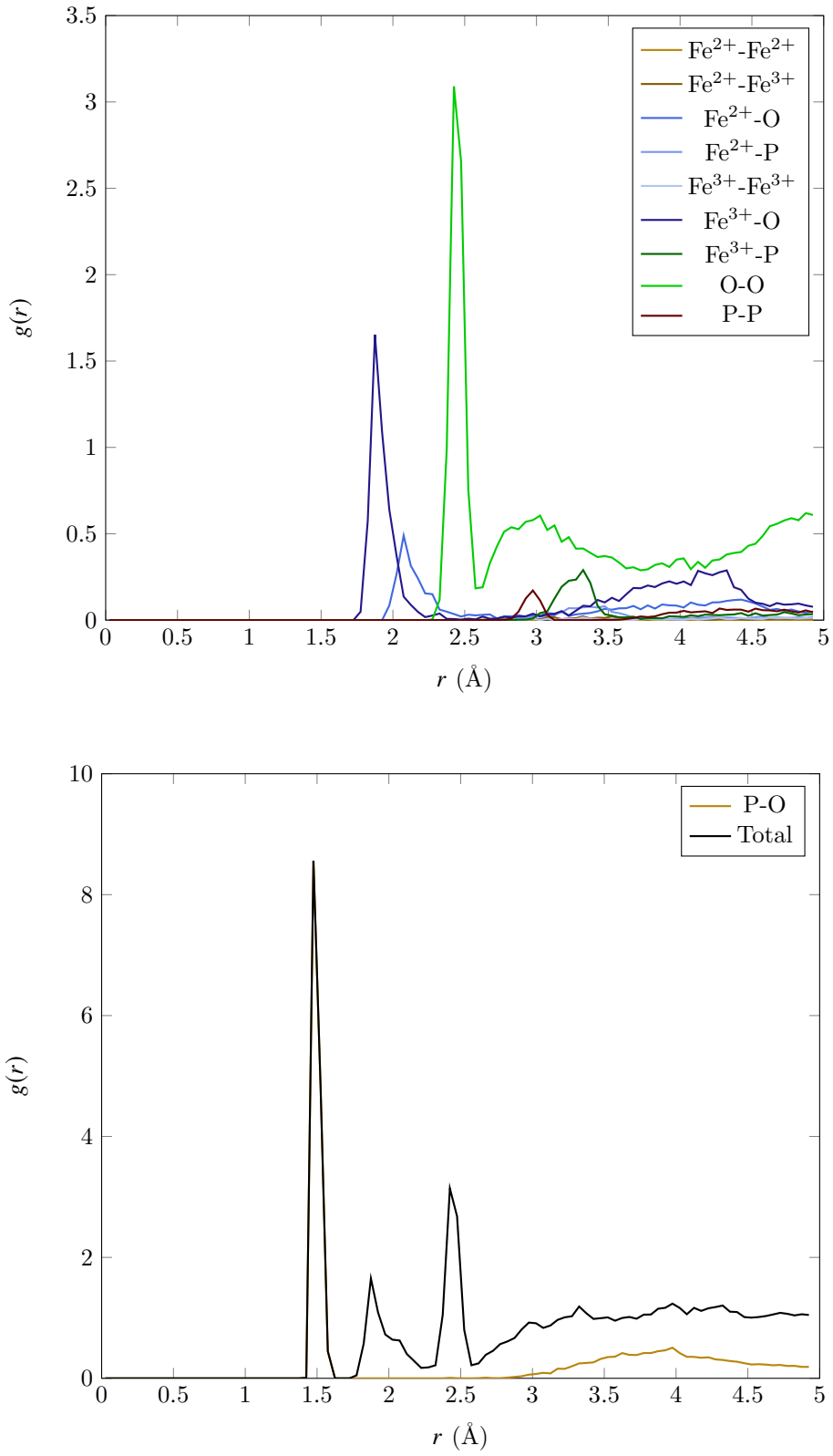

Figure 7.1: Partial and total radial distribution functions of the of the IPG1 glass structure.

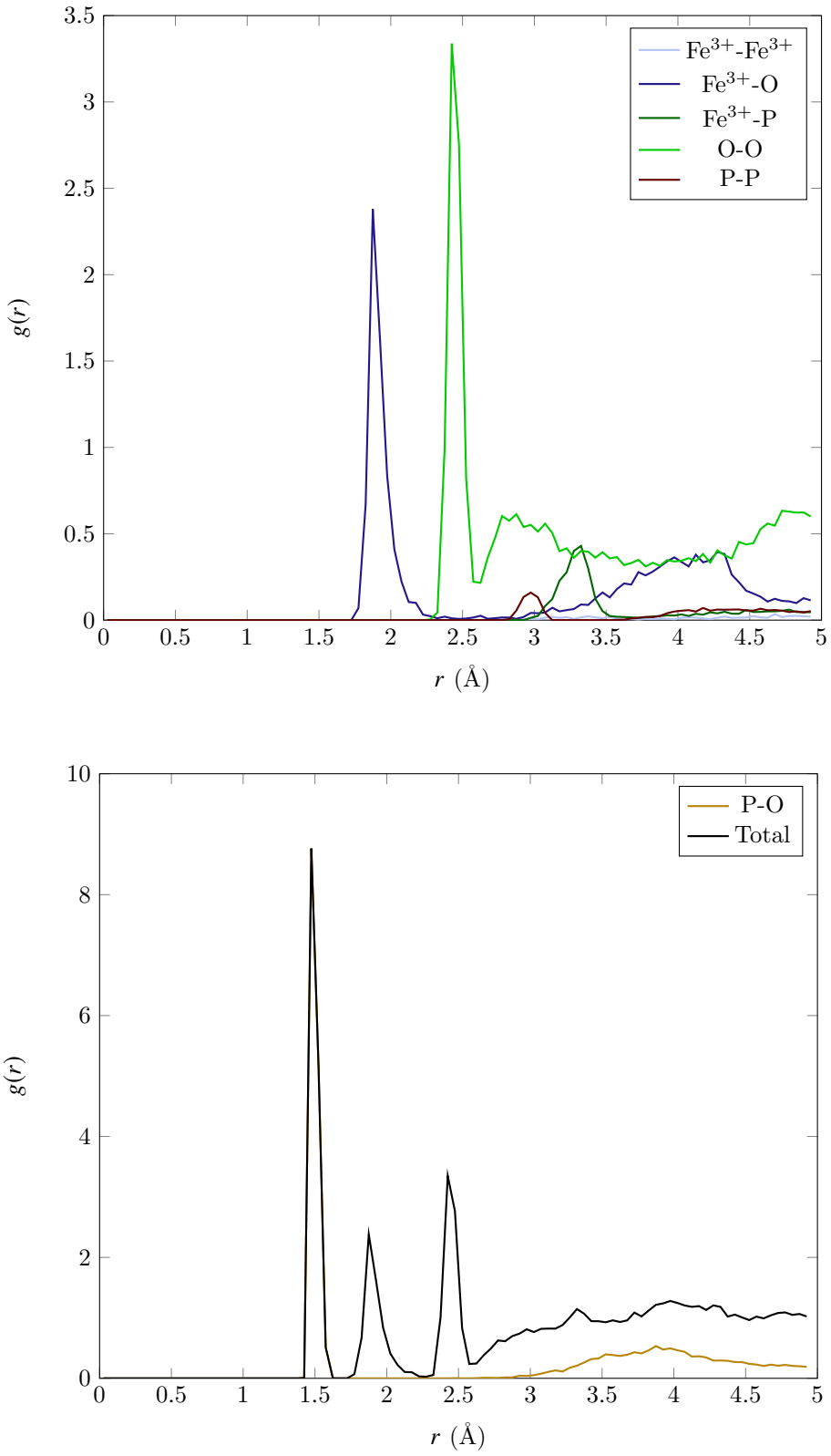

Figure 7.2: Partial and total radial distribution functions of the of the IPG2 glass structure.

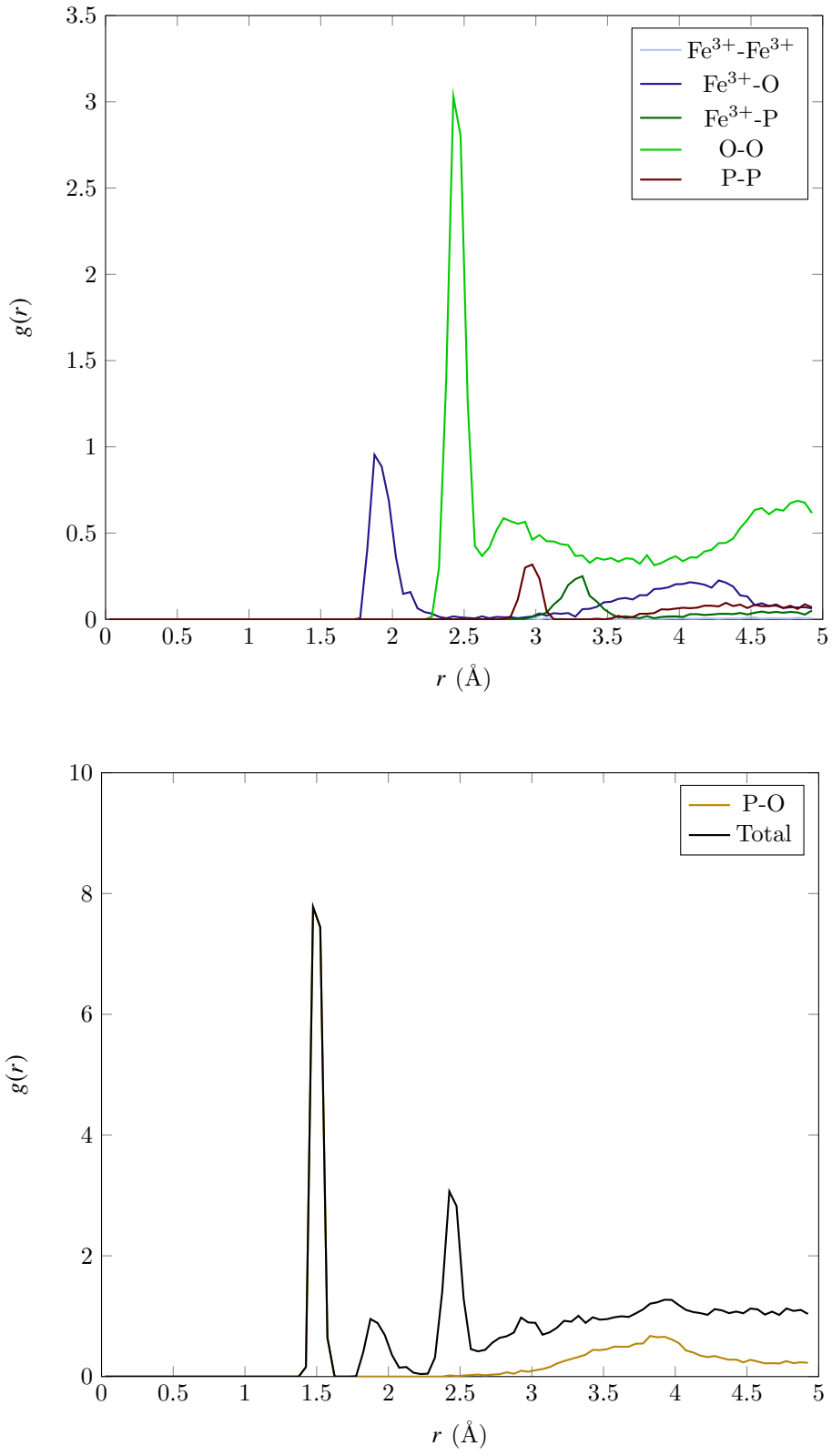

Figure 7.3: Partial and total radial distribution functions of the of the IPG3 glass structure.

The initial structures of random atomic arrangements were first equilibrated at 6000 K and then quenched to room temperature at a rate of 5×10^{12} K/s. Finally, the system was energy minimized at 0 K using the conjugate gradient method. For the simulation of the structures, a single 4 GHz Intel Core i7 processor was used. Due to the relatively low computational power, authors were only able to quench small systems of around 2000 atoms and the large systems used in this analysis were generated by stacking multiple copies of quenched cells to generate a simulation cell of the desired size.

At this point, it is important to notice that the work of Jolley et. al. [13] is based on an important approximation, since they assumed that the $Fe^{2+}-O/Fe^{3+}-O$ ions of the structures maintain their valence during the simulation

In Figs. 7.1-7.3 the radial distribution functions of the three structures are shown. It is clear that the first minimum of the total RDF is governed by the P-O bonds. This is the only pair for which the first minimum of the partial RDF is smaller than the first minimum of the total RDF. Consequently, it is assumed - as is natural since iron atoms act as network modifiers - that the only existing bonds of the structure are between phosphorus and oxygen atoms.

7.2.1 Creating a radiation damage cascade

The creation of a damage cascade was also performed by Jolley et. al. [13]. Each of the structures was subjected to radiation damage, by selecting a primary knock-on atom (PKA) which was given a 4 keV excess of kinetic energy along a random direction. The cascade formation was simulated for a total of 4 ps in the NVE ensemble. Since the NVE ensemble does not preserve temperature, the temperature of the system increased from 0 K to 32 K by the end of the simulation.

7.3 Algorithmic details for defect analysis

The defect counting method was used by Jolley et. al. [13], to study the effects of radiation damage in the three modelled structures. In their work, these authors calculated the displacement of atoms from the position they occupied in the undamaged structure, and characterized a particle as a defect if that distance was greater than 1.2 Å (Fig. 7.4).

For the calculation of the Steinhardt and Hermite order parameters performed in this work by the author, the standard approach was used: An output file was generated, containing the trajectories of the atoms at every 100 timesteps of the simulation, generating 401 snapshots in total to be analysed using the partial SOP/HOP methods. Additionally, for each snapshot, a primitive ring statistics analysis was performed, to get detailed information regarding the effect of the radiation in the silica network of the glasses.

For the calculation of Steinhardt and Hermite order parameters, and based on the radial distribution functions of the systems, a bond between two atoms exists - as discussed previously - if the interatomic distance between the two atoms is smaller from the first minimum of both the partial and the total radial distribution function. Consequently, for the three simple structures under investigation, the only existing bonds are between phosphorus and oxygen atoms.

7.4 Results

7.4.1 Defect counting

According to the work of Jolley et. al. [13], for the IPG1 glass, it is clear that the number of displaced Fe^{2+} and Fe^{3+} atoms is almost the same at every timestep, despite the fact that the number of Fe^{3+} atoms was twice as large as Fe^{2+} (Fig. 7.4). Consequently, it can be argued that Fe^{3+} atoms are more resistant to radiation damage [13]. The number of displaced phosphorus atoms is slightly higher in comparison with the Fe^{2+} and Fe^{3+} atoms, while displaced oxygen atoms are almost 6 times higher. For all species, a small peak in the number of displaced atoms just after 0.50 ps is observed. Their number is slightly reduced for the next 0.50 ps and remains constant until the end of the simulation. However, as seen in Figs. 7.8, 7.12 and 7.16, these results are in contrast with the changes in the coordination numbers of the phosphorus atoms. Thus, as was the case for borosilicate glass structures, the number of displaced atoms is not sufficient to identify bond-defected atoms.

7.4.2 Partial Steinhardt order parameters

In Figs. 7.5, 7.6 and 7.7, the plots of $Q_6(Q_4)$ for the phosphorus atoms of the IPG1 glass are shown for the initial structure at t = 0.00 ps, at t = 0.50 ps where the maximum of displaced atoms is observed and for the final structure at t = 4.00 ps respectively. It is clear, that PO_4 tetrahedra are characterized by a single geometry, since all data points for t = 0.00 ps are found in the same area of the $Q_6(Q_4)$ plots. At the time of maximum damage, several P atoms are found away from the well defined region formed by the 4-coordinated atoms and are associated with at least one bond defect. Actually, for t = 0.50 ps most of the defected atoms are 3-coordinated and only a few are 2-coordinated. At the end of the simulation however, only 3-coordinated defected phosphorus atoms are found, implying a degree of recovery of the phosphorus network.

The single geometry of the PO_4 units makes it possible to apply the method described in the previous chapters to calculate at every stage of the simulation the number of phosphorus atoms associated with bond defects (Fig. 7.8). As is clear when compared with the number of phosphorus atoms with coordination number less than 4, Steinhardt order parameters provide a very accurate estimation of the number of P atoms associated with at least one bond defect. In contrast with the maximum number of displaced atoms, which is observed for t = 0.50 ps, the maximum number of P atoms associated with bond defects is observed at t = 0.25 ps. At the maximum damage, only 220 P atoms have bond defects (0.25% of the total P atoms) while by the end of the simulation, almost 2/3 of them have recovered their bonds leaving only about 65 defect atoms, which accounts for 0.075% of the total P atoms.

By comparing the results with the number of displaced atoms, it is apparent that at the maximum damage stage, the number of displaced atoms is actually smaller than the number of bond-defected phosphorus atoms while at the end of the simulation it is higher. By combining these results it can be argued that during the first stages of the creation of the damage cascade, the light oxygen atoms are displaced from their initial positions faster than the phosphorus atoms, resulting in the creation of bond defected phosphorus atoms. As the damage progresses, the phosphorus atoms are also displaced from their initial positions by distances comparable with those travelled

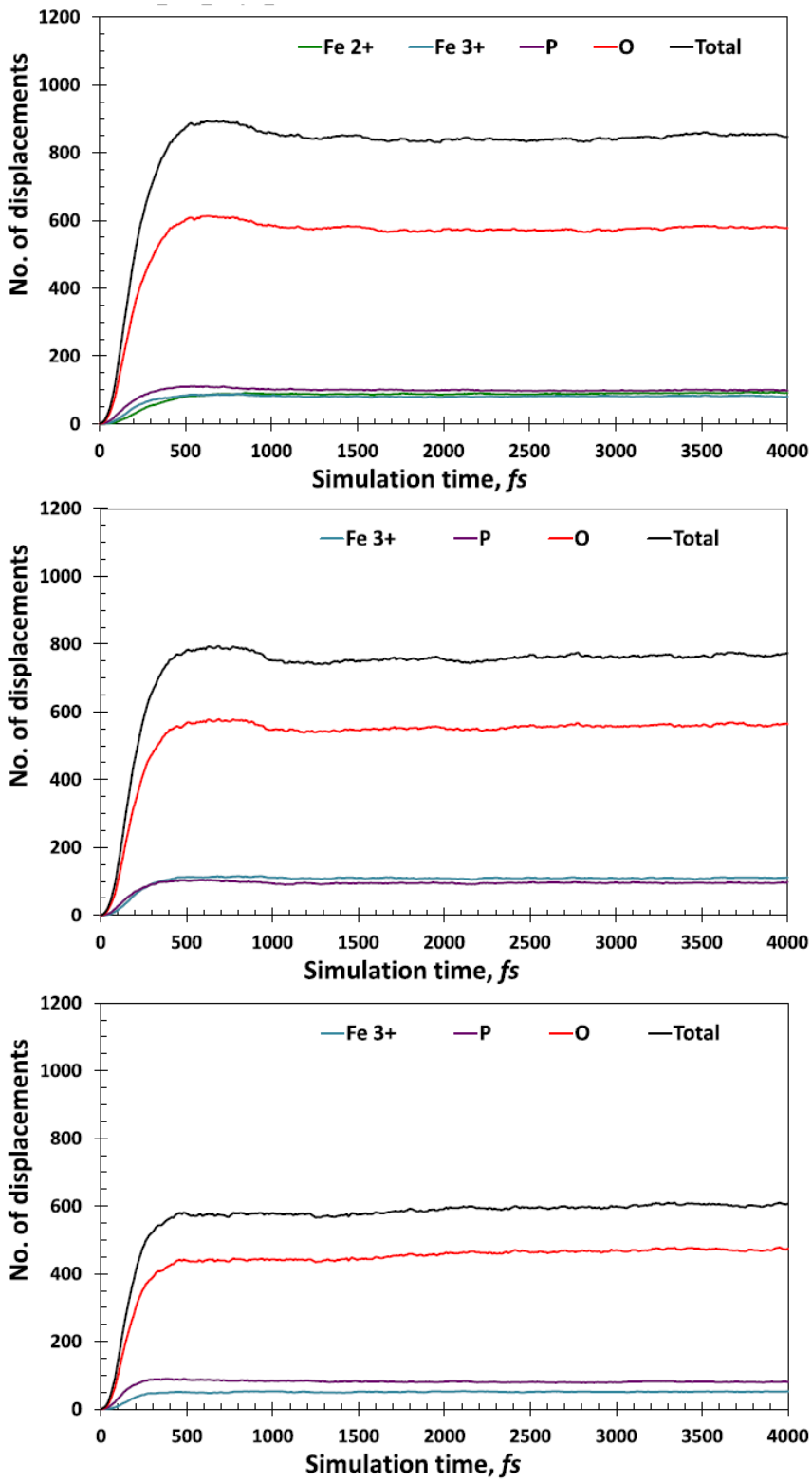

Figure 7.4: The number of displaced atoms as a function of time for the IPG1 (**top**), IPG2 (**middle**) and IPG3 (**bottom**) iron phosphate glass structures simulated by Jolley et. al. [13].

by their neighbouring oxygen atoms and finally they are reconnected, although they are displaced from their initial positions by more than 1.2 Å.

For the IPG2 glass, results are slightly different, as phosphorus atoms are more heavily defected in comparison with IPG1 glass. For all the stages of the simulation, apart from the 3- and 2-coordinated P atoms, atoms with coordination number 0 and 1 (Figs. 7.9, 7.10 and 7.11) were identified. The partial Steinhardt order parameters method was used to identify the number of phosphorus atoms associated with bond defects, as shown in Fig. 7.12. The maximum number of defected phosphorus atoms is observed for t = 0.40 ps, where 290 P atoms (0.33% of the total) are associated with at least one bond defect. By the end of the simulation, about 1/3 of the atoms are recovered and there are about 200 P atoms remaining defected (0.23% of the total P atoms). The differences can be explained based on the different composition of the two glasses. However, existing experiments suggest that the energy threshold per atom is higher for Fe^{3+} and O atoms in comparison with Fe^{2+} atoms and consequently, IPG1 glass should be more resistant to radiation damage. Although the percentage of remaining defect atoms is almost three times higher in comparison with those for the IPG1 glass, the percentage is quite low and characteristic of the tolerance of the system in radiation damage.

Finally, the behaviour of the IPG3 glass is closer to that of the IPG1 glass. $Q_6(Q_4)$ plots for this structure are demonstrated in Figs. 7.13, 7.14 and 7.15, while the number of phosphorus atoms associated with bond defects is shown in Fig. 7.16. At the maximum damage phase, 334 phosphorus atoms are associated with at least one bond defect, a number that accounts for just 0.3% of the total phosphorus atoms. By the end of the simulation, 2/3 of the atoms are recovered, leaving just 100 atoms with a bond defect (0.095% of the total phosphorus atoms). This structure is slightly less resistant than IPG1 glass, but it is also more tolerant to radiation damage in comparison with IPG2 glass.

In terms of the geometry of the oxygen neighbours, for the initial undamaged structures, it is clear that the $Q_6(Q_4)$ data points form a single compact area for every glass. It is safe to argue that the local angular distribution of the oxygen neighbours of the PO_4 units exhibits very small variations. However, as the damage progresses, the area covered by the 4-coordinated phosphorus atoms is extended, reflecting the changes in the shape of the PO_4 tetrahedra due to radiation damage. Additionally, the defected 3-coordinated phosphorus atoms cover a wide area on the $Q_6(Q_4)$ plots. Consequently, the 3 remaining oxygen atoms are arbitrarily distributed around the phosphorus atoms. As for the 2-coordinated defected atoms, they cover a significant part of the curve corresponding to the Steinhardt order parameters for atoms with 2 neighbours, but away from the points corresponding to interdimensional atoms. At the end of the simulation, the areas corresponding to the remaining 3- and 4-coordinated phosphorus atoms are shrunk in comparison with the state of maximum damage. However, the resulting regions for the 4-coordinated phosphorus atoms, is extended when compared with those of the undamaged structure, especially for the IPG3 glass. Thus, although there is a significant recovery of the PO_4 tetrahedra, the angular distribution of the oxygen neighbours exhibits variations that are not observed in an undamaged structure.

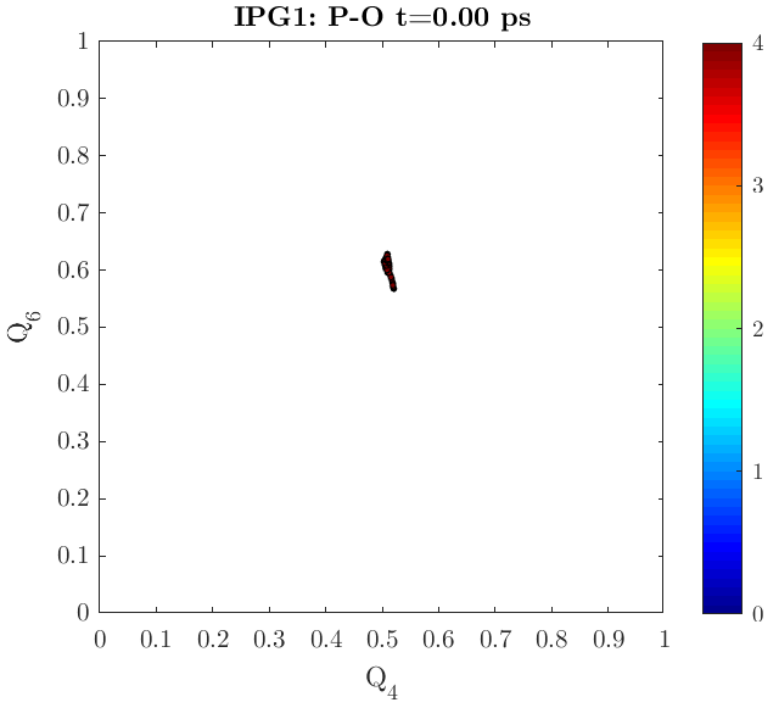

Figure 7.5: $Q_6(Q_4)$ plot of the phosphorus atoms of the IPG1 glass at t = 0.00 ps, highlighting the coordination number, as indicated in the colourbar next to the plots.

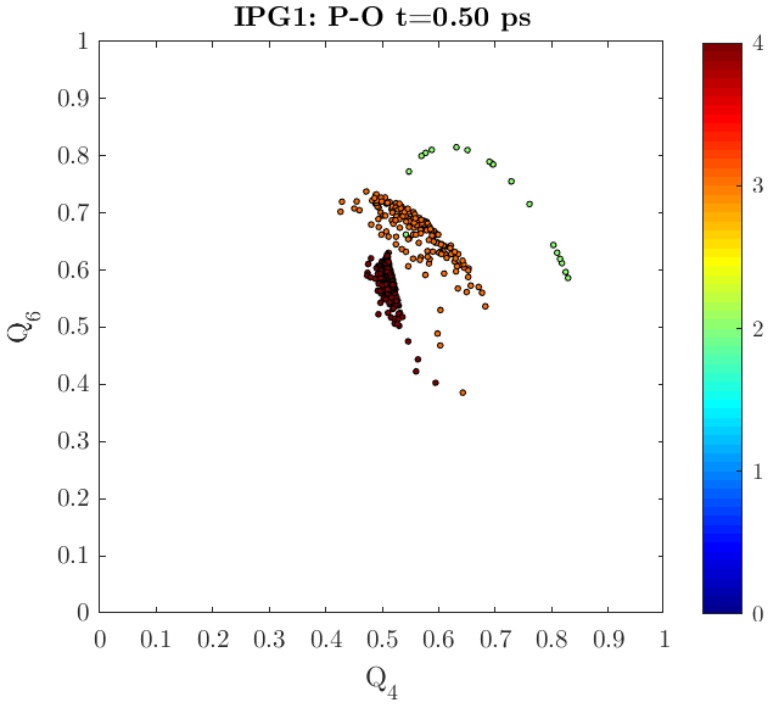

Figure 7.6: $Q_6(Q_4)$ plot of the phosphorus atoms of the IPG1 glass at t = 0.50 ps, highlighting the coordination number, as indicated in the colourbar next to the plots.

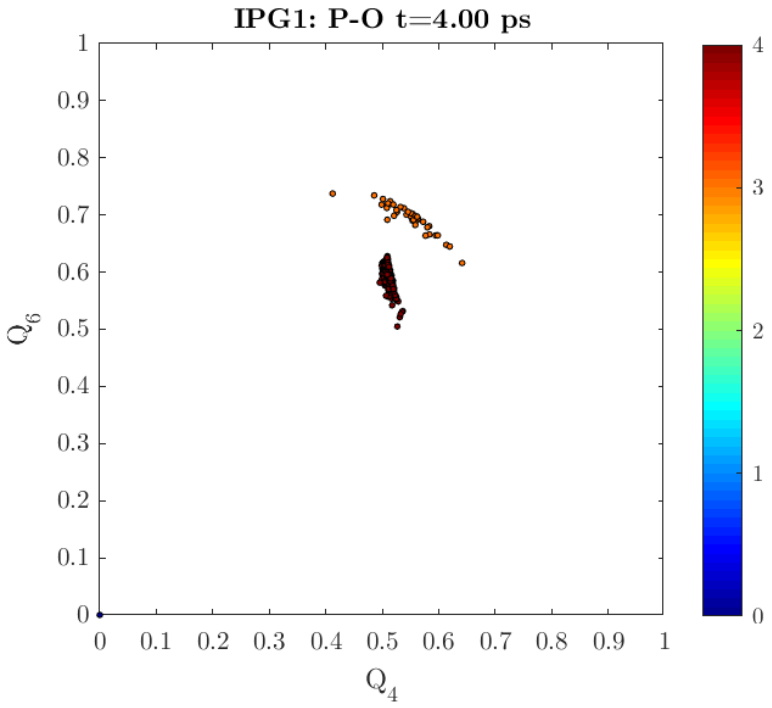

Figure 7.7: $Q_6(Q_4)$ plot of the P atoms of the IPG1 glass in the final damaged structure, highlighting the coordination number, as indicated in the colourbar next to the plots.

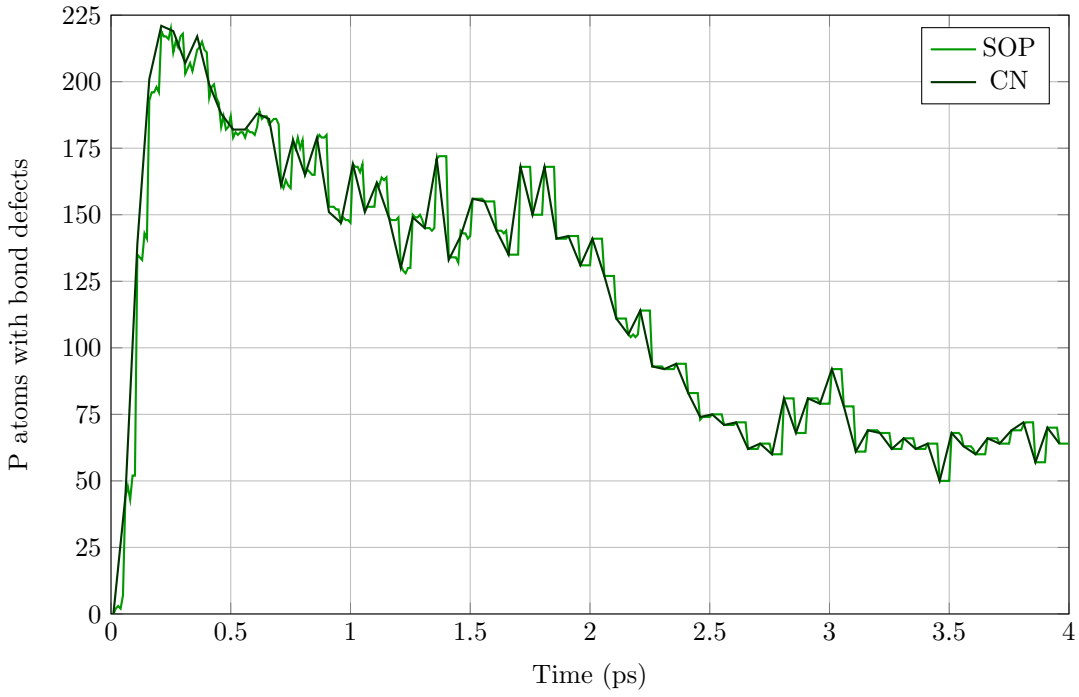

Figure 7.8: Number of phosphorus atoms of the IPG1 glass identified with bond defects using the partial Steinhardt order parameters method.

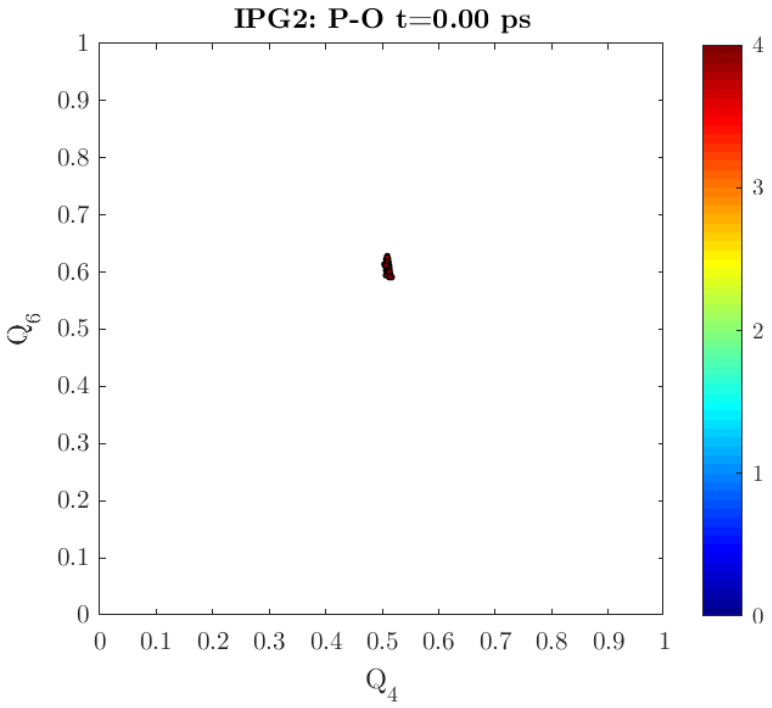

Figure 7.9: $Q_6(Q_4)$ plot of the P atoms of the IPG2 glass at t = 0.00 ps, highlighting the coordination number, as indicated in the colourbar next to the plots.

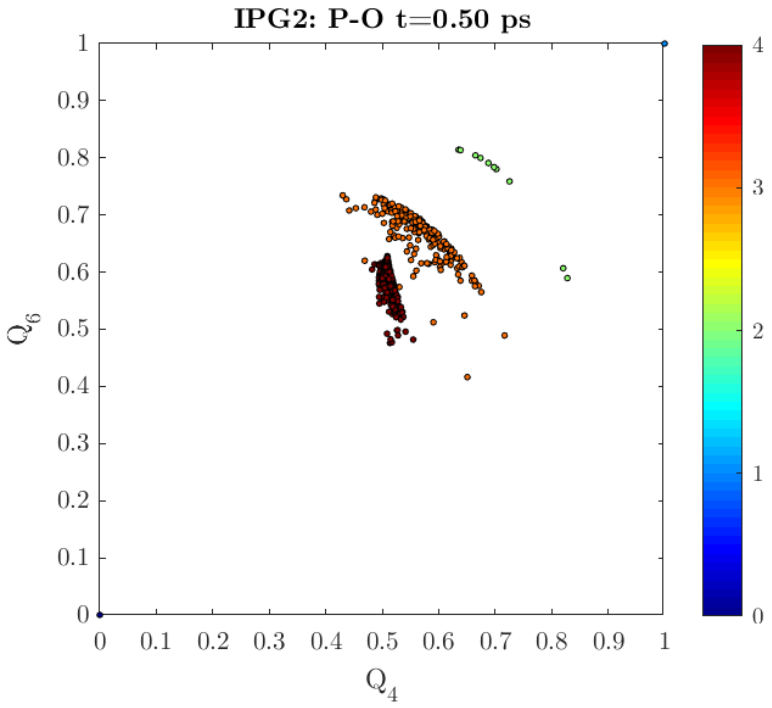

Figure 7.10: $Q_6(Q_4)$ plot of the P atoms of the IPG2 glass at t = 0.50 ps, highlighting the coordination number, as indicated in the colourbar next to the plots.

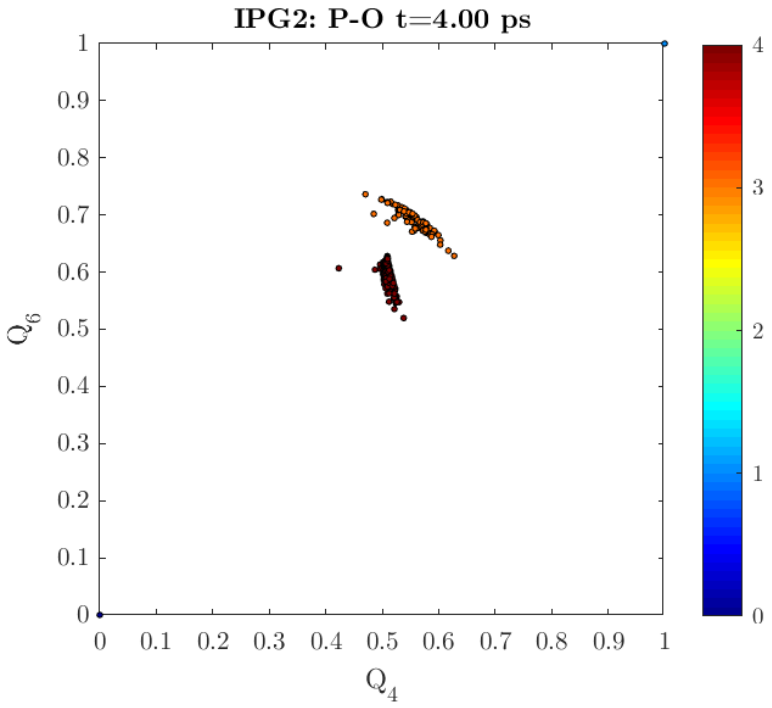

Figure 7.11: $Q_6(Q_4)$ plot of the P atoms of the IPG2 glass in the final damaged structure, highlighting the coordination number, as indicated in the colourbar next to the plots.

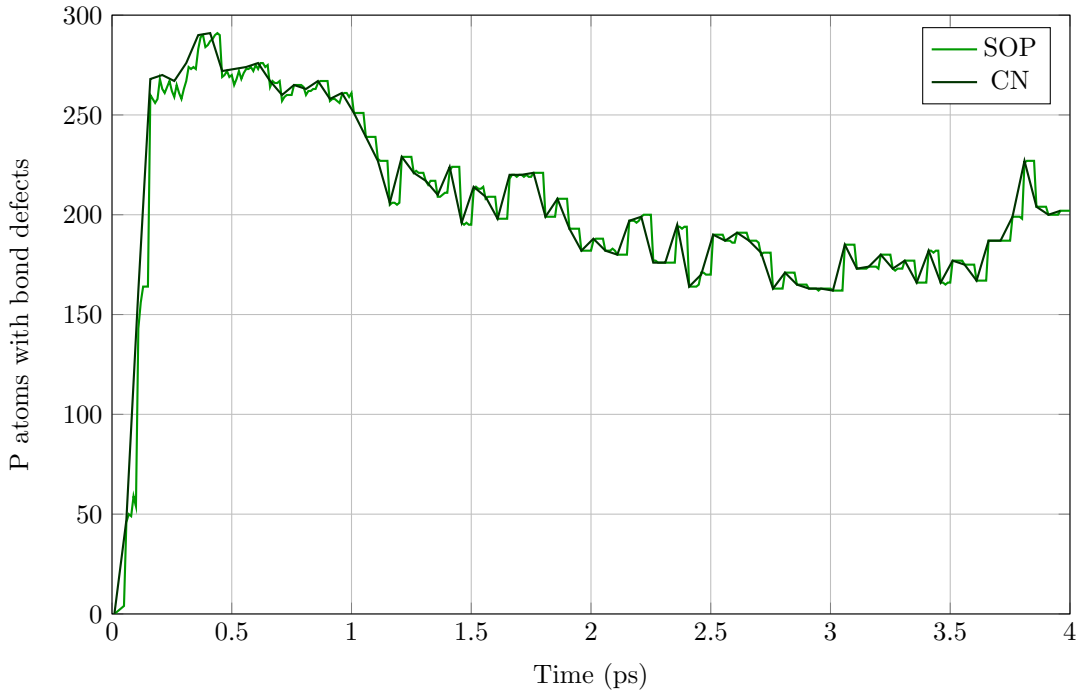

Figure 7.12: Number of phosphorus atoms of the IPG2 glass identified with bond defects using the partial Steinhardt order parameters method.

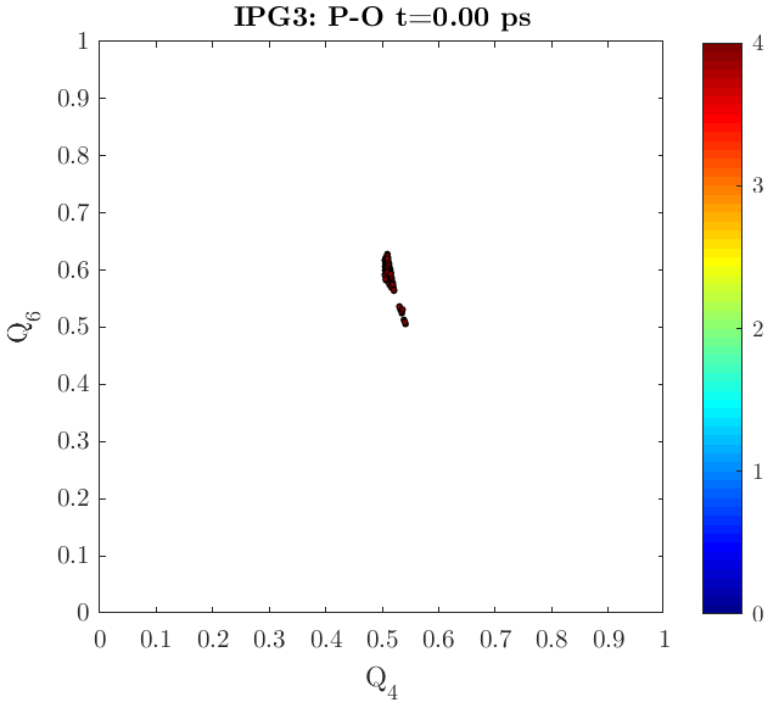

Figure 7.13: $Q_6(Q_4)$ plot of the P atoms of the IPG3 glass at t = 0.00 ps, highlighting the coordination number, as indicated in the colourbar next to the plots.

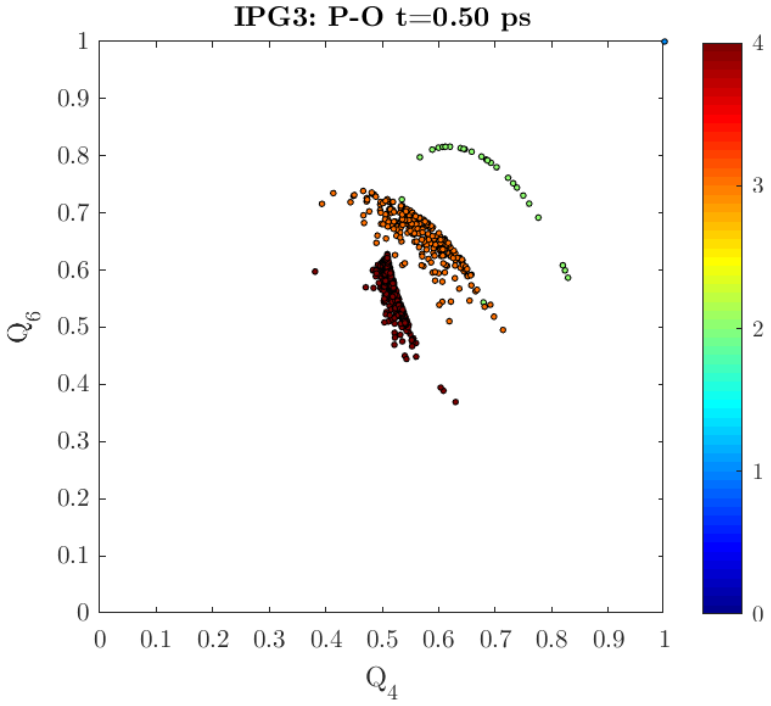

Figure 7.14: $Q_6(Q_4)$ plot of the P atoms of the IPG3 glass at t = 0.50 ps, highlighting the coordination number, as indicated in the colourbar next to the plots.

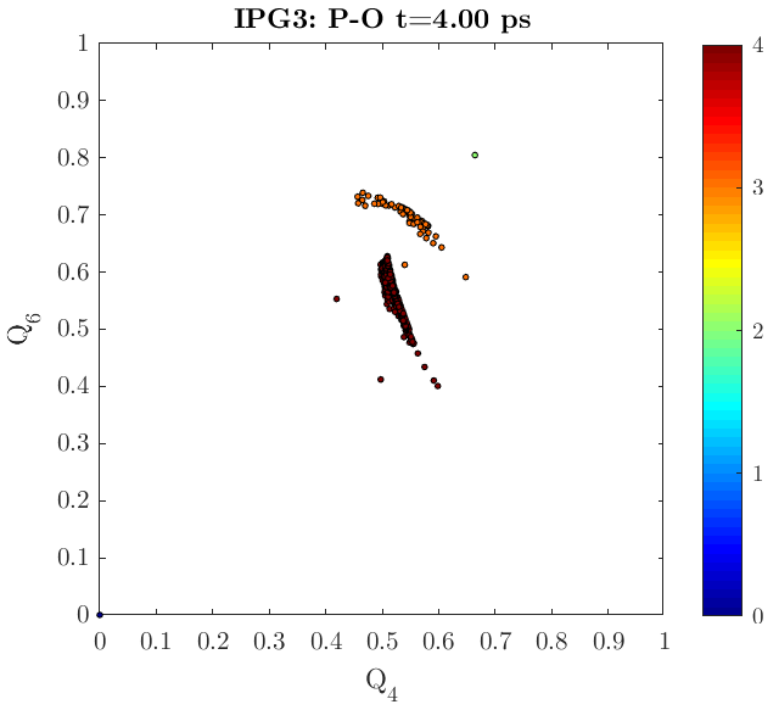

Figure 7.15: $Q_6(Q_4)$ plot of the P atoms of the IPG3 glass in the final damaged structure, highlighting the coordination number, as indicated in the colourbar next to the plots.

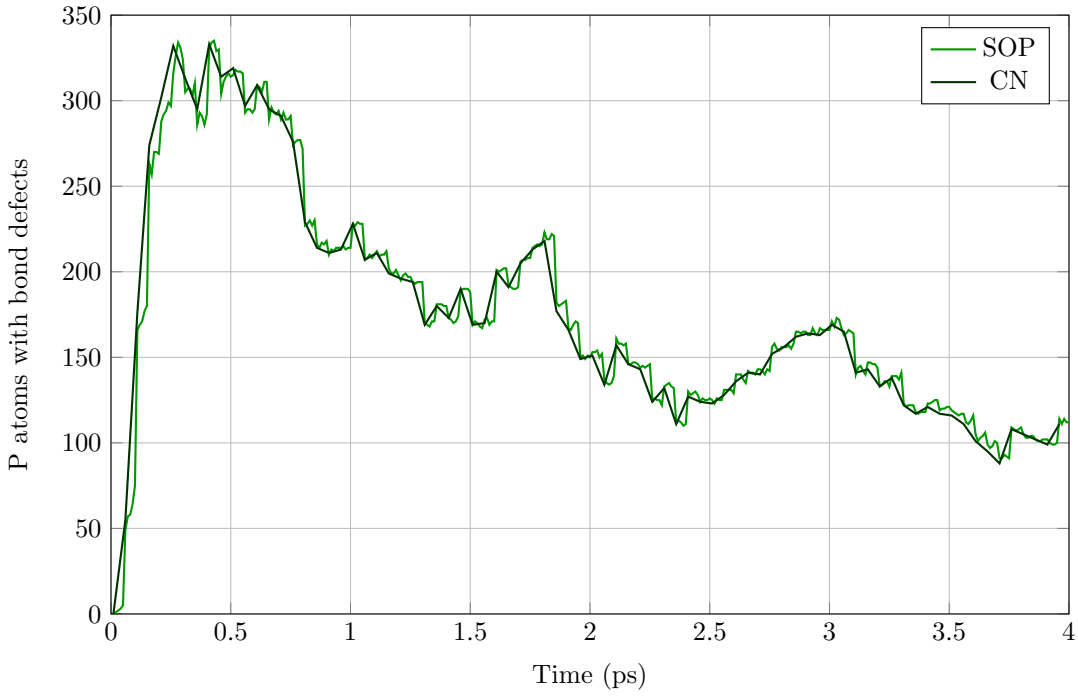

Figure 7.16: Number of phosphorus atoms of the IPG3 glass identified with bond defects using the partial Steinhardt order parameters method.

7.4.3 Partial Hermite order parameters

Along with Steinhardt order parameters, for the three structures, Hermite order parameters were calculated. In Figs. 7.17-7.19, 7.21-7.23 and 7.25-7.27, the plots of $R_6(R_4)$ for the phosphorus atoms of the IPG1, IPG2 and IPG3 glass are shown for the initial structure at t = 0.00 ps, at t = 0.50 ps where the maximum of displaced atoms is observed, and for the final structure at t = 4.00 ps respectively.

In terms of the number of phosphorus atoms associated with at least one bond defect (Figs. 7.20, 7.24 and 7.28), information retrieved from the $R_6(R_4)$ is almost identical to those extracted using Steinhardt order parameters for all three structures. The single geometry of the PO_4 tetrahedra is obvious in the plot for t = 0.00 ps as all data points are found in the same area. Phosphorus atoms associated with bond defects are progressively found away from that region, making it easy to identify these atoms.

Plots of R_4 against R_6 can be used to extract information regarding the average P-O bond length. From Figs. 7.17, 7.21 and 7.25, it is clear that since the data points form a very compact area, there are very small variations in the P-O distance. However, as seen in Figs. 7.18, 7.22 and 7.26, the radiation damage event, apart from creating phosphorus atoms with coordination number less than 4, expands the area covered by the 4-coordinated phosphorus atoms, suggesting an alteration in the P-O bond lengths in the PO_4 tetrahedra. This effect is more intense for the IPG2 glass, for which the data points of several atoms are spread relatively away from the compact area of the 4-coordinated phosphorus atoms. Additionally, for all three structures, the 3- and 2-coordinated phosphorus atoms formed during the damage event also appear to have significant variations in the average distance from their oxygen neighbours. At t = 4.00 ps (figs. 7.19, 7.23 and 7.27), the areas corresponding to the 3- and 4-coordinated phosphorus atoms are slightly contracted suggesting a small restoration of the average P-O bond length.

7.4.4 Primitive ring statistics

The simple iron phosphate glass structures modelled for this work contain only P-O bonds and consequently, a search for even ordered primitive rings consisting of consecutive phosphorus and oxygen atoms was performed. However, the search failed to find any rings. This observation is in-line with experimental studies on alkali phosphate glasses stating that there is a large number of non-bridging oxygens in the PO_4 units that prevents the formation of rings [11]. A possible explanation can be suggested using the coordination numbers of the oxygen atoms, as presented in Table 7.4. From this table it is clear that the majority of the oxygen atoms are 2-coordinated. This means that these atoms, when connected form P-O chains while the 3- and 4-coordinated oxygen atoms can form bifurcations that in general favour the formation of rings. However, in all structures there is also a large number of oxygen atoms that accept only one phosphorus neighbour and consequently create end-points in the P-O chains preventing the formation of rings.

There are other possibilities to get information regarding the connectivity, such as the study of the P-O chains within the structures. Although such methods are out of the scope of this work package it would be extremely interesting to perform such research in future projects.

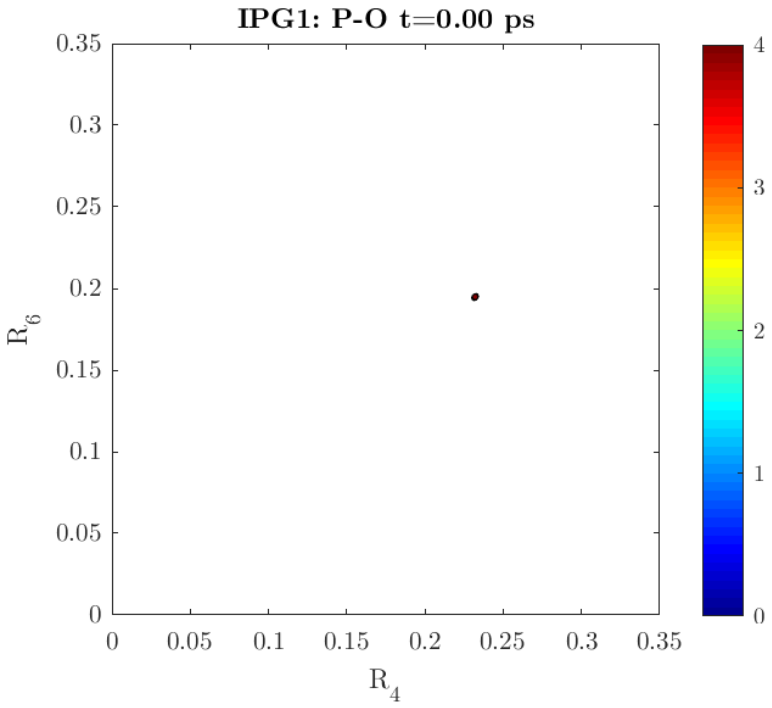

Figure 7.17: $R_6(R_4)$ plot of the P atoms of the IPG1 glass at t = 0.00 ps, highlighting the coordination number, as indicated in the colourbar next to the plots.

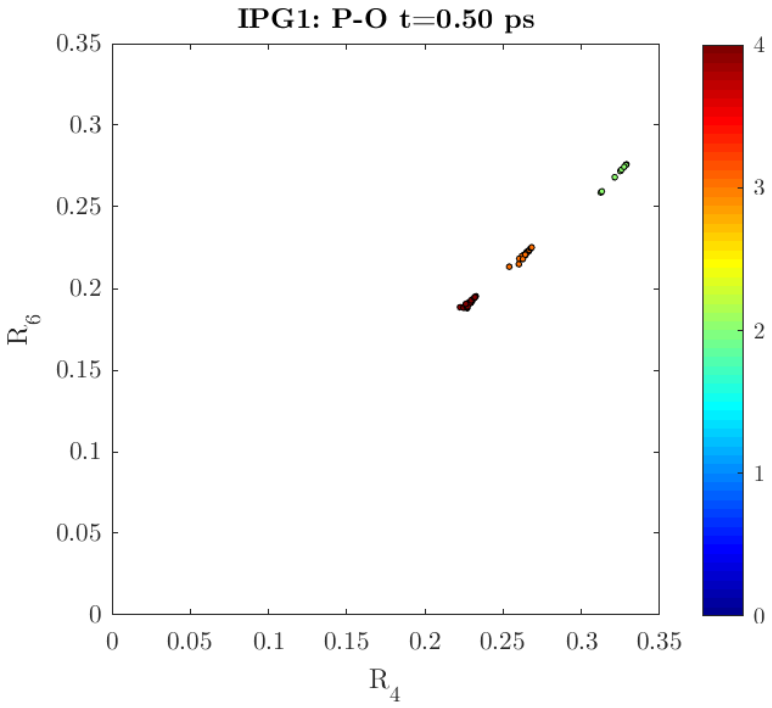

Figure 7.18: $R_6(R_4)$ plot of the P atoms of the IPG1 glass at t = 0.50 ps, highlighting the coordination number, as indicated in the colourbar next to the plots.

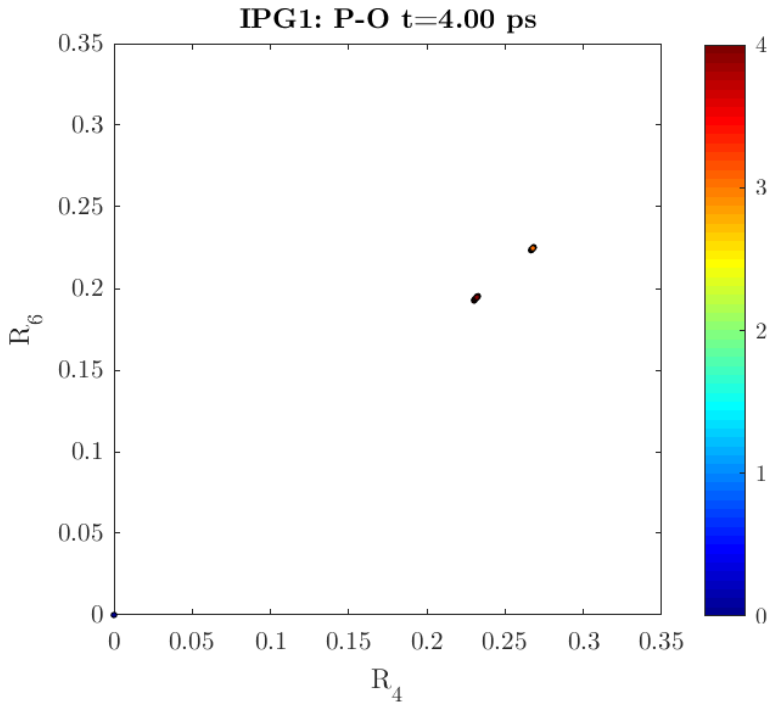

Figure 7.19: $R_6(R_4)$ plot of the P atoms of the IPG1 glass in the final damaged structure, highlighting the coordination number, as indicated in the colourbar next to the plots.

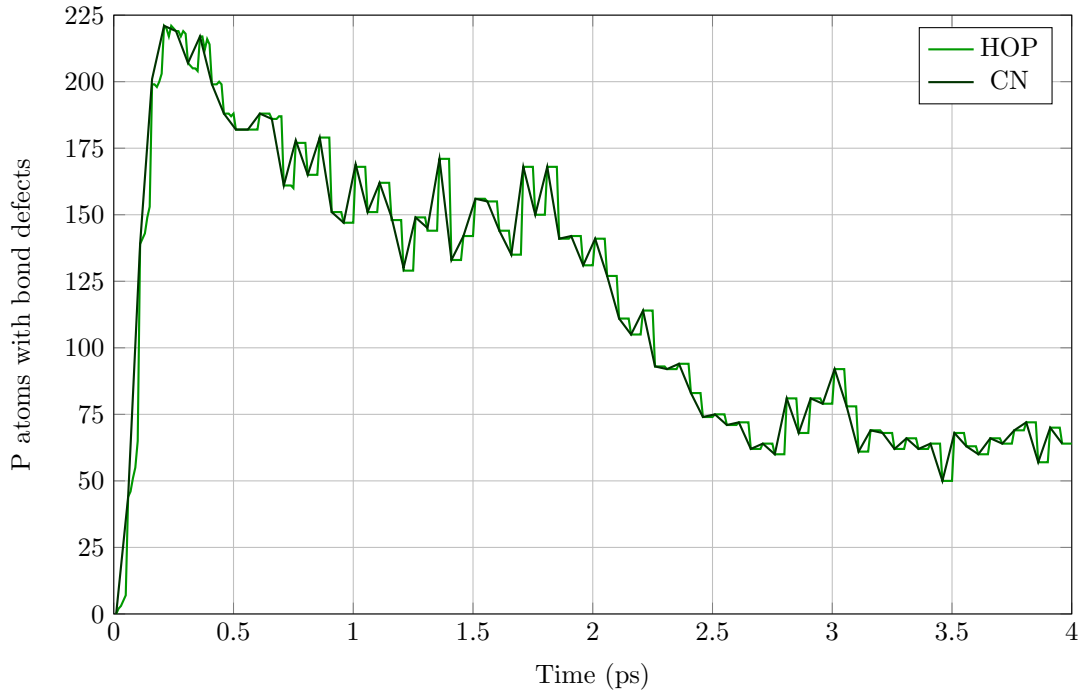

Figure 7.20: Number of phosphorus atoms of the IPG1 glass identified with bond defects using the partial Hermite order parameters method.

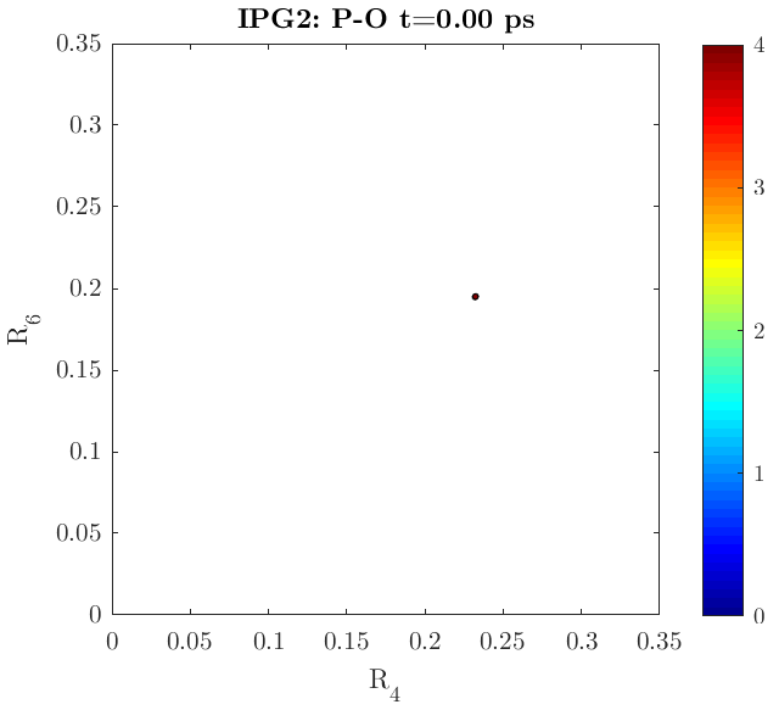

Figure 7.21: $R_6(R_4)$ plot of the P atoms of the IPG2 glass at t = 0.00 ps, highlighting the coordination number, as indicated in the colourbar next to the plots.

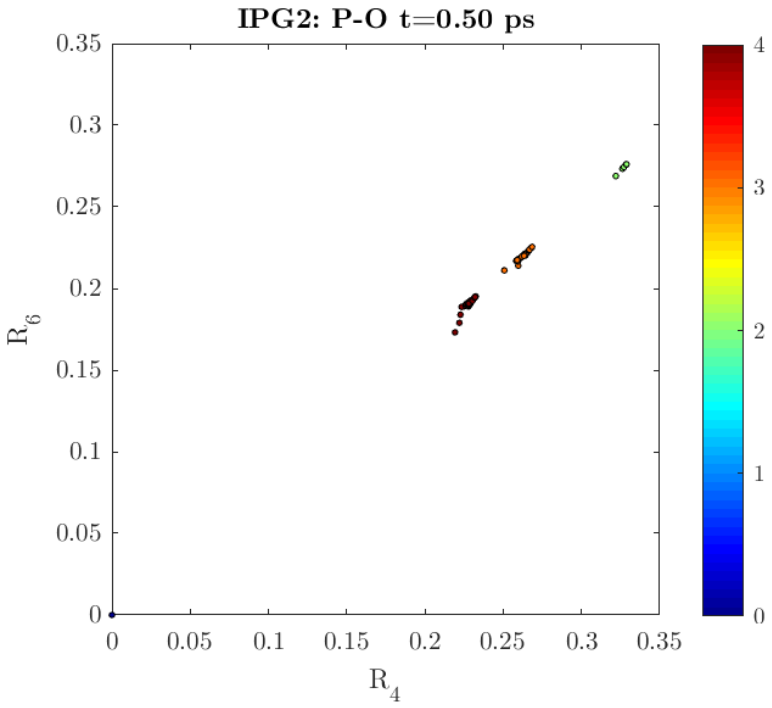

Figure 7.22: $R_6(R_4)$ plot of the P atoms of the IPG2 glass at t = 0.50 ps, highlighting the coordination number, as indicated in the colourbar next to the plots.

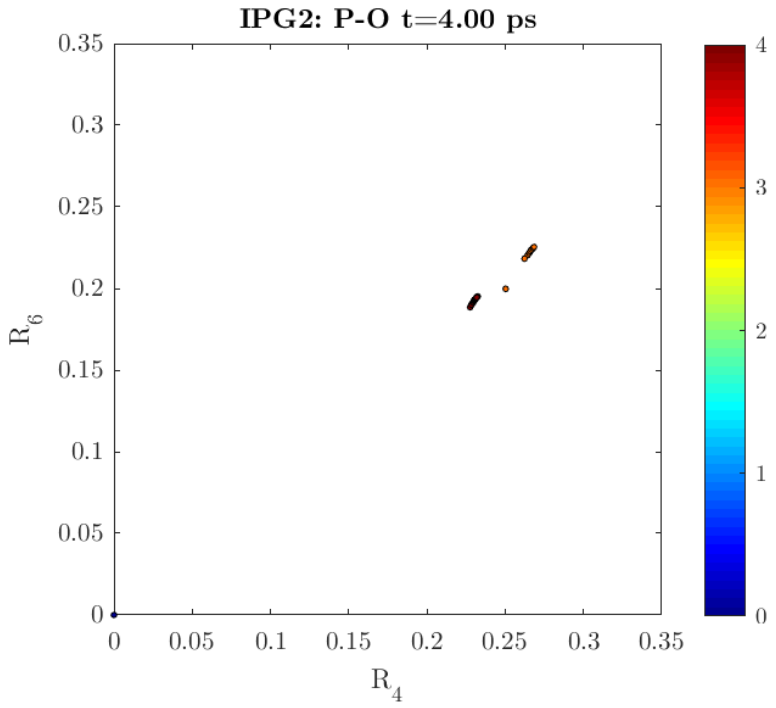

Figure 7.23: $R_6(R_4)$ plot of the P atoms of the IPG2 glass in the final damaged structure, highlighting the coordination number, as indicated in the colourbar next to the plots.

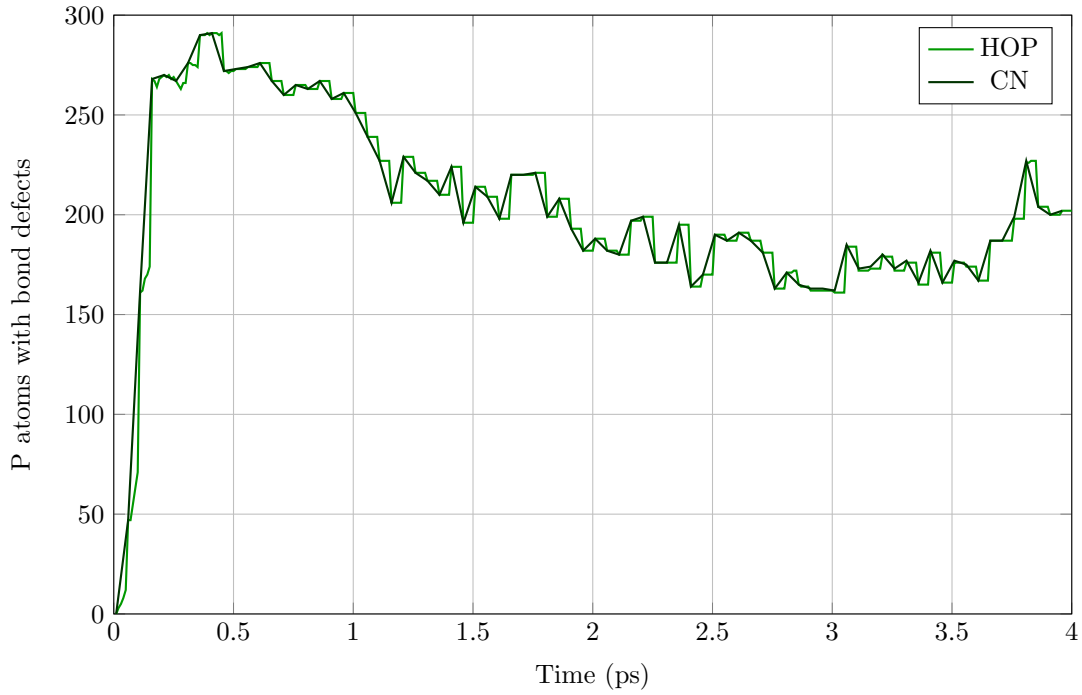

Figure 7.24: Number of phosphorus atoms of the IPG2 glass identified with bond defects using the partial Hermite order parameters method.

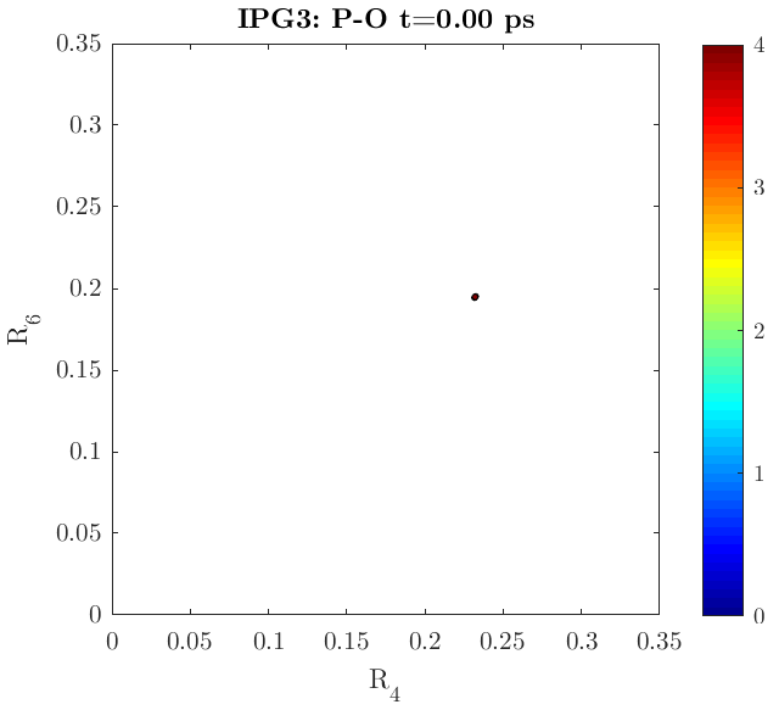

Figure 7.25: $R_6(R_4)$ plot of the P atoms of the IPG3 glass at t = 0.00 ps, highlighting the coordination number, as indicated in the colourbar next to the plots.

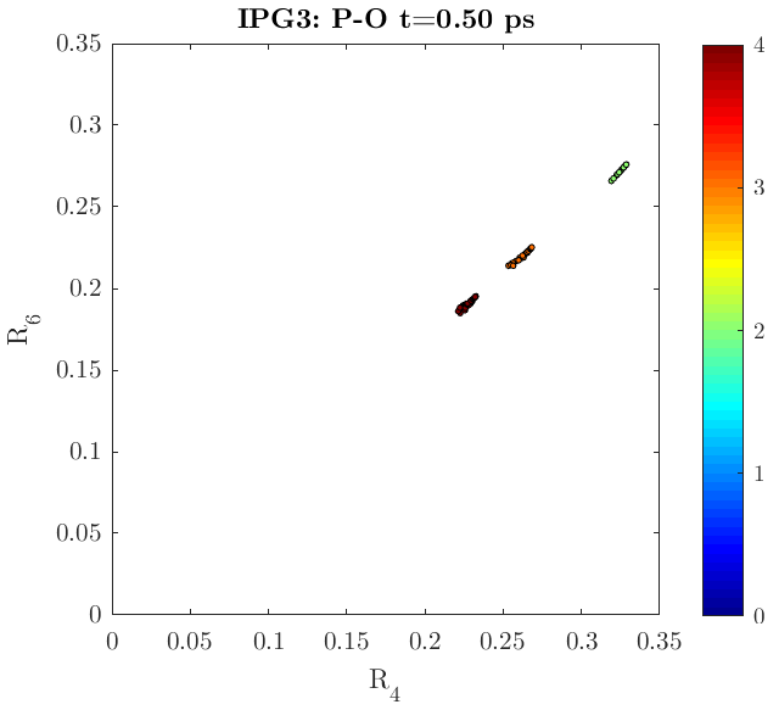

Figure 7.26: $R_6(R_4)$ plot of the P atoms of the IPG3 glass at t = 0.50 ps, highlighting the coordination number, as indicated in the colourbar next to the plots.

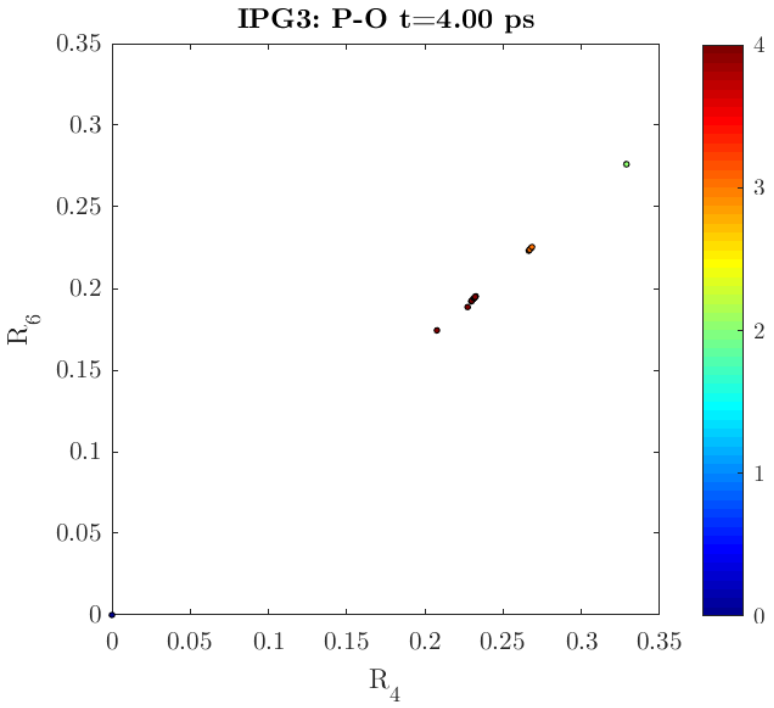

Figure 7.27: $R_6(R_4)$ plot of the P atoms of the IPG3 glass in the final damaged structure, highlighting the coordination number, as indicated in the colourbar next to the plots.

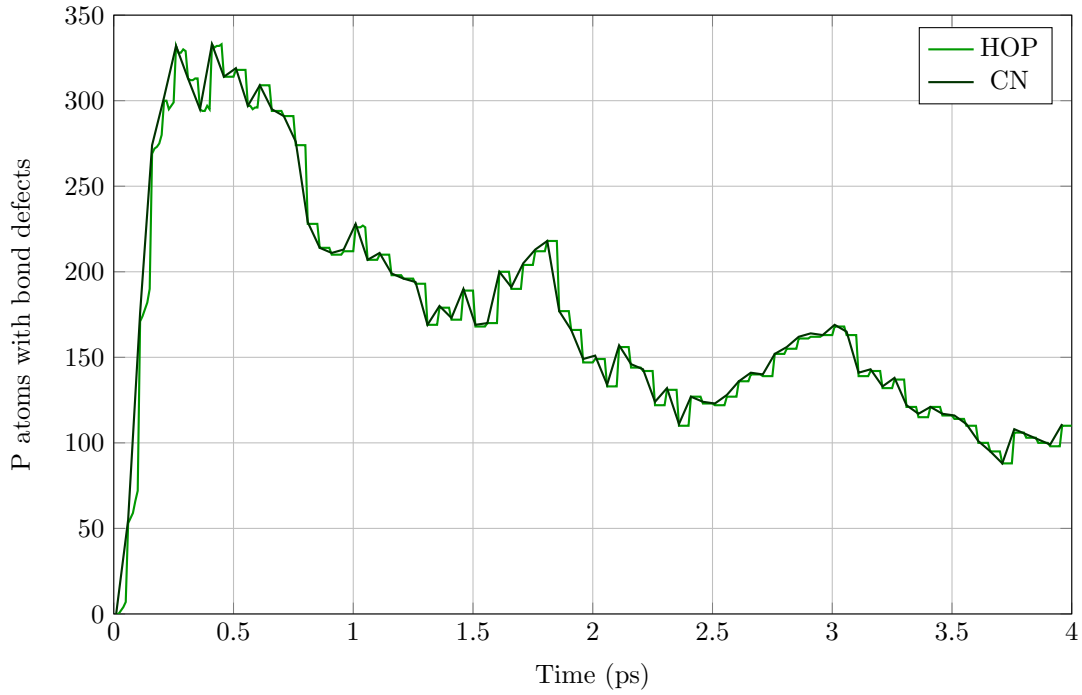

Figure 7.28: Number of phosphorus atoms of the IPG3 glass identified with bond defects using the partial Hermite order parameters method.

Table 7.4: The number of oxygen atoms with different coordination number in the three structures.

	Coordination number			
Structure	1	2	3	4
IPG1	8088	257808	35424	1080
IPG2	14688	283824	9936	0
IPG3	49788	262332	2808	0

7.5 Topological description of the redox states of the irradiated IPG1 glass

Although iron atoms are not directly bonded with oxygen atoms, partial Steinhardt order parameters and/or Hermite order parameters can be used to explore qualitatively the transition of both Fe^{2+} and Fe^{3+} atoms between their possible states during the creation of the damage cascade. This method is demonstrated analytically for the IPG1 glass (which contains both Fe^{2+} and Fe^{3+}) ions using Steinhardt order parameters. For the iron species of the undamaged iron phosphate glass structures have various numbers of closest oxygen neighbours, making it difficult to determine the number of damaged bonds from the $Q_6(Q_4)$ plots. For example, as shown in Fig. 7.29, Fe^{2+} with different numbers of closest oxygen neighbours are mixed in the $Q_6(Q_4)$ for both the initial undamaged structure and the final damaged configuration. For simplicity, an iron atom with n closest oxygen neighbours will be referred to have a coordination number equal to n or n-coordinated, despite the absence of actual bonds between iron and oxygen atoms. To distinguish the different coordination numbers, a roman subscript will be used. For example the 3-coordinated Fe^{2+} atoms will be referred as Fe^{2+}_{III}

As in the case of the B-O bonds of the SBN12 and SBN14 borosilicate glasses, atoms of the same species can be separated into groups, according to their coordination number in the initial undamaged structure. For each stage of the radiation damage simulation, Q_6 is plotted against Q_4 for the Fe^{2+}-O, and Fe^{3+}-O pairs and for all the possible coordination numbers.

For the IPG1 glass, the initial coordination number of the Fe^{2+} species varies between 3 and 6, for the Fe^{3+} between 4 and 6. As the damage proceeds, several Fe^{2+}-O, Fe^{3+}-O are broken and the coordination numbers are between 0 and 6 for both iron states. In Figs. 7.30-7.41, the $Q_6(Q_4)$ plots for the Fe^{2+} atoms for the initial coordination numbers 3, 4, 5 and 6 and for t = 0.00 ps, t = 0.50 ps - where according to the defect counting method the maximum number of displaced atoms is observed - and t = 4.00 ps.

Fe^{2+} atoms: The originally Fe^{2+}_{III} atoms are concentrated in three different regions corresponding to three different angular geometries (Fig. 7.30). At t = 0.50 ps, only a few of the originally Fe^{2+}_{III} atoms have lower coordination. A large number of atoms are transformed into Fe^{2+}_{IV} atoms and very few of them 5-coordinated (Fig. 7.31). The distribution of the data points for all the coordination numbers suggests a great variety in the relative angular position of the oxygen atoms around the reference Fe^{2+} atoms. The plots also suggest that all the atoms belonging in one of the initial three geometries around point $(0.66, 0.52)$ are transformed into either Fe^{2+}_{III} atoms with

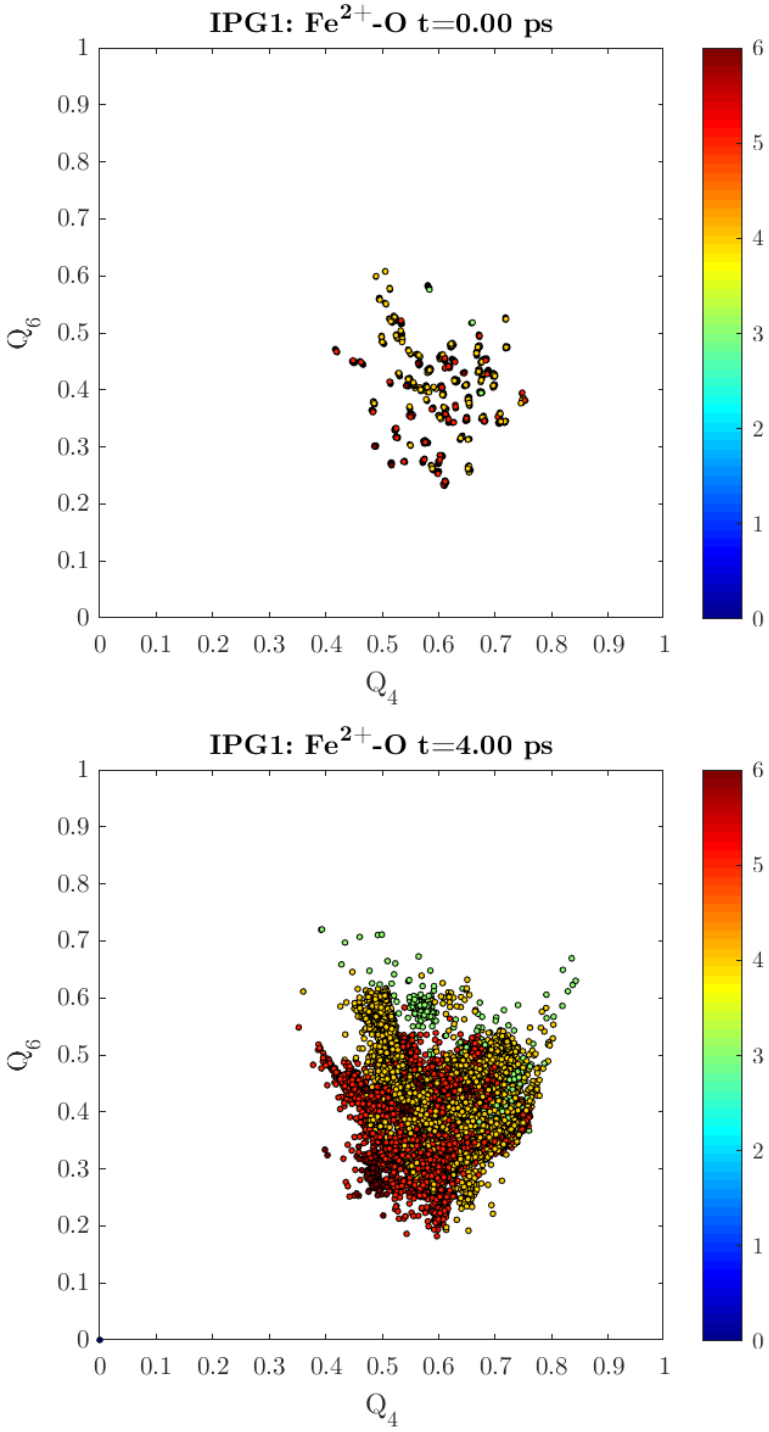

Figure 7.29: $Q_6(Q_4)$ plots of the undamaged (top) and the damaged (bottom) IPG1 glass structure. The colourbar indicates the coordination number of Fe^{2+} atoms.

different geometries, or into Fe^{2+} with different coordination number. This can be explained if the free energy minimum corresponding to the specific geometry is not very deep and it favours either the capture of an additional oxygen or the displacement of the oxygen atoms to form other

possible arrangements. In the final structure (Fig. 7.32), there are no atoms with coordination number lower than 3. However there is a large number of Fe^{2+}_{IV} atoms mainly concentrated in three regions. The majority of the Fe^{2+}_{III} atoms that are transformed into 4-coordinated are found around point $(0.7, 0.5)$. However, a large number of those atoms are still dispersed away from this region suggesting an arbitrary angular distribution of oxygen atoms. Also, some of the 3-coordinated atoms belonging to the geometry around point $(0.66, 0.52)$ are recovered and only a few are distributed away from the initial 3 regions, suggesting a recovery of the geometry of the Fe^{2+}_{III} atoms.

Fe^{2+} atoms that were initially 4-coordinated (Fig. 7.33) are dispersed into a large number of data points in the $Q_6(Q_4)$ plots, that are characteristic of the different geometries of the non-bonded $Fe^{2+}O_4$ units. For t = 0.50 ps (Fig. 7.34), several atoms receive coordination numbers different from 4 and so they are associated with a transformation between different coordination numbers. Most of the defected atoms seem to be transformed into Fe^{2+}_{V} and Fe^{2+}_{III} and a smaller number show coordination numbers lower than 3. The angular distribution of oxygen atoms around the reference iron particle shows large variety. In the final structure (Fig. 7.35), only atoms with coordination numbers 0, 3, 4, 5 and 6 are found. The geometry of Fe^{2+}_{IV} atoms is extended around the data points corresponding to the initial structure. It is also observed, that 3-coordinated atoms resulted from 4-coordinated atoms are found away from the regions defined by the originally Fe^{2+}_{III} atoms for both t = 0.50 ps and t = 4.00 ps and consequently they have different geometries from the originally Fe^{2+}_{III} atoms.

Initially 5-coordinated Fe^{2+} atoms behave in a similar manner (Figs. 7.36-7.38). As the damage

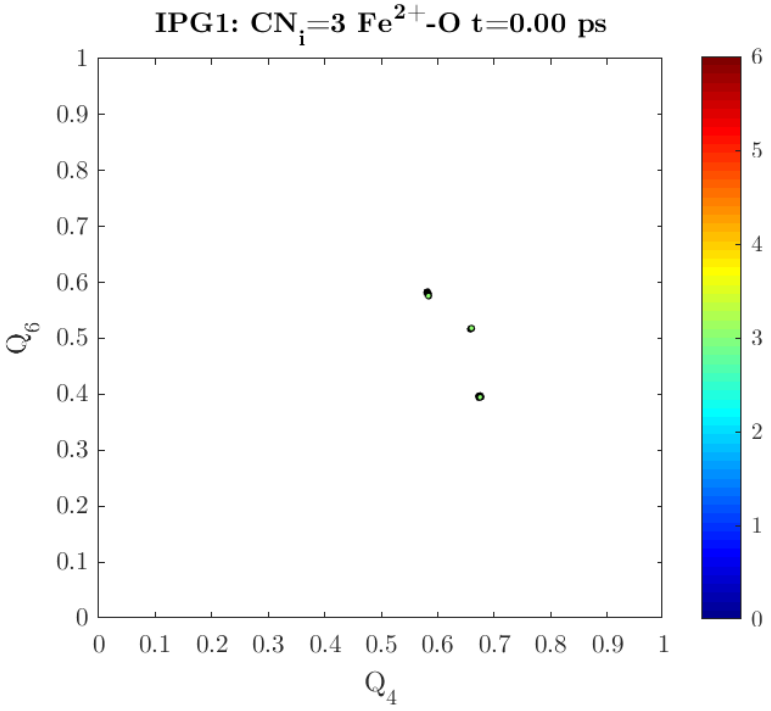

Figure 7.30: $Q_6(Q_4)$ plot of the Fe^{2+} atoms of the IPG1 glass with initial coordination number 3 at t = 0.00 ps. The colourbar indicates the coordination number of Fe^{2+} at the specific time.

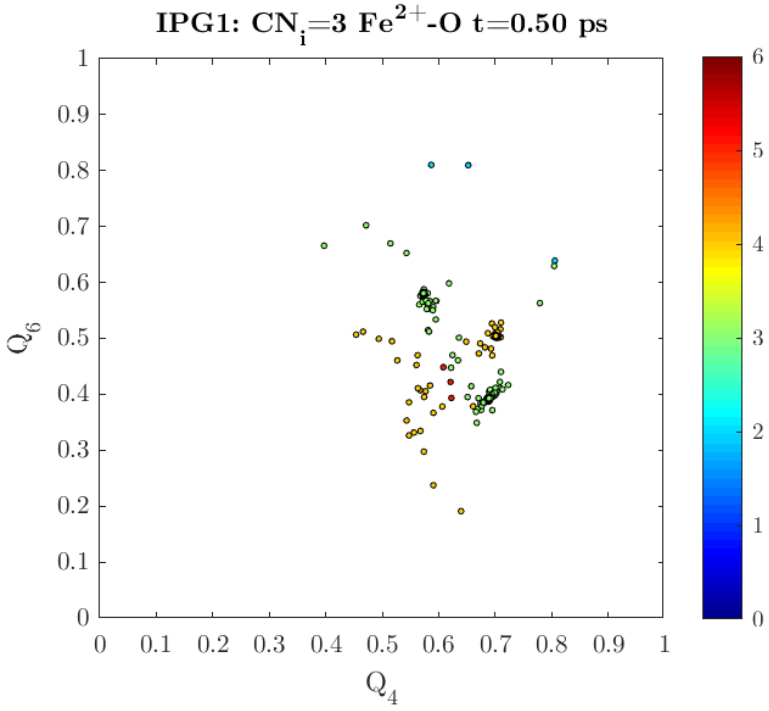

Figure 7.31: $Q_6(Q_4)$ plot of the Fe^{2+} atoms of the IPG1 glass with initial coordination number 3 at t = 0.50 ps. The colourbar indicates the coordination number of Fe^{2+} at the specific time.

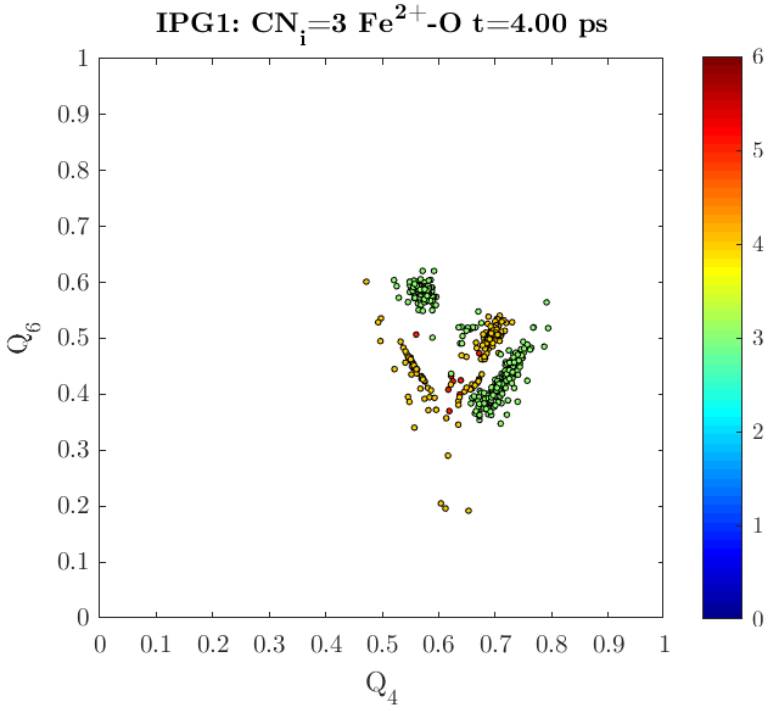

Figure 7.32: $Q_6(Q_4)$ plot of the Fe^{2+} atoms of the IPG1 glass with initial coordination number 3 at t = 4.00 ps. The colourbar indicates the coordination number of Fe^{2+} at the specific time.

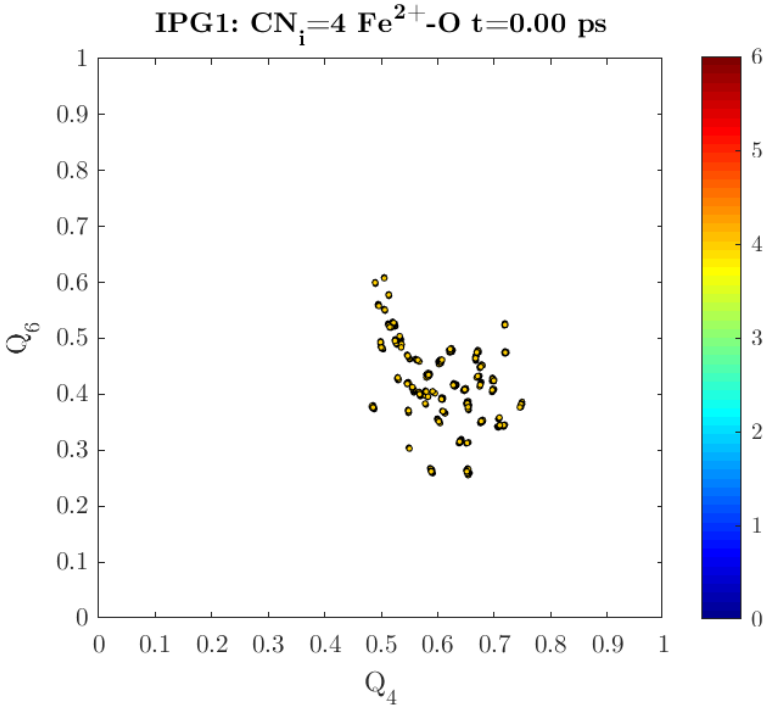

Figure 7.33: $Q_6(Q_4)$ plot of the Fe^{2+} atoms of the IPG1 glass with initial coordination number 4 at t = 0.00 ps. The colourbar indicates the coordination number of Fe^{2+} at the specific time.

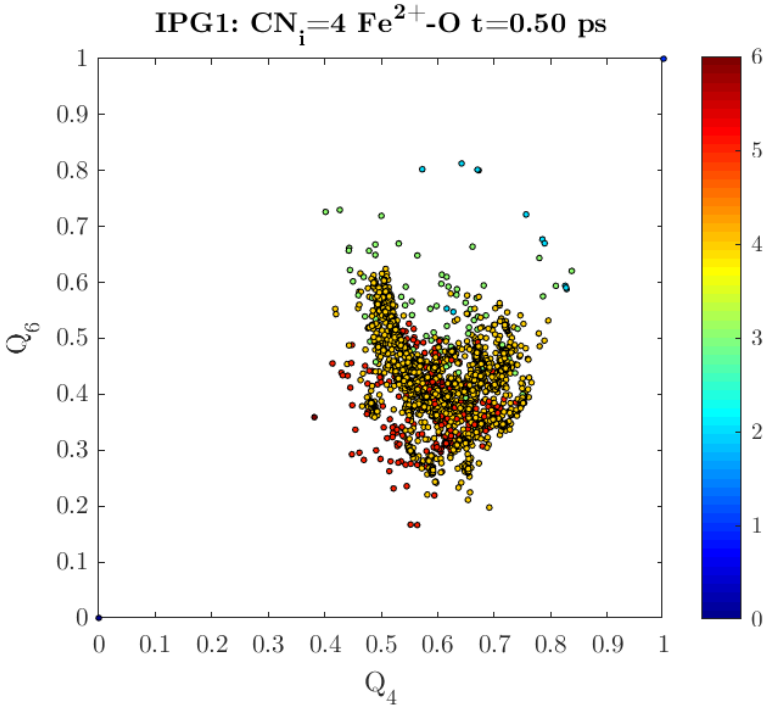

Figure 7.34: $Q_6(Q_4)$ plot of the Fe^{2+} atoms of the IPG1 glass with initial coordination number 4 at t = 0.50 ps. The colourbar indicates the coordination number of Fe^{2+} at the specific time.

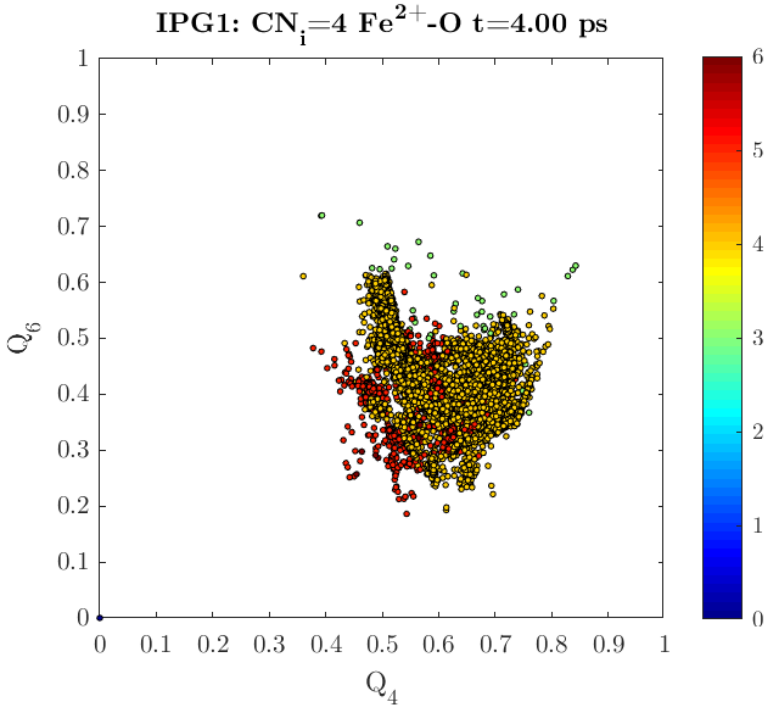

Figure 7.35: $Q_6(Q_4)$ plot of the Fe^{2+} atoms of the IPG1 glass with initial coordination number 4 at t = 4.00 ps. The colourbar indicates the coordination number of Fe^{2+} at the specific time.

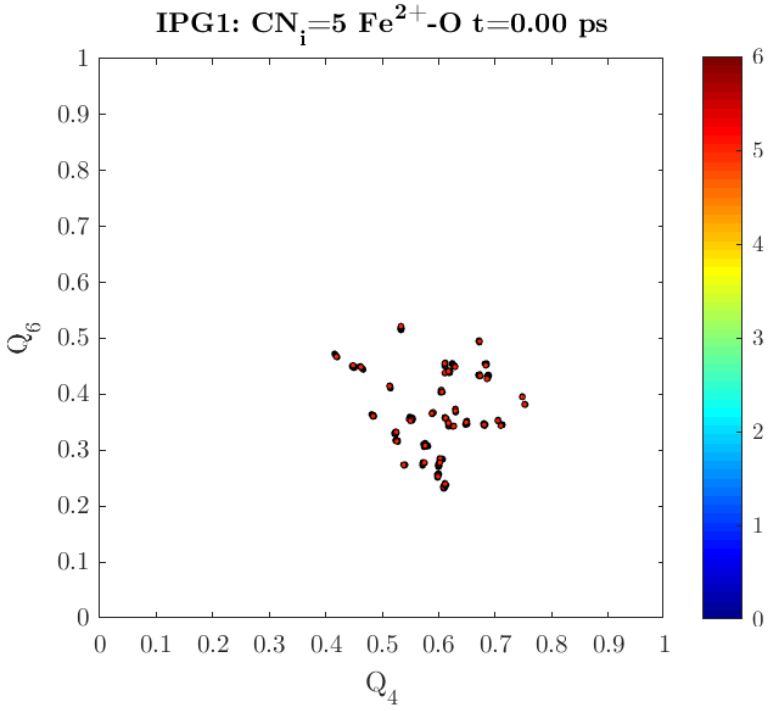

Figure 7.36: $Q_6(Q_4)$ plot of the Fe^{2+} atoms of the IPG1 glass with coordination number 5 at t = 0.00 ps. The colourbar indicates the coordination number of Fe^{2+} at the specific time.

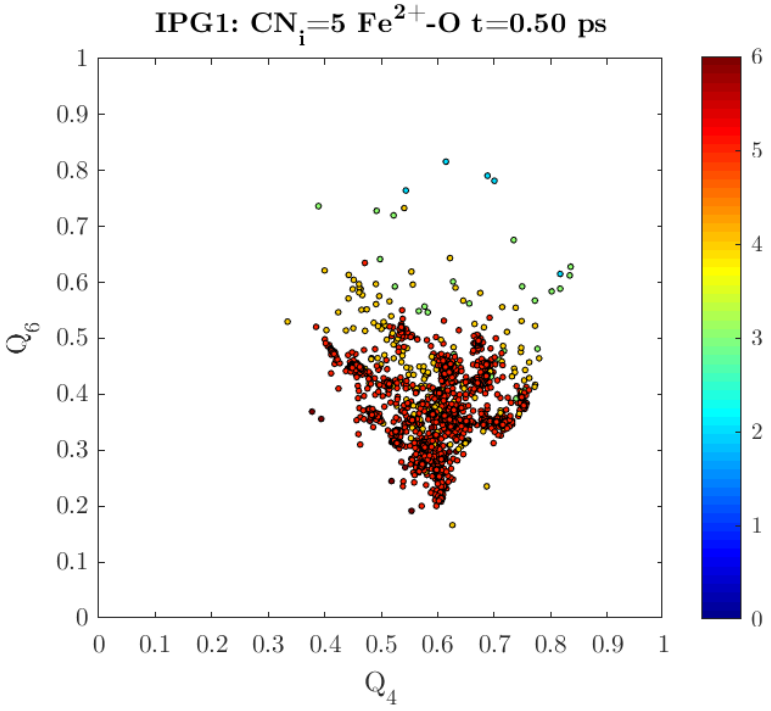

Figure 7.37: $Q_6(Q_4)$ plot of the Fe^{2+} atoms of the IPG1 glass with initial coordination number 5 at t = 0.50 ps. The colourbar indicates the coordination number of Fe^{2+} at the specific time.

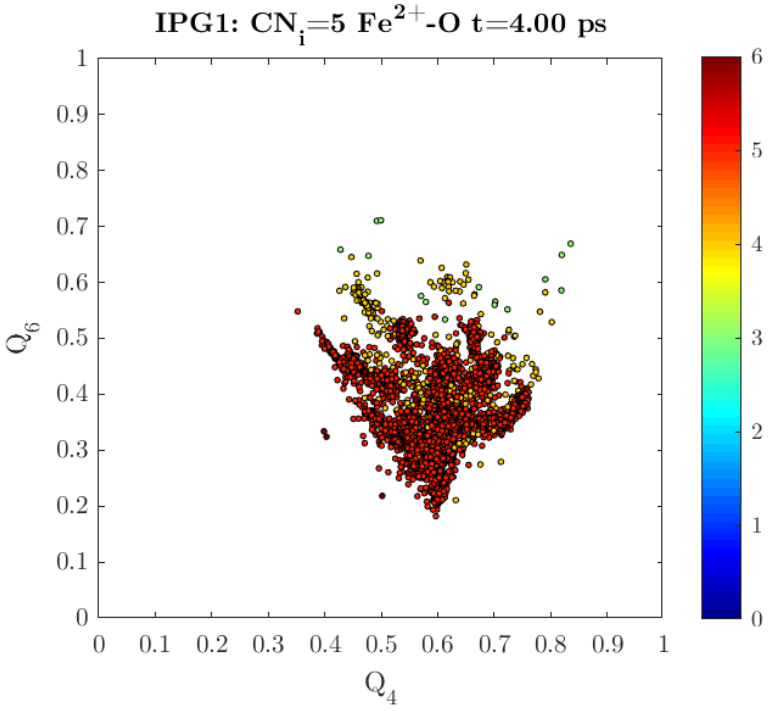

Figure 7.38: $Q_6(Q_4)$ plot of the Fe^{2+} atoms of the IPG1 glass with initial coordination number 5 at t = 4.00 ps. The colourbar indicates the coordination number of Fe^{2+} at the specific time.

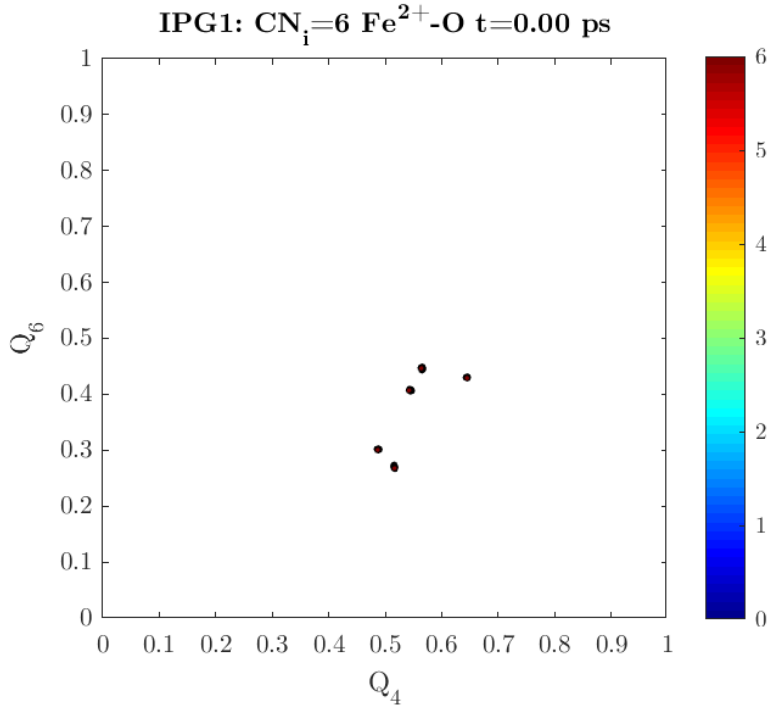

Figure 7.39: $Q_6(Q_4)$ plot of the Fe^{2+} atoms of the IPG1 glass with initial coordination number 6 at t = 0.00 ps. The colourbar indicates the coordination number of Fe^{2+} at the specific time.

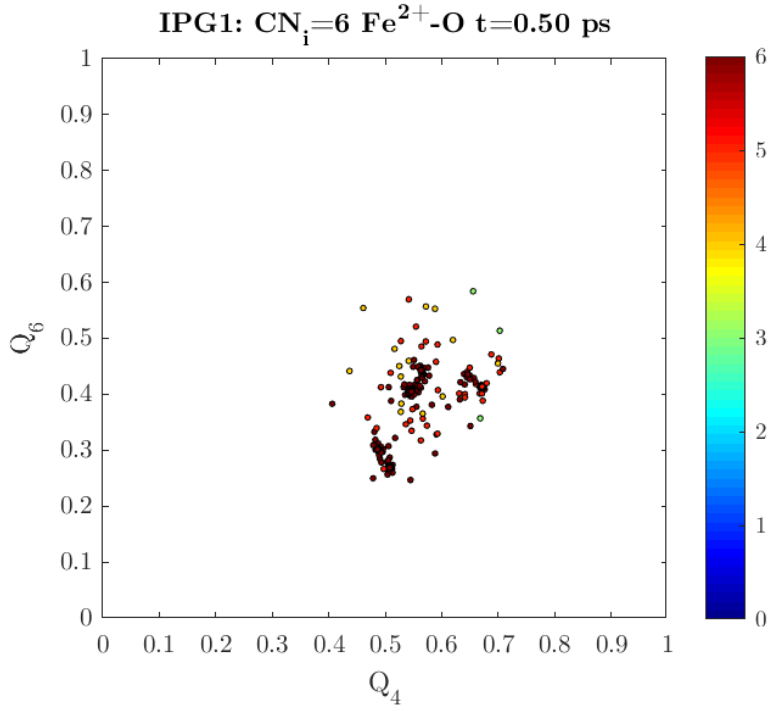

Figure 7.40: $Q_6(Q_4)$ plot of the Fe^{2+} atoms of the IPG1 glass with initial coordination number 6 at t = 0.50 ps. The colourbar indicates the coordination number of Fe^{2+} at the specific time.

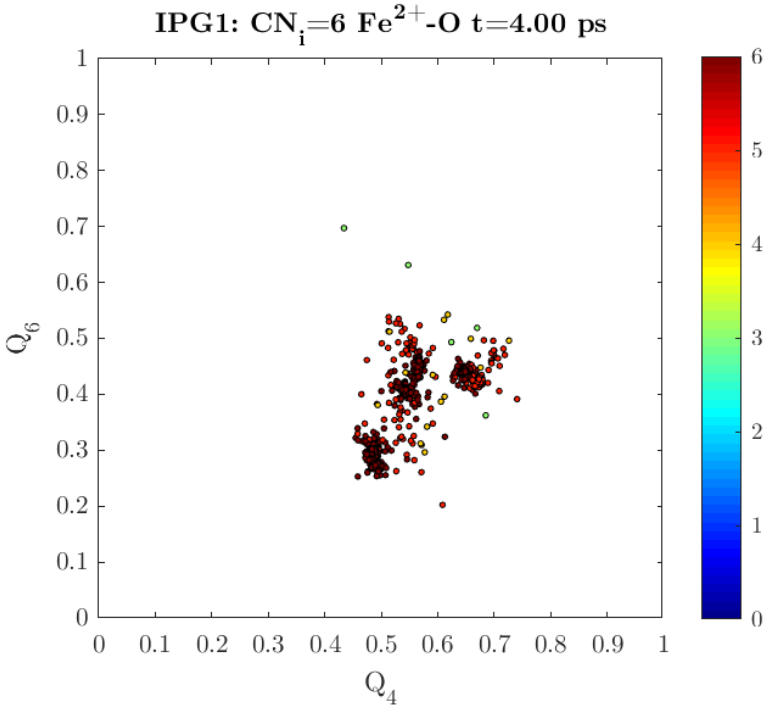

Figure 7.41: $Q_6(Q_4)$ plot of the Fe^{2+} atoms of the IPG1 glass with initial coordination number 6 at t = 4.00 ps. The colourbar indicates the coordination number of Fe^{2+} at the specific time.

progresses, several atoms are transformed to Fe^{2+}_{III} and Fe^{2+}_{IV} and only a few of them have a coordination number equal to 2. Finally, Fe^{2+} atoms with coordination number 6 in the undamaged structure, are initially found in 5 different groups representing 5 different geometries of non-bonded $Fe^{2+}O_6$ units (Fig. 7.39). Radiation damage results into transforming several 6-coordinated atoms into the lower coordinated atoms Fe^{2+}_{IV} and Fe^{2+}_{V}. This behaviour is observed for both the mid-stage of the damage process (Fig. 7.40) as well as in the final structure (Fig. 7.41).

Fe^{3+} atoms: In general, Fe^{3+} atoms behave in a similar manner to the Fe^{2+} atoms. Originally 4- and 5-coordinated Fe^{3+} show various geometries reflected in the large number of groups identified in the $Q_6(Q_4)$ plots (Figs. 7.42 and 7.45), while the Fe^{3+}_{VI} atoms show a single geometry (Fig. 7.48).

At the maximum of the damage, at t = 0.50 ps, a number of Fe^{3+}_{IV} atoms are transformed into Fe^{3+}_{V} (Fig. 7.43) and vice versa (Fig. 7.46) while some 6-coordinated atoms are transformed in Fe^{3+}_{V}. Several Fe^{3+}_{IV} and less Fe^{2+}_{V} atoms are found as Fe^{2+}_{II} and Fe^{3+}_{III}. Additionally, some Fe^{3+}_{V} atoms are found at point $(0,0)$ suggesting that the oxygen neighbours are at large distance from these atoms.

However, at the end of the simulation, at t = 4.00 ps (Figs. 7.44, 7.47 and 7.50), although several Fe^{3+}_{IV} and Fe^{2+}_{VI} atoms are transformed into Fe^{3+}_{V} and via versa, there are actually no defected Fe^{3+} atoms with coordination number lower than 4, except only a few Fe^{3+}_{V} atoms found at point $(0,0)$.

To summarise, it is clear that during the creation of the damage cascade, the majority of the Fe^{3+} and Fe^{3+} atoms are transformed between their possible coordination numbers. The local environment of the iron atoms in terms of the angular distribution of the closest oxygen neighbours

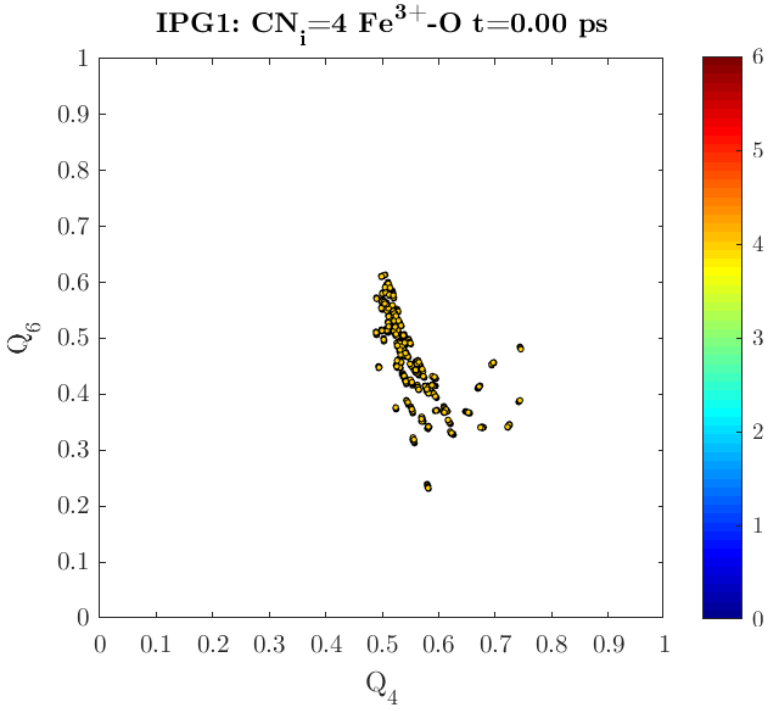

Figure 7.42: $Q_6(Q_4)$ plot of the Fe^{3+} atoms of the IPG1 glass with initial coordination number 4 at t = 0.00 ps. The colourbar indicates the coordination number of Fe^{3+} at the specific time.

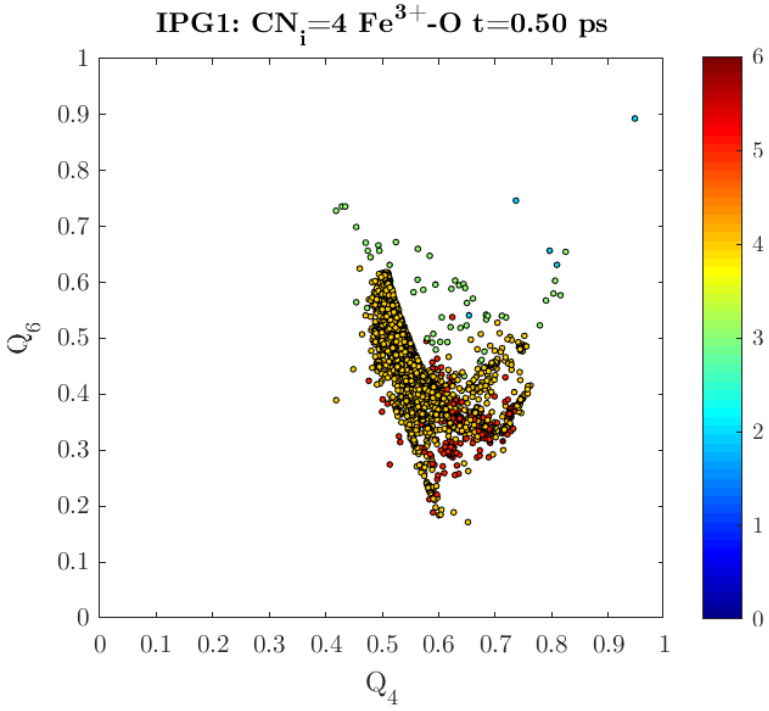

Figure 7.43: $Q_6(Q_4)$ plot of the Fe^{3+} atoms of the IPG1 glass with initial coordination number 4 at t = 0.50 ps. The colourbar indicates the coordination number of Fe^{3+} at the specific time.

varies significantly as a result of the impact event. However, at the end of the simulation, almost no atoms are found with coordination numbers lower than 3 and 4 respectively and consequently it can be argued that the regions around iron atoms are strongly recovered. The qualitative results for the Fe^{3+} atoms of the IPG2 and IPG3 glass structures are almost identical to those of the IPG1, revealing similar transitions between the different possible coordination numbers.

It would be possible to perform a similar qualitative analysis using the Hermite polynomials. However, the $R_6(R_4)$ plots will provide information regarding the number of closest oxygen neighbours - which is already extracted using Steinhardt order parameters - and the average $Fe^{2+/3+}-O$ distance which is of limited interest since there are no actual bonds between iron and oxygen atoms and consequently this distance does not correspond to an actual bond length.

7.6 Conclusions

Radiation damage simulations were performed on three different iron phosphate glass models, designated as IPG1, IPG2 and IPG3 (Table 7.1). For these structures the only existing bonds are between phosphorus and oxygen atoms. Steinhardt order and Hermite order parameters were used to estimate the number of phosphorus atoms that are associated with at least one P-O bond defect. The results show that at the maximum damage state the percentage of defect phosphorus atoms is 0.25%, 0.33% and 0.30% respectively. By the end of the simulation, the respective percentages reduced to abut 0.075%, 0.23% and 0.095% suggesting a high level of tolerance to radiation damage. By these means it can be argued that IPG1 is the most tolerant structure. For the IPG1 and IPG3 glasses, these numbers are slightly higher than the percentage of displaced phosphorus atoms, as calculated by Jolley et. al. [13], while for the IPG2 glass they are almost double. This suggests that the number of displaced atoms is not a reliable way to estimate the extent of radiation damage in terms of defect atoms. The number of bond-defected P atoms calculated using Hermite order parameters method (Figs. 7.20, 7.20 and 7.20) are extremely close to the respective number calculated using Steinhardt order parameters, enhancing the reliability of the two methods.

In terms of the angular distribution of oxygen atoms neighbouring with phosphorus atoms, Steinhardt order parameters revealed that in an undamaged iron phosphate structure, the PO_4 units form tetrahedra with very similar geometry. A cascade event however, apart from creating defect P atoms, alters the geometry of these tetrahedra and the relative positions of the oxygen atoms surrounding the reference phosphorus atoms show a wider range of values. This effect is weaker for the IPG2 glass which on the contrary exhibits the highest percentage of defected phosphorus atoms. Hermite order parameters however suggest that although the undamaged structures have very consistent P-O bond lengths, the irradiated IPG2 glass is associated with a wider range of average bond length values in comparison with the other two structures. It can be argued that a radiation damage event in the IPG1 and IPG3 glasses mainly affects the O-P-O angles while in the IPG2 glass results in variations in the P-O bond lengths.

In addition to the above, Steinhardt order parameters were used to explore the redox states of the iron atoms of the IPG1 glass. The results show that in the initial structure, both Fe^{2+} and Fe^{3+} atoms are found with various numbers of closest non-bonded oxygen neighbours. For Fe^{2+} the coordination number varies between 3 and 6 while for Fe^{3+} it varies between 4 and 6. The geometries of these arrangements have great variety. However, the data points on the $Q_6(Q_4)$

plots corresponding to the iron atoms are grouped into small and well defined areas, suggesting that these geometries are not arbitrary. As the damage progresses, the number of closest oxygen neighbours alters significantly, suggesting a strong modification of the network of the structure. Additionally, the well defined areas corresponding to the various relative angular positions of the closest neighbouring oxygen atoms are extended to a high degree. This suggest that the radiation damage event results in the modification of the network in a way that several oxygen atoms occupy arbitrary positions around iron atoms.

It is important to notice that primitive ring statistics analysis in the three iron phosphate glass structures revealed the total absence of primitive rings. This can only be explained by the fact that the vast majority of oxygen atoms in the structures appear to have a coordination number equal to two, which is ideal to form P-O chains but at the same time prohibits the formation of rings. Although a number of 3-coordinated oxygen atoms exist in the structures, the simultaneous existence of oxygen atoms with coordination number equal to 1 can lead to endpoints in the chains which also work against the formation of rings. This result is in-line with experimental observations of the phosphate glasses, according to which the large number of non-bridging oxygens prevents the formation of rings and instead, the glass network is formed by PO_4 chains [11].

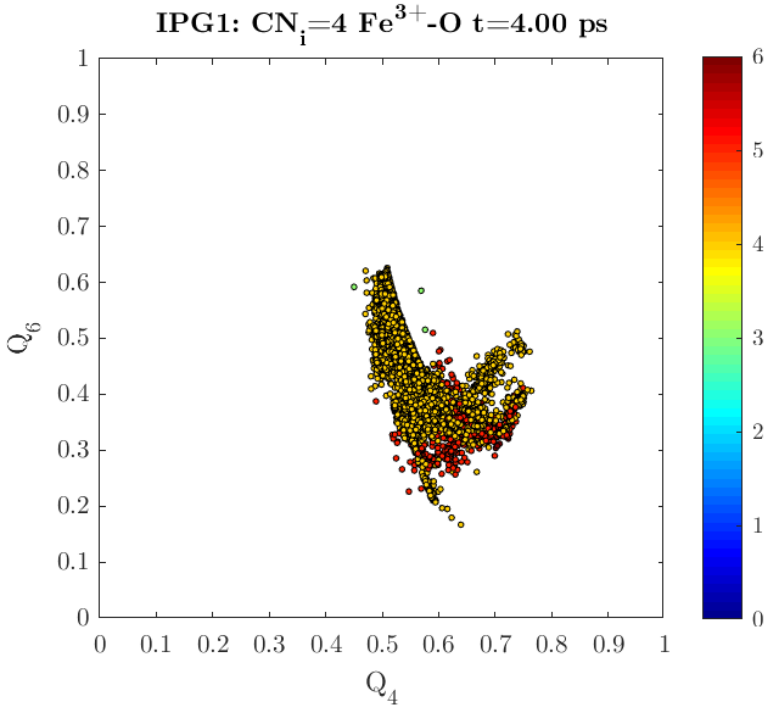

Figure 7.44: $Q_6(Q_4)$ plot of the Fe^{3+} atoms of the IPG1 glass with initial coordination number 4 in the final damaged structure. The colourbar indicates the coordination number of Fe^{3+} at the specific time.

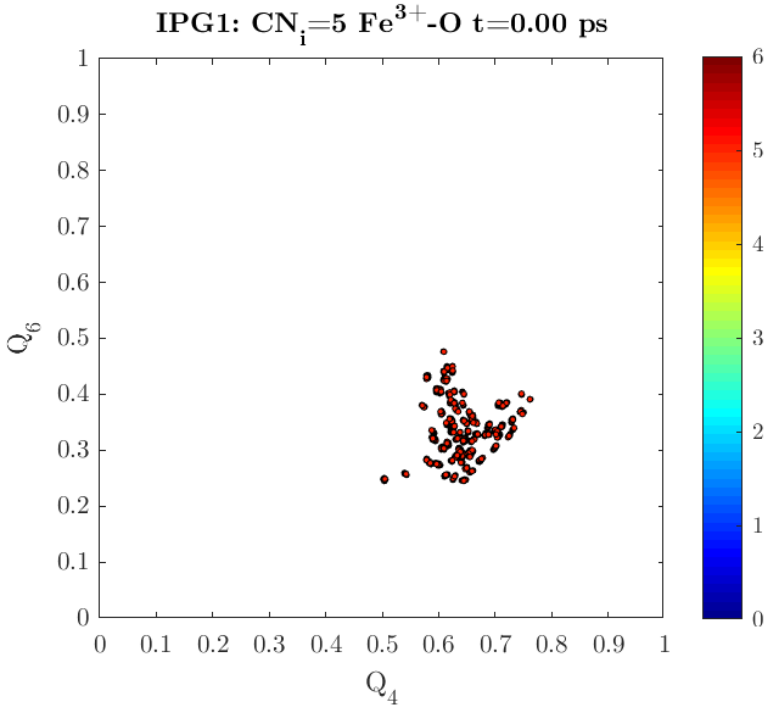

Figure 7.45: $Q_6(Q_4)$ plot of the Fe^{3+} atoms of the IPG1 glass with coordination number 5 at t = 0.00 ps. The colourbar indicates the coordination number of Fe^{3+} at the specific time.

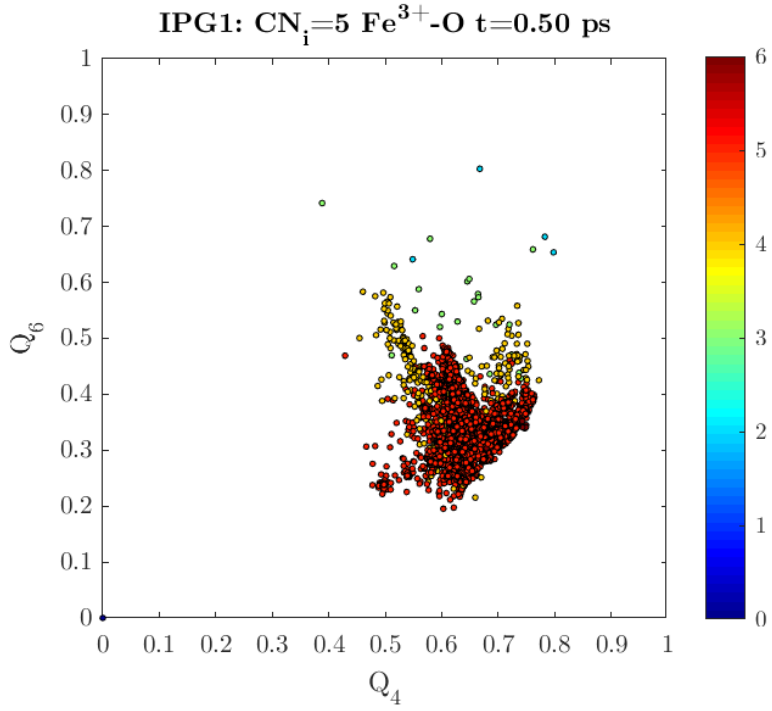

Figure 7.46: $Q_6(Q_4)$ plot of the Fe^{3+} atoms of the IPG1 glass with initial coordination number 5 at t = 0.50 ps. The colourbar indicates the coordination number of Fe^{3+} at the specific time.

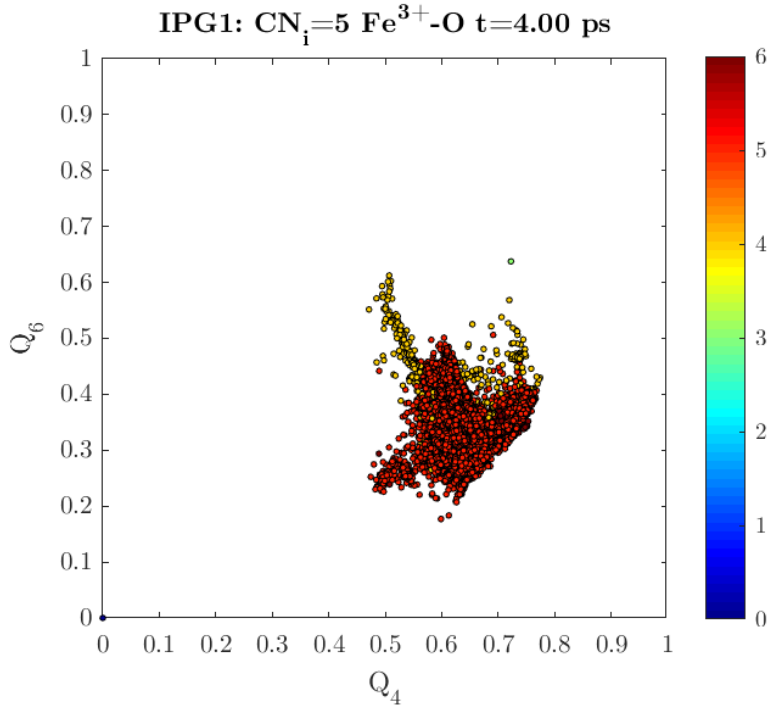

Figure 7.47: $Q_6(Q_4)$ plot of the Fe^{3+} atoms of the IPG1 glass with initial coordination number 5 in the final damaged structure. The colourbar indicates the coordination number of Fe^{3+} at the specific time.

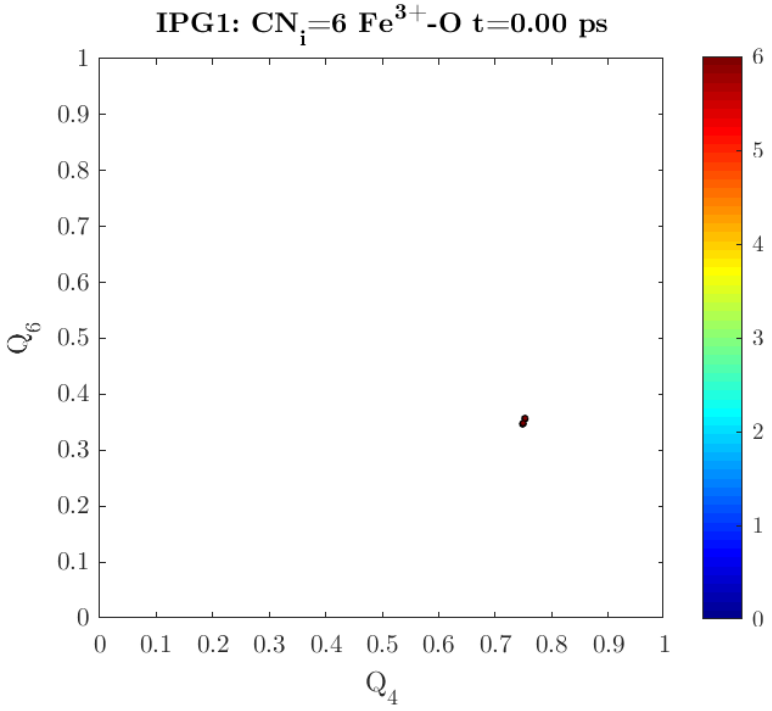

Figure 7.48: $Q_6(Q_4)$ plot of the Fe^{3+} atoms of the IPG1 glass with initial coordination number 6 at t = 0.00 ps. The colourbar indicates the coordination number of Fe^{3+} at the specific time.

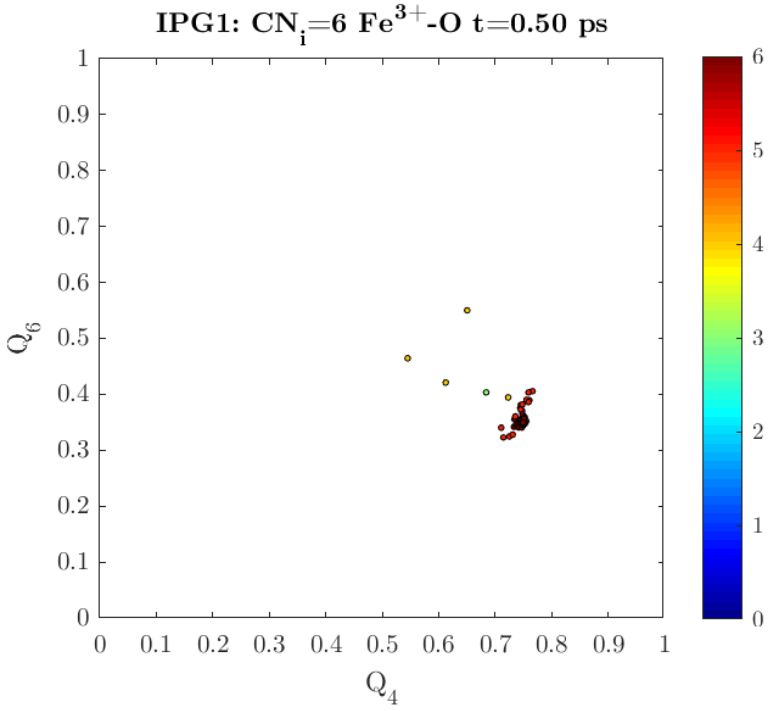

Figure 7.49: $Q_6(Q_4)$ plot of the Fe^{3+} atoms of the IPG1 glass with initial coordination number 6 at t = 0.50 ps. The colourbar indicates the coordination number of Fe^{3+} at the specific time.

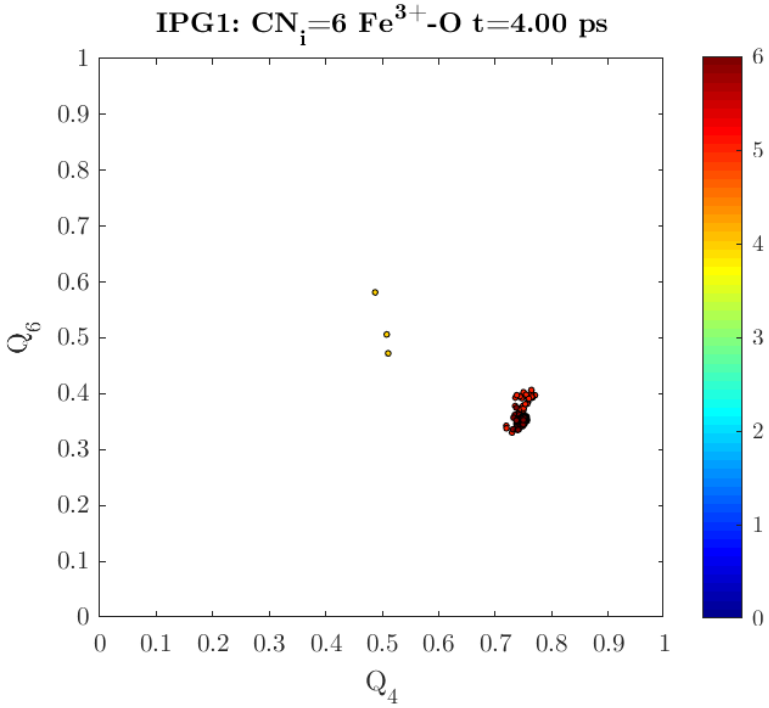

Figure 7.50: $Q_6(Q_4)$ plot of the Fe^{3+} atoms of the IPG1 glass with initial coordination number 6 in the final damaged structure. The colourbar indicates the coordination number of Fe^{3+} at the specific time.

Chapter 8

Conclusions and proposed further work

8.1 Conclusions

The work presented in this thesis is part of the DREAM II project, aiming to create computer models of irradiated borosilicate and iron phosphate glasses, that will assist the efforts towards the development of reliable and durable vitrified wasteforms for the immobilisation of High Level Waste. The work package presented here aimed to investigate the radiation damage effects in irradiated computer models of borosilicate and iron phosphate glasses, by using existing and novel topological methods.

Our approach involved the development of novel topological methods based on modified sets of Steinhardt order parameters and the Hermite order parameters introduced in this work. The development of the new methods was achieved using a computer model of an irradiated zircon crystal, generated using molecular dynamics simulations. The molecular dynamics simulations allow the study of materials from a dynamic perspective in relatively short time and extract information regarding the structural changes of a structure under irradiation. Once the methods were developed, they were compared against the traditional Wigner-Seitz method to demonstrate their superiority and emphasise the additional information that can be extracted regarding the dynamic behaviour of a system under irradiation when using a topological approach. The topological methods developed in this work, are expected to provide new insights towards the characterisation of structures and contribute significantly in the scientific literature.

The next step was to apply this topological approach on irradiated borosilicate and iron phosphate glass models, also generated using molecular dynamics simulations. The main contribution of this work is that the usage of the partial Steinhardt and Hermite order parameters provides a new insight regarding the behaviour of the irradiated glasses in terms of bond defect atoms, that was absent from the existing literature. A second method was also developed in this work, based on the species specific Steinhardt and Hermite order parameters. Although this method was able to predict with good accuracy the number of defect particles in the irradiated zircon crystal, it failed to do the same in the irradiated glass structures.

Additional information regarding the behaviour of the glass network was extracted by performing a primitive ring statistics analysis on the irradiated glass models. This method succeeded in providing information regarding the behaviour of the network in the borosilicate glasses, suggesting a strong recovery of the structure. However, it was not possible to do the same in the iron phosphate structures, as no primitive rings were found, something that was expected based on the existing literature [11].

The main discovery from the topological analysis is that the borosilicate and iron phosphate glasses used in this study show great tolerance to irradiation since only a very small fraction of atoms are associated with a bond defect after the recovery of the structure. Actually, this number is much lower compared to the number of defect atoms calculated using the Wigner-Seitz method suggesting that the latter overestimates the damage effects in amorphous materials.

In the following sections we provide an in depth set of conclusions, following the structure of this thesis, and a discussion on future work than could be done, both experimental and computational, to validate the results and further develop the topological methods introduced in this thesis.

8.1.1 Development of topological methods towards the characterisation of radiation damage

The development of the new topological approaches was based on the study of a radiation damaged zircon crystal that was used as a test structure. To create the zircon crystal model, molecular dynamics simulations were performed. The radiation damage cascade was created by assigning a 4 keV excess of kinetic energy to a particle of the system, simulating the primary knocked atom, resulting from the collision with the recoil nuclei of an alpha decay event. The energy of the projectile was relatively high for the size of the structure. However, the purpose of the irradiated zircon crystal model was not to study with accuracy the effects of radiation damage in a zircon crystal. Our purpose was to create an extended damage cascade in the structure that would be easy to quantify and analyse in order to develop new topological methods towards the characterisation of radiation damage effects.

Steinhardt order parameters are well known for providing information regarding the angular distribution of atoms around a reference particle. The standard calculation approach includes all the atoms with a sphere of specific radius, centred on the reference particle. However, when applied to the test system - the zircon crystal - this approach did not prove sufficient to characterise the radiation damage effects in terms of bond defects, since within the sphere can be included atoms that are not bonded with the reference particle. To overcome this discrepancy, two novel approaches were proposed. In the first approach the partial Steinhardt order parameters were calculated only for the bonded atoms surrounding a reference particle, and for each of the neighbouring species separately. In the second approach, the species specific Steinhardt order parameters were calculated for the atoms of the same species A within the first coordination shell of the $g_{A-A}(r)$ radial distribution function.

Using the partial Steinhardt order parameters approach it was possible to determine with good accuracy the number of zirconium and silicon atoms that were associated with at least one bond defect. The results revealed that zircon crystal has a high degree of tolerance to radiation damage especially in the Si-O bonds which seems to be completely recovered. Zr-Si and Zr-O bonds also demonstrate a high degree of recovery with a small number of broken bonds remaining in the system. It was also possible to retrieve qualitative information regarding the angular geometry of the bonded particles around the reference atoms. It was found that the geometry of the non defected SiO_4 and ZrO_8 units is only a little affected by the cascade event. However the low coordinated units resulting from the collision of atoms exhibit a large variety in the angular distribution of oxygen atoms around the reference Zr/Si particles, reflected in the extended areas covered by the

corresponding data points in the $Q_6(Q_4)$ plots. Additionally, during the decay event, several Si-Zr-Si angles are taking values away from the ideal bond angle of 180°. However, at the end of the simulation, the majority of the affected Si-Zr-Si triplets recover to an almost linear conformation.

The species specific Steinhardt order parameters method was proved accurate for the estimation of the number of defect particles resulting from a radiation damage event. For the silicon and zirconium atoms there was a very good agreement with the Wigner-Seitz method. However, for the oxygen atoms, the species specific Steinhardt order parameters method show a good agreement with the Wigner-Seitz method only at the first stages of the simulation, where the damage cascade is created. In the recovery region, our method seems to significantly overestimate the number of defect atoms. However, the species specific Steinhardt order parameters method has the ability to identify and count as defect atoms the antisites, that are not calculated using the DL_POLY 4 inbuilt routine. When calculating the number of defect particles using the Wigner-Seitz method and taking into account the antisites, the results are much closer to those obtained by our method. However, there is still a considerable difference between the two methods that needs to be addressed.

The novel Hermite order parameters were also introduced in this work and developed using the test zircon crystal structure, in order to obtain additional information regarding the radial distribution of the atoms surrounding a reference particle. Two sets of parameters was introduced, the partial Hermite order parameters and the species specific Hermite order parameters calculated in the same way as the respective Steinhardt order parameters. This approach provided details regarding the average first neighbour distance and the bond lengths between the different bonded pairs. When applied to the zircon crystal, Hermite polynomial parameters results for the number of particles associated with bond defects or the number of defect atoms are almost identical to those retrieved using the Steinhardt order parameters method. Hermite polynomial parameters depend only on the distance r between the reference particles and their neighbours, in contrast with Steinhardt order parameters that depend only on the spherical angles θ and ϕ. Since the results obtained using the two methods converge to the same values, it may be argued that they can be used as a cross validating set of methods for the characterization of radiation damage in terms of defect particles. Additional information extracted regarding the average bond length shows that the distance between all the possible pairs is affected by the impact event.

8.1.2 Topological analysis of irradiated borosilicate and iron phosphate glass models

The models of the irradiated borosilicate glass models followed a similar approach to the one for the zircon crystal. The initial stage was to create a random arrangement of the atoms comprising the glass based on a fcc lattice. Then, molecular dynamics simulations were performed to melt the glasses at a high temperature, above the melting point of each glass and then quench them rapidly at room temperature at a rate fast enough to avoid the recrystallisation of the structure. Radiation damage cascades were created using the same method as for the zircon crystal model, using a 1 keV projectile. The models of the iron phosphate glass models were provided by our collaborators at Loughborough University [13].

When the partial Steinhardt and Hermite order parameters methods were applied to the models of the SBN12 and SBN14 borosilicate glasses, in terms of the number of bond-defect particles, the

results were quite similar. Both methods suggest that these glasses demonstrate high tolerance to radiation damage, with the SBN14 performing slightly better. The majority of the damage is located at the B-O bonds. For the SBN14 glass, only 6.4% of the boron atoms are related with bond defects by the end of the simulation while the respective percentage for the SBN12 glass rises to 8.8%. As suggested by Steinhardt order parameters, the angular geometry of the BO_4 tetrahedra converges at all stages of the simulation. Thus, radiation damage does not affect the relative positions of the oxygens bonded to the 4-coordinated boron atoms no matter if they were originally 4-coordinated or created by the transformation of previously 3-coordinated boron atoms. On the other hand, Hermite polynomial parameters reveal that the average B-O bond length of the BO_4 units is affected by the recoil event during the creation of the damage cascade. However, at the end of the simulation, the distribution of data points into the $R_6(R_4)$ plots, corresponding to BO_4 units is very close to the one of the undamaged structure, suggesting a recovery of the B-O distance in these units. For the 3-coordinated boron atoms forming the BO_3 units, the results show the opposite behaviour in comparison with the BO_4 units. During the simulation, the angular distribution of the oxygen neighbours is affected more in comparison with the respective of the BO_4 units, while the radial distribution seems to be affected insignificantly. As for the silica network, while during the simulation it is obvious that several Si-O bonds are broken, at the final recovered structure almost all Si-O bonds are restored, reflecting the high recovery of the silica network within the structures. The geometry of the SiO_4 tetrahedra shows variations in the undamaged structure and is not affected by the displacement of the particles during the creation of the damage cascade. On the other hand, the resulting low coordination silicon atoms appear to have an arbitrary angular and radial distribution of the remaining bonded oxygen neighbours.

For the borosilicate glasses it was also possible to perform a primitive ring statistics analysis to identify the effect of radiation damage in the network of the material. In detail, all the primitive rings of the structure were identified and the number of rings per boron and silicon node as well as the average ring size was calculated for both glasses. For the SBN12 glass, the result suggest that the creation of the damage cascade results in the destruction of a number of the dominant 12- 14 and 16-sized rings accompanied by the formation of higher order rings consisting of 26, 34, 36 and 38 nodes. It is important to note that for the stage of maximum damage, the curves of rings per node forms a distinct peak in the position of the 26-sized rings. At the final structure, the distribution of rings is very close to that of the undamaged structure with slightly decreased number of 14-, 16- and 18-sized rings and an increased number of rings consisting of 10 and 22 nodes. The SBN14 glass behaves in a similar manner. The initial structure is governed by 14-, 16- and 18- sized rings and the number of rings per node demonstrates three characteristic peaks at the positions of the 14-, 18- and 28- sized rings. During the creation of the damage cascade, the number of 18-sized rings is decreased significantly and the peak at the position of the 28-sized rings is diminished. There is a small but observable decrease in the number of 10-, 12- and 14- sized rings. Similarly to the SBN12, a small increase of the 26-, 34- and 38- sized rings is also observed. At the end of the simulation, rings with sizes 10 to 14 are completely restored. 18-sized rings also exhibit a degree of recovery accompanied by an increase of number of 28-sized rings. Additionally, the calculation of the average ring size for both structures revealed that for the SBN12 glass, radiation damage favours the creation of smaller rings while the average ring size slightly increases for the SBN14.

For the iron phosphate structures, a similar analysis was performed. The results extracted using the partial Steinhardt and Hermite order parameters methods revealed that all three iron phosphate glass structures (Table 7.1) show high degree of resistance to radiation damage, as by the end of the simulation, only 0.25%, 0.33% and 0.30% pf the phosphorus atoms of structures IPG1, IPG2 and IPG3 respectively are related to P-O defects. Steinhardt order parameters and Hermite polynomial parameters also suggest that the geometry of the PO_4 units is very consistent in the undamaged structure. However, during the creation of a damage cascade, both the angular and radial distribution of the oxygen neighbours bonded to the phosphorus atoms is slightly altered. For the IPG1 and IPG3 glasses it appears that the P-O bond lengths are not affected as much as the relative position of the neighbouring oxygen atoms, while for the IPG2 glass the effect is stronger for the bond lengths. By the end of the simulation, the distribution of data points in the $Q_6(Q_4)$ and $R_6(R_4)$ plots, corresponding to the 4-coordinated phosphorus atoms is quite close to the one of the initial undamaged structure, suggesting a recovery of both the bond lengths and O-P-O bond angles.

Steinhardt order parameters were also used to explore the effect of the radiation damage on the angular distribution of oxygen atoms around iron atoms of the structure - although no bond between oxygen and iron atoms exists. The analysis was performed for the IPG1 glass consisting of both Fe^{2+} and Fe^{3+} iron redox states. It was found that Fe^{2+} atoms can be surrounded by 3 to 6 closest oxygen atoms while the Fe^{3+} can be surrounded by 4 to 6. The angular distribution of the oxygen atoms around the reference iron atoms exhibits a great variety for the initial undamaged structure. However, regardless of the number of closest oxygen atoms, iron atoms appear to form groups of similar geometries. When the recoil event occurs, this classification appears to diminish and the distribution of oxygen atoms extends to a level that can be regarded as arbitrary, suggesting a strong modification of the network of the structures.

It is important to note that when attempting to apply the primitive rings statistics analysis in the iron phosphate glasses, it was found that no primitive rings with size up to 40 exists in the structure, mainly due to the high number of low coordinated non-bridging oxygen atoms, with coordination number equal to 1, that act as end points in the P-O chains and prevent the formation of rings.

The second topological method developed based on the species specific Steinhardt and Hermite order parameters was also applied on the glass models used in this study. However, none of the parameters that were calculated ($Q_0 - Q_{10}$ and $R_0 - R_{16}$) showed a desired damaged like behaviour and consequently it was impossible to correlate the number of particles with a parameter value greater than the average with the number of defect particles in these systems.

8.2 Further work

8.2.1 Extending the timescales and the system size of the simulations

The simulations performed in this work were in the ps timescale and nm length scale. Although the structural information retrieved by these simulations is important, it is necessary to perform simulations for larger systems at longer timescales. The larger system size will allow us to create simulations using even higher kinetic energy for the impact particle. The simulations of the

borosilicate glasses involved a 1 keV energy projectile, while those for the iron phosphate glasses were performed with a 4 keV impact particle. However, the average kinetic energy of an alpha particle resulting from an α decay is 5 keV, which means that the simulations describe the damage created by relatively low energy α particles. However, the α decay process in real glass wasteforms is expected to produce a large number of high energy α particles, that will create more severe cascades that will probably decrease the tolerance of the wasteforms to radiation damage. Longer time scales will be able to provide a more complete image regarding the cascade evolution and the recovery of the wasteforms after an impact event. For the iron phosphate glasses used in this study, it is clear that the evolution on the number of particles associated with a bond defect was not able to form a plateau (Figs. 7.8, 7.12, 7.16, 7.20, 7.24 and 7.28). Consequently it is not possible to determine with high accuracy the extent of the damage at the recovery region. For this, there are several simulation techniques that can be used, including Kinetic Monte Carlo, Dissipative Particle Dynamics, Temperature Accelerated Dynamics or even Smooth Particle Applied Mechanics.

8.2.2 Multiple projectile simulations

Molecular dynamics simulations performed in this study, assumed that the damage cascade is created by a single projectile. However, in real systems this is not the case, as there can be multiple projectiles affecting a specific area of the structure at a relatively short timescale. To study the damage accumulation in these structures, additional molecular dynamics simulations can be performed following two different approaches. The first is to start a simulation with one projectile particle and then, at a random time within the simulation, create a second projectile or, alternatively, it is possible to generate a series of cascade simulations, using the final damage structures of one simulation as a starting point for the following simulation. The first method will provide information on how the structure of a glass wasteform is affected due to almost simultaneous decay events at a small region, while the second will determine the behaviour under continuous decay events. For these simulations, it is recommended to use large structures to allow the cascades to be created in a larger volume of the material and explore the effects of creating overlapping cascades.

8.2.3 Simulations in various ensembles

The damage cascades in this study were created under the constant volume NVT dynamics. This prevents the systems from changing shape and size during the simulations. However, it is observed experimentally that the glass wasteforms tend to swell under self irradiation. To explore such effects it is necessary to perform simulations using different dynamics. The isobaric-isothermal NPT ensemble can be an alternative as it will allow the system size to change during the simulation. This will be useful for studying isotropic swelling of the structure. For anisotropic swelling, it is necessary to allow the simulation box to change both its volume and shape. A potential approach is to use flexible NPT dynamics, in which the shape of the simulation box is allowed to change during the simulation by allowing the cell angles to be flexible, and not fixed to a specific geometry.

8.2.4 Improvement of the interaction potentials

The glass compositions used in this work were relatively simple and did not correspond to one of the actual glass wasteforms used in the industry. This is because the accurate potentials developed to describe the pair interactions in borosilicate glasses are limited to Si–O, B–O and Na–O interactions, while for the phosphate glasses are limited to the P–O, Fe^{2+}–O, Fe^{3+}–O and O–O interactions. It is important to develop a more complete set of potentials that will be able to describe more interactions - for example for the Li–O, Mg–O and Al–O pairs. That will allow the modelling of borosilicate structures that will be much closer to the experimental in terms of composition. This will give the opportunity to study in great detail the composition effects using computer simulations. Additionally, for the iron phosphate glasses it is important to perform simulations with improved interaction potentials that will take into account the transformation between the redox states of the iron ions during the creation of a radiation damage cascade. The development of such potentials can be performed with ab initio methods such as Density Functional Theory.

8.2.5 Actinide doping simulations

In the existing simulations, it was assumed that a recoil event transferred the kinetic energy of an α particle to an atom of a system that was used as a primary knock atom to create the radiation damage cascade. Additionally, there were no nuclear fusion elements in the structures that can affect the behaviour of the wasteform. It would be beneficial to perform simulations in which the structure would be doped with actinides and the decay event would be simulated with accuracy using an actual recoil nucleus and an α particle that would be responsible for the creation of the damaged region. For this it would be necessary to develop potentials that will be able to describe with accuracy the interaction between the actinides and the glass atoms comprising the wasteform. Performing such simulations will allow the investigation of the effects of various radioactive loads on the behaviour and tolerance of the wasteforms.

8.2.6 Investigation of chain formation in iron phosphate glasses

As discussed previously, the existence of a large number of non-bridging oxygen atoms in the PO_4 tetrahedra of the iron phosphate glass network, prevents the formation of rings and favours the formation of chains. Consequently, it was possible to study the effects of the radiation damage in the phosphorus network of the structures. This could be done by developing an algorithm that will allow the study of chains in an amorphous materials and explore how the length and possibly the shape of the chains is changing during the creation of the radiation damage cascade.

8.2.7 Experimental validation of the computer models

Probably the most important part of the future work that needs to be performed is to validate the results of the molecular dynamics simulations and topological analysis performed in this study using an experimental approach. This can be achieved by applying experimental methods such as X-ray Absorption Spectroscopy (XAS) technique to real glass wasteforms with glass composition as close as possible to the simulated structures. XAS has the ability to determine the local geometric

structure in amorphous solids and liquids. Performing such experiments and analysing the local geometric structure will provide information regarding the local connectivity and network of glass atoms in both the cascade and undamaged areas. These results can be compared to those retrieved from the molecular dynamics simulations and topological analysis of the glass models. A successful experimental validation will place of the proposed topological methods on a solid rock basis and will contribute significantly towards the accurate characterisation of the damage effects in a large variety of wasteforms using computational methods.

Appendix A

Steinhardt order parameters mathematical details

A.1 The effect of the coordination number

A.1.1 Reference particle with one neighbour

In case the reference particle has only one neighbour, first and second kind Steinhardt order parameters are given by

$$\langle Q_{\ell,m}\rangle^{(i)} = Y_\ell^m(\theta,\phi) \qquad \text{and} \qquad Q_\ell^{(i)} = \left[\frac{4\pi}{2\ell+1}\sum_{m=-\ell}^{\ell}|Y_\ell^m(\theta,\phi)|^2\right]^{1/2}. \tag{A.1}$$

Replacing tesseral spherical harmonics, we get

$$Q_\ell^{(i)} = \left[\frac{8\pi}{2\ell+1}\sum_{m=-\ell}^{\ell} c_{\ell,|m|}^2[P_\ell^{|m|}(\cos\theta)]^2\sin^2(|m|\phi) + \frac{4\pi}{2\ell+1}c_{\ell,0}^2[P_\ell^0(\cos\theta)]^2 + \right.$$
$$\left. + \frac{8\pi}{2\ell+1}\sum_{m=1}^{\ell} c_{\ell,m}^2[P_\ell^m(\cos\theta)]^2\cos^2(m\phi)\right]^{1/2}, \tag{A.2}$$

which results to

$$Q_\ell^{(i)} = \sqrt{\frac{4\pi}{2\ell+1}}\left[c_{\ell,0}^2[P_\ell^0(\cos\theta)]^2 + 2\sum_{m=1}^{\ell} c_{\ell,m}^2[P_\ell^m(\cos\theta)]^2\right]^{1/2} \tag{A.3}$$

By substituting associated Legendre polynomials, it can be proven that for all ℓ values and for one neighbour all the second kind Steinhardt order parameters are equal to 1, thus

$$Q_\ell^{(i)}(N_b=1) = \left[\frac{4\pi}{2\ell+1}\sum_{m=-\ell}^{\ell}|Y_\ell^m(\theta,\phi)|^2\right]^{1/2} = 1. \tag{A.4}$$

A.1.2 Reference particle with two or more neighbours

When the reference particle has 2 neighbours, first kind Steinhardt order parameters are given by

$$\langle Q_{\ell,m}\rangle^{(i)} = \frac{1}{2}\left[Y_\ell^m(\theta_1,\phi_1) + Y_\ell^m(\theta_2,\phi_2)\right], \tag{A.5}$$

and so

$$|\langle Q_{\ell,m}\rangle^{(i)}|^2 = \frac{1}{4}\left[|Y_\ell^m(\theta_1,\phi_1)|^2 + |Y_\ell^m(\theta_2,\phi_2)|^2 + 2Y_\ell^m(\theta_1,\phi_1)Y_\ell^m(\theta_2,\phi_2)\right]. \tag{A.6}$$

Thus second kind Steinhardt order parameters are given by

$$Q_\ell^{(i)} = \frac{1}{2}\left[\frac{4\pi}{2\ell+1}\sum_{m=-\ell}^{\ell}|Y_\ell^m(\theta_1,\phi_1)|^2 + \frac{4\pi}{2\ell+1}\sum_{m=-\ell}^{\ell}|Y_\ell^m(\theta_2,\phi_2)|^2 + \right.$$
$$\left. + \frac{8\pi}{2\ell+1}\sum_{m=-\ell}^{\ell}Y_\ell^m(\theta_1,\phi_1)Y_\ell^m(\theta_2,\phi_2)\right]^{1/2}, \tag{A.7}$$

and using (4.35)

$$Q_\ell^{(i)} = \frac{1}{2}\left[2 + \frac{8\pi}{2\ell+1}\sum_{m=-\ell}^{\ell}Y_\ell^m(\theta_1,\phi_1)Y_\ell^m(\theta_2,\phi_2)\right]^{1/2}. \tag{A.8}$$

Following the same procedure we can find for N_b neighbours that

$$Q_\ell^{(i)} = \frac{1}{N_b}\left[N_b + \frac{8\pi}{2\ell+1}\sum_{m=-\ell}^{\ell}\sum_{j=1}^{N_b-1}\sum_{k>j}^{N_b}Y_\ell^m(\theta_j,\phi_j)Y_\ell^m(\theta_k,\phi_k)\right]^{1/2}. \tag{A.9}$$

A.2 Steinhardt order parameters of simple cubic crystals

The calculation of Steinhardt order parameters of simple cubic cells requires the calculation of the tesseral spherical harmonics for various θ and ϕ values. For $\theta = 0$, $\cos\theta = 1$ and eq. (4.12) for $m \neq 0$ gives $P_{\ell,m}(1) = 0$ and so the only non-zero tesseral spherical harmonics for $\theta = 0$ are given for $m = 0$. Combining eq. (4.18) and (4.21) it can be shown that

$$Y_{\ell,m}(0,\phi) = \sqrt{\frac{2\ell+1}{4\pi}}\delta_{m,0}, \tag{A.10}$$

and so they are independent of angle ϕ. For $\theta = \pi/4$ things are far more complicated. To start with, $\cos(\pi/4) = \sqrt{2}/2$ and so eq. (4.12) gives

$$P_{\ell,m}(\sqrt{2}/2) = \frac{1}{2^{\ell+\frac{m}{2}}}\sum_{k=0}^{\ell-m}2^{-\frac{k}{2}}d_k(\ell,m), \tag{A.11}$$

and eq. (4.21) results in

$$Y_{\ell,m}(\tfrac{\pi}{4},\phi) = \begin{cases} \dfrac{c_{\ell,|m|}}{\sqrt{2}}\dfrac{1}{2^{\ell+\frac{|m|}{2}}}\left[\displaystyle\sum_{k=0}^{\ell-|m|}2^{-\frac{k}{2}}d_k(\ell,|m|)\right]\sin(|m|\phi), & \text{for} \quad m<0 \\ c_{\ell,0}\dfrac{1}{2^\ell}\displaystyle\sum_{k=0}^{\ell}2^{-\frac{k}{2}}d_k(\ell,0), & \text{for} \quad m=0 \\ \dfrac{c_{\ell,m}}{\sqrt{2}}\dfrac{1}{2^{\ell+\frac{m}{2}}}\left[\displaystyle\sum_{k=0}^{\ell-m}2^{-\frac{k}{2}}d_k(\ell,m)\right]\cos(m\phi), & \text{for} \quad m>0 \end{cases} \tag{A.12}$$

Using the term

$$e_{i,jk+l} = \sum_{k=0}^{\infty}\delta_{i,jk+l}, \tag{A.13}$$

which is actually a sum over different Kronecker's delta terms, the spherical harmonics can be written in a compact form as

$$\begin{aligned} Y_{\ell,m}(\tfrac{\pi}{4},\phi) =& \frac{1}{2^\ell} c_{\ell,0} \left[\sum_{k=0}^{\ell} 2^{-\frac{k}{2}} d_k(\ell,0)\right] \delta_{m,0} + \\ &+ \frac{1}{2^{\ell+\frac{|m|+1}{2}}} c_{\ell,|m|} \left[\sum_{k=0}^{\ell-|m|} 2^{-\frac{k}{2}} d_k(\ell,|m|)\right] \sin(|m|\phi) e_{m,-k-1} + \\ &+ \frac{1}{2^{\ell+\frac{m+1}{2}}} c_{\ell,m} \left[\sum_{k=0}^{\ell-m} 2^{-\frac{k}{2}} d_k(\ell,m)\right] \cos(m\phi) e_{m,k+1}, \end{aligned} \tag{A.14}$$

For $\theta = \pi/4$, only the tesseral spherical harmonics for $\phi = 0$ and $\phi = \pi/2$ require calculation. For $\phi = 0$, $\cos(m\phi) = 1$ and $\sin(|m|\phi) = 0$ and so

$$Y_{\ell,m}(\tfrac{\pi}{4},0) = \frac{1}{2^{\ell+\frac{m+1}{2}}} c_{\ell,m} \left[\sum_{k=0}^{\ell-m} 2^{-\frac{k}{2}} d_k(\ell,m)\right] \left(\sqrt{2}\delta_{m,0} + e_{m,k+1}\right), \tag{A.15}$$

and the only non-zero terms are for $m \geq 0$. For $\phi = \pi/2$ on the other hand

$$\sin(|m|\pi/2) = (-1)^{\frac{1}{2}(|m|-1)} e_{m,-2k-1} \qquad \text{and} \qquad cos(m\pi/2) = (-1)^{\frac{m}{2}} e_{m,2k}, \tag{A.16}$$

so

$$\begin{aligned} Y_{\ell,m}(\tfrac{\pi}{4},\tfrac{\pi}{2}) =& \frac{(-1)^{\frac{1}{2}(|m|-1)}}{2^{\ell+\frac{|m|+1}{2}}} c_{\ell,|m|} \left[\sum_{k=0}^{\ell-|m|} 2^{-\frac{k}{2}} d_k(\ell,|m|)\right] e_{m,-2k-1} + \\ &+ \frac{1}{2^{\ell+\frac{m+1}{2}}} c_{\ell,m} \left[\sum_{k=0}^{\ell-m} 2^{-\frac{k}{2}} d_k(\ell,m)\right] \left[\sqrt{2}\delta_{m,0} + (-1)^{\frac{m}{2}} e_{m,2k+1}\right], \end{aligned} \tag{A.17}$$

and the non-zero terms are for negative odd m values, $m = 0$ and positive even m values. For $\theta = \cos^{-1}(1/\sqrt{3})$

$$\begin{aligned} Y_{\ell,m}(\cos^{-1}(\tfrac{1}{\sqrt{3}}),\phi) =& \frac{1}{2^\ell} c_{\ell,0} \left[\sum_{k=0}^{\ell} 3^{-\frac{k}{2}} d_k(\ell,0)\right] \delta_{m,0} + \\ &+ \frac{1}{2^{\ell-\frac{|m|-1}{2}} 3^{\frac{|m|}{2}}} c_{\ell,|m|} \left[\sum_{k=0}^{\ell-|m|} 3^{-\frac{k}{2}} d_k(\ell,|m|)\right] \sin(|m|\phi) e_{m,-k-1} + \\ &+ \frac{1}{2^{\ell-\frac{m-1}{2}} 3^{\frac{m}{2}}} c_{\ell,m} \left[\sum_{k=0}^{\ell-m} 3^{-\frac{k}{2}} d_k(\ell,m)\right] \cos(m\phi) e_{m,k+1}, \end{aligned} \tag{A.18}$$

These spherical harmonics needs to be calculated for $\phi = \pi/4$ and $\phi = 3\pi/4$. It can be proven that

$$\begin{aligned} \sin(|m|\pi/4) =& \frac{1}{\sqrt{2}} \left[(-1)^{\frac{1}{4}(|m|-1)} e_{m,-4k-1} + (-1)^{\frac{1}{4}(|m|-3)} e_{m,-4k-3}\right] + \\ &+ (-1)^{\frac{1}{4}(|m|-2)} e_{m,-4k-2}, \end{aligned} \tag{A.19}$$

and

$$\cos(m\pi/4) = \frac{1}{\sqrt{2}}\left[(-1)^{\frac{1}{4}(m-1)}e_{m,4k+1} - (-1)^{\frac{1}{4}(m-3)}e_{m,4k+3}\right] - \\ - (-1)^{\frac{1}{4}(m-4)}e_{m,4k+4}, \tag{A.20}$$

The final form of the tesseral spherical harmonics for $(\theta,\phi) = (\cos^{-1}(1/\sqrt{3}),\pi/4)$ is

$$\begin{aligned} Y_{\ell,m}(\cos^{-1}(\tfrac{1}{\sqrt{3}}),\tfrac{\pi}{4}) = &\frac{1}{2^\ell}c_{\ell,0}\left[\sum_{k=0}^{\ell} 3^{-\frac{k}{2}} d_k(\ell,0)\right]\delta_{m,0} + \\ &+ \sum_{j=1,3}\left[\frac{(-1)^{\frac{1}{4}(|m|-j)}}{2^{\ell+1-\frac{|m|}{2}}3^{\frac{|m|}{2}}}c_{\ell,|m|}\left[\sum_{k=0}^{\ell-|m|} 3^{-\frac{k}{2}} d_k(\ell,|m|)\right]e_{m,-4k-j}\right] + \\ &+ \frac{(-1)^{\frac{1}{4}(|m|-2)}}{2^{\ell-\frac{|m|-1}{2}}3^{\frac{|m|}{2}}}c_{\ell,|m|}\left[\sum_{k=0}^{\ell-|m|} 3^{-\frac{k}{2}} d_k(\ell,|m|)\right]e_{m,-4k-2} + \\ &+ \sum_{j=1,3}\left[\frac{(-1)^{\frac{1}{4}(m+j-2)}}{2^{\ell+1-\frac{m}{2}}3^{\frac{m}{2}}}c_{\ell,m}\left[\sum_{k=0}^{\ell-m} 3^{-\frac{k}{2}} d_k(\ell,m)\right]e_{m,4k+j}\right] - \\ &- \frac{(-1)^{\frac{1}{4}(m-4)}}{2^{\ell-\frac{m-1}{2}}3^{\frac{m}{2}}}c_{\ell,m}\left[\sum_{k=0}^{\ell-m} 3^{-\frac{k}{2}} d_k(\ell,m)\right]e_{m,4k+4}, \end{aligned} \tag{A.21}$$

while for $\phi = 3\pi/4$, spherical harmonics can be calculated using the symmetry relation

$$Y_{\ell,m}(\cos^{-1}(\tfrac{1}{\sqrt{3}}),\tfrac{3\pi}{4}) = (-1)^m Y_{\ell,m}(\cos^{-1}(\tfrac{1}{\sqrt{3}}),\tfrac{\pi}{4}) \tag{A.22}$$

Finally, for $\theta = \pi/2$ it is $\cos(\pi/2) = 0$ and $P_\ell^m(0) = d_0(\ell,m)/2^\ell$. Consequently

$$\begin{aligned} Y_{\ell,m}(\tfrac{\pi}{2},\phi) = &\frac{1}{2^\ell}c_{\ell,0}d_0(\ell,0)\delta_{m,0} + \frac{1}{2^{\ell+\frac{1}{2}}}c_{\ell,|m|}d_0(\ell,|m|)\sin(|m|\phi)e_{m,-k-1} + \\ &+ \frac{1}{2^{\ell+\frac{1}{2}}}c_{\ell,m}d_0(\ell,m)\cos(m\phi)e_{m,k+1}. \end{aligned} \tag{A.23}$$

It is required to calculate the above tesseral spherical harmonics for $\phi = 0, \pi/4, \pi/2$ and $3\pi/4$. For $\phi = 0$

$$Y_{\ell,m}(\tfrac{\pi}{2},0) = \frac{1}{2^\ell}c_{\ell,0}d_0(\ell,0)\delta_{m,0} + \frac{1}{2^{\ell+\frac{1}{2}}}c_{\ell,m}d_0(\ell,m)e_{m,k+1}, \tag{A.24}$$

for $\phi = \pi/4$

$$\begin{aligned} Y_{\ell,m}(\tfrac{\pi}{2},\tfrac{\pi}{4}) = &\frac{1}{2^\ell}c_{\ell,0}d_0(\ell,0)\delta_{m,0} + \sum_{j=1,3}\frac{(-1)^{\frac{1}{4}(|m|-j)}}{2^{\ell+1}}c_{\ell,|m|}d_0(\ell,|m|)e_{m,-4k-j} + \\ &+ \frac{(-1)^{\frac{1}{4}(|m|-2)}}{2^{\ell+\frac{1}{2}}}c_{\ell,|m|}d_0(\ell,|m|)e_{m,-4k-2} + \sum_{j=1,3}\frac{(-1)^{\frac{1}{4}(m+j-2)}}{2^{\ell+1}}c_{\ell,m}d_0(\ell,m)e_{m,4k+j} - \\ &- \frac{(-1)^{\frac{1}{4}(m-4)}}{2^{\ell+\frac{1}{2}}}c_{\ell,m}d_0(\ell,m)e_{m,4k+4}, \end{aligned} \tag{A.25}$$

for $\phi = \pi/2$

$$Y_{\ell,m}(\tfrac{\pi}{2},\tfrac{\pi}{2}) = \frac{1}{2^{\ell}} c_{\ell,0} d_0(\ell,0)\delta_{m,0} + \frac{(-1)^{\frac{1}{2}(|m|-1)}}{2^{\ell+\frac{1}{2}}} c_{\ell,|m|} d_0(\ell,|m|) e_{m,-2k-1} + \\ + \frac{(-1)^{\frac{m}{2}}}{2^{\ell+\frac{1}{2}}} c_{\ell,m} d_0(\ell,m) e_{m,2k+2}, \tag{A.26}$$

and finally for $\phi = 3\pi/4$

$$Y_{\ell,m}(\tfrac{\pi}{2},\tfrac{3\pi}{4}) = (-1)^m Y_{\ell,m}(\tfrac{\pi}{2},\tfrac{\pi}{4}) \tag{A.27}$$

For the first neighbour shell of the primitive cubic cell, first kind Steinhardt order parameters are given by

$$\langle Q_{\ell,m}\rangle^{(i)} = \frac{1}{6}\sum_{j=1}^{6} Y_{\ell,m}(\theta_j,\phi_j) = \\ = \frac{1}{6}\left[Y_{\ell,m}(0,\phi_p) + Y_{\ell,m}(\pi,\phi_p) + \sum_{k=0}^{3} Y_{\ell,m}(\tfrac{\pi}{2},\tfrac{k\pi}{2}) \right], \tag{A.28}$$

and by using the symmetry of tesseral spherical harmonics, the parameters become

$$\langle Q_{\ell,m}\rangle^{(i)} = \frac{1}{6}\left[1+(-1)^{\ell-m}\right] Y_{\ell,m}(0,\phi_p) + \frac{1}{6}\left[1+(-1)^{m}\right]\left[Y_{\ell,m}(\tfrac{\pi}{2},0) + Y_{\ell,m}(\tfrac{\pi}{2},\tfrac{\pi}{2})\right] = \\ = \frac{1}{3} Y_{\ell,m}(0,\phi_p) e_{\ell-m,2k} + \\ + \frac{1}{3}\left[Y_{\ell,m}(\tfrac{\pi}{2},0) + Y_{\ell,m}(\tfrac{\pi}{2},\tfrac{\pi}{2})\right](e_{m,-2k-2} + e_{m,2k}). \tag{A.29}$$

Replacing tesseral spherical harmonics

$$\langle Q_{\ell,m}\rangle^{(i)} = \frac{1}{3}\left[c_{\ell,0}\left[e_{\ell,2k} + \frac{1}{2^{\ell-1}} d_0(\ell,0)\right]\delta_{m,0} + \frac{1}{2^{\ell-\frac{1}{2}}} c_{\ell,m} d_0(\ell,m) e_{m,4k+4}\right] \tag{A.30}$$

In the above relation the only non zero terms can be found for $m = 4k$. Since $d_0(\ell,m) \neq 0$ only for $\ell - m =$ even, it can be argued that for $\ell =$ odd, $\langle Q_{\ell,m}\rangle^{(i)} = 0$. So

$$\langle Q_{\ell,m}\rangle^{(i)} = \frac{1}{3}\left[c_{\ell,0}\left[1 + \frac{1}{2^{\ell-1}} d_0(\ell,0)\right]\delta_{m,0} + \frac{1}{2^{\ell-\frac{1}{2}}} c_{\ell,m} d_0(\ell,m) e_{m,4k+4}\right] e_{\ell,2k}. \tag{A.31}$$

Second order Steinhardt order parameters require the calculation of the squared norm of $\langle Q_{\ell,m}\rangle^{(i)}$ which is given by

$$\left|\langle Q_{\ell,m}\rangle^{(i)}\right|^2 = \frac{1}{9} c_{\ell,0}^2 \left[1 + \frac{1}{2^{\ell-1}} d_0(\ell,0)\right]^2 \delta_{m,0} e_{\ell,2k} + \\ + \frac{1}{9}\frac{1}{2^{2\ell-1}} c_{\ell,m}^2 d_0^2(\ell,m) e_{m,4k+4} e_{\ell,2k}. \tag{A.32}$$

Thus

$$Q_{\ell}^{(i)} = \frac{1}{3}\left[\left[1 + \frac{1}{2^{\ell-1}} d_0(\ell,0)\right]^2 + \frac{1}{2^{2\ell-1}}\sum_{m=0}^{\ell}\frac{(\ell-m)!}{(\ell+m)!} d_0^2(\ell,m) e_{m,4k+4}\right]^{\frac{1}{2}} e_{\ell,2k}. \tag{A.33}$$

For the atoms that lie exclusively in the second neighbour shell, first kind Steinhardt order parameters are given by

$$\langle Q_{\ell,m}\rangle^{(i)} = \frac{1}{12}\sum_{k=0}^{3}\left[Y_{\ell,m}(\tfrac{\pi}{4},\tfrac{k\pi}{2}) + Y_{\ell,m}(\tfrac{3\pi}{4},\tfrac{k\pi}{2}) + Y_{\ell,m}(\tfrac{\pi}{2},\tfrac{k\pi}{2}+\tfrac{\pi}{4})\right] \tag{A.34}$$

Using the symmetry of tesseral spherical harmonics the above equation results in

$$\begin{aligned}\langle Q_{\ell,m}\rangle^{(i)} =& \frac{1}{3}\left[Y_{\ell,m}(\tfrac{\pi}{4},0) + Y_{\ell,m}(\tfrac{\pi}{4},\tfrac{\pi}{2})\right] e_{\ell,2k}(e_{m,-2k,-2} + e_{m,2k}) + \\ &+ \frac{1}{6}\left[Y_{\ell,m}(\tfrac{\pi}{2},\tfrac{3\pi}{4}) + Y_{\ell,m}(\tfrac{\pi}{2},\tfrac{5\pi}{4})\right](e_{m,-2k,-2} + e_{m,2k}).\end{aligned} \tag{A.35}$$

Thus, the only non-zero terms exist for ℓ, m = even. Substituting tesseral spherical harmonics this gives

$$\begin{aligned}\langle Q_{\ell,m}\rangle^{(i)} =& \frac{1}{3}\frac{1}{2^{\ell}}c_{\ell,0}\left[2\left[\sum_{k=0}^{\ell}2^{-\frac{k}{2}}d_k(\ell,0)\right] + d_0(\ell,0)\right]\delta_{m,0}e_{\ell,2k} + \\ &+ \frac{1}{3}\frac{(-1)^{\frac{m}{4}}}{2^{\ell+\frac{1}{2}}}c_{\ell,m}d_0(\ell,m)e_{m,4k+4}e_{\ell,2k}.\end{aligned} \tag{A.36}$$

The squared norm of the first kind Steinhardt order parameters is

$$\begin{aligned}\left|\langle Q_{\ell,m}\rangle^{(i)}\right|^2 =& \frac{1}{9}\frac{1}{2^{2\ell}}c_{\ell,0}^2\left[2\left[\sum_{k=0}^{\ell}2^{-\frac{k}{2}}d_k(\ell,0)\right] + d_0(\ell,0)\right]^2\delta_{m,0}e_{\ell,2k} + \\ &+ \frac{1}{9}\frac{1}{2^{2\ell+1}}c_{\ell,m}^2 d_0^2(\ell,m)e_{m,4k+4}e_{\ell,2k},\end{aligned} \tag{A.37}$$

and so

$$\begin{aligned}Q_{\ell}^{(i)} =& \frac{1}{3\cdot 2^{\ell}}\left[\left[2\left[\sum_{k=0}^{\ell}2^{-\frac{k}{2}}d_k(\ell,0)\right] + d_0(\ell,0)\right]^2 + \right. \\ &\left. + \frac{1}{2}\left[\sum_{m=0}^{\ell}\frac{(\ell-m)!}{(\ell+m)!}d_0(\ell,m)e_{m,4k+4}\right]\right]^{\frac{1}{2}}e_{\ell,2k}.\end{aligned} \tag{A.38}$$

For the third neighbour shell, first kind Steinhardt order parameters are

$$\langle Q_{\ell,m}\rangle^{(i)} = \frac{1}{8}\sum_{k=0}^{3}\left[Y_{\ell,m}(\cos^{-1}(\tfrac{1}{\sqrt{3}}),\tfrac{k\pi}{2}+\tfrac{\pi}{4}) + Y_{\ell,m}(\cos^{-1}(-\tfrac{1}{\sqrt{3}}),\tfrac{k\pi}{2}+\tfrac{\pi}{4})\right], \tag{A.39}$$

which gives

$$\begin{aligned}\langle Q_{\ell,m}\rangle^{(i)} =& \frac{1}{2^{\ell}}c_{\ell,0}\left[\sum_{k=0}^{\ell}3^{-\frac{k}{2}}d_k(\ell,0)\right]\delta_{m,0}e_{\ell,2k} - \\ &- \frac{(-1)^{\frac{1}{4}(m-4)}}{2^{\ell-\frac{m-1}{2}}3^{\frac{m}{2}}}c_{\ell,m}\left[\sum_{k=0}^{\ell-m}3^{-\frac{k}{2}}d_k(\ell,m)\right]e_{m,4k+4}e_{\ell,2k}.\end{aligned} \tag{A.40}$$

The squared norm is

$$|\langle Q_{\ell,m}\rangle^{(i)}|^2 = \frac{1}{2^{2\ell}} c_{\ell,0}^2 \left[\sum_{k=0}^{\ell} 3^{-\frac{k}{2}} d_k(\ell,0)\right]^2 \delta_{m,0} + \\ + \frac{1}{2^{2\ell-m+1}3^m} c_{\ell,m}^2 \left[\sum_{k=0}^{\ell-m} 3^{-\frac{k}{2}} d_k(\ell,m)\right]^2 e_{m,4k+4}, \tag{A.41}$$

and second order Steinhardt order parameters are given by

$$Q_\ell^{(i)} = \frac{1}{2^\ell}\left[\left[\sum_{k=0}^{\ell} 3^{-\frac{k}{2}} d_k(\ell,0)\right]^2 + \right. \\ \left. + \frac{1}{2}\sum_{m=0}^{\ell}\left(\frac{2}{3}\right)^m \frac{(\ell-m)!}{(\ell+m)!}\left[\sum_{k=0}^{\ell-m} 3^{-\frac{k}{2}} d_k(\ell,m)\right]^2 e_{m,4k+4}\right]^{\frac{1}{2}} e_{\ell,2k}. \tag{A.42}$$

As in the previous cases, all terms with ℓ = odd are zero and the only terms that contribute to the values of $Q_\ell^{(i)}$ are for $m = 4k$.

Appendix B

Primitive ring statistics code details

Step 1: Identifying all the links in the network.

The simulation cell is expanded in a way similar to the expansion performed for the calculation of Steinhardt order parameters. The difference is that the expansion distance is defined by the maximum ring size L we need to calculate and is equal to $r_{\max}(L/2)$, where $r_{\max}$ is the maximum bond length in the system as defined by the first maximum of the partial radial distribution functions. Once the cell is expanded, all the bonds are identified. The number of linked nodes for each node is stored in the array `LNKS(:)` and the identification number of each linked node is stored into the 2D array `NODLNKD(:,:)`

Listing B.1: Djikstra simplified algorithm for the identification of single-source shortest paths [159]

```
1       DO J=1, RATOMS
2         LVLREF(I,J)=LVLREFREQ+2
3       END DO
4       NODSRC=NODEREF(I)
5       LVLREF(I,NODSRC)=0
6       QUEUE(1)=NODSRC
7       QUEBGN=0
8       QUEEND=1
9       DO WHILE (QUEBGN QUEEND)
10        QUEBGN=QUEBGN+1
11        NODCRT=QUEUE(QUEBGN)
12        LVLPRB=LVLREF(I,NODCRT)+1
13        DO LNKSCRT=1, LNKS(NODCRT)
14          NODPRB=NODLNKD(NODCRT,LNKSCRT)
15          IF (LVLREF(I,NODPRB)>LVLPRB) THEN
16            LVLREF(I,NODPRB)=LVLPRB
17            IF (LVLPRB<LVLREFREQ) THEN
18              QUEEND=QUEEND+1
19              QUEUE(QUEEND)=NODPRB
20            END IF
21          END IF
22        END DO
23      END DO
```

Step 2: Creating a distance levels reference map.

In this extended cell, four reference source nodes are selected, usually as near as possible to four of the corners of the extended cell. For these reference nodes, the shortest path lengths with all other nodes of the system are calculated and stored in a one dimensional matrix, that will be used to search for shortcuts between any pair of nodes on a ring under examination. The reference shortest distance matrix is calculated using the following simplified Djikstra algorithm [167], proposed by Yuan & Cormack [159], written in `FORTRAN 95`. For each of the reference nodes `I`, the shortest paths lengths `LVLREF(:,:)` of every other node in the system is set to an initial value of `LVLREFREQ+2` (lines 1-3), where `LVLREFREQ` needs to be selected carefully to be greater than the maximum shortest distance in the system. A simple way to set this number, is to divide the diagonal length of the extended cell by the minimum bond length of the system. Let d be the result of the division. `LVLREFREQ` is set to be an integer number one order of magnitude higher than the integer part of d. The first reference node is selected as a source node `NODSRC` (line 4) and its reference distance is set to zero (line 5). The source node is then set to be the first node in the list for the identification of shortest paths (line 6). Two integers, `QUEBGN` and `QUEEND` are then selected in order to direct the search to the next linked node (lines 7-8). The following loop (lines 9-22) is used to estimate the length of the shortest paths to each node. In lines 12-14, the source node is selected as the first in the list and a predefined distance `LVLPRB` from the source node is set to be 1 higher than the distance level of the node in the list. Afterwards (lines 13-22) all the linked nodes are examined. The first linked node is set as `NODPRB` (line 14) and its distance level `LVLREF(I,NODPRB)` from the reference node is checked. If it is lower than the predefined level `LVLPRB`, it means that the node was already checked and the next linked node is examined. If it is higher (line 15), it is set equal to the predefined level `LVLPRB` (line 16) and if this level is lower than the requested level, the list is updated (lines 17-20) with the examined node. The shortest path search concludes when `QUEEND=QUEBGN` and this happens only when all the nodes are examined.

Step 3: Finding shortest paths

Once the reference distance map is created, for a given source node, the shortest paths levels `LVLDIST(:)` of all other nodes of the system up to the requested level `LVLREQ` - which is equal to the half of the maximum ring size, are calculated using the simplified Djikstra Algorithm described above, just by replacing `LVLREF(:,:)` with `LVLDIST(:)`. It is worth pointing out that, depending on the maximum ring size, several nodes of the system will appear have a distance level equal to `LVLREQ+2`. However, these nodes were never examined to find the actual distance level since ot is equal to or higher than the requested level. Additionally, the distance level of each source node will be found equal to zero and this must be the only node with zero distance level.

Step 4: Finding Prime-mid-nodes

With the shortest paths from the given source node, to any node of the network known, up to the requested level, the next step is to identify prime-mid-nodes. For odd rings, we just need to search for nodes which have at least one linked node with the same level distance level from the source

node, while for even rings, we need to identify nodes with at least one linked node with a distance level lower by 1. The FORTRAN 95 code to identify prime-mid-nodes for a given source node I is given below. For every node in the network, we define an integer PRIMMN(:) set to zero (line 1) that helps identify if a node is a prime-mid-node. Integers OPMN and EPMN are used to identify the number of linked nodes with the desired level, and initially they are set to zero (lines 3-4). Nodes are examined only if the distance levels is higher than 1 and lower than or equal to the required level LVLREQ (line 5). In lines 6-16, all the distance level of all the linked nodes is examined. If the distance level of the linked node is equal to the level of node under investigation, an odd prime-mid-node is identified (lines 7-19) and if the level is lower by 1, a potential even prime-mid-node is found (lines 10-12). Based on the number of linked nodes that have the required distance level, the node can be classified as prime-mid-node and PRIMMN(:) is set to 1 (line 13). Finally, the total number of prime-mid-nodes PNM is calculated and each prime-mid-node receives an index PMNINDEX(:) (lines 18-23), to be able to identify it at a later stage.

Listing B.2: Algorithm for the identification of prime-mid-nodes, developed using pseudo-code published by Yuan & Cormack [159]

```
1      DO J=1, RATOMS
2        PRIMMN(J)=0
3        OPMN=0
4        EPMN=0
5        IF (LVLDIST(J)>0 .AND. LVLDIST(J)<=LVLREQ) THEN
6          DO K=1, LNKS(J)
7            IF (LVLDIST(NODLNKD(J,K))==LVLDIST(J) .AND. IODD==1) THEN
8              OPMN=OPMN+1
9            END IF
10           IF (LVLDIST(NODLNKD(J,K))==LVLDIST(J)-1 .AND. IODD==0) THEN
11             EPMN=EPMN+1
12           END IF
13           IF (OPMN>=1 .OR. EPMN=2) PRIMMN(J)=1
14         END DO
15       END IF
16     END DO
17     PMN=0
18     DO J=1, RATOMS
19       IF (PRIMMN(J)==1) THEN
20         PMN=PMN+1
21         PMNINDEX(PMN)=J
22       END IF
23     END DO
```

Step 5: Forming rings

Once all the prime-mid-nodes are known, the ring forming process is initialized. The idea is that for even rings, each pair of paths connecting the source node to a prime-mid-node form a ring while for odd rings any path of one of the prime-mid-nodes forms a ring with a path of its pair prime-mid-node. This can be done using code B.4. During the ring forming procedure, all the nodes forming the shortest paths must be identified and for this the recursive subroutine SRTPATH_RECORD (code B.3) is used. In code B.4, we first set the total number of paths that

connect the current prime-mid-node with the source node and the number of rings to zero (lines 1-2). In lines 3-4, the current node under investigation `NODCRT` is set to the current prime-mid-node and its distance level `LVLCRT` is set. In line 5, the distance level `LVLPRIM` of the prime-mid-node is set. The difference between `LVLCRT` and `LVLPRIM` is that the first will change dynamically as the recursive subroutine `SRTPATH_RECORD` will search for the nodes forming the ring. Before calling the subroutine `SRTPATH_RECORD`, we also set the first node of the path `SRTPTHX(:)` to be the current prime-mid-node. In line 7, the recursive subroutine is called (code B.3) and all the linked nodes of the prime-mid-node are checked.

In code B.3, for each linked node `NDPRB` we examine the distance level `LVLPRB` from the source node. If the level is by 1 less than the level of the current prime-mid-node (line 11), the node is added to the path (line 12) and the subroutine is called again to examine the neighbours of the last identified node. The process stops when the distance level of a node is equal to zero and the source node is found (line 6). In this case, a path is identified and receives an ID number (line 7) and all the nodes of the part are recorded in the array `SRTPTH(:,:)`.

Listing B.3: Subroutine to identify all the nodes forming a path [159]

```
1  RECURSIVE SUBROUTINE SRTPTH_RECORD(NODCRT,LVLCRT,PTHS,LVLPRIM,LNKS,NODLNKD,
       LVLDIST,SRTPTH,SRTPTHX)
2
3  DO LNKSCRT=1, LNKS(NODCRT)
4    NODPRB=NODLNKD(NODCRT,LNKSCRT)
5    LVLPRB=LVLDIST(NODPRB)
6    IF (LVLPRB==0) THEN
7      PTHS=PTHS+1
8      DO LVL=1, LVLPRIM
9        SRTPTH(PTHS,LVL)=SRTPTHX(LVL)
10     END DO
11   ELSE IF (LVLPRB==LVLCRT-1) THEN
12       SRTPTHX(LVLPRB)=NODPRB
13       CALL SRTPTH_RECORD(NODPRB,LVLPRB,PTHS,LVLPRIM,LNKS,NODLNKD,LVLDIST,SRTPTH
             ,SRTPTHX)
14   END IF
15 END DO
```

Once the paths from the current prime-mid-node to the current source node are formed, the process returns to code B.4 and the ring forming process takes place (line 8). There are two options, one for even rings for which `IODD=0` (line 8) and for odd rings with `IODD=1` (line 23). For even rings it is quite straightforward to form rings, since every pair of paths from the current prime-mid-node to the current source node forms a ring. The formation is achieved with the double loop over all the paths (lines 9-21). However there is a chance that the two paths that form the ring might have a common node (apart from the source node and the prime-mid-node). These rings will not be primitive and we can filter them out by comparing the nodes of the two paths at the same level (lines 12-14). The `PAIR` variable is used to identify the distance levels that have different nodes, and if this number is 1 less than the distance level of the prime-mid-node (line 15), the two paths have no common nodes and a ring is formed (line 16). To identify the ring at a later stage, each of the paths forming the ring receive a unique ID using the array `QUERNG(:,:)`. For the odd rings things are more complicated. The first step is to copy the number of paths for the

current prime-mid-node using variable OPTH (line 24) and then we check all the linked nodes (line 25) to identify the other node of the prime-mid-nodes pair, which have the same distance level as the current prime-mid-node (line 26). In this statement, we require that the index of the pair prime-mid-node is greater than the index of the current prime-mid-node, to avoid finding the same pair twice. Once the pair node is found, we need to form again the paths from this pair node to the current source node (lines 27-32). Note that before calling the subroutine SRTPH_RECORD, variable PTHS is set to an initial value equal to the number of paths of the current prime-mid-node (line 31). Once the paths of the pair prime-mid-node are identified, we can form the rings by pairing any path of the current prime-mid-node with any path of the pair prime-mid-node (lines 33-45) following the same procedure as for the even rings.

Listing B.4: Algorithm to form all the rings of a given source node, developed using pseudo-code published by Yuan & Cormack [159].

```
1        PTHS=0
2        RNGS=0
3        NODCRT=PMNINDEX(J)
4        LVLCRT=LVLDIST(NODCRT)
5        LVLPRIM=LVLDIST(NODCRT)
6        SRTPTHX(LVLPRIM)=NODCRT
7        CALL SRTPTH_RECORD(NODCRT,LVLCRT,PTHS,LVLPRIM,LNKS,NODLNKD,LVLDIST,SRTPTH
             ,SRTPTHX)
8        IF (IODD==0) THEN
9          DO PATH1, PTHS-1
10           DO PATH2=PATH1+1, PTHS
11             PAIR=0
12             DO LVL=1, LVLPRIM
13               IF (SRTPTH(K,LVL)/=SRTPTH(L,LVL)) PAIR=PAIR+1
14             END DO
15             IF (PAIR==LVLPRIM-1) THEN
16               RNGS=RNGS+1
17               QUERNG(RNGS,1)=PATH1
18               QUERNG(RNGS,2)=PATH2
19             END IF
20           END DO
21         END DO
22       END IF
23       IF (IODD==1) THEN
24         OPTH=PTHS
25         DO K=1, LNKS(PMNINDEX(J))
26           IF (LVLDIST(NODLNKD(PMNINDEX(J),K))==LVLDIST(PMNINDEX(J)) .AND.
                 NODLNKD(PMNINDEX(J),K)>PMNINDEX(J)) THEN
27             NODCRT=NODLNKD(PMNINDEX(J),K)
28             LVLCRT=LVLDIST(NODCRT)
29             LVLPRIM=LVLDIST(NODCRT)
30             SRTPTHX(LVLPRIM)=NODCRT
31             PTHS=OPTH
32             CALL SRTPTH_RECORD(NODCRT,LVLCRT,PTHS,LVLPRIM,LNKS,NODLNKD,LVLDIST,
                   SRTPTH,SRTPTHX)
33             DO PATH1=1, OPTH
34               DO PATH2=OPTH+1, PTHS
35                 PAIR=0
```

```
36                 DO LVL=1, LVLPRIM
37                   IF (SRTPTH(PATH1,LVL)/=SRTPTH(PATH2,LVL)) PAIR=PAIR+1
38                 END DO
39                 IF (PAIR==LVLPRIM) THEN
40                   RNGS=RNGS+1
41                   QUERNG(RNGS,1)=PATH1
42                   QUERNG(RNGS,2)=PATH2
43                 END IF
44               END DO
45             END DO
46           END IF
47         END DO
48       END IF
```

Step 6: Checking for shortcuts and identify primitive rings

The final step of the process is to validate that the rings formed are indeed primitive rings. This is done by using code B.5. Logical variable `GOAL_FOUND` is used to state if a shortcut is found or not. Initially it is assumed that no shortcut exists for the ring under investigation (line 1). For a given pair of source node and prime-mid-node all the rings formed are examined (line 2), using the paths stored for each ring (lines 3-4). If the distance level of the prime-mid-node is `LVLPRIM`, to classify the ring as primitive it is necessary to verify that there is no path with length shorter than `LVLPRIM` between any two unlinked nodes in the ring. The pair of nodes is selected using variables `NODCHK` and `NODMID` (lines 8-9), for which the sum of distance levels is initially equal to the distance level of the prime-mid-node. To identify any possible shortcut, a four point detection method is applied (lines 10-32), using the recursive subroutine shown in code B.6.

This method uses the reference distance level map `LVLREF(:,:)` calculated at the first step of the procedure. In Fig. B.1 a 2D analogue of the method is illustrated. The four reference nodes occupy positions near the corner of the expanded simulation cell and we examine a 12-order ring. The distance level between the source node and the prime-mid-node is equal to 6. Assume that we want to search for a shortcut between nodes 3 and 12. The shortest path that connects these two nodes across the ring has a length equal to 5 ($3-4-5-6-P-12$). If a shortcut exists, it should have a maximum length 4. Thus, we check if there is a path, connecting nodes 3 and 12 with length ≤ 4. Let L_1, L_2, L_3 and L_4 be the distance levels of node 3 from the four reference nodes. If a shortcut with maximum length equal to 4 between nodes 3 and 12 exists, the distance levels of node 12 from the reference nodes should lie in the limits $L_i - 4 \leq l_i < L_i + 4$, $i = 1, 2, 3, 4$.. Thus, by comparing the distance levels of the two nodes from the reference nodes we can determine if a shortest path exists. If the distance level of node 12 from the reference nodes is not within these limits, a shortcut does not exist. Schematically, if we make the simplification that nodes with the same distance level from a reference node form a circular arc, a shortcut would exist if node 12 was within the overlapping arc of the four shells. However, the fact that the distance level of node 3 from the reference nodes is within the specified limits does not guarantee the existence of a shortcut and a further investigation needs to be carried out.

Before calling the subroutine `PAIR_SEARCH` to identify shortcuts (code B.6), we use the reference distance levels of node `NODMID` to set the upper and lower limits for the distance levels of node

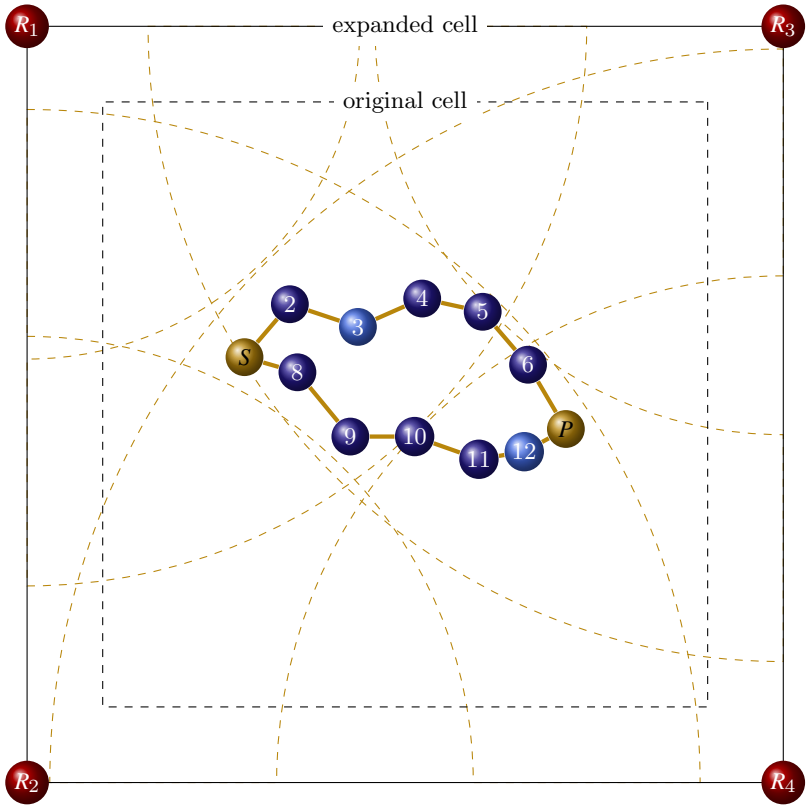

Figure B.1: Illustration of the 4 point detection method used to identify shortcuts between any pair of nodes of a ring.

NODCHK from the reference nodes (lines 10-13). Lines 14 and 15 provide two additional limits defined the same way, related with the distance level of MIDNODE from the source node, useful when the distance level of node NODCHK is within the defined limits. After calling subroutine PAIR_SEARCH, if a shortcut is found, the ring is not a primitive ring and the search is directed to the next ring. However, before proceeding to the next ring, we can check if any other rings have the same pair of NODCHK and NODMID (lines 19-30). If they do, QUERNG(:,1) is set to zero and the specific ring is omitted from the next search.

Listing B.5: Algorithm to identify all primitive rings for a given source node [159]

```
1       GOAL_FOUND=.FALSE.
2       DO IRNG=1, RNGS
3         PTH1=QUERNG(IRNG,1)
4         PTH2=QUERNG(IRNG,2)
5         IF (PTH1>0) THEN
6           DO LVLMAX=LVLPRIM, LVLPRIM+IODD
7             DO LVLCHK=1, LVLMAX-1
8               NODCHK=SRTPTH(PTH1,LVLCHK)
9               NODMID=SRTPTH(PTH2,LVLMAX-LVLCHK)
10              DO K=1, 4
11                LIMIT(K,1)=LVLREF(K,NODMID)+LVLPRIM-1
12                LIMIT(K,2)=LVLREF(K,NODMID)-LVLPRIM+1
13              END DO
```

```
14              LIMIT(5,1)=LVLDIST(NODMID)+LVLPRIM-1
15              LIMIT(5,2)=LVLDIST(NODMID)-LVLPRIM+1
16              CALL PAIR_SEARCH(NODCHK,NODMID,LIMIT,GOAL_FOUND,LNKS,NODLNKD,
                    LVLDIST,LVLREF)
17              IF (GOAL_FOUND) THEN
18                GOAL_FOUND=.FALSE.
19                DO IRGX=IRNG+1, RNGS
20                  P1X=QUERNG(IRGX,1)
21                  P2X=QUERNG(IRGX,2)
22                  IF (P1X>0) THEN
23                    IF (SRTPTH(P1X,LVLCHK)==NODCHK .AND. SRTPTH(P2X,LVLMAX-
                          LVLCHK)==NODMID) THEN
24                      QUERNG(IRGX,1)=0
25                    END IF
26                    IF (SRTPTH(P2X,LVLCHK)==NODCHK .AND. SRTPTH(P1X,LVLMAX-
                          LVLCHK)==NODMID) THEN
27                      QUERNG(IRGX,1)=0
28                    END IF
29                  END IF
30                END DO
31                GO TO 200
32              END IF
33            END DO
34          END DO
35          RINGSTAT(I,2*LVLPRIM+IODD)=RINGSTAT(I,2*LVLPRIM+IODD) +1
36        END IF
37        200 CONTINUE
38      END DO
```

Subroutine `PAIR_SEARCH` (code B.6), used to identify shortcuts between any pair of nodes in a ring, initially examines the distance levels of the nodes linked with `NODCHK` with the reference nodes (lines 9-11) and if they are not within the limits defined by the reference nodes, no shortcut is found, and the ring is counted as a primitive in line 35 of code B.5. If the distance level of the neighbours is within the limits defined by the four reference nodes, an additional check is performed by comparing the distance levels of the linked node with the limits defined by the distance level of `NODMID` from the source node (lines 12-13). Once again, if the distance level is outside those limits, the analysis proceeds by identifying the ring as positive. If not, the upper and lower limits in the distance levels are decreased and increased by one respectively (lines 13-16) and the subroutine is called again (line 17) to check this time a node linked to `NODPRB` (which is linked to node `NODMID` under examination). If at any point of the search `NODCHK` is found (lines 3-5, 18), it means that a shortcut exists and the search ends (lines 5,19).

Listing B.6: Subroutine to identify shortcuts in a ring [159].

```
1  RECURSIVE SUBROUTINE PAIR_SEARCH(NODCRT,NODGOAL,LIMIT,GOAL_FOUND,LNKS,NODLNKD,
       LVLDIST,LVLREF)
2
3  IF (NODCRT==NODGOAL) THEN
4    GOAL_FOUND=.TRUE.
5    RETURN
6  END IF
7  DO LNKSCRT=1, LNKS(NODCRT)
```

```
    NODPRB=NODLNKD(NODCRT,LNKSCRT)
    DO IREF=1, 4
      IF (LVLREF(IREF,NODPRB)>=LIMIT(IREF,1) .OR. LVLREF(IREF,NODPRB)<=LIMIT(IREF
          ,2)) GO TO 100
    END DO
    IF (LVLDIST(NODPRB)>=LIMIT(5,1) .OR. LVLDIST(NODPRB)<=LIMIT(5,2)) GO TO 100
    DO IREF=1, 5
      LMTX(IREF,1)=LIMIT(IREF,1)-1
      LMTX(IREF,2)=LIMIT(IREF,2)+1
    END DO
    CALL PAIR_SEARCH(NODPRB,NODGOAL,LMTX,GOAL_FOUND,LNKS,NODLNKD,LVLDIST,LVLREF)
    IF (GOAL_FOUND) THEN
      RETURN
    END IF
    100 CONTINUE
  END DO
```

Bibliography

[1] IAEA, "Power reactor information system." https://pris.iaea.org/pris/, 2010. [Online; accessed 14 August 2018].

[2] IAEA, "Chain fission yields." https://www-nds.iaea.org/sgnucdat/c1.htm, 2015. [Online; accessed 14 August 2018].

[3] WNA Information Library, "World uranium mining production." http://www.world-nuclear.org/information-library/nuclear-fuel-cycle/mining-of-uranium/world-uranium-mining-production.aspx, 2018. [Online; accessed 10 August 2018].

[4] WNA Information Library, "Nuclear fuel and its fabrication." http://www.world-nuclear.org/information-library/nuclear-fuel-cycle/conversion-enrichment-and-fabrication/fuel-fabrication.aspx, 2018. [Online; accessed 16 August 2018].

[5] WNA Image Library, "Pressurised water reactor." http://www.world-nuclear.org/gallery/reactor-diagrams/pressurized-water-reactor.aspx, 2018. [Online; accessed 8 August 2018].

[6] WNA Image Library, "Boiling water reactor." http://www.world-nuclear.org/gallery/reactor-diagrams/boiling-water-reactor.aspx, 2018. [Online; accessed 8 August 2018].

[7] WNA Image Library, "Pressurised heavy water reactor." http://www.world-nuclear.org/gallery/reactor-diagrams/pressurized-heavy-water-reactor.aspx, 2018. [Online; accessed 8 August 2018].

[8] WNA Image Library, "Advanced gas-cooled rreactor." http://www.world-nuclear.org/gallery/reactor-diagrams/advanced-gas-cooled-reactor.aspx, 2018. [Online; accessed 8 August 2018].

[9] WNA Information Library, "Nuclear power in the united kingdom." http://www.world-nuclear.org/information-library/country-profiles/countries-t-z/united-kingdom.aspx, 2018. [Online; accessed 8 August 2018].

[10] NDA, "Radioactive wastes in the uk: A summary of the 2016 inventory." https://ukinventory.nda.gov.uk/wp-content/uploads/sites/18/2017/03/High-Level-Summary-UK-Radwaste-Inventory-2016.pdf, 2016. [Online; accessed 21 August 2018].

[11] A. Varshneya, "Fundamentals of inorganic glasses." Society of Glass Technology: http://www.sgt.org/SGTNews/2005/SGTN05_19-22.pdf, 2005. [Online; accessed 14 September 2016].

[12] K. O. Trachenko, M. T. Dove, T. Geisler, I. Todorov, and B. Smith, "Radiation damage effects and percolation theory," *Journal of Physics: Condensed Matter*, vol. 16, pp. 2623–2627, 2004.

[13] K. Jolley and R. Smith, "Iron phosphate glasses: Structure determination and radiation tolerance," *Nuclear Instruments and Methods in Physics Research B*, vol. 374, pp. 8–13, 2016.

[14] WNA Information Library, "Nuclear power reactors." http://www.world-nuclear.org/information-library/nuclear-fuel-cycle/nuclear-power-reactors/nuclear-power-reactors.aspx, 2018. [Online; accessed 8 August 2018].

[15] J. M. Delaye and D. Ghaleb, "Molecular dynamics simulation of low-energy atomic displacement cascades in a simplified nuclear glass," *Journal of Nuclear Materials*, vol. 244, pp. 22–28, 1997.

[16] J. M. Delaye and D. Ghaleb, "Displacement cascades in a borosilicate glass: Influence of the level of polymerization on the cascade morphology," *Nuclear Instruments and Methods in Physics Research B*, vol. 135, pp. 201–206, 1998.

[17] J. M. Delaye and D. Ghaleb, "Volume change origin in glasses subjected to ballistic collisions: Molecular dynamics simulations," *Nuclear Instruments and Methods in Physics Research B*, vol. 191, pp. 10–16, 2002.

[18] J. M. Delaye, S. Peuget, G. Bureau, and G. Calas, "Molecular dynamics simulation of radiation damage in glasses," *Journal of Non-Crystalline Solids*, vol. 357, pp. 2763–2768, 2011.

[19] A. Abbas, Y. Serruys, D. Ghaleb, J. M. Delaye, B. Boizot, B. Reynard, and G. Calas, "Evolution of nuclear glass structure under α-irradiation," *Nuclear Instruments and Methods in Physics Research B*, vol. 166-167, pp. 445–450, 2000.

[20] L. Dewan, L. W. Hobbs, and J. M. Delaye, "Topological analysis of the structure of self-irradiated sodium borosilicate glass," *Journal of Non-Crystalline Solids*, vol. 358, pp. 3427–3432, 2012.

[21] A. Abbas, J. M. Delaye, D. Ghaleb, and G. Calas, "Molecular dynamics study of the structure and dynamic behavior at the surface of a silicate glass," *Journal of Non-Crystalline Solids*, vol. 315, pp. 187–196, 2003.

[22] L. H. Kieu, J. M. Delaye, L. Cormier, and C. Stolz, "Development of empirical potentials for sodium borosilicate glass systems," *Journal of Non-Crystalline Solids*, vol. 357, pp. 3313–3321, 2011.

[23] B. Al-Hasni and G. Mountjoy, "Structural investigation of iron phosphate glasses using molecular dynamics simulation," *Journal of Non-Crystalline Solids*, vol. 357, pp. 2775–2779, 2011.

[24] K. Jolley, R. Smith, and J. Kitheri, "Borosilicate glass potentials for radiation damage simulations," *Nuclear Instruments and Methods in Physics Research B*, vol. 352, pp. 140–144, 2015.

[25] K. Robinson, G. V. Gibbs, and P. H. Ribbe, "The structure of zircon: A comparison with garnet," *Americal Mineralogist*, vol. 56, pp. 782–789, 1971.

[26] R. M. Hazen, "Crystal structure and compressibility of zircon at high pressure," *Americal Mineralogist*, vol. 64, pp. 196–201, 1979.

[27] R. J. Finch, J. M. Hanchar, P. W. O. Hoskin, and P. C. Burns, "Rare-earth elements in synthetic zircon: Part 2. A single-crystal X-ray study of xenotime substitution," *American Mineralogist*, vol. 86, pp. 681–689, 2001.

[28] K. O. Trachenko, D. M. T., and E. K. H. Salje, "Atomistic modelling of radiation damage in zircon," *Journal of Physics: Condensed Matter*, vol. 13, pp. 1947–1959, 2001.

[29] R. Devanathan, L. R. Corrales, and W. J. Weber, "Molecular dynamics simulation of disordered zircon," *Physical Review B*, vol. 69, pp. 1–9, 2004.

[30] J. Yu, R. Devanathan, and W. J. Weber, "Unified interatomic potential for zircon, zirconia and silica systems," *Journal of Materials Chemistry*, vol. 19, pp. 3923–3930, 2009.

[31] J. Kitheri, K. Jolley, and R. Smith, "Iron phosphate glasses: Structure determination and displacement energy thresholds, using a fixed charge potential model," *Journal of Non-Crystalline Solids*, vol. 411, pp. 137–144, 2015.

[32] J. J. Duderstadt and L. J. Hamilton, *Nuclear Reactor Analysis*. New York: Wiley, 1976.

[33] WNA Information Library, "Physics of nuclear energy." http://www.world-nuclear.org/information-library/nuclear-fuel-cycle/introduction/physics-of-nuclear-energy.aspx, 2018. [Online; accessed 6 August 2018].

[34] USNRC, "Fuel cycle facilities." http://www.nrc.gov/materials/fuel-cycle-fac.html, 2016. [Online; accessed 11 September 2016].

[35] WNA Information Library, "The nuclear fuel cycle." http://www.world-nuclear.org/information-library/nuclear-fuel-cycle/introduction/nuclear-fuel-cycle-overview.aspx, 2017. [Online; accessed 15 August 2018].

[36] WNA Information Library, "Conversion and deconversion." http://www.world-nuclear.org/information-library/nuclear-fuel-cycle/conversion-enrichment-and-fabrication/conversion-and-deconversion.aspx, 2017. [Online; accessed 15 August 2018].

[37] WNA Information Library, "Uranium enrichment." http://www.world-nuclear.org/information-library/nuclear-fuel-cycle/conversion-enrichment-and-fabrication/uranium-enrichment.aspx, 2018. [Online; accessed 11 August 2018].

[38] IAEA, "The nuclear fuel cycle." https://www.iaea.org/sites/default/files/nfc0811.pdf, 2011. [Online; accessed 11 September 2016].

[39] IAEA, "Cumulative fission yields." http://www-nds.iaea.org/sgnucdat/c3.htm, 2010. [Online; accessed 14 September 2016].

[40] WNA Information Library, "Processing of used nuclear fuel." http://www.world-nuclear.org/information-library/nuclear-fuel-cycle/fuel-recycling/processing-of-used-nuclear-fuel.aspx, 2018. [Online; accessed 16 August 2018].

[41] WNA Information Library, "Mixed Oxide (MOX) Fuel." http://www.world-nuclear.org/information-library/nuclear-fuel-cycle/fuel-recycling/mixed-oxide-fuel-mox.aspx, 2017. [Online; accessed 17 August 2018].

[42] V. I. Golubev, V. V. Dolgov, V. A. Dulin, A. V. Zvonarev, E. Y. Smetanin, L. A. Kochetkov, V. V. Korobeinikov, V. G. Liforov, G. N. Manturov, I. P. Matveenko, and A. M. Tsibulya, "Fast-reactor actinoid transmutation," *Atomic Energy*, vol. 74, p. 83, 1993.

[43] Urenco, "Separative work unit." https://urenco.com/about-us/business-activity/nuclear-fuel-supply-chain/separative-work-unit/, 2018. [Online; accessed 15 August 2018].

[44] WNA Information Library, "Radioactive waste management." http://www.world-nuclear.org/information-library/nuclear-fuel-cycle/nuclear-wastes/radioactive-waste-management.aspx, 2018. [Online; accessed 21 August 2018].

[45] M. I. Ojovan and W. E. Lee, *An introduction to nuclear waste immobilisation.* Amsterdam: Elsevier, 2005.

[46] WNA Information Library, "Treatment and conditioning of nuclear waste." http://www.world-nuclear.org/information-library/nuclear-fuel-cycle/nuclear-wastes/treatment-and-conditioning-of-nuclear-wastes.aspx, 2018. [Online; accessed 23 August 2018].

[47] M. I. Ojovan, W. E. Lee, R. J. Hand, and N. V. Ojovan, "Corrosion of nuclear waste glasses in non-saturated conditions: Time-temperature behaviour." http://isl.group.shef.ac.uk/papers/MIOCorrosionICG2004paper.pdf, 2006. [Online; accessed 15 September 2016].

[48] M. I. Ojovan and W. E. Lee, "Glassy wasteforms for nuclear waste immobilization," *Metallurgical and Materials Transactions A.*, vol. 42, no. 4, p. 837, 2010.

[49] NRC, *Nuclear wastes: Technologies for separation and transmutation.* Washington DC: National Academy Press, 1996.

[50] M. T. Harrison, "Vitrification of High Level Waste in the UK," *Procedia Materials Science*, vol. 7, pp. 10–15, 2014.

[51] WNA Information Library, "Storage and disposal of radioactive waste." http://www.world-nuclear.org/information-library/nuclear-fuel-cycle/nuclear-wastes/storage-and-disposal-of-radioactive-wastes.aspx, 2018. [Online; accessed 23 August 2018].

[52] NDA, "Implemeting Geological Disposal - Annual report," tech. rep., Department of Business, Energy & Industrial Strategy, 2016.

[53] Department of Business, Energy and Industrial Development, "Implementing geological disposal." https://assets.publishing.service.gov.uk/government/uploads/system/uploads/attachment_data/file/676396/GDF_Annual_Report_2016-2017.pdf, 2017. [Online; accessed 24 August 2018].

[54] R. C. Ewing, W. J. Weber, and F. W. J. Clinard, "Radiation effects in nuclear waste forms for high-level radioactive waste," *Progress in Nuclear Energy*, vol. 29, no. 2, pp. 63–127, 1985.

[55] D. S. Barker, *Igneous rocks*. New Jersey: Prentice Hall, 1983.

[56] W. Lutze and R. C. Ewing, *Radioactive waste forms for the future*. Amsterdam: North-Holland, 1988.

[57] L. L. Hench, D. E. Clark, and J. Campbell, "High level waste immobilization forms," *Nuclear Chemical Waste Management*, vol. 5, p. 149, 1884.

[58] A. B. Harker, *Radioactive waste forms for the future*, ch. Tailored ceramics, pp. 335–392. Amsterdam: North-Holland, 1988.

[59] C. Adelhelm, C. Bauer, S. Gahlert, and G. Ondracek, *Radioactive waste forms for the future*, ch. Ti-O: A ceramic matrix, pp. 393–426. Amsterdam: North-Holland, 1988.

[60] P. J. Hayward, *Radioactive waste forms for the future*, ch. Glass-ceramics, pp. 427–494. Amsterdam: North-Holland, 1988.

[61] P. J. Boatner and B. C. Sales, *Radioactive waste forms for the future*, ch. Monazite, pp. 495–564. Amsterdam: North-Holland, 1988.

[62] C. Kittel, *Introduction to solid state physics*. New York: John Wiley & Sons, Inc., 6th ed., 1986.

[63] K. Laaziri, S. Kycia, S. Roorda, M. Chicoine, J. L. Robertson, J. Wang, and S. C. Moss, "High-energy x-ray diffraction study of pure amorphous silicon," *Physical Review B*, vol. 60, pp. 13520–13533, Nov 1999.

[64] S. Roorda, R. A. Hakvoort, A. van Veen, P. A. Stolk, and F. W. Saris, "Structural and electrical defects in amorphous silicon probed by positrons and electrons," *J. Appl. Phys.*, vol. 72, no. 11, 1992.

[65] B. E. Warren, "The diffraction of X-Rays in glass," *Physical Review*, vol. 45, p. 657, 1934.

[66] K. J. Rao, *Structural chemistry of glasses*. Elsevier SCience & Technology Books, 2002.

[67] J. Animesh, *Introduction*, pp. i–xviii. Wiley-Blackwell, 2016.

[68] G. Urbain, Y. Bottinga, and P. Richet, "Viscosity of liquid silica, silicates and aluminosilicates," *Geochim Cosmochim Acta*, vol. 46, pp. 1061–1072, 1982.

[69] R. L. Cormia, J. D. Mackenzie, and D. Turnbull, "Kinetics of melting and crystallization of phosphorus pentoxide," *Journal of Applied Physics*, vol. 34, no. 8, pp. 2239–2244, 1963.

[70] W. Zachariasen, "The atomic arrangement in glass," *Journal of the American Chemical Society*, vol. 54, p. 3841, 1932.

[71] A. Smekal, "Structure of glass," *Journal of the Society of Glass Technology*, vol. 35, p. 411, 1951.

[72] K. H. Sun and M. L. Huggins, "Energy additivity in oxygen-containing crystals and glasses," *Journal of Physical and Colloid Chemistry*, vol. 51, p. 438, 1947.

[73] H. Rawson in *Proceedings of the IV International Congress on Glass*, (Paris), p. 62, 1956.

[74] R. K. Kalia, A. Nakano, P. Vashishta, C. Rountree, L. Brutzel, and S. Ogata, "Multiresolution atomistic simulations of dynamic fracture in nanostructured ceramics and glasses," *International Journal of Fracture*, vol. 121, no. 1-2, pp. 71–79, 2003.

[75] K. H. Sun, "Fundamental condition of glass formation," *Journal of the American Ceramic Society*, vol. 30, no. 9, pp. 277–281, 1947.

[76] R. Barrioy, R. Kernerz, M. Micoulautz, and G. G. Naumisyz, "Evaluation of the concentration of boroxol rings in vitreous B_2O_3 by the stochastic matrix method," *J. Phys. Condens. Matter*, vol. 9, pp. 9219–9234, 1997.

[77] G. Ferlat, T. Charpentier, A. Seitsonen, A. Takada, M. Lazzeri, L. Cormier, G. Calas, and M. F., "Boroxol rings in liquid and vitreous B_2O_3 from first principles," *Physical Review Letters*, vol. 101, no. 6, p. 065504, 2008.

[78] P. Balta and E. Balta, *Introduction to the Physical Chemistry of the Vitreous State*. Bukarest: Editura Academiei, 1976.

[79] U. Selvaraj and K. J. Rao, "Infrared spectroscopic study of mixed-alkali effect in borate glasses," *Spectrochimica Acta Part A: Molecular Spectroscopy*, vol. 40, no. 11, pp. 1081–1085, 1984.

[80] M. E. Milberg, J. G. O'Keefe, R. A. Verhelst, and H. O. Hooper, "Boron coordination in sodium borosilicate glasses," *Physics and Chemistry of Glasses*, vol. 13, pp. 79–84, 1972.

[81] Y. Yun, S. Feller, and P. Bray, "Correction and addendum to nuclear magnetic-resonance studies of the glasses in the system $Na_2O–B_2O_3–SiO_2$," *Journal of Non-Crystalline Solids*, vol. 33, pp. 273–277, 1979.

[82] P. Bray, A. Geissberger, F. Bucholtz, and I. Harris, "Glass structure," *Journal of Non-Crystalline Solids*, vol. 52, pp. 45–66, 1982.

[83] W. Dell, P. Bray, and S. Xiao, "B-11 NMR-studies and structural modeling of Na_2O-B_2O_3-SiO_2 glasses of high soda content," *Journal of Non-Crystalline Solids*, vol. 58, pp. 1–16, 1983.

[84] D. Feil and S. Feller, "The density of sodium borosilicate glasses related to atomic arrangements," *Journal of Non-Crystalline Solids*, vol. 119, pp. 103–111, 1990.

[85] D. Manara, A. Grandjean, and D. R. Neuville, "Advances in understanding the structure of borosilicate glasses: a raman spectroscopy study," *American Mineralogist*, vol. 94, pp. 777–784, 2009.

[86] J. Li, T. Lenosky, C. J. Forst, and S. Yip, "Thermochemical and mechanical stabilities of the oxide scale of ZrB_2+SiC and oxygen transport mechanisms," *Journal of the American Ceramic Society*, vol. 91, no. 5, pp. 1475–1480, 2008.

[87] J. J. Hudgens and S. W. Martin, "Glass transition and infrared spectra of low-alkali, anhydrous lithium phosphate glasses," *Journal of the American Ceramic Society*, vol. 76, no. 7, pp. 1691–1696, 1993.

[88] W. Stoch, P. and. Szczerba, W. Bodnar, M. Ciecinka, A. Stoch, and E. Burkel, "Structural properties of iron-phosphate glasses: spectroscopic studies and ab initio simulations," *Physical Chemistry Chemical Physics*, vol. 16, pp. 19917–19927, 2014.

[89] D. E. Day and C. S. Ray, "A review of iron phosphate glasses and recommendations for vitrifying Hanford waste," tech. rep., Missouri University of Science and Technology, Rolla, MO, 2013. Report Prepared for Idaho National Laboratory.

[90] R. K. Brow, C. M. Arnes, X. Yu, and D. E. Day, "An XPS study of iron phosphate glasses," *Phys. Chem.*, vol. 35, no. 3, p. 132, 1994.

[91] J. G. Vaughan and D. L. Kinser, "Electrical resistivity surface for FeO-Fe2O3-P2O5 glasses," *Journal of the American Ceramic Society*, vol. 58, no. (7-8), pp. 326–329, 1975.

[92] K. Xu, P. Hrma, W. Um, and J. Heo, "Iron phosphate glasses for immobilization of ^{99}tc," *Journal of Nuclear Materials*, vol. 441, pp. 262–266, 2013.

[93] X. Yu, D. E. Day, G. J. Long, and R. K. Brow, "Properties and structure of sodium-iron phosphate glasses," *Journal of Non-Crystalline Solids*, vol. 215, no. 1, pp. 21–31, 1997.

[94] F. Wedgwood and A. Wright, "Short range antiferromagnetic ordering in vitreous $Fe_2O_3-P_2O_5$," *Journal of Non-Crystalline Solids*, vol. 21, no. 1, pp. 95–105, 1976.

[95] G. Marasinghe, K. M., C. Ray, D. Day, M. Shumsky, W. Yelon, C. Booth, P. Allen, and D. Shuh, "Structural features of iron phosphate glasses," *Journal of Non-Crystalline Solids*, vol. 222, pp. 144–152, 1997.

[96] W. Weber, R. Ewing, C. Angell, G. Arnold, A. Cormack, J. Delaye, D. Griscom, L. Hobbs, A. Navrotsky, D. Price, A. Stoneham, and M. Weinberg, "Radiation effects in glasses used for immobilization of high-level waste and plutonium disposition," *Journal of Materials Research*, vol. 12, pp. 1946–1975, 1997.

[97] W. Weber, A. Navrotsky, S. Stefanovsky, E. Vance, and E. Vernaz, "Materials science of high-level nuclear waste immobilization," *MRS Bulletin*, vol. 34, pp. 46–53, 2009.

[98] H. Geiger and J. M. Nuttall, "The ranges of the α particles from various radioactive substances and a relation between range and period of transformation," *Philosophical Magazine, Series 6*, vol. 22, no. 130, pp. 613–621, 1911.

[99] K. D. Reeve and J. L. Woolfrey, "Accelerated irradiation testing of SYNROC using fast neutrons: I.First results on barium hollandite, perovskite, and undoped SYNROC B," *Journal of the Australian Ceramic Society*, vol. 16, pp. 10–15, 1980.

[100] J. F. DeNatale and D. G. Howitt, "Importance of ionization damage to nuclear waste storage in glass," *Am. Ceram. Sot. Bull.*, vol. 66, pp. 1393–1396, 1987.

[101] S. Gutierez, G. ang Peuget, J. A. Hinks, G. Greaves, S. E. Donnelly, E. Oliviero, and C. Jegou, "Helium bubble formation in nuclear glass by in-situ TEM ion implantation," *Journal of Nuclear Materials*, vol. 452, no. 1-3, pp. 565–568, 2014.

[102] I. W. Donald, B. L. Metcalfe, and R. N. J. Taylor, "Review: The immobilization of high-level radioactive wastes using ceramics and glasses," *Journal of Materials Science*, vol. 32, pp. 5851–5887, 1997.

[103] J. M. J. Perez, D. F. Bickford, D. E. Day, D. S. Kim, S. L. Lambert, S. L. Marra, D. K. Keepler, D. M. Stratchan, M. B. Triplett, J. D. Vienna, and R. S. Wittman, "High-level waste melter study report," tech. rep., Pacific Northwest National Laboratory, Richland, WA, 2001.

[104] M. J. Plodinec, P. D. Soper, N. E. Bibler, and J. L. Kessler, "SRP radioactive glass studies: Small-scale process development and product performance. SRL Report DPMS," *Savannah River Laboratory*, 1982.

[105] N. E. Bibler, *Scientific Bask for Nuclear Waste Management*, vol. 6, ch. Effects of alpha, gamma, and alpha-recoil radiation on borosilicate glass containing Savannah River Plant defense high-level nuclear waste. New York: Elsevier, 1982.

[106] D. D. Walker, M. D. Dukes, M. J. Plodinec, and N. E. Bibler, "Effect of radiation on leaching of borosilicate glass containing defense high level nuclear waste," in *181st National Meeting of the American Chemical Society*, (Atlanta, GA), E. I. du Pont de Nemours & Co. and Alken, SC., 1981.

[107] H. K. Manaktala, "An assessment of borosilicate glass as a high-level wasteform," tech. rep., Center for Nuclear Waste Regulatory Analyses, San Antonio, TX, 1992.

[108] G. B. Mellinger and L. A. Chick, "Effects of composition on waste glass properties," in *Ceramics in Nuclear Waste Management* (T. D. Chikalla and J. E. Mendel, eds.), (Cincinnati), pp. 213–217, 1979.

[109] M. J. Plodinec, *Scientific Basis for Nuclear Waste Management*, ch. Viscosity and Electrical Conductivity of Glass Melts as a Function of Waste Composition, pp. 31–35. New York: Plenum Press, 1979.

[110] G. Gehlhoff and M. Thomas, "The physical properties of glass in relation to its composition part II," *Zeitzchrift fur Techniske Physik*, vol. 7, no. 3, pp. 105–126, 1926.

[111] R. P. Turcotte and J. W. Wald, "Devitrification behaviour in a zinc borosilicate nuclear waste glass," tech. rep., Pacific Northwest Laboratories, Richland, WA, 1978.

[112] E. Schiewer, "The borosilicate glass for "PAMELA"," *Radioactive Waste Management and the Nuclear Fuel Cycle*, vol. 7, no. 2, pp. 121–138, 1986.

[113] D. E. Day, Z. Wu, C. S. Ray, and P. Hrma, "Chemically durable iron phosphate glass wasteforms," *Journal of Non-Crystalline Solids*, vol. 241, pp. 1–12, 1998.

[114] S. L. Lambert and D. S. Kim, "Tank waste remediation system: High-Level Waste Feed processability assessment report," tech. rep., Westinghouse Hanford Company, Richland, WA, 1994.

[115] H. Li, J. D. Darab, P. A. Smith, M. J. Scweiger, D. E. Smith, and P. Hrma, *Nuclear Materials Management*, vol. 14. Northbrook, IL: Institute of Nuclear Materials Management, 1995.

[116] W. Weber and R. Ewing, *Uranium-Cradle to Grave*, vol. 43 of *Short Course Series*, ch. Ceramic Waste Forms for Uranium and Transuranium Elements, pp. 317–336. Quebec: Mineralogical Association of Canada, 2013.

[117] W. Weber, "The effect of radiation on nuclear waste forms," *Journal of Metals*, vol. 43, no. 7, pp. 35–39, 1991.

[118] S. Peuget, C. Mendoza, E. A. Maugeri, J. M. Delaye, R. Caraballo, T. Charpentier, M. Tribet, O. Bouty, and C. Jegou, "Alpha decays impact on nuclear glass structure," *Procedia Materials Science*, vol. 7, pp. 252–261, 2014.

[119] W. J. Weber and F. P. Roberts, "A review of radiation effects in solid nuclear waste forms," *Nuclear Technology*, vol. 60, pp. 178–198, 1983.

[120] W. J. Weber, "Radiation effects in nuclear waste glasses," *Nuclear Instruments and Methods in Physics Research*, vol. B32, pp. 471–479, 1988.

[121] W. J. Weber, "Radiation and thermal ageing on nuclear waste glass," *Procedia Materials Science*, vol. 7, pp. 237–246, 2014.

[122] J. M. Delaye and D. Ghaleb, "Molecular dynamics analysis of volume change in a nuclear glass model subjected to a displacement cascade," *Nuclear Instruments and Methods in Physics Research B*, vol. 153, pp. 157–162, 1999.

[123] G. Bureau, J. M. Delaye, S. Peuget, and G. Calas, "Molecular dynamics study of structural changes versus deposited energy dose in a sodium borosilicate glass," *Nuclear Instruments and Methods in Physics Research B*, vol. 266, pp. 2707–2710, 2008.

[124] X. Yu, D. E. Day, G. J. Long, and R. K. Brow, "Properties and structure of sodium-iron phosphate glasses," *Journal of Non-Crystalline Solids*, vol. 215, pp. 21–31, 1997.

[125] X. Yu and D. E. Day, "Effect of raw materials on the redox state of iron and properties of iron phosphate glasses," in *Proceedings 17th International Congress on Glass*, vol. 2, pp. 45–51, 1995.

[126] M. G. Mesko and D. E. Day, "Immobilization of spent nuclear fuel in iron phosphate glasses," *Journal of Nuclear Meterials*, vol. 273, pp. 27–36, 1999.

[127] S. V. Stefanovsky, O. I. Stefanovsky, M. I. Kadyko, I. A. Presniakov, and B. F. Nyasoedov, "The effect of Fe_2O_3 substitution for Al_2O_3 on the phase composition and structure of sodium-aluminum-iron phosphate glasses," *Journal of Non-Crystalline Solids*, vol. 425, pp. 138–145, 2015.

[128] R. C. Ewing and L. M. Wang, "Phosphates as nuclear waste forms," *Reviews in Mineralogy and Geochemistry*, vol. 48, no. 1, pp. 673–699, 2002.

[129] P. Sengupta, "A review on immobilization of phosphate containing high level nuclear wastes within glass matrix - Present status and future challenges," *Journal of Hazardous Materials*, vol. 235–236, pp. 17–28, 2012.

[130] C. L. Dube, M. C. Stennett, A. S. Gandy, and N. C. Hyatt, "Simulation of alpha decay of actinides in iron phosphate glasses by ion irradiation," *Nuclear Instruments and Methods in Physics Research B*, vol. 371, pp. 424–428, 2016.

[131] H. J. C. Berendsen, J. P. M. Postma, W. F. van Gunsteren, A. DiNola, and J. R. Haak, "Molecular dynamics with coupling to an external bath," *The Journal of Chemical Physics*, vol. 81, no. 8, pp. 3684–3690, 1984.

[132] I. T. Todorov, W. Smith, K. Trachenko, and M. T. Dove, "DL_POLY_3: New dimensions in molecular dynamics simulations via massive parallelism," *Journal of Materials Chemistry*, vol. 16, pp. 1911–1918, 2006.

[133] S. Nosé, "A unified formulation of the constant temperature molecular-dynamics methods," *The Journal of Chemical Physics*, vol. 81, no. 1, pp. 511–519, 1984.

[134] W. G. Hoover, "Canonical dynamics: Equilibrium phase-space distributions," *Physical Review A*, vol. 31, no. 3, pp. 1695–1697, 1985.

[135] H. C. Andersen, "Molecular dynamics at constant pressure and/or temperature," *The Journal of Chemical Physics*, vol. 72, pp. 2384–2393, 1980.

[136] G. S. Grest and K. Kremer, "Molecular-dynamics simulation for polymers in the presence of a heat bath," *Phys. Rev. A*, vol. 35, no. 5, pp. 3628–3631, 1986.

[137] M. P. Allen and D. J. Tildesley, *Computer simulation of liquids*. New York: Oxford University press, 1991.

[138] S. Melchionna, G. Ciccotti, and H. B. L., "Hoover NPT dynamics for systems varying in shape size," *Molecular Physics*, vol. 78, no. 3, 1993.

[139] L. Verlet, "Computer "Experiments" on Classical Fluids. I, Thermodynamical Properties of Lennard-Jones Molecules," *Phys. Rev.*, vol. 159, pp. 98–103, 1967.

[140] W. C. Swope, H. Andersen, P. Berens, and K. Wilson, "A computer simulation method for the calculation of equilibrium constants for the formation of physical clusters of molecules: Application to small water clusters," *The Journal of Chemical Physics*, vol. 76, no. 1, p. 648, 1982.

[141] N. W. Ashcroft and N. D. Mermin, *Solid State Physics*. New York: Holt, Rinehart and Winston, 1976.

[142] Lennard-Jones, J. E., "On the Determination of Molecular Fields," *Proceedings of the Royal Society of London A*, vol. 106, no. 738, pp. 463–477, 1924.

[143] Z. H. Stachurski, *Fundamentals of amorphous solids: Structure and properties*. Beijing: Higher education press, 2015.

[144] R. Buckingham, "The classical equation of state of gaseous helium, neon and argon," in *Proceedings of the Royal Society of London. Series A, Mathematical and Physical Sciences*, vol. 168, pp. 264–283, 1938.

[145] F. Jensen, *Introduction to Computational Chemistry*. Chichester, England: John Wiley & Sons, 2nd ed., 2007.

[146] J. Ziegler, J. P. Biersack, and U. Littmark, *The Stopping and Range of Ions in Matter*, vol. 1. Boston: Springer US, 1985.

[147] J. D. Gale, "GULP: General Utility Lattice Program: a computer program for the symmetry adapted simulation of solids," *The Journal of Chemical Society, Faraday Transactions*, vol. 93, pp. 629–637, 1997.

[148] F. Stillinger and T. Weber, "Computer simulation of local order in condensed phases of silicon," *Physical Review B*, vol. 31, pp. 5262–5271, 1985.

[149] B. P. Feuston and S. Garofalini, "Empirical three-body potential for vitreous silica," *J. Chem. Phys.*, vol. 89, pp. 5818–5824, 1988.

[150] C. M. Marcelli, B. D. Todd, and R. J. Sadus, "On the relationship between two-body and three-body interactions from nonequilibrium molecular dynamics simulation," *The Journal of Chemical Physics*, vol. 115, no. 20, pp. 9410–9413, 2001.

[151] U. Essmann, L. Perera, M. L. Berkowitz, T. Darden, H. Lee, and P. L. G., "A smooth article mesh Ewald method," *The Journal of Chemical Physics*, vol. 103, p. 8577, 1995.

[152] F. Gou, G. N. Greaves, W. Smith, and R. Winter, "Molecular dynamics simulation of sodium borosilicate glasses," *Journal of Non-Crystalline Solids*, vol. 293-295, pp. 539–546, 2001.

[153] L. W. Hobbs, *Engineering of Crystalline Materials Properties: State of the Art in Modeling, Design and Applications*, ch. Topological Approaches to the Structure of Crystalline and Amorphous Atom Assemblies, pp. 193–230. Dordrecht: Springer Netherlands, 2008.

[154] P. J. Steinhardt, D. R. Nelson, and M. Ronchetti, "Bond-orientational order in liquids and glasses," *Physical Review B*, vol. 28, pp. 784–805, Jul 1983.

[155] L. W. Hobbs, F. W. Clinard, S. J. Zinkle, and R. C. Ewing, "Radiation effects in ceramics," *Journal of Nuclear Materials*, vol. 216, 1994.

[156] L. W. Hobbs, "The role of topology and geometry in the irradiation-induced amorphization of network structures," *Journal of Non-Crystalline Solids*, vol. 182, no. 1-2, 1995.

[157] L. W. Hobbs, A. Sreeram, C. E. Jesurum, and B. Berger, "Structural freedom, topological disorder and the irradiation-induced amorphization of ceramic structures," *Nuclear Instruments and Methods in Physics Research B: Beam Interaction with Materials and Atoms*, vol. 116, 1996.

[158] L. W. Hobbs, C. E. Jesurum, V. Pulim, and B. Berger, "Local topology of silica networks," *The Philosophical Magazine A*, vol. 78, 1998.

[159] X. Yuan and A. N. Cormack, "Efficient algorithm for primitive ring statistics in topological networks," *Computational Materials Science*, vol. 24, pp. 343–360, 2002.

[160] C. S. Marians and L. W. Hobbs, "Network properties of crystalline polymorphic of silica," *Journal of Non-Crystalline Solids*, vol. 124, p. 242, 1990.

[161] K. Goetzke and H.-J. Klein, "Properties and efficient algorithmic determination of different classes of rings in finite and infinite polyhedral networks," *Journal of Non-Crystalline Solids*, vol. 127, no. 2, pp. 215–220, 1991.

[162] R. J. Finch and J. M. Hanchar, "Structure and chemistry of zircon and zircon-group minerals," *Reviews in Mineralogy and Geochemistry*, vol. 53, no. 1, p. 1, 2003.

[163] J. A. Speer, *Reviews in Mineralogy Vol 5: Orthosilicates*, ch. Zircon, pp. 67–112. 1982.

[164] M. J. Sanders, M. Leslie, and C. R. A. Catlow, "Interatomic potentials for SiO_2," *Journal of the Chemical Society, Chemical Communication*, no. 19, pp. 1271–1273, 1984.

[165] M. W. D. Cooper, M. J. D. Rushton, and R. W. Grimes, "A many-body potential approach to modelling the thermomechanical properties of actinide oxides," *Journal of Physics: Condensed Matter*, vol. 26, p. 105401, 2014.

[166] M. I. Ojovan, "Glass for nuclear waste immobilization," in *Waste Materials Conference*, 2007.

[167] T. H. Cormen, C. E. Leiserson, R. L. Rivest, and C. Stein, *Introduction to Algorithms*. The MIT Press, 3rd ed., 1990.